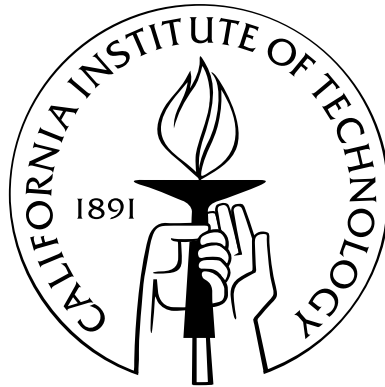# Topics in Gravitational-Wave Science: Macroscopic Quantum Mechanics and Black Hole Physics

Thesis by

Huan Yang

In Partial Fulfillment of the Requirements

for the Degree of

Doctor of Philosophy

California Institute of Technology

Pasadena, California

2013

(Submitted May 23, 2013)

Dedicated to my parents

Fuxi Yin and *Ganqin Yang*

Acknowledgments

There is a Chinese saying that goes, "it takes ten years to sharpen a sword." It took me the continuous effort of many years to become an qualified "sword" (with a Ph.D.), ready for cutting through the fog of unknowns at the frontier of physics. Along my way, studying physics during these years, I have received enormous encouragement and assistance from my family, my friends and my colleagues. I am grateful for the help of all of them, and I shall acknowledge them in chronological order.

First I would like to thank my parents Fuxi Yin and Ganqin Yang. They taught me the really important things in life and they showed me how to build my character with integrity, honesty and sheer tenacity. There were times when I was confused and uncertain about my future, but they always told me to follow my heart and they always supported my decisions. My parents greatly helped me to define who I am.

I am also thankful to Kip Thorne and Nai-Chang Yeh. I worked with Kip since my sophomore year. He brought me into the field of general relativity, which has become one of my main research interests. He influenced me not only through his scientific wisdom, but also his way of interacting with people and his positive energy. Nai-Chang was my senior thesis advisor. During my time working in her lab, I was truly impressed by her passion and attitude toward doing research. As a female professor, she is also very generous to her students. I would like to thank for all her help in my past studies.

I want to give special thanks to my Ph.D thesis advisor Yanbei Chen. As an advisor and as a physicist, he is my favorite type: very considerate to students, always curious about problems in physics and full of ideas. I enjoyed spontaneous discussions with him about many branches of physics, and I learned a lot from him about ways of looking at and solving physics problems. I am also grateful for his encouragement and painstaking effort to teach me how to write scientific articles and give clear presentations .

I also want to express my thankfulness to Rana Adhikari, Koji Arai, Jenne Driggers, Jan Harms, Larry Price, David Yeaton-Massey, Nicholas Smith and my colleagues in the TAPIR group: David Nichols, Aaron Zimmerman, Fan Zhang, Bassam Helou, Chad Galley, Jeffrey Kaplan, Anil Zenginoglu, Yasushi Mino, Tanja Hinderer, Jeandrew Brink, Haixing Miao and Roland Haas. I am lucky to have the chance to work with all these brilliant people. We had a lot of fruitful discussions

and many of them have turned into chapters of this thesis.

I would like to acknowledge Stefan Danilishin, Thomas Corbitt, Kentaro Somiya, Yiqiu Ma, Farid Khalili and Sergey Vyatchanin and all the other members of the Macroscopic Quantum Mechanics (MQM) discussion group. I also want to thank other colleagues outside Caltech: Howard Wiseman, Scott Hughes, Emanuele Berti, Sam Dolan, Marc Casals, Yi Pan, Steven Detweiler, Steve Carlip, Da-Shin Lee, Bei-lok Hu, Ting Yu, Walter Strunz, Matthew Evans and Ian Vega. I enjoyed and benefitted from stimulating discussions with all of them.

I want to thank the two other members of my thesis committee who have not been mentioned before: Christopher Hirata and Christian Ott, for giving me very valuable advice and comments on my thesis research as well as presentation skills.

Finally, I would like to acknowledge JoAnn Boyd and Shirley Hampton for their assistance on administration matters.

Abstract

The theories of relativity and quantum mechanics, the two most important physics discoveries of the 20th century, not only revolutionized our understanding of the nature of space-time and the way matter exists and interacts, but also became the building blocks of what we currently know as modern physics. My thesis studies both subjects in great depths — this intersection takes place in gravitational-wave physics.

Gravitational waves are "ripples of space-time", long predicted by general relativity. Although indirect evidence of gravitational waves has been discovered from observations of binary pulsars, direct detection of these waves is still actively being pursued. An international array of laser interferometer gravitational-wave detectors has been constructed in the past decade, and a first generation of these detectors has taken several years of data without a discovery. At this moment, these detectors are being upgraded into second-generation configurations, which will have ten times better sensitivity. Kilogram-scale test masses of these detectors, highly isolated from the environment, are probed continuously by photons. The sensitivity of such a quantum measurement can often be limited by the Heisenberg Uncertainty Principle, and during such a measurement, the test masses can be viewed as evolving through a sequence of nearly pure quantum states.

The first part of this thesis (Chapter 2) concerns how to minimize the adverse effect of thermal fluctuations on the sensitivity of advanced gravitational detectors, thereby making them closer to being quantum-limited. My colleagues and I present a detailed analysis of coating thermal noise in advanced gravitational-wave detectors, which is the dominant noise source of Advanced LIGO in the middle of the detection frequency band. We identified the two elastic loss angles, clarified the different components of the coating Brownian noise, and obtained their cross spectral densities.

The second part of this thesis (Chapters 3 – 7) concerns formulating experimental concepts and analyzing experimental results that demonstrate the quantum mechanical behavior of macroscopic objects — as well as developing theoretical tools for analyzing quantum measurement processes. In Chapter 3, we study the open quantum dynamics of optomechanical experiments in which a single photon strongly influences the quantum state of a mechanical object. We also explain how to engineer the mechanical oscillator's quantum state by modifying the single photon's wave function.

In Chapters 4–5, we build theoretical tools for analyzing the so-called "non-Markovian" quantum

measurement processes. Chapter 4 establishes a mathematical formalism that describes the evolution of a quantum system (the plant), which is coupled to a non-Markovian bath (i.e., one with a memory) while at the same time being under continuous quantum measurement (by the probe field). This aims at providing a general framework for analyzing a large class of non-Markovian measurement processes. Chapter 5 develops a way of characterizing the non-Markovianity of a bath (i.e.,whether and to what extent the bath remembers information about the plant) by perturbing the plant and watching for changes in the its subsequent evolution. Chapter 6 re-analyzes a recent measurement of a mechanical oscillator's zero-point fluctuations, revealing nontrivial correlation between the measurement device's sensing noise and the quantum rack-action noise.

Chapter 7 describes a model in which gravity is classical and matter motions are quantized, elaborating how the quantum motions of matter are affected by the fact that gravity is classical. It offers an experimentally plausible way to test this model (hence the nature of gravity) by measuring the center-of-mass motion of a macroscopic object.

The most promising gravitational waves for direct detection are those emitted from highly energetic astrophysical processes, sometimes involving black holes — a type of object predicted by general relativity whose properties depend highly on the strong-field regime of the theory. Although black holes have been inferred to exist at centers of galaxies and in certain so-called X-ray binary objects, detecting gravitational waves emitted by systems containing black holes will offer a much more direct way of observing black holes, providing unprecedented details of space-time geometry in the black-holes' strong-field region.

The third part of this thesis (Chapters 8 – 11) studies black-hole physics in connection with gravitational-wave detection.

Chapter 8 applies black hole perturbation theory to model the dynamics of a light compact object orbiting around a massive central Schwarzschild black hole. In this chapter, we present a Hamiltonian formalism in which the low-mass object and the metric perturbations of the background spacetime are jointly evolved. Chapter 9 uses WKB techniques to analyze oscillation modes (quasi-normal modes or QNMs) of spinning black holes. We obtain analytical approximations to the spectrum of the weakly-damped QNMs, with relative error $O(1/L^2)$, and connect these frequencies to geometrical features of spherical photon orbits in Kerr spacetime. Chapter 11 focuses mainly on near-extremal Kerr black holes, we discuss a bifurcation in their QNM spectra for certain ranges of (l, m) (the angular quantum numbers) as $a/M \to 1$. With tools prepared in Chapter 9 and 10, in Chapter 11 we obtain an analytical approximate for the scalar Green function in Kerr spacetime.

Contents

Chapter 1

Introduction

This thesis is an assembly of ten research papers that span across several disciplines of physics, which are all related to the on-going effort of gravitational-wave detection. According to the different aspects of gravitational-wave science they involve, the following ten chapters of this thesis can be naturally divided into three parts. In Part I (Chapter 2), we study the physics of advanced gravitational-wave detectors, in particular how thermal fluctuations affect the detectors' sensitivity. In Part II (Chapters 3 – 7), motivated by the fact that gravitational-wave detectors are continuously monitoring kilogram-scale test masses near the quantum limit, we study Macroscopic Quantum Mechanics. In Part III (Chapters 8 – 11), we study physics of gravitational-wave sources, in particular black-hole perturbation theory. Correspondingly, this introductory chapter has also been divided into three sections. In each section, we shall first provide background for the corresponding part of the thesis, and then briefly discuss the motivation and summarize the main results of each chapter in that part.

1.1 Physics of advanced gravitational wave detectors

1.1.1 An overview of laser interferometer gravitational-wave detectors

The existence of gravitational wave (GW) is one of the most powerful predictions of general relativity (GR); directly measuring GW is an important test of GR. GWs interact very weakly with matter, but often carry a large amount of energy — for equal-mass binary black-hole mergers, up to 5% of the binaries' total mass energy is converted to and radiated away by GWs [1]. Because gravitational radiation serves as an important component of many astrophysical and cosmological processes, and because GWs are not easily damped by interacting with matter, GW detection will open a new window for the human being to observe the universe. With experimental progress in the past decade, it is getting clearer that we will soon enter a new era with a whole new branch of astronomy — gravitational-wave astronomy.

In the past five years, an international array of first-generation long-baseline laser-interferometer GW detectors have operated at their design sensitivities. This array included: the LIGO detectors (US, two 4 km detectors H1 and L1, one 2 km detector H2) [2], the VIRGO detector (France and Italy, 3 km) [3], the GEO 600 detector (UK and Germany, 600 m) [4] and the TAMA detector (Japan, 300 m) [5]. Up till now, with most of the first-generation data analysis finished, no direct detection of GW has been made, and this is consistent with astrophysical estimates. In order to achieve first detection, and subsequently develop a fruitful observational program of GW astronomy, the GW community must keep upgrading their detectors for better sensitivity. At this moment, while second-generation detectors (for example the Advanced LIGO detectors in the US) are in construction, experimental techniques aimed for third-generation detectors are being researched and prototyped. These prototype experiments include: the 300-m CLIO cryogenic detector (Kamioka, Japan) [6], the AEI 10-m prototype (under construction in Hannover, Germany) [7], the Glasgow 10-m prototype (Glasgow, UK) [8], the 80-m high-power facility (Gingin, Australia) [9], and table-top experiments with small test masses (MIT/ANU/NAOJ) [10].

The typical configuration of a long-baseline laser interferometer GW detector is a Michelson interferometer with km-scale arms and kg-scale suspended test masses serving as mirrors. The suspension frequencies are usually around 1 Hz, therefore allowing the isolation of ground motion at frequencies ~ 10 Hz and above — at these frequencies, the test masses act as free masses. Laser light is incident from, and mostly returns to the "bright port" of the Michelson interferometer — if the mirrors remain at their equilibrium positions — and in this case only a small amount of light is allowed to emerge from the "dark port" of the interferometer. As arm lengths change differentially (e.g., due to incoming GWs), additional signal light emerges from the dark port. At the photodetector, the signal light beats with the static output light from the dark port to give a linear signal proportional to the amplitude of the gravitational wave. Optical cavities are often used in the arms (therefore there are two mirrors in each arm) in order to increase light power in the arms and amplify the signal light. The interferometer's performance is further amplified when "recycling mirrors" are further placed at the bright and dark ports.

As we consider GWs with frequencies below the free spectral range of the arm cavity, i.e., $c/(2L)$ (with L the arm length, 10s of kHz) and above the resonant frequency of the test masses' translational motion, a gravitational wave with amplitude h can be viewed as causing relative displacements $\sim Lh/2$ between the mirrors (with a geometrical factor that depends on its polarization), while causing no effect on the propagation of light. We can therefore regard GW detectors as displacement measuring devices; their sensitivity for measuring the displacement is limited by *force noises* which disturb the motion of test masses, and *readout noises* which add random output fluctuations to the displacement signal. These noises may have both classical and quantum origins (see Fig. 1.1).

In Fig. 1.1, we show the noise budget of Advanced LIGO detectors (in terms of strain-referred
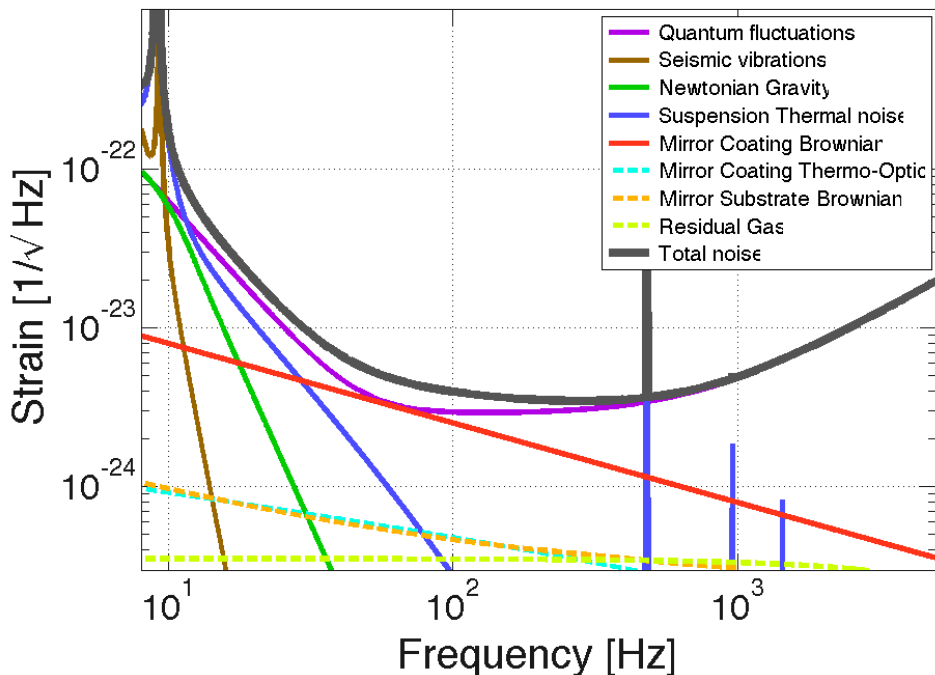
Figure 1.1: (Color online.) Square root of strain noise spectrum for several of Advanced LIGO's major noise sources. In its detection band 10 Hz – several kHz, Advanced LIGO's sensitivity is mainly constrained by quantum noise and coating Brownian noise (red curve).

noise spectral density). This figure shows several major types of noise that are of classical origin [11]:

- *Suspension thermal noise* (blue curve in Fig. 1.1), which arises from thermal fluctuations in the wires that are used to suspend the test masses.

- *Gravity gradient noise* (dark green curve in Fig. 1.1), which arises from differential fluctuations of the Newtonian gravitational field at the locations of the test masses. The dominant component of this noise arises due to surface seismic waves [12].

- *Excess gas noise* (light green curve in Fig. 1.1), which is mainly produced by gas molecules in the beam tube. The high frequency component of this noise arises from molecules randomly moving through the laser beam, causing phase noise, while at low frequencies the random impacts of molecules on the mirror surfaces dominate [13].

- *Seismic noise* (brown curve in Fig. 1.1), which is the mirror position fluctuation induced by ground vibrations. It is the main noise source below 10 Hz.

- *Coating Thermo-optic noise*(teal curve in Fig. 1.1), which is a combination of *coating thermoelastic noise* and *coating thermorefractive noise*. Temperature fluctuations in the dielectric coating and the nearby area in the mirror substrate cause both geometric random deformations

of the coating and random variations in the coating materials' refractive index. The geometric deformation affects the position of the mirror surface, causing thermoelastic noise, while the refractive index change affects the phase probed by the light beam, which partially penetrates into the coating layers, causing thermorefractive noise. Evans *et al.* proved that by careful design of coating structure these two pieces of noise can almost cancel each other in Advanced LIGO mirrors[15].

- *Brownian noise* (red curve in Fig. 1.1), which includes coating Brownian noise and substrate Brownian noise. At constant temperature T, each elastic eigenmode of the mirror possesses $k_{\mathrm{B}}T$ energy according to equal partition theorem. Because of the mechanical losses, the thermal spectrum of these modes all have a tail to the low frequency end, and the sum of all these contributions gives the Brownian noise. Because coatings (quality factor $\sim 10^3$) are much more lossy than the substrate (quality factor $\sim 10^7 - 10^8$), coating Brownian noise is much higher than substrate Brownian noise, and turns out to be higher than all other classical noises in the advanced LIGO detection band. This is the main motivation for us to carefully analyze coating Brownian noise in Chapter 2.

In Fig. 1.1, quantum noise is shown in purple curve. This includes quantum radiation pressure noise, photon shot noise and sensing noise due to optical loss and inefficient photo-detection. The sensing noise due to optical or photo-detection loss is an important component of the quantum noise budget, but it can be improved by using better optical systems. The shot noise and radiation pressure noise together is often subject to a sensitivity bound for general quantum measurement, as will be shown below (and in the Section 1.2 from a different perspective). Let us approximate LIGO mirrors as free masses and, for simplicity, assume there are no arm cavities. The displacement-referred noise spectrum due to radiation-pressure fluctuation for a free mass m is

$$S_x^{\mathrm{rp}}(\Omega) = \frac{I_0 \omega_0 \hbar}{m^2 \Omega^4 c^2}, \tag{1.1}$$

where ω_0 is the angular frequency of the laser beam and I_0 is the optical power. The stronger the power of the laser, the higher the rate of random photons that will impinge on the mirror, hence the higher the radiation-pressure noise. On the other hand, the displacement-referred spectrum of shot noise is

$$S_x^{\mathrm{sh}} = \frac{\hbar c^2}{I_0 \omega_0} \tag{1.2}$$

which is inversely-proportional to the number of sensing photons — increasing the rate of sensing photons will improve the our accuracy of position measurement.

Because shot noise and radiation pressure noise depend oppositely on the intensity of light, the sum of these two noises are limited by a bound regardless of light power, which is usually referred

as *Standard Quantum Limit* (SQL) as first realized by Braginsky in the 1960s [17, 18]:

$$S_x = S_x^{\text{rp}} + S_x^{\text{sh}} = \frac{I_0 \omega_0 \hbar}{m^2 \Omega^4 c^2} + \frac{\hbar c^2}{I_0 \omega_0} \geq S_x^{\text{SQL}}(\Omega) \equiv \frac{2\hbar}{m\Omega^2}. \tag{1.3}$$

Here $m = M/4$ is the reduced mass of the four test masses (each with a mass of M). As we will show later in Sec. 1.2, once these GW detectors enter this quantum regime, in addition to detecting gravitational waves with higher sensitivity, one can also use these interferometers to probe quantum behaviors of macroscopic test masses. In this case, SQL serves as a benchmark for a successful macroscopic quantum mechanics (MQM) experiment.

1.1.2 Brownian thermal noise of mirrors with multilayer coatings (Chapter 2)

Chapter 2 is a research paper published as:

- T. Hong, H. Yang, E.K. Gustafson, R.X. Adhikari and Y. Chen, *Brownian thermal noise in multilayer coated mirrors*, Physical Review D **87**, 082001 (2013).

1.1.2.1 Motivation and significance

This was my first Ph.D. research project, in which I studied coating Brownian thermal noise (CBTN) for optical systems. This piece of thermal noise is not only the dominant classical noise source in the advanced LIGO detection band, but also a limiting factor for controlling laser stability and setting laser frequency standard [38]. It is therefore important to understand different components of this noise and their correlations, as well as to investigate possible ways to reduce the noise. Before our work, many still believed that CBTN could be lowered by careful designs of the structure of the multi-layer coating. In addition, the gravitational-wave community was not using the correct loss angle to describe the mechanical losses that are associated with the coating Brownian noise. As our work gives a solid description of the weak noise correlation, it is clear now that the bulk part of CBTN can hardly be improved by the coating design — one will have to use low-loss coating materials or high-Young's-modulus substrate materials to reduce the CBTN. Our work also pointed out the correct loss angles to characterize the coating materials' mechanical losses — assuming that they are isotropic and formulated experimental strategies that will allow the direct measurement of both angles. Finally, our analysis also paved the way toward further calculations of thermal noises with anisotropic coating materials.

1.1.2.2 Summary of main results

We start Chapter 2 by expressing the amplitude and phase of the reflected light in terms fluctuations in all aspects of the coating structure, thereby identifying all components of coating thermal noise. For example, we show that coating noise arise not only from layer thickness fluctuations (as one might naively think at first sight), but also from fluctuations of the interface between the coating and substrate, which can also be driven by internal fluctuating stresses of the coating. After applying the fluctuation-dissipation theorem, we find that thickness fluctuations of different coating layers are incoherent with each other, although they may correlate with fluctuations of the coating-substrate interface (depending on the loss angles, which will be discussed later). This is because the fluctuating stress in any coating layer does not affect thicknesses of the other layers, yet it may influence the bending of coating-substrate interface. Based on the formulas we obtained for cross spectral densities, roughly 70% of Advanced LIGO's coating Brownian noise is due to coating-substrate interface fluctuations, because Young's modulus of the more lossy type of coating material (Ta_2O_5) was assumed to be much higher than the Young's modulus of the substrate. This piece of noise turns out to be inversely proportional to the Young's modulus of the substrate material, which means it can be reduced by using stiffer substrate materials.

Previously [43], the vertical and horizontal loss angles $\phi_\perp$, $\phi_\parallel$ of an isotropic material are defined such that given a periodic driving force, the energy dissipated per radian is

$$W_{\text{diss}} = \phi_\perp U_\perp + \phi_\parallel U_\parallel, \ U_{\text{tot}} = U_\perp + U_\parallel \tag{1.4}$$

where the total elastic energy U_{tot} is separated into vertical component $U_\perp$ (perpendicular to the surface) and horizontal component $U_\parallel$ (parallel to the surface). In Chapter 2, we show that for materials with nonzero poisson ratios, $U_\perp$ and $U_\parallel$ could be negative for certain ways of applying external forces. This means neither $U_\perp$ nor $U_\parallel$ is a reasonable candidate for energy. We instead propose to use shear and bulk loss angles ϕ_Σ, ϕ_Θ, associated with the bulk and shear elastic energy such that

$$W_{\text{diss}} = \phi_\Sigma U_\Sigma + \phi_\Theta U_\Theta, \ U_{\text{tot}} = U_\Sigma + U_\Theta. \tag{1.5}$$

According to elasticity theory, the bulk and shear energies U_Σ, U_Θ are both positive definite (see Chapter 2 for their definitions). In fact, for isotropic materials, this is the only well-defined way to classify loss angles. Since most recent experiments for loss angles all measure quality factors of bending modes for 2-D thin plates, they only give information about one particular combination of shear and bulk loss angles. In order to break this degeneracy and obtain two loss angles separately, we need another independent type of measurement. This can be achieved by measuring torsional modes of a coated cylinder, which gives information only for the shear loss angle. Combining the

proposed experiment with previous measurements, bulk and shear loss angles can be determined separately.

In Chapter 2 we also point out a new contribution to coating Brownian noise that had not been discussed before. As briefly explained earlier, this noise is due to refractive-index fluctuations induced by strain fluctuations, via the photoelastic effect. The photoelastic noise not only imposes a fluctuating phase shift to light propagating within the coating — the inhomogeneity caused by this noise also back-scatters some of the propagating light. All the backscattered light add up together to a new piece of phase noise, which we refer as "backscattered noise". There is one subtlety we encountered when computing this noise — mathematically the self correlation of Brownian strain fluctuations is a δ function in position space, and so is the resulting refractive-index fluctuation. This δ function apparently causes a divergence problem during the calculation of the backscattered noise. Fortunately, since the average of fluctuations over any small volume is finite, the total noise is in fact regular. After a careful treatment, we successfully obtained a regular expression for the back-scattered noise. For advanced LIGO coatings, the back-scattered noise is less than 5% of the total coating Brownian noise, because light only penetrates into the first few coating layers, and because the back-scattering is relatively weak in the first place. However, for other optics experiments using mirrors with far fewer coating layers, this could be a more important part of total coating Brownian noise.

1.1.2.3 My specific contributions

I derived the formulas for cross spectral density between strain fluctuations at different locations, and I also did the calculation for back-scattered noise. I was in charge of revising the manuscript and answering questions from the referees during the peer-review process and production stages.

1.2 Macroscopic Quantum Mechanics (MQM)

1.2.1 Background

The theory of continuous measurement, namely a single quantum system under continuous monitoring, was first considered for GW detectors in the 1960s. In recent years, the field of "quantum optomechanics", namely the study of interactions between light with mechanical systems — especially ones with macroscopic scales — in the quantum regime, has become very active. As Feynman suggested in his *Lectures on Gravitation*: *"It is possible that quantum mechanics fails at large distances and for larger objects"*; it remains physically interesting and important to test quantum mechanics at macroscopic scales. In recent years, rapid experimental progresses have been made towards demonstrating the quantum-mechanical behavior of a macroscopic object, which include

successfully preparing one degree of freedom of a macroscopic object into the quantum ground state [19], as well as generating squeezed light though its interaction with a macroscopic oscillator [20]. There are several excellent review articles on this subject: one of them is written by Chen [21], which emphasizes quantum measurement and testing quantum mechanics; the other one is written by Aspelmeyer, Kippenberg and Marquart [22], which discusses cavity optomechanics from an experimental point view. In this section we will only discuss a few basics that are relevant for Part II of this thesis.

1.2.1.1 The input-output formalism of linear quantum measurement theory

Let us illustrate the input-output formalism of linear quantum measurement theory using a simple example. Suppose a laser beam with intensity I_0 and frequency ω_0 is targeting on a test object with mass m and mechanical frequency ω_m. With phase reference (the plane where the phase is set to zero) chosen at the equilibrium position of the test object, the input electrical field can be written as

$$\hat{E}_{\rm in}(t) = \left[\sqrt{2I_0/\hbar\omega_0} + \hat{a}_1(t)\right]\cos\omega_0 t + \hat{a}_2(t)\sin\omega_0 t \tag{1.6}$$

with $\hat{a}_1, \hat{a}_2$ being the amplitude and phase quadratures of the fluctuation, their cross spectral density given by:

$$S_{a_1}(\Omega) = S_{a_2}(\Omega) = 1,\ S_{a_1 a_2}(\Omega) = 0. \tag{1.7}$$

The reflected electric field $\hat{E}_{\rm out}(t)$ is just

$$\hat{E}_{\rm out}(t) = \hat{E}_{\rm in}(t - 2\hat{x}/c), \tag{1.8}$$

where $2\hat{x}/c$ is the extra delay time. Similar to the input field, the output field can also be decomposed as:

$$\hat{E}_{\rm out}(t) = \left[\sqrt{2I_0/\hbar\omega_0} + \hat{b}_1(t)\right]\cos\omega_0 t + \hat{b}_2(t)\sin\omega_0 t. \tag{1.9}$$

According Eq. (1.8), the output quadrature fields $\hat{b}_1, \hat{b}_2$ and input quadrature fields $\hat{a}_1, \hat{a}_2$ are related to each other by

$$\hat{b}_1(t) = \hat{a}_1(t) \tag{1.10}$$

$$\hat{b}_2(t) = \hat{a}_2(t) + 2\sqrt{\frac{2I_0\omega_0}{\hbar c^2}}\hat{x}. \tag{1.11}$$

We have to measure the phase quadrature $\hat{b}_2$ to gain position information of the test object. On

the other hand, the Heisenberg equations of motion of the test object are given by:

$$\dot{\hat{x}} = \hat{p}/m$$

$$\dot{\hat{p}} = 2\sqrt{\frac{2\hbar\omega_0 I_0}{c^2}}\hat{a}_1(t) + f_{\text{ext}}(t) - m\omega_m^2\hat{x}\,. \tag{1.12}$$

For simplicity, we have neglected the DC part of radiation pressure force, as it is expected to be balanced by other DC forces. The first term in $\dot{\hat{p}}$ is the fluctuating piece of radiation pressure and the second term is the external force on the test object. Eq. (1.10) together with Eq. (1.12) describe both the dynamics of this simple optomechanical system and the output signal channel. This *input-output formalism* is generalized to describe more sophisticated systems in Chapter 4–7.

1.2.1.2 The standard quantum limit

We introduced the Standard Quantum Limit (SQL) for the position sensitivity of GW detectors in Sec. 1.1. It was obtained by minimizing the sum of photon shot noise and radiation pressure noise in the output light field. In fact, as originally showed by Braginsky and Khalili, the SQL can be regarded as a benchmark for any quantum measurements performed on a test object, and it is directly related to the Heisenberg uncertainty principle. Below we shall explain it from a generalized linear quantum measurement point of view. A more detailed justification can be found in [21] or [18].

According to the free mass's Heisenberg equations of motion, momentum $\hat{p}$ is a conserved quantity and the position operator at time t is given by

$$\hat{x}(t) = \hat{x}(0) + \frac{\hat{p}(0)}{m}t, \tag{1.13}$$

which also means that

$$[\hat{x}(t), \hat{x}(t')] = i\hbar(t' - t)/m. \tag{1.14}$$

From the above expression, it is clear that the Heisenberg operators of position do not commute at different times. In fact , if we were to measure both positions in a continuous quantum measurement, the Heisenberg uncertainty relation would suggest that

$$\Delta x(t)\Delta x(t') \geq \frac{\hbar}{2m}|t - t'|. \tag{1.15}$$

Imagine we send a sequence of light pulses to measure the positions, with the time intervals between neighboring pulses equal to τ. No matter how strong the pulses are, Eq. (1.15) tells us that

the measurement uncertainty Δx is at least

$$\Delta x \sim \sqrt{\frac{\hbar\tau}{2m}}. \tag{1.16}$$

The corresponding noise spectral density (at $\Omega \sim 1/\tau$) is then given by

$$S_x(\Omega) \sim \Delta x^2 \tau \sim \frac{\hbar}{2m\Omega^2} \tag{1.17}$$

which recovers the SQL we obtained in Sec. 1.1.

1.2.2 Open quantum dynamics of single-photon optomechanical devices (Chapter 3)

Chapter 3 is based on the following preprint:

- Ting Hong, Huan Yang, Haixing Miao, Yanbei Chen, *Open quantum dynamics of single-photon optomechanical devices*, arXiv:1110.3348 [quant-ph].

1.2.2.1 Motivation and signficance

This work was inspired by Marshall *et al.* [40], where the authors proposed to measure the effect of the (speculated) gravity-induced-decoherence using a Michelson interferometer with Fabry-Perot cavity arms (one with a movable end mirror, the other with fixed mirrors), and driven by a single photon. Based on the time evolution of the interference pattern's visibility on the dark port, Marshall *et al.* claimed that they could determine the decoherence rate of the total system — yet in their calculations they had assumed that the single photon starts off already as a coherent superposition in either of the Fabry-Perot cavities, instead of having to enter them from the outside. Therefore, they did not have to consider the spatial mode of the incoming photon, either. Such single-photon driven devices have also been studied by Rabl [41] and Nunnenkamp *et al.* [42]. Unlike Rabl and Nunnenkamp *et al.*, who studied systematically the statistics of the out-going photons and the steady state reached by the mechanical oscillator, we focused instead on the fringe visibility of a single-photon interferometer, and the conditional quantum state of the mechanical oscillator upon the detection of an outgoing photon —- explicitly accounting for the spatial mode of the incoming photon. We obtained an exact analytical solution for the system's quantum mechanical equations of motion, including details about the exchange of the single photon between the cavity mode and the external continuum. This result is one of the few known exact solutions for *nonlinear quantum open systems*. Using our exact solution, we found Marshall *et al.*'s calculation result only approximately correct when the incoming photon has a much broader frequency width than the cavity's linewidth, in which case the photon has a small chance of entering the cavity in the first

place, thereby lowering the efficiency of the experiment, and making it potentially more susceptible to imperfections. Furthermore, we presented a method to construct the non-classical quantum state of the mechanical oscillator by modulating the single photon's profile, which sheds light on future technologies of quantum-state engineering.

1.2.2.2 Summary of main results

In Chapter 3, we start with a total system with the Hamiltonian:

$$\hat{H} = \frac{i}{2} \int_{-\infty}^{\infty} (\partial_x \hat{c}_x^\dagger \hat{c}_x - \hat{c}_x^\dagger \partial_x \hat{c}_x) \, dx + \omega_0 \hat{a}^\dagger \hat{a} + i\sqrt{\gamma}(\hat{c}_0 \hat{a}^\dagger - \hat{a}\hat{c}_0^\dagger) + \frac{\hat{p}_y^2}{2m} + \frac{1}{2}m\omega_m^2 \hat{y}^2 + k\hat{a}^\dagger \hat{a}\hat{y}. \quad (1.18)$$

The first term is the Hamiltonian for a freely propagating single photon: the field with $x < 0$ is propagating toward the cavity, while the field with $x > 0$ is the propagating away from the cavity. The second term in Eq. (1.18) is Hamiltonian for the optical mode of the cavity (one that is closest to being excited by the single photon). The third term indicates that the cavity's front mirror is located at $x = 0$; the reflection of the electromagnetic field on the front mirror, i.e the transition from c_{0-} to c_{0+} is naturally captured by this term. The next two terms are the mechanical oscillator's kinetic and potential energies, while the last term describes the interaction between the cavity's optical mode and the mechanical oscillator.

This Hamiltonian can be used to model the optomechanical device previously studied by Marshall et al. [40], which is a Michelson interferometer with an Fabry-Perot cavity in each arm, one of them with a movable end mirror. The system is driven by a single photon injected from one of the input ports of the Michelson interferometer. However, Marshall *et al.* neglected the free-propagation Hamiltonian for their single photon. They instead assumed that the photon was initially prepared in a "Schrödinger-cat state", namely a coherent superposition of either being in one of the cavities or being in the other, with equal probability, which was experimentally unrealistic.

Without coupling to the outside, the photon-mirror Hamiltonian is known to be analytically solvable. This is no-trivial, because we have a cubic term in the Hamiltonian. The analytic solution is only possible because this nonlinearity is very special. Now, adding the coupling to the outside field, the system is more complex. However, we have been able to explicitly solve the single-photon case. We then applied this analytical solution to the experimental setup in [40], which has a Michelson interferometer. The resulting time evolution of the interferometer's fringe visibility displays interesting new features when the incoming photon's frequency uncertainty is narrower or comparable to the cavity's line width — only in the limiting case of a much broader-band input photon does the result return to that of Marshall *et al.*. In this case the photon is not very likely to enter the cavity and interact with the mirror, making the experiment less efficient and more susceptible to imperfections.

Given the exact solution of the total system's joint wave function, we show that after the detection of the single photon at the interferometer's dark port, the mechanical oscillator's conditional quantum state can be obtained and (for the same photon arrival time) it depends linearly on the initial profile of the single photon (it also depends on the arrival time of the photon, but not linearly). We then discover a family of initial wavefunctions of the single photon for which the resulting mechanical oscillator's asymptotic-conditional-states are displaced number states. Since the set of all number states forms a complete basis, it is natural to see that ideally we can prepare the mechanical oscillator's quantum state by engineering the single photon's wavefunction. In reality, there are a lot of restrictions on quantum state preparation. *First*, the optomechanical coupling has to be strong. We define a constant β as

$$\beta = \frac{k/(2\omega_m)}{\sqrt{\hbar m \omega_m/2}} = \left[\frac{\hbar \omega_0}{c}\right] \sqrt{\frac{2}{\hbar m \omega_m}} \left[2\omega_m \frac{L}{c}\right]^{-1}, \qquad (1.19)$$

which is the momentum kick of the photon (to the oscillator during one radian of mechanical oscillation) divided by the ground state momentum uncertainty $\sqrt{\hbar m \omega_m/2}$ (L is the cavity length). The first requirement is $\beta > 1$, which means the momentum kick from the photon needs to be big enough to substantially change the mirror state. The *second* requirement is that the cavity bandwidth be smaller than the mechanical frequency $\gamma < \omega_m$. This is to ensure the photon stays inside the cavity long enough to affect the mirror motion. The *third* requirement is that the thermal decoherence effect has to be small within one mechanical oscillation period, which is a generic condition for all MQM experiments. With all requirements satisfied, we show that preparing a mechanical quantum state with high occupation number generally has a low probability of success — in other words, a large number of experimental trials are needed. For example, with $\beta \sim 1$, the probability of successfully preparing a state with occupation number less than 8 and fidelity $\geq 90\%$ is about 0.1%. Although the requirements are stringent, we do show that in the strong-coupling regime, by engineering the incoming photon's wave function, it is possible to prepare a movable mirror into an arbitrary quantum state of a multi-dimensional Hilbert space.

1.2.2.3 My specific contributions

I worked out the quantum evolution of the total system given the total Hamiltonian in Eq. (1.18) and initial wave function of the single photon. I also discovered and analyzed the possibility of preparing quantum states by modifying the input photon wave function. The initial draft of the paper was written by me, and it was later significantly revised by Chen.

1.2.3 Theory of non-Markovian quantum measurement processes (Chapters 4 and 5)

Chapters 4 and 5 are based on one paper and one preprint:

- Huan Yang, Haixing Miao, and Yanbei Chen, *Nonadiabatic elimination of auxiliary modes in continuous quantum measurements*, Physical Review A **85** , 040101 (2012).

- Huan Yang, Haixing Miao, Yanbei Chen, *Reveal non-Markovianity of open quantum systems via local operations*, arXiv:1111.6079 [quantum-ph] (2011).

1.2.3.1 Motivation and significance

In many cases, scientists are interested in studying the interaction between a quantum object and its surrounding bath. This interaction correlates the system and its bath, so that the bath also carries quantum information about the system. For Markovian interactions, when we trace out the bath, the evolution of system's density matrix at any time t is independent of its previous history, because the bath never feeds back its past information about the system (only instantaneous information is fed back); for non-Markovian interactions, because the bath continuously feeds back its past information to the system, knowing the system's quantum state at one time t is not enough to determine its later evolution. Although the *mathematical* definition for non-Markovianity was given in a rigorous manner, there is still a great deal of effort, in the field, going into trying to identify and characterize *physical* properties of non-Markovian dynamics. In Chapter 4, we construct two very general types of continuous measurement models that exhibit non-Markovianity; for each scenario, we provide theoretical tools that help obtain the system's evolution equations. In Chapter 5, we propose a new way to physically characterize non-Markovianity, by perturbing the system and watching how its subsequent evolution differs from the unperturbed case; we show that this method is capable of revealing some of the previously "hidden" non-Markovianity. Work in this chapter partly answers the question of how to describe a measurement process involving non-Markovianity, which has been argued back and forth for years, and in certain scenarios can lead to efficient algorithms for simulating quantum evolutions.

1.2.3.2 Summary of main results

Non-Markovianity naturally arises in many interesting quantum systems, e.g., cavity QED [46], photosynthesis [47] and cold atoms [48]. A common theoretical tool for investigating non-Markovian open quantum systems is the non-Markovian stochastic Schröedinger equation (also called the state-diffusion equation) or equivalently the master equation [52–54]. The underlying assumption usually made is that no information concerning the environment (i.e., the bath) is collected; however, in

most experimental setups, a measurement device is an indispensable part, especially when we want to control the dynamics of the system via feedback [55]. While it is clear the Markovian quantum measurement processes can be described by stochastic master equations, the physical meaning of non-Markovian stochastic master equations had been controversial. Recent discussions between Diósi and Wiseman *et. al.* [56, 57] highlight this issue: initially Diósi tried to give a quantum trajectory interpretation of the non-Markovian Stochastic Schrödinger Equation (SSE), i.e., claiming that it describes a pure state evolution under a continuous measurement of a particular operator of the system that is non-local in time. It is now clear that this interpretation is incorrect, as was shown explicitly by Wiseman *et. al.* [57] and later by Diósi himself [56].

In Chapter 4, instead of trying to find scenarios that can be described by non-Markovian SSEs, we start with a quantum system under the continuous quantum measurement, and study two important scenarios in which non-Markovianity can arise: the first one is an indirect measurement of the system via a measurement of its bath, which has a finite memory; the second one is a direct measurement of the system, but the measurement device has non-trivial quantum correlations in time.

In the *first* scenario, the total system is composed of a plant plus auxiliary degrees of freedom (DOFs) plus Markovian probe field, and the dynamics of the auxiliary DOFs are linear. The interaction between the plant and the auxiliary DOFs is non-Markovian, which means these auxiliary DOFs store information about the plant, in other words, they are entangled with the plant. As a result, if we trace out the auxiliary DOFs, the plant would be in a mixed state. In fact, in many cases people are only interested in the quantum evolution of the plant, and it is often too expensive to keep track of the whole systems's evolution. The question is then whether one can trace out the auxiliary DOFs and directly obtain a self-contained equation for the plant's quantum evolution under quantum measurement. The answer has been known to be affirmative in the case when measurement result was discarded. The density matrix of the plant can be shown to satisfy its own master equation, which can be deduced using a quantum trajectory technique developed by Strunz and Diosi. In Chapter 4 we prove that with some modifications, this technique can be generalized to incorporate continuous quantum measurement. In particular, with some tedious but nevertheless straightforward calculations, we obtain explicit stochastic master equations for the plant in the limit of weak coupling or linear coupling between the plant and the auxiliary DOFs. For more general cases, the stochastic master equation can be written in the form of perturbative expansion, which closes itself when the system has a finite-dimension Hilbert space. In short, this model not only describes a general class of non-Markovian measurement scenarios, but also offers an efficient way of simulating those systems numerically.

In the *second* scenario, we study systems composed by only a plant and a probe field, with probe-field components that interact with the system at different times correlated with each other. In this case, the non-Markovianity of the measurement process does not come from the interaction between

the plant and the probe field, but rather arise from the statistical correlation between entangled probe fields that interact with the plant at different times. There is no known master equation description for this scenario, and we have to apply a path integral technique to describe the plant's quantum evolution. We deduce the evolution equation for the plant's Wigner function (which has a one-to-one correspondence with the density matrix) in two examples that are of particular experimental relevance: (i) a linear continuous measurement, and (ii) a nonlinear energy measurement, both with correlated input probe field. Other interesting cases in this category are subject to future investigation.

The above two scenarios characterize two important aspects of non-Markovian quantum measurement. By developing techniques that obtain evolution equations for the plant in these two scenarios, we manage to develop a general understanding of non-Markovian quantum measurement.

Chapter 5 concerns how to characterize the non-Markovianity of plant-bath interaction. The basic idea is to have two identical copies of the same plant-bath system. In copy (A), at a particular moment in time, we instantaneously perturb the plant's Hamiltonian and return it back afterwards, and then watch the difference between the subsequent evolution of this copy's density matrix ρ_A and that of the other copy (B), ρ_B. In order to measure the difference between these two quantum states or density matrices, we use the trace distance, which is defined as

$$d(\rho_A, \rho_B) = Tr|\rho_A - \rho_B|. \tag{1.20}$$

For Markovian systems, this trace distance always decreases in time, as the plant gradually loses information about its initial state to the bath. For non-Markovian systems, information can slosh back and forth between the plant and the bath. In certain cases, the trace distance may temporarily increase in time, as the plant recovers part of its information from the bath. As we perturb the plant's Hamiltonian at one time, its non-Markovian bath responds to the perturbation and feed backs some of the information it stores at later times. The time retardation depends on the plant-bath coupling strength, as well as the bath's memory timescale. Using this "perturbation+observation" approach, we are effectively investigating the "Green function" of the bath with respect to small perturbations. In general, for any non-Markovian scenario, in which the bath stores a non-trivial amount of plant information, by choosing an appropriate instantaneous perturbation in its Hamiltonian, the plant can always restore part of its information from the bath — we refer to this effect as "dynamical recovering" [58]. Dynamical recovering can be contrasted with "dynamical decoupling", where a series of instantaneous perturbative Hamiltonians are applied onto the plant to prevent it from losing information to the bath. As "dynamical decoupling" has already been experimentally demonstrated in the past [59, 60], we hope this "dynamical recovering" phenomenon will attract attention from experimentalists in the near future.

1.2.3.3   My specific contributions

For Chapter 4, I gave the initial formulation of non-Markovian measurement model and applied it to the simple two-level-atom-in-cavity system. For Chapter 5, I found an example in which two identical systems interact with two baths separately — one bath is clear Markovian while the other has a memory, and hence non-Markovian. I also found a way to break the degeneracy between the above two systems, by perturbing the system's Hamiltonian and monitoring the response.

1.2.4   Probing mechanical oscillators near their zero points (Chapter 6)

Chapter 6 is based on a research paper published as:

- Farid Ya. Khalili, Haixing Miao, Huan Yang, Amir H. Safavi-Naeini, Oskar Painter, and Yanbei Chen, *Quantum back-action in measurements of zero-point mechanical oscillations*, Physical Review A **86**, 033840 (2010).

1.2.4.1   Motivation and signficance

In this work, we analyzed an experiment done by Oskar Painter's research group [62], which raised a controversy at the time about whether experiment did reveal the "quantumness" of a mechanical oscillator. By applying linear quantum measurement theory, we were able to establish firmly that: (i) the oscillator in the experiment was indeed prepared at a level of displacement fluctuations that was very close to being at the zero point, and that (ii) the quantum back-action noise of the light used to probe the mechanical oscillator was correlated with its quantum sensing noise. Through (ii), this experiment became the first to confirm the existence of back-action noise in optomechanics experiments, and to demonstrate that it can be correlated with the sensing noise, a feature that will be very useful for schemes of quantum measurement that requires "back-action evasion".

1.2.4.2   Summary of main results

The main idea of the experiment by Safavi-Naeini *et al.* is to parametrically couple two optical modes to a mechanical vibrational mode in a patterned silicon nano-beam. One optical mode — the cooling mode — is pumped with a relatively high power at a "red" detuning (lower than resonance), and is used to cool the mechanical mode via radiation pressure damping; the other optical mode — the readout mode — has a much lower pumping power and is used for probing the mechanical motion. The readout laser frequency ω_{lr} is detuned from the resonant frequency ω_r of the readout mode by either $-\omega_m$ or $+\omega_m$, where ω_m is the mechanical resonant frequency. The observed spectrum of the readout laser is asymmetric with respect to the detuning $\Delta \equiv \omega_r - \omega_{lr}$. Specifically, in the positive-detuning case ($\Delta = +\omega_m$), the spectrum has a smaller amplitude than that in the negative-detuning case. The area I_+ enclosed by the spectrum in the positive-detuning case, *after*

subtracting out the noise floor away from the mechanical resonant frequency, is proportional to the thermal occupation number $\langle n \rangle$ of the mechanical oscillator, while, in the negative-detuning case $(\Delta = -\omega_m)$, the enclosed area is $I_- \propto \langle n \rangle + 1$. The spectrum asymmetry is given by

$$\eta \equiv \frac{I_-}{I_+} - 1 = \frac{1}{\langle n \rangle} \tag{1.21}$$

where the asymmetry was interpreted as arising from quantized motion of the mechanical oscillator, and is related to the difference between the rate of phonon absorption from the oscillator, proportional to $\langle n \rangle$, and phonon emission rate, proportional to $\langle n \rangle + 1$ [62].

In Chapter 6, we provide an alternative viewpoint to Ref. [62], by emphasizing more the role of quantum back-action and its relation to the quantization of the mechanical oscillator. First of all, we separate the experimental system into two parts. The cooling mode, the mechanical oscillator, and the environmental thermal bath couples to together forms the first part, which can be viewed as providing an *effective mechanical oscillator* nearly at the ground state, but with a quality factor significantly lower than the intrinsic quality factor of the mechanical mode. It is the zero-point fluctuation of this effective oscillator that we shall be probing. The second part of the system consists of the readout mode, which couples to the effective oscillator (the first part of the system) through its displacement alone. The second part provides us with a probe-field output $\hat{y}$, which contains information about the zero-point fluctuation of the effective mechanical oscillator.

Using linear quantum measurement theory, we show that the output spectra S_{yy} for the two opposite detunings, $\Delta = \pm \omega_m$, are different from each other:

$$S_{yy}(\omega)|_{\Delta=-\omega_m} \neq S_{yy}(\omega)|_{\Delta=\omega_m}. \tag{1.22}$$

This difference can be traced back to the correlation that exists between the sensing noise and the back-reaction noise. This correlation in turn arises from the quantum coherence between the mechanical oscillator and the measuring device, which builds up during the measurement process. As earlier works had indicated, the correlation between sensing noise and back-action noise is key to improving sensitivities beyond the standard quantum limit. As a consequence, this experiment with nanomechanical oscillators demonstrates a effect much sought after by the gravitational-wave-detection community.

1.2.4.3   My specific contributions

My contributions to the paper [61] was mainly at Section II, where we point out the connection between this optomechanical experiment and previous experiments in atomic physics.

1.2.5 Macroscopic quantum mechanics in a classical spacetime (Chapter 7)

Chapter 7 is based on the research paper published as:

- Huan Yang, Haixing Miao, Da-Shin Lee, Bassam Helou, Yanbei Chen, *Macroscopic Quantum Mechanics in a Classical Spacetime*, Physical Review Letters, **110**, 170401 (2013).

1.2.5.1 Motivations and significance

This work was initiated by Chen, who was thinking about the problem of scalar waves propagating in a curved spacetime. He later realized that it was also a model for quantized matter coupled with a classical spacetime, and urged me to think about the non-relativistic limit of this model and the possibility of testing it with experiments. We analyzed the non-relativistic evolution equation of a many-particle system in this model, and showed that the center-of-mass (CM) evolution can be singled out from evolution of internal degrees of freedom — this enabled us to derive the evolution equation for CM alone, which can be monitored and manipulated at quantum levels by state-of-the-art optomechanics experiments. We further showed that mass concentration inside a crystal (around the lattice sites) makes the CM motion deviate from standard quantum mechanics at a level that might be visible by a carefully designed lab-scale optomechanics experiment.

1.2.5.2 Summary of main results

Testing the nature of gravity is a prominent problem in modern physics. Apart from the standard formulation of linearized quantum gravity [68], which seems rather implausible to test in the lab, several signatures have been conjectured: (i) *gravity decoherence* [70–80], where gravity introduces decoherence to macroscopic quantum superpositions; (ii) modifications to canonical quantization motivated by the existence of a minimum length scale [81–83], and (iii) *semiclassical gravity* [84–86], which will be the subject of this chapter. As originally suggested by Møller [84] and Rosenfeld [85], spacetime structure might *still remain classical* even if it is sourced by matters of quantum nature, if we impose ($G = c = 1$):

$$G_{\mu\nu} = 8\pi \langle \psi | \hat{T}_{\mu\nu} | \psi \rangle . \tag{1.23}$$

Here $G_{\mu\nu}$ is the Einstein tensor of a (3+1)-dimensional classical spacetime, $\hat{T}_{\mu\nu}$ is the operator for the energy-stress tensor, and $|\psi(t)\rangle$ is the wave function of all matters that evolve within this classical spacetime.

Equation. (7.1) reduces to the so-called Schrödinger-Newton equation in the non-relativistic limit. For a system with n non-relativistic particles, if we denote their joint wave function as $\varphi(t, \mathbf{X})$ with $3n$-D vector $\mathbf{X} \equiv (\mathbf{x}_1, \cdots, \mathbf{x}_n)$ and $\mathbf{x}_k$ the 3-D spatial coordinate of k-th particle, then the many-

particle SN equation, obtained by Diosi and Penrose [69, 73], can be written as

$$i\hbar\partial_t\varphi = \sum_k \left[-\frac{\hbar^2\nabla_k^2}{2m_k} + \frac{m_k\,U(t,\mathbf{x}_k)}{2} \right]\varphi + V(\mathbf{X})\varphi\,, \tag{1.24}$$

where $V(\mathbf{X})$ is the potential energy for non-gravitational interactions, while the Newtonian potential U is given by

$$\nabla^2 U(t,\,\mathbf{x}) = 4\pi \sum_j \int \mathrm{d}^{3n}\mathbf{X}\,|\varphi(t,\mathbf{X})|^2 m_j\,\delta(\mathbf{x}-\mathbf{x}_j)\,. \tag{1.25}$$

Many-particle wave-functions are generally very fragile and difficult to model. Previously, it was proposed to test the above equation in the single-particle case [86]. However, in order to satisfy the single-particle approximation, the object's size has to be smaller than the width of its wave function. This requirement limits the mass of the object and hence the gravitational interaction energy. In addition, the dynamical and decoherence timescales for a small object are usually too short compared with its gravitational interaction timescale. As a result, it is very difficult for single particle tests to achieve the desired sensitivity.

In Chapter 7, we show that it is possible to single out CM evolution from other degrees of freedom (DOFs) for a macroscopic object with many particles. Moreover, in certain parameter regimes, the CM wavefunction approximately satisfies the following SN equation:

$$i\hbar\frac{\partial\Psi}{\partial t} = \left[-\frac{\hbar^2\nabla^2}{2M} + \frac{1}{2}M\omega_{\mathrm{CM}}^2 x^2 + \frac{1}{2}M\omega_{\mathrm{SN}}^2(x-\langle x\rangle)^2 \right]\Psi. \tag{1.26}$$

Here $\langle x\rangle \equiv \langle\Psi|\hat{x}|\Psi\rangle$ is the expectation value of the CM position; ω_{CM} is the eigenfrequency in absence of gravity, determined by how the CM is confined; and ω_{SN} is a characteristic frequency due to the self-gravitational effect, which depends on material properties and temperature. For silicon crystal at low temperatures, ω_{SN} is approximately $\sim 0.036\mathrm{s}^{-1}$.

Using the CM Schrödinger-Newton equation (7.2), we solve the equations of motion for the first ($\langle x\rangle, \langle p\rangle$) and second ($V_{\mathrm{xx}}, V_{\mathrm{pp}}, V_{\mathrm{xp}}$) moments of position and momentum, and find they oscillate at different frequencies. The mean position and momentum $\langle x\rangle, \langle p\rangle$, which carry classical information about the object, remain oscillating at frequency ω_{CM}; the seconds moments, or more precisely the noise ellipse, which is related to quantum uncertainties, oscillates at a new frequency $\omega_q = \sqrt{\omega_{\mathrm{SN}}^2 + \omega_{\mathrm{CM}}^2}$. Obviously, we can test this SN model by experimentally verifying if there are separate oscillation frequencies for first and second moments of a mechanical oscillator. On the other hand, we find an alternative way which is experimentally easier to implement — by sending a probe light and measure the noise spectrum of the outgoing field. According to Eq. (7.2), there will be two resonant peaks in the spectrum: one is driven by thermal noise and peaked at ω_{CM}; the other is driven by the quantum radiation pressure noise and resonant at ω_q. The experimental goal is therefore to distinguish these two (possible) peaks in the spectrum. To achieve this goal, we need the quantum

radiation pressure noise to be comparable to thermal noise, and the separation between those two peaks to be smaller than the peak width. The latter requirement is equivalent to

$$Q \gtrsim (\omega_{\mathrm{CM}}/\omega_{\mathrm{SN}})^2. \tag{1.27}$$

For oscillators made from silicon crystals with $\omega_{\mathrm{SN}} \approx 0.036\,\mathrm{s}^{-1}$, if $\omega_{\mathrm{CM}} \approx 2\pi \times 10\,\mathrm{Hz}$, Eq. (7.24) requires $Q \gtrsim 3 \times 10^6$, which is challenging but possible [87]. If a lower-frequency oscillator, e.g., a torsional pendulum with $\omega_{\mathrm{CM}} \approx 2\pi \times 0.1\,\mathrm{Hz}$ [88] can be probed with back-action noise comparable to thermal noise, in that case we only require $Q \gtrsim 3 \times 10^2$.

By analyzing the CM motion of a macroscopic object under classical gravity, we have demonstrated: (i) A model in which classical theory interfaces with a quantum theory. (ii) Optomechanics for macroscopic object is the regime (probably the only known so far) in which both self-gravitational effect and quantum effect are important. (iii) It is experimentally possible to use CM motion of a macroscopic oscillator to test semiclassical gravity or more specifically the non-relativistic limit of Eq. (7.1).

1.2.5.3   My specific contributions

I performed the derivation of the CM Schrödinger-Newton equation, while Chen greatly refined my error estimates. I also wrote the initial draft of the paper, which was revised by Miao and Chen, with a number of useful suggestions from Lee.

1.3   Black hole perturbation theory

1.3.1   Background

Many gravitational-wave-emitting processes end with the formation of a black hole. For example, in the final stage of a binary black-hole merger, the spacetime is approximately a perturbed Kerr spacetime. The metric perturbations gradually radiate to infinity or get absorbed by the black hole, and eventually the whole spacetime settles down to a Kerr spacetime. In the past, various analytical tools were developed to describe the evolution of a perturbed black holes's spacetime.

For *Schwarzschild black holes*, Reggie and Wheeler [23] and Zerilli [24] showed the metric perturbations can be decomposed into spherical harmonics and the different spherical harmonic components evolve independently. For each spherical component with l, m, there are 10 metric quantities to be determined (except for $l = 0, 1$ case). Because there are 4 Bianchi identities to be satisfied and 4 gauge freedoms for the coordinates choice, only $10 - 4 - 4 = 2$ out of 10 metric quantities are truly independent. They chose a specific gauge (usually referred as Reggie-Wheeler gauge) and it turns out in this gauge one can derive evolution equations for the two independent metric quantities.

These results were further generalized by Moncrief, who recombined these 10 metric quantities to obtain 2 independent gauge invariant quantities. He also derived separated evolution equations for them:

$$\frac{\partial^2 \psi_{\mathrm{p}}}{\partial t^2} - \frac{\partial^2 \psi_{\mathrm{p}}}{\partial r_*^2} + V_{\mathrm{p}} \psi_{\mathrm{p}} = 0. \tag{1.28}$$

Here $r_* = r + 2M \log(r/2M - 1)$ and p corresponds to the parity of the field. ψ_{p} are the gauge invariant quantities with even or odd parity and the potential terms V_{p} are given in Chapter 8. In addition, the horizon is located at $r = 2M$ or $r_* = -\infty$, whereas spatial infinity is at $r = +\infty$ or $r_* = +\infty$. .

Kerr black holes do not have spherical symmetry. There is as yet no way to write down a single wave equation with separable angular and radial/time dependence which can be used to generate all other metric perturbations. However, Teukolsky managed to show [26] that certain components of curvature perturbations on the Kerr background obey separable wave equations in the frequency domain (the wave equations are listed in Chapters 10–12). In particular, these curvature quantities are the Newman-Penrose (NP) curvature scalars Ψ_0 and Ψ_4 [27], both of which are gauge invariant under infinitesimal gauge transformations at linear perturbative order. Physically speaking, the quantity Ψ_0 originates from gravitational waves that go into the black horizon, whereas Ψ_4 originates from gravitational waves that radiate towards infinity. As a result, it is convenient to apply Ψ_4 in numerical relativity simulations for wave extraction at infinity. In addition, with certain gauge choices, algorithms have been developed to reconstruct full metric perturbations from Ψ_0 and Ψ_4. For example, Chrzanowski [28], Kegeles and Cohen [29], Stewart [30] and Wald [31] demonstrated the metric reconstruction procedure in ingoing and outgoing radiation gauges. For systems with quasi-periodic dynamics and adiabatic evolution (such as Extreme Mass Ratio Inspiral or EMRI in Kerr spacetime), frequency domain analysis is accurate and much more efficient than time-domain methods. In those cases, the Teukolsky formalism becomes very useful. In other cases, however, where the adiabatic approximation does not hold or the frequency domain method is not accurate enough, we still need to solve coupled wave equations for the 10 metric perturbation quantities in order to determine the system's evolution.

Although the perturbations of a Kerr black hole generically decay in time (see [32] for the proof of Kerr spacetime's linear stability), these perturbations can still be decomposed into eigenmodes, each with a complex eigenfrequency. These eigenmodes are usually referred as *Quasinormal Modes* (QNMs), and they serve as an important tool in black hole perturbation theory (see [33–36] for reviews). In absence of external incoming waves, it is natural to require the boundary condition of these modes to outgoing at infinity and ingoing at the horizon. For Eq. (1.28) which describes

Schwarzschild perturbation, this is equivalent to requiring $\psi_{\mathrm{e/o}} \propto e^{-i\omega_{ln}(t+r_*)}$ when $r_* \to -\infty$, and $\psi_{\mathrm{e/o}} \propto e^{-i\omega_{ln}(t-r_*)}$ when $r_* \to \infty$. With these boundary conditions Eq. (1.28) can be solved in the frequency domain. There are a series of eigenmodes, which are indexed by angular number l and overtone n. Their frequencies ω_{ln} are complex numbers with negative imaginary parts. This agrees with [32] because ω_I with positive imaginary parts corresponds to growing or unstable modes.

For Kerr black holes the boundary condition at horizon has to be modified to take into account frame dragging effect. Ψ_4 becomes (see Chapter 10 for more details)

$$
\begin{aligned}
\Psi_4 &\propto \frac{1}{r^5}e^{-i(\omega_{lmn}-m\omega_+)(t+r_*)}, \quad r_* \to -\infty, \\
&\propto \frac{1}{r}e^{-i\omega_{lmn}(t-r_*)}, \quad r_* \to +\infty
\end{aligned}
\tag{1.29}
$$

and Ψ_0 becomes

$$
\begin{aligned}
\Psi_0 &\propto \frac{1}{r}e^{-i(\omega_{lmn}-m\omega_+)(t+r_*)}, \quad r_* \to -\infty, \\
&\propto \frac{1}{r^5}e^{-i\omega_{lmn}(t-r_*)}, \quad r_* \to +\infty
\end{aligned}
\tag{1.30}
$$

where $\omega_+ = Ma/(2r_+)$ is the horizon frequency, $a = J/M$ is the black hole's spin parameter and $r_+ = M + \sqrt{M^2 - a^2}$ is the outer-horizon radius. Similar to the Schwarzschild case, a series of eigenmodes can be obtained by combining the Teukolsky equation Eq. (1.28) with boundary conditions in Eq. (1.29). Since Kerr black holes do not have spherical symmetry, the degeneracy of azimuthal degrees of freedom is broken and Kerr QNMs are indexed by l, n and azimuthal number m. In general ω_{lmn}s are complex numbers with negative imaginary frequencies, with a few exceptions for extreme Kerr black holes ($a = M$).

1.3.2 First-order perturbative Hamiltonian equations of motion for a point particle orbiting a Schwarzschild black hole (Chapter 8)

Chapter 8 is based on the following preprint:

- Huan Yang, Haixing Miao, Yanbei Chen, *First-Order Perturbative Hamiltonian Equations of Motion for a Point Particle Orbiting a Schwarzschild Black Hole*, arXiv:1211.5410 [gr-qc].

1.3.2.1 Motivation and significance

Chen was initially thinking about coherently evolving a test particle and the gravitational perturbation in a Schwarzschild spacetime. One natural way is to include both the gravitational perturbation and the test particle into the same Hamiltonian. Following this line, we successfully constructed a Hamiltonian formalism for this problem, in which the particle's equations of motion and the field's

wave equations can be naturally derived from the Hamilton-Jacobi equations, and the gauge choices are no longer limited to Lorenz gauge. Our Hamiltonian formalism allows more flexible gauge choices than other approaches, and introduces more efficient evolution schemes.

1.3.2.2 Summary of main results

Simulating Extreme Mass Ratio Inspirals (EMRIs) is one of the outstanding problems in gravitational physics. A EMRI system often includes a supermassive black hole and an object with much smaller mass. EMRI is astrophysically interesting because a supermassive black hole is believed to exist in every galaxy; it is also conceptually intriguing because black-hole perturbation theory can be naturally applied here. However, computationally this is a difficult problem for numerical relativity simulations because of the large separation in length scales. Even in terms of black-hole perturbation theory, since the small mass object is often approximated as a point mass to avoid dealing with its equation of state, a special regularization procedure has to be performed to remove metric singularities on the point mass's worldline.

The most common approach for metric regularization was developed by Detweiler and Whiting [90, 91]. The basic idea is to separate the metric perturbation h into a regular piece h_R and a singular piece h_S. The singular piece diverges at the particle's location but does not have any effect on the particle's motion; it can be obtained by a local expansion of the Green function. The regular field satisfies the homogeneous Einstein's equation and is responsible for the geodesic deviation of the particle's motion in the background spacetime; it is obtained by subtracting the singular field from the full field. Using this regularization technique, there are two major approaches for numerically evolving the test particle and the metric perturbation. One way is the *mode sum* approach, developed by Barack and Ori [92], which decomposes each of the 10 metric components into spherical harmonics, and solves 10 coupled 1+1 wave equations for each (l, m). The particle equation of motion is then regularized mode-by-mode, by subtracting a series of regularization parameters for each (l, m). This mode sum method has already been implemented by Warburton et al. [93] for the Schwarzschild gravitational EMRI problem. In the second approach, one directly applies a 3+1 decomposition of spacetime geometry, and tries to obtain the regular field directly — by obtaining a field $\tilde{h}_R$ which is approximately the Detweiler-Whiting h_R near the particle, but gradually becomes the full field at null infinite and near horizon. As shown by Vega and Detweiler [94], the field $\tilde{h}_R$ satisfies a wave equation with out-going boundary condition at infinity and horizon, but with a source that can be computed from the Detweiler-Whiting singular field h_S. Diener and Vega [95] have implemented this method for a scalar particle orbiting a Schwarzschild black hole.

In Chapter 8, we formulate a Hamiltonian approach towards the EMRI problem in the Schwarzschild background, with the aim of providing a new angle to view this problem. In our approach, the trajectory of a point particle and its gravitational metric perturbation are self-consistently evolved in

a spherically decomposed 1+1 scheme. Following the work of Moncrief, we write down an action for perturbations in space-time geometry, combine that with the action for a point-particle moving through this space-time, and then obtain Hamiltonian equations of motion for metric perturbations and the particle's coordinates, as well as their canonical momenta. Hamiltonian equations for the metric-perturbation and their conjugate momenta, for even and odd parities, reduces to Zerilli-Moncrief and Regge-Wheeler master equations with source terms, which are gauge invariant, plus auxiliary equations that specify gauge. Hamiltonian equations for the particle, on the other hand, now include effect of metric perturbations — with these new terms derived from the same interaction Hamiltonian that had lead to those well-known source terms. In this way, space-time geometry and particle motion can be evolved in a self-consistent manner, in principle in any gauge. However, the point-particle nature of our source requires regularization, and we outline how the Detweiler-Whiting approach can be applied. In this approach, a singular field can be obtained analytically using the Hadamard decomposition of the Green's function; while the regular field, which needs to be evolved numerically, is the result of subtracting the singular field from the total metric perturbation. In principle, any gauge that has the singular-regular field decomposition is suitable for our self-consistent scheme. In reality, however, this freedom is only possible if our singular field has a high enough level of smoothness. For a singular field with minimum quality, one can adopt the Lorenz gauge condition, which we have recast into our formalism: for each l and m, we have 2 wave equations to evolve odd and even parity gauge invariant quantities and 8 first order differential equations to fix the Lorenz gauge and determine all the metric components.

1.3.2.3   My specific contributions

I performed most of the analytical calculations in this work, and also wrote the initial version of the paper, which was greatly revised by Chen.

1.3.3   Quasinormal mode spectrum of Kerr black holes and its geometric interpretation (Chapter 9)

Chapter 9 is a research paper published as:

- Huan Yang, David A. Nichols, Fan Zhang, Aaron Zimmerman, Zhongyang Zhang, and Yanbei Chen, *Quasinormal-mode spectrum of Kerr black holes and its geometric interpretation*, Physical Review D **86** 104006 (2012).

1.3.3.1   Motivation and significance

Initially Chen found numerically that for certain Kerr black hole spins there are degenerate frequencies among different sets of quasinormal modes (QNMs). In order to explain this degeneracy, an

analytical understanding for Kerr QNM frequency is needed. We worked out the QNM frequency formula in the eikonal limit $l \gg 1$ using WKB techniques, which agrees with numerical results very well. Using the analytical formula, the mode degeneracies are naturally explained and moreover, we showed these Kerr QNMs are intimately related to null particles moving in spherical orbits of Kerr. In this work we have built up analytical tools which are not only applicable for analyzing Kerr QNMs but has also been proved to be useful for the work in later Chapters 10–11.

1.3.3.2 Summary of main results

Quasinormal modes (QNMs) of black-hole spacetimes are the characteristic modes of linear perturbations of black holes that satisfy an outgoing boundary condition at infinity and an ingoing boundary condition at the horizon. For generic Kerr black holes, they are well understood and can be calculated quite accurately, for example using the numerical algorithm developed by Leaver [97]. In addition, for modes with $l \gg 1$, there is a well-known, intuitive geometric correspondence between high-frequency quasinormal modes of slowly-rotating Kerr black holes and null geodesics that reside on the light-ring (often called spherical photon orbits) [98]:

$$\omega_{lmn} \approx L\frac{1}{\sqrt{27}M} + m\frac{2a}{27M^2} - iN\frac{1}{\sqrt{27}M} \tag{1.31}$$

where $L \equiv l + 1/2$ and $N = n + 1/2$. The real part of the mode's frequency relates to the Keplerian orbital frequency for the spherical photon orbit $1/(\sqrt{27}M)$, and the Lense-Thiring-precession frequency of the orbit $2S/(3M)^3 = 2a/(27M^2)$ (S is the angular momentum of the Kerr black hole); the imaginary part of the frequency corresponds to the Lyapunov exponent of the orbit $1/(\sqrt{27}M)$. As a result, we may expect closed photon orbits to play an important role in the structure of a spacetime's QNM. It is however nontrivial to generalize this geometric correspondence to generic Kerr black holes. The main difficulty comes from the fact that radial and angular Teukolsky equation both contain two constants to be determined by the boundary conditions — angular and radial eigenvalues, and hence these two second-order differential equations have to be solved jointly.

Instead of directly solving the joint second-order differential equations, we try to derive the algebraic relations between the two eigenvalues based on the two Teukolsky equations. The first relation was worked out by Iyer and Will [99]. They used the fact that the radial Teukolsky equation describes a scattering problem, and applied WKB techniques to show $V(\omega_R, r_0) = V'(\omega_R, r_0) = 0$ and:

$$\omega_I = (n + 1/2)\frac{\sqrt{2d^2V_r/dr_*^2}}{\partial V_r/\partial \omega}\Bigg|_{r_0, \omega_R} \tag{1.32}$$

where r_0 is the peak position and $\omega_{lmn} = \omega_R - i\omega_I$ (the angular eigenvalue A_{lm} is implicitly contained

in the expression for V_r). The second relation was discovered by us, by noticing that the angular Teukolsky equation can be transformed into a boundary state problem, which is extensively studied in quantum mechanics. We apply a WKB approximation on this bound-state problem, and obtain the second relation between angular eigenvalue A_{lm} and QNM frequency ω_R

$$\int_{\theta_-}^{\theta_+} d\theta \sqrt{a^2 \omega_R^2 \cos^2 \theta - \frac{m^2}{\sin^2 \theta} + A_{lm}^R} = (L - |m|)\,\pi\,, \tag{1.33}$$

where the integral is performed in the classical regime (integrand ≥ 0). Comparing our WKB calculation to the leading-order, geometric-optics approximation to scalar-wave propagation in the Kerr spacetime, we then draw a correspondence between the real parts of the parameters of a quasinormal mode and the conserved quantities of spherical photon orbits. At next-to-leading order in this comparison, we relate the imaginary parts of the quasinormal-mode parameters to the Lyapunov exponent of the scalar wave. In particular, the QNM frequency is

$$\omega_{lmn} = L\omega_{\mathrm{orb}} + m\omega_{\mathrm{prec}} - iN\gamma + O(1/L) \tag{1.34}$$

where ω_{orb} is the orbital frequency of the corresponding photon orbit, ω_{prec} is the corresponding precession frequency and γ is the Lyapunov component of the orbit.

The above QNM formula is checked against numerical scalar QNM values and the relative errors are shown to be under $0.06/L^2$. Moreover, it manifests the geometric correspondence between Kerr QNMs and the null rays propagating in spherical orbits of Kerr spacetime. With the correspondence, we also make other observations about features of the QNM spectrum of Kerr black holes that have simple geometric interpretations. First, we find that for near extremal Kerr black holes with $a/M \to 1$, a significant fraction of the QNMs have their real frequencies approach m times the angular frequency of the horizon and a decay rate that rapidly falls to zero; we explain this in terms of a large number of spherical photon orbits that collect on the horizon for extremal Kerr holes. This phenomenon will be further investigated in Chapter 10. Second, we use the geometric-optics interpretation given by Eq. (9.3) to explain a degeneracy in the QNM spectrum of Kerr black holes, in the eikonal limit, which also manifests itself, approximately, for small l. The degeneracy occurs when the orbital and precession frequencies, ω_{orb} and ω_{prec} are rationally related (i.e., $\omega_{\mathrm{orb}}/\omega_{\mathrm{prec}} = p/q$ for integers p and q) for a hole of a specific spin parameter, and when the corresponding spherical photon orbits close. By substituting this result into Eq. (9.3), one can easily see that modes with l and m become degenerate with those of indexes $l' = l + kq$ and $m' = m - kp$ for any non-negative integer k, in the eikonal limit.

1.3.3.3 My specific contributions

I performed most of the analytical calculations in this work, and wrote the initial draft of the paper, which was dramatically improved by all the authors.

1.3.4 Quasinormal mode bifurcation for near extreme Kerr black holes (Chapter 10)

Chapter 10 is partially based on the following paper:

- Huan Yang, Fan Zhang, Aaron Zimmerman, David A. Nichols, Emanuele Berti, and Yanbei Chen, *Branching of quasinormal modes for nearly extremal Kerr black holes*, Physical Review D **87**, 041502 (2013).

1.3.4.1 Motivations and significance

Chapter 10 is a natural extension of the findings we present in Chapter 9. We systematically investigated the near extreme Kerr (NEK) QNMs, and found the criteria to separate two regimes in the QNM spectrum. In one of the regimes we discovered mode-bifurcation phenomena at certain black-hole spins, and we gave a physical interpretation — a single potential well splits into two as we increase a/M and this causes the mode spectrum to bifurcate. We also applied our new understanding about NEK QNMs to investigate late time tails of NEK spacetime, which turned out to behave like $1/t$ at early times and exponentially at later times. Our work clarified long-standing controversies in understanding NEK QNMs and suggested possibly a verifiable optical/GW-signal for astrophysical NEK black holes.

1.3.4.2 Summary of main results

In 1980, Detweiler used an approximation to the radial Teukolsky equation for NEK BHs to show that QNMs with angular indices $l = m$ have a long decay time [101]. Using Detweiler's result, Sasaki and Nakamura [102] calculated QNM frequencies analytically and Andersson proposed long-lived emission from NEK BHs [103]. However, there remains a long-standing controversy in the literature about what set of QNMs decay slowly [104], whether long-lived radiation is possible [105], and whether the imaginary part of the QNM frequencies vanishes as $a \to 1$ (compare [102, 105] with [104]). Despite the importance of this problem, our present understanding of the QNM spectrum of NEK BHs is inconclusive.

In Chapter 11, we show that the NEK geometry has two distinct sets of QNMs: zero-damping modes (ZDMs) and damped modes (DMs). ZDMs are associated with the near-horizon geometry of the BH, and they exist for *all* allowed values of l and $m \geq 0$. DMs are associated with peaks of the potential barrier; in the eikonal limit, they exist when $\mu \equiv m/(l + 1/2) \leq 0.74$. This implies

that ZDMs and DMs coexist if $0 \leq \mu \leq 0.74$. For generic l, we argue that the existence of DM is equivalent to the existence of a peak for the external potential barrier. It turns out that there is no peak outside the horizon when (for simplicity we take $M = 1$)

$$\frac{7}{4}m^2 - s(s+1) - {}_sA_{lm}\left(\omega = \frac{m}{2}\right) > 0, \qquad (1.35)$$

where s is the spin of the perturbation field and ${}_sA_{lm}$ is the angular eigenvalue. Equation (1.35) is expected to separate the single-mode and double-mode regimes and this is numerically verified for $2 \leq l \leq 100$ and $s = (0, -2)$. Our results for modes of arbitrary l, m gives us the following, coherent picture of the two phase regimes. An extrema of the potential always exists at the horizon of the NEK black hole, supporting a family of QNMs whose damping is proportional to the surface gravity and vanishes in the extremal limit. Meanwhile, for equatorial modes ($m = l$), there is a second peak of the potential, away from the horizon, which supports a number of additional modes. The decay of these modes is controlled by the width of this secondary peak, and remains nonzero even for an extreme Kerr black hole. As we consider modes with higher m, which we can describe as having progressively smaller inclination angles relative to the equator in the sense of the geometric correspondence with null orbits, the secondary peak moves closer to the horizon. This second peak joins onto the horizon and vanishes entirely for some m. For equatorial modes ($m = l$), there is always only the horizon peak, supporting the ZDMs.

It is known that in the cases of Schwarzschild and slowly spinning Kerr black holes, the QNMs of a given l, m are indexed by a single overtone number n and that their decay rate monotonically increases with increasing n. This is in direct contrast to the results we have just obtained, where there are two distinct families of modes for NEK, and no unique way to index them at a given spin. We are led to the conclusion that there is some transitional behavior at a large spin, where in the double phase regime a single family of QNMs branches into two families with different properties, the DMs and ZDMs. In order to explore the bifurcation effect, we numerically compute QNM frequency values as we increase a. We indeed observe the bifurcation of spectrum for various l's, and demonstrate the existence of bifurcation in the double-phase regime and the absence of bifurcation in the single-phase regime. By developing a technique to transform the radial Teukolsky equation into a bound-state problem, QNM wave functions become bounded (before the transformation QNM wave functions diverge at $r_* \to \pm\infty$). By applying this technique and examining the QNM wavefunction, we discuss an analytic model of the bifurcation in terms of the parametric potential-well splitting of an oscillator in quantum mechanics.

Finally, we apply our new analytical expressions to study the power-law tail for the quasi normal ringing of a NEK black hole. It was argued by Glampedakis and Anderson [106] that the perturbation of rapidly rotating black holes decays as $1/t$ at late times. Their argument used a less accurate NEK

QNM frequency formula. With our new understandings, we show that the collective ringing of ZDMs generates a $1/t$ tail when $t\sqrt{1-a} \ll 1$, but eventually becomes an exponential decay in the long run. On the other hand, for extreme Kerr black holes the $1/t$ tail lasts forever. Our formula fit nicely with previous numerical results in [106, 107], where they see both $1/t$ and exponential tails.

1.3.4.3 My specific contributions

My contributions to this work are mainly the analytical part of the content: the derivation of the phase boundaries, the physical interpretation and demonstration of the mode bifurcation and the tail calculations.

1.3.5 An analytical approximation for the scalar Green function in Kerr spacetime (Chapter 11)

Chapter 11 is a paper in preparation.

1.3.5.1 Motivation and significance

I had the idea of computing the scalar Green function of Kerr spacetime after reading the paper by Dolan and Ottewill [108], which describes how to approximatly calculate the Green function of Schwarzschild spacetime using QNMs. At that time it was difficult to generalize their technique for Kerr spacetime, as Kerr QNMs were poorly understood. After finishing the work we present in Chapter 10, I noticed that we have the right tools to compute the Kerr Green function and then I performed the computation in this chapter. This work is not fully complete yet, with additional numerical verification needed before submitting for publication.

1.3.5.2 Summary of main results

The scalar Green function $G(x, x')$ is defined as

$$\Box G(x, x') = \frac{1}{\sqrt{-g}} \partial_\mu \left(\sqrt{-g} g^{\mu\nu} \partial_\nu G_{\text{ret}} \right) = \delta^{(4)}(x - x') \tag{1.36}$$

where $g_{\mu\nu}$ is given by the background's metric, which is the Kerr metric in our case. For Schwarzschild background spacetime, Dolan and Ottewill [108] used a spectra method to relate scalar Green function to quasinormal modes. By adopting a matched expansion technique, they managed to obtain an approximate analytical form of the Green function. Moreover, they showed the Green's function is singular on the lightcone, and it has the four-fold singular structure as $\delta(\sigma), 1/\sigma, -\delta(\sigma), -1/\sigma$. σ is the Synge's world function. This four-fold singular structure matches the earlier expectation by Casals et. al [109, 110], which is proved using the Hadamard ansatz of the direct part of the Green's

function. On the other hand, Zenginoglu and Galley [111] used numerical method to obtain the time domain scalar Green function in Schwarzschild background. They also observe the four-fold singular structure as caustic echos.

In this work, I solve for the Green function by decomposing it in the frequency domain. Similar to the Schwarzschild case, this quantity can be evaluated using residue theorem and divided into three pieces. The first piece ("direct part") is the integral on the high frequency arc, it is expected to be zero after very short amount of time [97]. The second piece is the integral on the branch cut on the imaginary frequency axis. It contributes to the power-law decay at later times and is also non-negligible at early times [112]. The final piece comes form the QNM poles, and it is important only at early and mid times. For simplicity, we focus on the QNM contribution to the Green's function and study its early time behavior.

With the knowledge we gained in Chapter 9, I wrote down the expression for Kerr QNM frequency in the eikonal limit. WKB treatment for QNM wave function typically fails near the peak of the potential barrier. As a result, I had to obtain WKB solutions on both sides of the potential barrier's peak and apply the asymptotic expansion technique to match them properly. Putting everything together I obtained an approximate QNM part of Green function, which agreed with Dolan and Ottewill's result in the non-rotation limit. In addition, I show that the Green function is related with spherical photon orbits, and it also recovers the four fold singular structure of Green functions that are seen in Schwarzschild [108] and other spacetimes [112]. In future work I will check this Green function against numerical results from Zenginoglu [113].

1.3.5.3 My specific contributions

I performed all the calculations up to this point and wrote an initial draft of the paper, with numerous comments and suggestions from Chen.

Bibliography

[1] E. Barausse, V. Morozova and L. Rezzolla, Astrophys. J. **758**, 63 (2012).

[2] A. Abramovici *et al.*, Science **256** 325 (1992).

[3] http://www.virgo.infn.it.

[4] http://geo600.aei.mpg.de.

[5] http://tamago.mtk.nao.ac.jp.

[6] K. Yamamoto *et al.*, J. Phys.: Conf. **122**, 012002 (2008).

[7] http://10m-prototype.aei.uni-hannover.de/.

[8] D. Robertson *et al.*, Rev. Sci. Instrum. **66**, 4447 (1995).

[9] C. Zhao *et al.*, J. Phys.: Conf. Ser. **32**, 368 (2006).

[10] T. Corbitt *et al.*, Phys. Rev. Lett., **98**, 150802 (2007).

[11] P. Fritschel, Proc. SPIE, **4856**, 282 (2003).

[12] S. Hughes and K. Thorne, Phys. Rev. D **58**, 122002 (1998).

[13] M. Zucker and S. Whitcomb, http://www.ligo.caltech.edu/docs/P/P940008-00.pdf.

[14] http://www.ligo.caltech.edu/advLIGO.

[15] M. Evans *et al.*, Phys. Rev. D **78**, 102003 (2008).

[16] http://wwwcascina.virgo.infn.it/advirgo/.

[17] V. B. Braginsky, Sov. Phys. JETP **26**, 831 (1968).

[18] V. B. Braginsky, and F. Khalili, *Quantum Measurement*, Cambridge University Press (1992).

[19] T. J. Kippenberg and K. J. Vahala, Science **321**, 1172 (2008).

[20] A. Safavi-Naeini *et al*, arXiv:1302.6179.

[21] Y. Chen, arXiv: 1302.1924

[22] M. Aspelmeyer, T. Kippenberg and F. Marquart, arXiv: 1303.0733

[23] T. Regge and J. A. Wheeler, Phys. Rev. **108** 1063, (1957).

[24] F. Zerilli, Phys. Rev. Lett., **24** 737 (1970).

[25] V. Moncrief, Annals of Physics, **88** 343, (1974).

[26] S. Teukolsky, Astrophys. J. **185** 635, (1973).

[27] E. Newman and R. Penrose, J. Math. Phys. **3**, 566 (1962).

[28] P. Chrzanowski, Phys. Rev. D **11**, 2042 (1975).

[29] L. Kegeles and J. Cohen, Phys. Rev. D **19**, 1641 (1979).

[30] J. Stewart, Proc. R. Soc. Lond. A **367**, 527 (1979).

[31] R. Wald, Phys. Rev. Lett. **41**, 203 (1978).

[32] B. Whiting, J. Math. Phys. **30**, 1301 (1989).

[33] K. Kokotas and B. Schmidt, Living Rev. Relativity **2**, 2 (1999).

[34] H. Nollert, Class. Quant. Grav. **16**, R159 (1999).

[35] E. Berti, V. Cardoso and A. Zhidenko, Class. Quant. Grav. **26**, 163001 (2009).

[36] R. Konoplya and A. Zhidenko, Rev. Mod. Phys. **83**, 793 (2011).

[37] T. Hong, H. Yang, E. Gustafson, R. Adhikari and Y. Chen, Phys. Rev. D **87**, 082001 (2013).

[38] G. Cole, W. Zhang, M. Martin, J. Ye and M. Aspelmeyer, arXiv: 1302.6489.

[39] T. Hong, H. Yang, H. Miao and Y. Chen, arXiv: 1110:3348.

[40] W. Marshall, C. Simon, R. Penrose and D. Bouwmeester, Phys. Rev. Lett **91** 130401 (2003).

[41] P. Rabl, Phys. Rev. Lett. **107**, 063601 (2011).

[42] A. Nunnenkamp, K. Børkje, and S. M. Girvin, Phys. Rev. Lett. **107**, 063602 (2011).

[43] G. Harry et al., Class. Quantum. Grav. **24**, 405 (2007).

[44] H. Yang, H. Miao and Y. Chen, Phys. Rev. A. **85**, 040101, (2012).

[45] H. Yang, H. Miao and Y. Chen, arXiv: 1111.6079.

[46] J. Majer *et al.* Nature **449**, 443, (2007).

[47] H. Lee, Y. Cheng and G. Fleming, Science **316**, 1462, (2007).

[48] S. Diehl *et al.* Nature Physics **4**, 878, (2008).

[49] M. M. Wolf *et al.*, Phys. Rev. Letter. **101**, 150402 (2008).

[50] H. P. Breuer, E. M. Laine, and J. Piilo, Phys. Rev. Lett. **103**, 210401 (2009).

[51] A. Rivas, S. F. Huelga, and M. B. Plenio, Phys. Rev. Lett. **105**, 050403 (2010).

[52] N. Gisin, and I. C. Percival, J. Phys. A: Math. Gen. **25** 5677 (1992).

[53] L. Diósi, N. Gisin, and W. T. Strunz, Phys. Rev. A **58**, 1699 (1998).

[54] L. Diósi, and W. Strunz, Phys. Lett. A **235**, 569 (1997).

[55] H. M. Wiseman, and G. J. Milburn, *Quantum Measurement and Control*, Cambridge University Press, 2010.

[56] L. Diósi, Phys. Rev. Lett. **100**, 080401 (2008).

[57] H. W. Wiseman, and J. M. Gambetta, Phys. Rev. Lett. **101**, 140401 (2008).

[58] L. Viola, E. Knill, and S. Lloyd, Phys. Rev. Lett. **82**, 2417 (1999).

[59] M. J. Biercuk, H. Uys, A. P. VanDevender, N. Shiga, W. M. Itano, and J. J. Bollinger, Nature **458**, 996 (2009).

[60] G. de Lange *et al.*, Science **330**, 60 (2010).

[61] F. Khalili, H. Miao, H. Yang *al.*, Phys. Rev. A. **86**, 033840 (2012).

[62] A. Safavi-Naeini *et al.*, Phys. Rev. Lett. **108**, 033602 (2012).

[63] K. Ni *et al.*, Phys. Rev Lett. **108** 214302 (2012)

[64] A. Geraci, S. Papp and J. Kitching, Phys. Rev. Lett. **105** 101101 (2010).

[65] A. Arvanitaki and A. Geraci, Phys. Rev. Lett. **110** 071105 (2013).

[66] D. Chang *et al.*, Proc. Natl. Acad. Sci. USA. **107** 1005 (2009).

[67] H. Yang, H. Miao, D. Lee, B. Helou and Y. Chen, Phys. Rev. Lett. **110** 170401, (2013).

[68] P. M. Bonifacio *et al.*, Class. Quantum Grav. **26**, 145013 (2009).

[69] L. Diósi, Phys. Lett. A **105**, 199 (1984).

[70] L. Diósi L, Phys. Lett. A **120**, 377 (1987).

[71] L. Diósi, Phys. Rev. A. **40**, 1165 (1989).

[72] L. Diósi and J. J. Halliwell, Phys. Rev. Lett. **81**, 2846 (1998).

[73] R. Penrose, Gen. Rel. Grav. **28**, 581 (1996).

[74] R. Penrose, *The Road to Reality: A Complete Guide to the Laws of the Universe,* Alfred A. Knopf inc., New York (2005).

[75] W. Marshall, C. Simon, R. Penrose, and D. Bouwmeester, Phys. Rev. Lett. **91**, 130401 (2003).

[76] T. Hong *et al.*, arXiv:1110.3349 [quant-ph] (2011).

[77] J. van Wezel and T. H. Oosterkamp, Proc. R. Soc. A **468**, 35 (2012).

[78] R. Kaltenbaek *et al.*, Exp. Astron. **34**, 123 (2012).

[79] O. Romero-Isart *et al.*, Phys. Rev. Lett. **107**, 020405 (2011).

[80] O. Romero-Isart, Phys. Rev. A **84**, 052121 (2011).

[81] M. Maggiore, Phys. Lett. B, **319**, 83 (1993).

[82] S. Das and E. C. Vagenas, Phys. Rev. Lett **101**, 221301 (2008).

[83] I. Pikovski *et al.*, Nature Phys. **8**, 393 (2012).

[84] C. Moller, *Les Theories Relativistes de la Gravitation* Colloques Internationaux CNRX 91 ed A Lichnerowicz and M-A Tonnelat (Paris: CNRS) (1962).

[85] L. Rosenfeld, Nucl. Phys. **40**, 353 (1963).

[86] S. Carlip, Class. Quantum Grav. **25**, 154010 (2008).

[87] T. Corbitt *et al.*, Phys. Rev. Lett. **98**, 150802 (2007); Phys. Rev. Lett. **99**, 160801 (2007); Phys. Rev. A **73**, 023801 (2006).

[88] K. Ishidoshiro *et al.*, Phys. Rev. Lett. **106**, 161101 (2011).

[89] H. Yang, H. Miao and Y. Chen, arXiv: 1211.5410.

[90] S. Detweiler, Phys. Rev. Lett. **86**1931 (2001).

[91] S. Detweiler, E. Messaritaki and B. F. Whiting, Phys. Rev. D **67** 104016 (2003).

[92] L. Barack and A. Ori, Phys. Rev. D **66** 084022 (2002).

[93] N. Warburton, S. Akcay, L. Barack, J. R. Gair and N. Sago, Phys. Rev. D **85** 061501 (2012); B. Wardell, private communication.

[94] I. Vega and S. Detweiler, Phys. Rev. D **77** 084008 (2008).

[95] P. Diener, I. Vega, B. Wardell and S. Detweiler, Phys. Rev. Lett. **108** 191102 (2012).

[96] H. Yang, D. Nichols, F. Zhang, A. Zimmerman, Z. Zhang and Y. Chen, Phys. Rev. D **86** 104006 (2012).

[97] E. W. Leaver, Proc. R. Soc. Lond. A **402**, 285 (1985).

[98] V. Ferrari and B. Mashhoon, Phys. Rev. D **30**, 295 (1984).

[99] S. Iyer and C. M. Will, Phys. Rev. D **35**, 3621 (1987).

[100] H. Yang, F. Zhang, A. Zimmerman, D. Nichols, E. Berti and Y. Chen, Phys. Rev. D **87** 041502 (2012).

[101] S. Detweiler, Astrophys. J. **239** 292 (1980).

[102] M. Sasaki and T. Nakamura, Gen. Rel. Grav. **22**, 1351 (1990).

[103] N. Anderson, Classical Quant. Grav. **10**, L61 (1993).

[104] S. Hod, Phys. Rev. D **78** 084035 (2008).

[105] V. Cardoso, Phys. Rev. D **70** 127502 (2004).

[106] K. Glampedakis, N. Anderson, Phys. Rev. D **64** 104021, (2001).

[107] E. Harms, S. Bernuzzi, B. Brügmann, arXiv:1301.1591 (2013).

[108] S. Dolan and A. Ottewill, Phys. Rev. D **84** 104002, (2011).

[109] M. Casals, S. R. Dolan, A. C. Ottewill and B. Wardell, Phys. Rev. D **79**, 124043, (2009).

[110] M. Casals, S. R. Dolan, A. C. Ottewill and B. Wardell, Phys. Rev. D **79**, 124044, (2009).

[111] A. Zenginoglu, C. R. Galley, Phys. Rev. D **86** 064030, (2012)

[112] M. Casals, B. C. Nolan, arXiv:1204.0407.

[113] A. Zenginoglu, private Communication.

Part I

Topics in gravitational wave detectors

Chapter 2

Brownian thermal noise in multilayer coated mirrors

We analyze the Brownian thermal noise of a multi-layer dielectric coating, used in high-precision optical measurements including interferometric gravitational-wave detectors. We assume the coating material to be isotropic, and therefore study thermal noises arising from shear and bulk losses of the coating materials. We show that coating noise arises not only from layer thickness fluctuations, but also from fluctuations of the interface between the coating and substrate, driven by fluctuating shear stresses of the coating. Although thickness fluctuations of different layers are statistically independent, there exists a finite coherence between the layers and the substrate-coating interface. In addition, photoeleastic coefficients of the thin layers (so far not accurately measured) further influences the thermal noise, although at a relatively low level. Taking into account uncertainties in material parameters, we show that significant uncertainties still exist in estimating coating Brownian noise.

2.1 Introduction

Brownian thermal noise in the dielectric coatings of mirrors limits some high precision experiments which use optical metrology. This thermal noise is currently a limit for fixed spacer Fabry-Perots used in optical clock experiments [1] and is estimated to be the dominant noise source in the most sensitive band of modern gravitational wave detectors (e.g., advanced LIGO, GEO, Advanced VIRGO and KAGRA) [2–6]. Recent work has indicated the possibility of reducing the various kinds of internal thermal noise by redesigning the shape of the optical mode [7, 8] or the structure of the multi-layer

coating [9, 10]. In this paper, we seek a more comprehensive understanding of coating Brownian noise. We first identify all thermally fluctuating physical properties (e.g., different components of the strain tensor) of the coating that can lead to coating Brownian noise, and calculate how each of them contributes (linearly) to the total noise; we then calculate their individual levels of fluctuation, as well as cross correlations between pairs of them, using the fluctuation dissipation theorem [11–13]. In this way, as we compute the total coating Brownian noise, it will be clear how each factor contributes, and we will be in a better position to take advantage of possible correlations between different components of the noise.

As a starting point, we will assume each coating layer to be isotropic, and hence completely characterized by its complex bulk modulus K and shear modulus μ—each with small imaginary parts related to the energy loss in the bulk and shear motions. The complex arguments of these moduli are often referred to as *loss angles*. While values of K and μ are generally known, loss angles of thin optical layers vary significantly according to the details of the coating process (i.e., how coating materials are applied onto the substrate and their composition). Since the loss angles are small, we will use K and μ to denote the real parts of the bulk and shear moduli, and write the complex bulk and shear moduli, $\tilde{K}$ and $\tilde{\mu}$ as

$$\tilde{K} = K(1 + i\phi_B), \quad \tilde{\mu} = \mu(1 + i\phi_S). \tag{2.1}$$

Here we have used subscripts B and S to denote bulk and shear, because these will be symbols for bulk strain and shear strain.

Note that our definition differs from that in previous literature, which used $\phi_\parallel$ and $\phi_\perp$ to denote losses induced by elastic deformations parallel and perpendicular to the coating-substrate interface [14]. As we shall argue in Appendix 2.C, $\phi_\parallel$ and $\phi_\perp$ cannot be consistently used as independent loss angles of a material. Only when assuming $\phi_\parallel = \phi_\perp = \phi_S = \phi_B$ will the previous calculation agree with ours — if we ignore light penetration into the coating. There is, a priori, no reason why these loss angles should all be equal, although this assumption has so far been compatible with existing ring-down measurements and direct measurements of coating thermal noise [15].

Brownian thermal fluctuations of a multilayer coating can be divided as follows: (i) thickness fluctuation of the coating layers, (ii) fluctuation of the coating-substrate interface, and (iii) refractive index fluctuations of the coating layers associated with longitudinal (thickness) and transverse (area) elastic deformations—as illustrated in Figure 2.1. Using what is sometimes referred to as Levin's direct approach [12] (based on the fluctuation dissipation theorem), and writing the coating Brownian noise as a linear combination of the above fluctuations, allows the construction of a corresponding set of forces acting on the coating and calculation of the thermal noise spectrum from the the dissipation associated with the simultaneous application of these forces. This has been carried out by Gurkovsky
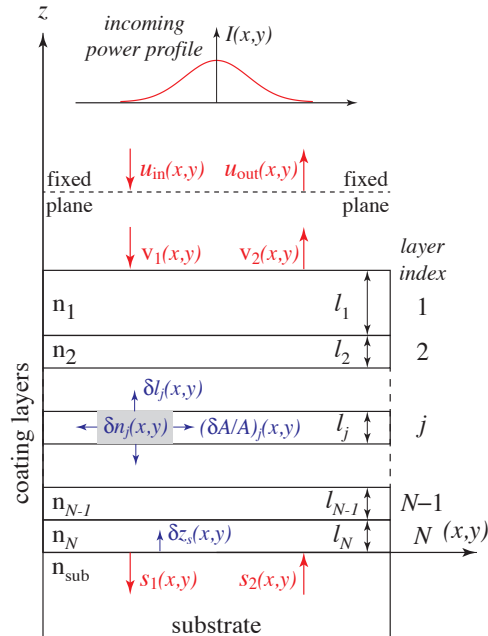
Figure 2.1: Drawing of a mirror coated with multiple dielectric layers. Shown here are the various fluctuations that contribute to coating noise, i.e., fluctuations in the amplitude and phase of the returning light caused by fluctuations in the geometry [including: layer thickness δl_j, layer area stretch $(\delta A/A)_j$, interface height z_s of the coating-substrate configuration] and in the refractive indices $\delta n_j(x, y, z)$ of the layers.

and Vyatchanin [16], as well as Kondratiev, Gorkovsky and Gorodetsky [17]. However, in order to obtain insights into coating noise that have proven useful we have chosen to calculate the cross spectral densities for each of (i), (ii), and (iii), and provide intuitive interpretations of each. We will show, in Sec. 2.4, that (i) and (ii) above are driven by both bulk and shear fluctuations in the coating, in such a way that thickness fluctuations of the j-th layer δl_j, or in transverse locations separated by more than a coating thickness, are mutually statistically independent, yet each δl_j is correlated with the fluctuation of the coating-substrate interface z_s—because z_s is driven by the *sum* of thermal stresses in the coating layers. We will also show that when coating thickness is much less than the beam spot size, the only significant contribution to (iii) arises from longitudinal (thickness) fluctuations, see Appendix 2.A.4 for details.

   This paper is organized as follows. In Sec. 2.2, we express the amplitude and phase of the reflected field in terms of fluctuations in the coating structure, thereby identifying the various components of coating thermal noise. In Sec. 2.3, we introduce the loss angles of isotropic coating materials, and use the fluctuation-dissipation theorem to calculate the cross spectral densities of the coating thermal noise ignoring light penetration into the multi-layer coating. In Sec. 2.4, we discuss in detail the cross spectra of all the components of the coating structure fluctuation, thereby obtaining the full formula for coating thermal noise, taking light penetration within the muli-layers into account.

The key formulas summarizing phase and amplitude noise spectrum are given in Eq. (2.94) and Eq. (2.95). In Sec. 2.5, we discuss the effect of light penetration on coating thermal noise, using typical optical coating structures. In Sec. 2.6, we discuss the dependence of thermal noise on the material parameters, and optimize the coating structure in order to lower the thermal noise. In Sec. 2.7, we discuss how only one combination of the two loss angles have been measured in past experiments, and how other different combinations can be measured using a new experimental geometry. Finally, we summarize our main conclusions in Sec. 2.8.

2.2   Components of the coating thermal noise

In this section, we express the coating thermal noise in terms of the elastic deformations of the coated substrate.

2.2.1   Complex reflectivity

As illustrated in Figure 2.1, we consider a laser field normally incident (along the $-z$ direction) onto the mirror, with complex amplitude profile $u_{\text{in}}(x, y)$ at a fixed reference plane (dashed line in the figure) and intensity profile $I(x, y) = |u_{\text{in}}(x, y)|^2$. Henceforth in the paper, we shall use arrows (e.g., $\vec{x}$) to denote the 2-dimensional vector (x, y) in the *transverse plane*, and boldface letters (e.g., $\mathbf{x}$) to denote 3-dimensional vectors.

Because the coating thickness is much less than the beam spot size, the reflected field (traveling along the $+z$ direction) at transverse location $\vec{x}$ has an amplitude given by

$$u_{\text{out}}(\vec{x}) = \rho_{\text{tot}}(\vec{x}) u_{\text{in}}(\vec{x}),$$

(2.2)

which only depends on the complex reflectivity $\rho_{\text{tot}}(\vec{x})$ and the complex amplitude of the incident field $u_{\text{in}}(\vec{x})$, at the same location $\vec{x}$ — assuming no incident light from the substrate (i.e., $s_2 = 0$). Here $\rho_{\text{tot}}(\vec{x})$ can be separated into three factors, as

$$\rho_{\text{tot}}(\vec{x}) = \frac{u_{\text{out}}(\vec{x})}{u_{\text{in}}(\vec{x})} = \left[\frac{u_{\text{out}}(\vec{x})}{v_2(\vec{x})}\right] \left[\frac{v_1(\vec{x})}{u_{\text{in}}(\vec{x})}\right] \left[\frac{v_2(\vec{x})}{v_1(\vec{x})}\right]$$

(2.3)

in which $v_1(\vec{x})$ is the incident complex amplitude at the coating-air interface, while $v_2(\vec{x})$ is the reflected complex amplitude at that interface.

The first two phase factors on the right-hand side of Eq. (2.3) are gained by the light when traveling across the gap between the fixed reference plane (see Fig. 2.1) and the coating-air interface;

we therefore obtain, up to a constant phase factor,

$$\left[\frac{u_{\text{out}}(\vec{x})}{v_2(\vec{x})}\right]\left[\frac{v_1(\vec{x})}{u_{\text{in}}(\vec{x})}\right] = e^{-2ik_0\left[\delta z_s(\vec{x})+\sum_{j=1}^{N}\delta l_j(\vec{x})\right]} \tag{2.4}$$

where $k_0 = \omega_0/c$ is the wave number of the laser (ω_0 its angular frequency) in vacuum, $\delta z_s(\vec{x})$ is the vertical displacement of the coating-substrate interface (from its zero point), and $\delta l_j(\vec{x})$ is the thickness fluctuation of the j-th coating layer — both evaluated at a transverse location $\vec{x}$.

The remaining complex reflectivity $v_2(\vec{x})/v_1(\vec{x})$ can be determined as a function of the phase shift experienced by the field in each layer, as well as the reflectivity of each interface, as described in detail in Sec. 2.5. We can write:

$$v_2/v_1 = \rho[\phi_1(\vec{x}),\ldots,\phi_N(\vec{x}); r_{01}(\vec{x}),\ldots,r_{Ns}(\vec{x})]. \tag{2.5}$$

Here ρ is the complex reflectivity of a multi-layer coating, measured at the coating-air interface, which in turn depends on the optical thickness $\phi_j(\vec{x})$ of each layer ($j = 1,\ldots,N$) and the reflectivity $r_{p,p+1}(\vec{x}) \equiv r_p(\vec{x})$ of each interface, ($p = 0,\ldots,N$, with $p = N+1$ representing the substrate, and $p = 0$ the vacuum outside the coating). Assembling the above equations (2.3)–(2.5), we obtain:

$$\rho_{\text{tot}}(\vec{x}) = e^{-2ik_0\left[\delta z_s(\vec{x})+\sum_{j=1}^{N}\delta l_j(\vec{x})\right]}\rho[\{\phi_j(\vec{x})\}; \{r_p(\vec{x})\}] \tag{2.6}$$

Brownian thermal forces lead to fluctuations in both the real and imaginary parts of this complex reflectivity. Fluctuations in the argument of the complex reflectivity phase modulates the outgoing light and directly produce sensing noise. Fluctuations in the magnitude, on the other hand, amplitude modulate the outgoing light, and produce a ponderomotive force noise.

2.2.2 Thermal Phase and Amplitude Noise

Brownian thermal fluctuations in coating geometry and refractive index modify the complex reflectivity $\rho_{\text{tot}}(\vec{x})$ defined in Eq. (2.6). The real and imaginary parts of

$$\delta \log \rho_{\text{tot}}(\vec{x}) = \frac{\delta \rho_{\text{tot}}(\vec{x})}{\rho_{\text{tot}}(\vec{x})} \tag{2.7}$$

encode the amplitude/intensity and phase fluctuations of the reflected light at position $\vec{x}$ on the mirror surface. In particular, intensity fluctuation of the reflected light is given by

$$\frac{\delta I(\vec{x})}{I(\vec{x})} = 2\frac{\delta|\rho_{\text{tot}}(\vec{x})|}{|\rho_{\text{tot}}(\vec{x})|} = 2\text{Re}\left[\delta \log \rho_{\text{tot}}(\vec{x})\right] \tag{2.8}$$

while phase fluctuation is given by

$$\delta\phi(\vec{x}) = \delta \arg\left[\rho_{\mathrm{tot}}(\vec{x})\right] = \mathrm{Im}\left[\delta \log \rho_{\mathrm{tot}}(\vec{x})\right]. \tag{2.9}$$

In this way, if we further write

$$\xi(\vec{x}) - i\zeta(\vec{x}) = -\frac{i}{2k_0}\delta\left[\log \rho_{\mathrm{tot}}\right], \tag{2.10}$$

with both ξ and ζ real-valued functions of $\vec{x}$, with the dimensionality of displacement; they will represent phase and amplitude noise, respectively. In particular, from Eq. (2.9), we have

$$\delta\phi(\vec{x}) = 2k_0\xi(\vec{x}). \tag{2.11}$$

Because we measure the mirror's position through the additional phase shift gained by the light after being reflected, through the relation $\Delta\phi = 2k_0\Delta x$, Eq. (2.11) indicates that $\xi(\vec{x})$ is the displacement noise due to phase fluctuations of the reflected light imposed by the coating.

The quantity ζ (which, like ξ, is a length) is connected to amplitude/intensity noise via

$$2k_0\zeta(\vec{x}) = \mathrm{Re}\left[\delta \log \rho_{\mathrm{tot}}\right] = \frac{\delta I(\vec{x})}{2I(\vec{x})}. \tag{2.12}$$

As we shall discuss in Sec. 2.2.5, ζ will cause a fluctuating force on the mirror, and can eventually be converted to a displacement noise via a dimensionless factor, although the effect will turn out to be small for gravitational-wave detectors.

Inserting the dependence of ρ_{tot} on ρ, l_j and z_s [Cf. Eq. (2.6)], we obtain

$$\begin{aligned}
\xi(\vec{x}) - i\zeta(\vec{x}) &= -\delta z_s(\vec{x}) - \sum_{l=1}^{N}\delta l_j(\vec{x}) \\
&\quad - \sum_{j=1}^{N}\frac{i}{2k_0}\left[\frac{\partial \log \rho}{\partial \phi_j}\cdot\delta\phi_j(\vec{x})\right] \\
&\quad - \sum_{p=0}^{N}\frac{i}{2k_0}\left[\frac{\partial \log \rho}{\partial r_p}\cdot\delta r_p(\vec{x})\right].
\end{aligned} \tag{2.13}$$

The first two terms are due to the motion of the coating-air interface at location $\vec{x}$ and thickness fluctuations of the layers, while the last two terms are due to light penetration into the coating layers (see Fig. 2.5). In particular, the third term is due to fluctuations in the total phase the light gains when propagating within the j-th layer, while the fourth term is due to the (effective) reflectivity of the p-th interface (with $p = 0$ indicating the coating-air interface), whose origin will be explained below.

2.2.3 Fluctuations $\delta\phi_j$ and δr_p

Light propagating within the coating layers are affected by the *photoelastic* effect, namely an *isothermal* fluctuation in $\delta n_j(\mathbf{x})$ (note here that $\mathbf{x}$ is a 3-D vector) due to fluctuating Brownian stresses exerted onto the coating materials. Assuming *isotropy* of the coating materials, we can write

$$\delta n_j(\mathbf{x}) = \beta_j^L S_{zz}(\mathbf{x}) + \beta_j^T \left[S_{xx}(\mathbf{x}) + S_{yy}(\mathbf{x}) \right] \tag{2.14}$$

with

$$\beta_j^L \equiv \left(\frac{\partial n_j}{\partial \log l} \right)_{A_j}, \quad \beta_j^T \equiv \left(\frac{\partial n_j}{\partial \log A} \right)_{l_j}. \tag{2.15}$$

Here L stands for longitudinal, and T stands for transverse, and the subscript A_j and l_j indicate fixing transverse area and longitudinal length, respectively. We have also used the usual strain definition

$$S_{ij} \equiv \frac{1}{2} \left[\frac{\partial u_i}{\partial x_j} + \frac{\partial u_j}{\partial x_i} \right] \tag{2.16}$$

where $u_i(\mathbf{x})$, $i = 1, 2, 3$ are components of the displacement vector of the mass element at position $\mathbf{x}$. Refer to Appendix 2.B for more details regarding defining the elasticity quantities, and Appendix 2.A.1 for more details on the photo elastic effect.

We note that in Eq. (2.14) S_{zz} is the fractional increase in length (i.e., linear expansion) in the longitudinal direction, while $S_{xx} + S_{yy}$ is the fractional increase in the transverse area. According to Appendix 2.A.4, we can ignore the second term representing area fluctuations in Eq. (2.14) when the beam spot size is much larger than the coating thickness. In this case, we write β_j in place for β_j^L, whose value can be expressed in terms of a particular component of the photo elastic tensor, see Eq. (2.119).

As we discuss in Appendix 2.A.2, the first term of Eq. (2.14) causes two effects for light propagating along each direction (i.e., $+z$ and $-z$): it adds an additional phase shift, and it back-scatters a fraction of the light into the opposite direction. As we show in Appendix 2.A.3 [c.f. Eqs. (2.130)–(2.132)], these effects can be accounted for by modifying the phase shift $\delta\phi_j$ of each coating layer and changing the reflectivity δr_j of interface, in the following manner:

$$\delta\phi_j = k_0 \Big[(n_j + \beta_j)\delta l_j - \frac{1 - r_j^2}{2r_j} \beta_j \delta l_j^c$$
$$+ \frac{1 + r_{j-1}^2}{2r_{j-1}} \beta_{j-1} \delta l_{j-1}^c \Big], \tag{2.17}$$
$$\delta r_j = k_0 t_j^2 \beta_j \delta l_j^s. \tag{2.18}$$

Here we have defined

$$\delta l_j^c = -\int_0^{l_j} S_{zz}(z_{j+1} + z)\cos(2k_0 n_j z)dz\,, \tag{2.19}$$

$$\delta l_j^s = -\int_0^{l_j} S_{zz}(z_{j+1} + z)\sin(2k_0 n_j z)dz \tag{2.20}$$

for $j \geq 1$, $\delta l_0^s = \delta l_0^c = 0$, and

$$z_j \equiv \sum_{n=j}^{N} l_n \tag{2.21}$$

marks the z-coordinate of the top surface of the j-th layer. We can also write

$$\delta l_j = \int_0^{l_j} S_{zz}(z_{j+1} + z)dz\,. \tag{2.22}$$

Note that

$$\begin{array}{c} \text{total coating} \\ \text{thickness} \end{array} \equiv z_1 > z_2 > \ldots > z_{N+1} \equiv 0. \tag{2.23}$$

Note that δr_j, as well as the last two terms in $\delta\phi_j$ are due to back-scattering, and have not been considered by previous authors.

Inserting Eqs. (2.17), (2.18) into Eq. (2.13), we obtain:

$$\xi(\vec{x}) - i\zeta(\vec{x}) = -z_s(\vec{x}) - \sum_{j=1}^{N} \int_{z_{j+1}}^{z_j} \left[1 + \frac{i\epsilon_j(z)}{2}\right] u_{zz}(\vec{x}, z)dz \tag{2.24}$$

where

$$\begin{aligned}
\epsilon_j(z) &= (n_j + \beta_j)\frac{\partial \log \rho}{\partial \phi_j} \\
&\quad - \beta_j \Bigg[\frac{1 - r_j^2}{2r_j}\frac{\partial \log \rho}{\partial \phi_j} \\
&\quad\quad - \frac{1 + r_j^2}{2r_j}\frac{\partial \log \rho}{\partial \phi_{j+1}}\Bigg]\cos[2k_0 n_j(z - z_j)] \\
&\quad - t_j^2 \beta_j \frac{\partial \log \rho}{\partial r_j}\sin[2k_0 n_j(z - z_{j+1})]\,, \tag{2.25}
\end{aligned}$$

a term that accounts for all effects associated with light penetration. Here we need to formally define

$$\frac{\partial \log \rho}{\partial \phi_{N+1}} = 0 \tag{2.26}$$

because ϕ_{N+1} does not really exist. Alternatively, we can also write formulas separately for ξ and

ζ, using only real-valued quantities. For ξ, we have,

$$
\begin{aligned}
\xi(\vec{x}) \;=\;& -z_s(\vec{x}) \\
& -\sum_{j=1}^{N}\left[\mathcal{T}_j^{\xi}\delta l_j(\vec{x})+\mathcal{T}_j^{\xi c}\delta l_j^c(\vec{x})+\mathcal{T}_j^{\xi s}\delta l_j^s(\vec{x})\right],
\end{aligned}
\tag{2.27}
$$

where

$$
\mathcal{T}_j^{\xi} \;=\; 1-\frac{n_j+\beta_j}{2}\mathrm{Im}\left(\frac{\partial\log\rho}{\partial\phi_j}\right),
\tag{2.28}
$$

$$
\begin{aligned}
\mathcal{T}_j^{\xi c} \;=\;& -\frac{\beta_j}{4}\mathrm{Im}\left(\frac{\partial\log\rho}{\partial\phi_j}\right)\left(\frac{1-r_j^2}{r_j}\right) \\
& +\frac{\beta_j}{4}\mathrm{Im}\left(\frac{\partial\log\rho}{\partial\phi_{j+1}}\right)\left(\frac{1+r_j^2}{r_j}\right),
\end{aligned}
\tag{2.29}
$$

$$
\mathcal{T}_j^{\xi s} \;=\; -\frac{\beta_j t_j^2}{2}\mathrm{Im}\left(\frac{\partial\log\rho}{\partial r_j}\right),
\tag{2.30}
$$

are transfer functions from the various δl's to the displacement-equivalent thermal noise (see Fig. 2.6). For ζ, we have

$$
\zeta(\vec{x})=\sum_{j=1}\left[\mathcal{T}_j^{\zeta}\delta l_j(\vec{x})+\mathcal{T}_j^{\zeta c}\delta l_j^c(\vec{x})+\mathcal{T}_j^{\zeta s}\delta l_j^s(\vec{x})\right]
\tag{2.31}
$$

where

$$
\mathcal{T}_j^{\zeta} \;=\; \frac{n_j+\beta_j}{2}\mathrm{Re}\left(\frac{\partial\log\rho}{\partial\phi_j}\right),
\tag{2.32}
$$

$$
\begin{aligned}
\mathcal{T}_j^{\zeta c} \;=\;& \frac{\beta_j}{4}\mathrm{Re}\left(\frac{\partial\log\rho}{\partial\phi_j}\right)\left(\frac{1-r_j^2}{r_j}\right) \\
& -\frac{\beta_j}{4}\mathrm{Re}\left(\frac{\partial\log\rho}{\partial\phi_{j+1}}\right)\left(\frac{1+r_j^2}{r_j}\right),
\end{aligned}
\tag{2.33}
$$

$$
\mathcal{T}_j^{\zeta s} \;=\; \frac{\beta_j t_j^2}{2}\mathrm{Re}\left(\frac{\partial\log\rho}{\partial r_j}\right).
\tag{2.34}
$$

For an arbitrary stack of dielectrics, ζ is comparable to the part of ξ [c.f. Eq. (2.25)] that involves light penetration into the layers. In practice, however, for highly reflective stacks, the real parts of $\partial\log\rho/\partial\phi_j$ and $\partial\log\rho/\partial r_j$ all turn out to be small, and therefore fluctuations in ζ (which correspond to amplitude fluctuations) should be much less than fluctuations in ξ (which corresponds to phase fluctuations).

2.2.4 Mode selection for phase noise

So far we have dealt with phase and amplitude noise as functions at each location $\vec{x}$ on the mirror surface. However, there is only one displacement noise that the light will sense. In this and the next subsection, we show how $\xi(\vec{x})$ and $\zeta(\vec{x})$ should be converted into measurement noise. In doing so, we recognize that only one spatial optical mode is injected on resonance in the optical cavity, and this mode has a complex amplitude of $u_0(\vec{x})$ at the mirror surface. Now suppose we have $u_{\text{in}} = u_0(\vec{x})$ incident on the mirror surface, we will then have $u_{\text{out}}(\vec{x}) = \rho_{\text{tot}}(\vec{x})u_0(\vec{x})$, which contains not only the resonant mode, but also other modes, which do not resonate in the cavity.

Let us select only the component of $u_{\text{out}}(\vec{x})$ that is in the resonant spatial mode that is driven, then we have a complex reflectivity of

$$\bar{\rho} = \frac{\int u_0^*(\vec{x})u_{\text{out}}(\vec{x})d^2\vec{x}}{\int u_0^* u_0 d\vec{x}} = \frac{\int \rho_{\text{tot}}(\vec{x})I(\vec{x})d^2\vec{x}}{\int I(\vec{x})d^2\vec{x}}, \tag{2.35}$$

specifically for the resonant mode, and hence independent of $\vec{x}$. Here we have defined $I(\vec{x}) \equiv |u_0(\vec{x})|^2$. Note that the bar on top of $\bar{\rho}$ represents averaging over the phase front, instead of averaging over time.

Now, inserting Eq. (2.10) as definitions for $\xi(\vec{x})$ and $\zeta(\vec{x})$ into Eq. (2.35), we obtain the fluctuating part of $\bar{\rho}$

$$\frac{\delta\bar{\rho}}{\bar{\rho}} = 2ik_0(\bar{\xi} - i\bar{\zeta}), \tag{2.36}$$

where

$$\bar{\xi} \equiv \frac{\int \xi(\vec{x})I(\vec{x})d^2\vec{x}}{\int I(\vec{x})d^2\vec{x}}, \quad \bar{\zeta} \equiv \frac{\int \zeta(\vec{x})I(\vec{x})d^2\vec{x}}{\int I(\vec{x})d^2\vec{x}}. \tag{2.37}$$

Note that $2ik_0\bar{\xi}$ is the additional phase gained by the returning light, while $2k_0\bar{\zeta}$ is the relative change in amplitude [see discussions in Sec. 2.2.2]. Focusing first on $\bar{\xi}$, we note that this creates the same phase change as that gained by the reflected light if the mirror does not deform but instead is displaced along the beam by $\bar{\xi}$. In this way, $\bar{\xi}$ is an error in our measurement of the mirror's displacement.

2.2.5 Conversion of amplitude noise into displacement

The amplitude thermal noise can produce a spurious GW signal by modulating the radiation pressure acting on the mirror, which in turn drives spurious mirror motion. Let us first consider a single-bounce scenario, in which an incoming beam with intensity profile $I(\vec{x})$, unaffected by thermal noise, is reflected with an intensity profile $I(\vec{x}) + \delta I(\vec{x})$, with $\delta I(\vec{x})$ induced by amplitude thermal noise.

In this case, the mirror feels a thermal-noise-induced recoil force of

$$F_{\text{th}}^{\text{single}} = \int \frac{\delta I(\vec{x})}{c} d^2 \vec{x}. \tag{2.38}$$

Using Eqs. (2.12) and (2.37), we obtain

$$F_{\text{th}}^{\text{single}} = \frac{4I_0 k_0}{c} \bar{\zeta} \tag{2.39}$$

with I_0 the power incident on the mirror. If the mirror is within a cavity, then we need to consider both the increase in the circulating power (which we denote by I_c) with respect to the input power, and the coherent build-up of amplitude modulation within the cavity. We also note that now both the incident and reflected beams contain amplitude modulation, and that we must also consider the effect of this amplitude modulation on the input mirror.

If we restrict ourselves to a single optical cavity on resonance, then the force thermal noise below the cavity bandwidth is given by

$$F_{\text{th}}^{\text{cav}} = \frac{16 k_0 I_c}{c\sqrt{T_{\text{i}}}} \bar{\zeta}. \tag{2.40}$$

Here I_c is the circulating power in the arm cavity. Suppose both input and end mirrors have the same mass M, then the spectrum of cavity length modulation driven by the amplitude thermal noise at angular frequency Ω is given by

$$\sqrt{S_{\text{th}}^{\text{amp}}(\Omega)} = \frac{2}{M\Omega^2} \sqrt{S_{F_{\text{th}}^{\text{cav}}}} = \frac{32\omega_0 I_c}{m\Omega^2 c^2 \sqrt{T_{\text{i}}}} \sqrt{S_{\bar{\zeta}}}. \tag{2.41}$$

Note that $\bar{\zeta}$ has the units of displacement, and therefore the pre-factor in front of $\sqrt{S_{\bar{\zeta}}}$ in Eq. (2.41) is a dimensionless conversion factor from $\bar{\zeta}$ to displacement noise. For Advanced LIGO, this cannot be completely dismissed at this stage, because

$$\frac{32\omega_0 I_c}{m\Omega^2 c^2 \sqrt{T_{\text{i}}}} = 18 \cdot \frac{I_c}{800\,\text{kW}} \cdot \frac{40\,\text{kg}}{m} \cdot \left[\frac{10\,\text{Hz}}{\Omega/(2\pi)}\right]^2 \sqrt{\frac{0.03}{T_{\text{i}}}}. \tag{2.42}$$

Nevertheless, as we will show in Sec. 2.5.2, the minor amplification factor here is not enough to make amplitude noise significant, because ζ is much less than ξ, for the coatings we consider.

2.3 Thermal noise assuming no light penetration into the coating

In this section, we compute the coating Brownian noise assuming that the incident light does not penetrate into the coating. This means light is promptly reflected at the coating-air interface, and

therefore we should only keep the first two terms on the right-hand side of Eq. (2.13), which leads to $\zeta = 0$. We therefore consider only coating phase noise ξ, in particular its weighted average over the mirror surface, $\bar{\xi}$, see Eq. (2.37).

2.3.1 The Fluctuation-Dissipation Theorem

The Fluctuation-Dissipation Theorem relates the near-equilibrium thermal noise spectrum of a generalized coordinate q to the rate of dissipation in the system when a generalized force acts directly on this coordinate. More specifically, the thermal noise spectrum of q at temperature T is given by [13]

$$S_q(f) = \frac{k_B T}{\pi^2 f^2} \text{Re}[Z(f)] \tag{2.43}$$

where f is frequency, $Z(f)$ is the mechanical impedance (inverse of admittance), or

$$Z(f) = -2\pi i f q(f)/F(f). \tag{2.44}$$

Alternatively, suppose we apply a sinusoidal force

$$F(t) = F_0 \cos(2\pi f t) \tag{2.45}$$

with amplitude F_0 acting directly on q, Eq. (2.43) can also be written as

$$S_x(f) = \frac{4k_B T}{\pi f} \frac{W_{\text{diss}}}{F_0^2} = \frac{4k_B T}{\pi f} \frac{U}{F_0^2} \phi \tag{2.46}$$

where W_{diss} is the energy dissipated per cycle of oscillation divided by 2π (in other words, W_{diss} is the average energy loss per radian), U is the peak of the stored energy in the system, and ϕ is the loss angle, defined by

$$\phi = \text{Re}[Z(f)]/\text{Im}[Z(f)]. \tag{2.47}$$

It is important to note that ϕ is, in general, frequency dependent. However, for an elastic body, if the frequency is low enough (well below the first eigenfrequency), then U can be computed using the quasi-static approximation, because it is equal to the elastic energy stored in the equilibrium configuration when a constant force F_0 is applied to the system.

2.3.2 Mechanical energy dissipations in elastic media

It is straightforward to apply Eq. (2.46) to calculate the thermal noise component due to fluctuation of the position of the coating-air interface — the weighted average [c.f. Eq. (2.35)] of the first two

terms of Eq. (2.13). This can be obtained by applying a force F with a pressure profile proportional to $I(\vec{x})$ to the mirror surface (coating-air interface). In this case, elastic energy can be divided into bulk energy U_B and shear energy U_S [Chapter I of Ref. [18]], with

$$U_{\text{coating}} = U_B + U_S = \int_{\text{coating}} \left(\frac{K}{2}\Theta^2 + \mu\Sigma_{ij}\Sigma_{ij} \right) dV \,, \tag{2.48}$$

where Θ is the expansion, and Σ_{ij} is the shear tensor (see Appendix 2.B for details). If we give small imaginary parts to K and μ, writing

$$\tilde{K} = K(1 + i\phi_{\text{B}}) \,, \quad \tilde{\mu} = \mu(1 + i\phi_{\text{S}}) \tag{2.49}$$

then W_{diss} can be written as

$$W_{\text{diss}} = \phi_B U_B + \phi_S U_S. \tag{2.50}$$

Here have introduced the loss angles ϕ_B and ϕ_S, which are associated with the dissipation of expansion energy density and the shear energy density, respectively. Note that our way of characterizing loss differs from previous work by Harry, et. al. [14], because for isotropic materials, ϕ_B and ϕ_S are the two fundamentally independent loss angles that characterize the dissipation of bulk and shear elastic energy; were we to literally adopt $\phi_\perp$ and $\phi_\parallel$ as done in Ref. [14], and consider them independent from each other, then the dissipated energy defined this way can turn out to be negative if certain force distributions are applied onto the mirror, which would be unphysical. See Appendix 2.C for more details.

Once we have introduced ϕ_{B} and ϕ_{S}, other elastic moduli also gain small imaginary parts correspondingly. For example, for the most widely used Young's modulus and Poisson ratio, because

$$K = \frac{Y}{3(1 - 2\sigma)}, \quad \mu = \frac{Y}{2(1 + \sigma)} \tag{2.51}$$

we can write

$$\tilde{Y} = Y(1 + i\phi_Y) \tag{2.52}$$

with

$$\phi_Y = \frac{(1 - 2\sigma)\phi_B + 2(1 + \sigma)\phi_S}{3} \tag{2.53}$$

and

$$\tilde{\sigma} = \sigma + \frac{i}{3}(1 - 2\sigma)(1 + \sigma)(\phi_B - \phi_S) \,. \tag{2.54}$$

Since $-1 < \sigma < 1/2$, we have $(1 - 2\sigma)(1 + \sigma) > 0$, therefore $\tilde{\sigma}$ has a positive imaginary part as ϕ_B is greater than ϕ_S, and vice versa. To understand the physical meaning of the imaginary part of

the Poisson ratio, one has to realize that Young's modulus and the Poisson ratio together describe the elastic response of a rod. Suppose we apply an oscillatory tension uniformly along a rod at a very low frequency, whether the area of the rod leads or lags the length of the rod depends on the relative magnitudes of the bulk and shear loss angles. In the situation when the two loss angles ϕ_B and ϕ_S are equal to each other, the Poisson's ratio is real, and we only need to deal with one loss angle ϕ_Y — although there is reason to assume the equality of these two angles.

If the coating material is made into the shape of a one-dimensional rod, and if we only consider its elongational, bending or torsional modes, then the Young's modulus is the appropriate elastic modulus associated with these modes, and ϕ_Y is the appropriate loss angle to apply. However, this is not directly relevant for coating thermal noise. An elastic modulus that will actually prove useful is that of the *two-dimensional (2-D) flexural rigidity* of a thin plate made from the coating material,

$$D = \frac{Yh}{12(1-\sigma^2)} = |D|(1 + i\phi_D) \tag{2.55}$$

where h is the thickness of the plate, with

$$\phi_D = \frac{(1 - \sigma - 2\sigma^2)\phi_B + 2(1 - \sigma + \sigma^2)\phi_S}{3(1-\sigma)} . \tag{2.56}$$

As we shall see in Sec. 2.7.1, this D is most easily measured through the quality factor of drum modes of a thinly coated sample — although this will not turn out to be the combination of loss angles that appears in the thermal noise of coated mirrors.

2.3.3 Thermal noise of a mirror coated with one thin layer

In the case where the coating thickness is much less than the size of the mirror substrate and the beam spot size, the elastic deformation of the substrate is not affected by the presence of the coating. As a consequence, if we include the elastic energy stored in the substrate U_{sub} with loss angle ϕ_{sub}, we can write

$$
\begin{aligned}
W_{\mathrm{diss}} &= \phi_{\mathrm{sub}} U_{\mathrm{sub}} + \phi_B U_B + \phi_S U_S \\
&\approx \left[\phi_{\mathrm{sub}} + \phi_B \frac{U_B}{U_{\mathrm{sub}}} + \phi_S \frac{U_S}{U_{\mathrm{sub}}} \right] U_{\mathrm{sub}}.
\end{aligned} \tag{2.57}
$$

With the assumption of thin coating and half-infinite substrate, the total strain energy stored in the sample can be considered as U_{sub}. In such a way the coating adds on to the substrate loss angle as additional, effective angles

$$\phi_{\mathrm{coated}} = \phi_{\mathrm{sub}} + \frac{U_B}{U_{\mathrm{sub}}} \phi_B + \frac{U_S}{U_{\mathrm{sub}}} \phi_S. \tag{2.58}$$

Note that when the total coating thickness l is much less than the beam spot size w_0, we have $U_B/U_{\text{sub}} \sim U_S/U_{\text{sub}} \sim l/w_0 \ll 1$. Unfortunately, however, ϕ_B and ϕ_S are found to be so much larger than the substrate loss angle ϕ_{sub} that in practice coating thermal noise still dominates over substrate thermal noise.

Now suppose we would like to measure a weighted average of the position of the mirror surface,

$$q = \bar{\xi} = \int d^2\vec{x}\, w(\vec{x}) z(\vec{x}) \tag{2.59}$$

with [Cf. Eq. (2.37)]

$$w(\vec{x}) = \frac{I(\vec{x})}{\int I(\vec{x}) d^2\vec{x}} \tag{2.60}$$

and $z(\vec{x})$ the position of the coating-air interface at transverse location $\vec{x}$.

According to Sec. 2.3.1, we need to apply a pressure profile of

$$f(\vec{x}) = F_0 w(\vec{x}) \tag{2.61}$$

onto the upper surface of the coating, which we shall also refer to as the coating-air interface. Straightforward calculations give

$$
\begin{aligned}
\frac{U_B}{F_0^2} =\ & \frac{(1-2\sigma_c)l}{3}\left[\frac{Y_c}{Y_s^2}\frac{(1-2\sigma_s)^2(1+\sigma_s)^2}{(1-\sigma_c)^2}\right.\\
&+\frac{1}{Y_s}\frac{2(1-2\sigma_s)(1+\sigma_s)(1+\sigma_c)}{(1-\sigma_c)^2}\\
&\left.+\frac{1}{Y_c}\frac{(1+\sigma_c)^2}{(1-\sigma_c)^2}\right]\int w^2(\vec{x})d^2\vec{x},
\end{aligned}
\tag{2.62}
$$

$$
\begin{aligned}
\frac{U_S}{F_0^2} =\ & \frac{2l}{3}\left[\frac{Y_c}{Y_s^2}\frac{(1-\sigma_c+\sigma_c^2)(1+\sigma_s)^2(1-2\sigma_s)^2}{(1-\sigma_c)^2(1+\sigma_c)}\right.\\
&-\frac{(1+\sigma_c)(1-2\sigma_c)(1-2\sigma_s)(1+\sigma_s)}{Y_s(1-\sigma_c)^2}\\
&\left.+\frac{(1-2\sigma_c)^2(1+\sigma_c)}{Y_c(1-\sigma_c)^2}\right]\int w^2(\vec{x})d^2\vec{x}.
\end{aligned}
\tag{2.63}
$$

Here l is coating thickness; for Young's modulus Y and Poisson's ratio σ, substrates c and s represent coating and substrate, respectively. Directly following Eqs. (2.46) and (2.50) will give rise to a noise spectrum of

$$S_{\bar{\xi}} = \frac{4k_B T}{\pi f}\left[\phi_B \frac{U_B}{F_0^2} + \phi_S \frac{U_S}{F_0^2}\right] \tag{2.64}$$

where U_B/F_0^2 and U_S/F_0^2 are given by Eqs. (2.62) and (2.63) respectively.

Here we can define

$$\int w^2(\vec{x})d^2\vec{x} = \frac{\int d^2\vec{x} I^2(\vec{x})}{\left[\int d^2\vec{x} I(\vec{x})\right]^2} \equiv \frac{1}{\mathcal{A}_{\text{eff}}} \tag{2.65}$$

as the inverse of an *effective beam area*. Therefore noise power in q is proportional to coating thickness and inversely proportional to beam area. In particular, for a Gaussian beam with

$$I(\vec{x}) \propto \exp\left(-\frac{\vec{2}x^2}{w_0^2}\right) \tag{2.66}$$

the effective area is $\mathcal{A}_{\text{eff}} = \pi w_0^2$.

Let us compare our results to previous calculations using $\phi_\perp$ and $\phi_\parallel$. As it turns out, if we assume $\phi_S = \phi_B$, then formulas for thermal noise agree with Eq. (22) in Ref. [14]. To illustrate the different roles now played by ϕ_B and ϕ_S, let us take the very simple case of $Y = Y_c = Y_s$ and $\sigma = \sigma_c = \sigma_s$, where

$$\frac{\delta U_B}{F_0^2} = \frac{4l}{3Y\mathcal{A}_{\text{eff}}}(1+\sigma)^2(1-2\sigma), \tag{2.67}$$

$$\frac{\delta U_S}{F_0^2} = \frac{2l}{3Y\mathcal{A}_{\text{eff}}}(1+\sigma)(1-2\sigma)^2. \tag{2.68}$$

Using Eq. (2.64), we can get the power spectral density of the single layer non-penetration coating thermal noise as

$$\begin{aligned} &S_{\bar{\xi}}(f) \\ &= \frac{8k_B T(1-\sigma-2\sigma^2)l}{3\pi f Y\mathcal{A}_{\text{eff}}}[2(1+\sigma)\phi_B + (1-2\sigma)\phi_S]. \end{aligned} \tag{2.69}$$

From Eq. (2.69), we can see that the bulk loss and shear loss contribute differently to the total noise. More importantly, at least in the simple case where $Y_c = Y_s$, the combination of ϕ_B and ϕ_S is approximately $2\phi_B + \phi_S$, which differs significantly from the combination $\phi_{\text{tot}} \approx \phi_B + 2\phi_S$ measured by the ring-down experiments that have been performed so far [19–21]. This will be discussed in detail in the rest of Sec. 2.7.

2.3.4 Discussions on the correlation structure of thermal noise

Before proceeding to more detailed calculations of Brownian noise that involve light penetrating into the coating layers, we would like to gain more insight into thermal noise by inspecting our existing expressions of coating thermal noise [Eqs. (2.62)–(2.64)] more carefully. We note that

$$S_{\bar{\xi}} \propto l \int w^2(\vec{x}) d^2\vec{x}. \tag{2.70}$$

where the coefficient of proportionality depends only on material property. From such a dependence on coating and beam geometries, we deduce that (i) each point on the coating-air interface fluctuates along the z direction independently, and (ii) materials at different z's within the coating also

contribute independently to coating thermal noise. These observations will be confirmed below in Sec. 2.4.

Finally, within the coefficient of proportionality [Cf. Eqs. (2.62) and (2.63)], we found three types of dependence on the Young's moduli of the coating and substrate materials: terms proportional to $1/Y_c$ are expected to arise from fluctuations in coating thickness, terms proportional to Y_c/Y_s^2 can be interpreted as arising from coating thermal stresses driving the substrate-coating interface, while terms proportional to $1/Y_s$ are therefore interpreted as correlations between the above two types of noise.

2.4   Cross spectra of thermal noise components

In this section, we compute the cross spectra of each component of coating thermal noise, and assemble the formula for the spectral density of the total noise. Specifically, in Sec. 2.4.1, we compute the cross spectra of the thickness fluctuations between any two uniform sublayers of the coating, and obtain the cross spectrum of S_{zz}; in Sec. 2.4.2, we compute the cross spectra involving height fluctuation z_s of the coating-substrate interface, i.e., $S_{S_{zz}z_s}$ and $S_{z_s z_s}$; in Sec. 2.4.3, we dissect the above results and analyze the separate roles of bulk and shear fluctuations; in Sec. 2.4.4, we write down the full formula for coating thermal noise.

2.4.1   Coating-thickness fluctuations

Let us start by calculating thickness fluctuations of individual layers and correlations between them. Following Levin's approach, we imagine applying two pairs of opposite pressures,

$$f_1(\vec{x}) = F_0 w_1(\vec{x}), \quad f_3(\vec{x}) = F_0 w_3(\vec{x}) \tag{2.71}$$

in the z direction on layer1 and layer 3, as shown in Fig. 2.2, with thickness of l_1 and l_3, respectively. Here $w_1(\vec{x})$ and $w_3(\vec{x})$, like the $w(\vec{x})$ used in Eq. (2.59), provide the shape of the pressure profiles. Note that we apply pairs of forces, and each pair must be equal and opposite in direction because we are interested in learning about the fluctuations of the *thickness*, instead of the location, of the layers.

We assume that layers I and III are each made from a single type of material, yet there could be arbitrary number of different material sub layers in II. As it will turn out, the precise locations of layers I and III along the z direction does not affect the result, *as long as they do not overlap*, or in other words, layer II has non-zero thickness.

Throughout this paper, we shall assume that the beam spot size is much less than the radius of the mirror, so that we can make the approximation that the mirror surface is an infinite two-dimensional

plane. In this case, we perform a spatial Fourier transformation for the applied pressure,

$$\tilde{f}_j(\vec{k}) = \int e^{i\vec{k}\cdot\vec{x}} f_j(\vec{x}) \, d^2\vec{x} = F_0 \tilde{w}_j(\vec{k}) \,, \; j = 1, 3 \,, \tag{2.72}$$

and carry out our calculations for strain and stress distributions in the coating-substrate system in the Fourier domain.

We further assume that the coating thickness is much less than the beam spot size, which is the inverse of the maximum spatial frequency contained in $\tilde{w}_{1,3}$. This means we only need to consider $\vec{k}$'s with $|\vec{k}|l \ll 1$, with l the total coating thickness. According to calculations in Appendix 2.B, non-zero components of the stress and strain tensors in Layers I and III are found to be (in the spatial Fourier domain)

$$\tilde{T}^{\mathrm{I}}_{xx} = \tilde{T}^{\mathrm{I}}_{yy} = \frac{\sigma_1 \tilde{w}_1}{1 - \sigma_1} F_0 \,, \quad \tilde{T}^{\mathrm{I}}_{zz} = \tilde{w}_1 F_0 \,, \tag{2.73}$$

$$\tilde{S}^{\mathrm{I}}_{zz} = -\frac{(1 - 2\sigma_1)(1 + \sigma_1)\tilde{w}_1}{Y_1(1 - \sigma_1)} F_0 \,, \tag{2.74}$$

and

$$\tilde{T}^{\mathrm{III}}_{xx} = \tilde{T}^{\mathrm{III}}_{yy} = \frac{\sigma_3 \tilde{w}_3}{1 - \sigma_3} F_0 \,, \quad \tilde{T}^{\mathrm{III}}_{zz} = \tilde{w}_3 F_0 \,, \tag{2.75}$$

$$\tilde{S}^{\mathrm{III}}_{zz} = -\frac{(1 - 2\sigma_3)(1 + \sigma_3)\tilde{w}_3}{Y_3(1 - \sigma_3)} F_0 \,, \tag{2.76}$$

respectively.

Note that deformations within layer I only depend on $\tilde{w}_1$ (not $\tilde{w}_3$), while deformations within layer III only depends on $\tilde{w}_3$ (not $\tilde{w}_1$) — while regions outside these layers are found to have vanishing strain and stress. This means we can treat deformations caused by each pair of forces independently, as long as layer I and layer III do not overlap. The deformations are also independent of the thickness of the layers. The vanishing of deformations outside these layers means that when we introduce additional pairs of opposite forces, the new deformations introduced will be constrained within those new layers — as long as those new layers do not overlap with existing ones. This independence originates from the linearity of elastic response, and the fact that coating strains induced by force applied on a single surface within the coating, as discussed in Appendix 2.B, do not depend on distance away from that surface, as seen in Eqs. (2.159)–(2.166). The situation here is analogous to the electrostatics of several pairs of oppositely-charged infinite parallel planes.

In terms of thermal noise, such a distribution of elastic deformations corresponds to a dissipation energy that consists of two independent terms, each corresponding to one layer and proportional to its thickness:

$$\frac{W_{\mathrm{diss}}}{F_0^2} = W_{11}l_1 \int w_1^2 d^2\vec{x} + W_{33}l_3 \int w_3^2 d^2\vec{x}. \tag{2.77}$$

Here we have defined, for $j = 1, 3$:

$$W_{jj} \equiv \frac{(1 - 2\sigma_j)(1 + \sigma_j)}{3(1 - \sigma_j)^2 Y_j} \left[\frac{1 + \sigma_j}{2} \phi_B^j + (1 - 2\sigma_j)\phi_S^j \right]. \tag{2.78}$$

This means the fluctuation of

$$q \equiv \int [w_1(\vec{x})\delta l_1(\vec{x}) + w_3(\vec{x})\delta l_3(\vec{x})] \, d^2\vec{x} \tag{2.79}$$

is given by

$$S_q = \frac{4k_B T}{\pi f} \sum_{j=1,3} \left[W_{jj} l_j \int w_j^2(\vec{x}) d^2\vec{x} \right]. \tag{2.80}$$

The absence of a cross term between w_1 and w_3 means that fluctuations in $\delta l_1(\vec{x})$ and $\delta l_3(\vec{x}')$ are uncorrelated — and hence statistically independent. Furthermore, within each layer, in the same spirit as the discussions in Sec. 2.3.4, the particular form of dependence on l_j and $w_j(\vec{x})$ indicates that S_{zz} fluctuations at different 3-D locations (within this layer) are all uncorrelated and have the same spectrum. In this way, we obtain the cross spectral density of S_{zz} at two arbitrary 3-D locations within the coating:

$$S_{S_{zz}S_{zz}}^{ij}(\vec{x}, z; \vec{x}', z') = \frac{4k_B T}{\pi f} \delta_{ij}\delta^{(2)}(\vec{x} - \vec{x}')\delta(z - z')W_{jj}. \tag{2.81}$$

Here we have assumed that $(\vec{x}, z)$ belongs to layer i, while $(\vec{x}', z')$ belongs to layer j. (The association to layers helps to identify the material property to be used in W_{jj}.)

2.4.2 Fluctuations of Coating-Substrate Interface and their correlations with coating thickness

To investigate the correlation between the height of the coating-substrate interface, $z_s(\vec{x})$ and the thickness of each coating layer, $\delta l_j(\vec{x})$, we apply an identical pair of pressures $f_1(\vec{x}) = F_0 w_1(\vec{x})$ at opposite sides of layer 1, and force $f_s(x, y) = F_0 w_s(\vec{x})$ onto the coating-substrate interface (along the $-z$ direction), as shown in Fig. 1. The same strain and stress as in Eqs. (2.73) and (2.74) are driven by $\tilde{f}_1$, which are only non-vanishing within layer I. On the other hand, $\tilde{f}_s$ drives uniform strain and stress over the entire coating, with non-vanishing components of stress and strain given by,

$$\|\tilde{T}_{ij}\| = \frac{\tilde{w}_s(1 - \sigma_s - 2\sigma_s^2)Y_c}{(1 + \sigma_c)\kappa^2 Y_s} \begin{bmatrix} \frac{k_x^2 + \sigma_c k_y^2}{1 - \sigma_c} & k_x k_y & 0 \\ k_x k_y & \frac{\sigma_c k_x^2 + k_y^2}{1 - \sigma_c} & 0 \\ 0 & 0 & 0 \end{bmatrix}, \tag{2.82}$$
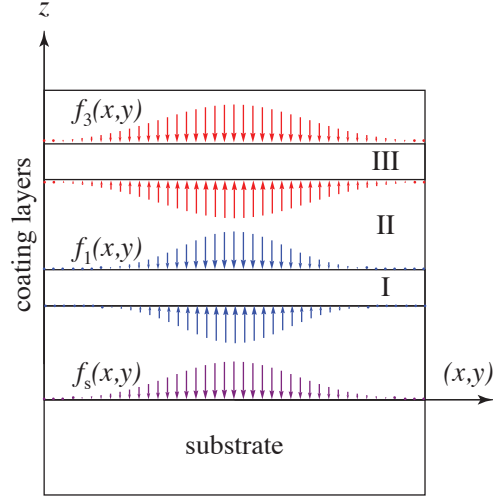
Figure 2.2: Illustrations of forces applied onto various interfaces within the coating. Each of layers I and III in the coating are assumed to be uniform (but they might each contain a different kind of material); region II denotes the entire gap between them, which may well contain many different dielectric layers. A pair of force distribution f_1 (f_3) with the same pressure profile but in opposite directions is exerted on opposite sides of layer I (III), while f_s is exerted on the coating-substrate interface. (Although each pair has the same pressure profile, they may be different from each other.) The three distributions may well have different profiles (as also illustrated in the figure).

$$\|\tilde{S}_{ij}\| = -\frac{\tilde{w}_s(1 - \sigma_s - 2\sigma_s^2)}{\kappa^2 Y_s} \begin{bmatrix} k_x^2 & k_x k_y & 0 \\ k_x k_y & k_y^2 & 0 \\ 0 & 0 & \frac{-\sigma_c}{1 - \sigma_c} \end{bmatrix}, \tag{2.83}$$

where Young's modulus Y_c and Poisson's ratio σ_c of the coating are given by values within layer I. The total dissipation in this case will have the following structure,

$$\frac{W_{\text{diss}}}{F_0^2} = l_1 \left[W_{11} \int w_1^2 d^2\vec{x} + 2W_{1s} \int w_1 w_s d\vec{x} + W_{ss} \int w_s^2 d^2\vec{x} \right], \tag{2.84}$$

with the first term arising from dissipation in layer I that is due to strain and stress driven by f_1, the second term also arising from dissipation in layer I arising from cross terms between strains and stresses caused by f_1 and f_s, and the third term arises from dissipations throughout the entire coating, due to strain and stress caused by f_s. Here W_{11} is the same as defined by Eq. (2.78), and

$$W_{js} = \frac{(1 - \sigma_s - 2\sigma_s^2)(1 - \sigma_j - 2\sigma_j^2)}{2(1 - \sigma_j)^2 Y_s}(\phi_B^j - \phi_S^j) \tag{2.85a}$$

$$W_{ss}^{(j)} = \frac{(1 - \sigma_s - 2\sigma_s^2)^2 Y_j}{(1 - \sigma_j)^2 Y_s^2} \left[\frac{1 - 2\sigma_j}{2}\phi_B^j + \frac{1 - \sigma_j + \sigma_j^2}{1 + \sigma_j}\phi_S^j \right]. \tag{2.85b}$$

Note that we have added a superscript (j) for W_{ss} to indicate that here the dissipation is due to the pair of forces applied on one thin layer alone.

Here again, the dependences on w_1^2 and w_s^2 indicate that fluctuations at different transverse locations, $\vec{x} \neq \vec{x}'$, are uncorrelated, while the l_1 in front of W_{11}, and the arbitrariness of l_1 means that S_{zz} fluctuations at different z locations within the thin layers are uncorrelated. The l_1 in front of both W_{1s} and W_{ss} indicates that all S_{zz} within layer I are correlated with z_s the same way, even though all of them are mutually uncorrelated.

This allows us to extract the following

$$S_{z_s z_s}(\vec{x}, \vec{x}') = \frac{4k_B T}{3\pi f} \delta^{(2)}(\vec{x} - \vec{x}') \sum_j l_j W_{ss}^{(j)}, \tag{2.86a}$$

$$S_{S_{zz} s_z}(\vec{x}; \vec{x}', z') = \frac{4k_B T}{3\pi f} \delta^2(\vec{x} - \vec{x}') W_{js}. \tag{2.86b}$$

Here for Eq. (2.86b), j is the layer with which z' is associated; and this labeling is to help identify which material parameter to use in W_{js}.

2.4.3 The anatomy of coating thermal noise

Here let us assemble Eqs. (2.81), (2.86a) and (2.86b) from the previous sections, and write:

$$S_{S_{zz} S_{zz}}^{ij}(\vec{x}, z; \vec{x}', z') = \frac{4k_B T}{3\pi f} \frac{(1+\sigma_j)(1-2\sigma_j)}{Y_j(1-\sigma_j)^2} \left[\frac{1+\sigma_j}{2}\phi_{Bj} + (1-2\sigma_j)\phi_{Sj}\right] \delta_{ij} \delta^{(2)}(\vec{x} - \vec{x}') \delta(z - z'),$$

$$\tag{2.87a}$$

$$S_{z_s z_s}(\vec{x}, \vec{x}') = \frac{4k_B T}{3\pi f} \frac{(1-\sigma_s - 2\sigma_s^2)^2}{Y_s^2} \sum_j \frac{Y_j l_j}{(1-\sigma_j)^2} \left[\frac{1-2\sigma_j}{2}\phi_{Bj} + \frac{1-\sigma_j + \sigma_j^2}{1+\sigma_i}\phi_{Sj}\right] \delta^{(2)}(\vec{x} - \vec{x}'),$$

$$\tag{2.87b}$$

$$S_{z_s S_{zz}}(\vec{x}; \vec{x}', z') = \frac{2k_B T}{3\pi f} \frac{(1-\sigma_s - 2\sigma_s^2)(1-\sigma_j - 2\sigma_i^2)}{Y_s(1-\sigma_j)^2} [\phi_{Bj} - \phi_{Sj}] \delta^2(\vec{x} - \vec{x}'). \tag{2.87c}$$

Here we have assumed that z belongs to the i-th layer and that z' belongs to the j-th layer, respectively. The thickness fluctuations of different layers are mutually independent [note the Kronecker delta in Eq. (2.87a)], while the thickness fluctuation of each layer is correlated with the height fluctuation of the coating-substrate interface [Eq. (2.87c)].

Fluctuations in the strain S_{zz} and the coating-substrate interface z_s, described by Eqs. (2.87a)–(2.87b), can be represented alternatively as being driven by a number of independent fluctuating fields that exist throughout the coating. Such a representation allows us to better appreciate the origin and the magnitude of these fluctuations.

In order to do so, let us first define $3N$ thermal noise fields (i.e., 3 for each coating layer), $n_j^B(\mathbf{x})$,

	Thickness (δ_j)	Surface height (z_s)
Bulk	$C_j^B = \sqrt{\dfrac{1+\sigma_j}{2}}$	$D_j^B = \dfrac{1 - \sigma_s - 2\sigma_s^2}{\sqrt{2(1+\sigma_j)}}\dfrac{Y_j}{Y_s}$
Shear A	$C_j^{S_A} = \sqrt{1 - 2\sigma_j}$	$D_j^{S_A} = -\dfrac{1 - \sigma_s - 2\sigma_s^2}{2\sqrt{1 - 2\sigma_j}}\dfrac{Y_j}{Y_s}$
Shear B	(none)	$D_j^{S_B} = \dfrac{\sqrt{3}(1 - \sigma_j)(1 - \sigma_s - 2\sigma_s^2)}{2\sqrt{1 - 2\sigma_j}(1 + \sigma_j)}\dfrac{Y_j}{Y_s}$

Table 2.1: Transfer functions from bulk and shear noise fields to layer thickness and surface height.

$n_j^{S_A}(\mathbf{x})$ and $n_j^{S_B}(\mathbf{x})$, all independent from each other, with

$$S_{n_j^B n_k^B} = \frac{4k_B T(1 - \sigma_j - 2\sigma_j^2)}{3\pi f Y_j (1 - \sigma_j)^2}\phi_B^j \delta_{jk}\delta^{(3)}(\mathbf{x} - \mathbf{x}'), \tag{2.88a}$$

$$S_{n_j^{S_A} n_k^{S_A}} = S_{n_j^{S_B} n_k^{S_B}} = \frac{4k_B T(1 - \sigma_j - 2\sigma_j^2)}{3\pi f Y_j (1 - \sigma_j)^2}\phi_S^j \delta_{jk}\delta^{(3)}(\mathbf{x} - \mathbf{x}'), \tag{2.88b}$$

and all other cross spectra vanishing. Here j labels coating layer, the superscript B indicates bulk fluctuation, while S_A and S_B label two types of shear fluctuations. The normalization of these fields are chosen such that each of these fields, when integrated over a length l_j along z, have a noise spectrum that is roughly the same magnitude as a single-layer thermal noise.

Noise fields $n_j^B(\mathbf{x})$, $n_j^{S_A}(\mathbf{x})$ and $n_j^{S_B}$ can be used to generate thickness fluctuations of the layers and the interface fluctuation (2.87a)–(2.87b) if we define

$$u_{zz}(\vec{x}, z) = C_j^B n_j^B(\vec{x}, z) + C_j^{S_A} n_j^{S_A}(\vec{x}, z) \tag{2.89}$$

and

$$\begin{aligned} z_s(\vec{x}) &= \sum_j \int_{L_{j+1}}^{L_j} dz \left[D_j^B n_j^B(\vec{x}, z) + D_j^{S_A} n_j^{S_A}(\vec{x}, z) \right. \\ &\qquad\qquad \left. + D_j^{S_B} n_j^{S_B}(\vec{x}, z) \right]. \end{aligned} \tag{2.90}$$

For each coating layer, C_j^B and D_j^B are transfer functions from the bulk noise field n_j^B to its own thickness δl_j and to surface height z_s, respectively; $C_j^{S_A}$ and $D_j^{S_A}$ are transfer functions from the first type of shear noise to thickness and surface height; finally $D_j^{S_B}$ is the transfer function from the second type of shear noise to surface height (note that this noise field does not affect layer thickness). Explicit forms of these transfer functions are listed in Table. 2.1.

Equations (2.89) and (2.90) owe their simple forms to the underlying physics of thermal fluctuations:

For *bulk noise*, i.e., terms involving n_j^B, the form of Eqs. (2.89) and (2.90) indicates that the interface fluctuation due to bulk dissipation is simply a sum of pieces that are directly proportional
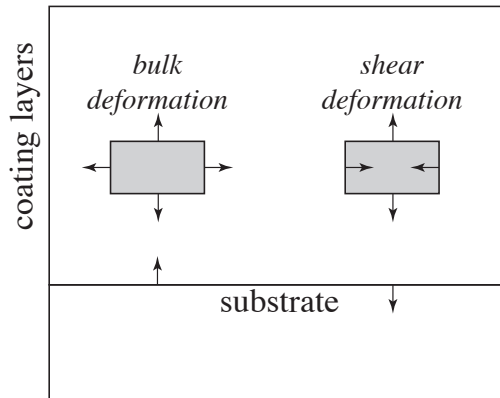
Figure 2.3: Illustration of the correlations between coating thickness δl_j and the height of the coating-substrate interface, z_s. On the left, for a bulk deformation: when a coating element is expanding, its expansion along the x-y plane lifts the coating-substrate interface upwards, causing additional motion of the coating-air interface correlated to that caused by the increase in coating thickness. On the right, a particular shear mode: when a coating element is expanding, its contraction along the x-y plan pushes the coating-substrate interface downwards, causing addition motion of the coating-air interface anti-correlated to that caused by the increase in coating thickenss.

to the bulk-induced thickness fluctuations of each layer. This means the thermal bulk stress in a layer drive simultaneously the thickness fluctuation of that layer and a fluctuation of the coating-substrate interface. The fact that D_j^B and C_j^B have the same sign means that when thickness increases, the interface also rises (with intuitive explanation shown in Figure 2.3). This sign of correlation is generally unfavorable because the two noises add constructively towards the rise of the coating-air interface.

For *shear noise*, the situation is a little more complicated, because unlike bulk deformations, there are a total of five possible shear modes. From Eq. (2.73) and (2.74), it is clear that f_1, applied on opposites of Layer I (Figure 2.2), only drives the $xx + yy - 2zz$ shear mode and the $xx + yy + zz$ bulk mode, while from Eq. (2.82) and (2.83), the force distribution f_s drives three shear modes of $xx - yy$, $xy + yx$, and $xx + yy - 2zz$. This means while thermal shear stresses in the $xx + yy - 2zz$ mode drives layer thickness and interface fluctuation simultaneously, there are additional modes of shear stress, $xx - yy$ and $xy + yx$, that only drive the interface without driving layer thickness. Our mode S_A, which drives both layer thickness and interface height, therefore corresponds to the physical shear mode of $xx + yy - 2zz$; our mode S_B, which only drives interface height, corresponds to the joint effect of the physical shear modes $xx - yy$ and $xy + yx$. It is interesting to note that for S_A, its contributions to δl_j and z_s are anti correlated, because C^{S_A} and D^{S_A} have opposite signs. This is intuitively explained in Fig. 2.3.

As an example application of Eqs. (2.89) and (2.90), if we ignore light penetration into the coating

layers, namely, when thermal noise is equal to

$$\xi^{\mathrm{np}} \equiv -z_s - \sum_j \delta l_j \tag{2.91}$$

we have

$$\xi^{\mathrm{np}} = -\sum_j \int_{L_j}^{L_{j+1}} dz \Big[\left(C_j^B + D_j^B \right) n_j^B$$
$$+ \left(C_j^{S_A} + D_j^{S_A} \right) n_j^{S_A}$$
$$+ D_j^{S_B} n_j^{S_B} \Big] \tag{2.92}$$

in which contributions from each layer have been divided into three mutually uncorrelated groups, each arising from a different type of fluctuation. Here we see explicitly that C^B and D^B sharing the same sign increases contributions from n^B, and C^{S_A} and D^{S_A} having opposite signs suppresses contributions from n^{S_A}.

Finally, we note that in the spectral density of ξ^{np}, contributions directly from coating thickness will be proportional to $|C_j^B|^2$ and $|C_j^{S_A}|^2$, and hence proportional to $1/Y_c$, those from interface height will be $|D_j^B|^2$, $|D_j^{S_A}|^2$ and $|D_j^{S_B}|2$, and hence proportional to Y_c/Y_s^2, while those from correlations will be proportional to $C_j^B D_j^B$ and $C_j^{S_A} D_j^{S_A}$, and hence proportional to $1/Y_s$. This confirms our anticipation at the end of Sec. 2.3.4.

2.4.4 Full formula for thermal noise

Now we give the complete formulas for amplitude and phase noise spectrum [Cf. Eq. (2.94) and Eq. (2.95)]. As we consider light penetration into the coating, we resort to Eq. (2.24), and write:

$$\xi(\vec{x}) - i\zeta(\vec{x})$$
$$= -\sum_j \int_{z_{j+1}}^{z_j} dz \Bigg\{ \left[\left[1 + \frac{i\epsilon_j(z)}{2} \right] C_j^B + D_j^B \right] n_j^B(\vec{x}, z)$$
$$+ \left[\left[1 + \frac{i\epsilon_j(z)}{2} \right] C_j^{S_A} + D_j^{S_A} \right] n_j^{S_A}(\vec{x}, z)$$
$$+ D_j^{S_B} n_j^{S_B}(\vec{x}, z) \right] \Bigg\}. \tag{2.93}$$

Here spectra of independent fields n_j^B, $n_j^{S_A}$ and $n_j^{S_B}$ have been given in Eqs. (2.88a)–(2.88b), ϵ is defined in Eq. (2.25), while the transfer functions Cs and Ds are listed in Table. 2.1.

We can then obtain the spectrum of phase noise (after averaging over the mirror surface, weighted

by the power profile of the optical mode) as

$$
\begin{aligned}
S_{\bar{\xi}} &= \sum_j \int_{z_{j+1}}^{z_j} \frac{dz}{\lambda_j} \left[\left[1 - \mathrm{Im}\frac{\epsilon_j(z)}{2} \right] C_j^B + D_j^B \right]^2 S_j^B \\
&+ \sum_j \int_{z_{j+1}}^{z_j} \frac{dz}{\lambda_j} \left[\left[1 - \mathrm{Im}\frac{\epsilon_j(z)}{2} \right] C_j^{S_A} + D_j^{S_A} \right]^2 S_j^S \\
&+ \sum_j \left[D_j^{S_B} \right]^2 \frac{l_j}{\lambda_j} S_j^S \\
&\equiv \sum_j q_j^B S_j^B + q_j^S S_j^S
\end{aligned}
\tag{2.94}
$$

and spectrum of amplitude noise as

$$
\begin{aligned}
S_{\bar{\zeta}} &= \sum_j \int_{z_{j+1}}^{z_j} \frac{dz}{\lambda_j} \left\{ \left[C_j^B \mathrm{Re}\frac{\epsilon_j(z)}{2} \right]^2 S_j^B \right. \\
&\left. + \left[C_j^{S_A} \mathrm{Re}\frac{\epsilon_j(z)}{2} \right]^2 S_j^S \right\}.
\end{aligned}
\tag{2.95}
$$

Here λ_j is the wavelength of light in layer j, and we have defined

$$
S_j^X \equiv \frac{4k_B T \lambda_j \phi_X^j (1 - \sigma_j - 2\sigma_j^2)}{3\pi f Y_j (1 - \sigma_j)^2 \mathcal{A}_{\mathrm{eff}}}, \quad X = B, S
\tag{2.96}
$$

which is at the level of coating thickness fluctuation of a single layer of dielectrics with material parameters identical to layer j and length equal to λ_j. Note that the quantity S_j^X only depends on the material properties (and temperature) of the layer, and is independent to the length of that layer; the quantities q_j^X (see Fig. 2.7), on the other hand, give us the relative thermal-noise contribution of each layer in a dimensionless way.

Note that the reason for keeping the integrals in Eqs. (2.94) and (2.95) is because ϵ has a z dependence, which originates from the fact that the back-scattering contributions to $\delta\phi_j$s and δr_js a weighted integral of u_{zz} within each layer [Cf. (2.17) and (2.18)].

2.5 Effect of light penetration into the coating

In this section, we synthesize results from Sec. 2.2 and Sec. 2.4, and compute the full Brownian thermal noise for coating configurations. We will illustrate how the light penetration affects the total noise in highly reflective coatings.

reflective surface   free propagation
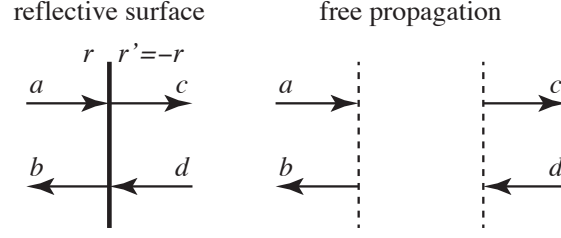
Figure 2.4: Two basic transformations involved in solving for optical fields in a multi-layer coating.

Parameter	Tantala(Ti$_2$O$_5$)	Silica(SiO$_2$)
Refractive index	2.07 [22]	1.45 [22]
Poisson's ratio	0.23 [23]	0.17[23]
Young's modulus (Pa)	1.4×10^{11}[24]	7×10^{10}[23]
Loss angle ($\phi_B = \phi_S$)	2.3×10^{-4}[25]	4.0×10^{-5}[26]
Photoelastic coefficient	-0.50 [27]	-0.41[28]

Table 2.2: Baseline material parameters.

2.5.1 Optics of multi-layer coatings

For completeness of the paper, we briefly review how light penetration coefficient $\partial \log \rho / \partial \phi_j$ can be calculated.

From an interface from layer i to j (here j is either $i+1$ or $i-1$), we denote the reflectivity and transmissivity of different layers by r_{ij} and t_{ij}: $r_{ij}^2 + t_{ij}^2 = 1$

$$r_{ij} = \frac{n_i - n_j}{n_i + n_j}. \tag{2.97}$$

We also define $n_{N+1} = n_1$, since that is the refractive index of the substrate.

A matrix approach can be applied to solve for the amplitude of light inside the layers, when we view the coating as made up of two elementary transformations, each representable by a matrix. In this approach, instead of writing out-going fields in terms of in-going fields, one writes fields to the right of an optical element in terms of those to the left. As illustrated in Figure 2.4, for reflection at an interface (left panel), we write

$$\begin{bmatrix} c \\ d \end{bmatrix} \equiv \mathbf{R}_r = \frac{1}{t} \begin{bmatrix} 1 & -r \\ -r & 1 \end{bmatrix} \begin{bmatrix} a \\ b \end{bmatrix}. \tag{2.98}$$

On the other hand, for propagation across a gap with phase shift ϕ, we have

$$\begin{bmatrix} c \\ d \end{bmatrix} \equiv \mathbf{T}_\phi = \begin{bmatrix} e^{i\phi} & 0 \\ 0 & e^{-i\phi} \end{bmatrix} \begin{bmatrix} a \\ b \end{bmatrix}. \tag{2.99}$$
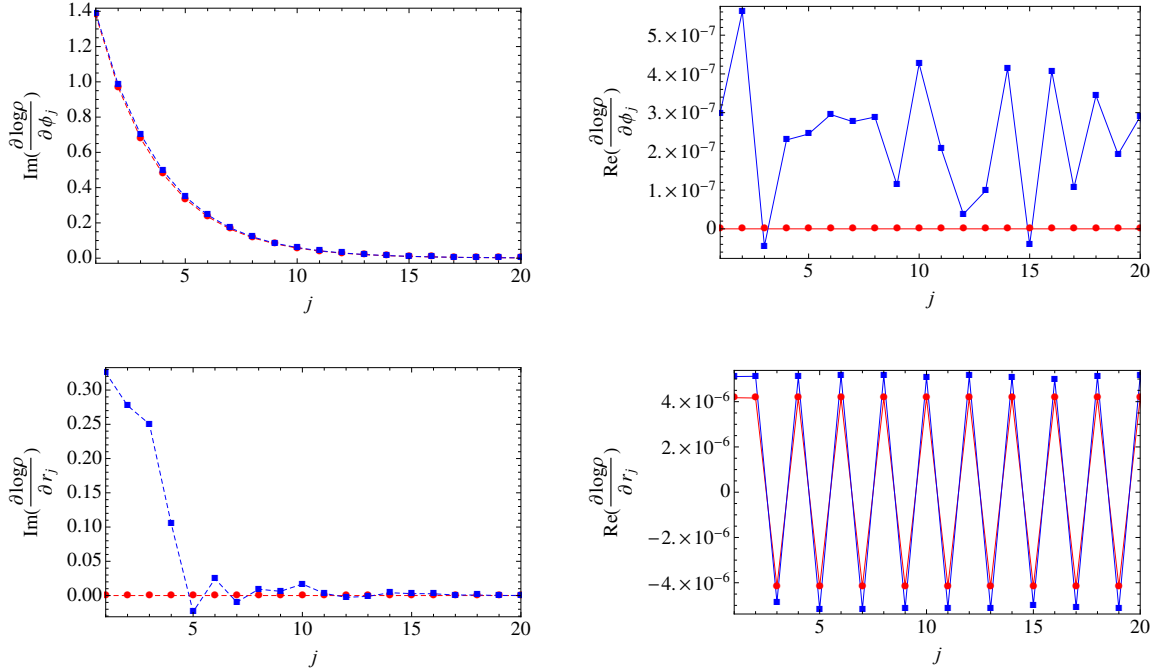
Figure 2.5: Real (solid curves) and imaginary (dashed curves) parts of $\partial \log \rho / \partial \phi_j$ (upper panel) and $\partial \log \rho / \partial r_j$ (lower panel), for conventional (red dot) and Advanced LIGO (blue square) coatings. [Note that $\mathrm{Re}(\partial \log \rho / \partial \phi_j) = 0$ for conventional coating.]

In this way, assuming the input and output field amplitude at the top surface of a multi-layer coating to be v_1 and v_2, and writing those right inside the substrate to be s_1 and s_2, we have

$$\left[\begin{array}{c} s_1 \\ s_2 \end{array} \right] = \left[\begin{array}{cc} M_{11} & M_{12} \\ M_{21} & M_{21} \end{array} \right] \left[\begin{array}{c} v_1 \\ v_2 \end{array} \right] = \mathbf{M} \left[\begin{array}{c} v_1 \\ v_2 \end{array} \right], \tag{2.100}$$

where $\mathbf{M}$ is given by

$$\mathbf{M} = \mathbf{R}_{r_{N,N+1}} \mathbf{T}_{\phi_{N-1}} \mathbf{R}_{r_{N-1,N}} \ldots \mathbf{R}_{r_{12}} \mathbf{T}_{\phi_1} \mathbf{R}_{r_{01}}. \tag{2.101}$$

The complex reflectivity is given by

$$\rho = -M_{21}/M_{22}. \tag{2.102}$$

2.5.2 Levels of light penetration in Advanced LIGO ETM Coatings

In Advanced LIGO, the coating stack is made from alternating layers of two materials: SiO_2 ($n_1 = 1.45$) and Ta_2O_5 ($n_2 = 2.07$). Here we consider the End Test-mass Mirror (ETM). In order to achieve very high reflectivity, the coating is made of 19 successive pairs of alternating SiO_2 and Ta_2O_5 layers, all $\lambda/4$ in thickness except the top one, which is $\lambda/2$. We will refer to this as the *conventional coating*. An alternative design has been made to allow the coating to operate at both
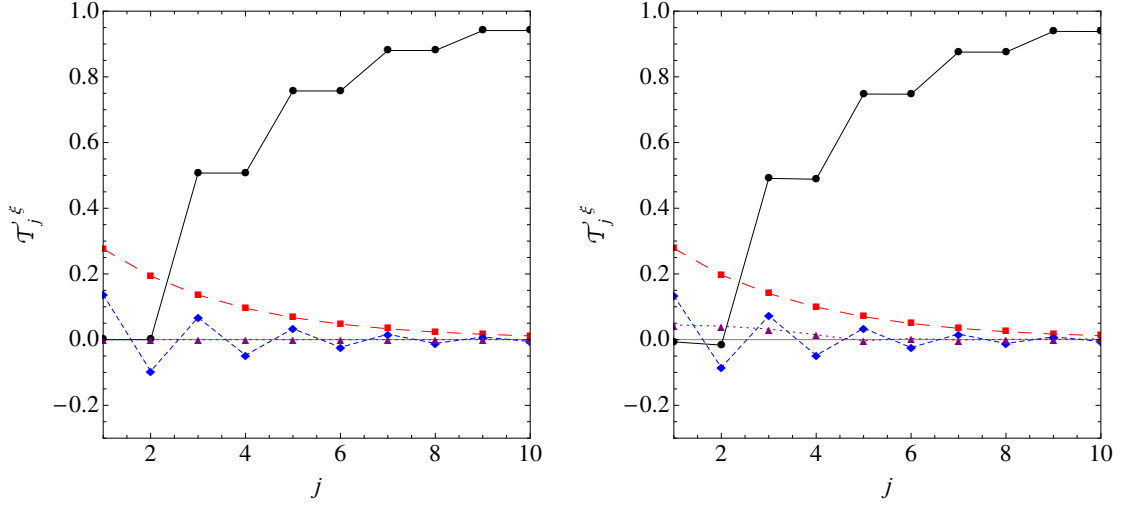
Figure 2.6: Light penetration into the first 10 layers of a 38-layer coating (left panel for conventional coating and right panel for Advanced LIGO coating). We plot the non-photoelastic part of $\mathcal{T}_j$ in black sold curves, the photoelastic part of $\mathcal{T}_j^s$ in long-dashed red curves, as well as $\mathcal{T}_j^s$(scaled by rms value of δl_j^c with respect to the rms value of δl_j, shown in short-dashed blue curves) and T_j^s (scaled by rms value of δl_j^s, shown in dotted purple curves). These plots indicate that for both structures, light penetration is restricted within the first 10 layers.

1064 nm and 532 nm. We shall refer to this as the *Advanced LIGO coating* (see Appendix. 2.D) [29].

In Fig. 2.5, we plot real and imaginary parts of $\partial \log \rho / \partial \phi_j$ and $\partial \log \rho / \partial r_j$ [see Eq. (2.13)], for both conventional and Advanced LIGO coating. Here we note that the real parts of these derivatives are at the order of 10^{-6}, which means $\bar{\zeta}$ is less than $\bar{\xi}$ by six orders of magnitude. This, together with considerations in Sec. 2.2.5, will make amplitude coating noise negligible.

In Eq. (2.27), we have divided contributions to ξ into four terms, the first, z_s, is the height of the coating-substrate interface, while the other three are related to fluctuations in layer thickness, δl_j, δl_j^c and δl_j^s, see Eqs. (2.27)–(2.30). We can illustrate the effect of light penetration by showing the relative size of these three contributions for each layer. In Figure 2.6, we carry out this illustration, for conventional coating on the left panel and for Advanced LIGO coating on the right. We use a solid black line to indicate the non-photoelastic part of $\mathcal{T}_j^\xi$ [i.e., terms not containing β_j, see Eq. (2.28)], and we use red-long-dashed, blue-short-dashed, and purple-dotted curves to indicate the photoelastic part of $\mathcal{T}_j^\xi$, $\mathcal{T}_j^{\xi c}\sqrt{\langle(\delta l_j^c)^2\rangle/\langle(\delta l_j)^2\rangle}$ and $\mathcal{T}_j^{\xi s}\sqrt{\langle(\delta l_j^s)^2\rangle/\langle(\delta l_j)^2\rangle}$, respectively. The weighting factors,

$$\sqrt{\langle(\delta l_j^c)^2\rangle/\langle(\delta l_j)^2\rangle} = \frac{1}{\sqrt{2}}\sqrt{1 + \frac{\sin 4\phi_j}{4\phi_j}}, \tag{2.103}$$

$$\sqrt{\langle(\delta l_j^s)^2\rangle/\langle(\delta l_j)^2\rangle} = \frac{1}{\sqrt{2}}\sqrt{1 - \frac{\sin 4\phi_j}{4\phi_j}}, \tag{2.104}$$
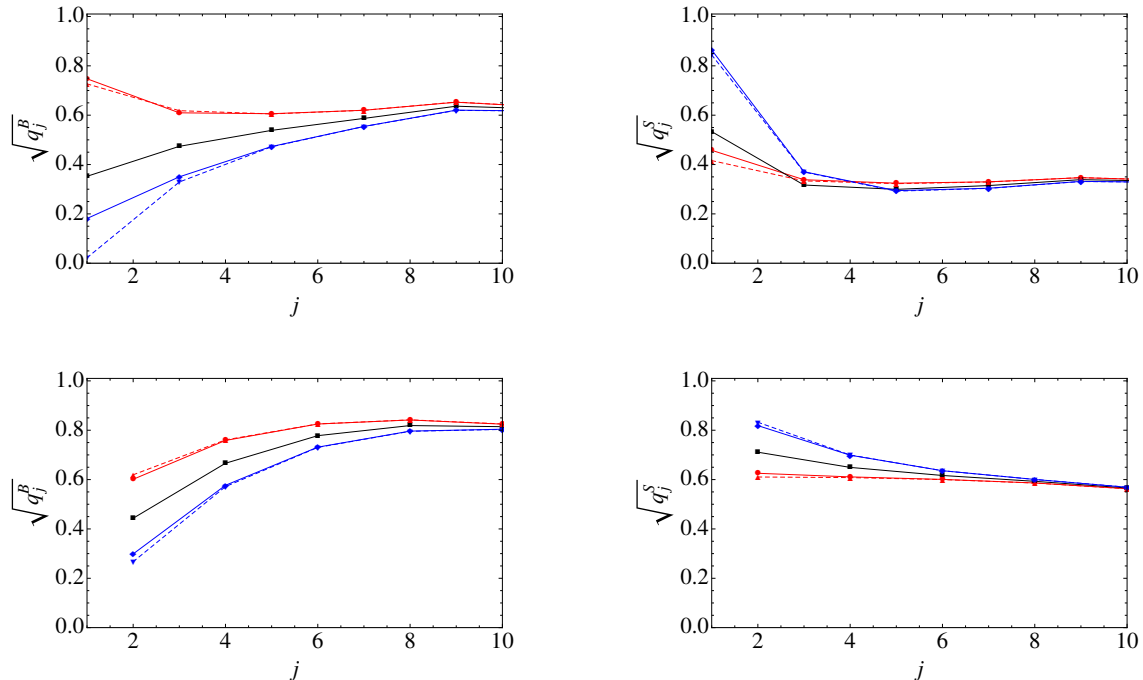
Figure 2.7: (Color online.) A break-down of thermal noise contributions from silica (upper panels) and tantala (lower panels) layers, from bulk (left panels) and shear (right panels) losses. Blue curves correspond to $\beta = -1$, black $\beta = 0$ and red $\beta = 1$. Dashed curves indicate results calculated without including back-scattering effects.

have been added for $\mathcal{T}_j^{\xi c}$ and $\mathcal{T}_j^{\xi s}$, respectively, to correct for the fact that δl_j^c and δl_j^s have different r.m.s. values compared to δl. Because of the lack of experimental data, we have assumed $\beta_j = -0.4$ identically. Note that in order to focus on the effect of light penetration, we have only showed the first 10 layers.

In the figure, the effect of light penetration into the coating layers is embodied in the deviation of the black solid curve from unity in the first few layers, and in the existence of the other curves. Although we cannot perceive the correlation between these contributions, we can clearly appreciate that only the first few layers are penetrated, and that the total effect of light penetration will be small. We should also expect the effect of photoelasticity (dashed curves) to be small, and the effect of back-scattering (which gives rise to $\mathcal{T}_j^{\xi c}$ and $\mathcal{T}_j^{\xi s}$, blue and purple dashed curves) to be even smaller.

2.5.3 Thermal noise contributions from different layers

Let us now examine the breakdown of the total coating noise by plotting the coefficients q_j^B and q_j^S in Eq. (2.94). In Fig. 2.7, we plot silica contributions on top panels, and tantala contributions on lower panels, with bulk contributions on left panels, and shear contributions on right panels. Here we use the baseline parameters shown in Table 2.2. As it turns out, the results for conventional
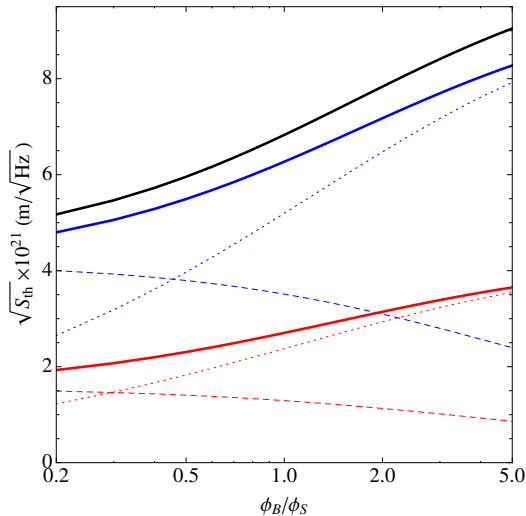
Figure 2.8: (Color online.) Variations in thermal noise contributions when ϕ_B/ϕ_S is varied. Contributions from tantala layers is shown in blue, those from silica layers are shown in red. The total thermal noise is in black. Bulk contributions are shown in dotted curves, while shear contributions are shown in dashed curves.

and Advanced LIGO coatings are hardly distinguishable from each other — therefore we only use the Advanced LIGO coating. The red curve uses $\beta = -1$, black uses $\beta = 0$ and blue uses $\beta = 1$. Superimposed onto the solid lines are dashed lines of each type, calculated without introducing the back-scattering terms; the effect is noticeable for the first few layers.

2.6 Dependence of thermal noise on material parameters

Experimental knowledge of coating materials is limited. Most notably, values of Young's moduli and Poisson's ratios of the coating materials are still uncertain, while only *one combination* of the two loss angles have been experimentally measured by ring-down experiments. In this section, we explore the possible variation in coating Brownian noise, away from the baseline configuration (Table 2.2), considering these uncertainties. We shall use the Advanced LIGO coating structure mentioned in the previous section.

2.6.1 Dependence on ratios between loss angles

In the baseline (Table 2.2), we have assumed that ϕ_B and ϕ_S are equal, but this is only out of our ignorance: experiments have only been able to determine one particular combination of these two angles. We now explore the consequence of having these loss angles not equal, while keeping fixed the combination measured by ring down rate of drum modes [see Eq. (2.110)].

In Figure 2.8, while fixing all other baseline parameters, we plot how each type of thermal noise
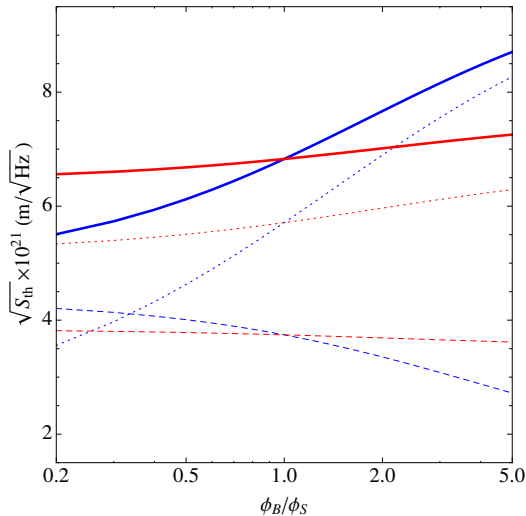
Figure 2.9: (Color online.) Variations in total noise when ϕ_B/ϕ_S is varied: (solid) total noise, (dotted) total bulk noise, (dashed) total shear noise. The red (blue) curve corresponds to only varying ϕ_B/ϕ_S for tantala (silica). With ϕ_B/ϕ_S of tantala or silica varying from 0.2 to 5, the change in total noise is 58.1% and 10.6% respectively.

(i.e., silica vs tantala, bulk vs shear) varies when the ratio ϕ_B/ϕ_S for both tantala and silica layers varies between 1/5 and 5. We use blue for tantala, red for silica, dotted for bulk, dashed for shear, and solid for the total of bulk and shear. In this configuration, tantala layers' contribution to thermal noise always dominate over silica layers, mainly due to the higher loss angle. As we vary the ratio between the loss angles, there is moderate variation of thermal noise. For the dominant tantala, as ϕ_B/ϕ_S varies from 1/5 to 5, there is a 30% change in thermal noise, while for silica, the change is a more significant 68%.

As we see from Fig. 2.8, a larger value of ϕ_B/ϕ_S gives rise to higher bulk, lower shear, and higher total noise — this is reasonable because bulk fluctuations drive correlated noise between a layer's thickness and the height of coating-substrate interface, while shear fluctuations drive anti-correlated noise, as shown in Fig. 2.3.

Moreover, the fact that variation is more significant for silica layers can be explained when we recall that thickness-induced thermal noise is proportional to $1/Y_c$, while surface-height-induced thermal noise is proportional to Y_c/Y_s^2. For silica layers, Y_c is assumed to be equal to Y_s, so the two types of noise being added (bulk) or subtracted (shear) are more comparable in magnitude; by contrast, the Young's modulus of tantala layers is significantly higher than that of the substrate, causing the noise to be dominated by fluctuations of the height of the coating-substrate interface, therefore making correlations between the two types of noise less important.

In Fig. 2.9, we plot variations in the total noise as we vary ϕ_B/ϕ_S for silica layers (blue) or tantala layers (red) only, and fix the other one. It shows that the variance of the tantala's loss angle
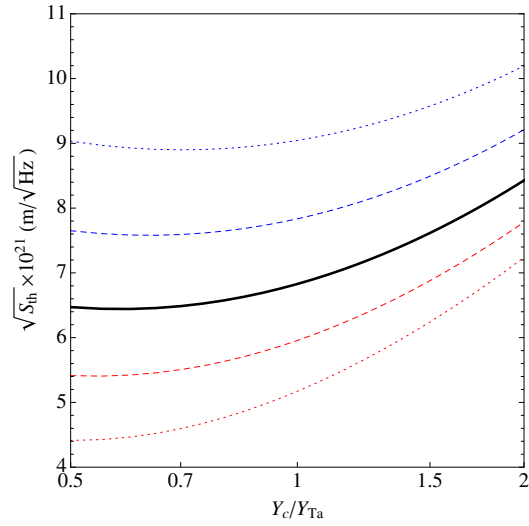
Figure 2.10: Thermal noise contribution from tantala, as its Young's modulus deviates from baseline value, for ϕ_B/ϕ_S=5 (blue dashed), 2 (blue dotted), 1 (black solid), 1/2 (red dotted), and 1/5 (red dashed).
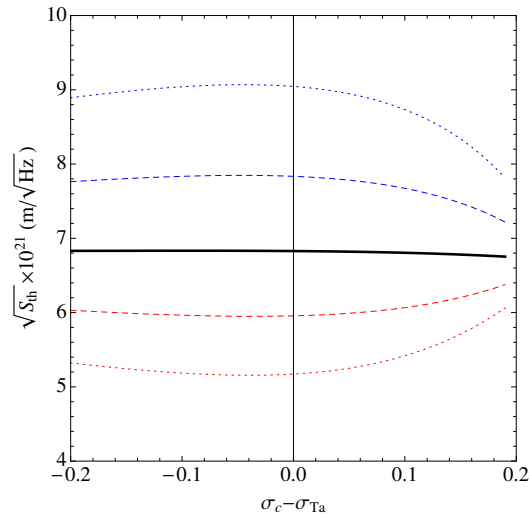
Figure 2.11: Thermal noise contribution from tantala, as its Poisson's ratio deviates from baseline value, for ϕ_B/ϕ_S=5 (blue dashed), 2 (blue dotted), 1 (black solid), 1/2 (red dotted), and 1/5 (red dashed).
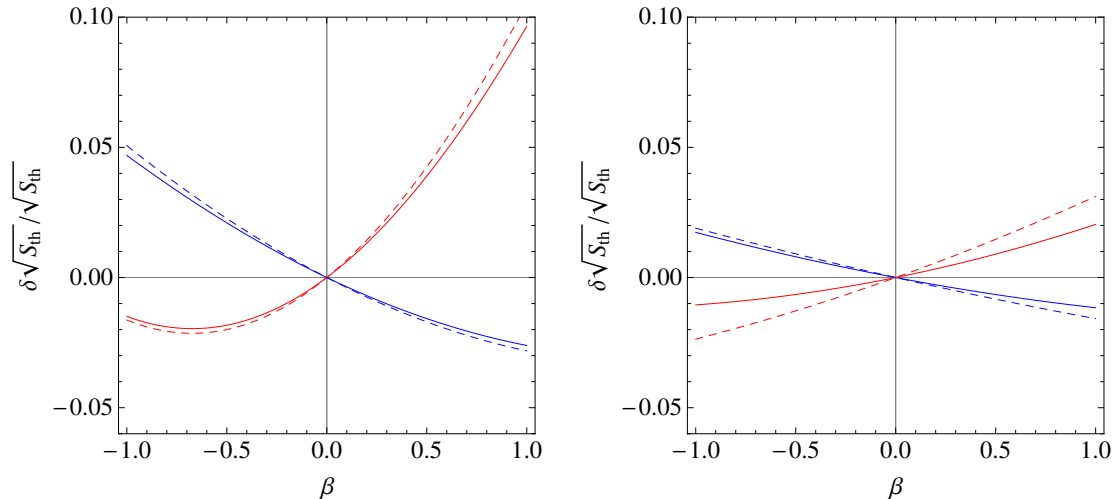
Figure 2.12: Fractional change in the contribution to thermal noise from all silica layers (left panel) and all tantala layers (right panel), due to bulk (blue) and shear (red) loss. Dashed lines indicate results calculated without including back-scattering terms.

will generate larger change of the total noise.

2.6.2 Dependence on Young's moduli and Poisson's ratios

Since the Young's modulus and Poisson's ratios of coating materials, especially of tantala, are also uncertain. In Fig. 2.10, we plot variations of tantala thermal noise when its Young's modulus varies from the baseline value by up to a factor of 2, for $\phi_B/\phi_S = 0.2, 0.5, 1, 2$ and 5. The noise is seen to vary by $\sim$15% as Young's modulus varies by a factor of ~ 2.

We can also explain the way the thermal noise varies as a function of Y_c. Starting from the baseline value, a lower Y_c leads to a lower thermal noise, until Y_c becomes comparable to Y_s (which we fix at the baseline value, equal to $0.5Y_{\mathrm{Ta}}$), and starts to increase again. Such a behavior is reasonable because thickness noise spectrum and interface noise spectrum are proportional to $\sim 1/Y_c$ and $\sim Y_c/Y_s^2$, respectively — as we decrease Y_c from the baseline Y_{Ta} value, we transition from interface fluctuation being dominant towards equal amount of both noises (which gives a minimum total noise), and then towards thickness fluctuation becoming dominant.

In Fig. 2.11, we explore the effect of varying coating Poisson's ratio, for the same values of ϕ_B/ϕ_S chosen in Fig. 2.10. In the baseline assumption of $\phi_B = \phi_S$, when bulk and shear have the same level of loss, thermal noise does not depend much on Poisson's ratio. However, if ϕ_B/ϕ_S turns out to differ significantly from 1, and if Poisson's ratio can be larger than the baseline value by more than ~ 0.1, then thermal noise can vary by $\sim 10\%$.

2.6.3 Dependence on photoelastic coefficients

Photoelastic properties of the coating materials are not yet well known. In Fig. 2.12, we plot the fractional change in thermal noise, separately for silica (left panel) and tantala (right pane), and for bulk (blue) and shear (red) losses, when we vary β between -1 and +1. Dashed curves are obtained ignoring back-scattering effects.

It is interesting to note that for small values of β, the dependence of noise on β has different trends for bulk and shear contributions. This is also related to the different types of correlations between thickness and interface height fluctuations. As we can see from the Figure, the effect of varying β is small, since it only affects thermal noise due to light penetration into the first few layers. If bulk and shear losses are indeed comparable, then cancelation between these two types of noises (especially for the more lossy tantala layers) will likely make the photo elastic effect completely negligible. Even in the case when one particular type of loss dominates, we shall expect at most $\sim 2\%$ contribution from photo-elasticity of the more lossy tantala — if we further assume that $|\beta| \sim 1$ [right panel of Fig. 2.12].

2.6.4 Optimization of coating structure

Although a standard highly reflective coating consists of $\lambda/4$ layers of alternating material capped by a $\lambda/2$ layer, this structure can be modified to lower thermal noise while still maintaining a high reflectivity for the 1064 nm carrier light, e.g., as shown by Agresti et al. [30]. As their results have indicated, for baseline coating parameters and neglecting light penetration into the coating layers [14], the optimal structure is more close to a stack of pairs of $\lambda/8$ (Ta_2O_5) and $3\lambda/8$ (SiO_2) layers, capped by a $\lambda/2$ (SiO_2) layer. This alternative coating structure shortens the total thickness of the more lossy tantala layers, while maintaining a high reflectivity for the light. The *Advanced LIGO type* coating given in Appendix 2.D, on the other hand, has been optimized considering reflectivity at both 1064 nm and 532 nm, as well as thermal noise — although light penetration into the layers have not been considered.

In this section, we carry out a numerical optimization taking penetration into account. We first fix the number N of layers (N is even, so we have $N/2$ pairs), and then for N, we use the Lagrange multiplier method to search for the constrained minimum of S_{th}, fixing T_{1064} and T_{532} (namely the power transmissivity, $1 - |\rho|^2$ assuming the coating is lossless, evaluated at 1064 nm and 532 nm, respectively). The quantity we seek to minimize (or, the *cost function*) is

$$y \equiv \sqrt{S_{th}} + \mu_1 T_{1064} + \mu_2 (T_{532} - 5\%)^2. \tag{2.105}$$

As we vary μ_1 and μ_2 and minimizing y, we obtain the constrained minimum of $\sqrt{S_{th}}$ for different pairs of (T_{532}, T_{1064}). The aim is to obtain a series of coating configurations with approximately 5%

transitivity for 532 nm, and with minimized thermal noise for a variable $3 - 20$ ppm transmissivity for 1064 nm. (Note that the choice of the cost function contains a certain level of arbitrariness.)

Since we are going to carry out minimization for a large number of multipliers over a large number of degrees of freedom, we have chosen to proceed gradually allowing only the first n pairs and last n pairs of layers to vary, while maintaining the same pair structure for $N/2 - n$ pairs in the middle (repeating doublets). In other words, our coating structure looks like:

$$\underbrace{\text{free}}_{2n \text{ layers}} \quad \underbrace{\text{repeating pair}}_{N - 2n \text{ layers}} \quad \underbrace{\text{free}}_{2n \text{ layers}} .$$

In this work, we found that it suffices to choose $n = 2$ (which corresponds to optimizing over 10 parameters); further increasing n does not lead to noticeable improvements. During our numerical optimization, we have adopted the *downhill simplex method* [31, 32].

target		Resulting Coating Structure									$\sqrt{S_{\text{th}}^{\text{opt}}}$			$\sqrt{S_{\text{th}}^{\lambda/4}}$
ϕ_B/ϕ_S	N	First 4 layers				Repeated Pair		Last 4 layers				$\frac{\phi_B}{\phi_S} = \frac{1}{5}$	$\frac{\phi_B}{\phi_S} = 1$	$\frac{\phi_B}{\phi_S} = 5$	
1/5	42	0.0479	0.1581	0.3430	0.1760	0.2919	0.1897	0.3164	0.1738	0.3178	0.1627	**5.01**	6.64	8.81	5.35
1	42	0.1020	0.1250	0.3267	0.1917	0.2911	0.1914	0.3110	0.1752	0.3196	0.1609	5.02	**6.64**	8.81	7.05
5	42	0.1118	0.0968	0.3353	0.1882	0.2893	0.1939	0.3135	0.1673	0.3199	0.1662	5.02	6.64	**8.81**	9.33

Table 2.3: Results of coating-structure optimization. We list optimized coating structures for $T_{1064} = 5$ ppm and $T_{532} = 5\%$, for three target values of ϕ_B/ϕ_S while fixing the measured effective loss angle ϕ_D [Eq. (2.56)] and other baseline material parameters [Table 2.2]. Thickness of coating layers are given in units of wavelength (for 1064 nm light). For each optimized coating structure, thermal noise is calculated separately for the same three values of ϕ_B/ϕ_S, and given in units of 10^{-21} m/$\sqrt{\text{Hz}}$ (thermal noise for the target ϕ_B/ϕ_S is given in boldface, and boldface numbers should be the minimum within its column); thermal noise spectra of the 38-layer $\lambda/4$ stack assuming the target ϕ_B/ϕ_S are also listed for comparison.
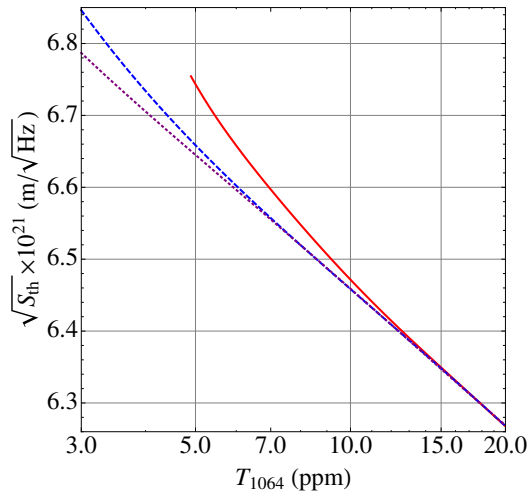
Figure 2.13: Optimized thermal noise versus transmissivity at 1064 nm, for a coating of 38 (red), 40 (blue), and 42 (purple) layers.

Results for baseline material parameters (Table. 2.2) and $N = 38$, 40 and 42 have been shown in Figure 2.13. This figure indicates that different numbers of layers should be chosen for different target T_{1064} – more layers are required for lower transmissivity (higher reflectivity). Overall, the optimal thermal noise varies by around $\sim 10\%$ as for T_{1064} from 3 to 20 ppm. In particular, for the standard Advanced LIGO requirement of 5 ppm (see first column of Table 2.3), 42 layers are found to be optimal. This is two more pairs or four more layers than the 38-layer $\lambda/4$ doublet, which has the minimum number of layers to reach 5 ppm. The larger number of layers here gets lower thermal noise (by 6 %) because the more lossy tantala layers are shortened, and the less lossy silica layers lengthened.

We have further optimized the structure when the ratio ϕ_B/ϕ_S is different from 1, while keeping fixed the effective loss angle measured so far — as done in Sec. 2.6.1. For $T_{1064} = 5$ ppm, we have listed results of optimized coating structure and thermal noise in the second and third columns of Table 2.3. The extent of variation found here is comparable to those obtained in Sec. 2.6.1 using a standard coating structure without optimization: the optimal coating structures consistently lower thermal noise by about 6%. In addition, as shown in Table 2.3, the optimal coating structure is robust against changes in ϕ_B/ϕ_S: structure obtained for any one of the values of the ratio is already almost optimal for all other ratios.

2.7 Measurements of loss angles

In this section, we study possible mechanical ringdown experiments that can be used to measure independently the bulk and shear loss angles, ϕ_B and ϕ_S of a coating material.

In a ringdown experiment, a sample with a high intrinsic Q is coated with a thin layer of the coating material in question. Due to the mechanical losses in the coating, the quality factor of the mechanical eigenmodes of the sample will be reduced [33, 34]. More specifically, for the nth eigenmode with resonant frequency f_n, if an e-folding decay time of τ_n is measured, then the quality factor is

$$Q_n = \pi f_n \tau_n \,, \tag{2.106}$$

while correspondingly, the loss angle is given by

$$\phi(f_n) = 1/Q_n \,, \tag{2.107}$$

which is equal to the fraction of energy dissipated per radian.
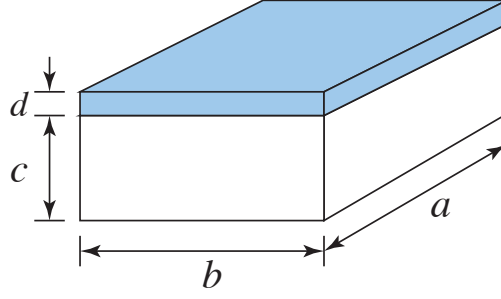
Figure 2.14: Rectangular shaped thin plate ($a \times b \times c$) with thin coating (thickness d): $c \ll a, b; d \ll c$. The transverse vibration mode is considered in this case

2.7.1 Bending modes of a thin rectangular plate

Figure 2.14 shows the schematic geometry of a rectangularly shaped sample, in which a thin coating layer with thickness d is deposited on a rectangular plate with dimensions $a \times b \times c$ ($c \ll a, b$), and d is much less than c. If we pay attention only to the bending (or, in other words, flexing) oscillations of the plate, the amount of energy stored in the coating layer, in the form of bulk and shear energies U_B and U_S, as a fraction of the entire energy U, can be calculated as

$$\frac{U_B}{U} = \frac{d}{3c}\frac{Y_c}{Y_s}\frac{(1-\sigma_s^2)(1-2\sigma_c)}{(1-\sigma_c)^2}, \tag{2.108}$$

$$\frac{U_S}{U} = \frac{2d}{3c}\frac{Y_c}{Y_s}\frac{(1-\sigma_s^2)(1-\sigma_c+\sigma_c^2)}{(1-\sigma_c)^2(1+\sigma_c)}. \tag{2.109}$$

Using Eq. (2.58), the total loss angle of the sample is

$$
\begin{aligned}
\phi &= \phi_{\text{sub}} \\
&+ \frac{d}{c}\frac{Y_c}{Y_s}\frac{1-\sigma_s^2}{1-\sigma_c^2}\left[\frac{\phi_B(1-\sigma_c-2\sigma_c^2)+2\phi_S(1-\sigma_c+\sigma_c^2)}{3(1-\sigma_c)}\right] \\
&= \phi_{\text{sub}} + \frac{|D_c|}{|D_s|}\phi_D.
\end{aligned}
\tag{2.110}
$$

It is not surprising that only the 2-D flexural rigidity D and its imaginary part appear in Eq. (2.110). During the bending of a thin plate with thin coating, both the substrate and the coating are described by the 2-D flexural rigidity, first introduced in Sec. 2.3.2 [see Eqs. (2.55) and (2.56) and Sec. 13 of Ref. [18]]. Because they both bend in the same way, the ratio of their elastic energies is given directly by the ratio of their flexural rigidities (each proportional to their thickness). The fraction of total energy lost in the coating needs to be multiplied by ϕ_D (of the coating material), and hence Eq. (2.110). As the oscillation of a thicker object is considered, as long as the coating only bends up and down (e.g., in a drum mode), then we expect the coating contribution to the loss angle to still be proportional to ϕ_D.
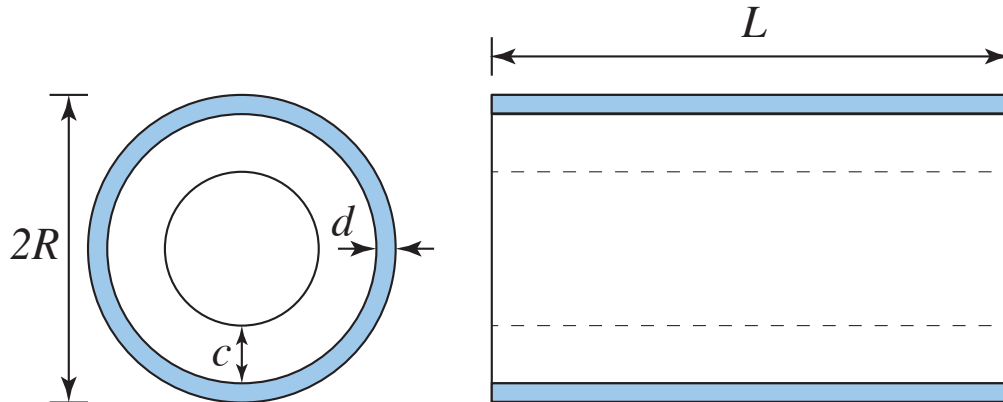
Figure 2.15: Thin cylindrical shell with thin coating outside. The first torsional eigenmodes of such a shell can be used to measure the shear loss angle of the coating.

As it turns out, the part of coating thermal noise due to bending of the coating-substrate interface [$S_{z_s z_s}$ in Eq. (2.87b)] also depends directly on ϕ_D, because the loss mechanism in this case is the same as during the oscillation of a drum mode — one only applies a perpendicular force from below the coating layer, while keeping $T_{zz} = 0$ within the layer.

It proves less straightforward to connect the thickness fluctuation part of thermal noise [$S_{u_z u_z}$ in Eq. (2.87a)] to the effective loss angle of either Y or D. Although the loss mechanism here is due to the compressing of a thin membrane from both sides, this membrane is not characterized by vanishing T_{xx} and T_{yy}, because the coating is attached to a substrate which provides restoring forces along the transverse (x and y) directions. However, in the case when the Poisson ratio σ_c of the coating vanishes, the thickness fluctuation does depend on the loss angle of the Young's modulus.

For our baseline parameters, mechanical dissipation is mostly contributed by the tantala layers, and because the Young's modulus of the tantala coating material is assumed to be much greater than that of the substrate, the largest contribution to the LIGO mirrors' Brownian noise is bending noise $S_{z_s z_s}$. This explains why the noise only varies by 30% (as noted in Sec. 2.6.1) even if no further measurements on the other loss angle is made.

2.7.2 Torsional modes of a coated hollow cylinder

Here we propose an approach with which we can measure another combination of loss angles. We consider a cylindrical shell with a thin, uniform coating layer outside, as shown in Fig. 2.15($c \ll R$, $d \ll c$). In this configuration, the surface deformations produce strains in the plane of shell according to the Donnell shell theory [35]. Here we assumed that there is only angular displacement in the shell, which means the longitudinal position of the cross section won't change. For a torsion mode,

we only have shear strain energy, the expressions are given by

$$\frac{U_B}{U} = 0 \tag{2.111}$$

$$\frac{U_S}{U} = \frac{d}{c}\frac{Y_c}{Y_s}\frac{(1+\sigma_s)}{(1+\sigma_c)}. \tag{2.112}$$

As a consequence, the total loss angle can be expressed as

$$\phi = \phi_{\text{sub}} + \frac{d}{c}\frac{Y_c}{Y_s}\frac{(1+\sigma_s)}{(1+\sigma_c)}\phi_S. \tag{2.113}$$

For a cylinder shell, according to the Donnell shell theory, the natural frequency of the n-th torsional mode is given by [36]

$$f_n = \frac{n}{2^{\frac{3}{2}}L}\left[\frac{Y}{\rho(1+\sigma)}\right]^{1/2}. \tag{2.114}$$

A more accurate calculation may be found by using the Flügge shell theory [37].

Using the values from Table 2.4, we can estimate the resonant frequency to be $9.2\,\text{kHz}$. The coating contribution to loss angle, assuming a ϕ_S of at least 10^{-5}, would be at least the order of 10^{-6}, which seems plausible to be extracted from ring-down measurements.

Table 2.4: Example parameters of a thin, uniformly coated cylindrical shell (SiO_2)

	L	R	c	d
unit(mm)	200	50	1	0.04

With the measurement of both the thin plate and cylinder shell, we can obtain ϕ_B and ϕ_S of the coating.

2.8   Conclusions

In this paper, we applied the fluctuation-dissipation theorem to obtain a *full set of correlation functions* (2.87a)–(2.87c) of Brownian thermal fluctuations of a multi-layer dielectric coating. In particular, we have related fluctuations of the coating thickness and the coating-substrate interface to *independent* bulk and shear thermal stresses associated with each coating layer. While those stresses not only induce thickness fluctuations of the layers themselves, they bend the coating-substrate interface and this bending noise had not been previously appreciated intuitively, although its effect has been incorporated into formulas, e.g., in Ref. [14]. As a result, we found that although thickness fluctuations of different coating layers are independent of each other, they each have partial correlations with the height fluctuations of the coating-substrate interface. Moreover, bulk loss creates a positive correlation between them, while shear loss creates a negative correlation. The entire picture is succinctly written mathematically in Eqs. (2.89) and (2.90). This coherence

material parameter	range	uncertainty in $\sqrt{S_x}$	for details, see
ϕ_B/ϕ_S	$0.2 - 5^1$	$\pm 37\%$	Sec. 2.6.1, Figs. 2.8, 2.9.
Y_{Ta}	factor of ~ 2	$\sim 60\%$	Sec. 2.6.2, Fig. 2.10.
σ_{Ta}	$\pm\, 0.2$	up to 10% if $\phi_B/\phi_S \neq 1$	Sec. 2.6.2, Fig. 2.11.
β	$-1 < \beta < +1$	$\pm 1\%$ ^{2}	Sec. 2.6.3, Fig. 2.12.

Table 2.5: Levels of thermal noise uncertainty caused by parameter uncertainties.

structure then gives coating Brownian noise in Eq. (2.93). Apart from having provided a pedagogical and systematic derivation of these noise components, the most important conceptual consequence of our work is to point out an uncertainty in coating loss angles. We have also incorporated the photo-elastic effect, the reflectivity fluctuations of the interfaces within the multilayer coating, and considered the effect of amplitude modulations caused by Brownian thermal noise. All of these turned out to be rather unimportant.

We have applied our formalism to mirrors that are to be used in Advanced LIGO detectors. As estimated in Sec. 2.6 and summarized in Table 2.5 (calculated for a typical candidate for the Advanced LIGO end test-mass mirror coating configuration), parameter uncertainties could lead to non-negligible corrections to coating Brownian noise calculations. The biggest uncertainties actually arise from the elastic moduli of coating materials — for example, current uncertainties in Young's modulus of the tantala coating material might lead up to 60% increase in thermal noise. Although photo-elastic coefficients for our coating materials are very uncertain, they do not significantly affect thermal noise since light does not penetrate through many layers.

It is rather remarkable that our lack of experimental knowledge about the loss angles, beyond what we had already obtained from the ring down of drum modes, would not give rise to a higher uncertainty in thermal noise. This is rather serendipitous, considering our path of understanding of the problem: for the baseline parameters of Advanced LIGO, the highest contribution to coating Brownian noise arises from the coating-substrate bending noise caused by losses in tantala layers, because these layers are much more lossy than the silica layers, and have been assumed to have a much higher Young's modulus than the substrate material. This bending noise, first elaborated by this work, turns out to be associated with the loss angle of the 2-D flexural rigidity, which in turn is directly connected to the decay of the drum modes of a thinly coated sample. This means the currently existing program [14] has been measuring the predominant loss angle all along, and has been compatible with direct measurements of coating thermal noise [15]. Nevertheless, the level of uncertainty noted in our study still warrants further experiments seeking the other loss angle, e.g., as outlined in Sec. 2.7. In addition, since future gravitational-wave detectors may use different substrate and coating materials, situations may arise when the loss angle measured now does not correlate with the total coating brownian noise.

At this moment, it is worth looking once more at the previously used loss angles, $\phi_\parallel$ and $\phi_\perp$ — although they are mathematically ill defined, they do correctly reflect the existence of two channels of loss. The $\phi_\parallel$ was meant to characterize losses incurred by the x-y deformations of the coating measurable when we do not compress the coating but instead drive its deformations using drum modes of the substrate. This loss angle is now replaced by the (mathematically well-defined) imaginary part of the flexural rigidity, for which extensive measurements have already been carried out. The $\phi_\perp$ was meant to characterize the losses incurred by compressing the coating layers. This has not been measured because it had not been obvious how to easily excite this mode of coating deformation (the most obvious way would be to compress the coating layer, but that is difficult); however, because the Young's modulus of the coating is much larger than that of the substrate, this difficult-to-measure loss angle should not contribute as much to the total coating noise. This said, in this work, we do come up with ways to measure both loss angles, ϕ_S and ϕ_B, without having to compress the coating layers — but instead by exciting different modes of substrate deformation. Of course, this is only possible because we have assumed that the material is isotropic — otherwise we may have to compress the coating to directly access the loss induced by such a deformation.

On the other hand, one may think of the possibilities of using substrate materials with higher Young's modulus to reduce the bending noise. Sapphire and Silicon are two viable choices because they both have higher Young's modulus than tantala. Using Eq. (2.87a)–(2.87c), it is straightforward to estimate the new coating brownian noise while replacing the substrate material by sapphire or silicon but keeping the same Advanced LIGO coating design. It turns out that the coating brownian noise will be reduced to 35% of its original power spectra value if we use silicon substrate or 32% if we use sapphire. However, there are other disadvantages for sapphire or silicon substrate that prevent us from using them for aLIGO mirrors. The main problem is that they both have very high thermal conductivity - much higher than fused silica. As a result, the substrate thermoelastic noise is one of the important noise source for both materials. For instance, if the aLIGO mirror was made of sapphire, the bulk thermoelastic noise would have about the same magnitude as the coating Brownian noise at 100 Hz. As for silicon substrate, the bulk thermoelastic noise is more than twice the size of its corresponding coating Brownian noise because silicon has even higher thermal conductivity than sapphire. One may refer to [40] for detailed methods to calculate bulk thermoelastic noise. Setting up the experiment in a cryogenic enviroment is a possible way to reduce the thermooptic noise.

Furthermore, our formula Eq. (2.93) can serve as a starting point for optimizing the material choice and structure design of the multi-layer coating taking light penetration effects into account. Our numerical results in Sec. 2.6.4 (see Table 2.3) have shown that optimization of the coating structure consistently offers a $\sim 6\%$ decrease in thermal noise, regardless of ϕ_B/ϕ_S. In fact, the optimal structure for these ratios are quite similar, and configurations obtained for each presumed

Coating	Ref. [14] (no light penetration)	Ref. [17] ($\beta = 0$ and no back scattering)	This work
$\lambda/4$	7.18	7.08	7.08
Advanced LIGO	6.93	6.82	6.83
Optimal	6.73	6.62	6.64

Table 2.6: Comparison of thermal noise spectral density (assuming $\phi_B = \phi_S$ and evaluated at $200\,\mathrm{Hz}$, in units of $10^{-21}\mathrm{m}/\sqrt{\mathrm{Hz}}$) between different works.

ratio of ϕ_B/ϕ_S are shown to work for other ratios interchangeably.

Upon completion of this manuscript, we noted that the optimization of the coating structure for the case assuming $\phi_B = \phi_S$ (and $\beta = 0$) has been carried out by Kondratiev, Gurkovsky and Gorodetsky [17]. [We note that their formalism is capable to treating $\beta \neq 0$ and $\phi_B \neq \phi_S$, as well as back-scattering induced by photo elasticity, but they did not explore the impact of these effects in their optimization.] Our results are compatible with theirs, if we also use these restrictions in parameter space and ignore back-scattering.

A comparison between our result, Kondratiev et al., and Harry et al. [14] (which ignores light penetration into the layers, and also effectively assumes $\phi_S = \phi_B$) would therefore illustrate the effects caused by ignoring photoelasticity and further ignoring light penetration into the coating. This is shown in Table 2.6. This again confirms that for total coating thermal noise, light penetration causes noticeable difference in coating thermal noise, while photoelasticity causes a negligible difference.

Acknowledgments

2.A Fluctuations of the complex reflectivity due to refractive index fluctuations

Brownian noise is not only caused by random strains, but also by the refractive-index fluctuations induced by such strains, through the photoelastic effect [Cf. Eqs. (2.13) and (2.14)]. We will quantify this contribution in this section.

2.A.1 The photoelastic effect

If we denote the displacement of coating mass elements as (u_x, u_y, u_z), then the relative coating-thickness change from its equilibrium value can be written as

$$\delta l/l = u_{z,z} \tag{2.115}$$

and the relative transverse area expansion can be written as

$$\delta A/A = u_{x,x} + u_{y,y}. \tag{2.116}$$

If we denote 2-dimensional displacement vectors along the x-y plane as $\vec{u} = (u_x, u_y)$, and two-dimensional gradient as $\vec{\nabla}$, then we have

$$\delta A/A = u_{x,x} + u_{y,y} = \vec{\nabla} \cdot \vec{u}. \tag{2.117}$$

We can then write the change in refractive index as

$$\delta n = \left[\frac{\partial n}{\partial \log l} \right]_{A_j} \frac{\delta l}{l} + \left[\frac{\partial n}{\partial \log A} \right]_{l_j} \vec{\nabla} \cdot \vec{u} \tag{2.118}$$

where $\partial n/\partial \log l$ and $\partial n/\partial \log A$ only depend on material properties. The two terms on the right-hand side of Eq. (2.118) represent refractive index change driven by relative length and area changes, respectively. The first term is given by [28]

$$\beta^L = \left[\frac{\partial n}{\partial \log l} \right]_A = -\frac{1}{2} n^3 CY \tag{2.119}$$

where C is the photoelastic stress constant, Y is the Young's modulus. For silica, $CY \approx 0.27$, therefore $\beta^L_{\text{SiO}_2} = -0.41$. The photoelastic coefficient can also be written as

$$\beta = -\frac{1}{2} n^3 p_{ij} \tag{2.120}$$
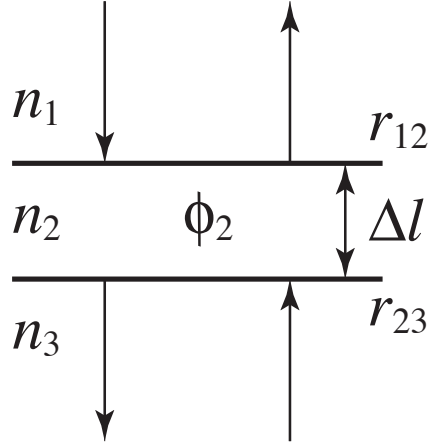
Figure 2.16: Light propagation across a thin layer (thickness of Δl) with fluctuating refractive index (from a uniform n_2 to an average of $n_2 + \delta n_2$ within this thin layer). The propagation matrix corresponding to this structure is given by Eq. (2.122).

where p_{ij} is the photo elastic tensor [39]. Some experiments have been done to measure this coefficient for tantala [27]. Empirically, the value of p_{ij} varies from -0.15 to 0.45 for Ta_2O_5 thin film fabricated in different ways. Here for the longitudinal photoelasticity, $\beta^{\mathrm{L}}_{\mathrm{Ta_2O_5}}$, we use -0.5 in our numerical calculation.

We shall next obtain formulas that will allow us to convert fluctuations in n into fluctuations in the complex reflectivity of the multi-layer coating.

2.A.2 Fluctuations in an infinitesimally thin layer

Because the coating is very thin compared with the Rayleigh associated with beam spot size, we model the phase shift of light gained during propagation along z as only determined the local refractive index. If the refractive index δn at a particular location $\delta n(z)$ is driven by longitudinal strain u_{zz} at that location, the fact that $\langle u_{zz}(z')u_{zz}(z'')\rangle \propto \delta(z' - z'')$ causes concern, because this indicates a high *variance* of δn at any given single point z, with a magnitude which is formally infinity. If we naively consider the reflection of light across any interface within the coating, e.g., at $z = z_0$, then the independent and high-magnitude fluctuations of $n(z_0-)$ and $n(z_0+)$ would lead to a dramatic fluctuation in the reflectivity

$$r = \frac{n(z_0-) - n(z_0+)}{n(z_0+) + n(z_0-)} \tag{2.121}$$

because, naively, $n(z_0-)$ and $n(z_0+)$ are uncorrelated and both have a variance of infinity.

However, two effects prevent the above divergence from actually taking place: (i) there is a finite correlation length for strain fluctuations (although not explicitly given in our current analysis) and

(ii) propagation of light averages over those fluctuations. The most convenient way to circumvent the above divergence is to always consider light propagation across a finite layer of materials. As shown in Fig. 2.16, let us consider three regions in the coating, with refractive indices n_1, n_2 and n_3 separated by two interfaces, with the length of the n_2 layer given by Δl — and here we only consider fluctuations in n_2. The entire transfer matrix (from below to above, in Fig. 2.16) is given by

$$\mathbf{M} = \mathbf{R}_{r_{12}} \mathbf{T}_{\phi_2} \mathbf{R}_{r_{23}} \tag{2.122}$$

following the same convention as in Sec. 2.2.3. Suppose the originally uniform n_2 now fluctuates, and after averaging over this thin layer, gives a mean refractive index of $n_2 + \delta n_2$, we use this as the refractive index of the entire layer, and then have

$$\delta\mathbf{M} = \frac{n_2}{\sqrt{n_1 n_3}} \begin{pmatrix} i & -i \\ i & -i \end{pmatrix} \delta n_2 \cdot k_0 \Delta l \tag{2.123}$$

Note that when $\Delta l \to 0$, $\delta n_2 \cdot \Delta l$ has a variance that approaches zero, and therefore $\delta\mathbf{M}$ is an infinitesimal matrix, and there is no divergence. [Note that when Δl is small enough, δn_2 has a variance that is comparable to the total variance of n, which is finite — therefore $\delta n_2 \cdot \Delta l \sim O(\Delta l)$.]

The physical meaning of Eq. (2.123) is the following: a random field of refractive index not only gives rise to a random phase shift (diagonal term), but also gives rise to a random reflectivity (non-diagonal term). The latter term is an additional contribution that has been ignored by previous analytical calculations.

2.A.3 The entire coating stack

Now we are ready to consider the entire multi-layer coating. Let us first focus on layer j of the coating stack, bounded by two interfaces with reflectivities r_{j-1} and r_j, respectively. Since the total transfer matrix of the entire stack is written as

$$\mathbf{M} = \cdots \mathbf{T}_{\phi_{j+1}} \mathbf{R}_{r_j} \mathbf{T}_{\phi_j} \mathbf{R}_{r_{j-1}} \cdots , \tag{2.124}$$

the reflectivity fluctuations with this layer will contribute to the matrix $\mathbf{T}_{\phi_j}$ above, which in turn will contribute to fluctuations in the entire $\mathbf{M}$. Consider a dz-thick sub-layer located at distance z' from the r_j boundary (lower boundary in Fig. 2.1), therefore at coordinate location $z = z_{j+1} + z'$ and integrate, we have

$$\mathbf{T}_{\phi_j} \to \mathbf{T}_{\phi_j} + k_0 \int_0^{l_j} \delta n(z_{j+1} + z) \mathbf{T}_{k_0 n_j z} \begin{bmatrix} i & -i \\ i & -i \end{bmatrix} \mathbf{T}_{k_0 n_j (l_j - z)} \, dz'$$

$$= \begin{bmatrix} 1 & \delta\eta_j \\ \delta\eta_j^* & 1 \end{bmatrix} \mathbf{T}_{\phi_j + k_0 \delta\bar{n}_j l_j} \tag{2.125}$$

where

$$\delta\bar{n}_j = \frac{1}{l_j} \int_0^{l_j} \delta n_j(z_{j+1} + z) dz \tag{2.126}$$

and

$$\delta\eta_j = -ik_0 \int \delta n_j(z_{j+1} + z) e^{2ik_0 n_j z} dz. \tag{2.127}$$

Here we have defined

$$z_j \equiv \sum_{n=j}^{N} l_n \tag{2.128}$$

to be the z coordinate of the top surface of layer j.

We need to adapt the new transfer matrix into the old form, but with modified $\{r_j\}$ and $\{\phi_j\}$. From Eq. (2.125), since $\delta\eta_j$ is complex, we need to adjust ϕ_j, r_j, as well as ϕ_{j+1}:

$$\mathbf{T}_{\phi_{j+1}} \mathbf{R}_{r_j} \mathbf{T}_{\phi_j}$$

$$\rightarrow \quad \mathbf{T}_{\phi_{j+1} + \delta\psi_j^+} \mathbf{R}_{r_j + \delta r_j} \mathbf{T}_{\phi_j + k_0 l_j \delta\bar{n}_j + \delta\psi_j^-}. \tag{2.129}$$

Here we have defined in addition

$$\delta r_j = -t_j^2 k_0 \int_0^{l_j} \delta n_j(z_{j+1} + z) \sin(2k_0 n_j z) dz \tag{2.130}$$

and

$$\delta\psi_j^{\pm} = \frac{r_j^2 \pm 1}{2r_j} k_0 \int_0^{l_j} \delta n_j(z_{j+1} + z) \cos(2k_0 n_j z) dz. \tag{2.131}$$

As we consider photoelastic noise of all the layers together, δr_j in Eq. (2.130) needs to be used for the effective fluctuation in reflectivity of each layer, while

$$\delta\phi_j = k_0 l_j \delta\bar{n}_j + \delta\psi_j^- + \delta\psi_{j-1}^+ \tag{2.132}$$

should be used as the total fluctuation in the phase shift of each layer.

2.A.4 Unimportance of transverse fluctuations

Connecting with the photoelastic effect, we have explicitly

$$\delta n_j(z, \vec{x}) = \beta_j^L u_{zz}(z, \vec{x}) + \beta_j^T \vec{\nabla} \cdot \vec{u}. \tag{2.133}$$

Here the vector $\vec{u}$ is the two-dimensional displacement vector (u_x, u_y) and $\vec{\nabla} \cdot$ is the 2-D divergence along the x-y plane. For terms that contain the transverse vector $\vec{u}$, we note that when a weighted average of ξ is taken over the mirror surface [see Sec. 2.2.4], they yield the following type of contribution

$$
\begin{aligned}
&\int_M I(\vec{x}) \left(\vec{\nabla} \cdot \vec{u} \right) d^2 \vec{x} \\
= &\int_{\partial M} dl (\vec{n} \cdot \vec{u} I) + \int_M \vec{u} \cdot \vec{\nabla} I \, d^2 \vec{x} \\
= &\int_M \vec{u} \cdot \vec{\nabla} I \, d^2 \vec{x}.
\end{aligned} \tag{2.134}
$$

Here M stands for the 2-d region occupied by the beam, and ∂M is the boundary on which power vanishes. As a consequence, the first term is zero according to the boundary condition, while the second term gains a factor of (l_i/w_0) with respect to other types of coating Brownian noise; here l_j is the thickness of the j-th layer, and w_0 the beam spot size. Since we always assume coating thickness l_i to be much smaller than the beam radius r_{beam}, we can neglect refractive index fluctuation due to area fluctuation.

2.B Elastic deformations In the coating

Throughout this paper, we assume the mirror substrate to be a half infinite space. We establish a Cartesian coordinate system, with (x, y) directions along the coating-substrate interface, and z direction orthogonal to the mirror surface (in the elasticity problem, we also ignore mirror curvature). This allows us to calculate elastic deformations in the spatial frequency domain. We will also assume the coating thickness to be much less than the beam spot size.

We denote the displacement along x, y and z directions as u_x, u_y and u_z. It is then straightforward to express the 3×3 strain tensor $\mathbf{S}$ in terms of their derivatives, and stress tensor $\mathbf{T}$ in terms of Hooke's Law:

$$
\begin{aligned}
S_{ij} &= \frac{1}{2} \left(\frac{\partial u_i}{\partial x_j} + \frac{\partial u_j}{\partial x_i} \right), & (2.135) \\
\Theta &= S_{ii}, & (2.136) \\
\Sigma_{ij} &= \frac{1}{2} [S_{ij} + S_{ji}] - \frac{1}{3} \delta_{ij} \Theta, & (2.137)
\end{aligned}
$$
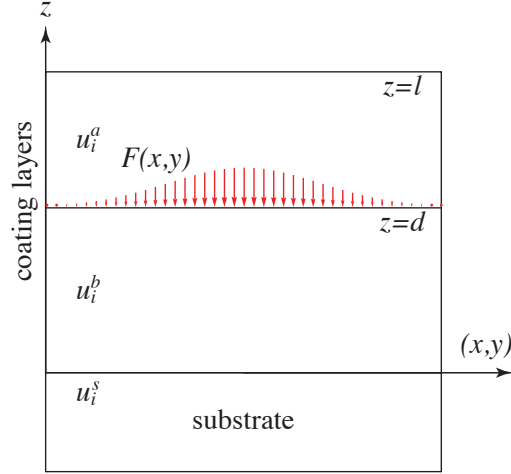
Figure 2.17: Sample with single layer coating, force is applied perpendicular to the air/coating interface.

$$T_{ij} = -K\Theta\delta_{ij} - 2\mu\Sigma_{ij}. \tag{2.138}$$

Here we have $x^j = (x, y, z)$, with Latin indices (like i and j) running from 1 to 3. Within any layer, it is straightforward to write down the most general solution of the elasticity equilibrium equation

$$T_{ij,j} = 0 \tag{2.139}$$

as

$$
\begin{aligned}
\tilde{u}_x &= ik_x[(\tilde{\alpha}_+ + \kappa z\tilde{\beta}_+)e^{\kappa z} + (\tilde{\alpha}_- - \kappa z\tilde{\beta}_-)e^{-\kappa z}] \\
&\quad - ik_y[\tilde{\gamma}_+ e^{\kappa z} + \tilde{\gamma}_- e^{-\kappa z}], \tag{2.140} \\
\tilde{u}_y &= ik_y[(\tilde{\alpha}_+ + \kappa z\tilde{\beta}_+)e^{\kappa z} + (\tilde{\alpha}_- - \kappa z\tilde{\beta}_-)e^{-\kappa z}] \\
&\quad + ik_x[\tilde{\gamma}_+ e^{\kappa z} + \tilde{\gamma}_- e^{-\kappa z}], \tag{2.141} \\
\tilde{u}_z &= -\kappa[\tilde{\alpha}_+ + \tilde{\beta}_+(-3 + 4\sigma + \kappa z)]e^{\kappa z} \\
&\quad + \kappa[\tilde{\alpha}_- + \tilde{\beta}_-(-3 + 4\sigma - \kappa z)]e^{-\kappa z}, \tag{2.142}
\end{aligned}
$$

where tilde denotes quantities in the x-y spatial-frequency domain, and $\kappa = \sqrt{k_x^2 + k_y^2}$. Namely

$$u_x(x, y, z) = \int \frac{dk_x dk_y}{(2\pi)^2} \tilde{u}(k_x, k_y, z) e^{-i(k_x x + k_y y)}. \tag{2.143}$$

We now consider a single-layer coating on a substrate (see Fig. 2.17), with the coating-substrate interface located at $z = 0$, and the coating-air interface at $z = l$. Suppose there is a force profile $F(x, y)$ exerted perpendicular to the surface at $z = d$, $0 < d < l$, and let us calculate the elastic

deformation field caused by F. The entire system is now divided into three regions, (a): $d < z < l$, (b): $0 < z < d$, and (s): $z < 0$. At the interfaces, we obtain the following 15 boundary conditions,

$$T_{iz}^a = 0, \quad z = l, \tag{2.144}$$

$$T_{xz}^a = T_{xz}^b, \; T_{yz}^a = T_{yz}^b, \; T_{zz}^b - T_{zz}^a = F, \quad z = d, \tag{2.145}$$

$$u_j^a = u_j^b, \quad z = d, \tag{2.146}$$

$$T_{iz}^b = 0, \; u_j^b = u_j^s, \quad z = 0, \tag{2.147}$$

as well as the condition that when $z \to -\infty$, $u_j^s \to 0$ (which leads to $\tilde{\alpha}_-^s = \tilde{\beta}_-^s = \tilde{\gamma}_-^s = 0$). We are left with 15 fields

$$(\tilde{\alpha}_\pm^a, \tilde{\beta}_\pm^a, \tilde{\gamma}_\pm^a, \tilde{\alpha}_\pm^b, \tilde{\beta}_\pm^b, \tilde{\gamma}_\pm^b, \tilde{\alpha}_+^s, \tilde{\beta}_+^s, \tilde{\gamma}_+^s) \tag{2.148}$$

which can be solved from the 15 boundary conditions. Assuming $\kappa d \ll 1$ and $\kappa l \ll 1$, we find that all $\tilde{\gamma}$ vanish, and

$$\tilde{\alpha}_+^a = \frac{F(1+\sigma_s)[2 - 3\sigma_s + \sigma_c(-3 + 4\sigma_s)]}{2Y_s\kappa^2(-1+\sigma_c)}, \tag{2.149}$$

$$\tilde{\alpha}_-^a = \frac{F(\sigma_c - \sigma_s)(1+\sigma_s)}{2Y_s\kappa^2(-1+\sigma_c)}, \tag{2.150}$$

$$\tilde{\beta}_+^a = -\frac{F(1+\sigma_s)(-3+4\sigma_s)}{4Y_s\kappa^2(-1+\sigma_c)}, \tag{2.151}$$

$$\tilde{\beta}_-^a = \frac{F(1+\sigma_s)}{4Y_s\kappa^2(1-\sigma_c)}, \tag{2.152}$$

$$\tilde{\alpha}_+^b = \frac{F(1+\sigma_s)[2 - 3\sigma_s + \sigma_c(-3+4\sigma_s)]}{2Y_s\kappa^2(-1+\sigma_c)}, \tag{2.153}$$

$$\tilde{\alpha}_-^b = \frac{F(\sigma_c - \sigma_s)(1+\sigma_s)}{2Y_s\kappa^2(-1+\sigma_c)}, \tag{2.154}$$

$$\tilde{\beta}_+^b = \frac{F[Y_s(1+\sigma) - Y_c(-3+\sigma_s+4\sigma_s^2)]}{4YY_s\kappa^2(-1+\sigma_c)}, \tag{2.155}$$

$$\tilde{\beta}_-^b = \frac{F[Y_s(1+\sigma_c) - Y_c(1+\sigma_s)]}{4YY_s\kappa^2(-1+\sigma_c)}, \tag{2.156}$$

$$\tilde{\alpha}_+^s = \frac{F(1+\sigma_s)(-1+2\sigma_s)}{Y_s\kappa^2}, \tag{2.157}$$

$$\tilde{\beta}_+^s = -\frac{F(1+\sigma_s)}{Y_s\kappa^2}. \tag{2.158}$$

We can therefore obtain the stain tensor in the frequency domain for the coating. The non-zero elements for region (a) are given by

$$S_{xx}^a = \frac{Fk_x^2(-1+2\sigma_s)(1+\sigma_s^2)}{Y_s\kappa^2}, \tag{2.159}$$

$$S_{yy}^a = \frac{Fk_y^2(-1+2\sigma_s)(1+\sigma_s^2)}{Y_s\kappa^2}, \tag{2.160}$$

$$S^a_{xy} = S_{yx} = \frac{Fk_xk_y(-1 + 2\sigma_s)(1 + \sigma_s^2)}{Y_s\kappa^2}, \tag{2.161}$$

$$S^a_{zz} = F\frac{\sigma_c(-1 + \sigma_s + 2\sigma_s^2)}{Y_s(-1 + \sigma_c)}, \tag{2.162}$$

while those in region (b) are given by

$$S^b_{xx} = \frac{Fk_x^2(-1 + 2\sigma_s)(1 + \sigma_s^2)}{Y_s\kappa^2}, \tag{2.163}$$

$$S^b_{yy} = \frac{Fk_y^2(-1 + 2\sigma_s)(1 + \sigma_s^2)}{Y_s\kappa^2}, \tag{2.164}$$

$$S^b_{xy} = S_{yx} = \frac{Fk_xk_y(-1 + 2\sigma_s)(1 + \sigma_s^2)}{Y_s\kappa^2}, \tag{2.165}$$

$$S^b_{zz} = F\left[\frac{-(1 + 2\sigma_c)}{Y_c} - \frac{\sigma_c(-1 + \sigma_s + 2\sigma_s^2)}{Y_s(1 - \sigma_c)}\right]. \tag{2.166}$$

Using linear superposition, as well as taking the appropriate limits of the above solution, it is straightforward to obtain elastic deformations in all the scenarios in Sec. 2.4, with forces applied on various surfaces, that are used to obtain cross spectra between different noises.

2.C   Definition of loss angle

In the past [14], the coating loss angle was defined in association with the parallel and perpendicular coating strains. The equation is written as

$$\phi_{\text{coated}} = \phi_{\text{sub}} + \frac{\delta U_\| d}{U}\phi_\| + \frac{\delta U_\perp d}{U}\phi_\perp \tag{2.167}$$

where $\delta U_\|$ and $\delta U_\perp$ are the energy density in parallel and perpendicular coating strains

$$\delta U_\| = \int_s \frac{1}{2}(S_{xx}T_{xx} + S_{yy}T_{yy})\,dxdy, \tag{2.168}$$

$$\delta U_\perp = \int_s \frac{1}{2}S_{zz}T_{zz}\,dxdy, \tag{2.169}$$

and where S_{ij} are the strains and T_{ij} are the stresses. While such a definition seems to be compatible with the symmetry of the system, the quantities $\delta U_\|$ and $\delta U_\perp$ cannot be used as energy, since in certain scenarios they each can become negative.

For example, we consider cube with surface area of each side A (poisson ratio σ, Young's modulus Y), and we uniformly apply two pairs of forces, one pair with magnitude f on opposite yz planes, the other with magnitude F on opposite xy planes, with $f \ll F$, as shown in Figure 2.18. According to the definition of Young's modulus and Poisson's ratio, up to leading order in f/F the non-vanishing

strains are,

$$S_{zz} = -\frac{F/A}{Y}, \quad S_{xx} = S_{yy} = \sigma\frac{F/A}{Y}. \tag{2.170}$$

On the other hand, for stress, we have, up to leading order in f/F,

$$T_{xx} = -f/A, \quad T_{yy} = 0, \quad T_{zz} = -F/A. \tag{2.171}$$

As a consequence, we have

$$\delta U_{\parallel} = S_{xx}T_{xx} + S_{yy}T_{yy} = -\sigma fF/(A^2Y) < 0 \tag{2.172}$$

which means $\delta U_{\parallel}$ is not a reasonable candidate for energy, at least with $\sigma \neq 0$. Since it is also true that $S_{xx}T_{xx} < 0$ we will arrive at

$$\delta U_{\perp} = S_{zz}T_{zz} < 0 \tag{2.173}$$

if we take this configuration and rotate by 90 degrees around the y axis, such that x rotates into z.
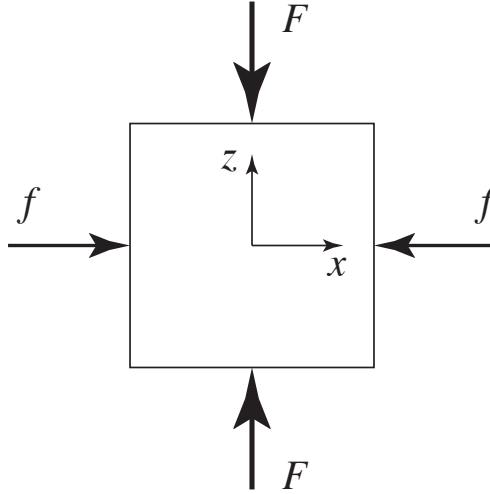
Figure 2.18: Solid cube with two pairs of forces applied on the side: $f \ll F$.

One reasonable way of defining the loss angle is to derive it from the fundamental elastic energy equation. The general form of the stored elastic energy density U can be written as

$$U = \frac{1}{2}K\Theta^2 + \mu\Sigma_{ij}\Sigma_{ij}, \tag{2.174}$$

$$U_B = \frac{1}{2}K\Theta^2, \tag{2.175}$$

$$U_S = \mu\Sigma_{ij}\Sigma_{ij}, \tag{2.176}$$

where K is called the *bulk modulus* and μ is the *shear modulus*. In the calculation, we use Young's

j	l_j				
1–5	0.497325	0.208175	0.289623	0.237274	0.250176
6–10	0.245330	0.249806	0.240129	0.270968	0.224129
11–15	0.251081	0.259888	0.260826	0.213460	0.290468
16–20	0.214524	0.273240	0.230905	0.259924	0.230020
21–25	0.275429	0.233086	0.270385	0.208581	0.273798
26–30	0.249741	0.267864	0.204698	0.292317	0.209712
31–35	0.278560	0.220264	0.282694	0.221687	0.268559
36–38	0.233460	0.270419	0.223050		

Table 2.7: Structure of an Advanced LIGO-like coating optimized jointly for dichroic operation and thermal noise. Thickness of each layer, given in units of wavelength (for light with vacuum-wavelength of 1064 nm), are listed here for the 38 layers. Note that $l_{1,3,5,...}$ are SiO$_2$ layers, while $l_{2,4,6,...}$ are Ta$_2$O$_5$ layers.

modulus Y and Poisson's ratio σ instead of K and μ. Their relation is given in Eq. (2.51). The expansion Θ and shear Σ are both irreducible tensorial parts of the strain tensor S,

$$\Theta = S_{ii}, \tag{2.177}$$

$$\Sigma = \frac{1}{2}(S_{ij} + S_{ji}) - \frac{1}{3}\delta_{ij}S_{kk}. \tag{2.178}$$

Note that the expansion and shear energy U_B and U_S are always positive, so it is consistent to define the loss angles ϕ_B and ϕ_S.

2.D   Advanced LIGO style coating

In Table 2.7, we provide the structure of the coating optimized jointly for dichroic operation and thermal noise.

Bibliography

[1] D. Meiser, *et al.* Phys. Rev. Lett. **102**, 163601 (2009).

[2] LIGO Scientific Collaboration, Rep. Prog. Phys. **72** (2009).

[3] G. M. Harry (for the LIGO Scientific Collaboration), Class. Quantum Grav. **27**, 084006 (2010).

[4] B. Willke et al., Class. Quantum Grav. **23** S207 (2006).

[5] The Virgo Collaboration, *Advanced Virgo Baseline Design,* note VIR027A09, May 16, (2009).

[6] K. Kuroda (on behalf of the LCGT Collaboration), Class. Quantum Grav. **27**, 084004 (2010).

[7] E. D'Ambrosio, Phys. Rev. D **67**, 102004 (2003); M. Bondarescu and K.S. Thorne, Phys. Rev. D **74** 082003 (2006); M. Bondarescu, O. Kogan and Y. Chen, Phys. Rev. D **78** 082002 (2008).

[8] G. Lovelace, Class. Quantum Grav. **24** 4491 (2007); J.-Y. Vinet, Living Rev. Relativity **12** 5 (2009).

[9] H. J. Kimble, B. L. Lev and J. Ye, Phys. Rev. Lett. **101**, 260602 (2008).

[10] M. Evans *et al.*, Phys. Rev. D **78**, 102003 (2008).

[11] G. González and P. Saulson, J. Acoust. Soc. Am. **96**, 207 (1994).

[12] Y. Levin, Phys. Rev. D **57**, 659 (1998).

[13] H. B. Callen and T. A. Welton, Phys. Rev. **83**, 34 (1951).

[14] G. M. Harry, A. M. Gretarsson, P. R. Saulson, S. E. Kittelberger, S. D. Penn, W. J. Startin, S. Rowan, M. M. Fejer, D. R. M. Crooks, G. Cagnoli, J. Hough and N. Nakagawa, Class. Quantum Grav. **19**, 897 (2002).

[15] A.E. Villar et al., Phys. Rev. D **81**, 122001 (2010).

[16] A. Gurkovsky and S. Vyatchanin, Phys. Lett. A **374**,3267 (2010).

[17] N. M. Kondratiev, A. G. Gurkovsky, and M. L. Gorodetsky, Phys. Rev. D **84**, 022001, (2011).

[18] L. D. Landau and E. M. Lifshitz, *Theory of Elasticity (Course of Theoretical Physics)*, Pergamon (1981).

[19] I.W. Martin, Class. Quantum Grav. **27**, 225020 (2010).

[20] G.M. Harry et al., Class. Quantum Grav. **24**, 405, (2007).

[21] S.D. Penn et al., Class. Quantum Grav. **20** 2917, (2003).

[22] R. Waynant and M. Ediger, *Electro-Optics Handbook*, McGraw-Hill (1994)

[23] M. M. Fejer, S. Rowan, G. Cagnoli, D. R. M. Crooks, A. Gretarsson, G. M. Harry, J. Hough, S. D. Penn, P. H. Sneddon and S. P. Vyatchanin, Phys. Rev. D **70**, 082003 (2004).

[24] P. J. Martin, A. Bendavid, M. Swain, R. P. Netterfield, T. J. Kinder, W. G. Sainty, D. Drage and L. Wielunski, Thin Solid Films **239**, 181 (1994).

[25] G. M. Harry, M. R. Abernathy, A. E. Becerra-Toledo, H. Armandula, E. Black, K. Dooley, M. Eichenfield, C. Nwabugwu, A. Villar, D. R. M. Crooks, G. Cagnoli, J. Hough, C. R. How, I. MacLaren, P. Murray, S. Reid, S. Rowan, P. H. Sneddon, M. M. Fejer, R. Route, S. D. Penn, P. Ganau, J. M. Mackowski, C. Michel, L. Pinard and A. Remillieux , Class. Quantum Grav. **24**, 405 (2007).

[26] S. D. Penn, P. H. Sneddon, H. Armandula, J. C. Betzwieser, G. Cagnoli, J. Camp, D. R. M. Crooks, M. M. Fejer, A. M. Gretarsson, G. M. Harry, J. Hough, S. E. Kittelberger, M. J. Mortonson, R. Route, S. Rowan and C. C. Vassiliou, Class. Quantum Grav. **20**, 2917 (2003).

[27] Y. Nakagawa *et al.*, Electronics and Communications in Japan, **(84)**, 46 (2001).

[28] J. Stone, Journal of Lightwave Technology **6**, 1245 (1988).

[29] G. Billingsley, private communication.

[30] J. Agresti, G. Castaldi, R. DeSalvo, V. Galdi, V. Pierro, and I. M. Pinto, LIGO-P060027-00-Z.

[31] J. A. Nelder and R. J. Mead, The Computer Journal, **7**, (1965).

[32] W. H. Press, S. A. Teukolsky, W. T. Vetterling, B. P. Flannery, "Numerical Recipes: The Art of Scientific Computing" (Third Edition), Section 10.5, Cambridge University Press (2007).

[33] A. Heptonstall, G. Cagnoli, J. Hough, S. Rowan, Phys. Lett. A **354**, 353, (2006).

[34] S. D. Penn, A. Ageev, D. Busby, G. M. Harry, A. M. Gretarsson, K. Numata, P. Willems, Phys. Lett. A **352**, 3, (2006).

[35] L. H. Donnell, NACA Report No. 479, (1933).

[36] Robert D. Blevins, *Formulas for Natural Frequency and Mode Shape*, Van Nostrand Reinhold Company, New York (1979).

[37] W. Flügge, *Stresses in Shells*, Springer-Verlag, New York (1973)

[38] S. E. Whitcomb, private communication.

[39] D. F. Nelson and M. Lax, Phys. Rev. Lett. **24** (1970).

[40] V. B. Braginsky, M. L. Gorodetsky, and S. P. Vyatchanin, Phys. Lett. A **271**, 303, (2000).

Part II

Topics in macroscopic quantum mechanics

Chapter 3

Open quantum dynamics of single-photon optomechanical devices

We study the quantum dynamics of a Michelson interferometer with Fabry-Perot cavity arms and one movable end mirror, and driven by a single photon — an optomechanical device previously studied by Marshall et al. as a device that searches for gravity decoherence. We obtain an exact analytical solution for the system's quantum mechanical equations of motion, including details about the exchange of the single photon between the cavity mode and the external continuum. The resulting time evolution of the interferometer's fringe visibility displays interesting new features when the incoming photon's frequency uncertainty is narrower or comparable to the cavity's line width — only in the limiting case of much broader-band photon does the result return to that of Marshall et al., but in this case the photon is not very likely to enter the cavity and interact with the mirror, making the experiment less efficient and more susceptible to imperfections. In addition, we show that in the strong-coupling regime, by engineering the incoming photon's wave function, it is possible to prepare the movable mirror into an arbitrary quantum state of a multi-dimensional Hilbert space.

3.1 Introduction

Recently, significant progress has been made in observing quantum effects in macroscopic mechanical systems [1]. As presented in the work of O'Connell *et al.* [2], a 6-GHz nano-mechanical oscillator was cooled down near its quantum ground state with dilution refrigeration, and later prepared into a Fock state by coupling the oscillator to a superconducting qubit. States with thermal occupation numbers

below unity have also been achieved with cavity-assisted radiation-pressure cooling, by Teufel *et al.* [3] and Safavi-Naeini *et al.* [4]. Further more, as shown by Gupta et al. [5] and Thompson et al. [6], it is possible to couple a single photon strongly with a mechanical degree of freedom, such that the momentum imparted by a single photon to a mechanical degree of freedom can be comparable to its initial momentum uncertainty.

In this paper, we study the open quantum dynamics of a nonlinear optomechanical device, namely a Michelson interferometer with Fabry-Perot cavities, one of them with a movable end mirror (acting as the mechanical oscillator). This device, driven by a single photon, was proposed by Marshall *et al.* [7, 8] as an experiment to search for Penrose's conjecture of gravity decoherence [9]. Such single-photon driven devices have also been more recently studied by Rabl [10] and Nunnenkamp *et al.* [11]. By taking advantage of the conserved quantity—the total number of photons in the system, we can obtain exact solutions to this system's quantum dynamics. Unlike Rabl and Nunnenkamp et al., who studied systematically the statistics of the out-going photons and the steady state reached by the mechanical oscillator, we focus instead on the fringe visibility of a single-photon interferometer, and the conditional quantum state of the mechanical oscillator upon the detection of an out-going photon.

The single-photon Michelson interferometer is shown schematically in Fig. 3.1, in which the port on the left is the input port, towards which the single photon is injected; the photon, after interacting with the Michelson interferometer, may exit either from the input port, or from the other open port. Each of the two arms consists of a high-finesse optical cavity; the setup of these two cavities are identical, except one of them has a movable end mirror, which acts as the mechanical oscillator that interacts with light in the cavity. The 50/50 beam splitter splits the quantum state of the entire mirror-light system into two components, one of them corresponding to the photon entering the fixed cavity (and leaving the oscillator at its initial state), the other corresponding to the photon entering the movable cavity (thereby modifying the oscillator's state through radiation pressure). We will set the displacement zero-point of the interferometer to have equal arm lengths, with each arm at an equal distance to the beamsplitter. At such a zero point, the photon injected from the input port will return to the input port with unit probability. Therefore we also call the input port the "bright port" and the other open port the "dark port". We can artificially tune the interferometer away from its zero point, e.g., by adjusting the fixed microscopic distances between the front mirrors and the beamsplitter. This changes the relative phase φ between the two superimposed components in the wave function of the entire system; the resulting variations in the probability density of the photon exiting the bright port at time t, quantified by the fringe visibility, is a measure of the degree of coherence between these two components at this moment in time.

In the case of low environmental temperature and in the absence of unexpected mechanisms of decoherence, Marshall *et al.* showed that the visibility will revive completely for every half of the

mechanical oscillation period. In obtaining such a result, they assumed the photon was initially already in either of the two cavity arms, and considered a closed evolution of the cavity mode and the mechanical oscillator. This assumption has also been widely used in analysis of such a nonlinear optomechanical device, e.g., by Bose *et al.* [12] and subsequent analysis of the Marshall experiment [7] by Bassi *et al* [13].
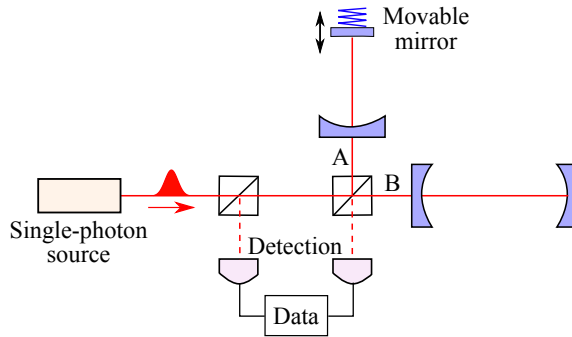
Figure 3.1: (Color online.) A schematic showing the single-photon interferometer. The external single photon excites the cavity mode which in turn interacts with the movable end mirror via radiation pressure. This is adapted from Fig. 1 of Ref. [7] with small modifications.

In a realistic experimental setup, it is necessary to take full account of the *open quantum dynamics* of this system, which involve the oscillator (the mirror), the cavity mode and the external continuous field, including how the single photon is coupled into the cavity in the first place. The open quantum dynamics depend on the wave function of the photon, whose Fourier transform is related to the frequency content of the photon. For example, if the photon has a short-pulse wave function with time-domain duration much less than the cavity storage time, which corresponds to a frequency uncertainty much larger than the cavity line width, then the photon will only enter the cavity with a small probability. By contrast, a narrowband photon (with frequency uncertainty below cavity line width) must have a wave packet duration much longer than cavity storage time, and therefore we must address the issue that the photon can be simultaneously inside and outside the cavity. The latter scenario, although more complicated, might be experimentally more favorable, as in this scenario the photon has a high probability to enter the cavity and to interact with the mirror much more strongly.

The outline of this article goes as follows: in Sec. 11.2, we will write down the Hamiltonian of our nonlinear optomechanical device and study the open quantum dynamics by solving the Shrödinger equation exactly; in Sec. 11.3, we will give a detailed analysis of the single-photon interferometer, and will calculate the interferometer's fringe visibility; in Sec. 11.4, we will show that the mechanical oscillator can be prepared to an arbitrary quantum state in a multi-dimensional Hilbert space, if we inject the single photon with a properly-designed profile into the interferometer; in Sec. 11.5, we will summarize our main results.

3.2 A Single cavity with one movable mirror
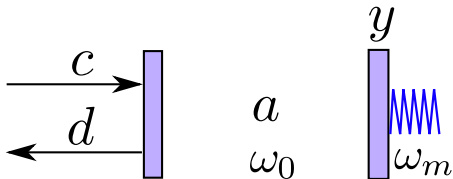
Figure 3.2: (Color online.) A schematic showing a single-photon interferometer with Fabry-Perot cavity and a movable mirror. The displacement of the mirror-endowed mechanical oscillator y is parametrically coupled to the cavity mode a, which has an eigenfrequency ω_0 with $y = 0$. The cavity mode in turn couples to the ingoing continuous field $c(x)$ and outgoing continuous field $d(x)$.

Before studying the entire single-photon interferometer, we first consider a single cavity, as shown schematically in Fig. 3.2. The cavity has one fixed mirror located at $x = 0$, and one movable mirror which acts as a mechanical oscillator. Here, assuming the injected photon to have a frequency content much less than the free spectral range of the cavity (which has a relatively high finesse), we will only consider one optical mode of the cavity (which we shall refer to as *the cavity mode*). By assuming a high finesse for the cavity, this mode couples to the external vacuum via single-photon exchange. At linear order in the mirror's motion and assuming low velocity, the coupling between the mirror and the cavity mode is parametric: the position y of the mirror modifies the eigenfreqeuncy of the cavity mode.

3.2.1 The Hamiltonian

Here we will write down the Hamiltonian of the system. For simplicity, we will use natural units with $\hbar = 1$ and $c = 1$ throughout this paper. The Hamiltonian of the external continuous optical field, in the position space representation, is given by

$$
\begin{aligned}
\hat{H}_o &= \frac{i}{2} \int_{-\infty}^{0} [(\partial_x \hat{c}_x^\dagger)\hat{c}_x - \hat{c}_x^\dagger \partial_x \hat{c}_x] \, \mathrm{d}x \\
&+ \frac{i}{2} \int_{-\infty}^{0} [(\partial_x \hat{d}_x^\dagger)\hat{d}_x - \hat{d}_x^\dagger \partial_x \hat{d}_x] \, \mathrm{d}x
\end{aligned}
\tag{3.1}
$$

where $\hat{c}_x$ and $\hat{d}_x$ are the annihilation operators for ingoing and outgoing fields at location x, respectively. Note that for the actual setup shown in Fig. 3.2, the ingoing and outgoing fields are on the same side of the front mirror, namely both at $x < 0$. Since the field operators at different locations commute with each other—$[\hat{c}_x\, \hat{c}_{x'}^\dagger] = \delta(x - x')$, we can fold the outgoing field from $[-\infty, 0]$ into $[0, +\infty]$, therefore just use $\hat{c}$ to denote both the ingoing and outgoing fields, with $\hat{c}_x(x < 0)$ for the

ingoing field and $\hat{c}_x (x > 0)$ for the outgoing field, namely

$$\hat{H}_o = \frac{i}{2} \int_{-\infty}^{\infty} (\partial_x \hat{c}_x^\dagger \hat{c}_x - \hat{c}_x^\dagger \partial_x \hat{c}_x) \, \mathrm{d}x. \tag{3.2}$$

The free Hamiltonian of the single cavity mode is given by

$$\hat{H}_c = \omega_0 \hat{a}^\dagger \hat{a}. \tag{3.3}$$

with $\hat{a}$ the annihilation operator and $[\hat{a}, \hat{a}^\dagger] = 1$.

The free Hamiltonian for the mechanical oscillator reads

$$\hat{H}_m = \frac{\hat{p}_y^2}{2m} + \frac{1}{2} m \omega_m^2 \hat{y}^2 \tag{3.4}$$

where $\hat{y}$ and $\hat{p}_y$ are the position and momentum operators, respectively.

The total interaction Hamiltonian H_I between the external continuum and the cavity mode in the rotating-wave approximation, and between the cavity mode and the mechanical oscillator, is given by

$$\hat{H}_I = i\sqrt{\gamma}(\hat{c}_0 \hat{a}\dagger - \hat{a}\hat{c}_0^\dagger) + k\hat{a}^\dagger \hat{a}\hat{y}. \tag{3.5}$$

Here $\gamma = \frac{T}{2L}$ is the cavity bandwidth with L being the cavity length; $k = \omega_0/L$ is the optomechanical coupling constant. The interaction between the cavity mode and the external continuum takes place at the front mirror with $x = 0$ and the Hamiltonian describes the exchange of photon between them. The total Hamiltonian is a sum of the free and the interaction parts, namely,

$$\hat{H} = \hat{H}_o + \hat{H}_c + \hat{H}_m + \hat{H}_I \,. \tag{3.6}$$

Note once more that by including only a single cavity mode resonant at frequency $\omega_0/(2\pi)$, we must make sure the frequency content of the injected light is focused well within a free spectral range, $c/(2L)$.

3.2.2 Structure of the Hilbert space

Even though the Hamiltonian contains a cubic term $\hat{a}^\dagger \hat{a}\hat{y}$, which implies a nonlinear dynamics, we have a conserved dynamical quantity—the total photon number:

$$\hat{a}^\dagger \hat{a} + \int_{-\infty}^{+\infty} \hat{c}_x^\dagger \hat{c}_x \, \mathrm{d}x, \tag{3.7}$$

which makes the system's evolution still analytically solvable, as also recognized by Rabl [10] and Nunnenkamp et al. [11]. Since the initial state of our system consists of one single photon, there can

only be one photon throughout the entire evolution. Mathematically, this means we only need to consider a one-photon subspace of the entire Hilbert space, which in turn consists of three disjoint subspaces, which corresponds to: $\mathcal{H}_{1-}$, which corresponds to an incoming photon towards the cavity; $\mathcal{H}_2$, which corresponds to a photon inside the cavity; and $\mathcal{H}_{1+}$, which corresponds to a photon leaving the cavity. All quantum states in this space can be written as:

$$
\begin{aligned}
|\psi\rangle \;=\; & \int_{-\infty}^{+\infty} f(x,t) e^{-i\omega_0(t-x)} |x\rangle_\gamma \otimes |\phi_1(x,t)\rangle_\mathrm{m}\, \mathrm{d}x \\
+ \;& \alpha(t) e^{-i\omega_0 t} \hat{a}^\dagger |0\rangle_\gamma \otimes |\phi_2(t)\rangle_\mathrm{m}\,.
\end{aligned}
\tag{3.8}
$$

Here

$$
|x\rangle_\gamma \equiv \hat{c}_x^\dagger |0\rangle_\gamma
\tag{3.9}
$$

is the "position eigenstate" of the single photon outside of the cavity, and $|0\rangle_\gamma$ is the optical vacuum; the subscripts γ and m indicate Hilbert spaces of light and movable mirror, respectively; $f(x,t)$ is a complex function of position ($-\infty < x < +\infty$) and time, $\alpha(t)$ is a complex function of time t alone; $|\phi_1(x,t)\rangle_\mathrm{m}$ and $|\phi_2(t)\rangle_\mathrm{m}$ are two *families of* state vectors that belong to the Hilbert space of the mechanical oscillator. At any given time, the $x < 0$ part of the integral term on the right-hand side corresponds to $\mathcal{H}_{1-}$, the $x > 0$ part of the integral term corresponds to $\mathcal{H}_{1+}$, while the non-integral term corresponds to $\mathcal{H}_2$. In general, all three terms will be present, which means the entire system's quantum state is a superposition of having the photon simultaneously present in all three possible locations. Note that the factors $e^{-i\omega_0(t-x)}$ and $e^{-i\omega_0 t}$ are added to "factor out" the free oscillation of the EM field, which has oscillation frequencies near ω_0.

By imposing normalization conditions of

$$
{}_\mathrm{m}\langle\phi_1(x,t)|\phi_1(x,t)\rangle_\mathrm{m} = {}_\mathrm{m}\langle\phi_2(t)|\phi_2(t)\rangle_\mathrm{m} = 1\,,
\tag{3.10}
$$

the probability for finding the photon at location x (with $x < 0$ indicating a photon propagating towards the cavity, and $x > 0$ a photon propagating away from the cavity) is given by

$$
p_\gamma(x,t) = |f(x,t)|^2
\tag{3.11}
$$

while the probability that the photon is in the cavity is given by $|\alpha^2(t)|$. In this way, the normalization condition of the joint quantum state

$$
\int_{-\infty}^{+\infty} |f(x,t)|^2 \mathrm{d}x + |\alpha^2(t)| = 1
\tag{3.12}
$$

is simply a statement about the conservation of total probability.

The function $f(x,t)$ can be viewed as the out-of-cavity photon's wave function, while $|\phi_1(x,t)\rangle_{\rm m}$ *for each x* can be viewed as the oscillator state that is entangled with *each possibility* for the out-of-cavity photon. On the other hand, $\alpha(t)$ can be viewed as the probability amplitude of the cavity mode, while $|\phi_2\rangle_{\rm m}$ can be viewed as the oscillator state that is entangled with the in-cavity photon.

To facilitate calculation, for any joint quantum state $|\psi\rangle$, we define

$$|\psi_1(x,t)\rangle_{\rm m} \equiv {}_\gamma\langle x|\psi\rangle e^{i\omega_0(t-x)} = f(x,t)|\phi_1(x,t)\rangle_{\rm m}, \tag{3.13}$$

$$|\psi_2(t)\rangle_{\rm m} \equiv \langle 0|a|\psi\rangle e^{i\omega_0 t} = \alpha(t)|\phi_2(t)\rangle_{\rm m}. \tag{3.14}$$

Here $|\psi_1(x,t)\rangle_{\rm m}$, $-\infty < x < +\infty$, is a series of vectors, parametrized by x, in the Hilbert space of the mechanical oscillator, while $|\psi_2(x,t)\rangle$ is a single vector in the Hilbert space of the mechanical oscillator. They together carry the full information of the quantum state of the entire system. To further appreciate the role of $|\psi_1\rangle_{\rm m}$ and $|\psi_2\rangle_{\rm m}$, we can project each of them into the position eigenstate of the oscillator, $|y\rangle_{\rm m}$, obtaining

$$\Phi_1(t,x,y) \equiv {}_{\rm m}\langle y|\psi_1\rangle_{\rm m} = f(x,t)\phi_1(y,x,t), \tag{3.15}$$

$$\Phi_2(t,y) \equiv {}_{\rm m}\langle y|\psi_2\rangle_{\rm m} = \alpha(t)\phi_2(y,t), \tag{3.16}$$

which can be viewed as the *joint wave functions* of the projection of the entire state into $\mathcal{H}_{1+} \oplus \mathcal{H}_{1-}$ and $\mathcal{H}_2$, respectively. Note that although $f(x,t)$ and $|\phi_1(x,t)\rangle_{\rm m}$ [and similarly $\alpha(t)$ and $|\phi_2(t)\rangle_{\rm m}$] share a phase ambiguity, $|\psi_1(x,t)\rangle_{\rm m}$ and $|\psi_2(t)\rangle_{\rm m}$, and hence $\Phi_1(t,x,y)$ and $\Phi_2(t,y)$, are well defined without ambiguity.

3.2.3 Initial, final States and photodetection

As special cases, we consider the quantum state of the system at $t = 0$ (the initial state), and at very late times (the final state). For the initial state, the photon is propagating towards the cavity, and the cavity is empty. This corresponds to $\alpha(0) = 0$, and $f(x,0) = 0$. In particular, we also presume the initial state to be *separable* between the photon and the oscillator, with

$$|\psi(0)\rangle = \int e^{i\omega_0 x} F(x)|x\rangle_\gamma \, \mathrm{d}x \otimes |\phi_0\rangle_{\rm m}. \tag{3.17}$$

Here $F(x)$ is the slowly-varying part of the initial wave function of the photon, and $|\phi_0\rangle_{\rm m}$ the initial wave function of the oscillator. In other words, we have

$$|\psi_1(t=0)\rangle_{\rm m} = F(x)|\phi_0\rangle_{\rm m}, \tag{3.18}$$

$$|\psi_2(t=0)\rangle_{\rm m} = 0 \tag{3.19}$$

with $F(x) = 0$ for $x > 0$. At a sufficiently late time T, the photon will leave the cavity with unity probability, and we expect $\alpha(T) = 0$ and $f(x, T) = 0$ for $x < 0$. Mathematically,

$$
\begin{aligned}
|\psi_1(x, t \geq T)\rangle_{\mathrm{m}} &= F_{\mathrm{out}}(x, t)|\phi(x, t)\rangle_{\mathrm{m}}, \\
|\psi_2(t \geq T)\rangle_{\mathrm{m}} &= 0
\end{aligned}
\tag{3.20}
$$

with $F_{\mathrm{out}}(t, x) = 0$ for $x < 0$ and $t > T$. This is an explicitly entangled state between the out-going photon and the mirror, if $|\phi(x, t)\rangle_{\mathrm{m}}$ for different values of x are not all proportional to the same state vector.

At an intermediate time $t > 0$, suppose a photodetector is placed at $x = L > 0$ (i.e., for out-going photons from the cavity), then the probability density for photon arrival time at T is given by

$$
p_L(T) = {}_{\mathrm{m}}\langle \psi_1(L, T)|\psi_1(L, T)\rangle_{\mathrm{m}}.
\tag{3.21}
$$

In addition, by detecting a photon at this particular instant, the oscillator is left at a *condition quantum state* of $|\phi(x, T)\rangle_{\mathrm{m}}$.

3.2.4 Evolution of the photon-mirror quantum state

Applying the operations ${}_\gamma\langle x|$ and ${}_\gamma\langle 0|a$ onto the (joint) Schrödingier equation

$$
i\hbar\frac{\mathrm{d}|\psi\rangle}{\mathrm{d}t} = \hat{H}|\psi\rangle
\tag{3.22}
$$

we will obtain coupled equations for $|\psi_1\rangle_{\mathrm{m}}$ and $|\psi_2\rangle_{\mathrm{m}}$. Throughout this section, we will mostly encounter states in the oscillator's Hilbert space, therefore we will ignore the subscript "m" unless otherwise necessary.

3.2.4.1 Free evolution

For $|\psi_1\rangle$, by applying ${}_\gamma\langle x|$ to both sides of Eq. (3.22) we obtain

$$
\left[\partial_t + \partial_x + i\,\hat{H}_m\right]|\psi_1(x, t)\rangle = -\sqrt{\gamma}\,\delta(x)|\psi_2(t)\rangle.
\tag{3.23}
$$

Equation (3.23), without the δ-function term, simply describes the propagation of the initial photon towards the cavity, and the free evolution of the oscillator. This is because when the single photon is outside the cavity, its propagation is free, while the oscillator's evolution is unaffected by light.

Equation (3.23), is a first-order partial differential equation with characteristics along $x - t = \mathrm{const}$. We hereby divide the $t > 0$ region of the t-x plane into three regions: (i) $x < 0$, (ii) $x > 0$ and $t > x$, and (iii) $x > 0$ and $t < x$, as shown in Fig. 3.3. We can discard region (iii) right away, because
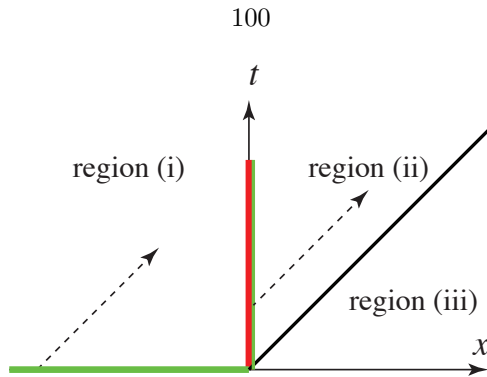
Figure 3.3: (Color online.) Three regions of the t-x plane and the free evolutions of $|\psi_1\rangle$. In region (i), the photon has not yet entered the cavity; the joint quantum state of the system is a simple free evolution of the initial quantum state, specified on $t = 0$, $x < 0$ (green horizontal half line), see Eq. (3.25). In region (ii), the photon and the oscillator evolve freely after the photon emerges from the cavity; the joint wave function depends on the wave function along $x = 0$, $t > 0$ (green vertical half line). The red line dividing regions (i) and (ii) corresponds to the δ-function in Eq. (3.23), which embodies the interaction between the outside photon and the in-cavity photon. Region (iii) is causally irrelevant to our experiment.

it is not causally connected with our experiment. In the interiors of regions (i) and (ii) separately, Eq. (3.23) has the following general solution,

$$|\psi_1(x,t)\rangle = e^{-\frac{i}{2}\hat{H}_m(t+x)}|C(t-x)\rangle \tag{3.24}$$

with $|C(v)\rangle$ an arbitrary state-valued function of v.

In region (i), $|C(v)\rangle$ can be specified by initial data along the half line of $t = 0$, $x < 0$; by using Eq. (3.24) twice, at (t, x) and $(0, x - t)$, we obtain [See Fig. 3.3]:

$$|\psi_1(x < 0, t)\rangle = F(x - t)\hat{U}_m(t)|\phi_0\rangle. \tag{3.25}$$

Here U_m is the evolution operator for the free oscillator, given by

$$\hat{U}_m(t) = e^{-i\hat{H}_m t}. \tag{3.26}$$

In terms of the Fock states $|n\rangle$, we have

$$\hat{U}_m(t) = \sum_n |n\rangle e^{-i\left(n+\frac{1}{2}\right)\omega_m t}\langle n|. \tag{3.27}$$

Equation (3.25) corresponds to the photon's wave packet freely propagating along the positive direction of the x axis and the mechanical oscillator independently evolving under its own Hamiltonian.

In region (ii), $|C(v)\rangle$ is specified by boundary data along the half line of $x = 0+$, $t > 0$, which

we denote by

$$|\psi_1(t)\rangle_{0+} \equiv |\psi_1(0+,t)\rangle . \tag{3.28}$$

By using Eq. (3.24) twice, at (t,x) and $(t-x,0)$, we obtain

$$|\psi_1(x>0,t)\rangle = \hat{U}_m(x)|\psi_1(t-x)\rangle_{0+} \tag{3.29}$$

Henceforth in the paper, $0+$ and $0-$ stand for $x \mapsto 0+$ (x approaches 0 from positive side of the axis) and $x \mapsto 0-$ (x approaches 0 from negative side of the axis) respectively. Equation (3.29) corresponds to the free evolution of the out-going photon and the mechanical oscillator.

3.2.4.2 Junction condition

The δ-function on the right-hand side of Eq. (3.23) relates the out-going photon to the decay of the in-cavity photon and the reflection of the in-going photon. To take this into account, we simply integrate both sides from $x=0-$ to $x=0+$, obtaining:

$$|\psi_1(0+,t)\rangle = |\psi_1(0-,t)\rangle - \sqrt{\gamma}|\psi_2(t)\rangle \tag{3.30}$$

This expresses the out-going wave as a combination of the promptly reflected incoming wave and the wave coming out from the cavity.

3.2.4.3 Coupled evolution

By applying $_\gamma\langle 0|a$ to both sides of Eq. (3.22) and using Eq. (3.30), we obtain:

$$\left[\partial_t + \frac{\gamma}{2} + i\hat{H}_\gamma\right]|\psi_2(t)\rangle = \sqrt{\gamma}|\psi_1(t)\rangle_{0-} . \tag{3.31}$$

Here as in Eq. (3.30), we have defined $|\psi_1\rangle_{0\pm} \equiv |\psi_1(0\pm,t)\rangle$. We have also defined

$$\hat{H}_\gamma \equiv \frac{\hat{p}_y^2}{2m} + \frac{m\omega_m^2(\hat{y}-\alpha)^2}{2} - \beta^2\omega_m \tag{3.32}$$

with

$$\alpha = -\frac{k}{m\omega_m^2}, \quad \beta = \frac{k}{\omega_m\sqrt{2m\omega_m}} . \tag{3.33}$$

The operator $\hat{H}_\gamma$ can be viewed as the modified Hamiltonian for the mirror when the photon is present in the cavity. Here α characterizes the shift in equilibrium position of the harmonic oscillator when the photon is inside the cavity and applies a constant force to the oscillator, while β (as seen from this equation) modifies the eigenfrequency of the harmonic oscillator. It is easy to work out

the eigenstates and eigenvalues of $\hat{H}_\gamma$: the eigenstates are

$$|\tilde{n}\rangle = e^{i\alpha\hat{p}_y}|n\rangle = \hat{D}(\beta)|n\rangle \tag{3.34}$$

which are simply displaced from the original Fock states in phase space, due to the change of equilibrium position, with

$$\hat{H}_\gamma|\tilde{n}\rangle = \left(n + \frac{1}{2} - \beta^2\right)\omega_m|\tilde{n}\rangle \tag{3.35}$$

which indicates an overall down-shift of eigenfrequency. Here we have further defined the displacement operator

$$\hat{D}(\beta) \equiv \exp[\beta(b^\dagger - b)] \tag{3.36}$$

with b and $b^\dagger$ the annihilation and creation operators for the free mechanical oscillator (i.e., before it couples to light). As we shall see in Sec. 11.5, β will become an important characterizing parameter of our optomechanical device; for example, $\beta \gtrsim 1$ is the regime in which the device is nonlinear.

For the photon, Eq. (3.31) means that the in-cavity photon is continuously driven by the incoming photon (right-hand side) and decays towards the out-going photon (as indicated by the $\gamma/2$ term in the bracket on the left-hand side). The above discussion, together with the initial data of $|\psi_2\rangle = 0$ at $t = 0$ gives

$$|\psi_2\rangle = \sqrt{\gamma}\int_0^t e^{-\frac{\gamma}{2}(t-t')}\hat{U}_\gamma(t-t')|\psi_1(t')\rangle_{0-} \tag{3.37}$$

where

$$\hat{U}_\gamma(t) \equiv e^{-i\hat{H}_\gamma t} = \sum_n |\tilde{n}\rangle e^{-i(n+1/2-\beta^2)\omega_m t}\langle\tilde{n}|, \tag{3.38}$$

which is the modified evolution operator of the oscillator when the photon is in the cavity.

3.2.4.4 Full evolution

The full evolution of the entire system's quantum state can now be obtained by combining Eqs. (3.29), (3.25), (3.30) and (3.37). In order to study the out-going photon, we only need to consider the region $x > 0$ and $t > x$ (see Fig. 3.3), because it emerges from the cavity at $t > 0$, and it propagates with $c = 1$. For this region, we obtain a compact-form solution of

$$|\psi_1(x,t)\rangle = \hat{M}|\phi_0\rangle \tag{3.39}$$

where $|\phi_0\rangle$ is the initial quantum state of the oscillator, and

$$\hat{M} = \int_0^{t-x} g(t-x,t')\hat{U}_m(x)\hat{U}_\gamma(t-x-t')\hat{U}_m(t')\mathrm{d}t'$$

$$= \int_0^{t-x} g(t-x,t')e^{i\beta^2\omega_m(t-x-t')}$$

$$\hat{D}(\beta e^{-i\omega_m x})\hat{D}(-\beta e^{i\omega_m(t'-t)})\hat{U}_m(t)\mathrm{d}t' \tag{3.40}$$

where

$$g(t,t') \equiv G(t-t')F(-t') \tag{3.41}$$

with

$$G(t) = \delta_+(t) + \gamma e^{-\frac{\gamma}{2}t} \tag{3.42}$$

the cavity's optical Green function. Here the subscript $+$ for the δ function indicates that its support lies completely in the region $t > 0$. Within the operator $\hat{M}$ [Eq. (3.40)], the factor g contains two terms, the first contains a δ-function and the second an exponential decay over time. The first term corresponds to the photon being promptly reflected by the cavity's front mirror, while the second term corresponds to the photon staying inside the cavity, for an amount of time equal to $t-x-t'$, which ranges from 0 to $t-x$. As a sanity check, it is straightforward to see that when mass of the oscillator approaches infinity, $\hat{U}_\gamma$ coincides with $\hat{U}_m$, and $\hat{M}$ simply describes the photon's propagation and the independent evolution of the oscillator.

3.3 Single-photon interferometer: Visibility

In this section, we will use the results of the previous section to analyze the single-photon interferometer.

3.3.1 The configuration

We consider a scheme proposed and analyzed by Marshall et al. [7], which is shown in Fig. 3.1. This Michelson interferometer (with 50/50 beamsplitter) has two arms: in the north arm, the end mirror in cavity A is movable, and initially prepared at a quantum state $|\phi_0\rangle$, whereas mirrors in cavity B, or east arm, are fixed. We assume the photon is injected from the west port, while a fixed photodetector is placed at the south port. Apart from mirror A being movable, the two cavities are otherwise identical: with the same input-mirror power transmissivity T, length L (for cavity A, counted from the zero-point of A's displacement). The front mirrors are placed at equal macroscopic distance from the beamsplitter, while there is a phase detuning of φ in arm B for ω_0 [1]. In our convention, if mirror A is at zero point and $\varphi = 0$, the photon will always return to the west port. Henceforth in the paper, we shall refer to the west port as the input port, and the south port the output port — although we may not always find the photon at the output port. Indeed,

---

[1]To give rise to a detuning, we assume that all optical frequencies we consider are centered around ω_0, and we offset the location of cavity B from symmetry by a length l such that $\omega_0 l = \varphi/2$.

whether and when the photon arrives at the photodetector is jointly determined by φ and the state of motion of mirror A.

In particular, we shall use $p(t)$ to denote the probability density for the photon to arrive at the detector at t (which can be measured by repeating the experiment many times). If we idealize the arrival time of the in-going photon (at the front mirror) to be $t = 0$, and ignore the macroscopic distance between the front mirrors, the beamsplitter, and the photodetector, then we are interested in $p(t)$ at $t \geq 0$. We further define an *instantaneous fringe visibility*

$$v(t) = \frac{p_{\max}(t) - p_{\min}(t)}{p_{\max}(t) + p_{\min}(t)}, \tag{3.43}$$

which measures the degree of coherence between the two components of returning photons at the beamsplitter, and can only become unity if at time t the joint mirror-photon quantum state is separable, as we shall see more clearly in Sec. 3.3.4.

3.3.2 The role of the beamsplitter and a decomposition of field degrees of freedom

In Sec. 3.2.3, we have studied in detail how the photon first affects the $x < 0$ components of the optical field out-side of a cavity, then interacts with the mirror, and finally returns back to the $x > 0$ components of the optical field. The scenario for a Michelson interferometer is slightly more complicated: we now need to consider a set of *input fields* that replaces the $x < 0$ single field in the single-cavity case, and a set of *output fields* which replaces the $x > 0$ single field.

As shown in Fig. 3.4, the annihilation operators of the input field for the two cavities are ($\hat{j}_-$, $\hat{k}_-$, $\hat{a}_-$, $\hat{b}_-$), while those of the output fields for the cavities are ($\hat{j}_+$, $\hat{k}_+$, $\hat{a}_+$, $\hat{b}_+$). Each of these fields are defined as a function of $-\infty < x < +\infty$, with $x = 0$ corresponding to the position of the beamsplitter, and positive direction along the arrow shown in Fig. 3.4. Ultimately, we need to calculate the fields of $\hat{j}_+$ and $\hat{k}_+$ in terms of $\hat{j}_-$ and $\hat{k}_-$.

Note that by allowing x to run through the entire real axis, we have assigned *two* input fields and two output fields to each point along the optical path (note here that "input" and "output" refer to the cavities, *not the beamsplitter*). This *redundancy* is necessary for a simplified treatment of the beamsplitter: instead of treating its internal dynamics, we simply view it as a mapping between the two different *representations* of the input and output fields. One representation ($\hat{j}_\pm$, $\hat{k}_\pm$) corresponds to the point of view of observers at the west and south ports, pretending that the beamsplitter does not exist; the other ($\hat{a}_\pm$, $\hat{b}_\pm$) corresponds to the point of view of observers at the east and north ports.

The conversion between the two representations takes the same form as the "input-output rela-
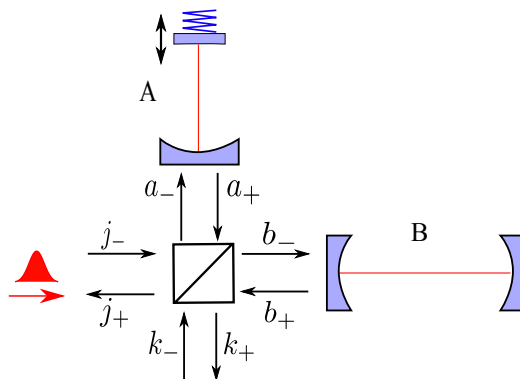
Figure 3.4: We illustrate the fields entering and exiting each of the four ports of the interferometer. We use arrows to define the positive sense of the coordinate used to label their locations. For each of them $x = 0$ corresponds to the location of the beamsplitter.

tion" of the beamsplitter:

$$\hat{b}_{\pm}(x) = \frac{\hat{j}_{\pm}(x) - \hat{k}_{\pm}(x)}{\sqrt{2}} \ , \ \hat{a}_{\pm}(x) = \frac{\hat{j}_{\pm}(x) + \hat{k}_{\pm}(x)}{\sqrt{2}} \ . \tag{3.44}$$

As an example, consider a quantum state in which an (instantaneous) photon is injected from the input port, which, according to the mapping in Eq. (5.1), has two equivalent representations:

$$\hat{j}_{-}^{\dagger}(x_0)|0\rangle = \frac{\hat{a}_{-}^{\dagger}(x_0) + \hat{b}_{-}^{\dagger}(x_0)}{\sqrt{2}}|0\rangle \ . \tag{3.45}$$

As time goes on, the quantum state evolves as $x_0 \rightarrow x_0 + t$. At any instant, the left-hand side represents a single photon propagating from west to east, and continuing through the location of the beamsplitter. The right-hand side represents a photon that has a two-component wave function, the first component propagates northwards, the second eastwards.

Although the two representations are equivalent, we still prefer to use the south-west representation when treating the generation and detection of photons, and the north-east representation when treating the light's interaction with the cavities.

3.3.3 Interactions between light and cavities

For each individual cavity, we intend to apply the result of Sec. 3.2.1. We note that $\hat{a}_{-}(x)$ (for $x < 0$) and $a_{+}(x)$ (for $x > 0$) defined in this section maps to the $\hat{c}(x)$ (for $x < 0$) and $\hat{d}(x)$ (for

$x > 0$) respectively, as defined in Sec. 3.2.1 and illustrated in Fig. 3.2. For this reason, we define

$$
\hat{a}(x) \equiv
\begin{cases}
\hat{a}_-(x)\,, & x < 0\,, \\[2ex]
\hat{a}_+(x)\,, & x > 0\,,
\end{cases}
\tag{3.46}
$$

and

$$
\hat{b}(x) \equiv
\begin{cases}
\hat{b}_-(x)\,, & x < 0\,, \\[2ex]
\hat{b}_+(x)\,, & x > 0\,.
\end{cases}
\tag{3.47}
$$

In this way, $a(x)$ and $b(x)$ here both map to $c(x)$ defined in Sec. 3.2.1. [The a and b here are not to be confused with operators of the optical mode and the mechanical oscillator — we shall always explicitly include the argument (x) for these continuum operators.] We further define

$$
\hat{j}(x) \equiv
\begin{cases}
\hat{j}_-(x)\,, & x < 0\,, \\[2ex]
\hat{j}_+(x)\,, & x > 0\,,
\end{cases}
\tag{3.48}
$$

and

$$
\hat{k}(x) \equiv
\begin{cases}
\hat{k}_-(x)\,, & x < 0\,, \\[2ex]
\hat{k}_+(x)\,, & x > 0\,.
\end{cases}
\tag{3.49}
$$

Furthermore, for fields a, b, j and k, the transformation relations Ea. (5.1) also apply.

Now suppose at $t = 0$, we have a photon coming from the input (west) port with arbitrary wave function $F(x)$ [like in Eq. (3.17), here $F(x) = 0$ for $x > 0$]. The initial quantum state of the entire optomechanical system is

$$
|\psi(0)\rangle \;=\; \int_{-\infty}^{0} \mathrm{d}x\, F(x)\hat{j}_-^\dagger(x)|0\rangle_\gamma \otimes |\phi_0\rangle_A.
\tag{3.50}
$$

Since we would like to investigate this state's evolution when the photon reaches the cavity, we covert into the north-east representation:

$$
|\psi(0)\rangle = \frac{1}{\sqrt{2}}\left[|\psi_A(0)\rangle + |\psi_B(0)\rangle\right].
\tag{3.51}
$$

Here we have defined

$$
|\psi_A(0)\rangle \;=\; \int_{-\infty}^{0} \mathrm{d}x\, F(x)\hat{a}^\dagger(x)|0\rangle_\gamma \otimes |\phi_0\rangle_A,
\tag{3.52}
$$

$$|\psi_B(0)\rangle = \int_{-\infty}^{0} dx\, F(x)\hat{b}^\dagger(x)|0\rangle_\gamma \otimes |\phi_0\rangle_A, \tag{3.53}$$

in which we have already taken Eqs. (10.32) and (3.47) into account.

Here $|\psi_A(0)\rangle$ corresponds to the case in which the photon enters cavity A with the movable mirror, and $|\psi_B(0)\rangle$ the case in which the photon enters cavity B with the fixed mirror. As time goes on, these two states evolve individually, and Eq. (3.51) remains true for $t > 0$. For the cavity A component $|\psi\rangle_A$, we have [cf. Eq. (3.39)]

$$|\psi_A(t)\rangle = \int_0^{t-x} dt'\, g(t-x,t')e^{i\beta^2\omega_m(t-x-t')}\hat{D}(\beta e^{-i\omega_m x})$$
$$\hat{D}(-\beta e^{i\omega_m(t'-t)})\hat{a}^\dagger(x)|\Phi(t)\rangle, \tag{3.54}$$

where we have defined

$$|\Phi(t)\rangle \equiv \hat{U}_m(t)|0\rangle_\gamma|\phi_0\rangle_A, \tag{3.55}$$

while for $|\psi\rangle_B$, we set $\beta \to 0$ and obtain

$$|\psi_B(t)\rangle = e^{i\varphi}\int_0^{t-x} dt'\, g(t-x,t')\hat{b}^\dagger(x)|\Phi(t)\rangle. \tag{3.56}$$

3.3.4 The final state

In order to describe the quantum state seen by the photodetector, we map a and b into j and k, only keeping the k component. We further project onto the single-photon basis of $_\gamma\langle 0|k(x)$, assuming $x = 0+$, obtaining

$$|\psi(t)\rangle_m = \frac{1}{2}\left[|\psi_A(t)\rangle_m + e^{i\varphi}|\psi_B(t)\rangle_m\right] \tag{3.57}$$

with

$$|\psi_A(t)\rangle_m = \int_0^t dt'\, g(t,t')\hat{O}(t-t')|\phi_0(t)\rangle, \tag{3.58}$$

$$|\psi_B(t)\rangle_m = \int_0^t dt'\, g(t,t')|\phi_0(t)\rangle, \tag{3.59}$$

with

$$|\phi_0(t)\rangle \equiv \hat{U}_m(t)|\phi_0\rangle \tag{3.60}$$

and

$$\hat{O}(t) \equiv e^{i\beta^2\omega_m t}\hat{D}(\beta)\hat{D}(-\beta e^{-i\omega_m t}), \tag{3.61}$$

in particular $\hat{O}(0) = 1$. In this way, we are using the same notation as Eq. (3.39), and we can use Sec. 3.2.3 for obtaining the photo-detection probability density at each time $t > 0$, which is given by

$$p(t) = \frac{\||\psi_A\rangle_m\|^2 + \||\psi_B\rangle_m\|^2 + 2\mathrm{Re}\left(e^{i\varphi}{}_m\langle\psi_A|\psi_B\rangle_m\right)}{4}, \tag{3.62}$$

which, when adjusting values of φ, leads to an instantaneous visibility of [Cf. (3.43)]:

$$v(t) = \frac{2|{}_m\langle\psi_A|\psi_B\rangle_m|}{\||\psi_A\rangle_m\|^2 + \||\psi_B\rangle_m\|^2}. \tag{3.63}$$

It relies on how different ψ_A is from ψ_B, which indicates how much the movable mirror in cavity A is capable of "learning" about the existence of the photon in cavity A. At any instant, if ψ_A is proportional to ψ_B (differ by a phase), the state of the movable mirror does not change, and therefore we have a perfect visibility. By contrast, if the photon is able to transform the movable mirror into a state substantially different from its freely evolving state, e.g., the orthogonal state in the extreme case, then we will have a significantly reduced visibility.

Similar to Eq. (3.39), here ψ_A and ψ_B each has a promptly reflected part [which arises from the δ-function part of $g(t,t')$], and a part in which the photon enters the cavity [which arises from the exponential decay part of $g(t,t')$]. It is the second part that contributes to the reduction of visibility.

3.3.5 Examples

We consider an experimental situation with the central frequency of the injecting photon tuned to the resonant frequency of the cavity, with a wave function of

$$F(x) = \sqrt{2\Gamma}e^{\Gamma x}\Theta(-x). \tag{3.64}$$

Here Γ measures the frequency-domain width of the photon. We further assume that the mechanical oscillator's eigenfrequency (when uncoupled with light) is equal to the cavity bandwidth, or $\omega_m = \gamma$. As in Ref. [7], we assume that the mechanical oscillator, i.e., the mirror, is initially prepared at its ground state:

$$|\phi_0\rangle = |0\rangle_A. \tag{3.65}$$

With these specializations, we have

$$|\psi_A(t)\rangle_m = C(t)\left[|0\rangle + \gamma|M(t)\rangle\right], \tag{3.66}$$

$$|\psi_A(t)\rangle_m = C(t)\left[|0\rangle + \gamma\int_0^t dt'\, f(t-t')|0\rangle\right], \tag{3.67}$$
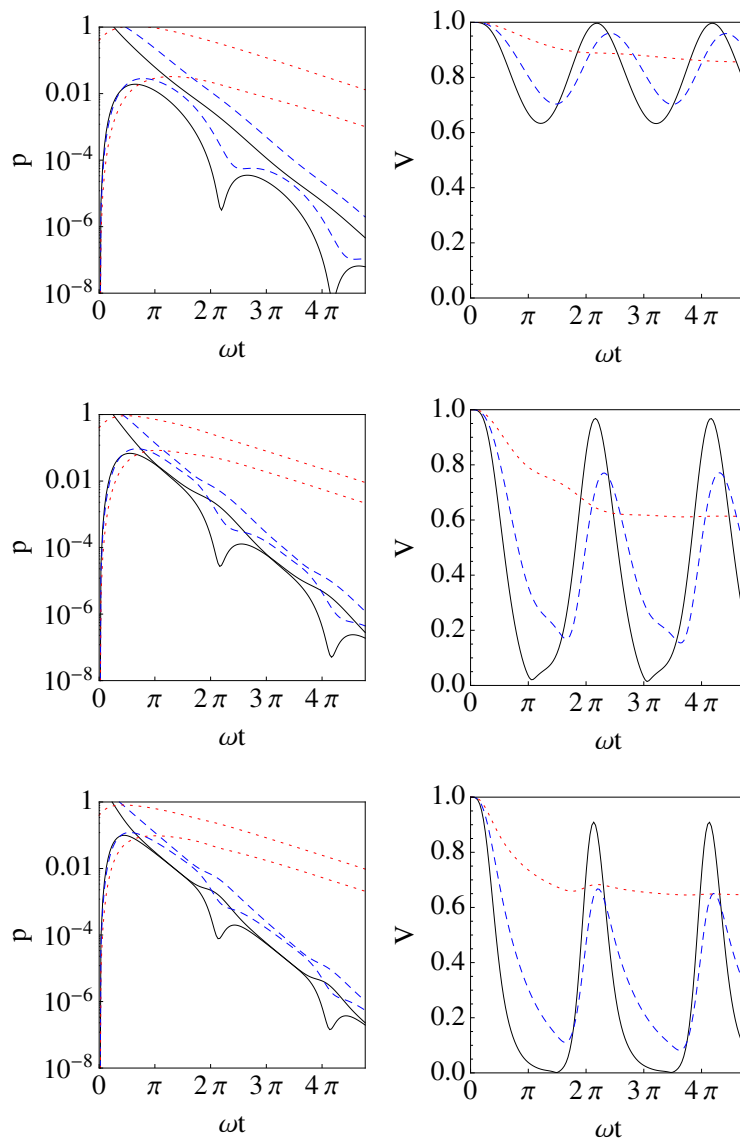
Figure 3.5: (Color online.) (left) Probability density and (right) fringe visibility for the photon to come out with different β (top-to-bottom: first row, $\beta = 0.5$; second row, $\beta = 1.2$; third row, $\beta = 2$). For each β, three different values of Γ are considered for comparison: $\Gamma = 0.2$ (red dotted), 1(blue dashed), 2(black solid). All the calculations assume $\gamma = 1, \omega_m = 1$. For probability density plots, the upper line of the same color is the maximum value of the probability density, the lower one is the minimum value.

with

$$C(t) \equiv \sqrt{2\Gamma} e^{-(\Gamma + i\omega_m/2)t} , \quad f(t) \equiv e^{(\Gamma - \gamma/2)t} \tag{3.68}$$

, and

$$|M(t)\rangle \equiv \int_0^t dt' \, f(t - t') e^{i\beta^2 \left[\omega_m(t-t') - \sin \omega_m(t-t') \right]}$$
$$\times \left| \beta - \beta e^{i\omega_m(t'-t)} \right\rangle. \tag{3.69}$$

By comparing with Sec. 3.3.4, we first find that visibility depends on the similarity between $|M(t)\rangle$ and its counterpart in Eq. (3.67): when they are similar to each other (e.g., when $\beta \lesssim 1$) or when they do not contribute significantly to $|\psi_{A,B}(t)\rangle_m$, the visibility will tend to be high. By contrast, in order to achieve a complete incoherence, we need $|M(t)\rangle$ to contribute significantly, and nearly orthogonal to $|0\rangle$ — and this *requires* $\beta \gtrsim 1$. The arrival probability density (3.62) and contrast defect (3.63) can be computed if we use

$$\langle 0|\beta \rangle = \langle 0|\hat{D}(\beta)|0\rangle = e^{-\beta^2/2}. \tag{3.70}$$

In Fig. 3.5, we plot the maximum and minimum of the probability density in the left panels, and visibility in the right panels, both as functions of time. We have chosen $\beta = 0.5$ for upper panels, $\beta = 1.2$ for middle panels and $\beta = 2$ for lower panels. In each panel, we have also shown curves with $\Gamma = 0.2$ (red dotted), $\Gamma = 1$ (blue dashed) and $\Gamma = 2$ (solid black). As β increases (as we move from upper to lower panels), the photon's ponderomotive effect on the movable mirror increases, therefore the visibility is able to vary more. This means $\beta \gtrsim 1$ is necessary (but not sufficient, see below) for visibility to substantially decay and then revive — a feature Ref. [7] has used to search for decoherence effects.

On the other hand, another condition for visibility to first decrease and then revive, and repeat on, seems to be $\Gamma \gtrsim 1$, as also indicated by each of the right panels of Fig. 3.5. In addition, as $\Gamma \gg 1$, our result becomes comparable to Ref. [7]. Qualitatively, this is because for $\Gamma \gg 1$, if a photon does arrive at a time around ~ 1, we can be sure the photon has interacted with the mirror — and we can roughly treat the photon as already within the cavity at $t = 0$.

Mathematically, for $t \gg 1/\Gamma$, the conditional quantum state of the mirror given photon detection at time t could be approximately written as :

$$\begin{aligned} |\psi\rangle_m &= \frac{\gamma}{\sqrt{2}a} e^{-(\gamma + i\omega_m)t/2} \\ &\quad \left[e^{i\varphi} |0\rangle + e^{i\beta^2 \omega_m t} \hat{D}(\beta) \left| -\beta e^{-i\omega_m t} \right\rangle \right] \\ &= \frac{\gamma}{\sqrt{2}a} e^{-(\gamma + i\omega_m)t/2} \end{aligned} \tag{3.71}$$

$$\left[e^{i\varphi}|0\rangle + e^{i\beta^2(\omega_m t - \sin \omega_m t)} \left| \beta - \beta e^{-i\omega_m t} \right\rangle \right]. \tag{3.72}$$

This is consistent with results of Ref. [7].

However, in order for $a \gg 1$ and to observe a revival of visibility, we have to wait till $t \geq 2\pi$. The probability for detecting the photon at such late times is exponentially small — as indicated by the left panels of Fig. 3.5. This means we may have to make a trade off between having a very sharp revival of visibility and being robust against loss and able to cumulate enough statistics within reasonable amount of time.

3.4 Conditional quantum-state preparation

In this section, we show how to engineer an arbitrary quantum state of the mechanical oscillator by injecting a single photon with specifically designed wave function and by post selecting the arrival time of the output photon. Note that unlike Refs. [10, 11], our state preparation procedure is conditional. This guarantees a pure quantum state for the mechanical oscillator, but requires a low decoherence rate and a high detection quantum efficiency for the out-going photon.

3.4.1 The configuration

The scheme is shown in Fig. 3.6. It is very similar to the single-photon interferometer discussed in the previous section, except that in the east arm we replace the cavity B with a perfectly reflected mirror B. In this case, most of the previous analyses are still valid: Eq. (3.57) to Eq. (3.59). The only difference is that the $g(t, t')$ function in Eq. (3.59) needs to be replaced by $\delta(t - t')$, as we have a perfectly reflecting mirror instead of a cavity here, namely,

$$|\psi_B(t)\rangle_{\mathrm{m}} = |\phi_0(t)\rangle. \tag{3.73}$$

To proceed, we further adjust the detuning phase φ in Eq. (3.57) such that at the dark port, the promptly reflected wave from the front mirror of cavity A exactly cancels the promptly reflected wave from the mirror B. In this case, having a photon emerging from our detection port (Fig. 3.6) automatically indicates that the photon has entered the cavity and interacted with the mirror, and Eq. (3.57) or the conditional quantum state of the mechanical oscillator (unnormalized) is given by:

$$|\psi(t)\rangle_{\mathrm{m}} = \frac{1}{2} \int_0^t \mathrm{d}t' \, g_p(t, t') \hat{O}(t - t') |\phi_0(t')\rangle \tag{3.74}$$

with

$$g_p(t, t') = \gamma e^{-\gamma/2(t - t')} F(-t'). \tag{3.75}$$
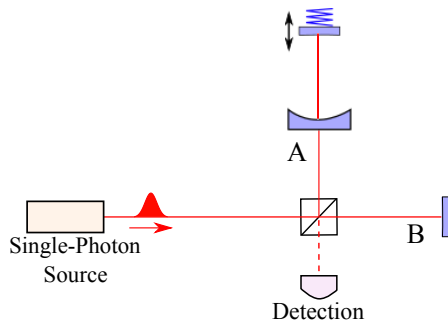
Figure 3.6: (Color online.) The sample device which uses a single photon to prepare a mechanical oscillator quantum state. Here the the detuning phase for the mirror on the east arm is adjusted such that the promptly reflected photon will come out from west port, with 0 probability coming out from south port.

As $g_p(t, t')$ is related to the input photon wave function $F(x)$, by modifying input photon wave function, we can therefore engineer the conditioning mechanical oscillator quantum state $|\psi(t)\rangle_m$. Even if there is a finite probability that the photon will come out through the west arm or the bright port, once we detect a photon at time t at the dark port, we know that it must come from arm A and it also has stayed in the cavity A for a certain amount of time.

3.4.2 Preparation of a single displaced-Fock state

First of all, we notice that when different in-coming photon wave function F's are used, if we keep conditioning over the *same* photon arrival time t, the conditional quantum states we obtain for the mechanical oscillator will depend linearly on F. In other words, if F_1 allows us to prepare $|\phi_1\rangle$, and F_2 allows us to prepare $|\phi_2\rangle$, then injecting a new photon with a superimposed wavefunction $F = \alpha_1 F_1 + \alpha_2 F_2$ will allow us to prepare $\alpha_1 |\phi_1\rangle + \alpha_2 |\phi_2\rangle$.

This means we only need to show how members of a complete basis can be prepared, and we choose this to be

$$|\psi(t)\rangle_\mathrm{m} = |\tilde{n}\rangle = \hat{D}(\beta)|n\rangle, \quad n = 0, 1, 2 \dots . \tag{3.76}$$

These displaced Fock states are simply Fock states of the oscillator when the photon is inside the cavity, see Eq. (3.34).

Let us assume that the mechanical oscillator is initially prepared at its ground state. Before studying preparation of an arbitrary conditional quantum state for the mechanical oscillator, we first show that we can prepare a conditional state with an arbitrary quantum number n, by injecting a photon with the following wave function:

$$F(x) = \sqrt{\gamma} e^{(\gamma/2 - i\beta^2 \omega_m + in\omega_m)x} \Theta(-x). \tag{3.77}$$
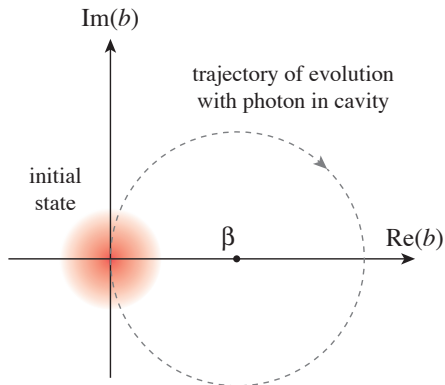
Figure 3.7: A sketch of the phase-space trajectory of the mechanical oscillator. The Wigner function of the initial state $|0\rangle$ is represented by the shaded disk, the dot marked with β on the real axis is the new equilibrium position of the oscillator when the photon is in the cavity, while the dashed circle is the trajectory of the oscillator's Wigner function when the photon is inside the cavity. Detection of the out-going photon at $t = 2n\pi/\omega_m$ corresponds to superimposing all mechanical-oscillator quantum states along the dashed trajectory, weighted by the photon's wave function.

As we plug Eq.(3.77) into Eq.(3.74) we obtain the conditional quantum state of

$$|\psi(t)\rangle_m = \frac{\hat{D}(\beta)\gamma^{3/2}e^{-\frac{\gamma}{2}t+i\beta^2\tau}}{2\omega_m} \int_0^\tau d\tau' e^{-in\tau'} |-\beta e^{i(\tau'-\tau)}\rangle \tag{3.78}$$

with $\tau \equiv \omega t$. This is a coherent superposition of coherent states, which in the complex amplitude domain all line up in a circle with radius β around the center located at complex amplitude equal to β; these states are parametrized mathematically by $\hat{D}(\beta)|-\beta e^{i\phi}\rangle$. These states are superposed with the same magnitude, but different phases, due to the decay rate of $\gamma/2$ in the F chosen by Eq. (3.77). Obtaining such a state is understandable, as given the photon detection at t, the actually time t' for the photon staying inside the cavity is uncertain, and we have to sum up all the possible contributions from 0 to t. This situation is illustrated in Fig. 3.7.

One important feature in the above expression is that the integrand is a periodic function. We denote

$$\tau \equiv \omega_m t = 2\pi N + \Delta\phi, \tag{3.79}$$

where N is some integer and $\Delta\phi$ is the residual phase ranging from 0 to 2π. In this way, the integral in Eq. (3.78) then becomes

$$\left[N\int_0^{2\pi} + \int_0^{\Delta\phi}\right] d\phi\, e^{-in\phi} |-\beta e^{i\phi}\rangle. \tag{3.80}$$

In the limit of $N \gg 1$, when the photon arrives at the photodetector with a delay large compared to the oscillator's oscillation period, the first term in Eq. (3.80) always dominates. This means we obtain the same conditional state if we restrict τ around an integer multiple of 2π, or make sure
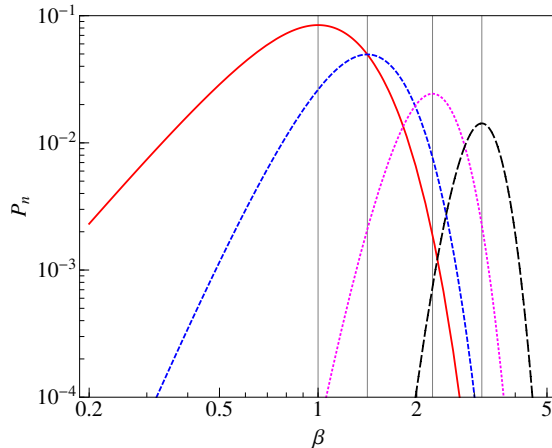
Figure 3.8: Probability for obtaining displaced Fock states $|\tilde{1}\rangle$ (red solid), $|\tilde{2}\rangle$ (blue dashed), $|\tilde{5}\rangle$ (magenta dotted) and $|\tilde{10}\rangle$ (black dash-dotted), a range of β and minimum state overlap of $1 - \epsilon$. Vertical gridlines are draw for $\beta = 1, \sqrt{2}, \sqrt{5}$ and $\sqrt{10}$; these are the locations where maxima of $P_{1,2,5,10}$ are reached.

it is large enough. This leads to the interesting effect that in the asymptotic limit of $\tau \to +\infty$, the conditional state will be independent of τ. In practice, however, although the integral (3.80) increases with N, the exponential decay factor in Eq. (3.78) always favors simply choosing $N = 1$. It is straightforward to evaluate this conditional state; using

$$\int_0^{2\pi} \mathrm{d}\phi \, e^{-in\phi} e^{e^{i\phi}\hat{a}^\dagger} |0\rangle = \frac{1}{n!} (\hat{a}^\dagger)^n |0\rangle \,, \tag{3.81}$$

we have

$$\begin{aligned}
\int_0^{2\pi} \mathrm{d}\phi \, e^{-in\phi} |-\beta e^{i\phi}\rangle &= \frac{2\pi (-\beta)^n e^{-\frac{\beta^2}{2}}}{\sqrt{n!}} |n\rangle \\
&= 2\pi |n\rangle\langle n | -\beta\rangle \,,
\end{aligned} \tag{3.82}$$

which means

$$|\psi\rangle_{\mathrm{m}} = \frac{\pi \gamma^{3/2} e^{-\frac{\pi\gamma}{\omega_m}} e^{2\pi i \beta^2}}{\omega_m} \frac{(-\beta)^n e^{-\frac{\beta^2}{2}}}{\sqrt{n!}} |\tilde{n}\rangle \,. \tag{3.83}$$

This is indeed proportional to $|\tilde{n}\rangle$, as promised. Here we have used

$$\langle -\beta | n \rangle = \frac{(-\beta)^n e^{-\beta^2/2}}{\sqrt{n!}} \,. \tag{3.84}$$

Since the probability for the returning photon to arrive at precisely $2\pi/\omega_m$ is zero, we must allow an interval around this target, which on the one hand provides us with a non-zero probability, but on the other hand makes the conditional state imprecise. If we require the actual conditional state

to have a high overlap with the target state (or high fidelity)

$$\frac{|_{\mathrm{m}}\langle\psi|\tilde{n}\rangle|}{\sqrt{_{\mathrm{m}}\langle\psi|\psi\rangle_{\mathrm{m}}}} \geq 1 - \epsilon \,, \tag{3.85}$$

then, by perturbing the integration upper bound of Eq. (3.82), we obtain the following requirement on the allowed photon arrival time

$$|\tau - 2\pi| \leq \Delta\tau \equiv \sqrt{8\pi^2\epsilon} \frac{|\langle-\beta|n\rangle|}{\sqrt{1 - \langle-\beta|n\rangle^2}} \,, \tag{3.86}$$

which, for each trial of the experiment, would happen with a probability of

$$\begin{aligned} P &= |_{\mathrm{m}}\langle\psi|\psi\rangle_{\mathrm{m}}|^2 \frac{2\Delta\tau}{\omega_m} \\ &= 2\sqrt{8\epsilon} \left(\frac{\pi\gamma}{\omega_m}\right)^3 e^{-\frac{2\pi\gamma}{\omega_m}} \frac{|\langle-\beta|n\rangle|^3}{\sqrt{1 - |\langle-\beta|n\rangle|^2}} \,. \end{aligned} \tag{3.87}$$

And this would be the probability with which we can create a conditional state with an overlap of at least $1 - \epsilon$ with the target.

From Eq. (3.87), we further notice that we should fix

$$\gamma/\omega_m = 3/(2\pi) \tag{3.88}$$

in order to obtain a maximized success probability of

$$P_n = \sqrt{8\epsilon} \frac{27}{4e^3} \frac{|\langle-\beta|n\rangle|^3}{\sqrt{1 - |\langle-\beta|n\rangle|^2}} \,. \tag{3.89}$$

For each n, the maximum of P_n is reached at $\beta = \sqrt{n}$. In Fig. 3.9, we plot P_n for a range of β, for $\epsilon = 0.1$, or a state overlap of $\geq 90\%$. We can see that the probability of producing $|\tilde{n}\rangle$ decreases rather quickly as n increases.

This dependence (3.89) on β comes from two sources, which we can understand better by going to the phase-space reference frame centered at the equilibrium position of the oscillator when the photon is inside the cavity. In this reference frame, the complex amplitude of the coherent states being superimposed are located on a circle with distance β away from the center, while the target we would like to prepare is simply the Fock state $|n\rangle$. Although the photon's wave function selects out an oscillator state proportional to $|n\rangle$, this post-selection does not improve the intrinsic overlap between all those that participate the superposition, which is actually proportional to

$$|\langle-\beta e^{i\phi}|n\rangle|^2 = |\langle-\beta|n\rangle|^2 \,. \tag{3.90}$$

This explains the dependence of $_m\langle\psi|\psi\rangle_m$ on beta. The other factor of dependence on β is that when the target state has a very low overlap with the individual members $|\beta e^{i\phi}\rangle$ of the superposition, the requirement for accuracy of photon arrival time, or $\Delta\tau$, increases, as shown in Eq. (3.86).

3.4.3 Preparation of an arbitrary state

Since the displaced number states form a complete basis we can expand any target state as

$$|\psi_{\text{tg}}\rangle = \sum_{n=0}^{+\infty} c_n|\tilde{n}\rangle\,, \quad \sum_{n=0}^{+\infty} |c_n|^2 = 1\,. \tag{3.91}$$

Since a linear combination of F's leads to a linear combination of conditional states, we simply need to apply the result of the last subsection and have

$$F(x) = \frac{\sqrt{\gamma}e^{(\gamma/2 - i\beta^2\omega_m)x}}{Z} \sum_{n=0}^{+\infty} \tilde{c}_n e^{in\omega_m x}\,, \tag{3.92}$$

with

$$Z \equiv \left[\sum_{j,k=0}^{+\infty} \frac{\tilde{c}_j\tilde{c}_k^*}{1 + i(j-k)\frac{\omega_m}{\gamma}}\right]^{1/2}\,, \tag{3.93}$$

$$\tilde{c}_n \equiv \frac{c_n}{\langle -\beta|n\rangle} = \sqrt{n!}(-\beta)^n e^{\beta^2/2} c_n\,. \tag{3.94}$$

This is an additional periodic modulation (with period $2\pi/\omega_m$) of the photon's wave function. We caution that in order for the summation in Eq. (3.92) to converge, if c_n does not go to zero for all $n \geq N$, then it must decay very fast when $n \to +\infty$, due to the presence of the $\sqrt{n!}$ factor (which grows faster than β^{-n}).

As in the previous subsection, we obtain the conditional state at $\tau \equiv \omega_m t = 2\pi, 4\pi, \ldots$, as well as any τ that is substantially large. Again, let us consider $\tau = 2\pi$; this gives the conditional state of

$$|\psi\rangle_m = \frac{\pi\gamma^{3/2}e^{-\frac{\pi\gamma}{\omega_m}}e^{2\pi i\beta^2}}{\omega_m Z}|\psi_{\text{tg}}\rangle\,. \tag{3.95}$$

We can use the same approach as the previous subsection to evaluate the probability with which this conditional state is achieved with a high overlap. For a minimum overlap of $1 - \epsilon$, we require

$$|2\pi - \tau| \leq \Delta\tau = \frac{\sqrt{8\pi\epsilon}}{\left|\sum_{m=0}^{+\infty}\tilde{c}_m\right|\sqrt{1 - |\langle -\beta|\psi_{\text{tg}}\rangle|^2}}\,. \tag{3.96}$$

Note that this $\Delta\tau$ diverges if $\sum_{m=0}^{+\infty}\tilde{c}_m = 0$, because in this case the overlap does not vary at $O[(\tau - 2\pi)^2]$ order. Assuming the target state to be generic, then the probability for obtaining this
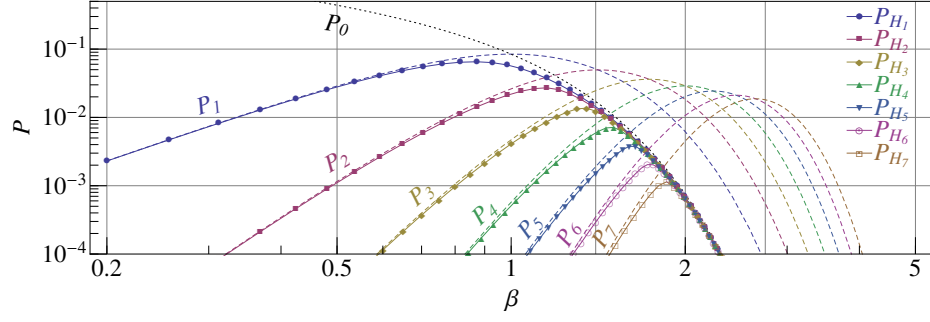
Figure 3.9: Minimum success probability for states in Hilbert spaces $\mathcal{H}_{1,2,\ldots 7}$ (solid curves with markers), together with success probability for producing single displaced Fock states, $P_{0,1,2,\ldots,7}$ (dashed curves without markers). Fidelity is fixed at 10%. Note that P_0 would become greater than 1 at low values of β — but in this case our approximation in obtaining $\Delta\tau$ breaks down.

state is

$$P_{|\psi\rangle} = 2\sqrt{8\epsilon} \, \frac{\left(\frac{\pi\gamma}{\omega_m}\right)^3 e^{-\frac{2\pi\gamma}{\omega_m}} \left[1 - \left|\sum_{n=0}^{+\infty}\langle-\beta|n\rangle^2 \tilde{c}_n\right|^2\right]^{-1/2}}{\left|\sum_{m=0}^{+\infty}\tilde{c}_m\right| \sum_{j,k=0}^{+\infty} \dfrac{\tilde{c}_j \tilde{c}_k^*}{1 + i\frac{(j-k)\omega_m}{\gamma}}} . \tag{3.97}$$

Here the choice of γ/ω_m depends on the target quantum state, but if we assume this dependence is weaker than the pre-factor, and continue to use Eq. (3.88), then we obtain

$$P_{|\psi\rangle} = \frac{27}{e^3}\sqrt{\frac{\epsilon}{2}} \, \frac{\left[1 - \left|\sum_{n=0}^{+\infty}\langle-\beta|n\rangle^2 \tilde{c}_n\right|^2\right]^{-1/2}}{\left|\sum_{m=0}^{+\infty}\tilde{c}_m\right| \sum_{j,k=0}^{+\infty} \dfrac{\tilde{c}_j \tilde{c}_k^*}{1 + \frac{2\pi i(j-k)}{3}}} . \tag{3.98}$$

As it turns out, $P_{|\psi\rangle}$ depends on the detail of $|\psi\rangle$ — even if we only try to create a combination of $|\tilde{0}\rangle$ and $|\tilde{1}\rangle$, the combination coefficients would lead to very different success probabilities. In order to provide a concrete measure of the ability of our state-preparation scheme, we have chosen to compute the minimum success probabilities of creating all the states in the mechanical oscillator's Hilbert subspaces spanned by the lowest displaced Fock states, e.g., $\mathcal{H}_1 \equiv \mathrm{Sp}\{|\tilde{0}\rangle, |\tilde{1}\rangle\}$, $\mathcal{H}_2 \equiv \mathrm{Sp}\{|\tilde{0}\rangle, |\tilde{1}\rangle, |\tilde{2}\rangle\}$, etc. We define

$$P_{\mathcal{H}_j} = \min_{|\psi\rangle \in \mathcal{H}_j} P_{|\psi\rangle}, \quad \mathcal{H}_j = \left\{\sum_{l=0}^{j} \alpha_l |\tilde{l}\rangle : \alpha_l \in \mathbb{C}\right\}. \tag{3.99}$$

In Fig. 3.9, we plot $P_{\mathcal{H}_1}$, $P_{\mathcal{H}_2}$, $\ldots$, $P_{\mathcal{H}_7}$ as functions of β (in solid purple curves). Because $\mathcal{H}_1 \subset \mathcal{H}_2 \subset \cdots \subset \mathcal{H}_7$, it is increasingly difficult to create all states in $\mathcal{H}_j$ with higher values of j, and therefore $P_{\mathcal{H}_1} \geq P_{\mathcal{H}_2} \geq \ldots P_{\mathcal{H}_7}$, namely our success probability decreases globally when j increases. In fact, as we overlay the single-Fock-state success probabilities P_0, P_1, $\ldots$, P_5, we also discover that for any $P_{\mathcal{H}_j}(\beta)$, it asymptotes to P_0 at higher β, and to P_j at lower β; moreover, the transition between these two asymptotic regions are brief, and the $P_{\mathcal{H}_j}(\beta)$ curves do not lie much below the

minimum of P_0 and P_j.

This asymptotic behavior can be understood from the behavior of P_n, the success probability for single (displaced) Fock states. For smaller β, it is much more difficult to prepare a higher Fock state, therefore, if β is sufficiently small, the difficulty of preparing $\mathcal{H}_j$ is dominated by the preparation of $|\tilde{j}\rangle$, the single most difficult state in the space to prepare — and therefore $P_{\mathcal{H}_j}$ agrees with P_j. Vice versa, for sufficiently large β, the difficulty of preparing $\mathcal{H}_j$ lies in the preparation of $\tilde{0}\rangle$, and therefore $P_{\mathcal{H}_j}$ would agree with P_0. The fast transition between the two extremes indicates that when trying to prepare states in $\mathcal{H}_j$, the difficulty either lies in $|\tilde{0}\rangle$, or in $|\tilde{j}\rangle$, and only for a small region of β the two difficulties might compete with each other — while none of the intermediate states contribute to the difficulty of state preparation. This is consistent with the relative locations of the P_n curves in Fig. 3.9: (i) for any β, $P_{1,2,\ldots,j-1}$ are always much greater than the minimum of P_0 and P_j, and (ii) as we move away from the β at which P_0 and P_j cross each other, their discrepancy increases quickly.

As a matter of practicality, we see that if we choose $\beta \approx 0.87$, the probability of achieving, with an overlap (or fidelity) above 90%, any superposition of $|\tilde{0}\rangle$ and $|\tilde{1}\rangle$ (i.e., any member of the subspace $\mathcal{H}_1$) is guaranteed to be above 6.3%. On the other end, with a probability of at least 0.1%, we can produce all states in the 8-dimensional subspace of $\mathcal{H}_7$.

3.5 Practical considerations

In order to realize such a state-preparation scheme, we need to fulfill the following three requirements. The *first* requirement is that the series in Eq. (3.92) be converging. This can be satisfied if $\beta \geq 1$. To see what this means, we restore all the physical units:

$$\beta = \frac{k/(2\omega_m)}{\sqrt{\hbar m \omega_m/2}} = \left[\frac{\hbar \omega_0}{c}\right]\sqrt{\frac{2}{\hbar m \omega_m}}\left[2\omega_m \frac{L}{c}\right]^{-1}. \tag{3.100}$$

It characterizes the momentum kick of photon $\hbar \omega_0/c$ to the oscillator during one oscillation period compared to the ground state momentum uncertainty $\sqrt{\hbar m \omega_m/2}$. The momentum kick from the photon needs to be big enough to substantially change the mirror state. The *second* requirement is that the cavity bandwidth be smaller than the mechanical frequency

$$\gamma < \omega_m. \tag{3.101}$$

This is because we need to wait at least several oscillation periods to approach the asymptotic state, and the photon should have sufficient duration such that we have a finite probability of detecting a photon at $t > \omega_m^{-1}$.

Combining the above two conditions, we obtain the following relation

$$\frac{\lambda}{\mathcal{F}} < \sqrt{\frac{\hbar}{2m\omega_m}} \qquad (3.102)$$

where λ is the optical wavelength of the photon, $\mathcal{F}$ is the cavity finesse. This means the cavity linear dynamical range must be less than the zero point uncertainty to realize the optomechanical nonlinearity. An alternative scheme has been proposed to make it more achievable experimentally [16].

The *third* requirement is that the thermal decoherence effect be small within one mechanical oscillation period, namely [cf. also Eq. (5) in Ref. [7]]:

$$Q > \frac{kT_E}{\hbar\omega_m}, \qquad (3.103)$$

where Q is the mechanical quality factor of the oscillator and T_E is the environmental temperature. These three requirements can be achieved experimentally, e.g., the current setups shown in Refs. [3, 4] and the one proposed in Ref. [6].

Finally, we require the the capability of generating a single photon with an arbitrary wave function with duration comparable to the mechanical oscillation frequency of the photon. This is possible with cavity QED systems, as has been discussed by Ref. [17–19].

3.6 Conclusions

We have presented an exact solution to the open quantum dynamics of an single-photon interferometer with a movable mirror. Since the photon number is preserved, we have been able to write the total wave function of the photon as three components: incoming photon, inside-cavity photon and out-going photon. We analyzed the details of how the photon exchanges between the cavity mode and the external continuous field.

We studied the fringe visibility of the interferometer in a specific case by injecting a single photon with exponentially decaying profile and with the movable mirror initially prepared at the ground state. This scheme has been proposed by Ref. [7] to explore decoherence of a macroscopic oscillator, although in that proposal the photon has been assumed to start off from inside the cavity. In the limit when the photon pulse is short (or $a \gg \gamma$), we did recover the result of Ref. [7], although our result deviates significantly when a becomes comparable to γ. We believe this is experimentally relevant, because in the case $a \gg \gamma$, the probability of the photon exiting from the detection port is very small, and therefore the experiment may suffer significantly from imperfections.

We have also studied the use of such nonlinear optomechanical interactions to prepare the mechanical oscillator into an arbitrary quantum state — similar to the proposal of Ref. [12], although

not having the requirement that the photon starts off from within the cavity. To realize this, we require that: (i) the optomechanical cavity must be working in the nonlinearity regime [i.e., the cavity's spatial line width must be less than the oscillator's zero-point position fluctuation, see discussions above Eq. (3.102)], (ii) the cavity's frequency width must be less than the mechanical oscillator's angular frequency, (iii) the thermal decoherence time must be less than several times the mirror's period of oscillation, and (iv) we must be able to engineer the single-photon wave function arbitrarily, at a time scale comparable to the mirror's oscillation period and with coherence time longer than the cavity storage time. Although we have shown mathematically that all quantum states whose expansion coefficients in the displaced Fock states $|\tilde{n}\rangle$ drop sufficiently fast as $n \to +\infty$ can be prepared by modulating the wave function of the incoming photon and conditioning over the arrival time of the returning photon, in practice we will be confined to the superposition of a handful of nearby displaced Fock states.

Acknowledgements

Bibliography

[1] Review articles by T. J. Kippenberg, and K. J. Vahala, Science **321**, 1172 (2008), and by F. Marquardt, and S. M. Girvin, Physics **2**, 40 (2009).

[2] A. D. O'Connell, M. Hofheinz, M. Ansmann, R. C. Bialczak, M. Lenander, E. Lucero, M. Neeley, D. Sank, H. Wang, M. Weides, J. Wenner, John M. Martinis, and A. N. Cleland, Nature **464**, 697 (2010).

[3] J. D. Teufel, T. Donner, Dale Li, J. W. Harlow, M. S. Allman, K. Cicak, A. J. Sirois, J. D. Whittaker, K. W. Lehnert, and R. W. Simmonds, Nature **475**, 359 (2011).

[4] A. H. Safavi-Naeini, J. Chan, J. T. Hill, T. P. M. Alegre, A. Krause, and O. Painter, arXiv:1108.4680 [quant-ph].

[5] S. Gupta, K.L. Moore, K.W. Murch, and D.M. Stamper-Kurn, Phys. Rev. Lett. **99**, 213601 (2007).

[6] J.D. Thompson, B.M. Zwickl, A.M. Jayich, F. Marquardt, S.M. Girvin and J.G.E. Harris, Nature 452, 72 (2008).

[7] W. Marshall, C. Simon, R. Penrose, and D. Bouwmeester, Phys. Rev. Lett. **91**, 130401 (2003).

[8] D. Kleckner, I. Pikovski, E. Jeffrey, L. Ament, E. Eliel, J. Brink, and D. Bouwmeester, New J. Phys. **10**, 095020 (2008).

[9] R. Penrose, Gen. Rel. Grav. **28** 581 (1996); Phil. Trans. R. Soc. Lond. A **356** 1927; *The Road to Reality: A Complete Guide to the Laws of the Universe*, Alfred A. Knopf, (2005).

[10] P. Rabl, Phys. Rev. Lett. **107**, 063601 (2011).

[11] A. Nunnenkamp, K. Børkje, and S. M. Girvin, Phys. Rev. Lett. **107**, 063602 (2011).

[12] S. Bose, K. Jacobs, and P. L. Knight, Phys. Rev. A **56**, 4175 (1997).

[13] A. Bassi, E. Ippoliti, S. L. Adler, Phys. Rev. Lett. **94**, 030401 (2005).

[14] U. Akram, N. Kiesel, M. Aspelmeyer and G. J Milburn., New J. Phys. **12**, 083030 (2010).

[15] A. Nunnenkamp, K. Børkje, J. G. E. Harris, and S. M. Girvin, Phys. Rev. A **82**, 021806 (2010).

[16] F. Y. Khalili, S. Danilishin, H. Miao, H. Muller-Ebhardt, H. Yang, and Y. Chen, Phys. Rev. Lett. **105**, 070403 (2010).

[17] C. K. Law, and H. J. Kimble, Journal of Modern Optics, **44**, 2067 (1997).

[18] J. McKeever, A. Boca, A. D. Boozer, R. Miller, J. R. Buck, A. Kuzmich, and H. J. Kimble, Science **303**, 1992 (2004).

[19] M. Keller, B. Lange, K. Hayasaka, W. Lange, and H. Walther, Nature (London) **431**, 1075 (2004).

Chapter 4

Towards understanding non-Markovian quantum measurement

In quantum measurement or control processes, there are often auxiliary modes coupling to the quantum system that we are interested in—they together form a *bath* or an environment for the system. The bath can have finite memory (non-Markovian), and simply ignoring its dynamics, i.e., adiabatically eliminating it, will prevent us from predicting the true quantum behavior of the system. We generalize the technique introduced by Strunz *et. al.* [Phys. Rev. Lett **82**, 1801 (1999)], and develop a formalism that allows us to eliminate the bath non-adiabatically in continuous quantum measurements, and obtain a non-Markovian stochastic master equation for the system which we focus on. This formalism also illuminates how to design the bath—acting as a quantum filter—to effectively probe interesting system observables, e.g., the Quantum-Nondemolition (QND) observable.

Based on paper by H. Yang, H. Miao and Y. Chen, Phys. Rev. A **85**, 040101 (R) (2013) and an unpublished note by the same set of authors. Copyright 2013 by the American Physical Society.

4.1   Introduction

Non-Markovianity naturally arises in many interesting quantum systems, e.g., cavity QED. In the theoretical side of the study, the common approach is to investigate the decoherence of the quantum system by using either the non-Markovian stochastic Schrödinger equation (also called the state diffusion equation) or equivalently the master equation [1–3]. The underlying assumption usually made is that no information concerning the environment (i.e., the bath) is collected; however, in most experimental setups, the measurement device is an indispensable part, especially when we want

to have good control over the dynamics of the system by implementing feedback control [4]. There are some ambiguities concerning how to correctly quantify the system dynamics under a continuous measurement when there is non-Markorvianity involved. Recent interesting discussions among Diósi and Wiseman *et. al.* [5, 6] highlight this issue. Diósi tried to give a quantum trajectory interpretation of the non-Markovian stochastic Schrödinger equation (SSE), i.e., claiming that it describes a pure state evolution under a continuous measurement of the system operator. It is now clear to us that this is not case, as shown explicitly by Wiseman *et. al.* and later by Diósi.

In this note, instead of trying to find the measurement correspondence of non-Markovian SSE, we start with a physical model for the continuous quantum measurement, and study two important scenarios in which non-Markovianity can arise: the first one is an indirect measurement of the system via a measurement of its bath which has finite memory; the second one is a direct measurement of the system, but where the measurement device initially has non-trivial quantum correlation. By clarifying the issues in these two scenarios, we try to develop a better understanding of non-Markovian quantum measurement in more general cases.

The outline of this note goes as follows: in section 11.2, we will build a physical model for a continuous measurement process, and point out the above scenarios in which non-Markovianity can arise; in section 11.3, we first use our model to reconsider a direct Markovian measurement of cavity mode, and recover the result in the literature; in section 11.4, we consider the first scenario of indirect measurement and derive the stochastic master equation, instead of pure-state SSE which generally does not exist for a non-Markovian measurement, as pointed out by Wiseman [6]. We solve two interesting examples in cavity QED and optomechanical systems exactly, and also present a perturbation method for more general systems when the coupling is weak; in section 11.5, we consider the second scenario of correlated measurement and derive the Wigner function by using a path-integral approach developed in Ref. [7]; in section 11.6, we will briefly mention more general scenarios of non-Markovian quantum measurement, and finnally conclude in section 4.7.

4.2   Quantum-classical interface: the measurement device
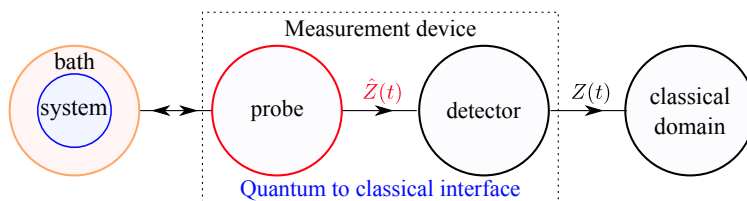
Figure 4.1: A schematic showing a general class of quantum measurement process. The probe and the detector together forms a measurement device that serves as a quantum-to-classical interface. The output of the quantum probe $\hat{Z}(t)$ becomes a c-number $Z(t)$ after the detection.

In this section, we will build a physical model for continuous measurement and derive the essential elements for an appropriate mathematical description. A general quantum measurement process is shown schematically in Fig. 4.1. The system is interacting with its bath which can have finite or infinite degrees of freedom (field). The bath degrees of freedom are partially or entirely coupled to a quantum probe. In order to be an adequate quantum probe, its output needs to be precisely measured by the detector (i.e., a von Neumann projective measurement), and there is no further quantum back action of the detector on the probe [1]. For this to be true, the probe output $\hat{Z}(t)$ has to commute at different times in the Heisenberg picture [9, 10], namely

$$[\hat{Z}(t), \hat{Z}(t')] = 0. \tag{4.1}$$

A continuous projective measurement of it by the detector gives a classical c-number data string $Z(t)$, which is then processed in the classical domain. This condition puts a rather tight constraint on the property of the probe. As shown in Ref. [9] and briefly discussed in appendix 6.4, *in a continuous linear quantum measurement, the probe that links the quantum and classical domains needs to be a continuous field with different degrees of freedom at different times. Measurement performed on the probe by the detector at one moment will therefore not have any dynamical back action on the measurement results at later moments. Its output gives rise to a well-defined measurable trajectory that has a classical reality.* To make it more concrete, in the later discussions, we will use a continuous optical field as a model for the probe field, of which the canonical quantities are the amplitude quadrature $\hat{o}_1 \equiv (\hat{o} + \hat{o}^\dagger)/\sqrt{2}$ and the phase quadrature $\hat{o}_2 \equiv (\hat{o} - \hat{o}^\dagger)/(i\sqrt{2})$ with $\hat{o}$ being the annihilation operator, which satisfies [2]:

$$[\hat{o}_1(t), \hat{o}_1(t')] = [\hat{o}_2(t), \hat{o}_2(t')] = 0, \quad [\hat{o}_1(t), \hat{o}_2(t)] = i\,\delta(t - t'). \tag{4.2}$$

Those different degrees of freedom, even though they are dynamical independent, can be statistically correlated. There are two cases: (i) the input probe field (before interacting with the bath and system) are uncorrelated; (ii) the input probe field are either classical or quantum mechanically correlated (quantum entanglement). Give such a model for the measurement device, there are three scenarios in which the effective dynamics of the system can be non-Markovian (after tracing out the bath and probe field):

1. The input probe field is uncorrelated, but the bath has a finite memory, i.e, non-Markovian dynamics.

---

[1] If it were not the case, we have to insert another additional probe in between the original probe and the detector such that this becomes true, and enlarge the original system. This serves as the Heisenberg cut [8], which is essential in order to have an unambiguous interpretation of the measurement result.

[2] We have neglected the spatial dependence of the field, as we use the interaction picture of the free Hamiltonian for the field, and compare the field at the same location but at different times. The propagation of the field is encoded in the time delay.

2. The input probe field is correlated, but the bath has no memory [3].

3. The input probe field is correlated and the system-bath dynamics is non-Markovian.

We will consider the first two scenarios by using physical models for the system and bath, and briefly discuss the last scenario.

4.3 Markovian measurement of a cavity mode
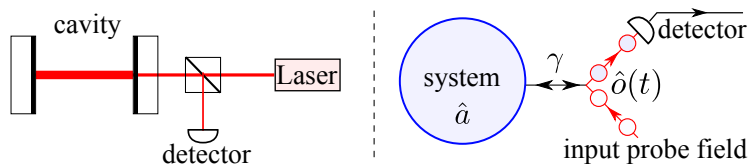
Figure 4.2: Schematics showing a Markovian measurement of a cavity mode with setup (left) and model (right).

Before considering non-Markovian measurement, we first study Markovian measurement of a cavity mode. From this example, not only can we recover the previous result in the literature, but is also an important step in studying the non-Markovian case in later sections, when the cavity mode acts as a intermediate bath that couples to the system. The Hamiltonian for such a measurement process in the rotating wave approximation is given by

$$\hat{H} = \hbar\,\omega_c \hat{a}^\dagger \hat{a} + \hbar\sqrt{\gamma}[\hat{a}\,\hat{o}^\dagger(t)e^{i\omega_0 t} + \hat{a}^\dagger\,\hat{o}(t)e^{-i\omega_0 t}]. \tag{4.3}$$

Here $\hat{a}$ is the annihilation operator for the cavity mode (system) and $[\hat{a},\,\hat{a}^\dagger] = 1$; ω_c is the resonant frequency of the cavity mode; $\hat{o}(t)$ is the annihilation operator for the external continuous optical field (probe field) in the interaction picture; ω_0 is the laser frequency. In the rotating frame of the laser frequency ω_0 (i.e., in the interaction picture of $\hbar\omega_0\hat{a}^\dagger\hat{a}$), it can be rewritten as

$$\hat{H} = \hbar\,\Delta\hat{a}^\dagger\hat{a} + \hbar\sqrt{\gamma}[\hat{a}\,\hat{o}^\dagger(t) + \hat{a}^\dagger\,\hat{o}(t)], \tag{4.4}$$

where detune frequency $\Delta \equiv \omega_c - \omega_0$ describes the offset between the laser and cavity resonant frequency.

We assume that the amplitude quadrature $\hat{o}_1$ of the optical field is measured by using a homodyne detection, and $y(t)$ is the measurement result. The evolution of the joint density matrix from t to $t + \mathrm{d}t$ is given by

$$\hat{\rho}(t + \mathrm{d}t) = \hat{\mathcal{P}}\hat{U}\hat{\rho}(t)\hat{U}^\dagger\hat{\mathcal{P}}/P[y(t)]. \tag{4.5}$$

---

[3]In this case, the bath degrees of freedom can be adiabatically eliminated; the system can be viewed as direct coupling to the probe field. One particular example of this scenario was considered by Diósi [5], which assumes a Gaussian correlated input probe field.

Here the projection operator $\hat{\mathcal{P}} = |y(t)\rangle\langle y(t)|$ with $|y(t)\rangle$ is the eigenstate of $\hat{o}_1$; the evolution operator $\hat{U} = e^{-i\hat{H}dt/\hbar}$; $P[y(t)]$ is the probability for measurement result. By tracing out the probe field, we obtain the reduced density matrix for the cavity mode conditional on the measurement result:

$$\hat{\rho}_a(t+dt) = \text{Tr}_o[\hat{\rho}(t+dt)] = \text{Tr}_o\left\{\delta[\hat{o}_1 - y(t)]\hat{U}\hat{\rho}(t)\hat{U}^\dagger\right\}/P[y(t)], \tag{4.6}$$

where we have used the fact that $\text{Tr}[\hat{\mathcal{P}}\hat{\rho}\hat{\mathcal{P}}] = \text{Tr}[\hat{\mathcal{P}}\hat{\rho}] = \text{Tr}\left\{\delta[\hat{o}_1 - y(t)]\hat{\rho}\right\}$. Before the interaction, we assume that the probe field and the cavity mode are separable, i.e., $\hat{\rho}(t) = \hat{\rho}_a(t) \otimes \hat{\rho}_o(t)$, and the input probe field is in vacuum state $\hat{\rho}_o(t) = |0\rangle\langle 0|$ [4]. Up to the first order of dt, we have

$$\hat{\rho}_a(t+dt) = \frac{1}{2\pi}\int d\xi\, e^{-i\xi y(t)}\text{Tr}_o\left[e^{i\xi\hat{o}_1(t)}\left\{\hat{\rho}(t) - \frac{i}{\hbar}[\hat{H}, \hat{\rho}(t)]dt - \frac{1}{2\hbar^2}[\hat{H}_{\text{int}}, [\hat{H}_{\text{int}}, \hat{\rho}(t)]]dt^2\right\}\right] + \mathcal{O}[dt^2], \tag{4.7}$$

where we introduce an auxiliary parameter ξ to rewrite the delta function; $\hat{H}_{\text{int}} \equiv \hbar\sqrt{\gamma}[\hat{a}\,\hat{o}^\dagger(t) + \hat{a}^\dagger\,\hat{o}(t)]$ and it is kept up to the second order in dt, because $\langle\hat{o}^\dagger\hat{o}\rangle \sim dt^{-1}$ and $[\hat{o}(t), \hat{o}^\dagger(t')] = \delta(t-t')$. After some lengthy but straightforward calculations, as shown in the Appendix 6.B, we obtain the stochastic master equation (SME):

$$d\hat{\rho}_a(t) = -i[\Delta\hat{a}^\dagger\hat{a}, \hat{\rho}_a(t)]dt - \gamma[\hat{a}^\dagger\hat{a}\hat{\rho}_a(t) + \hat{\rho}_a(t)\hat{a}^\dagger\hat{a} - 2\hat{a}\hat{\rho}_a(t)\hat{a}^\dagger]dt - i\sqrt{2\gamma}[\hat{a}\hat{\rho}_a(t) - \hat{\rho}_a(t)\hat{a}^\dagger - \langle\hat{a} - \hat{a}^\dagger\rangle\hat{\rho}_a(t)]dW, \tag{4.8}$$

where $\langle\hat{a}\rangle \equiv \text{Tr}_a[\hat{\rho}_a(t)\hat{a}]$ and dW is the Wiener increment and $dW^2 = dt$. The measurement result $y(t)$ satisfies

$$y(t)dt = -i\sqrt{\gamma}\langle\hat{a} - \hat{a}^\dagger\rangle dt + dW/\sqrt{2}. \tag{4.9}$$

This simply recovers the result obtained by Wiseman and Milburn [34] but from a different approach. If we ignore the fact that the measurement result and mean of dW is equal to zero, we simply obtain the Markovian master equation. We therefore can call the above SME Markovian SME.

Since, for this Markovian measurement, a pure initial state for the cavity mode will remain pure, we can write down the corresponding stochastic Schrödinger equation (an stochastic unraveling of the SME):

$$d|\psi\rangle = -i\Delta\hat{a}^\dagger\hat{a}|\psi\rangle dt - \gamma(\hat{a}^\dagger\hat{a} - 2\langle\hat{a}^\dagger\rangle\hat{a} + \langle\hat{a}^\dagger\rangle\langle\hat{a}\rangle)|\psi\rangle dt - i\sqrt{2\gamma}(\hat{a} - \langle\hat{a}\rangle)|\psi\rangle dW \tag{4.10}$$

with $|\psi\rangle$ defined through $|\psi\rangle\langle\psi| \equiv \hat{\rho}_a$.

---

[4] One should not be confused by the time dependence of $\hat{\rho}_o(t)$, as we are in the interaction picture. It can be viewed as introducing a new degree of freedom to interact with the system at each moment, and tracing it out afterwards

4.4 Non-Markovian quantum measurement: the first scenario

In this section, we will consider the first scenario of non-Markovian quantum measurement—an indirect measurement of the system via a measurement of its bath which has non-Markovian dynamics. To be concrete, we will consider specific examples to illustrate the measurement process. In subsection 4.4.1, we study the cavity QED model with atom-cavity interaction; in subsection 4.4.2, we consider a typical cavity-assisted optomechanical device, in which a mechanical oscillator is coupled to a cavity mode via radiation pressure.

4.4.1 Cavity QED: atom-cavity interaction
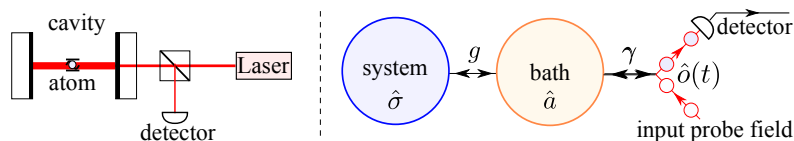
Figure 4.3: Schematics showing the cavity QED model under consideration. A two-level atom interacts with a cavity mode that is continuously interacting with an external continuous field. The cavity mode now becomes a bath instead of system as considered in the previous Markovian measurement case.

The model is shown schematically in Fig. 4.3. A two-level atom (system) is coupled to a cavity mode (bath) which, in turn, is coupled to the external continuous optical field (probe field). Such a system can exhibit a strong non-Markovianity if the cavity bandwidth is small—a long memory. The Hamiltonian can be written as

$$\hat{H} = \hbar\frac{\omega_q}{2}\hat{\sigma}_z + \hbar\,\Delta\hat{a}^\dagger\hat{a} + \hbar g(\hat{\sigma}_-\hat{a}^\dagger + \hat{\sigma}_+\hat{a}) + \hbar\sqrt{\gamma}[\hat{a}\,\hat{o}^\dagger(t) + \hat{a}^\dagger\,\hat{o}(t)], \qquad (4.11)$$

where $\hat{\sigma}_z$ is the Pauli matrix and $\hat{\sigma}_- = \hat{\sigma}_x - i\hat{\sigma}_y$ and $\sigma_+ = \hat{\sigma}_x + i\sigma_y$. Apart from the last additional term, it is the famous Jaynes-Cummings model. We again assume that the amplitude quadrature of the optical filed is measured. By using the result obtained in the previous section, we can immediately write down the stochastic master equation for the atom and the cavity mode:

$$\mathrm{d}\hat{\rho}_{\sigma a} = -\frac{i}{\hbar}[\hat{H}_\sigma + \hat{H}_a + \hat{H}_\mathrm{int},\ \hat{\rho}_{\sigma a}]\mathrm{d}t - \gamma[\hat{a}^\dagger\hat{a}\hat{\rho}_{\sigma a} + \hat{\rho}_{\sigma a}\hat{a}^\dagger\hat{a} - 2\hat{a}\hat{\rho}_{\sigma a}\hat{a}^\dagger]\mathrm{d}t - i\sqrt{2\gamma}[\hat{a}\hat{\rho}_{\sigma a} - \hat{\rho}_{\sigma a}\hat{a}^\dagger - \langle\hat{a} - \hat{a}^\dagger\rangle\hat{\rho}_{\sigma a}]\mathrm{d}W.$$

$$(4.12)$$

In order to obtain the equation for the atom only, we need to trace out the cavity mode. We will use the technics developed by Diósi and Strunz [3]. We first write the above equation in the

non-normalized Bargmann coherent state basis $|\alpha\rangle \equiv e^{\alpha \hat{a}^{\dagger}}|0\rangle$ and obtain

$$\mathrm{d}\hat{\rho}_{\sigma a} = -\frac{i}{\hbar}[\hat{H}_{\sigma}, \hat{\rho}_{\sigma a}]\mathrm{d}t - i\Delta(\alpha^*\partial_{\alpha^*} - \alpha\partial_{\alpha})\hat{\rho}_{\sigma a}\mathrm{d}t - i\,g(\hat{\sigma}_-\alpha^* + \hat{\sigma}_+\partial_{\alpha^*})\hat{\rho}_{\sigma a}\mathrm{d}t + i\,g(\hat{\rho}_{\sigma a}\hat{\sigma}_+\alpha + \partial_{\alpha}\hat{\rho}_{\sigma a}\hat{\sigma}_-)\mathrm{d}t$$

$$- \gamma(\alpha^*\partial_{\alpha^*} + \alpha\,\partial_{\alpha} - 2\,\partial_{\alpha}\partial_{\alpha^*})\hat{\rho}_{\sigma a}\,\mathrm{d}t - i\sqrt{2\gamma}[\partial_{\alpha} - \partial_{\alpha^*} - \langle\hat{a} - \hat{a}^{\dagger}\rangle]\hat{\rho}_{\sigma a}\,\mathrm{d}W. \tag{4.13}$$

The reduced atom density matrix is given by

$$\hat{\rho}_{\sigma} = \int \mathrm{d}^2\boldsymbol{\alpha}\,e^{-|\alpha^2|}\langle\alpha|\hat{\rho}_{\sigma a}|\alpha\rangle \equiv \int \mathrm{d}^2\boldsymbol{\alpha}\,e^{-|\alpha|^2}\hat{\rho}_{\sigma a}(\alpha^*, \alpha). \tag{4.14}$$

Instead of interpreting this as the standard tracing procedure, in Ref. [2], the authors interpret $\hat{\rho}_{\sigma a}(\alpha, \alpha^*)$ as the system state under a different parametrization of the Hamiltonian $\hat{H}(\alpha)$ with α being the parameter, which is a random variable with the joint Gaussian distribution $P(\alpha, \alpha^*) = e^{-|\alpha|^2}$, and Eq. (4.14) is a classical ensemble average, namely

$$\hat{\rho}_{\sigma} = \int \mathrm{d}^2\boldsymbol{\alpha}\,P(\alpha)\hat{\rho}_{\sigma}(\alpha^*, \alpha) \equiv M_{\alpha}[\hat{\rho}_{\sigma}(\alpha^*, \alpha)]. \tag{4.15}$$

By using the fact that, for a Gaussian probability distribution, $M_{\alpha}[\alpha\,\hat{\rho}_x(\alpha^*, \alpha)] = M_{\alpha}[\partial_{\alpha^*}\hat{\rho}_x(\alpha^*, \alpha)]$, we have

$$\mathrm{d}\hat{\rho}_{\sigma} = -\frac{i}{\hbar}[\hat{H}_{\sigma}, \hat{\rho}_{\sigma}]\mathrm{d}t - ig(\hat{\sigma}_-\bar{\partial}_{\alpha} + \hat{\sigma}_+\bar{\partial}_{\alpha^*})\hat{\rho}_{\sigma}\mathrm{d}t + i\,g(\bar{\partial}_{\alpha^*}\hat{\rho}_{\sigma}\hat{\sigma}_+ + \bar{\partial}_{\alpha}\hat{\rho}_{\sigma}\hat{\sigma}_-)\mathrm{d}t - i\sqrt{2\gamma}[\bar{\partial}_{\alpha} - \bar{\partial}_{\alpha^*} - \langle\hat{a} - \hat{a}^{\dagger}\rangle]\hat{\rho}_x\mathrm{d}W, \tag{4.16}$$

where we have defined $\bar{\partial}_{\alpha^*}\hat{\rho}_x \equiv M_{\alpha}[\partial_{\alpha^*}\hat{\rho}_x(\alpha^*, \alpha)]$.

To obtain something meaningful for the study of the state of atom, we need to replace ∂_{α^*} in the term of the operator for the atom. This has been extensively studied in Refs. [2, 33] for deriving SSE unraveling of the master equation. Here we will apply this technic. We first assume the following ansatz:

$$\partial_{\alpha^*}\hat{\rho}_x(\alpha^*, \alpha) = -i\hat{O}(t, \alpha^*)\hat{\rho}_x(\alpha^*, \alpha) \tag{4.17}$$

where $\hat{O}$ is only a function of the operators for an atom. The exact form for $\hat{O}$ can be derived by using the consistent condition:

$$\frac{\mathrm{d}}{\mathrm{d}t}[\partial_{\alpha^*}\hat{\rho}_x(\alpha^*, \alpha)] = \partial_{\alpha^*}[\frac{\mathrm{d}}{\mathrm{d}t}\hat{\rho}_x(\alpha^*, \alpha)]. \tag{4.18}$$

As shown in Appendix 4.C, we obtain

$$\hat{O}(t, \alpha^*) = e^{i(\omega_q - \Delta + i\gamma)t}f(t)\hat{\sigma}_- \equiv \hat{O}_0(t), \tag{4.19}$$

where function $f(t)$ satisfies the following nonlinear Riccati equation:

$$\dot{f}(t) = g\, e^{-i(\omega_q - \Delta + i\gamma)t} + g\, e^{i(\omega_q - \Delta + i\gamma)t} f^2(t), \tag{4.20}$$

with initial condition $f(0) = 0$. There is a closed-form solution for $f(t)$, but it is too cumbersome to show. Since $\hat{O}(t, \alpha^*) = \hat{O}_0(t)$ is independent of α^* we can easily obtain $\bar{\partial}_{\alpha^*}\hat{\rho}_x \equiv \hat{O}_0\hat{\rho}_x$. Finally, we obtain the non-Markovian stochastic master equation for the atom only:

$$\begin{aligned}
\mathrm{d}\hat{\rho}_\sigma = &- i\left[\frac{\omega_q}{2}\hat{\sigma}_z,\, \hat{\rho}_\sigma\right]\mathrm{d}t - g\left(\hat{\sigma}_+\hat{O}_0\hat{\rho}_\sigma + \hat{\rho}_\sigma\hat{O}_0^\dagger\hat{\sigma}_- - \hat{O}_0\hat{\rho}_\sigma\hat{\sigma}_+ - \hat{\sigma}_-\hat{\rho}_\sigma\hat{O}_0^\dagger\right)\mathrm{d}t \\
&+ \sqrt{2\gamma}[\hat{O}_0\hat{\rho}_\sigma + \hat{\rho}_\sigma\hat{O}_0^\dagger - \langle\hat{O}_0 + \hat{O}_0^\dagger\rangle\hat{\rho}_\sigma]\mathrm{d}W.
\end{aligned} \tag{4.21}$$

This equation describes a quantum measurement of $\hat{O}_0 + \hat{O}^\dagger$ which is equal to the atomic polarization $\hat{\sigma}_x$ filtered by the cavity mode, or a retarded observable in the description of Diósi [5].

It is rather remarkable in the sense it only involves the time-local density matrix, and this significantly reduces the computation effort for studying the atom dynamics. Instead of evolving the cavity mode and the atom all together as in the usual approach, we only need to consider a finite dimensional density matrix for the atom.

In addition, there is an important difference from the usual Markovian SME in the fact that the decoherence part is not exactly in a Lindblad form, and it can be effectively viewed as a non-Markovian quantum measurement of $\hat{\sigma}_-$. We can recover the Markovian case by taking the large cavity bandwidth limit $\gamma \gg \Delta, \omega_q, g$. In this case, the cavity mode enslaves to the dynamics of the atom, and it is easy to find

$$\hat{O}_0(t) \approx \frac{g}{\gamma}\hat{\sigma}_-, \tag{4.22}$$

and we simply have

$$\begin{aligned}
\mathrm{d}\hat{\rho}_\sigma = &- i\left[\frac{\omega_q}{2}\hat{\sigma}_z,\, \hat{\rho}_\sigma\right]\mathrm{d}t - (g^2/\gamma)\left(\hat{\sigma}_+\hat{\sigma}_-\hat{\rho}_\sigma + \hat{\rho}_\sigma\hat{\sigma}_+\hat{\sigma}_- - 2\hat{\sigma}_-\hat{\rho}_\sigma\hat{\sigma}_+\right)\mathrm{d}t \\
&+ \sqrt{2g^2/\gamma}[\hat{\sigma}_-\hat{\rho}_\sigma + \hat{\rho}_\sigma\hat{\sigma}_+ - \langle\hat{\sigma}_- + \hat{\sigma}_+\rangle\hat{\rho}_\sigma]\mathrm{d}W.
\end{aligned} \tag{4.23}$$

This also recovers the result with adiabatic elimination of the cavity mode in the literature, which corresponds to a direct Markovian measurement of $\hat{\sigma}_x$ with an effective measurement strength given by g^2/γ.

To confirm that Eq. (4.112) is the SME that correctly describes the conditional dynamics of the atom, we numerically solve and compare (i) the Markovian SSE for the joint atom-cavity wavefunction and (ii) the non-Makovian SME for the atom density matrix, to see whether they both give the same conditional means of $\hat{\sigma}_x$, $\hat{\sigma}_y$ and $\hat{\sigma}_z$. The numerical results are shown in Fig. 4.4. We have chosen $\omega_q = 1$, $\Delta = 1$ and $\gamma = 2$, and the atom-cavity initial state is $[|+\rangle_z + |-\rangle_z]/\sqrt{2} \otimes |0\rangle$. They
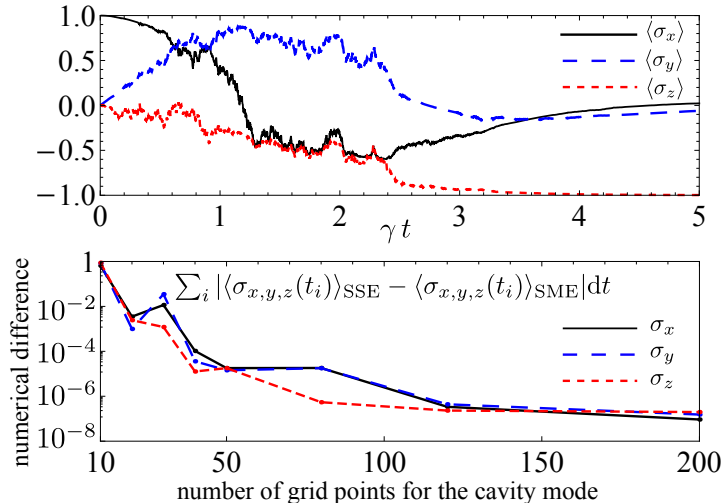
Figure 4.4: (Color online.) The top panel shows simulation results for the time evolution of $\langle\sigma_x\rangle$, $\langle\sigma_y\rangle$ and $\langle\sigma_z\rangle$ for one realization of dW. The bottom panel is the convergency of the accumulated numerical difference between the SSE and SME simulation results given different number of grid points for the cavity mode.

indeed agree with each other as shown by the convergency of their accumulated numerical difference.

4.4.2 Optomechanical device
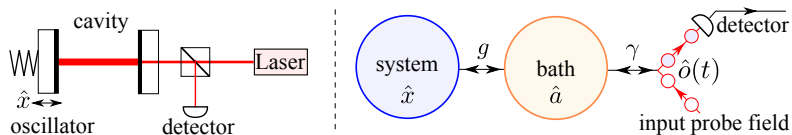
Figure 4.5: Schematics showing a typical optomechanical device. The displacement $\hat{x}$ of the mechanical oscillator is coupled to the cavity mode via radiation pressure.

There is another interesting system that has been studied extensively in the literature recently—an optomechanical device, which is shown schematically in Fig. 4.5. The interaction between the oscillator (system) and the cavity mode (bath) is mediated by radiation pressure. For a small cavity bandwidth (smaller than the mechanical oscillator frequency), the information can slosh back and forth between the oscillator and the cavity mode for many mechanical oscillator periods—again a strong non-Markovianity. The procedure to derive the reduced dynamics for the oscillator is similar to the atom case.

The corresponding Hamiltonian can be written as

$$\hat{H} = \frac{\hat{p}^2}{2m} + \frac{1}{2}m\omega_m^2\hat{x}^2 + \hbar\,\Delta\hat{a}^\dagger\hat{a} + \hbar\,g\hat{x}\hat{a}^\dagger\hat{a} + \hbar\sqrt{\gamma}[\hat{a}\,\hat{b}^\dagger(t) + \hat{a}^\dagger\,\hat{b}(t)]. \qquad (4.24)$$

Usually, the cavity mode is pumped by the laser with a large steady-state amplitude $\bar{\alpha}$, and we can

then obtain the linearized Hamiltonian by studying the change around $\bar{\alpha}$:

$$\hat{H} = \frac{\hat{p}^2}{2m} + \frac{1}{2}m\omega_m^2\hat{x}^2 + \hbar\,\Delta\hat{a}^\dagger\hat{a} + \hbar G\hat{x}(\hat{a}^\dagger + \hat{a}) + \hbar\sqrt{\gamma}[\hat{a}\,\hat{b}^\dagger(t) + \hat{a}^\dagger\,\hat{b}(t)] \tag{4.25}$$

with $G \equiv g\bar{\alpha}$. This is the quantum Brownian motion with a single-degree-of-freedom bath under continuous measurement. We again assume that we measure the amplitude quadrature of the optical field. Similar to the previous case, after tracing out the cavity mode and continuous optical field, the reduced non-Markovian SME is given by

$$\begin{aligned}
\mathrm{d}\hat{\rho}_x = &-\frac{i}{\hbar}\left[\frac{\hat{p}^2}{2m} + \frac{1}{2}m\omega_m^2\hat{x}^2,\ \hat{\rho}_x\right]\mathrm{d}t - G(\hat{x}\hat{O}\hat{\rho}_x + \hat{\rho}_x\hat{O}^\dagger\hat{x} - \hat{O}\hat{\rho}_x\hat{x} - \hat{x}\hat{\rho}_x\hat{O}^\dagger)\mathrm{d}t \\
&+ \sqrt{2\gamma}[\hat{O}\hat{\rho}_x + \hat{\rho}_x\hat{O}^\dagger - \langle\hat{O} + \hat{O}^\dagger\rangle\hat{\rho}_x]dW,
\end{aligned} \tag{4.26}$$

where

$$\hat{O}\hat{\rho}_x = [O_1(t)\hat{\rho}_x\hat{O}_0^\dagger + \hat{O}_0\hat{\rho}_x]/[1 - |O_1(t)|^2], \tag{4.27}$$

$$\hat{\rho}_x\hat{O}^\dagger = [O_1^*(t)\hat{O}_0\hat{\rho}_x + \hat{\rho}_x\hat{O}_0^\dagger]/[1 - |O_1(t)|^2] \tag{4.28}$$

with details of $\hat{O}_0$ and $O_1(t)$ shown in Appendix 4.D.

In the large cavity bandwidth limit $\gamma \gg \omega_m, \Delta$, and G, $\hat{O}$ is simply given by:

$$\hat{O} = G\hat{x}/\gamma, \tag{4.29}$$

and we again recovers the Markovian SME:

$$\mathrm{d}\hat{\rho}_x = -\frac{i}{\hbar}\left[\frac{\hat{p}^2}{2m} + \frac{1}{2}m\omega_m^2\hat{x}^2,\ \hat{\rho}_x\right]\mathrm{d}t - G^2/\gamma[\hat{x},\ [\hat{x},\hat{\rho}_x]]\mathrm{d}t + \sqrt{2G^2/\gamma}[\hat{x}\hat{\rho}_x + \hat{\rho}_x\hat{x} - 2\langle\hat{x}\rangle\hat{\rho}_x]dW. \tag{4.30}$$

If we ignore the the measurement result (by averaging over dW which has zero mean), we have

$$\mathrm{d}\hat{\rho}_x = -\frac{i}{\hbar}\left[\frac{\hat{p}^2}{2m} + \frac{1}{2}m\omega_m^2\hat{x}^2,\ \hat{\rho}_x\right]\mathrm{d}t - \frac{G^2}{\gamma}[\hat{x},\ [\hat{x},\hat{\rho}_x]]\mathrm{d}t, \tag{4.31}$$

which recovers the Markovian master equation for quantum Brownian motion.

4.4.3 Generalization to bath with many degrees of freedom

In the previous two sections, we used two specific examples to illustrate non-Markovian measurement in the first scenario—due to non-Markovian dynamics between the system and bath, a measurement on the bath gives rise to non-Markovian stochastic (conditional) evolution of the system quantum state. In those examples, the cavity mode serves as the bath, and it only has one degree of freedom.

In this section, we will generalize the result to the case with a many-degrees-of-freedom bath which is linearly coupled to the probe field. We consider the following Hamiltonian for such a case:

$$\hat{H} = \hat{H}_s + \sum_k \hbar \omega_k \hat{a}_k^\dagger \hat{a}_k + \sum_k \hbar g_k (\hat{L}\hat{a}_k^\dagger + \hat{L}^\dagger \hat{a}_k) + \sum_k \hbar \sqrt{\gamma_k}[\hat{a}_k \, \hat{o}^\dagger(t) + \hat{a}_k^\dagger \, \hat{o}(t)]. \tag{4.32}$$

Here $\hat{H}_s$ is the free part of the system Hamiltonian; $\hat{L}$ is an arbitrary operator of the system; g_k is the coupling strength between the system and the bath which consists of different modes with frequency ω_k; γ_k is the coupling strength between the bath and the probe field $\hat{o}$. Note that this Hamiltonian is still quite special. It excludes other possibilities: (i) some of the bath modes might not be coupled to the probe field, in which case we cannot access the information of those modes and they will contribute to decoherence of the system; (ii) different modes might be coupled to different probe fields, in which case we have multiple measurement output channels. In principle, we can include those complicated cases, but right now, we will just focus on this specific Hamiltonian, and postpone the discussion of more general cases until later.

The derivation of non-Markovian SME for the system is almost parallel to the single-degree-of-freedom case, and we can formally write down the reduced stochastic master equation for the system:

$$d\hat{\rho}_s = -\frac{i}{\hbar}[\hat{H}_s, \, \hat{\rho}_s] \, dt - \sum_k g_k(\hat{L}^\dagger \hat{O}_s \hat{\rho}_s + \hat{\rho}_s \hat{O}_k^\dagger \hat{L} - \hat{O}_k \hat{\rho}_s \hat{L}^\dagger - \hat{L}\hat{\rho}_s \hat{O}_k^\dagger) dt + \sum_k \sqrt{2\gamma_k}[\hat{O}_k \hat{\rho}_s + \hat{\rho}_s \hat{O}_k^\dagger - \langle \hat{O}_k + \hat{O}_k^\dagger \rangle \hat{\rho}_s] dW. \tag{4.33}$$

The operator $\hat{O}_k$ is defined through the following ansatz:

$$M_{\vec{\alpha}}[\partial_{\alpha_k^*} \hat{\rho}_s(t, \, \vec{\alpha})] = -i\hat{O}_k(t)\hat{\rho}_s(t). \tag{4.34}$$

Generally, it is quite difficult to find a closed form for $\hat{O}_k$ in terms of the system operator. Only in the following two cases, can we obtain relatively a simple expression for $\hat{O}_k$: (i) $\hat{L}$ is a linear function of the canonical variables of the system—linear coupling case; (ii) $g_k/\gamma_k < 1$—the weak coupling case, which allows us to find a perturbative solution. We will discuss these two cases in more detail.

Linear coupling.— We use the atom as an example with $\hat{H}_s = \hbar \frac{\omega_q}{2} \hat{\sigma}_z$, and choose $\hat{L} = \hat{\sigma}_-$. As shown in the Appendix 4.E, we can obtain

$$\hat{O}_k(t) = \sum_{k'} [e^{i(\omega_q \mathbf{I} - \mathbf{M})t}]_{kk'} f_{k'}(t)\hat{\sigma}_-, \tag{4.35}$$

with

$$\dot{f}_k(t) = \sum_{k'} g_{k'} [e^{-i(\omega_q \mathbf{I} - \mathbf{M})t}]_{kk'} - f_k(t) \sum_{k'k''} g_{k'} [e^{i(\omega_q \mathbf{I} - \mathbf{M})t}]_{kk'} f_{k''}(t) \tag{4.36}$$

and initial condition $f_k(0) = 0$. Here we have introduced identity matrix $\mathbf{I}$ and matrix $\mathbf{M}$:

$$\mathbf{M} \equiv \begin{bmatrix} \omega_1 - i\gamma_1 & -i\sqrt{\gamma_1\gamma_2} & \cdots \\ -i\sqrt{\gamma_1\gamma_2} & \omega_2 - i\gamma_2 & \vdots \\ \vdots & \cdots & \ddots \end{bmatrix}. \tag{4.37}$$

This recovers the result in subsection 4.4.1 when the bath has only one mode.

Similarly, if the system is a harmonic oscillator and $\hat{L} = \hat{b}$ is the annihilation operator, we will end with the same expression, expect that ω_q is replaced by the oscillator frequency and $\hat{\sigma}_-$ is replaced by $\hat{b}$.

Weak coupling— When the operator $\hat{L}$ is a nonlinear function of the system canonical variables, there will be no straightforward route to derive $\hat{O}_k$. If the coupling is weak, we can use the perturbation method and expand the solution in series of coupling strength. As shown in Appendix 4.F, we obtain

$$\hat{O}_k(t) = \sum_{k'} \int_0^t \mathrm{d}\tau [e^{-i\mathbf{M}\tau}]_{kk'} g_{k'} \, \hat{L}(-\tau)\hat{\rho}_s(t) + \mathcal{O}[g_k^2], \tag{4.38}$$

where $\hat{L}(-\tau) = e^{-i\hat{H}_s\tau/\hbar} \hat{L} \, e^{i\hat{H}_s\tau/\hbar}$ under free evolution and the matrix element $\mathbf{M}_{kk'} = \omega_k \, \delta_{kk'} - i\sqrt{\gamma_k\gamma_{k'}}$ with $\delta_{kk'}$ being the Kronecker delta. Basically, $\hat{\varrho}_k$ is equal to $\hat{L}\hat{\rho}_s$ convoluted with the Green's function of the bath. In other words, we are effectively coupled to a dynamical quantity of the system that is shaped by the bath—a quantum filter. One can therefore engineer the bath to measure desired observables of the system, e.g., a QND observable, as illustrated in the following two examples.

The first example is measuring mechanical energy quantization considered in Refs. [16–19], aiming at unequivocally demonstrating the quantumness of a macroscopic mechanical oscillator. In the proposed experiment, the position of a mechanical oscillator is quadratically coupled to a cavity mode, namely,

$$\hat{H}_{\mathrm{int}} = \hbar g \, \hat{x}^2(\hat{a} + \hat{a}^\dagger). \tag{4.39}$$

If the cavity bandwidth γ is less than the mechanical frequency ω_m, we expect a direct probe of the slowly-varying part of $\hat{x}^2$ which is proportional to the QND variable (energy or equivalently the phonon number $\hat{N}$). Indeed, from $\hat{x}(-\tau) = \hat{x}\cos\omega_m\tau - \hat{p}\sin\omega_m\tau$,

$$\hat{O} = g \int_0^t \mathrm{d}\tau \, e^{-\gamma\tau}\hat{x}^2(-\tau)\hat{\rho} \approx \frac{g}{\gamma}\hat{N}\hat{\rho}, \tag{4.40}$$

where we have ignored terms proportional to $e^{-\gamma t}$, as the characteristic measurement time scale is

γ^{-1}. The leading-order SME for the oscillator reads:

$$\mathrm{d}\hat{\rho} = - i[\omega_m \hat{N}, \, \hat{\rho}] \, \mathrm{d}t - g_{\mathrm{eff}}[\hat{X}^2, \, [\hat{N}, \, \hat{\rho}]]\mathrm{d}t$$
$$+ \sqrt{2g_{\mathrm{eff}}}[\{\hat{N}, \, \hat{\rho}\} - 2\langle\hat{N}\rangle\hat{\rho}]\mathrm{d}W \tag{4.41}$$

with $g_{\mathrm{eff}} = g^2/\gamma$. Note that such a measurement is not an exact QND measurement, because we have $[\hat{X}^2, \, [\hat{N}, \, \hat{\rho}]]$ instead of the usual Lindblad term $[\hat{N}, [\hat{N}, \hat{\rho}]]$. This term describes a two-phonon process that induces quantum jumps. However, after numerically solving this SME, we find that it does not have significant effects, and a QND measurement can indeed be effectively realized. This is in accord with the argument by Martin and Zurek [16]—the two-photon process happens at $2\,\omega_m$, which is strongly suppressed due to a small cavity bandwidth γ.

The second example is measuring the QND observable of a free mass—the momentum $\hat{p}$. This is of particular interest in quantum-limited force measurement with mechanical probes, e.g., detecting gravitational waves [20]. By monitoring the momentum change, one can detect the force signal without quantum back action, enabling surpassing of the Standard Quantum Limit (SQL) [21]. To achieve this, we can couple the position $\hat{x}$ of the free mass with two coupled cavity modes $\hat{a}_1$ and $\hat{a}_2$, of which the interaction Hamiltonian is given by:

$$\hat{H}_{\mathrm{int}} = \hbar\,\omega_s(\hat{a}_1\hat{a}_2^\dagger + \hat{a}_1^\dagger\hat{a}_2) + \hbar\,g\,\hat{x}(\hat{a}_1 + \hat{a}_1^\dagger), \tag{4.42}$$

where ω_s is the coupling constant between two cavity modes. The cavity mode $\hat{a}_1$ is coupled to external probe field. From Eq. (4.8), we derive that:

$$\hat{O} = 2g \int_0^t \mathrm{d}\tau\, e^{-\gamma\tau} \cos\left(\frac{\omega_s\tau}{2}\right) \hat{x}(-\tau)\hat{\rho} \approx \frac{4g}{\omega_s^2}\,\dot{\hat{x}}(0)\,\hat{\rho}, \tag{4.43}$$

where we have used the stationary-phase approximation by assuming $\omega_s \gg \gamma$, and also ignored terms proportional to $e^{-\gamma t}$. The effective observable is therefore equal to the momentum, as $\hat{p} = m\dot{\hat{x}}(0)$. Indeed, such a coupled-cavity scheme has been proposed as the so-called "speed-meter" for advanced gravitational-wave detectors [22].

4.5   Non-Markovian quantum measurement: The second scenario

In this section, we will consider the second scenario: the system-bath dynamics is Markovian but the input probe field is correlated before interacting the bath—such a correlation can be either classical or quantum (entanglement). Since the bath would simply follow the system dynamics in this case,

we will ignore the bath and consider a direct coupling between the system and the probe field.

In Ref. [5], Diósi tried to construct correlated infinity von Neumann detectors (correlated input field in our model) in order to prove that non-Markovian SSE describes the this kind of non-Markovian quantum measurement. Later on, Wiseman *et al.* [6] used two initially entangled detectors to disprove this. He showed that measurement on the first detector can create quantum entanglement between the system and the second unmeasured detectors. Therefore the system state is not pure anymore once we trace out the unmeasured detectors, and hence can not be described by non-Markovian SSE, namely, nonexistence of a pure-state quantum trajectory.

Here, we will use the formalism described in Ref. [7] to derive the system Wigner representation of the density matrix, i.e., the Wigner function in two cases: (i) linear continuous measurement, and (ii) nonlinear measurement of system energy, both with correlated input field.

4.5.1 linear continuous measurement
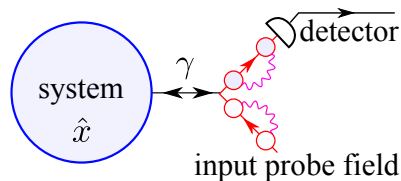
Figure 4.6: Schematic showing a non-Markovian quantum measurement with correlated input field (wiggly line denoting correlation schematically).

To be concrete, we study a continuous measurement of the position of an oscillator with the following Hamiltonian

$$\hat{H} = \frac{\hat{p}^2}{2m} + \frac{1}{2}m\omega_m^2\hat{x}^2 + \hbar\sqrt{\gamma}\,\hat{x}\,\hat{o}_1(t). \tag{4.44}$$

This is similar to what has been studied in Section 11.4, except that the cavity mode is now replaced by the oscillator and also the input optical field is correlated, as shown schematically in Fig. 4.6. To derive the conditional quantum state of the oscillator, we follow the general formalism outlined in Ref. [7]. The first step is to divide the process from 0 to t into N segments with $\mathrm{d}t = t/N$ and then to take the continuous limit. The n-th segment consists of: (i) *a free evolution,* which is described by the evolution operator: $\hat{U}_n \equiv \exp[-i\hat{H}_n\mathrm{d}t/\hbar]$ with $\hat{H}_n$ being the entire Hamiltonian at $t = n\,\mathrm{d}t$, and (ii) *measurement of the output phase quadrature* $\hat{y} = \hat{o}_2$, which is described by a projection operator: $\hat{\mathcal{P}}_n = |y_n\rangle\langle y_n|$ with y_n the measurement result of $\hat{o}_2$. After the entire process and conditioning on the measurement results $\boldsymbol{y} = (y_1, \cdots, y_N)$, the oscillator is projected into a conditional quantum state with density matrix:

$$\hat{\rho}_x(t|\boldsymbol{y}) = \mathrm{Tr}_o[\hat{\mathcal{P}}_{\boldsymbol{y}}\hat{\rho}(0)\,\hat{\mathcal{P}}_{\boldsymbol{y}}]/P[\boldsymbol{y}]. \tag{4.45}$$

Here Tr_o indicates tracing over the optical field; $\hat{\mathcal{P}}_{\boldsymbol{y}} \equiv \hat{\mathcal{P}}_N\hat{U}_N\cdots\hat{\mathcal{P}}_1\hat{U}_1$; $P[\boldsymbol{y}]$ the probability for

obtaining measurement results $\boldsymbol{y}$. $\hat{\rho}(0)$ is the initial state for the system and input field, and here we apply the usual assumption that the initial state is separable $\hat{\rho}(0) = \hat{\rho}_x(0) \otimes \hat{\rho}_o(0)$, but this is not a necessary requirement.

To derive the analytical expression for $\hat{\rho}(t|\boldsymbol{y})$, the usual applied approach is to use the path-integral approach by expressing the evolution operator in terms of a path integral, and derive the influence functional. Here, instead, we take the advantage of linear dynamics, in which case the Heisenberg equation of motion can be solved exactly. By inserting identity operator $\hat{I} = \hat{U}[(n-1)dt]\hat{U}^\dagger[(n-1)dt]$ in between $\hat{P}_{n-1}$ and $\hat{P}_n$, we obtain

$$\hat{\mathcal{P}}_{\boldsymbol{y}} = \hat{U}(t)\hat{\mathcal{P}}_N^{\mathrm{H}}\hat{\mathcal{P}}_{N-1}^{\mathrm{H}}\cdots\hat{\mathcal{P}}_1^{\mathrm{H}} \equiv \hat{U}(t)\hat{\mathcal{P}}_{\boldsymbol{y}}^{\mathrm{H}} \tag{4.46}$$

where $\hat{U}(t) \equiv \prod_{n=1}^N \hat{U}_n(dt)$ (time-ordered) and $\hat{\mathcal{P}}_n^{\mathrm{H}} \equiv \delta(\hat{y}_n^{\mathrm{H}} - y_n)$ with $\hat{y}_n^{\mathrm{H}} \equiv \hat{U}^\dagger(ndt)\,\hat{y}\,\hat{U}(ndt)$.

To obtain the Wigner function, we first evaluate its Fourier transform—the generating function:

$$\begin{aligned}
\mathcal{J}[\alpha_x, \alpha_p] &= \mathrm{Tr}_x[e^{i\alpha_x\hat{x}+i\alpha_p\hat{p}}\,\hat{\rho}_x(t|\boldsymbol{y})] \\
&= \mathrm{Tr}_{xo}[\hat{\mathcal{P}}_{\boldsymbol{y}}^{\mathrm{H}}\hat{U}^\dagger(t)e^{i\alpha_x\hat{x}+i\alpha_p\hat{p}}\hat{U}(t)\hat{\mathcal{P}}_{\boldsymbol{y}}^{\mathrm{H}}\hat{\rho}(0)]/P[\boldsymbol{y}] \\
&= \mathrm{Tr}_{xo}[e^{i\alpha_x\hat{x}(t)+i\alpha_p\hat{p}(t)}\hat{\mathcal{P}}_{\boldsymbol{y}}^{\mathrm{H}}\hat{\rho}(0)]/P[\boldsymbol{y}].
\end{aligned} \tag{4.47}$$

Here we have used the fact that, for general linear measurement,

$$[\hat{x}(t),\,\hat{y}^H(t')] = 0,\ \forall\, t' < t\,; \tag{4.48}$$

therefore $\hat{x}(t)$, $\hat{p}(t)$ and $\hat{\mathcal{P}}_{\boldsymbol{y}}^{\mathrm{H}}$ commute; we also use $\hat{\mathcal{P}}_{\boldsymbol{y}}^{\mathrm{H}}\hat{\mathcal{P}}_{\boldsymbol{y}}^{\mathrm{H}} = \hat{\mathcal{P}}_{\boldsymbol{y}}^{\mathrm{H}}$ which is equal to a product of the Dirac delta function $\prod_n \delta(\hat{y}_n - y_n)$ inside Tr. Since the output field at different times commutes

$$[\hat{y}_n^{\mathrm{H}},\, y_{n'}^{\mathrm{H}}] = 0, \tag{4.49}$$

the projection operator can be written as a path integral and, in the continuous limit, it is equal to

$$\hat{\mathcal{P}}_{\boldsymbol{y}}^{\mathrm{H}} = \prod_n \delta(\hat{y}_n^{\mathrm{H}} - y_n) = \int \mathcal{D}[\xi] \exp\left\{i\int_0^t dt'\,\xi(t')[\hat{y}(t') - y(t')]\right\}. \tag{4.50}$$

This is one of the most important steps for treating the correlated input field. Basically, instead of tracing out the optical field at each moment, we sum up the measurement result in terms of a trajectory in time and trace out the optical field all together after each moment.

The generating function is then

$$\mathcal{J}[\alpha_x, \alpha_p] = \int \mathcal{D}[\xi]\,\mathrm{Tr}_{xo}\left[\exp\left\{i\alpha_x\hat{x}(t) + i\alpha_p\hat{p}(t) + i\int_0^t dt\,\xi(t')[\hat{y}(t') - y(t')]\right\}\hat{\rho}(0)\right]P[y(t)]. \tag{4.51}$$

Given the Hamiltonian in Eq. (4.44), the Heisenberg equation can be easily solved, and we have

$$\hat{x}(t) = \hat{x}_q(t) + \int_0^t dt' G_x(t - t')\hbar\sqrt{\gamma}\,\hat{o}_1(t'),\qquad(4.52)$$

$$\hat{p}(t) = \hat{p}_q(t) + \int_0^t dt' G_p(t - t')\hbar\sqrt{\gamma}\,\hat{o}_1(t'),\qquad(4.53)$$

$$\hat{y}(t) = \hat{o}_2(t) + \sqrt{\gamma}\,\hat{x}(t).\qquad(4.54)$$

Here $\hat{x}_q(t) = \hat{x}(0)\cos\omega_m t + (m\omega_m)^{-1}\hat{p}(0)\sin\omega_m t$ is the the oscillator position under free evolution and $G_x(t) \equiv (m\omega_m)^{-1}\sin\omega_m t$ is the Green's function, and similar for $\hat{p}$; the time in $\hat{o}_{1,2}(t)$ is only for denoting the optical fields at different times, as we ignore their free evolution—optical detection is made right after their interaction with the oscillator; therefore, the statistics of $\hat{o}_{1,2}(t)$ are determined by the initial quantum state $\hat{\rho}_o(0)$ of the optical field.

Since all the Heisenberg operators can be solved exactly in terms of their initial value, the generating function can be solved once we specify the initial quantum state. In the special case of $\hat{\rho}_o(0) = \prod \otimes |0\rangle\langle 0|$, a vacuum input, we will simply return to the previous case of uncorrelated input field.

Gaussian-entangled state—we now consider the first non-trivial case that is studied by Diósi in Ref. [5]; the oscillator is in a Gaussian state and the input field is initially in a Gaussian entangled state. Since the linear dynamics will preserve the Gaussianity, the only relevant quantities are mean and the covariance. To derive the generating function more easily, it is better to simplify the statistics of the output field while keeping the information about the oscillator motion. We make a causal whitening of its correlation function, and introduce $\hat{z}$ as

$$\hat{z}(t) = \int_0^t dt' \sigma^{-1/2}(t,\,t')\hat{y}(t)\qquad(4.55)$$

where $\sigma(t,\,t')$ is the correlation function and $\sigma(t,\,t') \equiv \langle\hat{y}(t)\hat{y}(t')\rangle = \langle\hat{o}_2(t)\hat{o}_2(t')\rangle + \gamma\langle\hat{x}(t)\hat{x}(t')\rangle$. From its definition, $\hat{z}$ satisfies

$$\langle z(t)\hat{z}(t')\rangle = \delta(t - t').\qquad(4.56)$$

We can then decompose the oscillator position and momentum into two parts,

$$\hat{x}(t) \equiv \hat{R}_x(t) + \int_0^t dt' K_x(t,\,t')\hat{z}(t'), \quad \hat{p}(t) \equiv \hat{R}_p(t) + \int_0^t dt' K_p(t,\,t')\hat{z}(t'),\qquad(4.57)$$

where the residue parts $\hat{R}_x(t)$ and $\hat{R}_p(t)$ are not correlated with the output field, namely $\langle\hat{R}_{x,p}(t)\hat{y}(t')\rangle =$

0. K_x and K_p are the Wiener filter

$$K_x(t,\,t') = \langle \hat{x}(t)\hat{z}(t')\rangle, \quad K_p(t,\,t') = \langle \hat{p}(t)\hat{z}(t')\rangle. \tag{4.58}$$

With these new defined quantities, the generating function is proportional to (we ignore the unimportant normalization factor and normalize the Wigner function in the final step):

$$
\begin{aligned}
\mathcal{J}[\boldsymbol{\alpha}] &\propto \int \mathcal{D}[\xi]\,\mathrm{Tr}_{xo}\left[\exp\left\{i\boldsymbol{\alpha}[\hat{\boldsymbol{R}}(t) + \int_0^t \mathrm{d}t'\boldsymbol{K}(t,\,t')\hat{z}(t')]^{\mathrm{T}} + i\int_0^t \mathrm{d}t'\,\xi(t')[\hat{y}(t') - y(t')]\right\}\hat{\rho}(0)\right] \\
&\propto \int \mathcal{D}[\tilde{\xi}]\,\mathrm{Tr}_{xo}\left[\exp\left\{i\boldsymbol{\alpha}\hat{\boldsymbol{R}}^{\mathrm{T}}(t) + i\int_0^t \mathrm{d}t'\,\tilde{\xi}(t')[\hat{z}(t') - z(t')] + i\int_0^t \mathrm{d}t'\,\boldsymbol{\alpha}\boldsymbol{K}^{\mathrm{T}}(t,\,t')z(t')\right\}\hat{\rho}(0)\right]
\end{aligned}
\tag{4.59}
$$

where vectors $\boldsymbol{\alpha} \equiv (\alpha_x,\,\alpha_p)$, $\boldsymbol{K} = (K_x,\,K_p)$, $\tilde{\xi}(t) \equiv \int \mathrm{d}t'\sigma^{1/2}(t,\,t')\xi(t') + \boldsymbol{\alpha}\boldsymbol{K}^{\mathrm{T}}(t,\,t')$ and superscript T denotes transpose. By using Eq. (4.56) and $\langle e^{i\hat{A}}\rangle = e^{-\langle \hat{A}^2\rangle/2}$ for the Gaussian state, we obtain

$$
\begin{aligned}
\mathcal{J}[\boldsymbol{\alpha}] &\propto \int \mathcal{D}[\tilde{\xi}]\exp\left\{-\frac{1}{2}\boldsymbol{\alpha}\langle\hat{\boldsymbol{R}}^{\mathrm{T}}(t)\hat{\boldsymbol{R}}(t)\rangle\boldsymbol{\alpha}^{\mathrm{T}} - \frac{1}{2}\int_0^t \mathrm{d}t'\,\tilde{\xi}^2(t') - i\int_0^t \mathrm{d}t'\,\tilde{\xi}(t')z(t') + i\int_0^t \mathrm{d}t'\,\boldsymbol{\alpha}\boldsymbol{K}^{\mathrm{T}}(t,\,t')z(t')\right\} \\
&\propto \exp\left\{-\frac{1}{2}\boldsymbol{\alpha}\langle\hat{\boldsymbol{R}}^{\mathrm{T}}(t)\hat{\boldsymbol{R}}(t)\rangle\boldsymbol{\alpha}^{\mathrm{T}} + i\int_0^t \mathrm{d}t'\,\boldsymbol{\alpha}\boldsymbol{K}^{\mathrm{T}}(t,\,t')z(t')\right\}.
\end{aligned}
\tag{4.60}
$$

Finally, the Wigner function for the oscillator $W(x,p)$ is simply the inverse Fourier transform of $\mathcal{J}$ and we can easily obtain:

$$W(x,p) = \frac{1}{2\pi\sqrt{\det \mathbf{V}_c(t)}}\exp\left[-\frac{1}{2}(x - x_c,\,p - p_c)\mathbf{V}_c^{-1}(x - x_c,\,p - p_c)^{\mathrm{T}}\right], \tag{4.61}$$

where the conditional covariance matrix

$$\mathbf{V}_c(t) \equiv \langle\hat{\boldsymbol{R}}^{\mathrm{T}}(t)\hat{\boldsymbol{R}}(t)\rangle, \tag{4.62}$$

and the conditional mean

$$x_c = \int_0^t \mathrm{d}t'\,K_x(t,\,t')z(t'), \quad p_c = \int_0^t \mathrm{d}t'\,K_p(t,\,t')z(t'). \tag{4.63}$$

We therefore obtain the expression for the oscillator Wigner function given a general Gaussian correlated input field.

More explicitly, we can express the covariance matrix $\mathbf{V}_c(t)$ in terms of the correlation function among known quantities—$\hat{x}(t)$, $\hat{p}(t)$ and $\hat{y}(t)$ in Eq. (4.52), Eq. (4.53) and Eq. (4.54). Taking

$\langle \hat{R}_x(t)\hat{R}_x(t)\rangle$ for instance, we have

$$\langle \hat{R}_x(t)\hat{R}_x(t)\rangle = \langle x^2(t)\rangle - \int_0^t \mathrm{d}t'\, K_x^2(t,\,t') = \langle x^2(t)\rangle - \int_0^t \mathrm{d}t' \int_0^t \mathrm{d}t'' \langle \hat{x}(t)\hat{y}(t')\rangle \sigma^{-1}(t',\,t'')\langle \hat{y}(t'')\hat{x}(t)\rangle, \tag{4.64}$$

where

$$\langle \hat{x}^2(t)\rangle = \langle \hat{x}_q^2(t)\rangle + \hbar^2\gamma \int_0^t \mathrm{d}t' \int_0^t \mathrm{d}t'' G_x(t-t')C_{11}(t',\,t'')G_x(t-t''), \tag{4.65}$$

$$\langle \hat{x}(t)\hat{y}(t')\rangle = \sqrt{\gamma}\,\langle \hat{x}(t)\hat{x}(t')\rangle = \sqrt{\gamma}\,\langle \hat{x}_q(t)\hat{x}_q(t')\rangle + \hbar^2\gamma^{3/2} \int_0^t \mathrm{d}\tau \int_0^{t'} \mathrm{d}\tau' G_x(t-\tau)C_{11}(\tau,\,\tau')G_x(t'-\tau'), \tag{4.66}$$

and $C_{11}(t',\,t'') \equiv \mathrm{Tr}_o[\hat{o}_1(t')\hat{o}_1(t'')\hat{\rho}_o(0)]$ is the initial correlation function for the amplitude quadrature of the input optical field. Similarly, we can obtain $\langle \hat{R}_x(t)\hat{R}_p(t)\rangle$ and $\langle \hat{R}_p(t)\hat{R}_p(t)\rangle$. The key is to invert the correlation function of the output field $\sigma(t,\,t')$. It amounts to, instead of a local differential equation, an integral equation. This is the price we paid for solving the situation of a general correlated input field. In general, we have to resort to numerical tools for solving it. When the system approaches to a steady state with $t \to +\infty$, this can be solved in the frequency domain by using the Wiener-Hopf method, of which the details in such a stationary case is shown in Ref. [11].

Non-Gaussian entangled stat.—in the case of non-Gaussian entangled input field, e.g., a single photon state, the optical field at different times has a non-trivial quantum correlation—mean and correlation are not enough to quantify the quantum state. To treat this situation, we apply the same approach outlined in Ref. [7], but with a small modification due to the fact that here we are considering a non-stationary scenario with interaction starting from 0 instead of $-\infty$.

In the same manneras Ref. [7], we assume an arbitrary function $f(x)$ for the photon mode, and define the corresponding operator for creating such a photon:

$$\hat{\Gamma}^\dagger \equiv \int_{-\infty}^\infty \mathrm{d}x\, f(x)\hat{o}^\dagger(x) = \int_{-\infty}^\infty \mathrm{d}t\, f(t)\hat{o}^\dagger(t). \tag{4.67}$$

The general non-Gaussian quantum state of such a photon mode, in the P-presentation, can be written as

$$\hat{\rho}_o(0) = \int d\zeta |\zeta\rangle\langle\zeta| P(\zeta) = \int d\zeta\, e^{\zeta\hat{\Gamma}^\dagger - \zeta^*\hat{\Gamma}}|\mathbf{0}\rangle\langle\mathbf{0}|e^{-\zeta\hat{\Gamma}^\dagger + \zeta^*\hat{\Gamma}} P(\zeta). \tag{4.68}$$

By substituting it into Eq. (4.59) and using the Baker-Campbell-Hausdorff formula, we obtain

$$\mathcal{J}[\boldsymbol{\alpha}] \propto \int d^2\boldsymbol{\zeta}\, \mathcal{D}[\xi]\, e^{i[\zeta^*\hat{\Gamma}^\dagger - \zeta\hat{\Gamma}^\dagger,\,\hat{B}]}\mathrm{Tr}_{xo}\left[e^{i\hat{B}}\hat{\rho}_x(0) \otimes |\mathbf{0}\rangle\langle\mathbf{0}|\right] P(\boldsymbol{\zeta}), \tag{4.69}$$

with $\hat{B} \equiv \boldsymbol{\alpha}\hat{\boldsymbol{R}}^\mathrm{T}(t) + i\int_0^t \mathrm{d}t'\,\tilde{\xi}(t')[\hat{z}(t') - z(t')] + i\int_0^t \mathrm{d}t'\,\boldsymbol{\alpha}\boldsymbol{K}^\mathrm{T}(t,\,t')z(t')$. Written in this way, $\hat{B}$

averaging over the non-Gaussian state is transformed into averaging over the vacuum Gaussian state. The only addition term $[\zeta^*\hat{\Gamma} - \zeta\,\hat{\Gamma}^\dagger,\,\hat{B}]$ is a c-number, as $\hat{B}$ is a linear function of the optical field operator; we can therefore directly use the result that we obtain in the previous case with the Gaussian input field.

Apart from the actual value for specific terms, the final result for the oscillator Wigner function is formally identical to Eq. (16) in Ref. [7]:

$$W(\boldsymbol{x}) = \int d\boldsymbol{\zeta} \exp\left\{ -\frac{1}{2}(\boldsymbol{x} - \boldsymbol{x}_\zeta)\mathbf{V}_c^{-1}(\boldsymbol{x} - \boldsymbol{x}_\zeta)^{\mathrm{T}} - \frac{1}{2}\int_0^t dt'\left(z(t') - \zeta^*[\hat{\Gamma},\,\hat{z}(t')] + \zeta[\hat{\Gamma}^\dagger,\,\hat{z}(t')] \right)^2 \right\} P(\boldsymbol{\zeta}),$$
$$(4.70)$$

where $\mathbf{V}_c$ is given by Eq. (4.62), vector $\boldsymbol{x} = (x, p)$ and $\boldsymbol{x}_\zeta \equiv \boldsymbol{x}_c + \zeta^*[\hat{\Gamma}, \hat{\boldsymbol{R}}(t)] - \zeta[\hat{\Gamma}^\dagger, \hat{\boldsymbol{R}}(t)]$ with $\boldsymbol{x}_c$ defined in Eq. (4.63). This formula gives the conditional Wigner function for the oscillator as a function of the initial non-Gaussian state of the input field. The dependence on the initial Gaussian state of the oscillator is contained in the $\mathbf{V}_c(t)$.

To conclude, we have derived the conditional Wigner function of the oscillator in both cases of correlated Gaussian and more general non-Gaussian input probe fields. The assumption that we have made is linearity of the system dynamics such that the system operator can be solved by using the Heisenberg equation of motion. It can therefore be easily generalized to a linear system with many degrees of freedom.

4.5.2 Phonon number measurement

In the previous section, we consider position measurement with a correlated input field. Since position is not a conserved quantity for the oscillator, it is difficult to gain a straightforward insight into the final structure of the result. Here we consider a simpler example of phonon number measurement, which is a quantum non-demolition measurement. In addition, the operator is a nonlinear function of the oscillator position and momentum, though in a trivial way. The total Hamiltonian is given by

$$\hat{H} = \frac{\hat{p}^2}{2m} + \frac{1}{2}m\omega_m^2\hat{x}^2 + \sqrt{\gamma/\omega_m^2}\left(\frac{\hat{p}^2}{2m} + \frac{1}{2}m\omega_m^2\hat{x}^2 \right)\hat{o}_1(t) = \hbar\omega_m\hat{N} + \hbar\sqrt{\gamma}\hat{N}\hat{o}_1(t), \qquad (4.71)$$

where $\hat{N}$ is the phonon number operator.

Similarly, we assume measurement of the outgoing phase quadrature. Most of the steps are therefore the same as what as shown in the previous section, and the reduced density matrix for the oscillator, in the number state basis, is given by

$$\rho_{mn}(t) = \int \mathcal{D}[\xi]\mathrm{Tr}_{xo}\left[\hat{U}^\dagger(t)|n\rangle\langle m|\hat{U}(t)\exp\left\{ i\int_0^t dt\,\xi(t')[\hat{y}(t') - y(t')] \right\}\hat{\rho}(0) \right]/P[y(t)]. \qquad (4.72)$$

Note here we again used the fact that $U^\dagger(t)|n\rangle\langle m|U(t)$, which is a system operator at time t, commutes with the previous measurement output, and we also used $\mathcal{P}_{\boldsymbol{y}}^H \mathcal{P}_{\boldsymbol{y}}^H = \hat{\mathcal{P}}_{\boldsymbol{y}}^H$.

To make the analysis simple, we consider initially the oscillator and the input field are separable and study only a Gaussian entangled input field, which can be generalized to the case with a non-Gaussian input field as shown previously. Further, by using the fact that $\hat{N}$ is a conserved quantity, we have

$$\rho_{mn}(t) \propto \int \mathcal{D}[\xi] \mathrm{Tr}_o \left[\exp\left\{ i\omega_m(n-m)t + i\sqrt{\gamma} \int_0^t dt'(n-m)\hat{o}_1(t') i \int_0^t dt\, \xi(t')[\hat{y}(t') - y(t')] \right\} \hat{\rho}_o(0) \right] \rho_{mn}(0)$$

$$(4.73)$$

where we again ignore unimportant normalization factor and $\hat{y}(t) = \hat{o}_2(t) - \sqrt{\gamma}\,n$. Again, for Gaussian state, $\langle e^{i\hat{A}} \rangle = e^{-\langle \hat{A}^2 \rangle/2}$, the tracing over the input field can be worked out, and we have

$$\rho_{mn}(t) \propto \int \mathcal{D}[\xi] \exp\left\{ i\omega_m(n-m)t - i\int_0^t dt'\xi(t')[\sqrt{\gamma}\,n + y(t')] - \int_0^t dt' \int_0^t dt'' \frac{\gamma}{2}(n-m)^2 C_{11}(t', t'') \right.$$

$$\left. - \int_0^t dt' \int_0^t dt'' \sqrt{\gamma}(n-m)C_{12}(t', t'')\xi(t') - \frac{1}{2}\int_0^t dt' \int_0^t dt'' \xi(t')C_{22}(t', t'')\xi(t'') \right\} \rho_{mn}(0)$$

$$(4.74)$$

where the correlation function for the input optical field is given by $C_{jk}(t', t'') = \mathrm{Tr}_o[\hat{o}_j(t')\hat{o}_k(t'')\hat{\rho}_o(0)]$. After finishing the Gaussian path integral over ξ, we finally get

$$\rho_{mn}(t) \propto \exp\left\{ i\omega_m(n-m)t \right\} \times$$

$$\exp\left\{ -\int_0^t dt' \int_0^t dt'' \left[\frac{\gamma}{2}(n-m)^2 C_{11}(t', t'') + \frac{1}{2}f(m,n,t,t')C_{22}^{-1}(t', t'')f(m,n,t,t'') \right] \right\} \rho_{mn}(0)$$

$$(4.75)$$

where $f(m,n,t,t') \equiv \sqrt{\gamma}\,n + y(t') - i\int_0^t d\tau \sqrt{\gamma}\,(n-m)C_{1,2}(t',\tau)$, To obtain $\rho_{mn}(t)$ explicitly, we again need to invert the correlation function $C_{22}(t', t'')$ of the input field, and this is the same as the case considered in the previous section, which is a general feature of non-Markovianity.

We can recover the result for Markovian measurement by plugging in the following correlation function for the input field:

$$C_{1,1}(t, t') = C_{22}(t, t') = \frac{1}{2}\delta(t - t'), \quad C_{12}(t, t') = 0. \tag{4.76}$$

where the fact $1/2$ arises from the normalization we have used that gives $[\hat{o}_1(t), \hat{o}_2(t')] = i\delta(t - t')$. In this case, Eq. (4.75) can be rewritten as

$$\rho_{mn}(t) \propto \exp\left\{ i\omega_m(n-m)t - \frac{\gamma}{2}(n-m)^2 t - \int_0^t dt'[\sqrt{\gamma}\,n + y(t')]^2 \right\} \rho_{mn}(0). \tag{4.77}$$

We can now recover the normalization factor $P[y(t)]$ by using $\text{Tr}_x[\hat{\rho}_x] = 1$, and we have [5]

$$P[y(t)] = \exp\left\{-\int_0^t dt'[\sqrt{\gamma}\langle\hat{N}\rangle + y(t')]^2\right\}. \tag{4.78}$$

We therefore can write $y(t)$ in terms of a classical random process

$$y(t)dt = -\sqrt{\gamma}\langle\hat{N}\rangle dt + dW/\sqrt{2}, \tag{4.79}$$

with $dW^2 = dt$ the Wiener increment. From Eq. (4.77) and (4.79), we can obtain a differential equation for the normalized density matrix, and up to the first order of dt, we get

$$\rho_{mn}(t + dt) = \left[1 + i\omega_m(n-m)dt - \frac{\gamma}{2}(n-m)^2 dt - \sqrt{2\gamma}(n - \langle\hat{N}\rangle)dW\right]\rho_{mn}(t) \tag{4.80}$$

In the operator representation, we recover the standard Markovian stochastic master equation for phonon-number measurement:

$$d\hat{\rho}_x(t) = -\frac{i}{\hbar}[\hat{H}_x, \hat{\rho}_x(t)]dt - \frac{\gamma}{2}[\hat{N}, [\hat{N}, \hat{\rho}_x(t)]]dt - \sqrt{2\gamma}(\hat{N} - \langle\hat{N}\rangle)\hat{\rho}_x(t)dW. \tag{4.81}$$

4.5.3 Nonlinear measurement with initially entangled detector state

In previous sections we solved the case for linear measurement and energy measurement. The energy measurement example is instructive because the interaction is nonlinear although the calculation is simple. Now we try to study the case with interaction term $\gamma\Omega(\hat{x})a_1$. The system density matrix in the x representation at time t is

$$\hat{\rho}(x, x') = Tr_{s,o}[|||x'\rangle\langle x|\hat{\rho}]$$
$$= \int Da_2\langle x|\langle a_2|U(t, t - \Delta t)P(t - \Delta t)U(t - \Delta t, t - 2\Delta t)\cdots\hat{\rho}_i\cdots P(t - \Delta t)U^{-1}(t, t - \Delta t)|x'\rangle|a_2\rangle \tag{4.82}$$

The nice thing one can see from the last formula is that the evolution and projection operators can be viewed as acting on some initially factorized state $|a_2\rangle|x\rangle$. As a result, this part of expression can be evaluated by using the usual stochastic Schrodinger's equation method. Thus the density matrix becomes

---

[5] To derive this formula, we have replaced n in the exponent directly by $\langle\hat{N}\rangle$. This is due to the fact that for continuous measurement the variance is of the order of dt^{-1} at time t—a very weak measurement at any moment.

$$\hat{\rho}(x,x') = Tr_{left}[\int \int dx_1 dx_2 \phi(x,x_1,t)\phi(x',x_2,t)\langle x_1|\langle y_2 - \gamma\Omega(x_1)|\hat{\rho}_i|y_2 - \gamma\Omega(x_2)\rangle|x_2\rangle]. \quad (4.83)$$

where $\phi(x,x_1,t)$ satisfies the free evolution Schrodinger's equation

$$i\frac{\partial|\psi\rangle}{\partial t} = \hat{H}_x|\psi\rangle$$
$$\phi(x,x_1,t) = \langle x_1|\psi\rangle, \phi(x,x_1,0) = \delta(x-x_1). \quad (4.84)$$

4.6 Non-Markovian quantum measurement: General case
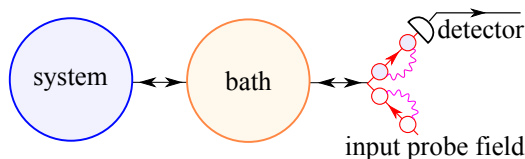
Figure 4.7: Schematic showing non-Markovian quantum measurement in a more general case with both non-Markovian dynamics and correlated input probe field.

After studying the first and second scenario, we now discuss briefly the general scenario: the input probe field is correlated and the system-bath dynamics is non-Markovian, as shown schematically in Fig. 4.7. There is no universal analytical method to solve the most general case. Only if the dynamics of the entire system is linear, can we then directly apply the approach used for treating the second scenario. We first solve the Heisenberg equation for the system, bath, and probe field, and express the operators at time t in terms of operators at $t = 0$, of which the quantum statistics can be easily determined from the initial quantum state. By tracing out the optical field and the bath degrees of freedom, we can then obtain the conditional Wigner function for the system only, in the same way as we derive Eq. (4.70).

4.7 Conclusion

To conclude, we have studied two important scenarios that give rise to an effective non-Markovian quantum measurement of the system: (i) a direct continuous measurement of the bath which couples to the system with non-Markovian dynamics; (ii) a direct measurement of the system with correlated probe field. For treating the first scenario, we used Strunz's method to eliminate the bath degrees of freedom to derive an effective non-Markovian stochastic master equation for the system. We explicitly worked out two interesting examples in cavity QED and optomechanical devices. In addition, we showed the perturbation approach for treating more general nonlinear system-bath

interaction. For the second scenario, we consider both a Gaussian and a non-Gaussian correlated input field. By taking advantage of linear dynamics and converting the influence of measurement in terms of a path integral, we can study non-local correlation of the input field, and derive the conditional Wigner function for the system. It seems to us that there is no transparent way to rewrite it in terms of a solution to a differential equation or Wigner transformation of some master equation, in contrast to the Markovian case. By studying these two scenarios, we can gain a better insight into non-Markovian quantum measurement for more general cases.

Acknowledgement

4.A   Linear continuous quantum measurement

Here we will show how the condition in Eq. (4.1) imposes the requirement that the probe should be a field in a linear continuous quantum measurement. This is adapted from Ref. [9] with small modifications to fit into the context of quantum measurement.

In a linear measurement, we couple the system and the probe linearly. The total Hamiltonian of the system and the probe can be then written as

$$\hat{H}_{\text{tot}} = \hat{H}_s + \hat{H}_p + \hbar\, g\, \hat{L} \otimes \hat{F}. \tag{4.85}$$

Here $\hat{H}_s$ and $\hat{H}_p$ are the free Hamiltonians for the system and probe; $\hat{L}$ and $\hat{F}$ are some arbitrary operators for the system and probe, respectively; g is the coupling constant.

In order to obtain information about L, the output needs be another operator of the probe, e.g., we denote it by $\hat{Z}$ and it does not commute with $\hat{F}$; otherwise, $\hat{Z}$ will simply undergo free evolution and contain no information about $\hat{L}$. We can then study the dynamics of the output from the Heisenberg equation of motion, and in the interaction picture, it is given by

$$\dot{\hat{Z}}_I(t) = \frac{i}{\hbar}[\hat{Z}_I(t),\, \hat{H}_{\text{I}}(t)]. \tag{4.86}$$

The solution reads

$$\hat{Z}_I(t) = \hat{Z}(0) + i\, g \int_0^t dt'[\hat{Z}_I(t),\, \hat{F}_I(t')]\hat{L}_I(t'). \tag{4.87}$$

Similarly for $\hat{F}_I(t)$ and $\hat{L}_I(t)$, we have

$$\hat{F}_I(t) = \hat{F}(0) + i\,g \int_0^t dt'[\hat{F}_I(t),\,\hat{F}_I(t')]\hat{L}_I(t'), \qquad (4.88)$$

$$\hat{L}_I(t) = \hat{L}(0) + i\,g \int_0^t dt'[\hat{L}_I(t),\,\hat{L}_I(t')]\hat{F}_I(t'). \qquad (4.89)$$

Due to the interaction term being bilinear—$\hat{L} \otimes \hat{F}$, we have

$$[\hat{Z}_I(t),\,\hat{F}_I(t')] \equiv C_{ZF}(t,t'), \quad [\hat{F}_I(t),\,\hat{F}_I(t')] \equiv C_{FF}(t,t'), \quad [\hat{L}_I(t),\,\hat{L}_I(t')] \equiv C_{LL}(t,t'), \qquad (4.90)$$

which are all c-numbers. Eqs. (4.87), (4.88), (4.89) are therefore a set of linear equations, and can be easily solved.

By applying a linear causal filter $K(t)$ to the output $\hat{Z}_I(t)$, we can introduce a $\hat{\mathcal{Z}}(t)$ that is directly equal to $\hat{L}(t)$ plus additional noise terms, and

$$\hat{\mathcal{Z}}(t) = \int_0^t dt'\,K(t-t')\hat{Z}_I(t) = g^{-1}\hat{L}(t) + \hat{\mathcal{Z}}_0(t) + i\,g \int_0^t dt'\,C_{LL}(t,\,t')\hat{\mathcal{F}}_0(t') \qquad (4.91)$$

where

$$C_{LL}(t,\,t') \equiv [\hat{L}_0(t),\,\hat{L}_0(t')] = [e^{i\hat{H}_0 t/\hbar}\hat{L}e^{-i\hat{H}_0 t/\hbar},\,e^{i\hat{H}_0 t'/\hbar}\hat{L}e^{-i\hat{H}_0 t'/\hbar}] \qquad (4.92)$$

is the response function. In general $C_{LL}(t,t')$ is non zero, one example being the harmonic oscillator and $C_{xx}(t,t') = [\hat{x}(t),\hat{x}(t')] = (m\omega_m)^{-1}\sin\omega_m(t-t')$ with ω_m being the eigenfrequency.

Since $\hat{Z}(t)$ commutes at different times, $\hat{\mathcal{Z}}(t)$ also commutes at different times:

$$0 = [\hat{\mathcal{Z}}(t),\,\hat{\mathcal{Z}}(t')] = C_{LL}(t,\,t') + [\hat{\mathcal{Z}}(t),\,\hat{\mathcal{Z}}(t')] + i\,g\left\{\int_0^{t'} d\tau\,C_{LL}(t',\tau)[\hat{\mathcal{Z}}(t),\hat{\mathcal{F}}(\tau)] + \int_0^t d\tau\,C_{LL}(t,\tau)[\hat{\mathcal{F}}(\tau),\,\hat{\mathcal{Z}}(t')]\right\}$$
$$- g^2 \int_0^t \int_0^{t'} d\tau d\tau'\,C_{LL}(t,\tau)C_{LL}(t',\tau')[\hat{\mathcal{F}}(\tau),\,\hat{\mathcal{F}}(\tau')]. \qquad (4.93)$$

As those terms on the left-hand side are different orders of some arbitrary coupling constant g, in order to for this to be satisfied, we therefore require

$$[\hat{\mathcal{Z}}(t),\,\hat{\mathcal{Z}}(t')] = 0, \quad [\hat{\mathcal{F}}(t),\,\hat{\mathcal{F}}(t')] = 0, \quad [\hat{\mathcal{Z}}(t),\,\hat{\mathcal{F}}(t')] = i\,\delta(t-t'), \qquad (4.94)$$

which has been proved in a more rigorous way in Ref [9]. This basically means that we can treat $\hat{\mathcal{Z}}(t)$ at different times as different degrees of freedom (a continuous field); $\hat{\mathcal{Z}}$ and $\hat{\mathcal{F}}$ are the corresponding canonical conjugate variables.

4.B   SME for measurement of cavity mode

Here we add the details for deriving SME as shown in Eq. (4.8). We start from Eq. (4.9):

$$\hat{\rho}_a(t + dt) = \frac{1}{2\pi P[y(t)]} \int d\xi\, e^{-i\xi y(t)} \text{Tr}_o \left[e^{i\xi\hat{o}_1(t)} \left\{ \hat{\rho}(t) - \frac{i}{\hbar}[\hat{H}, \hat{\rho}(t)]dt - \frac{1}{2\hbar^2}[\hat{H}_{\text{int}}, [\hat{H}_{\text{int}}, \hat{\rho}(t)]]dt^2 \right\} \right]$$
$$+ \mathcal{O}[dt^2]. \tag{4.95}$$

By plugging in the expression for $\hat{H}$ and $\hat{H}_{\text{int}}$, we have

$$\text{Tr}_o \left\{ e^{i\xi\hat{o}_1} \hat{\rho} \right\} = \langle e^{i\xi\hat{o}_1} \rangle \hat{\rho}_a, \tag{4.96}$$

$$\text{Tr}_o \left\{ e^{i\xi\hat{o}_1}[\hat{H}_{\text{int}}, \hat{\rho}] \right\} = \hbar\sqrt{\gamma}(\langle e^{i\xi\hat{o}_1}\hat{o}^\dagger \rangle \hat{a}\hat{\rho}_a + \langle e^{i\xi\hat{o}_1}\hat{o} \rangle \hat{a}^\dagger \hat{\rho}_o - \langle \hat{o}^\dagger e^{i\xi\hat{o}_1} \rangle \hat{\rho}_a \hat{a} - \langle \hat{o}\, e^{i\xi\hat{o}_1(t)} \rangle \hat{\rho}\hat{a}^\dagger), \tag{4.97}$$

and

$$\text{Tr}_o \left\{ e^{i\xi\hat{o}_1}[\hat{H}_{\text{int}}, [\hat{H}_{\text{int}}, \hat{\rho}]] \right\}$$
$$= \hbar^2\gamma(\langle e^{i\xi\hat{o}_1}\hat{o}^{\dagger 2} \rangle \hat{a}^2 + \langle e^{i\xi\hat{o}_1}\hat{o}^\dagger\hat{o} \rangle \hat{a}\hat{a}^\dagger + \langle e^{i\xi\hat{o}_1}\hat{o}^\dagger\hat{o} \rangle \hat{a}\hat{a}^\dagger + \langle e^{i\xi\hat{o}_1}\hat{o}\hat{o}^\dagger \rangle \hat{a}^\dagger\hat{a} + \langle e^{i\xi\hat{o}_1}\hat{o}^2 \rangle \hat{a}^{\dagger 2})\hat{\rho}_a \tag{4.98}$$
$$+ \hbar^2\gamma\hat{\rho}_a(\langle e^{i\xi\hat{o}_1}\hat{o}^{\dagger 2} \rangle \hat{a}^2 + \langle e^{i\xi\hat{o}_1}\hat{o}^\dagger\hat{o} \rangle \hat{a}\hat{a}^\dagger + \langle e^{i\xi\hat{o}_1}\hat{o}^\dagger\hat{o} \rangle \hat{a}\hat{a}^\dagger + \langle e^{i\xi\hat{o}_1}\hat{o}\hat{o}^\dagger \rangle \hat{a}^\dagger\hat{a} + \langle e^{i\xi\hat{o}_1}\hat{o}^2 \rangle \hat{a}^{\dagger 2})$$
$$+ 2\hbar^2\gamma(\langle \hat{o}^\dagger e^{i\xi\hat{o}_1}\hat{o}^\dagger \rangle \hat{a}\hat{\rho}_a\hat{a} + \langle \hat{o}\, e^{i\xi\hat{o}_1}\hat{o}^\dagger \rangle \hat{a}\hat{\rho}_a\hat{a}^\dagger + \langle \hat{o}^\dagger e^{i\xi\hat{o}_1}\hat{o} \rangle \hat{a}^\dagger\hat{\rho}_a\hat{a} + \langle \hat{o}\, e^{i\xi\hat{o}_1}\hat{o} \rangle \hat{a}^\dagger\hat{\rho}_a\hat{a}^\dagger) \tag{4.99}$$

where the average $\langle \hat{A} \rangle \equiv \text{Tr}_o[\hat{A}\rho_o(t)]$ is over the continuous optical field. Since we assume that the optical field is in a vacuum state[6], we have $\langle \hat{o}_1^2 \rangle = \langle \hat{o}_2^2 \rangle = \frac{1}{2dt}$[7] and those averages over the optical field can be easily worked out explicitly. Specifically,

$$\langle e^{i\xi\hat{o}_1} \rangle = e^{\frac{-\xi^2}{4dt}}, \quad \langle e^{i\xi\hat{o}_1}\hat{o} \rangle = 0, \quad \langle e^{i\xi\hat{o}_1}\hat{o}^\dagger \rangle = \frac{i\xi}{\sqrt{2}\,dt} e^{\frac{-\xi^2}{4dt}},$$

$$\langle e^{i\xi\hat{o}_1}\hat{o}^2 \rangle = 0, \quad \langle e^{i\xi\hat{o}_1}\hat{o}^{\dagger 2} \rangle = -\frac{\xi^2}{2dt^2} e^{\frac{-\xi^2}{4dt^2}}, \quad \langle e^{i\xi\hat{o}_1}\hat{o}\,\hat{o}^\dagger \rangle = \frac{1}{2dt} e^{\frac{-\xi^2}{4dt^2}},$$

$$\langle e^{i\xi\hat{o}_1}\hat{o}^\dagger\hat{o} \rangle = 0, \quad \langle \hat{o}\, e^{i\xi\hat{o}_1}\hat{o}^\dagger \rangle = \left(\frac{1}{dt} - \frac{\xi^2}{2dt} \right) e^{\frac{-\xi^2}{4dt^2}}, \quad \langle \hat{o}^\dagger e^{i\xi\hat{o}_1}\hat{o} \rangle = \frac{\xi^2}{4dt^2} e^{\frac{-\xi^2}{4dt}}.$$

All the other terms, e.g. $\langle \hat{o}e^{i\xi\hat{o}_1} \rangle$, can be obtained by taking the complex conjugate of $\langle e^{i\xi\hat{o}_1}\hat{o}^\dagger \rangle$ and setting $\xi \to -\xi$, so we will not list all of them. We then need to integrate over ξ, and we have

$$\int d\xi e^{-i\xi y - \frac{\xi^2}{4dt}} \xi = -4iy dt\sqrt{\pi dt}\, e^{-y^2 dt}, \tag{4.100}$$

$$\int d\xi e^{-i\xi y - \frac{\xi^2}{4dt}} \xi^2 = 4(dt - 2y^2 dt^2)\sqrt{\pi dt}\, e^{-y^2 dt}. \tag{4.101}$$

---

[6]In reality, it is a coherent state, but we are only interested in fluctuation around the steady-state amplitude.

[7]We have used the fact that $\delta(0)dt = 1$

By taking the trace of Eq. (4.95) and using the fact that $\text{Tr}_a[\hat{\rho}_a(t)] = 1$, we obtain, up to the order of dt,

$$P[y(t)] = \sqrt{\frac{\mathrm{d}t}{\pi}}\, e^{-y^2\mathrm{d}t}(1 - 2i\sqrt{\gamma}\langle \hat{a} + \hat{a}^\dagger \rangle y\mathrm{d}t) \approx \sqrt{\frac{\mathrm{d}t}{\pi}}\, e^{-(y+i\sqrt{\gamma}\langle \hat{a} - \hat{a}^\dagger \rangle)^2\mathrm{d}t}. \qquad (4.102)$$

Therefore, the measurement result can be viewed as a classical random process, as written in Eq. (4.9):

$$y(t)\mathrm{d}t = -i\sqrt{\gamma}\langle \hat{a} - \hat{a}^\dagger \rangle \mathrm{d}t + \mathrm{d}W/\sqrt{2} \qquad (4.103)$$

where dW is the Wiener increment and d$W^2 = $ dt. After replacing $y(t)$ inthe above formula by Eq. (4.95), it turns out all the counter rotating terms vanishe because the right-hand-side of Eq. (4.101) vanishes to the first order of dt, and finally we get the stochastic master equation for the cavity mode, shown in Eq. (4.8):

$$\mathrm{d}\hat{\rho}_a(t) = -i[\Delta\hat{a}^\dagger\hat{a},\, \hat{\rho}_a(t)]\mathrm{d}t - \gamma[\hat{a}^\dagger\hat{a}\hat{\rho}_a(t) + \hat{\rho}_a(t)\hat{a}^\dagger\hat{a} - 2\hat{a}\hat{\rho}_a(t)\hat{a}^\dagger]\mathrm{d}t$$
$$- i\sqrt{2\gamma}[\hat{a}\hat{\rho}_a(t) - \hat{\rho}_a(t)\hat{a}^\dagger - \langle \hat{a} - \hat{a}^\dagger \rangle\hat{\rho}_a(t)]\mathrm{d}W. \qquad (4.104)$$

4.C Operator $\hat{O}$ in the linear coupling case

To derive the operator $\hat{O}$, it is most convenient to use the stochastic Schrödinger equation counterpart of Eq. (4.12) and derive directly $\partial_{\alpha^*}|\psi(\alpha^*)\rangle$. The stochastic Schrödinger equation reads

$$\mathrm{d}|\psi\rangle = -\frac{i}{\hbar}(\hat{H}_x + \hat{H}_a + \hat{H}_{\mathrm{int}})|\psi\rangle\mathrm{d}t - \gamma(\hat{a}^\dagger\hat{a} - 2\langle\hat{a}^\dagger\rangle\hat{a} + \langle\hat{a}^\dagger\rangle\langle\hat{a}\rangle)|\psi\rangle\mathrm{d}t - i\sqrt{2\gamma}(\hat{a} - \langle\hat{a}\rangle)|\psi\rangle\mathrm{d}W. \quad (4.105)$$

We move into the interaction picture of $\hat{H}_x + \hat{H}_a + i\hbar\gamma\hat{a}^\dagger\hat{a}$, and define the evolution operator

$$\hat{U}(t) = \exp\left[-\frac{i}{\hbar}(\hat{H}_x + \hat{H}_a - i\hbar\gamma\hat{a}^\dagger\hat{a})t\right]. \qquad (4.106)$$

The wave function in the Schrödinger and the interaction picture are related by

$$|\psi\rangle = \hat{U}(t)|\psi\rangle_I. \qquad (4.107)$$

In contrast to the usual interaction picture, $\hat{U}$ is not unitary and the operator transforms as $\hat{a}_I(t) = \hat{U}^{-1}(t)\hat{a}\hat{U}(t)$, instead of $\hat{a}_I = \hat{U}^\dagger\hat{a}\hat{U}$. In the interaction picture, we have

$$\mathrm{d}|\psi\rangle_I = -ig(\hat{L}_I\hat{a}_I^\dagger + \hat{L}_I^\dagger\hat{a}_I) + \gamma(2\langle\hat{a}^\dagger\rangle\hat{a}_I - \langle\hat{a}^\dagger\rangle\langle\hat{a}\rangle)|\psi\rangle\mathrm{d}t - i\sqrt{2\gamma}(\hat{a}_I - \langle\hat{a}\rangle)|\psi\rangle\mathrm{d}W. \qquad (4.108)$$

In the coherence basis of the cavity mode, it can be rewritten as

$$d|\psi(\alpha^*)\rangle_I = -ig(\hat{L}_I e^{i(\Delta-i\gamma)t}\alpha^* + \hat{L}_I^\dagger e^{-i(\Delta-i\gamma)t}\partial_{\alpha^*})|\psi(\alpha^*)\rangle_I dt$$

$$+ \gamma[2e^{-i(\Delta-i\gamma)t}\langle\hat{a}^\dagger\rangle\partial_{\alpha^*} - \langle\hat{a}^\dagger\rangle\langle\hat{a}\rangle]|\psi(\alpha^*)\rangle_I dt \tag{4.109}$$

$$- i\sqrt{2\gamma}[e^{-i(\Delta-i\gamma)t}\partial_{\alpha^*} - \langle\hat{a}\rangle]|\psi(\alpha^*)\rangle_I dW \equiv \hat{\mathcal{H}}_{\text{eff}}(\alpha^*)|\psi(\alpha^*)\rangle_I dt. \tag{4.110}$$

We use the following Ansatz:

$$\partial_{\alpha^*}|\psi(\alpha^*)\rangle_I \equiv -i\hat{O}_I(t,\alpha^*)|\psi(\alpha^*)\rangle_I. \tag{4.111}$$

By comparing the resulting equation, we find out that the Schrödinger picture operator $\hat{O}(t,\alpha^*)$, which is defined in Eq. (4.17), and the interaction picture operator $\hat{O}_I(t,\alpha^*)$ are related by

$$\hat{O}(t,\alpha^*) = e^{-i(\Delta-i\gamma)t}e^{-\frac{i}{\hbar}\hat{H}_x t}\hat{O}_I(t,\alpha^*)e^{\frac{i}{\hbar}\hat{H}_x t}. \tag{4.112}$$

To derive $\hat{O}$, we use the consistent condition [2]:

$$\frac{d}{dt}[\partial_{\alpha^*}|\psi(\alpha^*)\rangle_I] = \partial_{\alpha^*}\left[\frac{d}{dt}|\psi(\alpha^*)\rangle_I\right], \tag{4.113}$$

which gives

$$\frac{d}{dt}\hat{O}_I(t,\alpha^*) = i\,\partial_{\alpha^*}\hat{\mathcal{H}}_{\text{eff}}(\alpha^*) + [\hat{\mathcal{H}}_{\text{eff}}(\alpha^*), \hat{O}_I(t,\alpha^*)]$$

$$= g\hat{L}_I e^{i(\Delta-i\gamma)t} + \sqrt{2\gamma}e^{-i(\Delta-i\gamma)t}(\langle\hat{a}^\dagger\rangle - i\sqrt{2\gamma}dW)\partial_{\alpha^*}\hat{O}(t,\alpha^*)$$

$$- ig[\hat{L}_I e^{i(\Delta-i\gamma)t}\alpha^* - i\hat{L}_I^\dagger e^{-i(\Delta-i\gamma)t}\hat{O}_I(t,\alpha^*), \hat{O}_I(t,\alpha^*)]. \tag{4.114}$$

For the case considered in the main text, $\hat{L} = \hat{\sigma}_-$ and $\hat{\sigma}_-^I = \hat{\sigma}\,e^{-i\omega_q t}$. We assume that

$$\hat{O}_I(t,\alpha^*) = f(t)\hat{\sigma}_- \equiv \hat{O}_0(t), \tag{4.115}$$

which is independent of α^*. A more systematic approach is to expand $\hat{O}_I(t,\alpha^*)$ in terms of α^* as in Ref. [33]. From the consistent condition, we obtain

$$\dot{f}(t) = g\,e^{-i(\omega_q-\Delta+i\gamma)t} + g\,e^{i(\omega_m-\Delta+i\gamma)t}f^2(t). \tag{4.116}$$

with initial condition $f(0) = 0$. Finally, by using Eq. (4.112), one can easily find out that

$$\hat{O}_0(t) = e^{i(\omega_q-\Delta+i\gamma)t}f(t)\hat{\sigma}_-. \tag{4.117}$$

4.D   Operator $\hat{O}$ for optomechanical interaction

Here we show the details for deriving the $\hat{O}$ operator for the optomechanical device considered in Section 11.3. The general procedure is similar the atom-cavity case, and the only complexity arises due to the dependence of $\hat{O}$ on α^*, but only to the linear order.

We again use the stochastic Schrödiner equation in the interaction picture of $\hbar(\omega_0 - i\gamma)\hat{a}^\dagger\hat{a}$ which is

$$d|\psi(\alpha^*)\rangle_I = -\frac{i}{\hbar}\left(\frac{\hat{p}^2}{2m} + \frac{1}{2}m\omega_m^2\hat{x}^2\right)|\psi(\alpha^*)\rangle_I dt - ig[e^{i(\omega_0 - i\gamma)t}\alpha^* + e^{-i(\omega_0 - i\gamma t)}\partial_{\alpha^*}]\hat{x}|\psi(\alpha^*)\rangle_I dt$$

$$+ \gamma[2e^{-i(\Delta - i\gamma)t}\langle\hat{a}^\dagger\rangle\partial_{\alpha^*} - \langle\hat{a}^\dagger\rangle\langle\hat{a}\rangle]|\psi(\alpha^*)\rangle_I dt - i\sqrt{2\gamma}[e^{-i(\Delta - i\gamma)t}\partial_{\alpha^*} - \langle\hat{a}\rangle]|\psi(\alpha^*)\rangle_I dW. \tag{4.118}$$

The $\hat{O}$ operator is similar to that which was obtained in Ref. [2] and it is a linear function of $\hat{x}$, $\hat{p}$ and α^*. We use the following ansatz and derive those functions by using the consistent condition:

$$\partial_{\alpha^*}|\psi(\alpha^*)\rangle_I = -i[f_0(t) + f_x(t)\hat{x} + f_p(t)\hat{p} + f_1(t)\alpha^*]|\psi(\alpha^*)\rangle_I \equiv -i\hat{O}_I(t,\alpha)|\psi(\alpha^*)\rangle_I. \tag{4.119}$$

The Schrodinger picture operator $\hat{O}(t,\alpha^*)$ and the interaction picture operator $\hat{O}_I(t,\alpha^*)$ here are related by

$$\hat{O}(t,\alpha^*) = e^{-i(\Delta - i\gamma)t}[f_0(t) + f_x(t)\hat{x} + f_p(t)\hat{p} + e^{-i(\Delta - i\gamma)t}f_1(t)\alpha^*] \equiv \hat{O}_0(t) + O_1(t)\alpha^*, \tag{4.120}$$

in which we define operator $\hat{O}_0$ and function O_1 by using the notation similar to Ref. [33]—subscripts 0 and 1 indicate the power dependence of α. From the consistent condition, those functions f satisfy the following equations

$$\dot{f}_0(t)dt = e^{-i(\Delta - i\gamma)t}[2\gamma\langle\hat{a}^\dagger\rangle f_1(t)dt - i\sqrt{2\gamma}\,f_1(t)dW - i\,g\,f_0(t)f_p(t)dt], \tag{4.121}$$

$$\dot{f}_x(t) = \omega_m f_p(t) + g\,e^{i(\Delta - i\gamma)t} - i\,g\,e^{-i(\Delta - i\gamma)t}[f_1(t) + f_x(t)f_p(t)], \tag{4.122}$$

$$\dot{f}_p(t) = -\omega_m f_x(t) - i\,g\,f_p^2(t)e^{-i(\Delta - i\gamma)t}, \tag{4.123}$$

$$\dot{f}_1(t) = g\,f_2(t)e^{i(\Delta - i\gamma)t} - i\,g\,f_2(t)f_3(t)e^{-i(\Delta - i\gamma)t} \tag{4.124}$$

with null initial condition.

To derive the SME, we need to average over α. By using the fact that $M_\alpha[\alpha^*\hat{\rho}_x(\alpha^*,\alpha)] = M_\alpha[\partial_\alpha\hat{\rho}_x(\alpha^*,\alpha)] = \hat{\rho}\hat{O}\dagger$, we obtain

$$\hat{O}\hat{\rho} = \hat{O}_0\hat{\rho} + O_1\hat{\rho}\hat{O}^\dagger, \tag{4.125}$$

$$\hat{\rho}\hat{O}^\dagger = \hat{\rho}\hat{O}_0^\dagger + O_1^*\hat{O}_0^\dagger\hat{\rho}. \tag{4.126}$$

We can then obtain Eqs. (4.27) and (4.28), namely

$$\hat{O}\hat{\rho}_x = [O_1\hat{\rho}_x\hat{O}_0^\dagger + \hat{O}_0\hat{\rho}_x]/[1 - |O_1|^2], \tag{4.127}$$

$$\hat{\rho}_x\hat{O}^\dagger = [O_1^*\hat{O}_0\hat{\rho}_x + \hat{\rho}_x\hat{O}_0^\dagger]/[1 - |O_1|^2]. \tag{4.128}$$

4.E   Operator $\hat{O}_k$ in the linear coupling case

Here we derive the $\hat{O}_k$ in the linear coupling case. The corresponding stochastic Schrödinger equation reads

$$\mathrm{d}|\psi\rangle = -\frac{i}{\hbar}(\hat{H}_x + \hat{H}_a)|\psi\rangle\mathrm{d}t - i\sum_k g_k(\hat{L}\hat{a}_k^\dagger + \hat{L}^\dagger\hat{a}_k)|\psi\rangle\mathrm{d}t$$
$$- \sum_{kk'}\sqrt{\gamma_k\gamma_{k'}}(\hat{a}_k^\dagger\hat{a}_{k'} - 2\langle\hat{a}_k^\dagger\rangle\hat{a}_{k'} + \langle\hat{a}_k^\dagger\rangle\langle\hat{a}_{k'}\rangle)|\psi\rangle\mathrm{d}t + \sum\sqrt{2\gamma_k}(\hat{a}_k - \langle\hat{a}_k\rangle)|\psi\rangle\mathrm{d}W. \tag{4.129}$$

Similar to the single-mode case, we move into the interaction picture of $\hat{H}_x + \hat{H}_a + i\hbar\sum_{kk'}\sqrt{\gamma_k\gamma_{k'}}\hat{a}_k^\dagger\hat{a}_{k'}$, and define the evolution operator

$$\hat{U}(t) = \exp\left[-\frac{i}{\hbar}\left(\hat{H}_x + \hat{H}_a + i\hbar\sum_{kk'}\sqrt{\gamma_k\gamma_{k'}}\hat{a}_k^\dagger\hat{a}_{k'}\right)t\right]. \tag{4.130}$$

The wave function and the operator in the Schrödinger and the interaction picture are related by

$$|\psi\rangle = \hat{U}|\psi\rangle_I, \quad \hat{o}_I = \hat{U}^{-1}\hat{o}\hat{U}. \tag{4.131}$$

Specifically, the annihilation operator for the bath $\hat{a}_k$ transforms as

$$\hat{U}^{-1}(t)\hat{a}_k\hat{U}(t) = \sum_{k'}e^{-i\mathbf{M}_{kk'}t}\hat{a}_{k'}, \quad \hat{U}^{-1}(t)\hat{a}_k^\dagger\hat{U}(t) = \sum_{k'}e^{i\mathbf{M}_{kk'}t}\hat{a}_{k'}^\dagger \tag{4.132}$$

where the dynamical matrix $\mathbf{M}$ is defined in Eq. (5.9). By using the coherent state basis for the bath, the stochastic master equation in the interaction picture reads

$$\mathrm{d}|\psi(\vec{\boldsymbol{\alpha}}^*)\rangle_I = -i\sum_{kk'}g_k\left(\hat{L}_Ie^{i\mathbf{M}_{kk'}t}\alpha_{k'}^* + \hat{L}_I^\dagger e^{-i\mathbf{M}_{kk'}t}\partial_{\alpha_{k'}^*}\right)|\psi(\vec{\boldsymbol{\alpha}}^*)\rangle_I\mathrm{d}t + \sum_{kk'k''}\sqrt{\gamma_k\gamma_{k'}}(2\langle\hat{a}_k^\dagger\rangle e^{-i\mathbf{M}_{k'k''}t}\partial_{\alpha_{k''}^*}$$
$$- \langle\hat{a}_k^\dagger\rangle\langle\hat{a}_{k'}\rangle)|\psi(\vec{\boldsymbol{\alpha}}^*)\rangle_I\mathrm{d}t + \sum_{kk'}\sqrt{2\gamma_k}(e^{-i\mathbf{M}_{kk'}t}\partial_{\alpha_{k'}^*} - \langle\hat{a}_k\rangle)|\psi(\vec{\boldsymbol{\alpha}}^*)\rangle_I\,\mathrm{d}W \equiv \mathcal{H}_{\text{eff}}(\vec{\boldsymbol{\alpha}}^*)|\psi(\vec{\boldsymbol{\alpha}}^*)\rangle_I. \tag{4.133}$$

Similarly, we use the following ansatz

$$\partial_{\alpha_k^*}|\psi(\vec{\boldsymbol{\alpha}}^*)\rangle_I = -i\hat{O}'_{Ik}(t, \vec{\boldsymbol{\alpha}}^*)|\psi(\vec{\boldsymbol{\alpha}}^*)\rangle_I. \tag{4.134}$$

It is related to the Schrödinger picture operator $\hat{O}'_k(t, \alpha^*)$ by

$$\hat{O}'_k(t, \vec{\alpha}^*) = \sum_{k'} e^{-i\mathbf{M}_{kk'}t} e^{-\frac{i}{\hbar}\hat{H}_x t} \hat{O}'_{Ik'}(t, \vec{\alpha}^*) e^{\frac{i}{\hbar}\hat{H}_x t}. \tag{4.135}$$

From the consistent condition:

$$\frac{\mathrm{d}}{\mathrm{d}t}[\partial_{\alpha_k^*}|\psi(\vec{\alpha}^*)\rangle_I] = \partial_{\alpha_k^*}\left[\frac{\mathrm{d}}{\mathrm{d}t}|\psi(\vec{\alpha}^*)\rangle_I\right], \tag{4.136}$$

we get

$$\frac{\mathrm{d}}{\mathrm{d}t}\hat{O}'_{Ik}(t, \alpha^*) = i\,\partial_{\alpha_k^*}\hat{\mathcal{H}}_{\mathrm{eff}}(\vec{\alpha}^*) + [\hat{\mathcal{H}}_{\mathrm{eff}}(\vec{\alpha}^*), \hat{O}'_{Ik}(t, \vec{\alpha}^*)]$$
$$= \sum_{k'} g_{k'}\hat{L}_I e^{i\mathbf{M}_{kk'}t} - i\sum_{k'k''} g_{k'}\left[\hat{L}_I e^{i\mathbf{M}_{k'k''}t}\alpha_{k''}^* - i\hat{L}_I^\dagger e^{-i\mathbf{M}_{k'k''}t}\hat{O}'_{Ik''}(t, \vec{\alpha}^*), \hat{O}'_{Ik}(t, \vec{\alpha}^*)\right]. \tag{4.137}$$

For the simple case considered in the main text, $\hat{L} = \hat{b}$, it is straightforward to get

$$\hat{O}'_{Ik}(t, \vec{\alpha}) = f_k(t)\hat{b} \tag{4.138}$$

with

$$\dot{f}_k(t) = \sum_{k'} g_{k'} e^{-i(\omega_m - \mathbf{M}_{kk'})t} - f_k(t)\sum_{k'k''} g_{k'} e^{i(\omega_m t - \mathbf{M}_{k'k''})t} f_{k''}(t). \tag{4.139}$$

By using Eq. (4.135), the Schrödinger picture operator is given by

$$\hat{O}_k(t) = \sum_{k'} e^{i(\omega_m - \mathbf{M}_{kk'})t} f_{k'}(t)\hat{b}. \tag{4.140}$$

This gives rise to Eq. (4.117) in the single-mode case.

4.F   Perturbative solution of $\hat{O}_k$

In this section, we will try to derive $\partial_{\alpha_k^*}\rho_x$ and $\langle\hat{a}_k\rangle$ in the case of the many-degrees-of-freedom bath. To illustrate the procedure, we first consider the case of the single-degree-of-freedom bath. The corresponding stochastic Schrödinger equation in the coherence basis of the cavity mode reads

$$\mathrm{d}|\psi(\alpha^*)\rangle = -\frac{i}{\hbar}(\hat{H}_x + \hat{H}_a)|\psi(\alpha^*)\rangle\mathrm{d}t - ig(\hat{L}\alpha^* + \hat{L}^\dagger\partial_{\alpha^*})|\psi(\alpha^*)\rangle\mathrm{d}t$$
$$- \gamma(\alpha^*\partial_{\alpha^*} - 2\langle\hat{a}^\dagger\rangle\partial_{\alpha^*} + \langle\hat{a}^\dagger\rangle\langle\hat{a}\rangle)|\psi(\alpha^*)\rangle\mathrm{d}t$$
$$+ \sqrt{2\gamma}(\partial_{\alpha^*} - \langle\hat{a}\rangle)|\psi(\alpha^*)\rangle\mathrm{d}W. \tag{4.141}$$

We do not use the interaction picture, as it is more convenient to study in the Schrödinger picture for this case.

In order to seek a perturbative solution to $\partial_{\alpha^*}|\psi(\alpha^*)\rangle$, we need to find a small dimensionless parameter. We notice that the characteristic memory time scale for the oscillator interacting with the cavity mode is γ^{-1}, after which the cavity mode is refreshed by the external field. Since the coupling strength between the oscillator and the cavity mode is g, the small dimensionless parameter is $\epsilon \equiv g/\gamma$. In addition, we know that g enters $|\psi(\alpha^*)\rangle$ as of $g\alpha^*$ (from the interaction term), we can make a Taylor expansion of $|\psi(\alpha^*)\rangle$ as α, which is equivalent to expansion in terms of ϵ [8], i.e.,

$$|\psi(\alpha^*)\rangle = |\psi\rangle(\epsilon^0) + \alpha^*\partial_{\alpha^*}|\psi\rangle(\epsilon^1) + \frac{1}{2}\alpha^{*2}\partial_{\alpha^*}^2|\psi\rangle(\epsilon^2) + \cdots . \tag{4.142}$$

By taking the partial derivative of Eq. (4.146), up to the first order of g, we have

$$d(\partial_{\alpha^*}|\psi\rangle) = -\frac{i}{\hbar}(\hat{H}_x + \hbar\Delta - i\hbar\gamma)(\partial_{\alpha^*}|\psi\rangle)dt - ig\hat{L}|\psi\rangle dt, \tag{4.143}$$

and we obtain

$$
\begin{aligned}
(\partial_{\alpha^*}|\psi(t)\rangle) &= (\partial_{\alpha^*}|\psi(0)\rangle) - ig\int_0^t dt' e^{-i(\Delta-i\gamma)(t-t')}e^{-i\hat{H}_x(t-t')/\hbar}\hat{L}|\psi(t')\rangle \\
&= -ig\int_0^t dt' e^{-i(\Delta-i\gamma)(t-t')}\hat{L}(t'-t)|\psi(t)\rangle
\end{aligned}
\tag{4.144}
$$

with $\hat{L}(t'-t) \equiv e^{-i\hat{H}_x(t-t')/\hbar}\hat{L}e^{i\hat{H}_x(t-t')/\hbar}$. We assume that the oscillator and the cavity mode are separable initially, and the cavity mode is in a vacuum state, in which case $|\psi(0)\rangle$ is independent of α^* and $\partial_{\alpha^*}|\psi(0)\rangle = 0$. Up to the first order of the interaction strength, we get

$$\hat{O}(t) = g\int_0^t dt' e^{-i(\Delta-i\gamma)(t-t')}\hat{L}(t'-t) + \mathcal{O}[g^2]. \tag{4.145}$$

Now, we can move on the the case of the bath with many degrees of freedom. The corresponding stochastic Schrödinger equation in the coherent state basis is

$$
d|\psi(\alpha^*)\rangle = -\frac{i}{\hbar}(\hat{H}_x + \hat{H}_a)|\psi(\alpha^*)\rangle dt - i\sum_k g_k(\hat{L}\alpha_k^* + \hat{L}^\dagger\partial_{\alpha_k^*})|\psi(\alpha^*)\rangle dt - \sum_{kk'}\sqrt{\gamma_k\gamma_{k'}}(\alpha_k^*\partial_{\alpha_{k'}^*} - 2\langle\hat{a}_k^\dagger\rangle\partial_{\alpha_{k'}^*})
$$
$$
+ \langle\hat{a}_k^\dagger\rangle\langle\hat{a}_{k'}\rangle)|\psi(\alpha^*)\rangle dt + \sum_k\sqrt{2\gamma_k}(\partial_{\alpha_k^*} - \langle\hat{a}_k\rangle)|\psi(\alpha^*)\rangle \, dW. \tag{4.146}
$$

Up to the first order of interaction strength g_k, we have

$$d(\partial_{\alpha_k^*}|\psi\rangle) = -\frac{i}{\hbar}(\hat{H}_x + \hbar\omega_k)(\partial_{\alpha_k^*}|\psi\rangle)dt - \sqrt{\gamma_k}\sum_{k'}\sqrt{\gamma_{k'}}(\partial_{\alpha_{k'}^*}|\psi\rangle)dt - ig_k\hat{L}|\psi\rangle dt + \mathcal{O}[g_k^2]. \tag{4.147}$$

---

[8]This is identical to Ting's expansion of $\hat{O}$ in terms of the random process [33].

It is a linearly coupled equation for $\partial_{\alpha_k^*}|\psi\rangle$. The solution can be formally written as

$$\partial_{\boldsymbol{\bar{\alpha}}^*}|\psi(t)\rangle = -i \int_0^t \mathrm{d}t' \exp\left[-\frac{i}{\hbar}(\hat{H}_x\mathbf{I} + \hbar\,\mathbf{M})(t-t')\right] \vec{\boldsymbol{g}}\,\hat{L}|\psi(t')\rangle = -i \int_0^t \mathrm{d}t' e^{-i\mathbf{M}(t-t')}\vec{\boldsymbol{g}}\,\hat{L}(t'-t)|\psi(t)\rangle,$$

(4.148)

where matrix $\mathbf{M}$ is defined in Eq. (5.9). We therefore obtain

$$\hat{O}(t) = \sum_{k'} \int_0^t \mathrm{d}t' e^{-i\mathbf{M}_{kk'}(t-t')} g_k\,\hat{L}(t'-t)\hat{\rho}_x + \mathcal{O}[g_k^2].$$

(4.149)

Bibliography

[1] N. Gisin, and I. C. Percival, J. Phys. A: Math. Gen. **25** 5677 (1992).

[2] L. Diósi, N. Gisin, and W. T. Strunz, Phys. Rev. A **58**, 1699 (1998).

[3] L. Diósi, and W. Strunz, Phys. Lett. A **235**, 569 (1997).

[4] H. M. Wiseman, and G. J. Milburn, *Quantum Measurement and Control*, Cambridge University Press, 2010.

[5] L. Diósi, Phys. Rev. Lett. **100**, 080401 (2008).

[6] H. W. Wiseman, and J. M. Gambetta, Phys. Rev. Lett. **101**, 140401 (2008).

[7] F. Khalili, S. Danilishin, H. Miao, H. Müller-Ebhardt, H. Yang, and Y. Chen, Phys. Rev. Lett. **105**, 070403 (2010).

[8] W. Heisenberg, *The Physical Principles of Quantum Mechanics*, University of Chicago, Chicago, IL, 1930.

[9] Refer to section II of A. Buonanno and Y. Chen, Phys. Rev. D **65**, 042001 (2002).

[10] Chapter VI in the book by V. B. Braginsky and F. Y. Farid, *Quantum Measurement*, Cambridge University Press, 1992.

[11] H. Müller-Ebhardt *et al.*, Phys. Rev A. **80**, 043802 (2009).

[12] E. A. Calzetta and B. L. Hu, *Nonequilibrium Quantum Field Theory*, Cambridge University Press, 2008.

[13] I. Martin and W. H. Zurek, Phys. Rev. Lett. **98**, 120401 (2007).

[14] J. D. Thompson *et al.*, Nature **452** 067015 (2008).

[15] G. J. Milburn, Quantum Semiclass. Opt. **8**, 269 (1996).

[16] I. Martin, and W. H. Zurek, Phys. Rev. Lett. **98**, 120401 (2007).

[17] J. Thompson *et al.*, Nature **452**, 72 (2008).

[18] A. M. Jayich *et al.*, New J. Phys. **10** 095008 (2008).

[19] H. Miao *et al.*, Phys. Rev. Lett. **103**, 100402 (2009).

[20] LIGO Scientific Collaboration, Rep. Prog. Phys. **72**, 076901 (2009).

[21] V. B. Braginsky, and F. Khalili, *Quantum Measurement*, Cambridge University Press (1992).

[22] P. Purdue, and Y. Chen, Phys. Rev. D **66**, 122004 (2002) and references therein.

[23] L. Diósi, Phys. Rev. A **85**, 034101 (2012) (2011).

[24] C. M. Caves, and B. L. Schumaker, Phys. Rev. A **31**, 3068 (1985).

[25] B. S. Schumaker, and C. M. Caves, Phys. Rev. A **31**, 3093 (1985).

[26] D. F. Walls, and G. J. Milburn, *Quantum Optics*, Springer-Verlag, Berlin (1994).

[27] L. Mandel, and E. Wolf, *Optical Coherence and Quantum Optics*, Cambridge University Press, Cambridge, England (1995).

[28] M. O. Scully, and M. S. Zubairy, *Quantum Optics*, Cambridge University Press, Cambridge, England (1997).

[29] C. M. Caves, Phys. Rev. D **33**, 1643 (1986).

[30] M. B. Mensky, *Continuous Quantum Measurements and Path Integrals*, IOP Publishing Ltd, London, England (1993).

[31] K. Jacobs, and D. A. Steck, Contemporary Physics, **47**, 279 (2006).

[32] R. P. Feynman and F. L. Vernon, Ann. Phys. (N.Y.) **24**, 118 (1963).

[33] T. Yu, L. Diósi, N. Gisin, and W. T. Strunz, Phys. Rev. A **60**, 91 (1999).

[34] H. M. Wiseman, and G. J. Milburn, Phys. Rev. A **47**, 642 (1993).

Chapter 5

Revealing non-Markovianity of open quantum systems via local operations

Non-Markovianity, as an important feature of general open quantum systems, is usually difficult to quantify with limited knowledge of how the plant, which we are interested in, interacts with its environment, the bath. It often happens that the reduced dynamics of the plant attached to a non-Markovian bath becomes indistinguishable from the one with a Markovian bath, if we let the plant-bath system freely evolve. Here we show that non-Markovianity can be revealed via applying local unitary operations on the plant—they will influence the plant dynamics at later times due to memory of the bath. This not only allows us to show non-Markovianity in those systems that are perviously considered as being Markovian, but also sheds light on protecting and recovering quantum coherence in non-Markovian systems, which will be useful for quantum-information processing.

Based on preprint by H. Yang, H. Miao, and Y. Chen, arXiv:1111.6079

5.1   Introduction

Recently, there have been many important theoretical and experimental studies of non-Markovian open quantum systems in the literature [1–5]. This is largely motivated by the quest for quantum information processing protocols that are robust under decoherence, as the basic information storing unit—the qubit—often interacts with a non-Markovian environment with which the noises at different times are correlated. If we can arbitrarily control the plant, e.g., the atomic spin, the non-Markovianity of the bath, in principle, allows us to completely decouple the spin from the environment, which is known as dynamical decoupling [6–8]. A good understanding and quantification of non-Markovian dynamics in open quantum systems can therefore lead to novel designs of quantum

devices that are less susceptible to environmentally-induced decoherence.

To quantify non-Markovianity, Breuer *et al.* proposed a measure based upon the evolution of the trace distance $\mathrm{Tr}|\hat{\rho}_1(t) - \hat{\rho}_2(t)|/2$ between two different initial quantum states of the plant $\hat{\rho}_1(0)$ and $\hat{\rho}_2(0)$ [3]. An increase in the trace distance gives a unequivocal signature of non-Markovianity, as it indicates that information flows from the environment back to the plant. There is another measure proposed by Rivas *et al.* [4]. The authors introduced an ancilla to entangle but not interact with the plant, whereas the plant is still interacting with the bath—an increase in the entanglement between the plant and the ancilla during evolution signifies the existence of non-Markovian dynamics between the plant and bath. Both measures have been compared theoretically [9, 10] and also tested in a recent novel experiment by Liu *et al.* [5].

These two measures focus on the reduced dynamics of the plant and do not provide details on how the bath and plant interact with each other. As the reduced dynamics contain limited knowledge of the bath and also critically depend on the initial state, it often happens that the plant dynamics is highly degenerate among different non-Markovian systems. In other words, the plant can effectively behave in the same way even when it is attached to vastly different baths—e.g., one a Markovian bath and the other a non-Markovian bath. In this letter, we propose a new criterion for non-Markivianity by exploring the memory effect in non-Markovian dynamics: *the dynamics is non-Markovian if a local unitary operation on the plant at a given moment can induce non-local influence on the plant dynamics at later times.* This allows us to reveal non-Markovianity in systems in which the reduced dynamics of the plant appear to be Markovian before applying local operations—e.g., it satisfies the time-local master equation with effective damping rates $\gamma_i(t) > 0$:

$$\dot{\hat{\rho}}_p(t) = -(i/\hbar)[\hat{H}_p(t), \hat{\rho}_p(t)] + \sum_i \gamma_i(t)\hat{\mathcal{L}}_i\hat{\rho}_p(t) \,, \tag{5.1}$$

where Lindblad terms $\hat{\mathcal{L}}_i\hat{\rho}_p = 2\hat{A}_i\hat{\rho}_p\hat{A}_i^\dagger - \{\hat{A}_i^\dagger\hat{A}_i, \hat{\rho}_p\}$ with $\hat{A}_i$ being plant operators [11, 12].
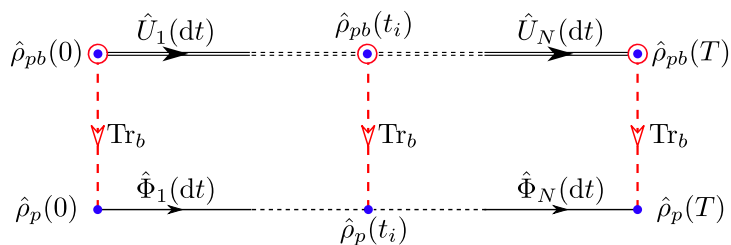
Figure 5.1: (Color online.) A schematic showing how the reduced dynamics of the plant emerges from the full dynamics of the plant-bath system by tracing over the bath state at each step.

5.2 Plant – bath dynamics

Reduced dynamics of the plant.—To introduce our new criterion for non-Markovianity, we first consider the reduced dynamics of the plant. Suppose the plant-bath system evolves from $t = 0$ to $t = T$. We divide this process into N small segments with increment $dt = T/N$. The plant-bath system undergoes a unitary evolution:

$$\hat{\rho}_{pb}(T) = \hat{U}_N(dt) \cdots \hat{U}_1(dt) \hat{\rho}_{pb}(0) \hat{U}_1^\dagger(dt) \cdots \hat{U}_N^\dagger(dt), \tag{5.2}$$

where $\hat{\rho}_{pb}$ is the plant-bath density matrix and $\hat{U}_i(dt)$ is the unitary evolution under the total Hamiltonian at t_i. The plant reduced dynamics is obtained by tracing over the bath at each step, as shown schematically in Fig. 5.1, and the reduced density matrix for the plant evolves as:

$$\hat{\rho}_p(T) = \hat{\Phi}_N(dt) \cdots \hat{\Phi}_i(dt) \cdots \hat{\Phi}_1(dt) \hat{\rho}_p(0), \tag{5.3}$$

where $\hat{\rho}_p \equiv \text{Tr}_b[\hat{\rho}_{pb}]$ and the super-operator $\hat{\Phi}_i(dt)$ is a trace-preserving dynamical map at $t = t_i$.

For general non-Markovian dynamics, the dynamical map $\hat{\Phi}_i(dt)$ relies on the history of the plant-bath state $\hat{\rho}_{pb}(t_k)$ ($t_k < t_i$). For Markovian dynamics, $\hat{\Phi}_i(dt)$ only locally depends on the plant-bath state, i.e., no memory, in a similar manner to the classical Markovian process. In the simplest case, $\hat{\Phi}_i(dt)$ is independent of time and the plant state—the dynamical map forms a semigroup with $\hat{\Phi}(t + \tau) = \hat{\Phi}(t)\hat{\Phi}(\tau)$. The corresponding generator is the Lindblad super-operator $\hat{\mathcal{L}}$, namely $\hat{\Phi}(t) = e^{\hat{\mathcal{L}}t}$, and the master equation for the plant is in the standard Lindblad form: $\dot{\hat{\rho}}_p(t) = -(i/\hbar)[\hat{H}_p, \hat{\rho}_p(t)] + \hat{\mathcal{L}}\hat{\rho}_p(t)$.

Criterion for non-Markovianity—to explore non-Markovianity, the key is to show the memory effect—the non-local dependence of the dynamical map on the plant-bath state. A natural way is to apply a certain local unitary operation on the plant-bath system at one moment and to study how it influences the plant dynamics at later times. In usual cases, only the plant can be manipulated and the bath, i.e., the environment, is not fully controllable. This leads to our new criterion for non-Markovianity in general open quantum systems:

The plant dynamics is non-Markovian if its dynamical maps at later times change under any local unitary operation $\hat{U}_p \otimes \hat{I}_b$ on the plant at any earlier moment t_k ($\hat{I}_b$ is the identity operator for the bath), namely, when $\hat{\rho}_{pb}(t_k) \rightarrow \hat{U}_p \otimes \hat{I}_b \, \hat{\rho}_{pb}(t_k) \hat{U}_p^\dagger \otimes \hat{I}_b$, the plant state at T:

$$\hat{\rho}_p(T) \neq \hat{\Phi}_N(dt) \cdots \hat{\Phi}_i(dt) \cdots \hat{\Phi}_{k+1}(dt) \hat{U}_p \hat{\rho}_p(t_k) \hat{U}_p^\dagger. \tag{5.4}$$

Here $\hat{\Phi}$ are dynamical maps before applying $\hat{U}_p \otimes \hat{I}_b$. The fact that the dynamical maps change at later times clearly indicates non-Markovianity, as we know for Markovian dynamics the dynamics

maps are invariant under such operations. If the dynamical maps do not change, it means that all the dynamical variables of the plant will follow the same equations of motion, before and after applying the unitary operations. Solely from the dynamical point of view, the dynamics cannot be treated as non-Markovian, as it is difficult to reveal the memory effect by studying dynamics of the plant variables alone. In the following, we will use two examples to illustrate this new criterion, and show that it can reveal non-Markovianity in systems inwhich the unperturbed dynamics (before applying the unitary operation) is indistinguishable from the Markovian one.

The first example—the first such example is the interesting spin-cavity system as shown in Fig. 5.2—a two-level atom coupled to a cavity mode which in turn couples to external continuum—a quantum Wiener process that is equivalent to a zero-temperature Markovian bath [13]. If we view the cavity mode and the external continuum together as the bath, the two-level atom—the plant— is effectively coupled to a damped cavity mode which is a non-Markovian dissipative bath. The corresponding Hamiltonian for this system is given by [14]:

$$
\begin{aligned}
\hat{H} =&\, \hbar(\omega_q/2)\hat{\sigma}_z + \hbar\,\Delta\hat{a}^\dagger\hat{a} + \hbar\,g(\hat{\sigma}_-\hat{a}^\dagger + \hat{\sigma}_+\hat{a}) \\
&+ \hbar\sqrt{\gamma}[\hat{a}\,\hat{b}_{\mathrm{in}}^\dagger(t) + \hat{a}^\dagger\,\hat{b}_{\mathrm{in}}(t)].
\end{aligned}
\tag{5.5}
$$

Here $\hat{\sigma}_z$ is the Pauli matrix and $\hat{\sigma}_\pm = \hat{\sigma}_x \pm i\hat{\sigma}_y$; $\hat{a}$ and $\hat{b}_{\mathrm{in}}$ are the annihilation operators of the cavity mode and the in-going field of the external continuum with $[\hat{a},\,\hat{a}^\dagger] = 1$ and $[\hat{b}_{\mathrm{in}}(t),\,\hat{b}_{\mathrm{in}}^\dagger(t')] = \delta(t-t')$; ω_q is the atom transition frequency and Δ is detune frequency of the cavity mode; g and γ are the corresponding coupling constants. After tracing over the external continuum, the joint density matrix of the atom and cavity satisfies the following Markovian master equation:

$$
\begin{aligned}
\dot{\rho}(t) =&- i\left[(\omega_q/2)\hat{\sigma}_z + \Delta\hat{a}^\dagger\hat{a} + g(\hat{\sigma}_-\hat{a}^\dagger + \hat{\sigma}_+\hat{a}),\,\hat{\rho}(t)\right] \\
&+ \gamma[2\hat{a}\hat{\rho}(t)\hat{a}^\dagger - \{\hat{a}^\dagger\hat{a},\,\hat{\rho}(t)\}].
\end{aligned}
\tag{5.6}
$$

To further obtain the master equation for the atom by eliminating the cavity mode, we need to know the initial state of the atom and the cavity mode. In the simplest case when they initially are separable and the cavity mode is in the vacuum state, namely $|\psi\rangle = |\psi_a\rangle \otimes |0\rangle$, as shown in Ref. [14],
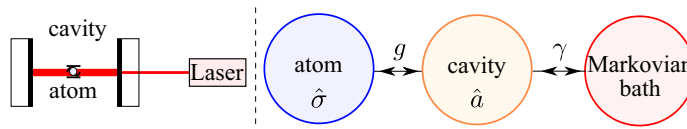
Figure 5.2: (Color online.) A schematic showing the atom-cavity system. The cavity mode is coupled to the external continuum field (a Markovian bath), and they together form an effective non-Markovian bath for the atom. (Adapted from Ref. [14]).

the reduced density matrix of the atom $\hat{\rho}_a(t)$ satisfies a time-local master equation:

$$\dot{\hat{\rho}}_a(t) = -i\left[\frac{\omega_q}{2}\hat{\sigma}_z + g\Im\{f(t)\}\hat{\sigma}_+\hat{\sigma}_-,\ \hat{\rho}_a(t)\right]$$

$$+ g\Re\{f(t)\}\left[2\,\hat{\sigma}_-\hat{\rho}_a(t)\hat{\sigma}_+ - \{\hat{\sigma}_+\hat{\sigma}_-,\ \hat{\rho}_a(t)\}\right], \tag{5.7}$$

where the time-dependent function $f(t)$ satisfies a Riccati equation: $\dot{f}(t) - i(\omega_q - \Delta + i\gamma)f(t) - g\,f^2(t) = g$ with an initial condition $f(0) = 0$, of which the solution is well-known. In the case with $\omega_q = \Delta$ and strong dissipation $\gamma \geq 2g$, $f(t)$ is real and positive, and we simply have

$$\dot{\hat{\rho}}_a(t) = -i\left[\frac{\omega_q}{2}\hat{\sigma}_z,\ \hat{\rho}_a(t)\right] + g\,f(t)\hat{\mathcal{L}}\hat{\rho}_a(t) \tag{5.8}$$

with $\hat{\mathcal{L}}\hat{\rho}_a(t) = 2\,\hat{\sigma}_-\hat{\rho}_a(t)\hat{\sigma}_+ - \{\hat{\sigma}_+\hat{\sigma}_-,\ \hat{\rho}_a(t)\}$. Such a master equation can also describe the case when the atom is directly coupled to the Markovian bath but with a time-dependent coupling rate, of which the Hamiltonian is

$$\hat{H} = \hbar(\omega_q/2)\hat{\sigma}_z + \hbar\sqrt{gf(t)}[\hat{\sigma}_-\,\hat{b}_{\rm in}^\dagger(t) + \hat{\sigma}_+\,\hat{b}_{\rm in}(t)]. \tag{5.9}$$

Basically, from this reduced dynamics alone, we cannot tell whether the underlying dynamics is Markovian or not, even though the atom-cavity interaction is highly non-Markovian when the cavity decay rate γ becomes comparable to the atom transition frequency ω_q. This master equation is simply an artifact of a specially-chosen initial state for the atom and the cavity. If we perturb the atom, e.g., by applying a π-pulse, the dynamics of the atom will deviate from the one described by Eq. (5.7) due to the memory of the cavity mode.

To show the change in the dynamical map for the plant after applying local operations, we
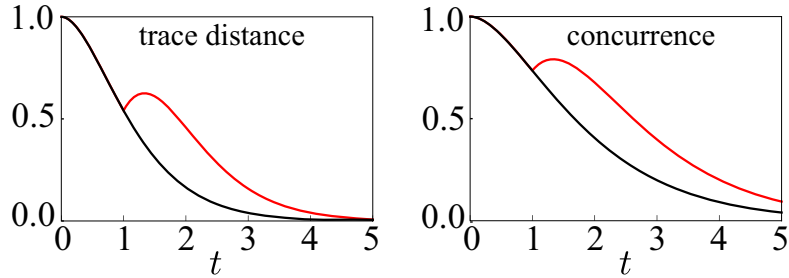
Figure 5.3: (Color online.) The left panel shows the change in the trace distance after applying a local unitary operation; the right panel shows the concurrence for the entanglement between the atom and a two-level ancilla. The black line shows the Markovian dynamics described by Eq. (5.8). We have chosen $\omega_q = \Delta = g = 1$, and $\gamma = 2g$. For evaluating the trace distance $\mathrm{Tr}|\hat{\rho}_1(t) - \hat{\rho}_2(t)|/2$, the two initial quantum states of the atom are $\hat{\rho}_1(0) = |1\rangle\langle1|$ and $\hat{\rho}_2(0) = |0\rangle\langle0|$. For evaluating the concurrence, the atom and ancilla are initially in the maximally entangled state: $\frac{1}{\sqrt{2}}[|0\rangle| \otimes |0\rangle + |1\rangle| \otimes |1\rangle]$.
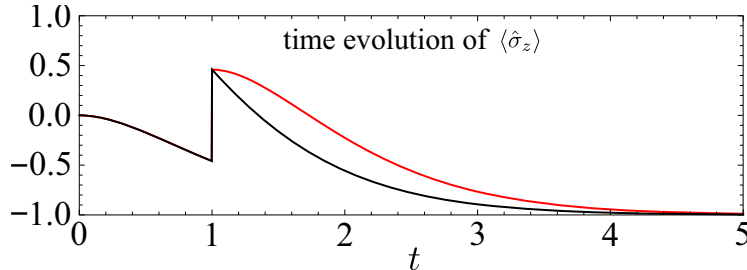
Figure 5.4: (Color online.) Plot showing the time evolution of $\langle\hat{\sigma}_z\rangle$ according to Markovian dynamics given in Eq. (5.10) (black) and to non-Markovian dynamics (red) with $\hat{\sigma}_z \otimes \hat{I}_c$ applied at $t = 1$. The initial atom-cavity state is $(|0\rangle + |1\rangle)/\sqrt{2} \otimes |0\rangle$.

numerically solve the master equation in Eq. (9.54a) for the joint atom-cavity density matrix. We use the same initially-separable quantum state for deriving Eq. (5.8) and in addition impose $\gamma = 2g$, so that when there is no unitary operation on the atom, the reduced density matrix of the atom simply follows Eq. (5.8) with $f(t) > 0$, which is a time-local Markovian master equation. In Fig. 5.3, we show the change of the trace distance and also the concurrence with and without introducing a local unitary operation on the atom $\hat{U} = \hat{\sigma}_z \otimes \hat{I}_c$ at $t = 1$ ($\hat{I}_c$ is the identity operator of the cavity mode). As we can see, after introducing a local operation on the atom, there is an increase in both the trace distance and the concurrence, which manifests the memory effect of the cavity mode. In contrast, if the atom were coupled to a Markovian bath with Hamiltonian given by Eq. (5.9), a local perturbation as $\hat{\sigma}_z \otimes \hat{I}_c$ will change neither the trace distance nor the concurrence.

Apart from the change of the trace distance or the concurrence, the change in the dynamical map can also show up in the expectation values of plant dynamical variables. Here, we take $\langle\hat{\sigma}_z\rangle \equiv \mathrm{Tr}[\hat{\rho}\,\hat{\sigma}_z]$ for illustration. In Fig. 5.4, we show the non-Markovian evolution $\mathrm{Tr}[\hat{\rho}\,\hat{\sigma}_z]$ due to the full dynamics described in Eq. (9.54a) and the Markovian evolution $\mathrm{Tr}_p[\hat{\rho}_p\hat{\sigma}_z]$ from Eq.(5.8) which gives:

$$\langle\dot{\hat{\sigma}}_z\rangle = -2gf(t)[1 + \langle\hat{\sigma}_z\rangle]. \tag{5.10}$$

Before applying the local operation there is no difference between them, as the reduced dynamics is indistinguishable from the Markovian case. They start to deviate from each other after the local unitary operation.

The second example—this new criterion can also be applied to study the recent experiment by Liu *et al.* [5]. In their setup, the polarization degree of freedom of photons acts as the plant, and it couples to the frequency degree of freedom which acts as the bath. They jointly undergo the following unitary evolution:

$$\hat{U}(t)|\lambda\rangle \otimes |\omega\rangle = e^{in_\lambda\omega t}|\lambda\rangle \otimes |\omega\rangle. \tag{5.11}$$

Here $\lambda = H, V$ representing the horizontal and vertical polarization states and $|\omega\rangle$ is the frequency
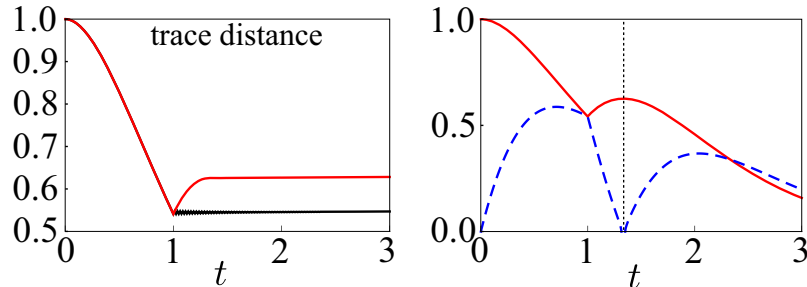
Figure 5.5: (Color online.) The left panel shows the time evolution of the trace distance of directly decoupling at $t = 1$ by applying a sequence of unitary operations on the plant in a short time interval, or a delay decoupling after applying $\hat{\sigma}_z \otimes \hat{I}_c$ in the atom-cavity example; the right panel shows that the maximal recovering is achieved when the atom and cavity mode are disentangled [solid curve is the trace distance (same as left panel) and the dashed curve is the concurrence for the atom-cavity entanglement].

eigenstate. In the experiment, the intial polarization state $|\phi\rangle = (|H\rangle \pm |V\rangle)/\sqrt{2}$ and the bath state $|\chi\rangle = \int d\omega\, g(\omega)|\omega\rangle$. After evolving for duration t, the joint state is $\hat{U}(t)|\phi\rangle \otimes |\chi\rangle$ which forms an entangled state:

$$\frac{1}{\sqrt{2}} \int d\omega\, g(\omega)(e^{in_H \omega t}|H\rangle \pm e^{in_V \omega t}|V\rangle) \otimes |\omega\rangle. \tag{5.12}$$

If we trace out the bath state $|\omega\rangle$, the polarization state starts decohering and its dynamics depends on the actual form of $g(\omega)$. By controlling $g(\omega)$, the time evolution of the trace distance can either monotonically decrease or oscillate. This was claimed to be the signature of switching between the Markovian and the non-Markovian regime in Ref. [5]. Interestingly, if we apply the unitary operation $\hat{\sigma}_x \otimes \hat{I}_\omega$ on the polarization at t and let it evolve for another time t, the final state is given by $\hat{U}(t)(\hat{\sigma}_x \otimes \hat{I}_\omega)\hat{U}(t)|\phi\rangle \otimes |\chi\rangle$ which is equal to

$$|\phi\rangle \otimes \int d\omega\, g(\omega)e^{i(n_H + n_V)\omega t}|\omega\rangle. \tag{5.13}$$

It is a separable state and the polarization state returns to its initial value $|\phi\rangle$, independent of the actual form of $g(\omega)$. This indicates that the dynamics is indeed non-Markovian regardless of the initial state of the bath, otherwise we would not recover the plant initial state at later times after applying the local unitary operation.

   Dynamical recoverin—the increase of quantum coherence, when the plant is perturbed with local unitary operations, can be important for quantum-information processing. This allows us to recover information concerning the plant that is stored in the bath, which we can call dynamical recovering. More importantly, by combining local operations with the dynamical decoupling protocols [6–8], we can characterize the bath dynamics by studying the maximal amount of information that we can recover at any given moment, which can help us find the optimal strategies for maintaining quantum

coherence. Take the atom-cavity system for example, in the left panel of Fig. 5.5, we show the time evolution of the trace distance for two different dynamical decoupling procedures—the first one is a direct decoupling at $t = 1$ while the second one is a delayed decoupling after a local operation at $t = 1$. The maximal difference in the trace distance not only can tell us the memory time scale of the bath but also information about the plant-bath entanglement dynamics. Indeed, we find that in this atom-cavity case, the maximal difference is achieved when the atom becomes disentangled with the cavity mode as shown in right panel of Fig. 5.5. In general, starting from any time t in the evolution, there should exist an optimal sequence of local operations on the plant for maximally recovering its information, which critically depends on the details of the plant-bath interaction.

Operationally, one can also define a measure for non-Markovianity based on such dynamical recovering. We introduce the set of plant state pairs with the initial trace distance D that is equal to 1: $\mathcal{M} = \{\{\hat{\rho}_1(0), \hat{\rho}_2(0)\}, \forall D\{\hat{\rho}_1(0), \hat{\rho}_2(0)\} = 1\}$. Suppose at moment t, $D\{\hat{\rho}_1(t), \hat{\rho}_2(t)\} = \alpha < 1$, the measure is:

$$\mathcal{N}_\alpha = \max_{\forall \tau, U_\tau} \frac{D\{\hat{\Phi}_{U_\tau}\hat{\rho}_1(t), \hat{\Phi}_{U_\tau}\hat{\rho}_2(t)\} - \alpha}{1 - \alpha}, \qquad (5.14)$$

where $\hat{\Phi}_{U_\tau}\hat{\rho}(t) \equiv \mathrm{Tr}_b[\hat{U}_p(\tau) \otimes \hat{I}_b \, \hat{\rho}_{pb}(t)\hat{U}_p^\dagger(\tau) \otimes \hat{I}_b]$ is a sequence of unitary maps for the plant from t to $t + \tau$. Obviously for Markovian systems $\mathcal{N}$ is equal to 0, and for the non-Markovian systems in which the plant can recover its initial states via local operations, the measure is equal to 1. In general, $\mathcal{N}_\alpha$ ranges between 0 and 1 depending on how strong the bath memory is, and also the moment t at which we start to apply unitary operations.

Experimental test—this new criterion can be tested experimentally, e.g. using the existing setup of Liu *et al.* [5]. The first step is the same as the one outlined by Breuer *et al.* [3]—one needs to carry out state tomography of the plant to measure the trace distance as a function of time. If there is an increase of trace distance, one can assert that the dynamics is non-Markovian by using the criterions of Breuer *et al.* However, if the trace distance decreases monotonically, one will need to take the next step by applying different unitary operations onto the plant at different times, and then repeat the tomography procedure to see whether the trace distance increases.

5.3 Conclusion

We have presented a new criterion for the existence of non-Markovianity in general open quantum systems—the non-Markovianity manifests in terms of non-local change in the dynamical map after applying local unitary operations on the plant. With this criterion, we can tell whether a time-local positive map is only an artifact of a special initial quantum state of the plant-bath system or not, and we have used the analytical solvable atom-cavity model and a recent experimental scheme to illustrate this point. This work, on the one hand, helps clarify some subtleties of non-Markovianity

in open quantum systems; on the other hand, it sheds light on designing appropriate non-Markovian baths for enhancing coherence in quantum information processing.

Acknowledgements.

Bibliography

[1] H. P. Breuer and F. Petruccione, *The Theory of Open Quantum Systems*, Oxford University Press, Oxford (2007).

[2] M. M. Wolf *et al.*, Phys. Rev. Letter. **101**, 150402 (2008).

[3] H. P. Breuer, E. M. Laine, and J. Piilo, Phys. Rev. Lett. **103**, 210401 (2009).

[4] A. Rivas, S. F. Huelga, and M. B. Plenio, Phys. Rev. Lett. **105**, 050403 (2010).

[5] B. H. Liu *et al.*, Nature Phys. (Advanced online publication) (2011).

[6] L. Viola, E. Knill, and S. Lloyd, Phys. Rev. Lett. **82**, 2417 (1999).

[7] M. J. Biercuk *et al.*, Nature **458**, 996 (2009).

[8] G. de Lange *et al.*, Science **330**, 60 (2010).

[9] P. Haikka, J. D. Cresser, and S. Maniscalco, Phys. Rev. A **83**, 012112 (2011).

[10] D. Chruściński, A. Kossakowski, and Á Rivas, Phys. Rev. A **83**, 052128 (2011).

[11] V. Gorini, A. Kossakowski, and E. Sudarshan, J. Math. Phys. **17**, 821 (1976).

[12] H. P. Breuer, Phys. Rev. A **70**, 012106 (2004).

[13] C. W. Gardiner, *Quantum Noise*, Springer-Verlag, Berlin, (1991).

[14] H. Yang, H. Miao, and Y. Chen, arXiv:1108.0963 [quant-ph] (2011).

Chapter 6

Quantum back-action in measurements of zero-point mechanical oscillations

Measurement-induced back action, a direct consequence of the Heisenberg uncertainty principle, is the defining feature of quantum measurements. We use quantum measurement theory to analyze the recent experiment of Safavi-Naeini *et al.* [Phys. Rev. Lett. **108**, 033602 (2012)], and show that results of this experiment not only characterize the zero-point fluctuation of a near-ground-state nanomechanical oscillator, but also demonstrate the existence of quantum back-action noise — through correlations that exist between sensing noise and back-action noise. These correlations arise from the quantum coherence between the mechanical oscillator and the measuring device, which build up during the measurement process, and are key to improving sensitivities beyond the Standard Quantum Limit.

6.1 Introduction

Quantum mechanics dictates that no matter or field can stay absolutely at rest, even at the ground state, for which energy is at minimum. A starting point for deducing this inevitable fluctuation is to write down the Heisenberg uncertainty principle

$$[\hat{x}, \hat{p}] = i\,\hbar\,, \tag{6.1}$$

which leads to:

$$\Delta x \cdot \Delta p \geq \hbar/2 \,. \tag{6.2}$$

Here $\hat{x}$ and $\hat{p}$ are the position and momentum operators, while Δx and Δp are standard deviations of position and momentum for an arbitrary quantum state. Eq. (6.2) means we cannot specify the position and momentum of a harmonic oscillator simultaneously, as a point in a classical phase space — the oscillator must at least occupy $\hbar/2$ area in the phase space. If the oscillator has mass of m and eigenfrequency of ω_m, then in the Heisenberg picture we can write

$$[\hat{x}_q(t), \, \hat{x}_q(t')] = \frac{i\hbar \sin \omega_m(t' - t)}{m\omega_m} \,, \tag{6.3}$$

which leads to:

$$\Delta x_q(t) \cdot \Delta x_q(t') \geq \frac{\hbar|\sin \omega_m(t' - t)|}{2m\omega_m} \,. \tag{6.4}$$

with $\hat{x}_q(t)$ the Heisenberg operator of the oscillator's position, quantum-mechanically evolving under the free Hamiltonian. Here $\Delta x_q(t)$ is the standard deviation of $\hat{x}_q(t)$ for an arbitrary quantum state. Eq. (6.4) means the position of a freely evolving quantum harmonic oscillator cannot continuously assume precise values, but instead, must fluctuate. This fluctuation carries the zero-point mechanical energy of $\hbar\omega_m/2$.

As a key feature of quantum mechanics, zero-point fluctuation of displacement is an important effect to verify when we bring macroscopic mechanical degrees of freedom into their ground states [1–8]. Needless to say, a continuous observation of the zero-point fluctuation of a macroscopic mechanical oscillator requires superb displacement sensitivity.

However, what constitutes an "observation of the quantum zero-point fluctuation" is conceptually subtle. Eqs. (6.3) and (6.4), which argue for the inevitability of the zero-point fluctuation, also dictate that the "exact amount" of the zero-point fluctuation cannot be determined precisely. More specifically, if we use a linear measurement device to probe the zero-point fluctuation, which has an output field of $\hat{y}(t)$, then we must at least have

$$[\hat{y}(t), \, \hat{y}(t')] = 0 \tag{6.5}$$

at all times, in order for y to be able to represent experimental data — with measurement noise simply due to the projection of the device's quantum state into simultaneous eigenstates of all $\{\hat{y}(t) : \, t \in \mathbb{R}\}$. This means $\hat{y}$ must be written as

$$\hat{y}(t) = \hat{\epsilon}(t) + \hat{x}_q(t) \tag{6.6}$$

with non-vanishing additional noise (error) $\hat{\epsilon}(t)$, which consists of degrees of freedom of the mea-

surement device and compensates the non-vanishing commutator of $\hat{x}_q{}^3$. In addition, during the measurement process, actual evolution of the mechanical displacement $\hat{x}$ must differ from its free evolution $\hat{x}_q$. This is because

$$\frac{[\hat{x}(t), \hat{x}(t')]}{i\hbar} \equiv \chi(t' - t) \tag{6.7}$$

is also the classical response function of x to an external force: any device that attempts to measure $\hat{x}$ by coupling it with an external observable $\hat{F}$, e.g., by adding a term proportional to $\hat{x}\hat{F}$ into the Hamiltonian, will have to cause non-zero disturbance. For this reason, we can expand the measurement error $\hat{\epsilon}$ into two parts: $\hat{z}$ — the sensing noise that is independent of mechanical motion, and $\hat{x}_{\mathrm{BA}}$ — additional disturbance to the mechanical motion from the measurement-induced back-action, and rewrite $\hat{y}(t)$ as:

$$\hat{y}(t) = \underbrace{\hat{z}(t) + \hat{x}_{\mathrm{BA}}(t)}_{\hat{\epsilon}(t)} + \hat{x}_q(t) = \hat{z}(t) + \hat{x}(t). \tag{6.8}$$

The mechanical displacement under measurement is therefore a sum of the freely-evolving operator $\hat{x}_q$ plus the disturbance $\hat{x}_{\mathrm{BA}}$ due to back action noise, namely, $\hat{x}(t) = \hat{x}_q(t) + \hat{x}_{\mathrm{BA}}(t)$.

The above lines of reasoning lies very much at the heart of linear quantum measurement theory, pioneered by Braginsky in the late 1960s and aimed at describing resonant-bar gravitational-wave detectors [11, 12], and later adapted to the analysis of laser interferometer gravitational-wave detectors by Caves [13]. A key concept in linear quantum measurement theory is the trade-off between sensing noise and back-action noise, which gives rise to the so-called Standard Quantum Limit (SQL). For optomechanical devices, sensing noise takes the form of quantum shot noise due to discreteness of photons, while the quantum back action is enforced by quantum fluctuations in the radiation pressure acting on the mechanical oscillators [13], which is therefore also called quantum radiation-pressure noise. It has been shown that the SQL, although not a strict limit for sensitivity, can only be surpassed by carefully designed linear measurement devices which take advantage of quantum correlations between the sensing noise and the back-action noise.

Observing signatures of quantum back-action, achieving and surpassing the associated SQL in mechanical systems are of great importance for the future of quantum-limited metrology, e.g., gravitational-wave detection [14–22]. At the moment, it is still experimentally challenging to directly observe quantum radiation-pressure noise in optomechanical devices due to high levels of environmental thermal fluctuations, and significant efforts are being made [4–8, 23]. One approach proposed by Verlot *et al.* [4] is, instead, to probe the quantum correlation between the shot noise and the radiation-pressure noise, which, in principle, is totally immune to thermal fluctuations.

---

[3]We note that Ozawa has developed a different formalism to quantify the issues that arise when attempts are made to measure non-commuting observables like $\hat{x}_q(t)$ [9, 10]. However, we have chosen to adopt the Braginsky-Khalili approach [11], because it is immediately applicable when the non-commuting observable is acting as a probe for an external classical force.

In this article, we analyze a recent experiment performed by Safavi-Naeini *et al.* [24], in which a radiation-pressure-cooled nanomechanical oscillator and a movable mirror of a high-finesse cavity is probed by a second beam of light, which is detuned from the cavity, for its zero-point mechanical oscillation. The out-going power spectrum of the second beam, near the mechanical resonant frequency, serves as an indicator of the oscillator's zero-point motion. It was experimentally observed that when the second beam is detuned on opposite sides to the cavity resonance, the out-going power spectra turn out to be different. Using theory of linear quantum measurements, we will show that this experiment not only probes the zero-point fluctuation of the mechanical oscillator at nearly ground state, but also illustrates vividly the non-trivial correlations between sensing noise and back-action noise — a much sought-after effect in the gravitational-wave-detection community. We further argue that what Ref. [24] observed is generic for attempts to measure the zero-point fluctuation: as soon as one tries to directly probe quantum zero-point fluctuation, that experiment will automatically introduce back-action noise, whose correlation with the sensing noise may give rise to an additional noise contribution at a similar level to the zero-point fluctuation of the oscillator. In the experiment reported by Ref. [24], this contribution is equal to the oscillator's zero-point fluctuation for one detuning of the readout beam, and exactly opposite for the other detuning. In addition, we will discuss quantum measurement devices that use a near-ground-state mechanical oscillator as a probe for an external classical force near its resonant frequency. We will focus on limitations imposed by the mechanical oscillator's zero-point fluctuation.

The outline of this article goes as follows: in Sec. 6.2, we will give a brief overview of the experiment by Safavi-Naeini *et al.*, and present an analysis of this experiment using quantum measurement theory; in Sec. 6.3, we will more broadly discuss the nature of mechanical zero-point fluctuation, show that in attempts to measure the zero-point fluctuation the contributions from sensing–back-action noise correlations can generically be comparable to the zero-point fluctuation itself, and discuss the connection between zero-point fluctuation and the SQL; we will conclude in Sec. 6.4.

6.2 A two-beam experiment that measures zero-point mechanical oscillation

In this section, we describe in Sec. 6.2.1 the experiment performed by Safavi-Naeini *et al.* reported in Ref. [24], put its results into the framework of linear quantum measurement theory in Sec. 6.2.2, and provide a detailed analysis in Sec. 6.2.3. In Sec. 6.2.4, we will comment on the connection between this viewpoint from quantum measurement and the scattering picture presented in Ref. [24].

6.2.1 Experimental setup and results

In the experiment, two spatial optical modes are coupled to a mechanical vibrational mode in a patterned silicon nanobeam. One spatial mode — the cooling mode — is pumped with a relatively high power at a "red" detuning (lower than resonance), and is used to cool the mechanical mode via radiation pressure damping [2]; the other cavity mode — the readout mode — has a much lower pumping power and is used for probing the mechanical motion. The readout laser frequency ω_{lr} is detuned from the resonant frequency ω_r of the readout mode by either $+\omega_m$ or $-\omega_m$. The observed spectrum of the readout laser is asymmetric with respect to the detuning $\Delta \equiv \omega_r - \omega_{lr}$. Specifically, in the positive-detuning case — $\Delta = \omega_m$, the spectrum has a smaller amplitude than that in the negative-detuning case. The area I_+ enclosed by the spectrum in the positive-detuning case, *after subtracting out the noise floor away from the mechanical resonant frequency*, is proportional to the thermal occupation number $\langle n \rangle$ of the mechanical oscillator, while, in the negative-detuning case, the enclosed area is $I_- \propto \langle n \rangle + 1$. Such asymmetry is illustrated in Fig. 6.1. In Ref. [24], we introduced the following figure of merit to quantify the asymmetry:

$$\eta \equiv \frac{I_-}{I_+} - 1 = \frac{1}{\langle n \rangle}. \tag{6.9}$$

We interpreted this asymmetry as arising from quantized motion of the mechanical oscillator-phonon, and is related to the difference between the rate of phonon absorption from the oscillator, proportional to $\langle n \rangle$, and phonon emission rate, proportional to $\langle n \rangle + 1$. It has been used for calibrating the thermal excitation of the vibrational mode of ions or cold atoms in electrical/optical traps [25–28]. If we view the measurement process as scattering between photons and phonons, the underlying physics is similar to the Raman scattering, e.g., in the spectroscopic analysis of crystals [29, 30]. The absorption of a phonon from the mechanical oscillator at frequency ω_m is associated with up-conversion of a pumping photon at ω_{lr} to a higher-frequency photon at $\omega_{lr} + \omega_m$ due to energy conservation — the so-called the anti-Stokes process; while the emission of a phonon into the mechanical oscillator is associated with down-conversion of a pumping photon to a lower-frequency photon at $\omega_{lr} - \omega_m$ —
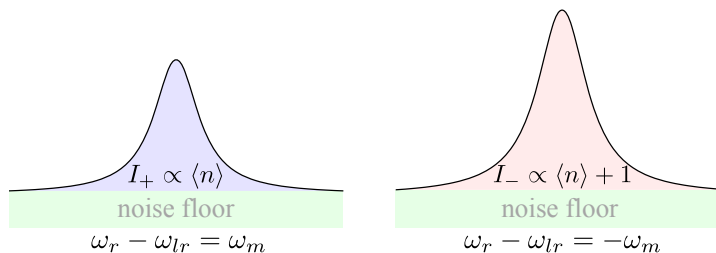
Figure 6.1: Figure illustrating the observed spectra of the readout laser in the positive-detuning case (left) and the negative-detuning case (right).

Figure 6.2: Figure illustrating the relation among different parts of the optomechanical system in the experiment. The thermal heat bath and the cooling mode together create an effective quantum heat bath for the mechanical oscillator which in turn couples to the readout mode.

the Stokes process. To probe the rates of these two processes from which we can infer $\langle n \rangle$, we need to take a photon-counting-type measurement to detect the emission spectra of (anti-)Stokes photons. However, in the experiment, we instead used the heterodyne scheme to measure the amplitude quadrature of the readout mode, which is the most convenient to realize with the setup that we had. Interestingly, by choosing the detuning $\Delta = \pm\omega_m$ and in the resolved-sideband regime, spectra of the amplitude quadrature are equal to emission spectra of the (anti-)Stokes photons plus a constant noise floor due to vacuum fluctuation of the light — the shot noise. We will elaborate on this point in Sec. 6.2.4 and show explicitly such a connection. Intuitively, one can view the cavity mode as an optical filter to selectively measure the emission spectra — for $\Delta = \omega_m$, the anti-Stokes process is significantly enhanced as the emitted photon is on resonance with respect to the cavity mode, and one therefore measures the spectrum for the anti-Stoke photons; while for $\Delta = -\omega_m$, the spectrum of the Stokes photon is measured.

6.2.2 Interpretation in terms of quantum measurement

Here we provide an alternative viewpoint to Ref. [24], but emphasizing more on the role of quantum back-action and its relation to quantization of the mechanical oscillator. First of all, we separate the experimental system into two parts. The cooling mode, the mechanical oscillator, and the environmental thermal bath the oscillator couples to (the left and middle boxes in Fig. 6.2) together is the first part, which can be viewed as providing an *effective mechanical oscillator* nearly at the ground state, but with a quality factor significantly lower than the intrinsic quality factor of the mechanical mode. It is the zero-point fluctuation of this effective oscillator that we shall be probing. The second part of the system consists of the readout mode (the box on the right of Fig. 6.2), which couples to the effective oscillator (the first part of the system) through displacement $\hat{x}$ alone. The second part provides us with an output $\hat{y}$, which contains information about the zero-point fluctuation of the effective mechanical oscillator.

6.2.2.1 The mechanical oscillator near ground state

Let us focus on the first part of the system (left two boxes of Fig. 6.2), the effective mechanical oscillator (because this will be a stand-alone subject of study in later discussions, we shall often ignore the word "effective"). The environmental heat bath and the cooling mode together form

a *quantum* heat bath with fluctuation close to the zero-point value. In steady state, the "free" mechanical displacement is determined by its coupling to this bath ("free" means in absence of the readout mode):

$$\hat{x}_q(t) = \int_{-\infty}^{t} \chi(t - t')\hat{F}_q(t')\mathrm{d}t' \,.$$

(6.10)

Here χ is the response function of the mechanical oscillator:

$$\chi(t - t') = -\frac{[\hat{x}(t), \hat{x}(t')]}{i\hbar} = e^{-\kappa_m |t-t'|/2}\frac{\sin \omega_m(t - t')}{m\omega_m} \,.$$

(6.11)

Note that we have an additional decay factor compared with Eq. (6.3), which describes an *idealized* free oscillator. The decay rate κ_m here is determined jointly by the intrinsic decay rate of the mechanical mode, and the optomechanical interaction between the mechanical mode and the cooling optical mode. The force $\hat{F}_q$ lumps together the fluctuating force acting on the mechanical mode by the environmental heat bath and the cooling mode. If the oscillator approaches the ground state only after applying the cooling mode, then one can show that $\hat{F}_q$ is dominated by fluctuation of the cooling mode.

The above two equations state that for a realistic mechanical oscillator with non-zero decay rate, its zero-point fluctuation in the steady state can be viewed as driven by the quantum heat bath surrounding it. We will returning to this prominent feature of linear quantum systems later in Sec. 6.3.1.

6.2.2.2   The quantum-measurement process

Let us now move on to the second part of the system (right box of Fig. 6.2), in which the readout mode serves as a linear position meter that measures the mechanical displacement. We can rewrite the disturbance $\hat{x}_{\mathrm{BA}}$ in Eq. (6.8) in terms of the back-action force $\hat{F}_{\mathrm{BA}}$ arising from radiation-pressure fluctuation of the readout mode, namely,

$$\hat{x}_{\mathrm{BA}}(t) = \int_{-\infty}^{t} \chi(t - t')\hat{F}_{\mathrm{BA}}(t')\mathrm{d}t' \,,$$

(6.12)

We have assumed that the readout mode does not modify the dynamics of the oscillator, which is a good approximation for the low pumping power used in the experiment. Written in the frequency domain, the readout mode output $\hat{y}$ [cf. Eq.(6.8)] is

$$\hat{y}(\omega) = \hat{z}(\omega) + \chi(\omega)\hat{F}_{\mathrm{BA}}(\omega) + \chi(\omega)\hat{F}_q(\omega).$$

(6.13)

where

$$\chi(\omega) = -\frac{1}{m(\omega^2 - \omega_m^2 + i\kappa_m\omega)}$$

(6.14)

is the Fourier transform of $\Theta(t)\chi(t)$, with Θ the Heaviside function, i.e., the positive half of $\chi(t)$ (even though $\chi(t)$ exists for both $t > 0$ and $t < 0$). The spectral density $S_{yy}(\omega)$ of $\hat{y}$ then reads:

$$S_{yy} = S_{zz} + 2\mathrm{Re}[\chi^* S_{zF}] + |\chi|^2 S_{FF}^{\mathrm{BA}} + |\chi|^2 S_{FF}^q. \tag{6.15}$$

Here these single-sided spectral densities are defined in a symmetrized way (see Appendix 6.4), which guarantees bilinearity for the cross spectrum and positivity for self spectrum; S_{zz} and S_{FF}^{BA} are the sensing-noise and back-action force noise spectrum, respectively; S_{zF} is the cross correlation between $\hat{z}$ and $\hat{F}_{\mathrm{BA}}$; the force spectrum of the effective quantum heat bath made up by the cooling mode and the environmental heat bath is given by

$$S_{FF}^q = (4\langle n \rangle + 2)\hbar m \kappa_m \omega_m, \tag{6.16}$$

and $\langle n \rangle$ is the thermal occupation number.

6.2.2.3 Asymmetry between spectra

Experimentally, it was observed that the output spectra S_{yy} for the two opposite detunings, $\Delta = \pm\omega_m$, are different — given the same thermal occupation number for the oscillator,

$$S_{yy}(\omega)|_{\Delta=-\omega_m} \neq S_{yy}(\omega)|_{\Delta=\omega_m}. \tag{6.17}$$

As we will show in the Section. 6.2.3 (following), when we flip the sign of the detuning Δ of the readout beam, the only term in S_{yy} that changes is S_{zF} — the correlation between the sensing noise and the back-action noise. In fact, according to Eq. (6.34), we have

$$S_{zF}(\omega) \approx -i\hbar\frac{\omega}{\Delta}, \tag{6.18}$$

in the resolved-sideband regime with the cavity bandwidth $\kappa_r \ll \omega_m$, which is the case in the experiment [24]. The asymmetry factor defined in Eq.(6.9) is given by:

$$\eta = \frac{2\int \mathrm{Re}[\chi^*(S_{zF}^- - S_{zF}^+)]\mathrm{d}\omega}{\int \left[|\chi|^2 S_{FF}^q + 2\mathrm{Re}(\chi^* S_{zF}^+)\right]\mathrm{d}\omega} = \frac{1}{\langle n \rangle}. \tag{6.19}$$

Here $S_{zF}^\pm$ is defined by $S_{zF}^\pm \equiv S_{zF}|_{\Delta=\pm\omega_m}$, and in particular around the mechanical resonant frequency ω_m, where $S_{zF}^\pm$ contributes to the above integral,

$$S_{zF}^\pm \approx \mp i\hbar. \tag{6.20}$$

The asymmetry, or effect of quantum correlation S_{zF}, is most prominent when the thermal occupation number approaches zero. Indeed, if we focus on the quantum fluctuation by taking the limit of $\langle n \rangle \to 0$, we obtain

$$\int 2\text{Re}(\chi^* S_{zF}^{\pm})\mathrm{d}\omega = \mp \int |\chi|^2 S_{FF}^q |_{\langle n \rangle = 0}\, \mathrm{d}\omega\,. \tag{6.21}$$

In other words, at the quantum ground state, contribution of the quantum correlation S_{zF} to the readout spectrum S_{yy} has the same magnitude as that of the zero-point fluctuation, while the sign of the correlation term depends on the sign of the detuning of the readout beam. *This means not only has the experiment probed the zero-point fluctuation of the mechanical oscillator, it has also demonstrated non-trivial correlations between sensing noise and back action at the quantum level.*

6.2.3   Detailed theoretical analysis

In this section, we supply a detailed calculation of the quantum dynamics and the output spectrum of the experiment. The dynamics for a typical linear optomechanical device has been studied extensively in the literature [31–33]; however, they have been focusing on the quantum state of the mechanical oscillator in ground-state cooling experiments, instead of treating the optomechanical device as a measurement device. Here we will follow Ref. [34] and derive the corresponding input-output relation — the analysis is the same as the one of quantum noise in a detuned signal-recycling laser interferometer which can be mapped into a detuned cavity [15, 35, 36]. We will focus only on the interaction between the readout cavity mode and the mechanical oscillator — the cooling mode and the thermal heat bath is taken into account by the effective dynamics of the oscillator as mentioned earlier.

The Hamiltonian of our optomechanical system can be written as [31–33]:

$$\hat{\mathcal{H}} = \hbar\omega_r \hat{a}^\dagger \hat{a} + \hat{\mathcal{H}}_{\kappa_r} + \hbar G_0 \hat{x}\hat{a}^\dagger \hat{a} + \frac{\hat{p}^2}{2m} + \frac{1}{2}m\,\omega_m^2 \hat{x}^2 + \hat{\mathcal{H}}_{\kappa_m}\,. \tag{6.22}$$

Here the first two terms describe the cavity mode including its coupling to the external continuum, the third term is the coupling between the cavity mode and the mechanical oscillator, $G_0 = \omega_r/L_c$ is the coupling constant with L_c the cavity length, the rest of the terms describes the dynamics of the effective oscillator (left and middle boxes in Fig. 6.2), with $\hat{\mathcal{H}}_{\kappa_m}$ summarizing the dynamics of the cooling mode and the thermal heat bath, as well as their coupling with the original mechanical oscillator.

In the rotating frame at the laser frequency, the *linearized* equations of motion for the perturbed

part — variation around the steady-state amplitude — read:

$$m(\ddot{\hat{x}} + \kappa_m \dot{\hat{x}} + \omega_m^2 \hat{x}) = \hat{F}_{\mathrm{BA}} + \hat{F}_q, \tag{6.23}$$

$$\dot{\hat{a}} + (\kappa_r/2 + i\Delta)\hat{a} = -i\,\bar{G}_0 \hat{x} + \sqrt{\kappa_r}\,\hat{a}_{\mathrm{in}}, \tag{6.24}$$

where the back-action force $\hat{F}_{\mathrm{BA}}$ is defined as:

$$\hat{F}_{\mathrm{BA}} \equiv -\hbar\,\bar{G}_0(\hat{a} + \hat{a}^\dagger), \tag{6.25}$$

and we introduce $\bar{G}_0 = \bar{a} G_0$ with $\bar{a}$ being the steady-state amplitude of the cavity mode and $\hat{a}_{\mathrm{in}}$ being the annihilation operator of the input vacuum field. The cavity output $\hat{a}_{\mathrm{out}}$ is related to the cavity mode by:

$$\hat{a}_{\mathrm{out}} = -\hat{a}_{\mathrm{in}} + \sqrt{\kappa_r}\,\hat{a}, \tag{6.26}$$

with κ_r the decay rate (the bandwidth) of the readout mode.

In the steady state, these equations of motion can be solved more easily in the frequency domain. Starting from the mechanical displacement, we get

$$\hat{x}(\omega) = \chi(\omega)[\hat{F}_{\mathrm{BA}}(\omega) + \hat{F}_q(\omega)]. \tag{6.27}$$

Here we have ignored modification to the mechanical response function χ due to the readout mode— a term proportional to $\bar{G}_0^2$, assuming that the pumping power is low. For the cavity mode, we invert Eq. (6.24) and obtain

$$\hat{a}(\omega) = \frac{\bar{G}_0\,\hat{x}(\omega) + i\sqrt{\kappa_r}\,\hat{a}_{\mathrm{in}}(\omega)}{\omega - \Delta + i\kappa_r/2}, \tag{6.28}$$

which leads to

$$\hat{F}_{\mathrm{BA}}(\omega) = \frac{2\,\hbar\,\bar{G}_0\sqrt{\kappa_r/2}[(\kappa_r/2 - i\omega)\hat{v}_1 + \Delta\,\hat{v}_2]}{(\omega - \Delta + i\kappa_r/2)(\omega + \Delta + i\kappa_r/2)}, \tag{6.29}$$

with $\hat{v}_1 \equiv (\hat{a}_{\mathrm{in}} + \hat{a}_{\mathrm{in}}^\dagger)/\sqrt{2}$ and $v_2 \equiv (\hat{a}_{\mathrm{in}} - \hat{a}_{\mathrm{in}}^\dagger)/(\sqrt{2}\,i)$ being the amplitude quadrature and the phase quadrature of the input vacuum field. When combining with Eq. (6.26), we obtain the output amplitude quadrature

$$\begin{aligned}
\hat{Y}_1(\omega) &= [\hat{a}_{\mathrm{out}}(\omega) + \hat{a}_{\mathrm{out}}^\dagger(-\omega)]/\sqrt{2} \\
&= \frac{(\Delta^2 - \kappa_r^2/4 - \omega^2)\hat{v}_1 - \kappa_r\Delta\,\hat{v}_2 + \sqrt{2\kappa_r}\,\bar{G}_0\Delta\,\hat{x}}{(\omega - \Delta + i\kappa_r/2)(\omega + \Delta + i\kappa_r/2)},
\end{aligned} \tag{6.30}$$

whose spectrum is measured experimentally. We put the above formula into the same format as Eq.(6.13) by normalizing $\hat{Y}_1$ with respect to the mechanical displacement $\hat{x}$, and introduce $\hat{y}(\omega)$ and

the corresponding sensing noise $\hat{z}(\omega)$:

$$\hat{y}(\omega) = \frac{(\Delta^2 - \kappa_r^2/4 - \omega^2)\hat{v}_1 - \kappa_r\Delta\hat{v}_2}{\sqrt{2\kappa_r}\,\bar{G}_0\Delta} + \hat{x}(\omega)$$

$$\equiv \hat{z}(\omega) + \chi(\omega)[\hat{F}_{\mathrm{BA}}(\omega) + \hat{F}_q(\omega)]\,. \tag{6.31}$$

Taking single-sided symmetrized spectral density of $\hat{y}$ (see Appendix 6.4), we obtain

$$S_{yy}(\omega) = S_{zz} + 2\mathrm{Re}[\chi^* S_{zF}] + |\chi|^2[S_{FF}^{\mathrm{BA}} + S_{FF}^q]\,, \tag{6.32}$$

where

$$S_{zz}(\omega) = \frac{(\Delta^2 - \kappa_r^2/4 - \omega^2)^2 + \kappa_r^2\Delta^2}{2\kappa_r\bar{G}_0^2\Delta^2}\,, \tag{6.33}$$

$$S_{zF}(\omega) = \frac{\hbar(\kappa_r/2 - i\,\omega)}{\Delta}\,, \tag{6.34}$$

$$S_{FF}^{\mathrm{BA}}(\omega) = \frac{2\hbar^2\bar{G}_0^2\kappa_r(\kappa_r^2/4 + \omega^2 + \Delta^2)}{(\Delta^2 - \kappa_r^2/4 - \omega^2)^2 + \kappa_r^2\Delta^2}\cdot f \tag{6.35}$$

Here we have used

$$\langle 0|\hat{v}_j(\omega)\hat{v}_k^\dagger(\omega')|0\rangle_{\mathrm{sym}} = \pi\,\delta_{jk}\,\delta(\omega - \omega')\ (j, k = 1, 2). \tag{6.36}$$

Indeed, only S_{zF} depends on the sign of detuning and contributes to the asymmetry. In the resolved-sideband case $\kappa_r \ll \omega_m$, and choosing detuning $|\Delta| = \omega_m$, S_{zF} can be approximated as the one shown in Eq. (6.18). For a weak readout beam, we can ignore S_{FF}^{BA}, which is proportional to $\bar{G}_0^2$, and the output spectra around ω_m for the positive- and negative-detuning cases can be approximated as

$$S_{yy}(\omega)|_{\Delta=\pm\omega_m} \approx \frac{\kappa_r}{2\bar{G}_0^2} + \frac{\hbar\kappa_m(2\langle n\rangle + 1 \mp 1)}{2m\omega_m[(\omega - \omega_m)^2 + (\kappa_m/2)^2]}\,, \tag{6.37}$$

from which one can easily obtain the dependence of the asymmetry factor η on $\langle n\rangle$ shown in Eq. (6.9).

Interestingly, even if the quantum back-action term S_{FF}^{BA} is much smaller than S_{FF}^q and has been ignored, given the weak readout mode used in the experiment, the asymmetry induced by quantum correlation is always visible as long as $\langle n\rangle$ is small. In addition, any optical loss in the readout mode only contributes a constant background — that is symmetric with respect to detuning — to the overall spectrum; therefore, the asymmetry is very robust against optical loss, and it can be observed without a quantum-limited readout mode, which is the case in the experiment.

6.2.4 Connection with the scattering picture

In the above, we have been emphasizing the viewpoint of position measurement, and interpreting the asymmetry as due to the quantum correlation between the sensing noise and the back-action

noise. Here we would like to show the connection between this viewpoint and the scattering picture in Ref. [24] that focuses on the photon-phonon coupling, and in addition, show how spectra of the amplitude quadrature measured in the experiment are related to emission spectra of the (anti-)Stokes photons that would have been obtained if we instead take a photon-counting measurement.

To illustrate these, we introduce the annihilation operator $\hat{b}$ for the phonon through the standard definition:

$$\hat{x} \equiv \sqrt{\hbar/(2m\omega_m)}(\hat{b} + \hat{b}^\dagger) \,, \tag{6.38}$$

which satisfies the commutator relation: $[\hat{b}, \hat{b}^\dagger] = 1$. In the rotating frame at the laser frequency, the Hamiltonian in Eq. (6.22) after linearization is given by:

$$\hat{\mathcal{H}} = \hbar\Delta\hat{a}^\dagger\hat{a} + \hat{\mathcal{H}}_{\kappa_r} + \hbar\bar{g}_0(\hat{a} + \hat{a}^\dagger)(\hat{b} + \hat{b}^\dagger) + \hbar\omega_m\hat{b}^\dagger\hat{b} + \hat{\mathcal{H}}_{\kappa_m} \,, \tag{6.39}$$

where $\bar{g}_0 \equiv \bar{G}_0\sqrt{\hbar/(2m\omega_m)}$. The third term is the photon-phonon coupling: $\hat{a}^\dagger\hat{b}$ describes the anti-Stokes process — the absorption of a phonon is accompanied by emission of a higher-frequency photon; and $\hat{a}^\dagger\hat{b}^\dagger$ describes the Stokes process — the emission of a phonon is accompanied by emission of a lower-frequency photon. The photon emission rate of these two processes can be estimated by using the *Fermi's golden rule*. Specifically, taking into account the finite bandwidth for the photon and phonon due to coupling to the continuum, the emission rate of the anti-Stokes photon at $\omega_{lr} + \omega$ reads

$$\begin{aligned}
\Gamma_{AS}(\omega) &= \bar{g}_0^2 \int \mathrm{d}\tau\, e^{i\omega\tau}\mathcal{D}(\omega)\langle\hat{b}^\dagger(\tau)\hat{b}(0)\rangle \\
&= \frac{\bar{g}_0^2\kappa_m\langle n\rangle\mathcal{D}(\omega)}{(\omega - \omega_m)^2 + (\kappa_m/2)^2} \,;
\end{aligned} \tag{6.40}$$

and the emission rate of the Stokes photon at $\omega_{lr} - \omega$ reads

$$\begin{aligned}
\Gamma_S(\omega) &= \bar{g}_0^2 \int \mathrm{d}\tau\, e^{-i\omega\tau}\mathcal{D}(-\omega)\langle\hat{b}(\tau)\hat{b}^\dagger(0)\rangle \\
&= \frac{\bar{g}_0^2\kappa_m(\langle n\rangle + 1)\mathcal{D}(-\omega)}{(\omega - \omega_m)^2 + (\kappa_m/2)^2} \,.
\end{aligned} \tag{6.41}$$

Here the density of state for the photons is determined by the cavity decay rate and detuning:

$$\mathcal{D}(\omega) \equiv \frac{\kappa_r/2}{(\omega - \Delta)^2 + (\kappa_r/2)^2} \,. \tag{6.42}$$

Were the cavity bandwidth much larger than the mechanical frequency ω_m, the density of state $\mathcal{D}(\omega)$ would become flat for frequencies around $\pm\omega_m$, and we would effectively have a scenario that is similar to the free-space Raman scattering as in the spectroscopic measurements of crystals [30]. By making a photon-counting-type measurement of the emitted (anti-)Stokes photons, one could

observe an asymmetric spectrum with two peaks (sidebands) around $\omega_r \pm \omega_m$ of which the profiles are given by the above emission rates.

The situation of our experiment is however different from the usual free-space Raman scattering spectroscopic measurement in the following two aspects: (i) *We are operating in the resolved-sideband regime* where the cavity bandwidth is much smaller than the mechanical frequency and the photon density of state is highly asymmetric for positive and negative sideband frequencies depending on the detuning. This basically dictates that we cannot measure two sidebands simultaneously, and we have to take two separate spectra by tuning the laser frequency. In the positive-detuning case $\Delta = \omega_m$, the anti-Stokes sideband is enhanced while the Stokes sideband is highly suppressed, as the photon density of state is peak around $\omega = \omega_m$; while in the negative-detuning case $\Delta = -\omega_m$, the situation for these two sidebands swaps. (ii) *We are using heterodyne detection scheme instead of photon counting*, where the outgoing field is mixed with a large coherent optical field (reference light) before the photodetector, to measure the output amplitude quadrature. On the one hand, this validates the picture of linear position measurement discussed in the previous sections. On the other hand, this introduces a noise floor due to vacuum fluctuation of the amplitude quadrature. Only by subtracting this noise floor, can we recover the emission spectra obtained by taking a photon-counting measurement. To illustrate this, we use the fact that

$$[\hat{Y}_1(\omega),\, \hat{Y}_1^\dagger(\omega')] = 0 \tag{6.43}$$

which is a direct consequence of $[\hat{y}(t),\, \hat{y}(t')] = 0$ ($\hat{y}$ is equal to $\hat{Y}_1$ normalized with respect to the mechanical displacement [cf. Eq. (6.31)]), and we have

$$\begin{aligned}
\langle \hat{Y}_1(\omega)\hat{Y}_1^\dagger(\omega')\rangle_{\text{sym}} &= \langle \hat{Y}_1^\dagger(\omega')\hat{Y}_1(\omega)\rangle \\
&= \frac{1}{2}[\langle \hat{a}_{\text{out}}(-\omega')\hat{a}_{\text{out}}^\dagger(-\omega)\rangle + \langle \hat{a}_{\text{out}}^\dagger(\omega')\hat{a}_{\text{out}}(\omega)\rangle].
\end{aligned} \tag{6.44}$$

This allows us to relate the output spectrum of the amplitude quadrature to the emission spectrum. Taking the positive-detuning case, $\Delta = \omega_m$ for instance, $\hat{a}_{\text{out}}(-\omega)$ contains mostly vacuum and negligible sideband signal due to suppression of the Stokes sideband around $\omega_{lr} - \omega_m$ by the cavity, namely, $\langle \hat{a}_{\text{out}}(-\omega')\hat{a}_{\text{out}}^\dagger(-\omega)\rangle \approx 2\pi\,\delta(\omega - \omega')$. Since the second term gives the emission spectrum for the output photons, the single-sided spectral density of the output amplitude quadrature reads:

$$S_{YY}(\omega) = 1 + 2\Gamma_{\text{out}}(\omega) \approx 1 + 2\Gamma_{\text{AS}}(\omega), \tag{6.45}$$

where we have used the fact that, given weak pumping power for the readout mode, $\Gamma_{\text{out}} = 1/[(2/\kappa_r) + (1/\Gamma_{\text{AS}})] \approx \Gamma_{\text{AS}}$. By normalizing the spectrum with respect to the mechanical dis-

placement, we have

$$S_{yy}(\omega)|_{\Delta=\omega_m} = \frac{\kappa_r}{2\bar{G}_0^2}[1 + 2\Gamma_{\text{AS}}(\omega)].\tag{6.46}$$

Similarly, by following the same line of thought, we get

$$S_{yy}(\omega)|_{\Delta=-\omega_m} = \frac{\kappa_r}{2\bar{G}_0^2}[1 + 2\Gamma_{\text{S}}(\omega)].\tag{6.47}$$

The above two equations give identical results to Eq. (6.37). We therefore make a direct connection between the spectra of amplitude quadrature measured in the experiment and the photon emission spectra that is obtained if making photon-counting measurements.

6.3 General linear measurements of the zero-point fluctuation

Based on the analysis of the specific experiment of Ref. [24] in the previous section, here we comment on the general features of linear quantum measurements including measuring zero-point fluctuation of a mechanical oscillator. We start by discussing the nature of the zero-point mechanical fluctuation in Sec. 6.3.1, proceed to discussion of measurements of it in Sec. 6.3.2, and finally end in Sec. 6.3.3 which discusses its effect on sensitivity for measuring external forces and the connection to the SQL.

6.3.1 The nature of zero-point mechanical fluctuation

First of all, let us take a closer look at the nature of the zero-point fluctuation of a realistic harmonic oscillator, which consists of a mechanical mode with eigenfrequency ω_m and finite decay rate κ_m. Suppose we initially decouple the oscillator from its environmental heat bath and turn on the coupling at $t = 0$. In the Heinserberg picture, the position and momentum of the oscillator at $t > 0$ will be

$$\hat{x}_q(t) = \hat{x}_{\text{free}}(t) + \int_0^t \chi(t - t')\hat{F}_q(t')\mathrm{d}t',\tag{6.48a}$$

$$\hat{p}_q(t) = \hat{p}_{\text{free}}(t) + m\int_0^t \partial_t\chi(t - t')\hat{F}_q(t')\mathrm{d}t',\tag{6.48b}$$

where

$$\hat{x}_{\text{free}}(t) = e^{-\kappa_m t/2}\left[\hat{x}(0)\cos\omega_m t + \frac{\hat{p}(0)}{m\omega_m}\sin\omega_m t\right],\tag{6.49a}$$

$$\frac{\hat{p}_{\text{free}}(t)}{m\omega_m} = e^{-\kappa_m t/2}\left[-\hat{x}(0)\sin\omega_m t + \frac{\hat{p}(0)}{m\omega_m}\cos\omega_m t\right]$$
$$- \frac{m\kappa_m}{2}\hat{x}_{\text{free}}(t),\tag{6.49b}$$

are contributions from the free evolution of the initial Schrödingier operators (i.e., undisturbed by the environment), which decay over time, and get replaced by contributions from the environmental heat bath [integrals on the right-hand side of Eqs. (6.48a) and (6.48b)]. Note that for any oscillator with non-zero decay rate, it is essential to have bath operators entering over time, otherwise the commutation relation between position and momentum:

$$[\hat{x}_q(t),\, \hat{p}_q(t)] = i\,\hbar \tag{6.50}$$

will not hold at $t > 0$ because of

$$[\hat{x}_{\text{free}}(t),\, \hat{p}_{\text{free}}(t)] = i\,\hbar\, e^{-\kappa_m t}\,. \tag{6.51}$$

This dictates that the heat bath must be such that the additional commutator from terms containing $\hat{F}_q$ exactly compensate for the decay in Eq. (6.51), which leads to the quantum fluctuation-dissipation theorem (see e.g., Ref. [37]).

It is interesting to note that this "replenishing" of commutators has a classical counterpart, since commutators are after all proportional to the classical Poisson Bracket. More specifically, for a classical oscillator with decay, we can write a similar relation for Poisson Brackets using the position and momentum of the oscillator, plus environmental degrees of freedom. The replenishing of the position-momentum Poisson Bracket by environmental variables, in classical mechanics, can also be viewed as a consequence of the conservation of phase-space volume, following the Liouville theorem. A decaying oscillator's phase-space volume will shrink, and violate the Liouville theorem — unless additional phase-space volume from the environmental degrees of freedom is introduced.

Nevertheless, the definitively quantum feature in our situation is a fundamental scale in the volume of phase space, $\hbar$. Here we note that if $\kappa_m \ll \omega_m$, when reaching the steady state with $\hat{x}_{\text{free}}$ and $\hat{q}_{\text{free}}$ decayed away, we have

$$\Delta x_q \cdot \Delta p_q \approx m\omega_m \int \frac{d\omega}{2\pi} S_{xx}^q(\omega)\,, \tag{6.52}$$

where $S_{xx}^q \equiv |\chi|^2 S_{FF}^q$. Although S_{xx}^q depends on the specific scenario, they are all constrained by a Heisenberg-like relation of,

$$S_{xx}^q(\omega) \geq 2\hbar\, \text{Im}\chi(\omega), \tag{6.53}$$

which is a straightforward consequence of the commutation relation in Eq. (6.11). The equality is achieved at the ground state [3]. This enforces the same Heisenberg uncertainty relation:

$$\Delta x_q \cdot \Delta p_q \geq \hbar/2, \tag{6.54}$$

---

[3] A generalization of this to thermal states will be the fluctuation-dissipation theorem [37].

as an ideal harmonic oscillator whose quantum fluctuations arise "on its own", instead of having to be driven by the surrounding environment. Therefore, in the steady state, the zero-point fluctuation of the mechanical oscillator can be viewed as being imposed by the environment due to linearity of the dynamics.

6.3.2 Measuring the zero-point fluctuation

Having clarified the nature of quantum zero-point fluctuations of a mechanical oscillator in the steady state, let us argue that the effects seen in Ref. [24] are actually generic when one tries to probe such fluctuations, namely: the correlation between sensing and back-action noise can be at the level of the zero-point fluctuation itself.

Let us start our discussion here from Eq. (6.5), namely,

$$[\hat{y}(t),\,\hat{y}(t')] = 0\,, \tag{6.55}$$

and the fact that $\hat{y}$ consists of sensing noise, back-action noise, and finally the zero-point fluctuation of the mechanical oscillator [cf. Eq. (6.8)]:

$$\hat{y}(t) = \frac{\hat{z}(t)}{\alpha} + \alpha \int_{-\infty}^{t} \chi(t-\tau)\hat{F}_{\mathrm{BA}}(\tau)\mathrm{d}\tau + \hat{x}_q(t)\,. \tag{6.56}$$

Here we have added a factor α, which labels the scaling of each term as the measurement strength which is proportional to the square root of the readout beam power. Let us assume that Eq. (6.55) continues to hold for the same set of $\hat{z}$ and $\hat{F}_{\mathrm{BA}}$, for a large set of α and χ: basically the measuring device works for different mechanical oscillators with different measuring strengths.

Since Eq. (6.55) remains valid for all values of α, we extract terms with different powers of scaling, and obtain

$$[\hat{z}(t),\,\hat{z}(t')] = \left[\hat{F}_{\mathrm{BA}}(t),\,\hat{F}_{\mathrm{BA}}(t')\right] = 0\,, \tag{6.57}$$

and

$$\int_{-\infty}^{t'} \chi(t'-\tau)\left[\hat{z}(t),\,\hat{F}_{\mathrm{BA}}(\tau)\right]\mathrm{d}\tau$$
$$-\int_{-\infty}^{t} \chi(t-\tau)\left[\hat{z}(t'),\,\hat{F}_{\mathrm{BA}}(\tau)\right]\mathrm{d}\tau$$
$$+\left[\hat{x}_q(t),\,\hat{x}_q(t')\right] = 0\,, \quad \forall\,t,\,t'\,. \tag{6.58}$$

This becomes

$$\int_{0}^{+\infty} \chi(\tau)\left[C_{zF}(t-\tau) - C_{zF}(-t-\tau)\right]\mathrm{d}\tau = -i\,\hbar\chi(t)\,, \tag{6.59}$$

for all values of t, where we have defined

$$C_{zF}(t' - t) \equiv \left[\hat{z}(t),\, \hat{F}_{\mathrm{BA}}(t')\right]. \tag{6.60}$$

Here the dependence is only through $t' - t$ because the system is time-invariant. We also note that since $\hat{z}$ is an out-going field, C_{zF} must vanish when $t > 0$ — otherwise any generalized force applied on $\hat{z}$ can still affect $\hat{F}$ at a later time [11, 35], which violates the causality. As proved in Appendix. 6.B, in order for Eq. (6.59) to be satisfied for all possible response functions of the oscillator, we must have

$$C_{zF}(t) = -i\,\hbar\delta_-(t), \tag{6.61}$$

where $\delta_-(t)$ is the Dirac delta function with support only for $t < 0$. In other words,

$$[\hat{z}(t),\, \hat{F}_{\mathrm{BA}}(t')] = -i\,\hbar\,\delta_-(t' - t). \tag{6.62}$$

Eq. (6.56), plus the commutation relations in Eqs. (6.57) and (6.62), then provide a general description of linear measuring devices which do not modify the dynamics of the mechanical oscillator — simply from the requirement that the out-going field operators at different times must commute [cf. Eq. (6.55)]. In particular, the non-vanishing commutator $[\hat{x}_q(t),\, \hat{x}_q(t')]$, which underlies the existence of the zero-point fluctuation, is canceled in a simple way by the non-vanishing commutator between the sensing noise and the back-action noise [cf. Eq. (6.62)].

Now turn to the noise content of the output $\hat{y}(t)$:

$$S_{yy} = \frac{S_{zz}}{\alpha^2} + 2\mathrm{Re}[\chi^* S_{zF}] + \alpha^2 S_{FF}^{\mathrm{BA}} + S_{xx}^q. \tag{6.63}$$

Let us consider experiments with relatively low measurement strength, so that the first term S_{zz}/α^2 from the sensing noise dominates the output noise. The next-order terms contain: (i) correlation between the sensing noise and the back-action noise — S_{zF}; and (ii) the mechanical fluctuation — S_{xx}^q. We assume nearly ground state for the mechanical oscillator

$$S_{xx}^q(\omega) \approx 2\hbar\,\mathrm{Im}\chi(\omega), \tag{6.64}$$

which, for $\kappa_m \ll \omega_m$, gives

$$\int \frac{\mathrm{d}\omega}{2\pi} S_{xx}^q(\omega) \approx \frac{\hbar}{2m\omega_m}. \tag{6.65}$$

If $S_{zF}(\omega)$ does not change noticeably within the mechanical bandwidth, then

$$\int \frac{\mathrm{d}\omega}{2\pi} 2\mathrm{Re}[\chi^*(\omega)S_{zF}(\omega)] \approx -\frac{1}{2m\omega_m}\mathrm{Im}S_{zF}(\omega_m)\,. \tag{6.66}$$

Because of Eq. (6.62), the typical magnitude for S_{zF} is naturally

$$|S_{zF}| \sim \hbar\,. \tag{6.67}$$

Therefore, contributions to the output noise from quantum correlation S_{zF} and mechanical fluctuation S_{xx}^q can generically become comparable to each other when the mechanical oscillator is approaching the quantum ground state. The result presented in Ref. [24] therefore illustrates two typical cases of this generic behavior [cf. Eq. (6.20)].

6.3.3 Measuring an external classical force in presence of zero-point fluctuation

Finally, let us discuss the role of zero-point fluctuation in force measurement, when the mechanical oscillator is used as a probe of an external classical force not far away from the mechanical resonant frequency. Because of the commutation relations shown in Eqs. (6.57) and (6.62), a Heisenberg uncertainty relation exists between $\hat{z}$ and $\hat{F}_{\mathrm{BA}}$, which, in terms of the single-sided symmetrized spectrum density, can be written as

$$S_{zz}(\omega)S_{FF}^{\mathrm{BA}}(\omega) - S_{zF}(\omega)S_{Fz}(\omega) \geq \hbar^2\,. \tag{6.68}$$

Note that because of Eq. (6.57), symmetrization is not necessary in the definition of S_{zz} and S_{FF}^{BA}. When the two noises are *not correlated* — $S_{zF} = S_{Fz} = 0$, the above inequality represents a trade-off between sensing noise $\hat{z}$ and back-action noise $\hat{F}_{\mathrm{BA}}$. Correspondingly, the force sensitivity S_F, which is obtained by normalizing the displacement sensitivity S_{yy} with respect to the mechanical response function χ, will have a lower bound:

$$\begin{aligned} S_F(\omega) \equiv \frac{S_{yy}(\omega)}{|\chi(\omega)|^2} &= \frac{S_{zz}(\omega)}{|\chi(\omega)|^2} + S_{FF}^{\mathrm{BA}}(\omega) + S_{FF}^q(\omega) \\ &\geq \frac{2\hbar}{|\chi(\omega)|} + (4\langle n\rangle + 2)\hbar\, m\kappa_m\omega_m\,. \end{aligned} \tag{6.69}$$

If the mechanical oscillator is in its quantum ground state, namely $\langle n\rangle = 0$, we obtain:

$$S_F(\omega) \geq \frac{2\hbar}{|\chi(\omega)|} + 2\hbar\, m\kappa_m\omega_m \equiv S_F^{\mathrm{Qtot}}\,. \tag{6.70}$$
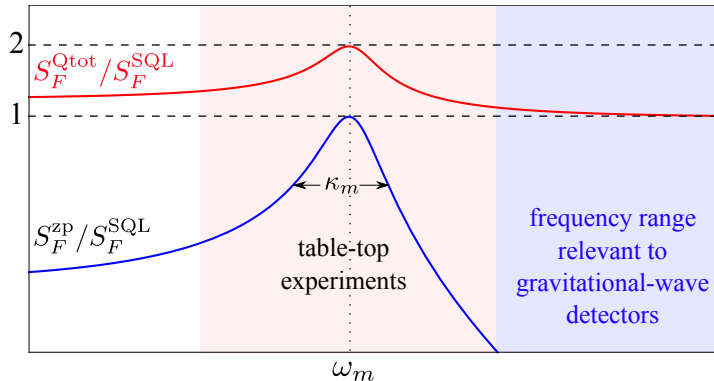
Figure 6.3: (Color online.) Figure illustrating that total quantum limitation S_F^{Qtot} (red) for force sensitivity and contribution from zero-point fluctuation S_F^{zp} (blue). For clarity, we divide both by the SQL and use log-log scale.

The first term is the Standard quantum limit for force sensitivity with mechanical probes [11, 12]:

$$S_F^{\text{SQL}} \equiv \frac{2\hbar}{|\chi(\omega)|} = 2\hbar m \sqrt{(\omega^2 - \omega_m^2)^2 + \kappa_m^2 \omega^2}\,. \tag{6.71}$$

The second term,

$$S_F^{\text{zp}} \equiv 2\hbar\, m\kappa_m\omega_m\,, \tag{6.72}$$

arising from the zero-point fluctuation due to mechanical quantization, also limits the sensitivity. As we can learn from Eqs. (6.68) and (6.69), the SQL S_F^{SQL} can be surpassed, in principle indefinitely, by building up quantum correlations between the sensing noise $\hat{z}$ and the back-action noise $\hat{F}_{\text{BA}}$ — although in practice the beating factor will be limited by the available optical power and the level of optical losses. However, the limit imposed by zero-point fluctuation cannot be surpassed — although can be mitigated by lowering κ_m.

Braginsky *et al.* [38] argued that mechanical quantization does not influence the force sensitivity when measuring a classical force with mechanical probes — one only needs to evaluate the quantum noise due to the readout field. But these authors had specifically pointed out that they were focusing on ideal mechanical probes with infinitely narrow bandwidth ($\kappa_m \to 0$) and observations outside of that frequency band. This corresponds to the situation of free-mass gravitational-wave detectors, in which the mechanical oscillator is the differential mode of four mirror-endowed test masses hung as pendulums with eigenfrequencies around $1\,\text{Hz}$ and very high quality factor, while the detection band is above $10\,\text{Hz}$, well outside the pendulum resonance. Indeed, from Eqs. (6.71) and (6.72), we see that the effect of zero-point fluctuation is only significant not far away from resonance — which confirms Braginsky *et al.*'s result. More specifically, if $\kappa_m \ll \omega_m$, we can write, for $|\omega - \omega_m| \ll \omega_m$,

$$S_F^{\text{SQL}} \approx S_F^{\text{zp}} \sqrt{1 + \left(\frac{\omega - \omega_m}{\kappa_m/2}\right)^2}\,. \tag{6.73}$$
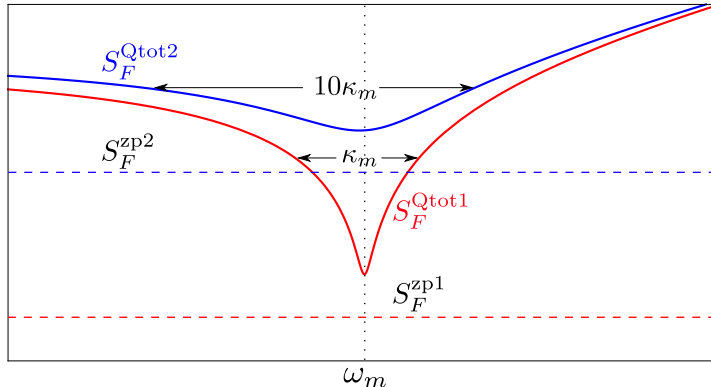
Figure 6.4: (Color online.) Figure illustrating effect of the mechanical decay rate (bandwidth) κ_m on S_F^{Qtot} (solid) and S_F^{zp} (dashed) — the larger the mechanical bandwidth, the lower the force sensitivity (This plot is also in the log-log scale).

In particular, the limit imposed by zero-point fluctuation is equal to SQL on resonance, and becomes less important as $|\omega - \omega_m|$ becomes comparable to or larger than the half bandwidth $\kappa_m/2$, as illustrated in Fig. 6.3.

Although the above relative comparison between the SQL and zero-point fluctuation indicates that the later plays a more important role near the oscillator's resonant frequency, it is straightforward to see from Eqs. (6.71) and (6.72) that on an absolute scale: (i) for a given oscillator at ground state, $S_F^{\text{SQL}}(\omega)$ is lower near mechanical resonance, while $S_F^{\text{zp}}(\omega)$ is independent from frequency, and (ii) at any frequency, lowering κ_m, while fixing ω_m and keeping the oscillator at ground state, always results in lower noise, as illustrated in Fig. 6.4. Now suppose we are free to choose from ground-state mechanical oscillators with different ω_m and κ_m as our probe, and that we are always able to reach the SQL at all frequencies, then: (i) if we know the frequency content of target signals, we should choose probes that are more resonant with the target, and (ii) regardless of signal frequency, we should always use probes with lower κ_m, or equivalently, higher mechanical quality factor.

6.4 Conclusion

We have shown, within the framework of quantum measurement theory, that the asymmetry in output spectra observed by Safavi-Naeini *et al.* can be explained as due to the quantum correlation between the sensing noise and the quantum back-action noise; this experiment therefore provides a clear signature of quantum back-action onto mechanical systems.

More broadly, we have shown that having quantum-noise correlations showing up at the same level as the zero-point fluctuations is a generic feature of measurements that attempt to measure the zero-point fluctuation. We have further shown that when an experimentally prepared ground-state mechanical oscillator is used as probe for classical forces near its resonant frequency, its mechani-

cal quantization — through zero-point displacement fluctuation — does impose an addition noise background. This additional noise does vanish when the oscillator's bandwidth approaches zero, i.e., when the oscillator becomes ideal.

Acknowledgements

6.A   Symmetrized cross spectral density

In this article, as in Ref. [14], we use the *single-sided* symmetrized cross spectral density, which, given a quantum state $|\psi\rangle$, is defined between a pair of operators $\hat{A}$ and $\hat{B}$ as:

$$S_{AB}(\omega)\delta(\omega - \omega') \equiv \frac{1}{\pi}\langle\psi|\hat{A}(\omega)\hat{B}^{\dagger}(\omega')|\psi\rangle_{\text{sym}}$$
$$= \frac{1}{2\pi}\langle\psi|\hat{A}(\omega)\hat{B}^{\dagger}(\omega') + \hat{B}^{\dagger}(\omega')\hat{A}(\omega)|\psi\rangle. \tag{6.74}$$

The symmetrization process here allows us to preserves bilinearity of $\tilde{S}$ on its entries, i.e.,

$$S_{A,c_1B+c_2C} = c_1^*S_{AB} + c_2^*S_{AC}, \tag{6.75a}$$

$$S_{c_1A+c_2B,C} = c_1S_{AC} + c_2S_{BC}. \tag{6.75b}$$

More importantly, we can show that

$$S_{AA} > 0 \tag{6.76}$$

for any field $\hat{A}$, even if $\left[\hat{A}(\omega), \hat{A}^{\dagger}(\omega')\right] \neq 0$. The positivity (6.76) allows us to interpret S_{AA} as the fluctuation variance per unit frequency band — as in the classical case.

6.B   Commutation relation between $\hat{z}$ and $\hat{F}$

Defining

$$f(t) \equiv C_{zF}(t) + i\hbar\delta_-(t) \tag{6.77}$$

we convert Eq. (6.59) into

$$\int_0^{+\infty} \chi(\tau) \left[f(t - \tau) - f(-t - \tau) \right] \mathrm{d}\tau = 0 \,. \tag{6.78}$$

Assuming analyticity of the Fourier transform of $f(t)$, it must be written as

$$\tilde{f}(\omega) = \sum_k \frac{f_k}{\omega - \omega_k} \tag{6.79}$$

with ω_k all located on the upper half of the complex plane (not including the real axis). Fourier transforming Eq. (6.78) gives us

$$\tilde{\chi}_+(\omega) \sum_k \left[\frac{f_k}{\omega - \omega_k} - \frac{f_k^*}{\omega - \omega_k^*} \right] = 0 \,, \quad \omega \in \mathbb{R} \,. \tag{6.80}$$

Because the set $\{\omega_k\}$ is within the upper-half complex plane (excluding the real axis), the set $\{\omega_k^*\}$ must be within the lower-half complex plane (excluding the real axis) — and the two sets do not intersect. For this reason, Eq. (6.80) requires f_k to all vanish, and hence

$$C_{zF}(t) = -i\hbar \, \delta_-(t) \,. \tag{6.81}$$

Bibliography

[1] T. J. Kippenberg and K. J. Vahala, Science **321**, 1172 (2008).

[2] F. Manquardt and S. M. Girvin, Physics **2**, 40 (2009).

[3] A. D. O' Connell *et al,* Nature **464**, 697 (2010).

[4] P. Verlot *et al,* Phys. Rev. Lett. **102**, 103601 (2009).

[5] J. D. Teufel *et al,* Nat. Nano. **4**, 820 (2009).

[6] G. Anetsberger *et al,* Nat. Phys. **5**, 909 (2009).

[7] K. Borkje, *et al,* Phys. Rev. A **82**, 013818 (2010).

[8] T. Westphal *at al,* arXiv:1111.7236.

[9] M. Ozawa, Phys. Rev. A **87**, 042105 (2003)

[10] J. Erhart *et al,* Nature Physics **8**, 185 (2012).

[11] V. B. Braginsky and F. Y. Khalili, *Quantum Measurement* (Cambridge University Press, 1992).

[12] V. B. Braginsky, JETP **26**, 831 (1968).

[13] C. M. Caves, Phys. Rev. Lett. **45**, 75 (1980).

[14] H. J. Kimble, Y. Levin, A. B. Matslo, K. S. Thorne and S. P. Vyatchanin, Phys. Rev. D **65**, 022002 (2001).

[15] A. Buonanno and Y. Chen, Phys. Rev. D **64**, 042006 (2001).

[16] P. Purdue and Y. Chen, Phys. Rev. D **66**, 122004 (2002),

[17] T. Corbitt *et al,* Phys. Rev. A. **73** 023801 (2006).

[18] T. Corbitt *et al,* Phys. Rev. Lett, **98**, 150802 (2007).

[19] T. Corbitt *et al,* Phys. Rev. Lett, **99**, 160801 (2007).

[20] F. Marino, F. S. Cataliotti, A. Farsi, M. S. Cumis and F. Marin, Phys. Rev. Lett **104** 073601 (2010).

[21] Y. Chen *et al,* Gen. Rel. Grav. **43**, 671 (2011).

[22] S. L. Danilishin and F. Y. Khalili, arXiv: 1203.1706.

[23] K. Yamamoto *et al,* Phys. Rev. A **81**, 033849 (2010).

[24] A. H. Safavi-Naeini *et al,* Phys. Rev. Lett **108**, 033602 (2012).

[25] F. Diedrich, J. C. Bergquist, W. M. Itano and D. J. Wineland, Phys. Rev. Lett **62**, 403 (1989).

[26] P. S. Jessen *et al,* Phys. Rev. Lett **69**, 49 (1992).

[27] C. Monroe *et al,* Phys. Rev. Lett **75**, 4011 (1995).

[28] N. Brahms, T. Botter, S. Schreppler, D. W. C. Brooks and D. M. Stamper-Kurn, Phys. Rev. Lett **108**, 133601 ()2012.

[29] T. R. Hart, R. L. Aggarwal and B. Lax, Phys. Rev. B **1**, 638 (1970).

[30] W. Hayes and R. London, *Scattering of Light by Crystals* (Dover Publications, 2004).

[31] F. Marquardt, J. P. Chen, A. A. Clerk and S. M. Girvin, Phys. Rev. Lett **99**, 093902 (2007).

[32] I. Wilson-Rae, N. Nooshi, W. Zwerger and T. J. Kippenberg, Phys. Rev. Lett **99**, 093901 (2007).

[33] C. Genes, D. Vitali, P. Tombesi, S. Gigan and M. Aspelmeyer, Phys. Rev. A **77**, 033804 (2008).

[34] H. Miao, S. Danilishin, H. Mueller-Ebhardt and Y. Chen, New Journal of Physics **12**, 083032 (2010).

[35] A. Buonanno and Y. Chen, Phys. Rev. D **65**, 042001 (2002).

[36] A. Buonanno and Y. Chen, Phys. Rev. D **67**, 062002 (2003).

[37] C. Gardiner and P. Zoller, *Quantum Noise* (Springer-Verlag, 2004).

[38] V. B. Braginsky, M. L. Gorodetsky, F. Y. Khalili, A. B. Marsko, K. S. Thorne and S. P. Vyatchanin, Phys. Rev. D **67** 082001 (2003).

Chapter 7

Macroscopic quantum mechanics in a classical spacetime

We apply the many-particle Schrödinger-Newton equation, which describes the co-evolution of an many-particle *quantum* wave function and a *classical* space-time geometry, to macroscopic mechanical objects. By averaging over motions of the objects' internal degrees of freedom, we obtain an effective Schrödinger-Newton equation for their centers of mass, which can be monitored and manipulated at quantum levels by state-of-the-art optomechanics experiments. For a single macroscopic object moving quantum mechanically within a harmonic potential well, its quantum uncertainty is found to evolve at a frequency different from its classical eigenfrequency — with a difference that depends on the internal structure of the object, and can be observable using current technology. For several objects, the Schrödinger-Newton equation predicts semiclassical motions just like Newtonian physics, yet quantum uncertainty cannot transferred from one object to another.

7.1 Introduction

Testing non-relativistic quantum mechanics on macroscopic objects has has been a minor approach in the search for effects of quantum gravity. Apart from the standard formulation of linearized quantum gravity [1], which seems rather implausible to test in the lab, several signatures have been conjectured: (i) *gravity decoherence* [2–12], where gravity introduces decoherence to macroscopic quantum superpositions; (ii) modifications to canonical quantization motivated by the existence of a minimum length scale [13–15]; and (iii) *semiclassical gravity* [16–18], which will be the subject of
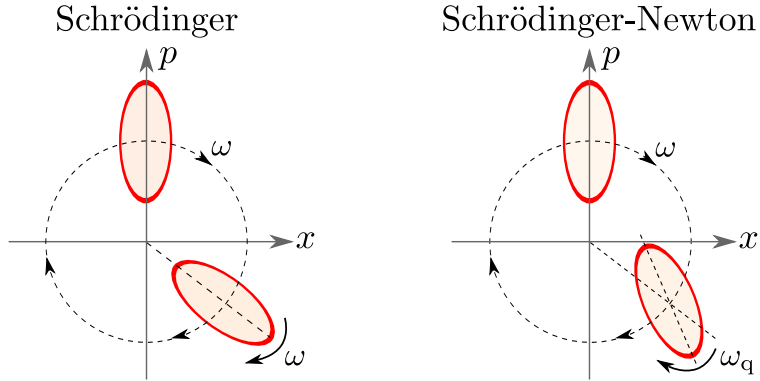
Figure 7.1: (Color online.) Left Panel: according to standard quantum mechanics, both the vector $(\langle x \rangle, \langle p \rangle)$ and the uncertainty ellipse of a Gaussian state for the CM of a macroscopic object rotate clockwise in phase space, at the same frequency $\omega = \omega_{CM}$. Right panel: according to the CM Schrödinger-Newton equation (7.2), $(\langle x \rangle, \langle p \rangle)$ still rotates at ω_{CM}, but the uncertainty ellipse rotates at $\omega_q \equiv (\omega_{CM}^2 + \omega_{SN}^2)^{1/2} > \omega_{CM}$.

this paper. As originally suggested by Møller [16] and Rosenfeld [17], spacetime structure might *still remain classical* even if it is sourced by matters of quantum nature, if we impose ($G = c = 1$):

$$G_{\mu\nu} = 8\pi \langle \psi | \hat{T}_{\mu\nu} | \psi \rangle . \tag{7.1}$$

Here $G_{\mu\nu}$ is the Einstein tensor of a (3+1)-dimensional classical spacetime, $\hat{T}_{\mu\nu}$ is the operator for the energy-stress tensor, and $|\psi(t)\rangle$ is the wave function of all matters that evolve within this classical spacetime.

Many arguments exist *against* semiclassical gravity. Some rely on the conviction that a classical system cannot properly integrate with a quantum system without creating contradictions. Others are based on "intrinsic" mathematical inconsistencies, the most famous one between Eq. (7.1), state collapse, and $\nabla^\nu G_{\mu\nu} = 0$ [19]. Towards the former argument, it is the aim of this paper to explicitly work out the effects of classical gravity on the quantum mechanics of macroscopic objects; which, although we will find them counterintuitive, do not seem dismissible right away. In fact, we shall find these effects "right on the horizon of testability" of current experimental technology. Towards the latter argument, we shall remain open minded regarding the possibility of getting rid of quantum state reduction while at the same time avoiding the many-world interpretation of quantum mechanics [20, 21] (also see the appendix).

The non-relativistic version of Eq. (7.1), the so-called Schrödinger-Newton (SN) equation, has been extensively studied for single particles [22–28]. In this paper, we consider instead a macroscopic object consisting of many particles, and will show that within certain parameter regimes, the Center-

of-Mass (CM) wavefunction approximately satisfies the following SN equation:

$$i\hbar\frac{\partial\Psi}{\partial t} = \left[-\frac{\hbar^2\nabla^2}{2M} + \frac{1}{2}M\omega_{\mathrm{CM}}^2 x^2 + \frac{1}{2}\mathcal{C}(x - \langle x\rangle)^2\right]\Psi. \tag{7.2}$$

Here $\langle x\rangle \equiv \langle\Psi|\hat{x}|\Psi\rangle$ is the expectation value of the CM position; ω_{CM} is the eigenfrequency in absence of gravity, determined by how the CM is confined; $\mathcal{C}$ is the SN coupling constant, from which we introduce $\omega_{\mathrm{SN}} \equiv \sqrt{\mathcal{C}/M}$. For Si crystal at $10\,\mathrm{K}$, we estimate $\omega_{\mathrm{SN}} \sim 0.036\,\mathrm{s}^{-1}$, much larger than the naively expected $\sqrt{G\rho_0}$ from the object's mean density ρ_0, due to the high concentration of mass near lattice points.

For a single macroscopic object prepared in a squeezed Gaussian state, Eq. (7.2) leads to different evolutions of expectation values and quantum uncertainties, as illustrated in Fig. 7.1. Such a deviation can be tested by optomechanical devices in the quantum regime [29–33]. For two macroscopic objects interacting through gravity, we show further, using the two-body counterpart of Eq. (7.2), that classical gravity cannot be used to transfer quantum uncertainties — experimental demonstration of this effect will be much more difficult than demonstrating modifications in single-object dynamics.

We emphasize that it is *not* our aim to use the SN equation to explain the collapse of quantum states, or to provide a pointer basis for gravity decoherence, as has been attempted in the literature [22–28]. We will take a conservative strategy, avoiding experimental regimes with exotic wavefunctions [10–12], and restraining ourselves to Gaussian states whose evolutions deviate little from predictions of standard quantum mechanics: just enough to be picked up by precision measurements. In this way, the solutions to SN equation we consider are much less complex than those in previous literature [22–28].

Many-particle SN equation— for n non-relativistic particles, if we denote their joint wave function as $\varphi(t, \mathbf{X})$ with $3n$-D vector $\mathbf{X} \equiv (\mathbf{x}_1, \cdots, \mathbf{x}_n)$ and $\mathbf{x}_k$ the 3-D spatial coordinate of k-th particle, then the many-particle SN equation, obtained by Diosi and Penrose [5, 22], is

$$i\hbar\partial_t\varphi = \sum_k\left[-\frac{\hbar^2\nabla_k^2}{2m_k} + \frac{m_k\,U(t, \mathbf{x}_k)}{2}\right]\varphi + V(\mathbf{X})\varphi\,, \tag{7.3}$$

where $V(\mathbf{X})$ is potential energy for non-gravitational interactions, while the Newtonian potential U is given by

$$\nabla^2 U(t, \mathbf{x}) = 4\pi\sum_j\int \mathrm{d}^{3n}\mathbf{X}\,|\varphi(t, \mathbf{X})|^2 m_j\,\delta(\mathbf{x} - \mathbf{x}_j)\,. \tag{7.4}$$

7.2 SN theory for macroscopic objects

The center of mass and the separation of scales.— equations (7.3) and (7.4) are still not suitable for experimental studies, because we cannot separately access each particle in a macroscopic object. In

optomechanical devices, a light beam often probes (hence acts back onto) the average displacements of atoms within the first few layers of the reflective coating of a mirror-endowed mass. Motion of this effective surface can often be well-approximated by the CM motion of the entire object; the error of this approximation is referred to as the "internal thermal noise", and has been shown to be suppressible below the free-mass Standard Quantum Limit (SQL) [34], a quantum level of CM motion defined by the object's total mass and the measurement time scale [35]. This suppression is possible because: (i) we tend to measure CM motion by averaging over a large number of atoms at the surface of the object, and (ii) we measure CM motion over a time scale much longer than the ones at which atoms oscillate due to thermal or zero-point fluctuations. Obtaining the SN equation for the CM is therefore central to the experimental test of this model. Before doing so, let us consider the separation of temporal and spatial scales in the motion of a macroscopic piece of crystal.

The scales of CM motion are determined externally by how we confine the object during measurement, and by how we measure it. Here we consider motions with $\omega_{CM}/(2\pi)$ from Hz to kHz scale. If thermal noise level is below the free-mass SQL [34], then one can either use optical or feedback trapping to create mechanical oscillators with coherence time τ_{CM} longer than $1/\omega_{CM}$ [36, 37]. Although not yet achieved, research towards sub-SQL devices in the Hz – kHz regime is being actively pursued [38, 39, 41]. In this regime, we have $\Delta x_{CM} \sim \sqrt{\hbar/(M\omega_{CM})}$; for $1\,\mathrm{g} < M < 10\,\mathrm{kg}$, $\Delta x_{CM} \sim 10^{-19}$–$10^{-17}\,\mathrm{m}$.

By contrast, the internal motions of atoms are due to excitation of phonons [44], with a total variance of [45]

$$\langle x^2 \rangle \equiv \frac{B^2}{8\pi^2} = \frac{\hbar^2}{mk_BT} \int_0^{+\infty} \frac{g(\nu)}{\xi} \left(\frac{1}{2} + \frac{1}{e^\xi - 1} \right) d\nu \tag{7.5}$$

where B is also known as the "B-factor" in X-ray diffraction, $\xi = h\nu/k_BT$, $g(\nu)$ is the phonon density of states, the first term in the bracket gives rise to zero-point uncertainty Δx_{zp}^2, while the second gives rise to thermal uncertainty Δx_{th}^2. These have been studied experimentally by X-ray diffraction, through measurements of the Debye-Waller factor [46], and modeled precisely (for Si crystal, see Ref. [47]). Much below the Debye temperature, one can reach $\Delta x_{th} \ll \Delta x_{zp}$, with most atomic motion due to zero-point fluctuations near the Debye frequency ω_D. For Si crystal, $\omega_D \sim 10^{14}\,\mathrm{s}^{-1}$, $\Delta x_{zp} = 4.86 \times 10^{-12}\,\mathrm{m}$, and $\Delta x_{th}(293\,\mathrm{K}) = 5.78 \times 10^{-12}\,\mathrm{m}$ [47]. At lower temperatures, $\Delta x_{th} \propto T$, therefore on the scale of $\sim 10\,\mathrm{K}$, at which our proposed experiment operates, we have $\Delta x_{zp} \gg \Delta x_{th} \gg \Delta x_{CM}$.

SN equation for the CM— for a crystal with n atoms, the CM is at $\mathbf{x}_{CM} = (1/n)\sum_k \mathbf{x}_k$, motion of the k-th atom in CM frame is $\mathbf{y}_k \equiv \mathbf{x}_k - \mathbf{x}_{CM}$. In standard quantum mechanics, for inter-atom interaction that only depends on the separation of atoms, the CM and internal DOFs are separable: $\varphi(t, \mathbf{X}) = \Psi_{CM}(t, \mathbf{x})\Psi_{int}(t, \mathbf{Y})$, with $3(n-1)$-D vector $\mathbf{Y} \equiv (\mathbf{y}_1, \cdots, \mathbf{y}_{n-1})$. The two wavefunctions

evolve independently:

$$i\hbar\partial_t\Psi_{\mathrm{CM}}(t,\mathbf{x}) = H_{\mathrm{CM}}\Psi_{\mathrm{CM}}(t,\mathbf{x}),\tag{7.6}$$

$$i\hbar\partial_t\Psi_{\mathrm{int}}(t,\mathbf{Y}) = H_{\mathrm{int}}\Psi_{\mathrm{int}}(t,\mathbf{Y}).\tag{7.7}$$

For classical gravity, let us first still assume separability: $\varphi = \Psi_{\mathrm{CM}}\Psi_{\mathrm{int}}$, and we will show this remains true (with negligible error) under evolution. Specifically, the sum of SN terms in Eq. (7.3) becomes

$$\begin{aligned}V_{\mathrm{SN}}(\mathbf{x},\mathbf{Y}) &= \sum_k m_k U(\mathbf{x}_k)/2\\ &= \sum_k \int \varepsilon\left[\mathbf{x}-\mathbf{z}+\mathbf{y}_k\right]\Psi_{\mathrm{CM}}^2(\mathbf{z})d^3\mathbf{z}.\end{aligned}\tag{7.8}$$

Here we have suppressed dependence on time and defined

$$\varepsilon(\mathbf{z}) = -\frac{Gm}{2}\int\frac{\tilde{\rho}_{\mathrm{int}}(\mathbf{y})}{|\mathbf{z}-\mathbf{y}|}d^3\mathbf{y}\tag{7.9}$$

as *half* the gravitational potential energy of a mass m at location $\mathbf{z}$ (in CM frame), due to the entire lattice, and

$$\tilde{\rho}_{\mathrm{int}}(\mathbf{y}) = m\sum_{j=1}^{n}\int\delta(\mathbf{y}-\mathbf{y}_j')|\Psi_{\mathrm{int}}(\mathbf{Y}')|^2 d^{3n-3}\mathbf{Y}'\tag{7.10}$$

is the CM-frame mass density. (Note: $\mathbf{y}_n \equiv -\sum_{j=1}^{n-1}\mathbf{y}_j$.) We will now have to show that V_{SN} approximately separates into a sum of terms that either only depend on $\mathbf{Y}$, or only on $\mathbf{x}$. Taylor expansion of V_{SN} in $\mathbf{x}$ and $\mathbf{z}$ leads to (for one direction):

$$\begin{aligned}V_{\mathrm{SN}} =& \sum_k \varepsilon(\mathbf{y}_k) + (x_{\mathrm{CM}} - \langle x_{\mathrm{CM}}\rangle)\sum_k \varepsilon'(\mathbf{y}_k)\\ &+ \frac{x_{\mathrm{CM}}^2 - 2x_{\mathrm{CM}}\langle x_{\mathrm{CM}}\rangle + \langle x_{\mathrm{CM}}^2\rangle}{2}\sum_k \varepsilon''(\mathbf{y}_k),\end{aligned}\tag{7.11}$$

with higher orders falling as powers of $\Delta x_{\mathrm{CM}}/\Delta x_{\mathrm{zp}} \ll 1$. Here in V_{SN}, the first term describes the leading SN correction to internal motion, and can be absorbed into H_{int}. The second term describes the interaction between CM motion and each individual atom — it can be shown to have negligible effects, because internal motions of different atoms are largely independent, and at much faster time scales. The third term is largely a correction to the CM motion; its main effect is captured if we replace it by its ensemble average over internal motion (again allowed by approximate independence

between atoms, see Supplementary Material): $\sum_k \varepsilon''(\mathbf{y}_k) \to \mathcal{C} \equiv \left\langle \sum_k \varepsilon''(\mathbf{y}_k) \right\rangle$, with

$$\mathcal{C} = -\frac{1}{2} \frac{\partial^2}{\partial z^2} \left[\int \frac{G\tilde{\rho}_{\text{int}}(\mathbf{y})\tilde{\rho}_{\text{int}}(\mathbf{y}')}{|\mathbf{z} + \mathbf{y} - \mathbf{y}'|} d\mathbf{y} d\mathbf{y}' \right]_{\mathbf{z}=0}, \tag{7.12}$$

which is half the double spatial derivative of the "self-gravitational energy" of the lattice as it is being translated. As this is independent from the internal motion $\mathbf{Y}$, we therefore obtain the leading correction to H_{CM}, which justifies Eq. (7.2) introduced at the beginning.

Estimates for ω_{SN} — Let us now estimate the magnitude of ω_{SN} from Eq. (7.12). We naively assume a homogeneous mass distribution with constant density ρ_0 leads to

$$\mathcal{C}^{\text{hom}} \approx GM\rho_0, \ \omega_{\text{SN}}^{\text{hom}} \approx \sqrt{G\rho_0}, \tag{7.13}$$

up to a geometric factor that depends on the shape of the object. This is a typical estimate for the gravity-decoherence time scale for a homogeneous object prepared in a nearly Gaussian quantum state with position uncertainty much less than its size [12]. Using the mean density of Si crystal, this is roughly $4 \times 10^{-4} \, \text{s}^{-1}$. However, mass in a lattice is *highly concentrated* near lattice sites; the realistic $\tilde{\rho}_{\text{int}}$ at low temperatures contains a total mass of m around each lattice point, Gaussian distributed with uncertainty of Δx_{zp} in each direction. This gives, through Eq. (7.12),

$$\omega_{\text{SN}}^{\text{crystal}} = \sqrt{Gm/(12\sqrt{\pi}\Delta x_{\text{zp}}^3)}. \tag{7.14}$$

For $\Delta x_{\text{zp}} \approx 4.86 \times 10^{-12} \, \text{m}$, we obtain $\omega_{\text{SN}}^{\text{Si}} \approx 0.036 \text{s}^{-1}$, nearly 100 times $\omega_{\text{SN}}^{\text{hom}}$. If we define

$$\Lambda = \left(\omega_{\text{SN}}^{\text{crystal}}/\omega_{\text{SN}}^{\text{hom}}\right)^2 = m/(12\sqrt{\pi}\rho_0\Delta x_{\text{zp}}^3), \tag{7.15}$$

then $\Lambda = 8.3 \times 10^3$ for Si crystal.

Evolutions of gaussian states and experimental Tests — As one can easily prove, Gaussian states remain Gaussian under Eq. (7.2); the self-contained evolution equations for first and second moments of $\hat{x}$ and $\hat{p}$, which completely determine the evolving Gaussian state, are given by:

$$\langle \dot{\hat{x}} \rangle = \langle \hat{p} \rangle / M, \qquad \langle \dot{\hat{p}} \rangle = -M\omega_{\text{CM}}^2 \langle \hat{x} \rangle, \tag{7.16}$$

$$\dot{V}_{xx} = 2V_{xp}/M, \quad \dot{V}_{pp} = -2M(\omega_{\text{CM}}^2 + \omega_{\text{SN}}^2)V_{xp}, \tag{7.17}$$

$$\dot{V}_{xp} = V_{pp}/M - M(\omega_{\text{CM}}^2 + \omega_{\text{SN}}^2)V_{xx}. \tag{7.18}$$

For covariance we have defined $V_{AB} \equiv \langle \hat{A}\hat{B} + \hat{B}\hat{A} \rangle / 2 - \langle \hat{A} \rangle \langle \hat{B} \rangle$. Eq. (7.16) indicates that $\langle \hat{x} \rangle$ and $\langle \hat{p} \rangle$ evolve the same way as a harmonic oscillator with angular frequency ω_{CM} — any *semiclassical* measurement of on $\langle \hat{x} \rangle$ and $\langle \hat{p} \rangle$ will confirm classical physics. On the other hand, evolution of second

moments (which represent *quantum uncertainty*), is modified to that of a harmonic oscillator with a different frequency (see Fig. 7.1):

$$\omega_{\mathrm{q}} \equiv \sqrt{\omega_{\mathrm{CM}}^2 + \omega_{\mathrm{SN}}^2} \, . \tag{7.19}$$

Equations (7.16)–(7.18) for Gaussian states can also be reproduced by a set of effective Heisenberg equations that contain expectation values:

$$\dot{\hat{x}} = \hat{p}/M \, , \quad \dot{\hat{p}} = -M\omega_{\mathrm{CM}}^2 \hat{x} - \mathcal{C}(\hat{x} - \langle \hat{x} \rangle) \, . \tag{7.20}$$

Classical gravity introduces a $\mathcal{C}$-dependent term to Eq. (7.20), in a way that only affects quantum uncertainty.

The most obvious test for the SN effect is to prepare a mechanical oscillator into a squeezed initial state, let it evolve for a duration τ, and carry out state tomography. We need to detect an extra phase $\Delta\theta = \omega_{\mathrm{CM}}\tau(\omega_{\mathrm{SN}}^2/\omega_{\mathrm{CM}}^2)$ in the rotation of the quantum uncertainty ellipse. This seems rather difficult because $\omega_{\mathrm{SN}}/\omega_{\mathrm{CM}}$ is often a very small number, yet $\omega_{\mathrm{CM}}\tau$ is often not large, either.

However, we have not taken advantage of the fact that $\Delta\theta$ is deterministic and repeatable. One way of doing so is to carry out a frequency-domain experiment. Suppose we use light (at ω_0) to continuously probe a mechanical object's position, with quantum back-action noise (in the form of radiation-pressure noise) comparable in level to thermal noise, as has been achieved by Purdy *et al.* [33]. The effective Heisenberg equations (valid for Gaussian states) for such an optomechanical device is given by:

$$\dot{\hat{x}} = \hat{p}/M \, , \tag{7.21}$$

$$\dot{\hat{p}} = -M\omega_{\mathrm{CM}}^2\hat{x} - 2\gamma_m\hat{p} - \mathcal{C}(\hat{x} - \langle \hat{x} \rangle) + \hat{F}_{\mathrm{BA}} + F_{\mathrm{th}} \tag{7.22}$$

$$\hat{b}_2 = \hat{a}_2 + n_x + (\alpha/\hbar)\hat{x} \, , \quad \hat{b}_1 = \hat{a}_1 \, . \tag{7.23}$$

Here γ_m is the damping rate, α is the optomechanical coupling constant, $\hat{F}_{\mathrm{BA}} \equiv \alpha\,\hat{a}_1$ is the quantum back action, and F_{th} is the classical driving force (e.g., due to thermal noise). $\hat{a}_{1,2}$ represents quadratures of the in-going optical field, and $\hat{b}_{1,2}$ those of the out-going field. (They correspond to amplitude and phase modulations of the carrier field at ω_0.) We have used n_x to denote sensing noise. As we show in the appedix, the outgoing quadrature $\hat{b}_2$ contains two prominent frequency contents, peaked at ω_{CM} (due to classical motion driven by thermal forces) and at ω_{q} (due to quantum motion driven by quantum fluctuation of light), respectively. Both have the same width (γ_m), and height (if thermal and back-action noises are comparable). In order to distinguish them, we require

$$S_{F_{\mathrm{th}}} \approx S_{F_{\mathrm{BA}}} \, , \quad Q \gtrsim (\omega_{\mathrm{CM}}/\omega_{\mathrm{SN}})^2 \, . \tag{7.24}$$

This indicates a SN-induced shift of $\Delta\theta \approx 2\pi/Q$ per cycle can be picked up by the frequency domain experiment, even in presence of classical thermal noise F_{th}.

For Si oscillators with $\omega_{\text{SN}} \approx 0.036\,\text{s}^{-1}$, if $\omega_{\text{CM}} \approx 2\pi \times 10\,\text{Hz}$, Eq. (7.24) requires $Q \gtrsim 3 \times 10^6$, which is challenging but possible [41]. If a lower-frequency oscillator, e.g., a torsional pendulum with $\omega_{\text{CM}} \approx 2\pi \times 0.1\,\text{Hz}$ [48] can be probed with back-action noise above thermal noise, then we only require $Q \gtrsim 3 \times 10^2$.

SN equation for two macroscopic objects— Now suppose we have two objects confined within potential wells frequencies $\omega_{1,2}$, and moving along the same direction as the separation vector $\mathbf{L}$ connecting their equilibrium positions (from 1 to 2). The standard approach for describing this interaction is to add a potential

$$V_g = \mathcal{E}'_{12}\left[x_{\text{CM}}^{(1)} - x_{\text{CM}}^{(2)}\right] + (\mathcal{C}_{12}/2)\left[x_{\text{CM}}^{(1)} - x_{\text{CM}}^{(2)}\right]^2 \tag{7.25}$$

into the Schrödinger equation, with

$$\mathcal{E}_{12} \equiv -\int d^3\mathbf{x}\,d^3\mathbf{y}\,\frac{G\tilde{\rho}_{\text{tot}}^{(1)}(\mathbf{x})\tilde{\rho}_{\text{tot}}^{(2)}(\mathbf{y})}{|\mathbf{L}+\mathbf{y}-\mathbf{x}|}, \quad \mathcal{C}_{12} \equiv \frac{\partial^2\mathcal{E}_{12}}{\partial L^2}, \tag{7.26}$$

with $\tilde{\rho}_{\text{tot}}^{(1)}$ and $\tilde{\rho}_{\text{tot}}^{(2)}$ the mass densities of objects 1 and 2, respectively. As has been argued by Feynman, this way of including gravity tacitly assumes that gravity is quantum. Although quantum operators have not been assigned for the gravitational field, they can be viewed as having been adiabatically eliminated due to their fast response: quantum information can transfer between these objects via gravity. Suppose $\omega_1 = \omega_2 = \omega$, then V_g modifies the frequency of the two objects' differential mode — allowing quantum state to slosh between them, at a frequency of $\Delta = |\omega_+ - \omega_-| = \mathcal{C}_{12}/(2M\omega)$.

Suppose we instead use the SN equation for the two macroscopic objects. In addition to modifying each object's own motion, we add a mutual term of

$$\begin{aligned} V_{\text{SN}} =& \mathcal{E}'_{12}\left[x_{\text{CM}}^{(1)} - x_{\text{CM}}^{(2)}\right] \\ & + \frac{\mathcal{C}_{12}}{2}\left[\left(x_{\text{CM}}^{(1)} - \langle x_{\text{CM}}^{(2)}\rangle\right)^2 + \left(x_{\text{CM}}^{(2)} - \langle x_{\text{CM}}^{(1)}\rangle\right)^2\right]. \end{aligned} \tag{7.27}$$

This V_{SN} makes sure that only $\langle x_{\text{CM}}\rangle$ gets transferred between the two objects the same way as in classical physics: *quantum uncertainty does not transfer from one object to the other.* To see this more explicitly for Gaussian states, we can write down the full set of effective Heisenberg equations governing these two CMs:

$$\begin{aligned} \dot{\hat{x}}_j =& \hat{p}_j/M_j\,, \\ \dot{\hat{p}}_j =& -M_j\omega_{\text{CM}}^2\hat{x}_j - \sum_{k,j}\left[\mathcal{E}'_{kj} + \mathcal{C}_{kj}\left(\hat{x}_j - \langle\hat{x}_k\rangle\right)\right]. \end{aligned} \tag{7.28}$$

It is clear that expectation values follow classical physics, and quantum uncertainties are confined within each object — and evolve with a shifted frequency. Although we have shown theoretically that the inability to transfer quantum uncertainty and the shift between ω_{CM} and ω_{q} *share the same origin*, in practice, observing the frequency shift for a single object will be much easier, because $\mathcal{C}_{12} \sim GM^2/L^3 \lesssim GM\rho_0 \ll \mathcal{C}_{11}, \mathcal{C}_{22}$, due to the lack of the amplification factor Λ in $\mathcal{C}_{12}$ [cf. Eq. (7.15)].

7.3   Discussion and conclusion

The lack of experimental tests on the quantum coherence of dynamical gravity makes us believe that semiclassical gravity is still worth testing [18]. Our calculations have shown that signatures of classical gravity in macroscopic quantum mechanics, although extremely weak, can be detectable with current technology. In particular, the classical self gravity of a single macroscopic object causes a much stronger signature than the classical mutual gravity between two separate objects: simply because the mass of a cold crystal is concentrated near lattice sites. We also speculate that the rate of gravity decoherence should also be expedited by $\Lambda^{1/2} \sim 100$ — if it is indeed determined by gravitational self energy [5, 6]. However, due to the lack of a widely-accepted microscopic model for gravity decoherence, this only makes it more hopeful for experimental attempts, but would not enforce a powerful bound if decoherence were not to be found.

Finally, since classical gravity requires the existence of a global wave function of the universe that does not collapse, (the unlikely case of) a positive experimental result will open up new opportunities of investigating the nature of quantum measurement.

Acknowledgement

7.A   Supplementary material for macroscopic quantum mechanics in a classical spacetime

7.A.1   A. Incompatibility between the many-world interpretation of quantum mechanics and classical gravity

At this moment, the only well-known (and widely accepted) interpretation of quantum mechanics that explains the phenomenology of quantum measurement without resorting to quantum-state reduction is the many-world interpretation of quantum mechanics [20]: the entire universe's wavefunction contains many branches, incorporating all possible measurement outcomes; each observer, however, can only perceive one of the branches, therefore experiencing the phenomenon of quantum-state reduction.

If we were to combine the many-world interpretation of quantum mechanics and classical gravity, the classical spacetime geometry will have to be determined by the expectation value of stress-energy tensor, which effectively averages over all possible measurement outcomes. Following Page and Geilker [21], let us consider the following gedankenexperiment. Suppose quantum measurement of $\hat{\sigma}_z$ of a spin-1/2 particle at a state of $(|+\rangle + |-\rangle)/\sqrt{2}$ determines whether we put a mass on the left or right side of a scale, then the combination of the many-world interpretation and classical gravity will predict a leveled scale, because the expectation value of matter densities on both sides are equal. This is in stark contrast with experimental facts.

Nevertheless, for many, including some of the authors, neither the concept of state reduction nor the many-world interpretation seems a satisfactory explanation of why we cannot predict the outcome of a quantum measurement. We therefore remain open minded towards the possibility of further interpretations/clarifications/modifications of quantum mechanics and the quantum measurement process that offer better explanations. For us, the Schrödinger-Newton equation is not ruled out right away, and is therefore still worth testing.

7.A.2   B. Separation between CM and internal degrees of freedom

In Eq. (11), we obtained the Schrödinger-Newton potential kept at quadratic order (in $\Delta x_{\mathrm{CM}}/\Delta x_{\mathrm{zp}} \ll 1$):

$$
\begin{aligned}
V_{\mathrm{SN}} &= \sum_k \varepsilon(\mathbf{y}_k) + (x_{\mathrm{CM}} - \langle x_{\mathrm{CM}}\rangle)\sum_k \varepsilon'(\mathbf{y}_k) \\
&+ \frac{1}{2}(x_{\mathrm{CM}}^2 - x_{\mathrm{CM}}\langle x_{\mathrm{CM}}\rangle + \langle x_{\mathrm{CM}}^2\rangle)\sum_k \varepsilon''(\mathbf{y}_k).
\end{aligned} \tag{B.1}
$$

As we shall argue, truncation at this order will give us the leading correction to CM motion, and it is also separable from corrections to the internal motion, therefore justifying the assumption of separability between the CM motion and internal DOFs. Higher order terms, being suppressed by powers of $\Delta x / \Delta x_{\text{zp}}$ are therefore negligible.

The first term

$$V_{\text{SN}}^{(0)} = \sum_k \varepsilon(\mathbf{y}_k) \tag{B.2}$$

is readily absorbed into H_{int}, which now becomes nonlinear. This is already the leading correction for the internal motion. Let us calculate the modulus of its contribution,

$$
\begin{aligned}
\|V_{\text{SN}}^{(0)} \varphi\| &= \left[\int \sum_{k,j} \varepsilon(\mathbf{y}_k) \varepsilon(\mathbf{y}_j) |\Psi_{\text{int}}(\mathbf{Y})|^2 d^{3n-3}\mathbf{Y} \right]^{1/2} \\
&\approx n \left(Gm^2 / \Delta x_{\text{zp}} \right).
\end{aligned}
\tag{B.3}
$$

The second term

$$V_{\text{SN}}^{(1)} = (x_{\text{CM}} - \langle x_{\text{CM}} \rangle) \sum_k \varepsilon'(\mathbf{y}_k) \tag{B.4}$$

describes the interaction between the CM and the internal motion of each of the atoms. In order to estimate its effect, let us first calculate the modulus of the change in φ it induces:

$$
\begin{aligned}
\|V_{\text{SN}}^{(1)} \varphi\| &= \Delta x_{\text{CM}} \left[\int \sum_{k,j} \varepsilon'(\mathbf{y}_k) \varepsilon'(\mathbf{y}_j) |\Psi_{\text{int}}(\mathbf{Y})|^2 d^{3n-3}\mathbf{Y} \right]^{1/2} \\
&\approx \sqrt{n} \left(Gm^2 / \Delta x_{\text{zp}} \right) \left(\Delta x_{\text{CM}} / \Delta x_{\text{zp}} \right).
\end{aligned}
\tag{B.5}
$$

Here we only have $\sqrt{n}$ (instead of n) because the integral will not vanish only when distribution of $\mathbf{y}_k$ and $\mathbf{y}_j$ are correlated, which only happens for nearby atoms. The other factor $\Delta x_{\text{CM}} / \Delta x_{\text{zp}}$ is due to the fact that this is the next order in the Taylor expansion. From the point of view of internal motion, $V_{\text{SN}}^{(1)}$ clearly gives a higher-order correction than $V_{\text{SN}}^{(0)}$, hence negligible. We will show that, even for CM motion, the contribution of $V_{\text{SN}}^{(1)}$ is also less than contribution from the next Taylor-expansion term $V_{\text{SN}}^{(2)}$.

Now turning to $V_{\text{SN}}^{(2)}$, let us split it into two terms

$$V_{\text{SN}}^{(2)} = \bar{V}_{\text{SN}}^{(2)} + \delta V_{\text{SN}}^{(2)}, \tag{B.6}$$

with

$$\bar{V}_{\text{SN}}^{(2)} = \frac{1}{2} (x_{\text{CM}}^2 - 2x_{\text{CM}} \langle x_{\text{CM}} \rangle + \langle x_{\text{CM}}^2 \rangle) \left\langle \sum_k \varepsilon''(\mathbf{y}_k) \right\rangle, \tag{B.7}$$

defined as the ensemble average, where

$$\left\langle \sum_k \varepsilon''(\mathbf{y}_k) \right\rangle \equiv \int \sum_k \varepsilon''(\mathbf{y}_k) |\Psi_{\text{int}}(\mathbf{Y})|^2 d^{3n-3}\mathbf{Y} \equiv \mathcal{C} \,, \tag{B.8}$$

and

$$\mathcal{C} = -\frac{1}{2} \frac{\partial^2}{\partial z^2} \left[\int \frac{G\tilde{\rho}_{\text{int}}(\mathbf{y})\tilde{\rho}_{\text{int}}(\mathbf{y}')}{|\mathbf{z} + \mathbf{y} - \mathbf{y}'|} d\mathbf{y} d\mathbf{y}' \right]_{\mathbf{z}=0} . \tag{B.9}$$

Note that $\bar{V}_{\text{SN}}^{(2)}$ does not depend explicitly on $\mathbf{Y}$, and hence is a correction to the Hamiltonian for the CM motion. It is straightforward to estimate that

$$\|\bar{V}_{\text{SN}}^{(2)}\varphi\| = nGm^2/\Delta x_{\text{zp}} \left(\Delta x_{\text{CM}}/\Delta x_{\text{zp}}\right)^2 . \tag{B.10}$$

This means, at any given time,

$$\|V_{\text{SN}}^{(1)}\varphi\|/\|\bar{V}_{\text{SN}}^{(2)}\varphi\| \approx \frac{1}{\sqrt{n}} \frac{\Delta x_{\text{zp}}}{\Delta x_{\text{CM}}} \approx \sqrt{\frac{\omega_{\text{CM}}}{\omega_D}} \ll 1 \,. \tag{B.11}$$

In addition, as we evolve in time, the effect of $V_{\text{SN}}^{(1)}$ oscillates around zero over a very fast time scale, while the effect of $\bar{V}_{\text{SN}}^{(2)}$ does not oscillate around zero — this further suppresses the relative contribution of $V_{\text{SN}}^{(1)}$. For this reason, we ignore $V_{\text{SN}}^{(1)}$ completely.

As for $\delta V_{\text{SN}}^{(2)}$, its effect is suppressed from $\bar{V}_{\text{SN}}^{(2)}$ by $\sqrt{n}$, because, much similar to Eq. (B.5), effects of different atoms do not accumulate unless they are very close to each other.

7.A.3   C. Effective Heisenberg equations of motion and coupling with optical field

The fact that Gaussian states leads to Gaussian states encourages us to look for *effective* Heisenberg equations of motion, which will at least be valid for Gaussian states. It is easy to find that

$$\dot{\hat{x}} = \hat{p}/M \,, \tag{C.1}$$

$$\dot{\hat{p}} = -M\omega_{\text{CM}}^2 \hat{x} - \mathcal{C}(\hat{x} - \langle\hat{x}\rangle) \tag{C.2}$$

will give the same set of first- and second-moment equations of motion as the SN equation. Note that in the Heisenberg picture, the initial state of the oscillator remains constant.

Let us now consider a more realistic scenario, in which the oscillator is damped with decay rate γ_m, driven with classical thermal noise and other classical driving; we also consider using light to sense the position of the mirror, in which we also suffer from sensing noise. The entire process can

be described by the following set of equations [cf. Eqs. (21), (22) and (23)]:

$$\dot{\hat{x}} = \hat{p}/M \,, \tag{C.3}$$

$$\dot{\hat{p}} = -M\omega_{\mathrm{CM}}^2 \hat{x} - 2\gamma_m \hat{p} - \mathcal{C}(\hat{x} - \langle\hat{x}\rangle) + \hat{F}_{\mathrm{BA}} + F_{\mathrm{th}} \,, \tag{C.4}$$

$$\hat{b}_2 = \hat{a}_2 + n_x + (\alpha/\hbar)\hat{x} \,, \quad \hat{b}_1 = \hat{a}_1 \,. \tag{C.5}$$

This set of equations can be solved first for $\langle\hat{x}\rangle$ by taking the expectation value of the first two equations, and then insert this back to obtain the entire solution. If we define

$$\chi_0 = -\frac{1}{M(\omega^2 + 2i\gamma_m\omega - \omega_{\mathrm{CM}}^2)} \tag{C.6}$$

$$\chi_g = -\frac{1}{M(\omega^2 + 2i\gamma_m\omega - \omega_{\mathrm{q}}^2)} \,, \tag{C.7}$$

then we can write, in the frequency domain,

$$\hat{b}_2 = \hat{a}_2 + (\alpha/\hbar)\chi_g\hat{F}_{\mathrm{BA}} + (\alpha/\hbar)\chi_0 F_{\mathrm{th}} + n_x \,. \tag{C.8}$$

Because both χ_g and χ_0 in the time domain are Green functions of stable systems, Eq. (C.8) represents the steady-state solution for the outgoing field, which is only determined by the ingoing optical field and the classical driving field — initial states of the mechanical oscillator do not matter (similar to the case of Ref. [49, 50]).

Equation (C.8) carries the separation between classical and quantum rotation frequencies in the previous section (Fig. 1) into the frequency spectrum of our measuring device: quantum back-action (radiation-pressure) noise $\hat{F}_{\mathrm{BA}}$ spectrum in the output port of the continuous measuring device is the same as an oscillator with frequency ω_{q}, and therefore peaks around ω_{q} — while classical noise F_{th} follows that of an oscillator with frequency ω_{CM}, and peaks at ω_{CM}. In order to look for such a signature, we will need classical force noise to be comparable in level to quantum noise, and have the two peaks to be resolvable,

$$\omega_{\mathrm{q}} - \omega_{\mathrm{CM}} \gtrsim \gamma_m \tag{C.9}$$

which means

$$Q \gtrsim (\omega_{\mathrm{CM}}/\omega_{\mathrm{SN}})^2 \tag{C.10}$$

where Q is the quality factor of the mechanical oscillator.

7.A.4 D. SN Equation for two macroscopic objects

Following the analysis in Appendix. A, here we deal with two macroscopic objects, and define

$$\mathbf{x}_k^{(I)} = \mathbf{X}^{(I)} + \mathbf{y}_k^{(I)} + \mathbf{x}_{\text{CM}}^{(I)}, \quad k = 1, \ldots, n_I, \quad I = 1, 2. \tag{D.1}$$

Here $\mathbf{X}^{(I)}$ is the zero point we use for describing object I, and n_I is the number of atoms object I contains. Following the same argument for deriving the single-object SN equation, we can still write the joint wavefunction as a product between the joint CM wavefunction and the internal wavefunctions,

$$\varphi = \Psi_{\text{CM}} \left[\mathbf{x}^{(1)}, \mathbf{x}^{(2)} \right] \Psi_{\text{int}}^{(1)} \left[\mathbf{Y}^{(1)} \right] \Psi_{\text{int}}^{(2)} \left[\mathbf{Y}^{(2)} \right]. \tag{D.2}$$

and show that this form will be preserved during evolution, even adding the SN term, which is now

$$V_{\text{SN}} = \frac{Gm^2}{2} \sum_{I,J=1}^{2} \sum_{i=1}^{n_I} \sum_{j=1}^{n_J} \frac{\left| \Psi_{\text{CM}}(\tilde{\mathbf{z}}^{(1)}, \tilde{\mathbf{z}}^{(2)}) \Psi_{\text{int}}^{(1)}(\tilde{\mathbf{Y}}^{(1)}) \Psi_{\text{int}}^{(2)}(\tilde{\mathbf{Y}}^{(2)}) \right|^2}{\left| \mathbf{L}^{(JI)} + \mathbf{x}^{(I)} + \mathbf{y}_i^{(I)} - \tilde{\mathbf{z}}^{(J)} + \tilde{\mathbf{y}}_j^{(J)} \right|} d\tilde{\mathbf{z}}^{(1)} d\tilde{\mathbf{z}}^{(2)} d\tilde{\mathbf{Y}}^{(1)} d\tilde{\mathbf{Y}}^{(2)}. \tag{D.3}$$

Here we have denoted

$$L^{(IJ)} \equiv X^{(J)} - X^{(I)}. \tag{D.4}$$

Terms with $I = J$ have already been dealt with, and give rise to the SN correction within object I. We will only have to deal with cross terms. In doing so, we shall assume each object's CM moves very little from its zero point, and carry out Taylor expansion. Note that because these objects are already macroscopically separated, with $L^{(IJ)}$ comparable to or greater than the size of each object, the expansion here will be valid for the cross term as long as the CM motion of each object is much less than its size.

The zeroth order expansion in CM motion, $V_{\text{SN}}^{(0)}$, gives rise to SN coupling between the objects' internal motions. Fortunately, that does not entangle their internal motions, and preserves the form of Eq. (D.2).

The first order in CM motion gives (after conversion of summation over atoms into ensemble average, the same as we did in Appendix B, and removing a constant):

$$\bar{V}_{\text{SN}}^{(1)} = -x_{\text{CM}}^{(1)} \mathcal{E}_{21}' - x_{\text{CM}}^{(2)} \mathcal{E}_{12}' = \left[x_{\text{CM}}^{(1)} - x_{\text{CM}}^{(2)} \right] \mathcal{E}_{12}' \tag{D.5}$$

where $\mathcal{E}_{12}$ is the interaction energy between the objects, as a function of their separation

$$\mathcal{E}_{12}(\mathbf{x}) \equiv - \int d^3\mathbf{y} d^3\mathbf{z} \frac{G \tilde{\varrho}_{\text{int}}^{(1)}(\mathbf{y}) \, \tilde{\varrho}_{\text{int}}^{(2)}(\mathbf{z})}{|\mathbf{z} + \mathbf{x} - \mathbf{y} + \mathbf{L}^{(12)}|}. \tag{D.6}$$

This describes the tendency of these objects to fall into each other. Similarly, we obtain the second order, which gives (apart from a constant)

$$\bar{V}_{\text{SN}}^{(2)} = \frac{\mathcal{E}_{12}''}{2} \left[\left(x_{\text{CM}}^{(1)} - \langle x_{\text{CM}}^{(2)} \rangle \right)^2 + \left(x_{\text{CM}}^{(2)} - \langle x_{\text{CM}}^{(1)} \rangle \right)^2 \right], \tag{D.7}$$

which justifies Eq. (27).

Bibliography

[1] P. M. Bonifacio *et al.*, Class. Quantum Grav. **26**, 145013 (2009).

[2] L. Diósi L, Phys. Lett. A **120**, 377 (1987).

[3] L. Diósi, Phys. Rev. A. **40**, 1165 (1989).

[4] L. Diósi and J. J. Halliwell, Phys. Rev. Lett **81**, 2846 (1998).

[5] R. Penrose, Gen. Rel. Grav. **28**, 581 (1996)

[6] R. Penrose, *The Road to Reality: A Complete Guide to the Laws of the Universe,* Alfred A. Knopf inc., New York (2005).

[7] W. Marshall, C. Simon, R. Penrose, and D. Bouwmeester, Phys. Rev. Lett. **91**, 130401 (2003).

[8] T. Hong *et al.*, arXiv:1110.3349 [quant-ph] (2011).

[9] J. van Wezel and T. H. Oosterkamp, Proc. R. Soc. A **468**, 35 (2012).

[10] R. Kaltenbaek *et al.*, Exp. Astron. **34**, 123 (2012).

[11] O. Romero-Isart *et al.*, Phys. Rev. Lett **107**, 020405 (2011).

[12] O. Romero-Isart, Phys. Rev. A **84**, 052121 (2011).

[13] M. Maggiore, Phys. Lett. B, **319**, 83 (1993).

[14] S. Das and E. C. Vagenas, Phys. Rev. Lett. **101**, 221301 (2008).

[15] I. Pikovski *et al.*, Nature Phys. **8**, 393 (2012).

[16] C. Moller, *Les Theories Relativistes de la Gravitation* Colloques Internationaux CNRX 91 ed A Lichnerowicz and M-A Tonnelat (Paris: CNRS) (1962).

[17] L. Rosenfeld, Nucl. Phys. **40**, 353 (1963).

[18] S. Carlip, Class. Quantum Grav. **25**, 154010 (2008).

[19] R. M. Wald, *General Relativity*, University of Chicago Press (1984).

[20] H. Everett III, Rev. Mod. Phys. 29, 454 (1957).

[21] D. N. Page and C. D. Geilker, Phys. Rev. Lett **47**, 979 (1981).

[22] L. Diósi, Phys. Lett. A **105**, 199 (1984).

[23] I. M. Moroz, R. Penrose, and P. Tod, Class. Quantum Grav. **15**, 2733 (1999).

[24] R. Harrison, I. Moroz, and K. P. Tod, Nonlinearity **16**, 101 (2002).

[25] P. J. Salzman and S. Carlip, arXiv:gr-qc/0606120 (2006).

[26] S. L. Adler, J. Phys. A **40**, 755 (2007).

[27] F. S. Guzmán and L. A. Urena-López. Phys. Rev. D **69**, 124033 (2004).

[28] J. R. Meter, Class. Quant. Grav. **28**, 215013, (2011). In this article, the authors assumed that the CM degree of freedom satisfies the single-particle SN equation. This is significantly different from what we have obtained. In particular, in the limiting case when the CM wave-function spread approaches zero, their SN term diverges due to divergence in the self-gravitational energy of a single particle, and the state changes dramtically. By contrast, our SN term also approaches zero in this case, as it arises from the change in many-particle grivitional energy induced by the CM motion, which decreases as the uncertainty in the CM motion decreases.

[29] See, e.g., recent review article by M. Aspelmeyer, P. Meystre, and K. Schwab, Physics Today **65**, 29 (2012).

[30] A. D. O'Connel *et al.*, Nature **464**, 697 (2010).

[31] J. Chan *et al.*, Nature **478**, 89 (2011).

[32] J. D. Teufel *et al.*, Nature **475**, 359 (2011).

[33] T. P. Purdy, R.W. Peterson, and C. A. Regal., arXiv:1209.6334 (2012).

[34] V. B. Braginsky and F. Ya. Khalili, *Quantum Measurement*, Cambridge University Press (1992).

[35] Y. Levin, Phys. Rev. D **57**, 659 (1998); T. Hong, *et al.*, arXiv:1207:6145 (2012).

[36] H. Müller-Ebhardt *et al.*, Phys. Rev. A **80**, 043802 (2009). H. Müller-Ebhardt, H. Rehbein, R. Schnabel, K. Danzmann, and Y. Chen , Phys. Rev. Lett. **100**, 013601 (2008); F. Khalili *et al.*, Phys. Rev. Lett. **105**, 070403 (2010).

[37] H. Miao *et al.*, Phys. Rev. A **81**, 012114 (2010).

[38] B. Abbott et al, New. J. Phys. **11**, 073032 (2009); A. R. Neben *et al.*, New. J. Phys. **14**, 115008 (2012).

[39] H. Miao *et al.*, *Comparison of Quantum Limits in Interferometer Topologies for 3rd Generation LIGO*, LIGO Document T1200008 (2012); S. L. Danilishin and F. Ya. Khalili, Living Rev. Relativity **15**, 5 (2012).

[40] See section C of the Supplementary Material

[41] T. Corbitt *et al.*, Phys. Rev. Lett **98**, 150802 (2007); Phys. Rev. Lett. **99**, 160801 (2007); Phys. Rev. A **73**, 023801 (2006).

[42] T. Westphal *et al.*, App. Phys. B, 1-7 (2012); S. Gossler, Class. Quantum Grav. **27**, 084023 (2010).

[43] T. Uchiyama *et al.*, Phys. Rev. Lett. **108**, 141101 (2012).

[44] C. Kittel, *Introduction to Solid State Physics*, 8th ed. *Wiley* (2004).

[45] M. Blackman and R. H. Fowler, Math. Proc. Cambridge Phil. Soc. **33**, 380 (1937).

[46] R. M. Housley and F. Hess, Phys. Rev. **146**, 517 (1966).

[47] C. Flensburg and R. F. Stewart. Phys. Rev. B **60**, 284 (1999).

[48] K. Ishidoshiro *et al.*, Phys. Rev. Lett **106**, 161101 (2011).

[49] V. B. Braginsky *et al.*, Phys. Rev. D **67**, 082001 (2003).

[50] F. Ya. Khalili *et al.*, Phys. Rev. A **86**, 033840 (2012).

Part III

Topics in black hole perturbation theory

Chapter 8

First-order perturbative hamiltonian equations of motion for a point particle orbiting a Schwarzschild black hole

We formulate a spherical harmonically decomposed 1+1 scheme to self-consistently evolve the trajectory of a point particle and its gravitational metric perturbation to a Schwarzschild background spacetime. Following the work of Moncrief, we write down an action for perturbations in space-time geometry, combine that with the action for a point-particle moving through this space-time, and then obtain Hamiltonian equations of motion for metric perturbations and the particle's coordinates as well as their canonical momenta. Hamiltonian equations for the metric-perturbation and their conjugate momenta, for even and odd parities, reduce to Zerilli-Moncrief and Regge-Wheeler master equations with source terms, which are gauge invariant, plus auxiliary equations that specify gauge. Hamiltonian equations for the particle, on the other hand, now include the effect of metric perturbations — with these new terms derived from the same interaction Hamiltonian that had lead to those well-known source terms. In this way, space-time geometry and particle motion can be evolved in a self-consistent manner, in principle in any gauge. However, the point-particle nature of our source requires regularization, and we outline how the Detweiler-Whiting approach can be applied. In this approach, a singular field can be obtained analytically using Hadamard decomposition of the Green's function; and the regular field, which needs to be evolved numerically, is the result of subtracting the singular field from the total metric perturbation. In principle, any gauge that has singular-regular field decomposition is suitable for our self-consistent scheme. In reality, however, this freedom is only possible if our singular field has a high enough level of smoothness. For a singular field with minimum quality, one can adopt the Lorenz

gauge condition, which we have recast into our formalism: for each l and m, we have 2 wave equations to evolve odd and even parity gauge invariant quantities and 8 first order differential equations to fix the Lorenz gauge and determine the metric components.

Preprint paper by H. Yang, H. Miao and Y. Chen, arXiv:1211.5410.

8.1 Introduction

In this paper, we discuss the motion of a small compact object (idealizing a black hole or neutron star) moving around a much more massive, Schwarzschild black hole — and the gravitational waves such a system would emit. In gravitational-wave astrophysics, this process is often referred to as an Extreme Mass-Ratio Inspiral (EMRI). This problem has attracted a lot of attention in recent years due to the possibility of directly detecting these waves using space-based [1–3] and even ground-based laser interferometer gravitational-wave detectors [4]. In EMRIs, the small object stays for a long time outside of the big black hole, emitting many cycles of gravitational waves — even in the strong-field region very close to the big black hole. This wave, if detected, will provide accurate information about the mass and the spin of big black hole, as well as parameters of the small object's orbit; one might even test whether the big black hole is indeed a Kerr background spacetime [5–8]. On the other hand, because it is the many cycles that would together lead to a detectable signal, it will be crucial (at least for the weaker sources) to get very accurate models for the waveforms (e.g., at the level of one or a few radians for the entire waveform, which may be up to 10^6 cycles) in order to be able to extract them from data [9].

Because the orbiting object is much smaller in mass, one expects the application of black-hole perturbation theory [10–12], successively to higher orders in mass ratio, would be a viable program towards solving the EMRI problem, just like Post-Newtonian theory has worked for the inspiral of comparable-mass compact objects [13]— although a direct application of post-Newtonian theory to EMRIs will not be very efficient because one expects the most interesting waves to be generated when the small object moves very close to the big black hole, with where post-Newtonian theory breaks down very fast. By contrast, full numerical simulation of the entire EMRI spacetime would be very expensive due to the large separation of scales and very long integration time that is required to providing meaningful information regarding the evolution of the orbit. Nevertheless, the most extreme mass ratio achieved so far in numerical relativity simulations is 1 : 100 [14].

When computing the leading-order waveform emitted by a small compact object moving in a black-hole background, one can idealize the small object as a test particle moving along a geodesic, and perturbations to the black-hole spacetime are sourced by a δ-function stress-energy tensor along that geodesic — with all other multipoles of the object ignored. However, if we would like to further

calculate the evolution of the object via coupling to the radiation field, we need to consider space-time geometry near the object, which formally diverges if we still use the point-particle model. From this point of view, a regularization procedure is necessary.

Historically there are two approaches toward regularization. The first involves matching the external (point-particle-generated perturbed black-hole) spacetime to the internal perturbed Schwarzschild spacetime of the small object — in a region where both are valid. This was proposed and carried out by Mino, Sasaki and Tanaka [15] as well as by Quinn and Wald [16], and later by Gralla, Pound, Poisson and others [17–19]. This approach, for the external spacetime of the object, has led to the separation of the total metric perturbation field into two pieces: $h = h_{\mathrm{dir}} + h_{\mathrm{tail}}$; h_{dir} is the light-cone contribution to metric perturbation from the point particle's δ-function stress energy tensor (the Hadamard direct part) and h_{tail} is the contribution inside the future light cone of the particle (the tail part). Mino et al. [15] and Quinn and Wald [16] proved that the regularized radiation reaction is solely contributed by h_{ret} which is everywhere continuous but not necessarily smoothly differentiable. This approach is useful when one knows the Green's function of the background spacetime.

The second method, usually called Detweiler-Whiting decomposition, keeps the point-particle description of the problem, but instead separates the total metric perturbation field h into a regular piece h_R and a singular piece h_S [20]. The singular piece diverges at the particles's location but does not have any effect on the particle's motion. It can be obtained by either transforming its expression in the local THZ (Thorne-Hartle-Zhang) coordinate system [21] to the background coordinate system or applying the Hadamard decomposition of the Green's function [22]. The regular field satisfies the homogeneous Einstein's equation and is responsible for the geodesic deviation of the particle's motion in background spacetime; it is obtained by subtracting the singular field from the full field.

The regularization procedures above normally provide, in a particular gauge, a force in terms of a geodesic orbit of a particle. In order to obtain the evolution of the particle and the out-going wave, one must construct an algorithm to compute the force, and use it to drive one's particle trajectory away from geodesic motion [17]. There are two major approaches towards the numerical implementation. One way is the *mode sum* approach, developed by Barack and Ori [23], which decomposes each of the 10 metric components into spherical harmonics, and solves 10 coupled 1+1 wave equations for each (l, m). Because of the modal decomposition, the metric component for each (l, m) is finite even at the particle's location. The particle equation of motion is then regularized mode-by-mode, by subtracting a series of regularization parameters for each (l, m) — these regularization parameters can be calculated either from the singular field of Detweiler and Whiting, or to the direct part of Mino, Sasaki and Tanaka. This mode sum method has already been implemented by Warburton et al. [24] for Schwarzschild gravitational EMRI problem.

In the second approach, one directly applies a 3+1 decomposition of spacetime, and tries to

obtain the regular field directly — by obtaining a field $\tilde{h}_R$ which is approximately the Detweiler-Whiting h_R near the particle, but gradually becomes the full field at null infinite and near horizon. As shown by Vega and Detweiler [25], the field $\tilde{h}_R$ satisfies a wave equation with out-going boundary condition at infinity and horizon, but with a source that can be computed from the Detweiler-Whiting singular field h_S. Diener and Vega [26] have implemented this method for a scalar particle orbiting a Schwarzschild black hole. In principal, this effective source method is also suitable for the 1+1 evolution scheme. In practice, translating the 3+1 effective source into spherical decomposed form and implementing it into a working code still requires a substantial amount of work.

In this paper, we formulate a Hamiltonian approach towards the EMRI problem in Schwarzschild background, with the aim of providing a new angle to view this problem. We will only write down the equations, but not attempt to solve them numerically. We start by generalizing Moncrief's (already spherical harmonic decomposed) quadratic action of perturbative Schwarzschild spacetime to include a point particle, and write down a joint Hamiltonian for the particle and the spherical harmonic decomposed field.

The total Hamiltonian leads naturally to a set of canonical equations that describe the joint evolution of the particle and the field. Moreover, since we are adopting Moncrief's formalism, the gauge invariant part of the perturbation fields are separated out from the rest of the degrees of freedom — these fields, together with lapse and shift, drive the rest of the fields. For each (l, m), there are 6 pairs of canonical quantities; 2 pairs are always gauge invariant, and evolve independently (but driven by the particle); among the other 4 pairs, 3 canonical momenta and 1 canonical coordinate correspond to the momentum and Hamiltonian constraints, while the other 3 canonical coordinate and 1 canonical momentum can be fixed by gauge choices.

Although the Hamiltonian approach provides a rather good way of organizing the fields, we have not found any stand-alone regularization technique — and must instead adopt an existing one. In principle, taking the 4 dimensional Detweiler-Whiting singular field h_S in any gauge, as long as their continuity survives the differential operations required for constructing our canonical field quantities, they can be readily used to obtain effective sources for $\tilde{h}_R$, the effective regular field. However, the currently available singular field only allows the use of Lorenz gauge, which means we will have to fix that gauge, evolving the 8 above mentioned equations.

This paper is organized as follows. In Sec. 11.3 we briefly review Moncrief's Hamiltonian approach for gravitational perturbations of the Schwarzschild metric. After that we introduce additional terms into the action that describe the point particle. From this new action, we rederive the odd and even parity metric perturbation master equations as well as the point mass equations of motion in Sec. 11.4. Note that for both odd and even parities, wave equations agree with the known master equations for Regge-Wheeler and Zerilli-Monrief functions with a point-particle source [27–29]. On the other hand, the point mass equations of motion are now subject to the influence of the background

metric and both odd and even parity metric perturbations. They have the physical meaning of the geodesic motion in the perturbed background spacetime. In Sec. 11.5, we will discuss possible ways to regularize the gauge invariant quantities and specific gauge choice, and hence obtain a fully regularized set of equations for both the metric perturbations and the point mass. We conclude in Sec. 11.6.

8.2   Review of Moncrief's Hamiltonian approach

The Arnowitt, Deser, and Misner (ADM) approach to general relativity [48] was established more than fifty years ago. In this approach, the Einstein-Hilbert action is written in a $3+1$ format similar to a constrained Hamiltonian dynamical system: the spatial 3-metric components are treated as canonical coordinates, while their conjugate momenta are related to components of the extrinsic curvature. The lapse and shift functions serve as Lagrange multipliers for the Hamiltonian and momentum constraints. As one varies the action with respect to the canonical coordinates (not including lapse and shift functions) and their conjugate momenta, a set of evolution equations can be obtained. As one varies the action with respect to the lapse and shift functions, a set of constraint equations are obtained — these equations are to be satisfied at the initial time, and will keep being satisfied if the above-mentioned evolution equations are followed. This approach rewrites Einstein's equations as an initial-value problem; it is closely related to the modern development of numerical relativity [47].

8.2.1   First-order perturbation of a static space-time in 3+1 form

Starting from this section, we review Moncrief's implementation of the ADM formalism to perturbed Schwarzschild spacetimes [30]. In general, for a static background spacetime, if we take spatial slices orthogonal to the time-like Killing vector $\vec{\partial}_t$, and use integration curves of $\vec{\partial}_t$ to identify points with the same spatial coordinates (on the spatial slices), we will have a constant 3-metric γ_{ij} (with determinant γ), vanishing extrinsic curvature, a lapse N that only depends on spatial coordinates, and a vanishing shift vector $N_j = 0$. Here and henceforth in the paper, we shall use $i, j, k, ... = 1, 2, 3$ to label spatial coordinates on each slice. If we have a perturbed 3-metric h_{ij}, their canonical conjugates p^{ij}, lapse perturbation N', and shift perturbation N'_j, then the perturbative part of the Einstein-Hilbert action, up to quadratic order in these perturbative quantities, can be written as: [30]

$$J = \int d^4x \left[p^{ij} \frac{\partial h_{ij}}{\partial t} - N'_i \mathcal{H}'^i - N' \mathcal{H}' - N \mathcal{H}^* \right] . \tag{8.1}$$

Here $\mathcal{H}'$ and $\mathcal{H}'^i$ are the Hamiltonian and momentum constraints, respectively,

$$\mathcal{H}'^i = -2p^{ij}_{|j}, \tag{8.2a}$$

$$\mathcal{H}' = -\gamma^{1/2}\left[h_{ij}{}^{|ij} - h_{|i}{}^{|i} - h_{ij}{}^{(3)}R^{ij}\right] \tag{8.2b}$$

and

$$\begin{aligned}
\mathcal{H}^* &= \gamma^{-1/2}\left[p^{ij}p_{ij} - \tfrac{1}{2}p^2\right] + \tfrac{1}{2}\gamma^{1/2}\tfrac{1}{2}h_{ij|k}h^{ij|k} \\
&+ \tfrac{1}{2}\gamma^{1/2}\left[-h_{ij|k}h^{ik|j} - \tfrac{1}{2}h_{|i}h^{|i} + 2h_{|i}h^{ij}{}_{|j}\right] \\
&+ \tfrac{1}{2}\gamma^{1/2}\left[hh^{ij}{}_{|ij} - hh_{ij}{}^{(3)}R^{ij}\right].
\end{aligned} \tag{8.3}$$

Here $^{(3)}R_{ij}$ is the Ricci tensor associated with γ_{ij}. The covariant derivative "$|$" here is with respect to the background 3 metric γ_{ij}.

The action J in Eq. (8.1) leads to a Hamiltonian system with constraints. In particular, variations with respect to the lapse function N' and shift function N'_j give rise to the constraint equations,

$$\mathcal{H}'^i = 0, \ \mathcal{H}' = 0 \tag{8.4}$$

while variations with respect to h_{ij} and π^{ij} give rise to the evolution equations:

$$\frac{\partial h_{ij}}{\partial t} = \frac{\delta H_T}{\delta \pi^{ij}}, \ \frac{\partial \pi^{ij}}{\partial t} = -\frac{\delta H_T}{\delta h_{ij}}. \tag{8.5}$$

Here we have defined

$$H_T = \int d^3x \left[N\mathcal{H}^* + N'\mathcal{H}' + N'_i\mathcal{H}'^i\right] \tag{8.6}$$

8.2.2 Degrees of freedom

Let us now count the number of degrees of freedom of this Hamiltonian system. Nominally, we start from 6 metric perturbations, plus 6 canonical momenta, governed by 6 pairs (i.e., 12) equations of motion. However, we have 4 constraints and 4 gauge degrees of freedom at all times; so in principle we should be able to cut down to 4 gauge independent functions, or 2 pairs of canonical degrees of freedom — this is what Moncrief worked out explicitly for Schwarzschild.

From a 3+1 point of view, we need to show that we indeed only have 4 independent data to specify for free at the initial time slice — and the evolution of these 4 independent data can already describe all solutions. For this, we note that when specifying the 12 *initial* perturbation functions, we need to subject them to 4 constraints, so there are 8 independent remaining degrees of freedom. However, we have 3 dimensional gauge within the slice, as well as an extra parameter determining

the slicing, so we have 4 additional functions that can be used to reveal initial data that are actually equivalent to each other — with 4 truly independent degrees of freedom left. The *evolution* these 4 functions will be supplemented by the 4 constraints and the 4 lapse/shift functions to complete the 12 functions.

In fact, we can make the above arguments a little more precise. Suppose, after a canonical transformation, we can transform the Hamiltonian and momentum constraints to become independent canonical coordinates and momenta. More specifically, let us label the Hamiltonian constraint the first canonical coordinate $\mathcal{Q}_0$, denote the conjugate momentum of $\mathcal{Q}_0$ as $\mathcal{P}_0$; let us then label the momentum constraints as $\mathcal{P}_{1,2,3}$, and label their conjugate coordinates as $\mathcal{Q}_{1,2,3}$. In other words, we have

$$\mathcal{Q}_0 = \mathcal{H}', \quad \mathcal{P}_i = \mathcal{H}'^i, \quad i = 1, 2, 3. \tag{8.7}$$

We will label the rest of the canonical coordinates $\mathcal{Q}_{4,5}$ and momenta $\mathcal{P}_{4,5}$. Noting that all components of the momentum constraints already have vanishing Poisson brackets with each other,

$$\left\{\mathcal{H}'^i, \mathcal{H}'^j\right\} = 0, \quad i, j = 1, 2, 3, \tag{8.8}$$

we only need to make sure that the Hamiltonian constraint have a vanishing Poisson bracket with all components of the momentum constraint:

$$\left\{\mathcal{H}', \mathcal{H}'^j\right\} = 0. \quad j = 1, 2, 3. \tag{8.9}$$

Thus it is rather straightforward to show if we look at the evolution equation for the Hamiltonian constraint:

$$\frac{d}{dt}\mathcal{H}' = \left\{\mathcal{H}', \mathcal{H}'^j\right\} N'_j + (\text{terms not involving shift}). \tag{8.10}$$

Now imagine we already have vanishing constraints initially, then in order to guarantee vanishing constraints during the subsequent evolution — regardless of the shift function N'_j we must ensure that the Poisson bracket $\left\{\mathcal{H}', \mathcal{H}'^j\right\}$ vanishes numerically. However, for linear perturbation theory, $\mathcal{H}'$ and $\mathcal{H}'^j$ are linear in the canonical coordinates and momenta, h_{ij} and p^{ij}, their Poisson brackets are simply numbers (or rather, functions of the spatial coordinate) that do not depend on these perturbative fields. In this way, the numerical vanishing of $\left\{\mathcal{H}', \mathcal{H}'^j\right\}$ in Eq. (8.10) is equivalent to Eq. (8.9) — hence Eq. (8.7) is always possible.

Next, let us consider the consequence of the important property that once $\mathcal{Q}_0$ and $\mathcal{P}_{1,2,3}$ start from 0, they must stay at 0. This means their time derivatives must only contain themselves — which means, in the Hamiltonian, quantities $\mathcal{P}_0$ and $\mathcal{Q}_{1,2,3}$ must only multiply $\mathcal{Q}_0$ and $\mathcal{P}_{1,2,3}$

$$\mathcal{P}_0 \cdot [\text{only } \mathcal{Q}_0 \text{ and } \mathcal{P}_{1,2,3}] \ \& \ \mathcal{Q}_{1,2,3} \cdot [\text{only } \mathcal{Q}_0 \text{ and } \mathcal{P}_{1,2,3}]. \tag{8.11}$$

	Odd Parity	Even Parity
Lapse		H_0
Shift	$h_0\ (l \geq 1)$	$H_1,\ h_0^*\ (l \geq 1)$
3-Metric	$h_1\ (l \geq 1),\ h_2\ (l \geq 2)$	$H_2,\ K,\ h_1^*\ (l \geq 1)\ ,\ G\ (l \geq 2)$

Table 8.1: List of lapse, shift and 3-metric perturbations

The absence of $\mathcal{Q}_{4,5}$ and $\mathcal{P}_{4,5}$ in the above terms means that the derivatives of $\mathcal{P}_{4,5}$ and $\mathcal{Q}_{4,5}$ cannot include $\mathcal{P}_0$ or $\mathcal{Q}_{1,2,3}$. This, plus the fact that $\mathcal{Q}_0$ and $\mathcal{P}_{1,2,3}$ vanish, means that the evolution of $\mathcal{P}_{4,5}$ and $\mathcal{Q}_{4,5}$ must be self contained, or:

$$\frac{d}{dt}\mathcal{P}_{4,5} \sim \mathcal{P}_{4,5}\&\mathcal{Q}_{4,5}\,,\quad \frac{d}{dt}\mathcal{Q}_{4,5} \sim \mathcal{P}_{4,5}\&\mathcal{Q}_{4,5}\,. \tag{8.12}$$

In this way, these 4 are the gauge-invariant canonical variables. Another 4 equations are driven by the above gauge-invariant quantities, plus lapse and shift:

$$\frac{d}{dt}\mathcal{P}_0 \quad \sim \quad \mathcal{P}_{4,5}\ \&\ \mathcal{Q}_{4,5}\ \&\ \mathcal{P}_0\ \&\ \mathcal{Q}_{1,2,3}\&N' \tag{8.13}$$

$$\frac{d}{dt}\mathcal{Q}_{1,2,3} \quad \sim \quad \mathcal{P}_{4,5}\ \&\ \mathcal{Q}_{4,5}\ \&\ \mathcal{P}_0\ \&\ \mathcal{Q}_{1,2,3}\&N'_{1,2,3}\,. \tag{8.14}$$

The final 4 equations are simply that the constraints vanish.

As we shall see below, in his treatment of Schwarzschild perturbations, Moncrief did follow the above general prescription — by directly using constraints as canonical coordinates and momenta. Note that this structure seems rather generic, and does not seem to be limited to Schwarzschild or even static spacetimes — of course, the question of whether one can separate these into different (l, m) components is another issue.

8.2.3 Schwarzschild perturbations

Let us return to perturbations of Schwarzschild. In our case, the background metric is

$$ds^2 = -\left(1 - \frac{2M}{r}\right)dt^2 + \frac{dr^2}{1 - \frac{2M}{r}} + r^2(d\theta^2 + \sin^2\theta d\phi^2) \tag{8.15}$$

and we choose to start with constant-t slices in this Schwarzschild coordinate system, and adopt spatial coordinates

$$(x^1, x^2, x^3) = (r, \theta, \phi). \tag{8.16}$$

In this way, we have $N = \sqrt{-1/g^{00}} = \sqrt{1 - 2M/r}$, and non-zero components of γ_{ij} given by

$$\gamma_{11} = \frac{1}{1 - 2M/r}\,,\quad \gamma_{22} = r^2\,,\quad \gamma_{33} = r^2\sin^2\theta\,. \tag{8.17}$$

We shall use $i, j, k = 1, 2, 3$ to label these spatial coordinates, and write components of the metric perturbation h_{ij} as functions of spacetime coordinates (t, r, θ, ϕ) — and separate the angular dependence by decomposing them into scalar, vectorial and tensorial spherical harmonics [27]

$$h_{AB}^{lm} = r^2 \left[K(t,r) U_{AB}^{lm} + G(t,r) V_{AB}^{lm} \right] + h_2(t,r) W_{AB}^{lm}, \tag{8.18a}$$

$$h_{rr}^{lm} = 1/f H_2(t,r) Y^{lm}, \tag{8.18b}$$

$$h_{rA} = h_1^*(t,r) Z_A^{lm} + h_1(t,r) X_A^{lm}. \tag{8.18c}$$

Here we have defined $f \equiv 1 - 2M/r$, and shall use $A, B, \ldots = 1, 2$ to label angular coordinates

$$(\Omega^1, \Omega^2) = (\theta, \phi). \tag{8.19}$$

The conjugate momenta p_{ij} can be similarly decomposed, while the decomposition of lapse and shift perturbations N', N_i' are [27]

$$h_{tt}^{lm} = f H_0(t,r) Y^{lm}, \tag{8.20a}$$

$$h_{tr}^{lm} = H_1(t,r) Y^{lm}, \tag{8.20b}$$

$$h_{tA}^{lm} = h_0^*(t,r) Z_A^{lm} + h_0(t,r) X_A^{lm}. \tag{8.20c}$$

Here we have used odd parity vector and tensor spherical harmonics X_A^{lm}, W_{AB}^{lm}, as well as even parity ones, $Z_A^{lm}, U_{AB}^{lm}, V_{AB}^{lm}$; their definitions can be found in [27, 28]; we have also listed them in Appendix 8.A. For each (l, m), $(l \geq 2)$, we have a total of 10 independent functions characterizing 10 independent metric components; 4 of them are lapse and shift perturbations: H_0 is lapse perturbation and H_1, h_0^*, h_0 are shift perturbations. The other 6 functions are spatial metric perturbations: $K, G, h_2, H_2, h_1^*, h_1$. For even parity, there is 1 lapse perturbation function H_0, 2 shift perturbation functions H_1, h_0^* and 4 spatial metric perturbation functions K, G, H_2, h_1^*. For odd parity, there are no lapse perturbation, 1 shift perturbation function h_0 and 2 spatial metric perturbation functions h_1, h_2 for odd parity. This list is shown in Table 8.1.

8.2.4   Odd parity $(l \geq 2)$

Let us first look at odd-parity perturbations, which contain spatial-metric perturbations h_1, h_2 [Eq. (8.18)] and shift perturbation h_0 [Eq. (8.20)]. All odd-parity infinitesimal coordinate transformations within the spatial slice can be represented using the odd-parity vector harmonic X_A^{lm},

$$\Omega_A' = \Omega_A + \sum_{lm} C^{lm}(r,t) X_A^{lm} = \Omega_A + C_A, \tag{8.21}$$

which, after applying

$$\delta h_{ij} = C_{i|j} + C_{j|i} \qquad (8.22)$$

lead to

$$\delta h_1 = C_{,r} - \frac{2}{r}C, \quad \delta h_2 = -2C. \qquad (8.23)$$

Moncrief defined new perturbation functions

$$k_1 = h_1 + \frac{1}{2}\left(h_{2,r} - \frac{2}{r}h_2\right), \quad k_2 = h_2, \qquad (8.24)$$

which transform as

$$\delta k_1 = 0, \, \delta k_2 = -2C. \qquad (8.25)$$

In other words, k_1 is invariant under infinitesimal coordinate transformations while k_2 is vulnerable to the specific choice of gauge. In terms of $k_{1,2}$, and their canonical conjugates $\tau_{1,2}$, the the odd-parity Hamiltonian [Eq. (8.6)] can now be expressed as

$$
\begin{aligned}
H_T &= \frac{1}{\lambda+1}\int dr\left\{\tau_1^2 + \frac{r^2 f}{\lambda}\left[\tau_2 - \frac{1}{2}\tau_{1,r} - \frac{1}{r}\tau_1\right]\right\} \\
&+ 2\lambda(\lambda+1)\int dr\, \frac{f}{r^2}k_1^2 - 2\int dr\, h_0\tau_2
\end{aligned}
\qquad (8.26)
$$

with

$$\lambda \equiv (l-1)(l+2)/2. \qquad (8.27)$$

Variation of the shift function h_0 in the Hamiltonian gives the odd-parity momentum constraint equation

$$\tau_2 = 0. \qquad (8.28)$$

Equations of motion for the dynamical variables take the form [30]

$$\frac{\partial k_1}{\partial t} = \frac{\delta H_T}{\delta \tau_1} = \frac{\tau_1}{2(\lambda+1)} + \frac{r^2\left[f\left(\tau_2 - \frac{(r^2\tau_1),_r}{2r^2}\right)\right]_{,r}}{2\lambda(\lambda+1)}, \qquad (8.29a)$$

$$\frac{\partial \tau_1}{\partial t} = -\frac{\delta H_T}{\delta k_1} = -\frac{4\lambda(\lambda+1)}{r^2}fk_1, \qquad (8.29b)$$

$$\frac{\partial k_2}{\partial t} = \frac{\delta H_T}{\delta \tau_2} = \frac{fr^2}{\lambda(\lambda+1)}\left[\tau_2 - \frac{(r^2\tau_1),_r}{2r^2}\right] - 2h_0, \qquad (8.29c)$$

$$\frac{\partial \tau_2}{\partial t} = -\frac{\delta H_T}{\delta k_2} = 0. \qquad (8.29d)$$

Here $\tau_2 = 0$ is constraint; (k_1, τ_1) is the gauge-invariant sector, which evolves independently (once setting $\tau_2 = 0$). The gauge is fixed by choosing h_0, which correspondingly fixes the evolution of k_2. (Note that τ_2 is constraint and should vanish.) As an example, the Regge-Wheeler gauge is obtained by imposing that $k_2 = 0$, which requires setting

$$h_0 = \frac{f(r^2 \tau_1)_{,r}}{4\lambda(\lambda + 1)}. \tag{8.30}$$

These odd-parity perturbation equations determine 2 out of the 6 spatial 3-metric components, and 3 out of the total 10 spacetime 4-metric components.

The Regge-Wheeler function frequently used in the literature to describe odd-parity perturbations [27–29, 41–43] is related to k_1 by

$$\psi_{\mathrm{RW}} = f k_1 / r : \tag{8.31}$$

ψ_{RW} is invariant under infinitesimal gauge transformations.

8.2.5 Even parity $(l \geq 2)$

For even parity, there are 4 spatial-metric perturbations, K, G, H_2, h_1^* [Eq. (8.18)], 1 lapse perturbation H_0 and 2 shift perturbations H_1, h_0^* [Eq. (8.20)]. Moncrief found it convenient to recombine K, G, H_2, h_1^* and define a new set of variables q_1, q_2, q_3, q_4. Like k_1 for odd parity perturbation, q_1 is invariant under the infinitesimal gauge transformation whereas q_2, q_3, q_4 are gauge dependent. The conversion between K, G, H_2, h_1^* and q_1, q_2, q_3, q_4 can be found in [30] and Appendix 8.B of this paper. In terms of the new coordinates and their conjugate momenta, $\pi_{1,2,3,4}$, the even parity Hamiltonian is given by:

$$
\begin{aligned}
H_T &= \int dr \left\{ -\frac{2}{r} f \pi_4 \left[r(\pi_1 - \pi_{2,r}) + \left(1 - \frac{M}{fr}\right) \pi_2 \right] \right\} \\
&+ \int dr \left\{ \frac{f}{2r^2\lambda} \left[\frac{\pi_3^2}{\lambda + 1} + 2\pi_3 \left[r\Lambda\pi_1 + \pi_2(r\Lambda)_{,r} \right] \right] \right\} \\
&+ \int dr \left\{ \frac{\lambda + 1}{2\lambda} f\Lambda^2 \pi_1^2 + \frac{\pi_4^2}{4(\lambda + 1)} - \frac{\lambda}{r\Lambda^2} q_1 q_2 \right\} \\
&+ \int dr \left\{ \frac{\lambda f}{2(\lambda + 1)\Lambda^2} (q_2 - q_{1,r})^2 + \frac{2\lambda^2}{r^2\Lambda^3} q_1^2 \right\} \\
&- \int dr \left\{ \frac{M q_2 (q_2 - q_{1,r})}{2(\lambda + 1)\Lambda r} + \frac{M q_2}{2r} \left(r q_{3,r} - \frac{2}{r} q_4 \right) \right\} \\
&+ \int dr \left\{ \frac{H_0 q_2}{2} + H_1 \pi_4 + h_0^* \left[\frac{2\pi_3}{r^2} - \frac{(r^2 \pi_4)_{,r}}{r^2} \right] \right\}. \tag{8.32}
\end{aligned}
$$

Here Λ is defined as

$$\Lambda \equiv 2 \left(\lambda + \frac{3M}{r} \right) = (l-1)(l+2) + \frac{6M}{r} . \tag{8.33}$$

From this Hamiltonian, it is straightforward to obtain the following canonical equations of motion:

$$\dot{q}_1 = -2f\pi_4 + \frac{f\Lambda}{\lambda r}\pi_3 + \frac{\lambda+1}{\lambda}f\Lambda^2\pi_1, \tag{8.34a}$$

$$\dot{\pi}_1 = \frac{\lambda q_2}{r\Lambda^2} - \frac{4\lambda^2}{r^2\Lambda^3}q_1 - \left[\frac{\lambda f}{(\lambda+1)\Lambda^2}(q_2 - q_{1,r})\right]_{,r}$$

$$+ \left[\frac{Mq_2}{2(\lambda+1)\Lambda r}\right]_{,r}, \tag{8.34b}$$

$$\dot{q}_2 = \frac{2f}{r^2}\pi_3 - \frac{2}{r}\left(f - \frac{M}{r}\right)\pi_4 - 2(f\pi_4)_{,r}, \tag{8.34c}$$

$$\dot{\pi}_2 = \frac{\lambda}{r\Lambda^2}q_1 - \frac{\lambda f}{(\lambda+1)\Lambda^2}(q_2 - q_{1,r}) - \frac{M}{2r}\left(rq_{3,r} - \frac{2}{r}q_4\right),$$

$$+ \frac{M(2q_2 - q_{1,r})}{2(\lambda+1)\Lambda r} - \frac{H_0}{2}, \tag{8.34d}$$

$$\dot{q}_3 = \frac{f\pi_3}{r^2\lambda(\lambda+1)} + \frac{f}{r^2\lambda}\left[r\Lambda\pi_1 + 2\lambda\pi_2\right] + \frac{2h_0^*}{r^2}, \tag{8.34e}$$

$$\dot{\pi}_3 = -\frac{M}{2}q_{2,r}, \tag{8.34f}$$

$$\dot{q}_4 = \frac{\pi_4}{2(\lambda+1)} + H_1 + r^2\left(\frac{h_0^*}{r^2}\right)_{,r}$$

$$-2f(\pi_1 - \pi_{2,r}) - \frac{2}{r}\left(f - \frac{M}{r}\right)\pi_2, \tag{8.34g}$$

$$\dot{\pi}_4 = -\frac{M}{r^2}q_2. \tag{8.34h}$$

By varying the lapse perturbation H_0 and the shift perturbations H_1, h_0^*, it is straightforward to obtain the Hamiltonian constraint equation

$$q_2 = 0 \tag{8.35}$$

as well as the even-parity momentum constraint equations

$$\pi_3 = \pi_4 = 0. \tag{8.36}$$

Note that (q_1, τ_1) is the even-parity gauge-invariant sectors; (π_2, q_3, q_4) are the gauge-dependent sector, which are determined after the lapse H_0 and shifts (H_1, h^*) are fixed.

For example, the even-parity Regge-Wheeler gauge is described by $q_3 = q_4 = \pi_2 = 0$, which requires initially setting $q_3 = q_4 = \pi_2 = 0$, and keeping it true by imposing $\dot{q}_3 = \dot{q}_4 = \dot{\pi}_2 = 0$ through setting the appropriate h_0^* [Eq. (8.34e)], H_1 [Eq. (8.34g)] and H_0 [Eq. (8.34d)]. These even-parity perturbation equations determine the other 4 of the 6 spatial 3-metric perturbations, and the other 7 out of the the 10 spacetime 4-metric perturbations.

Gauge invariant quantity ψ_{ZM} is commonly [27–29, 41–43] used for even parity perturbation and

it is defined by $q_1/(\lambda+1)/\Lambda$ or equivalently [42]

$$\psi_{\text{ZM}} = \frac{r}{\lambda+1} \left[K + \frac{2f}{\Lambda} \left(H_2 - r\frac{\partial K}{\partial r} \right) \right] + \frac{2f}{\Lambda} \left[\frac{r^2 \partial G}{\partial r} - 2h_1^* \right]. \tag{8.37}$$

8.2.6 Monopole and dipole perturbations

For $l \leq 1$, the evolution of 3-metric perturbations can all be fixed by the constraint equations plus arbitrary choices of lapse and shift functions. More specifically:

For $l = 0$, there are only even-parity perturbations. We have lapse perturbation H_0 and shift perturbation H_1, plus metric perturbations H_2 and K — while lapse perturbation h_{0*} and 3-metric perturbations G and h_1^* all vanish due to the non-existence of the vector and tensor harmonics Z and V. However, there still exists one Hamiltonian constraint and one momentum constraint. We can transform (H_2, K) into two new canonical coordinates, one of them the Hamiltonian constraint, the other the canonical conjugate of the momentum constraint — leaving no gauge-invariant perturbation fields.

For $l = 1$, even-parity perturbation, we have lapse perturbation H_0, shift perturbations H_1 and h_0^*, plus three non-vanishing 3-metric perturbation fields, namely H_2, K and h_1^*. However, there exists 1 Hamiltonian constraint and two momentum constraints, and we can transform (H_2, K, h_1^*) into the Hamiltonian constraint and the canonical conjugate of the two momentum constraints, also leaving no gauge-invariant perturbation fields.

For $l = 1$, odd-parity perturbation, we shift perturbation h_0, and one metric perturbation field, which is h_1. We also have one momentum constraint, therefore a spatial operation on h_1 will become the canonical conjugate of the momentum constraint, meaning we have no gauge-invariant perturbation field as well.

8.3   3+1 approach with point mass source

In this paper, we are interested in the joint evolution metric perturbations and the motion of a point particle. In this section, we will augment Moncrief's formalism with a point particle.

8.3.1   3+1 Formulation

Since Eq. (8.1) is the action for free metric perturbations alone, we need to add the action for the point particle. Using the prescriptions in [48], we can write:

$$
\begin{aligned}
J_m &= m \int d\tau \\
&= \int d^4x \, \delta^{(3)}(\mathbf{r} - \mathbf{Q}(t)) \left[P_i \frac{\partial x^i}{\partial t} - \mathcal{N} \left(g^{ij} P_i P_j + m^2 \right)^{1/2} \right]
\end{aligned}
$$

$$+ \quad \left[\mathcal{N}^i P_i \delta^{(3)}(\mathbf{r} - \mathbf{Q}(t)) \right]. \tag{8.38}$$

Here, regarding quantities of space-time geometry, we have $g_{ij} = \gamma_{ij} + h_{ij}$, the total perturbed spatial metric; $\mathcal{N} = N + N'$ the total lapse; and $\mathcal{N}_i = N_i'$ the total shift (recall that $N_i = 0$). Regarding the particle, P_j (j=1,2,3) are components of the 3-momentum, and $\mathbf{Q}(t)$ represents the spatial coordinates of the particle, which are, more specifically, $(R(t), \Theta(t), \Phi(t))$. The δ function is more explicitly written as

$$\delta^{(3)}(\mathbf{r} - \mathbf{Q}(t)) = \delta(r - R(t))\delta(\theta - \Theta(t))\delta(\phi - \Phi(t)). \tag{8.39}$$

From this action, we can read off the part of the Hamiltonian that involves the point particle, which includes the Hamiltonian of the point particle alone,

$$H_m(Q^k, P_k) = N(Q^k)\sqrt{\gamma^{ij}(Q^k)P_iP_j + m^2}, \tag{8.40}$$

which describes the geodesic motion of the particle, plus the interaction Hamiltonian that couples the particle and metric perturbations,

$$
\begin{aligned}
&H_{\text{int}}(Q^k, P_k, N', N_j', h_{ij}) \\
=&N'\sqrt{\gamma^{ij}P_iP_j + m^2} - \frac{N}{2}\frac{h_{ij}\gamma^{il}\gamma^{jm}P_lP_m}{\sqrt{\gamma^{ij}P_iP_j + m^2}}. \\
&-N_j'P^j
\end{aligned}
\tag{8.41}
$$

Here we have suppressed N', N, N_j', γ^{ij} and h_{ij}'s dependence on Q^k, for simplicity — but the reader is reminded that Q^k enters this interaction Hamiltonian through these quantities' dependence on Q^k. Note that H_{int} is *linear* in the metric perturbations N', N_j' and h_{ij}.

The total Hamiltonian for the combined system of point particle plus metric perturbations is

$$H_{\text{tot}} = \sum_{lm}(H_{\text{oddT}}^{lm} + H_{\text{evenT}}^{lm}) + 16\pi H_{\text{m}} + 16\pi H_{\text{int}}. \tag{8.42}$$

The 16π is actually the $2\kappa = 2(8\pi G)$ factor in the Einstein-Hilbert action and we are taking the Newton's constant G to be unity. We have now enlarged the set of canonical coordinates and momenta to include (Q^k, P_k).

The field-alone term in H_{tot} describes the free propagation of metric perturbations around Schwarzschild, the H_m term describes the geodesic motion of the point particle. It is H_{int} that couples the fields and the particle together: it allows the particle's motion to drive field perturbations, and field perturbations to act back onto the particle — with action and back-action described

in a self-consistent way.

Due to spherical symmetry of the background spacetime, we can assume that the point particle is confined within the equatorial plane, with $\Theta = \pi/2$, $P_\theta = 0$ — and we only need to deal with $R(t), \Phi(t)$. In addition, because H_{int} is linear in metric perturbations, we can divide it into the sum of an odd-parity component and an even-parity component — each component only involving one type of metric perturbations.

8.3.2 Odd parity $(l \geq 2)$

Odd-Parity metric perturbations are described in terms of odd-parity vector and tensor harmonics X_A^{lm}, W_{AB}^{lm} in Eq. (8.18) and Eq. (8.20). For later convenience, we denote by Π and Ξ,

$$\Pi = W_{AB}^{lm} P^A P^B, \ \Xi = X_A^{lm} P^A, \tag{8.43}$$

the contractions of these harmonics with angular components of momentum. Plugging odd-parity perturbations in Eqs. (8.18) and (8.20) into Eq. (8.41), and taking Eq. (8.43) into account, we obtain, for each (l, m),

$$
\begin{aligned}
&H_{\text{int}}^{\text{odd}} \\
&= \left[-h_0 \Xi - \frac{\sqrt{f}}{2} \frac{2h_1 P^r \Xi + h_2 \Pi}{\sqrt{\gamma_{ij} P^i P^j + m^2}} \right]\Bigg|_{r=R(t),\, \Omega=\tilde{\Omega}(t)}, \\
&= \int dr \int d^2\Omega \ \delta(r - R(t))\delta^{(2)}(\Omega - \tilde{\Omega}(t)) \\
&\qquad \left[-h_0 \Xi - \frac{\sqrt{f}}{2} \frac{2(k_1 - \frac{1}{2}k_{2,r} + \frac{1}{r}k_2)P^r \Xi + k_2 \Pi}{\sqrt{\gamma_{ij} P^i P^j + m^2}} \right].
\end{aligned}
\tag{8.44}
$$

Here we have used Ω to represent (θ, ϕ), and $\tilde{\Omega}(t)$ to represent $(\Theta(t), \Phi(t))$.

For any expression inside the definition of $H_{\text{int}}^{\text{odd}}$, for example γ_{ij}, it always appears along with a $\delta(r - R(t))$ function; therefore being a function of (r, θ, ϕ) instead of (R, Θ, Φ) does not seem to make a difference. However, because derivatives of fields are involved, we will encounter derivatives of δ functions in further calculations, and for a generic function $\mathcal{G}(r)$

$$\mathcal{G}(r)\delta'(r - R(t)) \neq \mathcal{G}(R(t))\delta'(r - R(t)). \tag{8.45}$$

This does not indicate an ambiguity in the equations of motion that we are ultimately going to obtain, but creates intermediate steps that may differ. This requires us to be careful with our conventions. Here we shall use the convention that all terms in the integrand on the right-hand side of Eq. (8.44), apart from the δ functions, only depend explicitly on (r, θ, ϕ), not on (R, Θ, Φ).

Taking the above convention for Eq. (8.44), the new constraint equation is

$$\tau_2 = -\frac{1}{2}\,\Xi\,\delta(r - R(t)).\tag{8.46}$$

The right-hand side is singular at the location of the point particle but zero elsewhere. Because H_{int} only contains metric perturbations, not their conjugate momenta, only the evolution of the momenta are affected. The evolution equations for τ_1 gains an additional term of:

$$\left.\frac{\partial \tau_1}{\partial t}\right|_{\text{add}} = -16\pi\frac{\delta H_{\text{int}}}{\delta k_1} = 16\pi\,\Xi\frac{P^r}{P^0}\delta(r - R(t)).\tag{8.47}$$

Similarly for τ_2, the additional term is

$$
\begin{aligned}
\left.\frac{\partial \tau_2}{\partial t}\right|_{\text{add}} &= -16\pi\,\frac{\delta H_{\text{int}}}{\delta k_2} = \frac{16\pi}{P^0}\left(\frac{\Pi}{2} - \frac{P^r}{r}\Xi\right)\delta(r - R(t)) \\
&\quad + \left[\frac{8\pi P^r}{P^0}\,\Xi\,\delta(r - R(t))\right]_{,r}, \\
&= \frac{16\pi}{P^0}\frac{\Pi}{2}\delta(r - R(t)) - \frac{1}{r}\left.\frac{\partial \tau_1}{\partial t}\right|_{\text{add}} - \frac{1}{2}\left[\frac{\partial \tau_1}{\partial t}\right]_{\text{add,r}}.
\end{aligned}\tag{8.48}
$$

It is easy to check that, up to linear order (i.e., inserting background geodesic equations of motion for the particle) this equation is consistent with the new constraint equation Eq (8.46). Combining the evolution equations for k_1, k_2, τ_1, τ_2 and noting $\psi_{\text{RW}} = fk_1/r$, we can derive the following master equation for ψ_{RW}

$$\left[-\frac{\partial^2}{\partial t^2} + \frac{\partial^2}{\partial r^{*2}} - V_{\text{odd}}^l(r)\right]\psi_{\text{RW}}(r, t) = S_{\text{odd}}(r, t),\tag{8.49}$$

where we have defined

$$r^* = r + 2M\log\left(r/2M - 1\right),\tag{8.50}$$

and

$$V_{\text{odd}}^l = \frac{2f}{r^2}\left(\lambda + 1 - \frac{3M}{r}\right).\tag{8.51}$$

The source term is

$$S_{\text{odd}} = \frac{4\pi f}{(\lambda + 1)r}\left[\frac{r^2}{\lambda}\left[\frac{f\Pi\delta(r - R(t))}{P^0}\right]_{,r} - \frac{2\,P^r\Xi\delta(r - R(t))}{P^0}\right].\tag{8.52}$$

Here the subscript "odd" means odd parity. This source term agrees with those derived in literature [11, 27, 28] as expected.

On the other hand, $H_{\text{int}}^{\text{odd}}$ introduces the following additional terms to the rate of change of the

point particle's coordinates:

$$\frac{dR}{dt}\bigg|_{\text{odd}} = 16\pi\frac{\partial H_{\text{int}}^{\text{odd}}}{\partial P_r} = -16\pi h_1\frac{f\,\Xi}{P^0}\left[1 - \frac{(P_r)^2}{(P^0)^2}\right]$$

$$+ 8\pi\frac{h_2\Pi\,P_r}{(P^0)^3} \tag{8.53a}$$

$$\frac{d\Phi}{dt}\bigg|_{\text{odd}} = 16\pi\frac{\partial H_{\text{int}}^{\text{odd}}}{\partial P_\phi}, = -16\pi\left[h_0 X^\phi - \frac{P_\phi[2h_1 P^r\Xi + h_2\Pi]}{2fr^2\sin\theta(P^0)^3}\right]$$

$$- \frac{16\pi}{P^0}\left[h_1 P^r X^\phi + h_2 W^{\phi\phi} P_\phi\right], \tag{8.53b}$$

where components of X^A, W^{AB} can be found in Appendix 8.A. Similarly, the rate of change of the point particle's momenta also gains the following additional terms:

$$\frac{dP_r}{dt}\bigg|_{\text{odd}} = -16\pi\frac{\partial H_{\text{int}}^{\text{odd}}}{\partial R} = 16\pi\left[h_{0,r}\Xi + \frac{2h_{1,r}P^r\Xi + h_{2,r}\Pi}{2\,P^0}\right]$$

$$+ 16\pi\left[2h_1 P^r\Xi + h_2\Pi\right]\left[\frac{1}{P^0}\right]_{,r}, \tag{8.54a}$$

$$\frac{dP_\phi}{dt}\bigg|_{\text{odd}} = -16\pi\frac{\partial H_{\text{int}}^{\text{odd}}}{\partial\Phi} = 16\pi\,h_0 P_\phi X_{,\phi}^\phi$$

$$+ 16\pi\left[\frac{2h_1 P^r P_\phi X_{,\phi}^\phi + h_2 W_{,\phi}^{\phi\phi}(P_\phi)^2}{2P^0}\right]. \tag{8.54b}$$

Note that such a term exists for each (l,m) with $l \geq 2$.

From the above equations of motion it is clear that the effect of odd-parity perturbations on the test particle's motion is determined once we know h_0, h_1, h_2 or h_0, k_1, k_2 and their spatial derivatives at $r = R(t)$; here h_0 and k_2 are related with the actual gauge choice and k_1 is gauge invariant. If we track back to the wave equation for ψ_{RW} or k_1, it is easy to see that k_1 must be discontinuous at $r = R(t)$ in order to obtain a source function $\delta'(r - R(t))$. On the other hand, the equation of motion for $dP_r/dt|_{\text{odd}}$ contains a term proportional to $k_{1,r}$. That means that this equation of motion is singular because it contains $\delta(r - R(t))$. This means the full metric perturbation is singular at the point particle's location, and directly applying full metric perturbation to the particle's equations of motion will introduce divergence. One has to apply a regularization scheme before one can use these equations for computation. This scheme must regularize gauge-invariant quantity k_1 as well as gauge-dependent terms h_2, h_0, since they all enter the particle's equation of motion. We will discuss possible regularization methods in Sec. 11.5.

8.3.3 Even parity $(l \geq 2)$

Even-parity metric perturbations are described in terms of the scalar harmonics Y^{lm}, vector harmonics Z_A^{lm} and tensor harmonics U_{AB}^{lm} and V_{AB}^{lm} [see Eqs. (8.18) and (8.20)]. For later convenience,

we define the following quantities,

$$\Pi_1 = U^{lm}_{AB} P^A P^B, \ \Pi_2 = V^{lm}_{AB} P^A P^B, \ \Xi' = Z^{lm}_A P^A \,, \tag{8.55}$$

which are contractions of the harmonics with angular components of the momentum. Even-parity metric perturbation fields include:

$$N' = -\frac{1}{2} f^{1/2} H_0 Y^{lm}, \ N'_r = H_1 Y^{lm}, \ N'_A = h_0^* Z^{lm}_A \,, \tag{8.56a}$$

$$h^{lm}_{rr} = \frac{H_2}{f} Y^{lm}, \ h^{lm}_{rA} = h_1^* Z^{lm}_A, \ h^{lm}_{AB} = r^2 (K U^{lm}_{AB} + G V^{lm}_{AB}) \,. \tag{8.56b}$$

The (l, m) component of the even-parity Hamiltonian is

$$H^{\text{even}}_{\text{int}} = \int dr \int d^2\Omega \ \delta(r - R(t)) \delta^{(2)}(\Omega - \tilde{\Omega}(t))$$
$$\left[-h_0^* \Xi' - H_1 Y^{lm} P^r + H_0 Y^{lm} P_0/2 \right.$$
$$- \frac{f^{-1}(P^r)^2 H_2 Y^{lm} + 2 h_1^* P^r \Xi'}{2P^0}$$
$$\left. - \frac{+r^2(K\Pi_1 + G\Pi_2)}{2P^0} \right]. \tag{8.57}$$

Here again we have used Ω to represent (θ, ϕ), and $\tilde{\Omega}(t)$ to represent $(\Theta(t), \Phi(t))$, and have defined $P_0 = -f P^0$. In addition, h_0^*, H_1 and H_0 are the lapse and shift perturbations, they serve as Lagrange multipliers in the Hamiltonian; K, H_2, h_1^* and G are 3-metric perturbations, they couple with the point-particle dynamical variables at its location, sourcing the interaction between the field and the test mass. The relation between K, H_2, h_1^*, G and Moncrief's q_1, q_2, q_3, q_4 are shown in Appendix 8.B. We recall the subtlety involving the δ function and its derivative mentioned below Eq. (8.44), and note that all terms in the integrand of Eq. (8.57), with the exception of the δ function, only depend explicitly on (r, θ, ϕ), but not on (R, Θ, Φ).

By varying h_0^*, H_1, H_0, we can obtain the new constraint equations:

$$q_2 = -16\pi P_0 Y^{lm} \delta(r - R(t)) \,, \tag{8.58a}$$

$$\pi_4 = 16\pi Y^{lm} P^r \delta(r - R(t)) \,, \tag{8.58b}$$

$$\pi_3 = 8\pi r^2 \Xi' \delta(r - R(t)) + 8\pi Y^{lm} [r^2 P^r \delta(r - R(t))]_{,r}. \tag{8.58c}$$

This means q_2, π_3 and π_4 are all divergent at the test particle's location and vanish everywhere else.

From $H^{\text{even}}_{\text{int}}$ [Eq. (8.57)], the evolution equation for π_1 gains the additional term of

$$\left. \frac{\partial \pi_1}{\partial t} \right|_{\text{add}} = -\frac{\lambda + 1}{rf} \left. \frac{\partial \pi_2}{\partial t} \right|_{\text{add}} + \left. \frac{\partial \pi_2}{\partial t} \right|_{\text{add,r}}$$

$$+ \frac{4\pi(P^r)^2 Y_{lm}}{P^0 f^2} \delta(r - R(t)) \tag{8.59}$$

and the evolution equation of π_2 gains

$$\frac{\partial \pi_2}{\partial t}\bigg|_{\text{add}} = \frac{4\pi[(P^r)^2 Y_{lm}\Lambda + 2(P^0)^2 r^2 f^2 \Pi]}{P^0 f(1 + \lambda)\Lambda} \delta(r - R(t))$$

$$+ \frac{16\pi f}{(\lambda + 1)\Lambda} \left[\frac{r(P^r)^2 Y_{lm}}{2fP^0} \delta(r - R(t)) \right]'. \tag{8.60}$$

Similar to the odd-parity case, the evolution equations for π_3, π_4 (up to linear order) are consistent with the constraint equations (8.58).

Combing the evolution equation for q_1, q_2, π_1, π_2 and the constraint equations, we will find that the gauge-invariant field ψ_{ZM} satisfies a wave equation with source term coming from the point particle:

$$\left[-\frac{\partial^2}{\partial t^2} + \frac{\partial^2}{\partial r^{*2}} - V^l_{\text{even}}(r) \right] \psi_{\text{ZM}}(r, t) = S_{\text{even}}(r, t), \tag{8.61}$$

with the potential V^l_{even} given by

$$V^l_{\text{even}} = \frac{4f}{r^2 \Lambda^2} \left[2\lambda^2 \left(\lambda + 1 + \frac{3M}{r} \right) \right.$$

$$\left. + \frac{18M^2}{r^2} \left(\lambda + \frac{M}{r} \right) \right], \tag{8.62}$$

and the source term S_e given by

$$S_e = \frac{2}{(\lambda + 1)\Lambda} \left\{ r^2 f(f^2 \frac{\partial}{\partial r} Q^{tt} - \frac{\partial}{\partial r} Q^{rr}) + r(\Lambda/2 - f)Q^{rr} \right.$$

$$\left. - \frac{2f^2}{r\Lambda} [\lambda(\lambda - 1)r^2 + (4\lambda - 9)Mr + 15M^2]Q^{tt} \right\}$$

$$+ \frac{2rf^2}{(\lambda + 1)\Lambda} Q^\flat + \frac{4f}{\Lambda} Q^r - \frac{f}{r} Q^\sharp. \tag{8.63}$$

Here the Qs are master functions describing spherical-harmonic decompositions of the point mass stress energy tensor. They are defined by

$$Q^{tt} = 8\pi \int T^{tt} Y^{lm*} d\Omega = \frac{8\pi P^0}{r^2} \delta[r - R(t)] Y^{lm*}[\Omega(t)], \tag{8.64a}$$

$$Q^{rr} = 8\pi \int T^{rr} Y^{lm*} d\Omega = \frac{8\pi(P^r)^2 \delta[r - R(t)] Y^{lm*}[\Omega(t)]}{r^2 P^0}, \tag{8.64b}$$

$$Q^r = \frac{8\pi r^2}{\lambda + 1} \int T^{rA} Z^{lm*}_A d\Omega = \frac{8\pi P^r \Xi'}{(\lambda + 1)P^0} \delta[r - R(t)], \tag{8.64c}$$

$$Q^\flat = 8\pi r^2 \int T^{AB} U^{lm*}_{AB} d\Omega = \frac{8\pi \Pi_1}{P^0} \delta[r - R(t)], \tag{8.64d}$$

$$Q^\sharp = \frac{8\pi r^4}{\lambda(\lambda + 1)} \int T^{AB} V^{lm*}_{AB} d\Omega = \frac{8\pi r^2 \Pi_2 \delta[r - R(t)]}{\lambda(\lambda + 1)P^0}. \tag{8.64e}$$

The source term in Eqs. (8.63) and (8.64) agrees with the previous derivation of Martel and Poisson [27, 28], and here we have adopted their notation.

In addition to the source term in the constraint equations and the field evolution equations, the particle-field interaction Hamiltonian also generates additional terms in the particle's equation of motion, which causes radiation reaction. These terms can be obtained by varying the interaction Hamiltonian with respect to point mass dynamical variables, in a similar manner as the odd parity case, for the canonical coordinate

$$
\begin{aligned}
\frac{dR}{dt}\bigg|_{\text{even}} &= 16\pi \frac{\partial H_{\text{int}}}{\partial P_r} \\
&= -16\pi \left[H_1 Y^{lm} f + \frac{H_0 Y^{lm} P^r}{2P^0} + \frac{f P_r H_2 Y^{lm}}{P^0} + \frac{f h_1^* \Xi'}{P^0} \right] \\
&\quad + 16\pi P_r \frac{(P^r)^2 / f H_2 Y^{lm} + 2h_1^* \Xi' P^r + r^2 (K\Pi_1 + G\Pi_2)}{2(P^0)^3} ,
\end{aligned}
\tag{8.65a}
$$

$$
\begin{aligned}
\frac{d\Phi}{dt}\bigg|_{\text{even}} &= 16\pi \frac{\partial H_{\text{int}}}{\partial P_\phi} \\
&= 16\pi \left\{ -h_0^* Z_{lm}^\phi - \frac{H_0 Y^{lm} P_\phi}{2r^2 P^0 \sin^2\theta} + \frac{P_\phi}{2 f r^2 \sin^2\theta (P^0)^3} \left[f^{-1}(P^r)^2 H_2 Y^{lm} + 2 h_1^* P^r \Xi' + r^2 (K\Pi_1 + G\Pi_2) \right] \right\} \\
&\quad - 16\pi \frac{h_1^* P^r Z^\phi + r^2 (KU^{\phi\phi} P_\phi + GV^{\phi\phi} P_\phi)}{P^0} ,
\end{aligned}
\tag{8.65b}
$$

and their conjugate momentum

$$
\begin{aligned}
\frac{dP_r}{dt}\bigg|_{\text{even}} &= -16\pi \frac{\partial H_{\text{int}}}{\partial R} \\
&= 16\pi \left\{ \Xi' \frac{\partial h_0^*(R)}{\partial R} + Y^{lm} P_r \frac{\partial (f H_1(R))}{\partial R} - \frac{1}{2} Y^{lm} \frac{\partial (H_0(R) P_0)}{\partial R} \right\} \\
&\quad + 16\pi \left\{ \frac{1}{2P^0} \left[(P_r)^2 Y^{lm} \frac{\partial (f H_2(R))}{\partial R} + 2 P_r \Xi' \frac{\partial (f h_1^*(R))}{\partial R} + \Pi_1 \frac{\partial (R^2 K(R))}{\partial R} + \Pi_2 \frac{\partial (R^2 G(R))}{\partial R} \right] \right\} \\
&\quad - \frac{8\pi}{(P^0)^2} \frac{\partial P^0}{\partial R} \left[f^{-1}(P^r)^2 H_2 Y^{lm} + 2 h_1^* P^r \Xi' + r^2 (K\Pi_1 + G\Pi_2) \right] ,
\end{aligned}
\tag{8.65c}
$$

$$
\begin{aligned}
\frac{dP_\phi}{dt}\bigg|_{\text{even}} &= -16\pi \frac{\partial H_{\text{int}}}{\partial \phi} \\
&= 16\pi \left[h_0^* \frac{\partial \Xi'}{\partial \phi} + H_1 P^r \frac{\partial Y^{lm}}{\partial \phi} - \frac{1}{2} H_0 P_0 \frac{\partial Y^{lm}}{\partial \phi} \right] \\
&\quad + \frac{8\pi}{P^0} \left[f^{-1}(P^r)^2 H_2 \frac{\partial Y^{lm}}{\partial \phi} + 2 h_1^* P^r \frac{\partial \Xi'}{\partial \phi} + r^2 G \frac{\partial \Pi_2}{\partial \phi} + r^2 K \frac{\partial \Pi_1}{\partial \phi} \right] .
\end{aligned}
\tag{8.65d}
$$

We have defined

$$
P^0(R) = \sqrt{ (P_r)^2 + \frac{(P_\phi)^2}{R^2 (1 - 2M/R) \sin^2\theta} + \frac{m^2}{1 - 2M/R} } .
\tag{8.66}
$$

This set of equations, together with the even-parity wave equation (8.61) and the odd-parity equations (8.49), (8.53a), (8.54a) and (8.54b), form a complete set of self-consistent evolution equations for both the point particle and the metric-perturbation fields.

Similar to the odd parity case, the even parity equations of motion also have a divergence problem. Because the wave equation (8.61) for ψ_{ZM} contains a source term as singular as $\delta'(r - R(t))$, ψ_{ZM}, or q_1, must be discontinuous at the point particle's location. According to the relation between H_2, G, h_1^*, K and q_1, q_2, q_3, q_4 shown in Appendix 8.A, K contains a $\delta(r - R(t))$-type term and H_2 even contains a $\delta'(r - R(t))$-type term. This means terms added to the particle's equation of motion are all singular at the particle's location. As a result, one has to *regularize* these equations of motion before they can be used for actual computations.

8.3.4 Monopole and dipole perturbations

Even though there are no gauge-invariant perturbations for these low-l components, metric perturbations at these orders do couple to the particle. The particle's perturbation to fields at these orders have been solved explicitly by Detweiler and Poisson [50], while their back-action to the particle's canonical equations can be obtained from expressions obtained for $l \geq 2$, simply removing those terms that do not exist in these low l's.

8.4 Regularization of test particle equation of motion

In order to obtain regular equations of motion for the point particle, we must carry out a *regularization procedure* that appropriately removes the divergences from the metric perturbation fields. While we have not been able to find a stand-alone regularization procedure in the 3+1 picture, currently existing regularization schemes can be adapted to our formalism. In this section, we shall outline, but not carry out, the procedure with which such a regularization could be done.

8.4.1 General Discussion

In particular, we shall discuss how the Detweiler-Whiting (DW) singular-regular decomposition [20, 21] approach could be used to regularize our canonical equations of motion.

In the DW approach, a metric perturbation field in a small but finite region around the point particle is decomposed into the sum of a regular piece (superscript "R") and a singular piece (superscript "S"):

$$h_{\mu\nu} = h_{\mu\nu}^R + h_{\mu\nu}^S \,. \tag{8.67}$$

The singular piece $h_{\mu\nu}^S$ corresponds to the deformed Schwarzschild solution around the small test mass as seen by a locally free falling observer on the background spacetime — it is singular as we

approach the location of the point particle; the regular piece h_R satisfies the linearized vacuum Einstein's equation and is everywhere regular (although it *does not* satisfy the out-going boundary condition at the null infinity and the down-going boundary condition at the future horizon). It is shown that $h_{\mu\nu}^S$ is the appropriate singularity to remove, and the point particle should travel along a geodesic of the perturbed spacetime that differs from the background by $h_{\mu\nu}^R$.

DW has shown that $h_{\mu\nu}^S$ can be approximated analytically in a local normal coordinate system built around the particle — such as the one introduced by Thorne and Hartle [36] and developed to higher orders by Zhang [44] (usually referred to as the THZ coordinate system). Another approach towards obtaining $h_{\mu\nu}^S$ is through the Hadamard singular Green function, as carried out by Hass and Poisson [22] as well as Warburton et al. [24]. The computation for $h_{\mu\nu}^S$ is carried out as an expansion in the proper distance away from the particle — and depending on the order to which this expansion is carried out, the corresponding $h_{\mu\nu}^R$ will only have a finite order of smoothness.

Among components of $h_{\mu\nu}^S$, h_{tt}^S is a lapse perturbation, h_{tr}^S and h_{tA}^S are shift perturbations, while h_{rr}^S, h_{rA}^S, and h_{AB}^S are 3-metric perturbations. One can carry out (l, m) decompositions of these quantities, using the appropriate harmonics, to obtain the singular pieces of our odd-parity metric-perturbation fields (h_0^S, h_1^S, h_2^S) and even-parity metric-perturbation fields $(H_0^S, H_1^S, h_0^{*S}, h_1^{*S}, H_2^S, K^S, G^S)$. In this way, the singular metric-perturbation fields come with a choice of gauge (through the singular pieces for lapse and shift) as well as 3-metric perturbations, around the worldline of the point particle. The (l, m)-decomposition coefficients of the singular metric fields are also referred to as *regularization parameters*.

It is anticipated that the mode-decomposed versions of these singular metric-perturbations fields should in general be discontinuous or singular at the radial location of the particle — but it is exactly these singularities that will cancel the ones we obtain for the full perturbations (i.e., $h_{\mu\nu}^{\text{full}}$), yielding

$$h_{\mu\nu}^R = h_{\mu\nu}^{\text{full}} - h_{\mu\nu}^S \tag{8.68}$$

which is regular.

More specifically in the 3+1 approach, we must first obtain the full metric (including lapse, shift and 3-metric perturbations), and then subtract the singular piece — resulting in the regular piece. A subtlety here is the choice of gauge: we obtain $h_{\mu\nu}^{\text{full}}$ using a particular choice of lapse and shift perturbations, and the arbitrariness of the choice suggests that the subtraction (8.68) will yield a regular result only if the full metric and the singular metric are computed in gauges that are related to each other through a smooth transformation in the region near the particle.

Note that the singular field is only defined in a region around the point particle — because the normal coordinate system (e.g., the THZ coordinate system), as well as the Hadamard decomposition of the Green function, is only valid within a distance away from the particle that is comparable to

space-time curvature. This does not prevent us from obtaining a regularized set of equations of motion for the point particle, because for that we will only need to obtain $h_{\mu\nu}^R$ around the location of the particle.

However, this has lead Vega and Detweiler (VD) [25] to develop a slight variant of the DW regularization approach, which further simplifies the regularization procedure. VD first assumed that we can obtain an $h_{\mu\nu}^S$ that has a definition everywhere in the spacetime, although this definition is physically meaningful only around the particle. They then proposed the application of a window function W, which is very flat around the location of the particle, but decays rapidly towards the horizon and infinity. In this way, if one defines an effective regular field, or *effective field* for short,

$$\tilde{h}_{\mu\nu}^R \equiv h_{\mu\nu}^{\text{full}} - W h_{\mu\nu}^S \,, \tag{8.69}$$

then the effective field $\tilde{h}_{\mu\nu}^R$ satisfies a wave equation with a regular source (the full source subtracted by the result obtained by inserting $\tilde{h}_{\mu\nu}^S \equiv W h_{\mu\nu}^S$ into the wave equation), as well as the out-going boundary condition at the future null infinity and the down-going boundary condition at the future horizon.

In this paper, we shall discuss how the effective-source approach can be adapted to our 3+1 Hamiltonian formalism — in even- and odd-parity cases.

8.4.2   Odd parity

Odd parity effective fields are $\tilde{h}_{0R}, \tilde{h}_{1R}, \tilde{h}_{2R}$, and their smoothness depends on the quality of our approximations for h_{0S}, h_{1S} and h_{2S}. We shall refer the regular field to be n-th order smooth if it has a smooth n-th order derivative. Right now, the singular field is available for the regular field to have 4-th order smoothness [49]. Let us first assume the order of smoothness is not an issue (e.g., assuming the singular piece to be available up to a rather high order), and later discuss options when the order of smoothness is limited.

8.4.2.1   An algebraic gauge

Out of the three metric quantities, one can construct a gauge invariant quantity — the Regge-Wheeler (RW) function and the other two degrees of freedom are fixed by one gauge choice and one constraint equation. First consider the gauge invariant quantity, its effective regularized piece $\tilde{\psi}_{\text{RWR}}$ given by

$$\tilde{\psi}_{\text{RWR}} = \frac{f}{r} \left[\tilde{h}_{1R} + \frac{1}{2} \left(\frac{\partial \tilde{h}_{2R}}{\partial r} - \frac{2}{r} \tilde{h}_{2R} \right) \right] \,, \tag{8.70}$$

while its effective singular piece $\tilde{\psi}_{\text{RW}}^S(r,t)$ is given similarly by $\tilde{h}_{1S}$, $\tilde{h}_{2S}$ (which are singular field components multiplied by the window functions).

The effective RW function satisfies the same wave equation as before [See Eq. (8.49)] but with a new source

$$\left[-\frac{\partial^2}{\partial t^2} + \frac{\partial^2}{\partial r^{*2}} - V_{\text{odd}}(r)\right]\tilde{\psi}_{\text{RWR}}(r,t) = S_{\text{oddR}}(r,t) \tag{8.71}$$

where the new source S_{odd}^R is simply the effective source, given by

$$S_{\text{oddR}}(r,t) = S_{\text{odd}}(r,t) - \left[-\frac{\partial^2}{\partial t^2} + \frac{\partial^2}{\partial r^{*2}} - V_{\text{odd}}(r)\right]\tilde{\psi}_{\text{RWS}}(r,t). \tag{8.72}$$

Given enough smoothness on the singular piece, a smooth enough $\tilde{\psi}_{\text{RWR}}$ can be obtained by solving Eq. (8.71) and imposing the out-going and down-going boundary conditions and infinity an the horizon. This $\tilde{\psi}_{\text{RWR}}$ can then be used to construct the rest of the gauge-dependent fields, imposing the gauge condition of, for example, $\tilde{h}_{1R} = 0$. We then obtain regular values for all the metric perturbation fields, as well as their derivatives, at the location of the point particle, and will be able to drive its motion. To carry out this computation, we will need the regular field to be 2-order smooth.

To be more specific, we can always do the coordinate transformation similar to Eq. (8.21) to shift $\tilde{h}_{1R}$ to 0. The gauge transformation function is given by

$$C^{lm}_{,r} - \frac{2}{r}C^{lm} = -\tilde{h}_{1R} \rightarrow C^{lm} = -r^2 \int dr \frac{\tilde{h}_{1R}}{r^2} \tag{8.73a}$$

$$x'_A = x_A + \sum_{lm} C^{lm} X^{lm}_A = x_A - r^2 \int dr \frac{\tilde{h}^{\text{odd}}_{rA}}{r^2}. \tag{8.73b}$$

After the gauge transformation, according to Eq. (8.21), the new $\tilde{h}'_{0R}, \tilde{h}'_{1R}, \tilde{h}'_{2R}$ are

$$\tilde{h}'_{1R} = 0, \tag{8.74a}$$

$$\tilde{h}'_{2R} = \tilde{h}_{2R} + 2r^2 \int dr \frac{\tilde{h}_{1R}}{r^2}, \tag{8.74b}$$

$$\tilde{h}'_{0R} = \tilde{h}_{0R} - r^2 \int dr \frac{\partial_t \tilde{h}_{1R}}{r^2}. \tag{8.74c}$$

Suppose the original effective field $\tilde{h}_R$ is a C^n function on the test mass's worldline, the coordinate transformation must be C^n smooth (Eq. (8.73)) and the new effective field is C^{n-1} smooth (Eq. (8.74)). Therefore $\tilde{h}_{1R} = 0$ is also a viable gauge for evolution because it can be smoothly transformed from the Lorenz gauge. For $n \geq 2$ the spatial derivative of the metric components would still be continuous. By imposing the $\tilde{h}_{1R} = 0$ algebraic gauge condition, $\tilde{h}_{2R}$ can be immediately obtained by solving

$$\frac{\partial \tilde{h}_{2R}}{\partial r} - \frac{2}{r}\tilde{h}_{2R} = \frac{2r}{f}\tilde{\psi}_{\text{RWR}}. \tag{8.75}$$

As τ_2 is fixed by the constraint equation Eq. (8.46) and τ_1 can be obtained by solving Eq. (8.84),

it is then straightforward to obtain $\tilde{h}_{0R}$ through Eq. (8.29)

$$\tilde{h}_{0R} = -\tilde{h}_{0S} - \frac{1}{2}\frac{\partial(\tilde{h}_{2R} + \tilde{h}_{2S})}{\partial t} + \frac{fr^2}{2\lambda(\lambda+1)}\left[\tau_2 - \frac{1}{2r^2}\frac{\partial(r^2\tau_1)}{\partial r}\right]. \tag{8.76}$$

Compared to the Lorenz gauge condition (in the following section), computing metric perturbations in this algebraic gauge is relatively easier although the effective fields are one order worse in smoothness.

8.4.2.2 Fixing Lorenz gauge

Another way to ensure the smoothness of the regular field is to resort to the known conclusion that if we keep the full field in the Lorenz gauge, the existing $n = 1$ singular field should be sufficient. This has been demonstrated by Refs. [15, 21, 37].

The Lorenz gauge condition,

$$\nabla^\mu \bar{h}_{\mu\nu} = 0 \tag{8.77}$$

where $\bar{h}_{\mu\nu}$ is the trace reversed metric perturbation $\bar{h}_{\mu\nu} = h_{\mu\nu} - 1/2\, g_{\mu\nu} h_{\alpha\beta} g^{\alpha\beta}$, converts into

$$r\frac{\partial h_0}{\partial t} + 2f\left(\frac{M}{r} - 1\right)h_1 - f^2 r\frac{\partial h_1}{\partial r} + \lambda f h_2 = 0 \tag{8.78}$$

for the (l, m) odd-parity perturbation fields. As we break this into singular and regular pieces, we obtain

$$r\frac{\partial \tilde{h}_{0R}}{\partial t} + 2f\left(\frac{M}{r} - 1\right)\tilde{h}_{1R} - f^2 r\frac{\partial \tilde{h}_{1R}}{\partial r} + \lambda f \tilde{h}_{2R} = A \tag{8.79}$$

for the effective regular field components, where A is given by

$$A = -r\frac{\partial \tilde{h}_{0S}}{\partial t} - 2f\left(\frac{M}{r} - 1\right)\tilde{h}_{1S} + f^2 r\frac{\partial \tilde{h}_{1S}}{\partial r} - \lambda f \tilde{h}_{2S}. \tag{8.80}$$

Combining Eqs. (8.70), (8.79) and (8.29), we have a set of first-order differential equations for $\tilde{h}_{0R}$ and $\tilde{h}_{2R}$

$$\partial_t\begin{bmatrix} \tilde{h}_{0R} \\ \tilde{h}_{2R} \end{bmatrix} = \begin{bmatrix} M_{11} & M_{12} \\ M_{21} & M_{21} \end{bmatrix}\begin{bmatrix} \tilde{h}_{0R} \\ \tilde{h}_{2R} \end{bmatrix} + \begin{bmatrix} N_1 \\ N_2 \end{bmatrix} \tag{8.81}$$

with

$$M_{11} = M_{22} = 0 \tag{8.82a}$$

$$M_{12} = -\frac{\lambda f}{r} + \left[f^2\frac{\partial}{\partial r} - \frac{2f}{r}\left(\frac{M}{r} - 1\right)\right]\left[\frac{1}{r} - \frac{\partial}{2\partial r}\right] \tag{8.82b}$$

$$M_{21} = -2, \tag{8.82c}$$

and

$$N_1 = \frac{A}{r} + \left[f^2 \frac{\partial}{\partial r} - \frac{2f}{r} \left(\frac{M}{r} - 1 \right) \right] \tilde{k}_{1R}, \tag{8.83a}$$

$$N_2 = \frac{fr^2}{\lambda(\lambda+1)} \left(\tau_2 - \frac{1}{2r^2} \frac{\partial(r^2 \tau_1)}{\partial r} \right). \tag{8.83b}$$

Here τ_2 is fixed by the constraint equation Eq. (8.46) and τ_1 can be obtained by solving Eq. (8.29)

$$\frac{\partial(\tilde{k}_{1R} + \tilde{k}_{1S})}{\partial t}$$
$$= \frac{\tau_1}{2(\lambda+1)} + \frac{r^2}{2\lambda(\lambda+1)} \frac{\partial}{\partial r} \left[f(\tau_2 - \frac{1}{2r^2} \frac{\partial(r^2 \tau_1)}{\partial r}) \right]. \tag{8.84}$$

At the initial time slice $t = 0$, we can impose the initial gauge condition that $\tilde{h}_{0R}(t = 0) = \tilde{h}_{2R}(t = 0) = 0$ and Eq. (8.81) determines the gauge condition evolution later on. Given $\tilde{h}_{0R}, \tilde{h}_{2R}$, Eq. (8.70) determines the value for $\tilde{h}_{1R}$ and therefore we can obtain the full set of regularized odd-parity fields.

8.4.3 Even parity

For even parity, we will follow similar procedures to the odd-parity case. Here we are dealing with seven effective field quantities: $\tilde{K}_R, \tilde{G}_R, \tilde{H}_{2R}, \tilde{H}_{1R}, \tilde{H}_{0R}, \tilde{h}_{1R}^*, \tilde{h}_{0R}^*$, compared to three field quantities in the odd-parity case. Out of these seven quantities, one can construct one gauge invariant perturbation quantity – Zerilli-Moncrief quantity; and the other six degrees of freedom are fixed by three gauge conditions and three constraint equations. The regular piece of the Zerilli-Moncrief function is given by

$$\begin{aligned} \tilde{\psi}_{ZMR} &= \frac{r}{\lambda+1} \left[\tilde{K}_R + \frac{2f}{\Lambda} \left(\tilde{H}_{2R} - r \frac{\partial \tilde{K}_R}{\partial r} \right) \right] \\ &+ \frac{2f}{\Lambda} \left(\frac{r^2 \partial \tilde{G}_R}{\partial r} - 2\tilde{h}_{1R} \right). \end{aligned} \tag{8.85}$$

It satisfies the following wave equation

$$\left[-\frac{\partial^2}{\partial t^2} + \frac{\partial^2}{\partial r^{*2}} - V_{\text{even}}(r) \right] \tilde{\psi}_{ZMR}(r, t) = S_{eR}(r, t) \tag{8.86}$$

with the effective source term S_{eR} given by

$$S_{eR}(r, t) = S_e(r, t) - \left[-\frac{\partial^2}{\partial t^2} + \frac{\partial^2}{\partial r^{*2}} - V_{\text{even}}(r) \right] \tilde{\psi}_{ZMS}(r, t). \tag{8.87}$$

With the outgoing wave boundary condition at spatial infinity and black hole horizon, one can solve the wave equation and obtain the numerical value for $\tilde{\psi}_{ZMR}$ or $\tilde{q}_{1R}$. On the other hand, the effective field $\tilde{q}_{2R}$ is fixed by the constraint equation

$$\tilde{q}_{2R} = q_2 - \tilde{q}_{2S} = -16\pi P_0 Y^{lm} \delta(r - R(t)) - \tilde{q}_{2S}\,. \tag{8.88}$$

Similar to the odd parity case, if the quality of the singular field is high enough, we can simply set the additional lapse $\tilde{H}_{0R}$ and shifts $(\tilde{H}_{1R}, \tilde{h}_{0R}^*)$ to zero, or to use an algebraic gauge for the gauge-dependent fields. Also similar to the odd parity, one way to limit our requirement for smoothness is to apply the Lorenz gauge condition Eq. (8.77), similar to what we did for the odd-parity case. In this case these Lorenz gauge conditions are given by

$$0 = (\lambda + 1)\frac{h_0^*}{r^2} + \left(\frac{M}{r} - 1\right)\frac{H_1}{r} - \frac{f}{2}\frac{\partial H_1}{\partial r}$$
$$+ \frac{1}{4}\frac{\partial(H_0 + H_2 + 2K)}{\partial t}\,, \tag{8.89a}$$

$$0 = \frac{M}{r}H_0 - 2(\lambda + 1)\frac{fh_1^*}{r} + \left(2 - \frac{3M}{r}\right)H_2 - 2fK$$
$$+ \frac{1}{2}rf\frac{\partial(H_0 + H_2 - 2K)}{\partial r} - r\frac{\partial H_1}{\partial t}\,, \tag{8.89b}$$

$$0 = f\left[\left(\frac{M}{r} - 1\right)h_1^* + \left(\frac{\lambda}{2}G + \frac{H_2 - H_0}{4}\right)r\right] + \frac{rf^2}{2}\frac{\partial h_1^*}{\partial r}$$
$$- \frac{r}{2}\frac{\partial h_0^*}{\partial t}\,. \tag{8.89c}$$

Combing the above equations with Appendix 8.A, Eq. (8.34) as well as the constraint Eq.(8.58), one can write down the evolution equation for $\tilde{G}_R, \tilde{h}_{1R}^*, \pi_2, \tilde{H}_{1R}, \tilde{h}_{0R}^*$ and a combination of effective field functions $I_R = \tilde{H}_{0R} + \tilde{H}_{2R} + 2\tilde{K}_R$. We also correspondingly define $I_S = \tilde{H}_{0S} + \tilde{H}_{2S} + 2\tilde{K}_S$.

$$\partial_t \begin{bmatrix} \tilde{G}_R \\ \tilde{h}_{1R}^* \\ \pi_2 \\ I_R \\ \tilde{H}_{1R} \\ \tilde{h}_{0R}^* \end{bmatrix} = \mathbf{M}' \begin{bmatrix} \tilde{G}_R \\ \tilde{h}_{1R}^* \\ \pi_2 \\ I_R \\ \tilde{H}_{1R} \\ \tilde{h}_{0R}^* \end{bmatrix} + \mathbf{N}' \tag{8.90}$$

Non-zero components of the matrix $\mathbf{M}'$ in Eq. (8.90) are given by

$$M_{13}' = \frac{2f}{r^2},\ M_{16}' = \frac{2}{r^2}; \tag{8.91a}$$

$$M_{23}' = 2f\partial_r - \frac{2}{r}\left(f - \frac{M}{r}\right),\ M_{25}' = 1,\ M_{26}' = \partial_r - \frac{2}{r}; \tag{8.91b}$$

$$M'_{31} = -\frac{r^2}{2}f\partial_r^2, \quad M'_{32} = \frac{f}{r}(2 - r\partial_r), \quad M'_{34} = -\frac{1}{2}; \tag{8.91c}$$

$$M'_{45} = -4\left(\frac{M}{r^2} - \frac{1}{r}\right) + 2f\partial_r, \quad M'_{46} = -\frac{4(\lambda+1)}{r^2}r; \tag{8.91d}$$

$$M'_{51} = \frac{M}{r^2} + \frac{f}{2}\partial_r, \quad M'_{52} = -\frac{4Mf}{r}\partial_r,$$

$$M'_{54} = -\frac{2f}{r^3}(4M + r + \lambda r); \tag{8.91e}$$

$$M'_{61} = \frac{\lambda f}{r} - (3 - 5M/r)f\partial_r - rf^2\partial_r^2, \quad M'_{62} = 3f^2\partial_r,$$

$$M'_{64} = -\frac{f}{2r}. \tag{8.91f}$$

Those of $\mathbf{N}'$ are given by

$$N'_1 = \frac{f\pi_3}{r^2\lambda(\lambda+1)} + \frac{f\Lambda\pi_1}{r\lambda} + \frac{2\tilde{h}_{0S}^*}{r^2} - \frac{\partial\tilde{G}_S}{\partial t}, \tag{8.92a}$$

$$N'_2 = \frac{\pi_4}{2(\lambda+1)} - 2f\pi_1 + \tilde{H}_{1S} + r^2\left(\frac{\tilde{h}_{0S}^*}{r^2}\right)_{,r} - \frac{\partial\tilde{h}_{1S}^*}{\partial t}, \tag{8.92b}$$

$$N'_3 = \frac{\lambda}{r\Lambda^2}q_1 - \frac{\lambda f}{(\lambda+1)\Lambda^2}(q_2 - q_{1,r}) - \frac{M}{2r}(r\frac{\partial\tilde{G}_S}{\partial r} - \frac{2}{r}\tilde{h}_{1S}^*)$$

$$+ \frac{M(2q_2 - q_{1,r})}{2(\lambda+1)\Lambda r} - \frac{\tilde{H}_{0S}}{2} + \frac{4\pi}{P^0}\frac{(P^r)^2 Y^{lm}}{f(\lambda+1)}\delta(r - R(t))$$

$$+ \frac{8\pi f}{\Lambda(\lambda+1)}\left[\frac{(P^r)^2 Y^{lm}}{fP^0}\delta(r - R(t))\right]_r$$

$$- \frac{8\pi}{P^0}\frac{r^2 f\Pi_1}{(\lambda+1)\Lambda}\delta(r - R(t)) + \frac{1}{4r(\lambda+1)\Lambda}\Big\{6(\lambda+1)\tilde{q}_{1R}$$

$$+ [12M - r(4+\Lambda)]\tilde{q}_{2R} + 2(r - 6M)\tilde{q}_{1R,r}\Big\}$$

$$+ \frac{1}{4(\lambda+1)\Lambda}\left[(\Lambda - 2\lambda)\tilde{q}_{1R,r} + 2rf(\tilde{q}_{2R,r} - \tilde{q}_{1R,rr})\right], \tag{8.92c}$$

$$N'_4 = -4(\lambda+1)\frac{\tilde{h}_{0S}^*}{r^2} - 4\left(\frac{M}{r} - 1\right)\frac{\tilde{H}_{1S}}{r} + 2f\frac{\partial\tilde{H}_{1S}}{\partial r} - \frac{\partial I_S}{\partial t} \tag{8.92d}$$

$$N'_5 = \frac{M}{r^2}\tilde{H}_{0S} - 2(\lambda+1)\frac{f\tilde{h}_{1S}^*}{r^2} + \left(\frac{2}{r} - \frac{3M}{r^2}\right)\tilde{H}_{2S} - \frac{2f}{r}\tilde{K}_S$$

$$+ \frac{2(M - r)(1 + \lambda)\tilde{q}_{1R} + rf(r(2+\Lambda) - 2M)(\tilde{q}_{2R} - \tilde{q}_{1R,r})}{r^3(1+\lambda)\Lambda}$$

$$+ \frac{1}{2}f\frac{\partial(\tilde{H}_{0S} + \tilde{H}_{2S} - \tilde{K}_S)}{\partial r} - \frac{\partial\tilde{H}_{1S}}{\partial t}, \tag{8.92e}$$

$$N'_6 = \frac{2f}{r}\left[\left(\frac{M}{r} - 1\right)\tilde{h}_{1S}^* + \left(\frac{\lambda}{2}\tilde{G}_S + \frac{\tilde{H}_{2S} - \tilde{H}_{0S}}{4}\right)r\right]$$

$$+ f^2\frac{\partial\tilde{h}_{1S}^*}{\partial r} - \frac{\partial\tilde{h}_{0S}^*}{\partial t}$$

$$
+ f \left\{ \frac{\tilde{q}_{2R} - \tilde{q}_{1R,r}}{2(\lambda + 1)} \right.
$$

$$
\left. + \left(1 + r \frac{\partial}{\partial r} \right) \left[\frac{\tilde{q}_{1R}}{r\Lambda} - \frac{f}{(\lambda + 1)\Lambda} \left(\tilde{q}_{2R} - \frac{\partial \tilde{q}_{1R}}{\partial r} \right) \right] \right\}. \tag{8.92f}
$$

We can pick the initial condition that $\tilde{G}_R = \tilde{h}^*_{1R} = \tilde{H}_{1R} = \tilde{h}^*_{0R} = I_R = \pi_2 = 0$. Eq. (8.90) determines their evolution later on. Once $\tilde{G}_R$ and $\tilde{h}^*_{1R}$ are known, $\tilde{K}_R$ and $\tilde{H}_{2R}$ can be obtained using Eq. (8.98). $\tilde{H}_{1R}$ is just $I_R - \tilde{H}_{2R} - 2\tilde{K}_R$ and then all effective fields for even parity are obtained following the above procedure. In reality, one may let the test particle freely evolve for a few cycles before turning on the radiation reaction in order for the initial junk radiation to go away. Another subtlety here is although $\tilde{G}_R, \tilde{h}^*_{1R}, \tilde{I}_R, \tilde{H}_{1R}, \tilde{h}^*_{0R}$ are all regular functions, π_2 may actually be divergent at $r = R(t)$. However, as long as the particle trajectory does not hit the grid point (which is the generic case and can be guaranteed by using some numerical algorithms), Eq. (8.90) can still be used for harmonic gauge evolution.

8.4.4 Monopole and dipole perturbations

Although there is no wave equation in the monopole and dipole cases, regularization does involve these orders. We need to carry out the steps described in the above, simply ignoring the step of solving the wave equation. This is discussed by Detweiler and Poisson [50], but unfortunately there is no known unique way to remove the singular piece of contribution from the $l = 0, 1$ modes. We will leave this for future investigation.

8.5 Conclusions and discussions

In this article we have taken a $3 + 1$ Hamiltonian approach toward the motion of a point particle around a Schwarzschild black hole. For the metric perturbation fields, we have simply adopted Moncrief's perturbative Hamiltonian (quadratic in these fields), and his canonical transformation to a new set of canonical coordinates and momenta which are either the Hamiltonian and momentum constraints themselves, their canonical conjugates, or gauge-invariant (see Sec. 8.2.2). For the point particle, we have inserted its own Hamiltonian plus an interaction Hamiltonian, with the former describing geodesic motion and the latter describing both (i) the particle sourcing metric perturbations and (ii) the metric perturbations acting back onto the particle. We have obtained these equations of motion explicitly — decomposed into (l, m) components ($l \geq 2$) and even and odd parities. For (i), the equations we obtain agree with the previous literature, obtaining wave equations for gauge-invariant functions that are sourced by the particle. In this way, we have obtained self-consistent evolution equations for both the particle and the metric-perturbation fields. In principle, depending

on the lapse and shift functions we choose, these self-consistent equations can be written for any gauge. The field equations we have will be in 1+1 (t and r) dimensions, and the gauge-invariant metric-perturbation fields are also decoupled from the rest of the fields.

As can be anticipated, this set of equations are singular due to the use of a point particle. While we have not been able to find a stand-alone 3+1 approach for regularization, we have shown that existing regularization schemes can be adopted to our scheme. The most straightforward approach would be to use the Detweiler-Whiting's singular-regular decomposition [21], combined with the Vega-Detweiler effective-source approach [25]. In the case when we have a high order approximation of the singular field, one can (i) solve the wave equation for the even- and odd-parity effective gauge-invariant fields, and (ii) fix an algebraically simple gauge for the effective metric, obtain all effective metric components, and calculate generalized forces acting on the particle. In this way, we will only have evolved one wave equation for each parity and each l (and all m's can be taken care of simultaneously) with an effective source, and will have used these waves, plus regularized gauge-fixing terms, to drive the motion of the particle in the self-consistent way. However, since we have not carried out this computation explicitly, it is not known up to what level of approximation we shall require for the singular field — although it may be substantially higher than what has been required before due to the multiple spatial derivatives used in defining the gauge-invariant quantities.

In case the requirement for the singular field in (ii) turns out to be too high, we have proposed to replace (ii) by (iii): choosing the Lorenz gauge for the full field, in which case it was known that the currently available approximations for the singular field is sufficient. In this case, in addition to the two wave equations, we require 2 odd-parity gauge-fixing equations, and 6 even-parity gauge fixing equations. This will be equivalent to decomposing Vega-Detweiler's and Warburton et al. [24]'s 3+1 calculations into a 1+1 form.

For $l = 0, 1$ metric perturbation fields do not have gauge-invariant components: a canonical transformation exists to transform them into either the constraints or their canonical conjugates. In this way, we only need step (ii) or (iii) in the above discussion — which we have not explicitly carried out.

Acknowledgement

8.A   Various tensor spherical harmonics

Here we list the components of the vector and tensor harmonics $X_A^{lm}, Z_A^{lm}, W_{AB}^{lm}, U_{AB}^{lm}, V_{AB}^{lm}$ in terms of scalar spherical harmonics and their partial derivatives. For the odd-parity vector harmonics X_A^{lm}, we have

$$X_\theta^{lm} = -\frac{1}{\sin\theta}\frac{\partial Y^{lm}}{\partial\phi}, \; X_\phi^{lm} = \sin\theta\frac{\partial Y^{lm}}{\partial\theta}\,. \tag{8.93}$$

For the even-parity vector harmonic Z_A^{lm}:

$$Z_\theta^{lm} = \frac{\partial Y^{lm}}{\partial\theta}, \; Z_\phi^{lm} = \frac{\partial Y^{lm}}{\partial\phi}\,. \tag{8.94}$$

For the identity tensor U_{AB}^{lm}:

$$U_{\theta\theta}^{lm} = Y^{lm}, \quad U_{\phi\phi}^{lm} = \sin^2\theta Y^{lm}, \quad U_{\theta\phi}^{lm} = U_{\phi\theta}^{lm} = 0\,. \tag{8.95}$$

For the even-parity, symmetric trace-free (STF) tensor harmonic V_{AB}^{lm}:

$$V_{\theta\theta}^{lm} = \left[\frac{\partial^2}{\partial\theta^2} + \frac{1}{2}l(l+1)\right] Y^{lm}\,, \tag{8.96a}$$

$$V_{\phi\phi}^{lm} = \left[\frac{\partial^2}{\partial\phi^2} + \cos\theta\sin\theta\frac{\partial}{\partial\theta} + \frac{1}{2}l(l+1)\sin^2\theta\right] Y^{lm}\,, \tag{8.96b}$$

$$V_{\theta\phi}^{lm} = V_{\phi\theta}^{lm} = \left[\frac{\partial^2}{\partial\theta\partial\phi} - \frac{\cos\theta}{\sin\theta}\frac{\partial}{\partial\phi}\right] Y^{lm}\,. \tag{8.96c}$$

And finally for the odd-parity tensor harmonic W_{AB}^{lm}:

$$W_{\theta\theta}^{lm} = \frac{-1}{\sin\theta}\left[\frac{\partial^2}{\partial\theta\partial\phi} - \frac{\cos\theta}{\sin\theta}\frac{\partial}{\partial\phi}\right] Y^{lm}\,,$$

$$W_{\phi\phi}^{lm} = \left[\sin\theta\frac{\partial^2}{\partial\theta\partial\phi} - \cos\theta\frac{\partial}{\partial\phi}\right] Y^{lm}\,,$$

$$W_{\theta\phi}^{lm} = W_{\phi\theta}^{lm} = \frac{1}{2}\left[\sin\theta\frac{\partial^2}{\partial\theta^2} - \frac{1}{\sin\theta}\frac{\partial^2}{\partial\phi^2} - \cos\theta\frac{\partial}{\partial\theta}\right] Y^{lm}\,. \tag{8.97}$$

8.B   Conversion of fields for even parity perturbations

The even parity perturbation quantities K, H_2, h_1^*, G and q_1, q_2, q_3, q_4 are related to each other by

$$K = \frac{q_1}{r\Lambda} - \frac{f}{(\lambda+1)\Lambda}(q_2 - q_{1,r}) - rf\left(q_{3,r} - \frac{2q_4}{r^2}\right)\,,$$

$$H_2 = \frac{(\Lambda-1)(\Lambda-2-2\lambda)}{2fr\Lambda}q_1 + \frac{q_2 - q_{1,r}}{2(\lambda+1)}$$

$$+ \quad r\left[\frac{q_1}{r\Lambda} - \frac{f}{(\lambda+1)\Lambda}(q_2 - q_{1,r})\right]_{,r}$$
$$- \quad f[r^2 q_{3,r} - 2q_4]_{,r} - \frac{M}{r^2}(r^2 q_{3,r} - 2q_4)$$
$$= \quad \frac{q_2 - q_{1,r}}{2(\lambda+1)} + (rK)_{,r} - K - \frac{1}{r}\left(1 - \frac{3M}{r}\right)\left[r^2 q_{3,r} - 2q_4\right]$$
$$G \quad = \quad q_3,$$
$$h_1^* \quad = \quad q_4. \tag{8.98}$$

Bibliography

[1] A. Abramovici, et al. Science **256** 325, (1992).

[2] S. Huges, Annals of Physics **303** 142, (2003).

[3] E. Flanagan and S. Hughes, New J Phys **7** 204, (2005).

[4] D.A. Brown et al., Phys. Rev. Lett **99**, 201102 (2007).

[5] F. D. Ryan, Phys. Rev. D **56** 1845, (1997).

[6] J. Brink, Phys. Rev. D **78** 102001, (2008); J. Brink, Phys. Rev. D **78** 102002, (2008); J. Brink, Phys. Rev. D **81** 022001, (2010); J. Brink, Phys. Rev. D **81** 022002, (2010).

[7] N.A. Collins and S.A. Hughes Phys. Rev. D **69** 124022 (2004).

[8] S.J. Vigeland and S.A. Hughes, Phys. Rev. D **81** 024030 (2010).

[9] C. Cutler and E. Flannagan, Phys. Rev. D **49** 2658, (1994).

[10] T. Regge and J. A. Wheeler, Phys. Rev. D **108** 1063, (1957).

[11] F. Zerilli, Phys. Rev. Lett **24** 737 (1970).

[12] S. Teukolsky, Astrophys. J **185** 635, (1973).

[13] L. Blanchet and G. Faye, Phys. Rev. D **63** 062005, (2001).

[14] C. Lousto and Y. Zlochower, Phys. Rev. Lett **106** 041101, (2011).

[15] Y. Mino, M. Sasaki, T. Tanaka, Phys. Rev. D **55** 3457 (1997).

[16] T. Quinn and R. M. Wald, Phys. Rev. D **56** 3381, (1997).

[17] S. E. Gralla, A. I. Harte, R. M. Wald, Phys. Rev. D **80** 024031, (2009); S. Gralla, R. Wald, arXiv:0907.0414.

[18] A. Pound, Phys. Rev. D **81** 024023, (2010).

[19] E. Poisson, A. Pound and I. Vega, Living Review in Relativity **7** 2011, arXiv:1102.0529.

[20] S. Detweiler, Phys. Rev. Lett **86**1931 (2001).

[21] S. Detweiler, E. Messaritaki and B. F. Whiting, Phys. Rev. D **67** 104016 (2003).

[22] R. Haas and E. Poisson, Phys. Rev. D **74**, 044009 (2006).

[23] L. Barack and A. Ori, Phys. Rev. D **66** 084002 (2002).

[24] N. Warburton, S. Akcay, L. Barack, J. R. Gair and N. Sago, Phys. Rev. D **85** 061501 (2012); B. Wardell, private communication.

[25] I. Vega and S. Detweiler, Phys. Rev. D **77** 084008 (2008).

[26] P. Diener, I. Vega, B. Wardell and S. Detweiler, Phys. Rev. Lett **108** 191102 (2012).

[27] K. Martel and E. Poisson, Phys. Rev. D **71**, 104003 (2005).

[28] K. Martel, Phys. Rev. D **69** 044025 (2004).

[29] K. Martel, Particles and Black Holes: Time Domain Integration of the Equations of Black Hole Perturbation Theory, University of Guelph, Ph.D thesis

[30] V. Moncrief, Annals of Physics, **88** 343, (1974).

[31] A. Taub, Commun. Math. Phys. **15** 235-254 (1969).

[32] A. Nagar and L. Rezzolla, Class. Quantum. Grav. **22** R167 (2005).

[33] C. Vishveshwara, Phys. Rev. D **1** 2870-2879 (1970).

[34] L. Edelstein and C. Vishveshwara, Phys. Rev. D **1** 3514-3517 (1970).

[35] B. Schutz, Astrophys. J. Suppl. Ser. **24** 343 (1972).

[36] K. S. Thorne and J. B. Hartel, Phys. Rev. D **31** 1815 (1985)

[37] L. Barack, Class. Quantum. Grav. **26** 213001 (2009)

[38] L. Barack, Yasushi Mino, Hiroyuki Nakano, Amos Ori and M. Sasaki, Phys. Rev. Lett **88** 091101 (2002).

[39] L. Barack and C. O. Lousto, Phys. Rev. D **66** 061502 (2002).

[40] I. Vega, P. Diener, W. Tichy and S. Detweiler, Phys. Rev. D **80** 084021 (2009).

[41] C. O. Lousto and R. H. Price, Phys. Rev. D **57** 1074 (1998).

[42] C. O. Lousto and R. H. Price, Phys. Rev. D **56** 6440 (1997).

[43] C. O. Lousto and R. H. Price, Phys. Rev. D **55** 2124 (1997).

[44] X. H. Zhang, Phys. Rev. D **34** 991 (1986).

[45] C. W. Misner, K. S. Thorne and J. A. Wheeler, *Gravitation*, W. H. Freeman (1973).

[46] S. Chandrasekhar, *The Mathematical Theory of Black Holes*, Oxford University Express (1983).

[47] T. W. Baumgarte and S. L. Shapiro, *Numerical Relativity: Solving Einstein's Equations on the Computer*, Cambridge University Press (2010).

[48] R. Arnowitt, S. Deser and C. Misner, Phys. Rev. **116** 5 1322-1330

[49] A. Heffernan, A. Ottewill, and B. Wardell, Phys. Rev. D **86** 104023, (2012).

[50] S. Detweiler and E. Poisson, Phys. Rev. D **69** 084019, (2004).

Chapter 9

Quasinormal-mode spectrum of Kerr black holes and its geometric interpretation

There is a well-known, intuitive geometric correspondence between high-frequency quasi-normal modes of Schwarzschild black holes and null geodesics that reside on the light-ring (often called spherical photon orbit): the real part of the mode's frequency relates to the geodesic's orbital frequency, and the imaginary part of the frequency corresponds to the Lyapunov exponent of the orbit. For slowly rotating black holes, the quasinormal-mode's real frequency is a linear combination of the orbit's precessional and orbital frequencies, but the correspondence is otherwise unchanged. In this paper, we find a relationship between the quasinormal-mode frequencies of Kerr black holes of arbitrary (astrophysical) spins and general spherical photon orbits, which is analogous to the relationship for slowly rotating holes. To derive this result, we first use the WKB approximation to compute accurate algebraic expressions for large-l quasinormal-mode frequencies. Comparing our WKB calculation to the leading-order, geometric-optics approximation to scalar-wave propagation in Kerr spacetime, we then draw a correspondence between the real parts of the parameters of a quasinormal mode and the conserved quantities of spherical photon orbits. At next-to-leading order in this comparison, we relate the imaginary parts of the quasinormal-mode parameters to coefficients that modify the amplitude of the scalar wave. With this correspondence, we find a geometric interpretation of two features of the quasinormal-mode spectrum of Kerr black holes: First, for Kerr holes rotating near the maximal rate, a large number of modes have nearly zero damping; we connect this characteristic to the fact that a large number of spherical photon orbits approach the horizon in this limit. Second, for black holes of any spins, the frequencies of specific sets of modes are degenerate; we find that this feature arises when the spherical photon or-

bits corresponding to these modes form closed (as opposed to ergodically winding) curves.

9.1 Introduction

Quasinormal modes (QNMs) of black-hole spacetimes are the characteristic modes of linear perturbations of black holes that satisfy an outgoing boundary condition at infinity and an ingoing boundary condition at the horizon (they are the natural, resonant modes of black-hole perturbations). These oscillatory and decaying modes are represented by complex characteristic frequencies $\omega = \omega_R - i\omega_I$, which are typically indexed by three numbers, n, l, and m. The decay rate of the perturbation increases with the overtone number n, and l and m are multipolar indexes of the angular eigenfunctions of the QNM.

9.1.1 Overview of quasinormal modes and their geometric interpretation

Since their discovery, numerically, in the scattering of gravitational waves in the Schwarzschild spacetime by Vishveshwara [1], QNMs have been thoroughly studied in a wide range of spacetimes, and they have found many applications. There are several reviews [2–6] that summarize the many discoveries about QNMs. They describe how QNMs are defined, the many methods used to calculate QNMs (e.g., estimating them from time-domain solutions [7], using shooting methods in frequency-domain calculations [8], approximating them with inverse-potential approaches [9] and WKB methods [10, 11], numerically solving for them with continued-fraction techniques [12, 13], and calculating them with confluent Huen functions [14, 15]), and the ways to quantify the excitation of QNMs (see, e.g., [16, 17]). They also discuss the prospects for detecting them in gravitational waves using interferometric gravitational-wave detectors, such as LIGO [18] and VIRGO [19], and for inferring astrophysical information from them (see, e.g., [20, 21] for finding the mass and spin of black holes using QNMs, [22, 23] for quantifying the excitation of QNMs in numerical-relativity simulations binary-black-hole mergers, and [24, 25] for testing the no-hair theorem with QNMs). There have also been several other recent applications of QNMs. For example, Zimmerman and Chen [26] (based on work by Mino and Brink [27]) study extensions to the usual spectrum of modes generated in generic ringdowns. Dolan and Ottewill use eikonal methods to approximate the modal wave function, and they use these functions to study the Green's function and to help understand wave propagation in the Schwarzschild spacetime [28–30].

Although QNMs are well understood and can be calculated quite precisely, it remains useful to

develop intuitive and analytical descriptions of these modes. Analytical insights into QNMs have come largely from two limits: the high-overtone limit $(n \gg 1)$ and the eikonal limit $(l \gg 1)$. In the high-overtone limit, the frequencies of a QNM are related to the surface gravity of the horizon (see e.g., [31, 32] for the numerical discovery for Schwarzschild black holes, [33] for an analytical proof for Schwarzschild holes, and [34, 35] for proofs for other spherically symmetric black-hole spacetimes). In this paper, we focus on the eikonal limit.

An important calculation in the eikonal limit $(l \gg 1)$ was performed by Ferrari and Mashhoon [9], who showed that for a Schwarzschild black hole, the QNM's frequency (which depends only on a multipolar index l and an overtone index n) can be written as

$$\omega \approx (l + 1/2)\Omega - i\gamma_L(n + 1/2). \tag{9.1}$$

The quantities Ω and γ_L are, respectively, the Keplerian frequency of the circular photon orbit and the Lyapunov exponent of the orbit, the latter of which characterizes how quickly a congruence of null geodesics on the circular photon orbit increases its cross section under infinitesimal radial perturbations [30, 36]. Equation (9.1) hints at an intriguing physical description of QNMs, first suggested by Goebel [37]: for modes with wavelengths much shorter than the background curvature, the mode behaves as if it were sourced by a perturbation that orbits on and diffuses away from the light ring on the time scale of the Lyapunov exponent. Thus, photon surfaces [38] play an important role in the structure of a spacetime's QNMs.

Ferrari and Mashhoon [9] also derived an analogous result to Eq. (9.1) for slowly rotating black holes. They showed for $l \gtrsim m \gg 1$, the real part of the frequency is given by

$$\Omega \approx \omega_{\text{orb}} + \frac{m}{l + 1/2}\omega_{\text{prec}}, \tag{9.2}$$

where ω_{orb} is now the Keplerian orbital frequency for the spherical photon orbit [1] and ω_{prec} is the Lense-Thiring-precession frequency of the orbit (which arises because of the slow rotation of the black hole). The term proportional to ω_{prec} also has a simple geometric-optics interpretation. Inertial frames near the high-frequency wave at the light ring are dragged with respect to inertial frames at infinity, and this frame dragging causes the perturbation's orbit to precess about the spin axis of the black hole with a frequency ω_{prec}. If the orbit is inclined at an angle of $\sin^2 \theta = m^2/l(l+1)$ (the ratio of angular momenta L_z^2/L^2 for quantized waves in flat space), then the projection of the precessional velocity onto the orbital plane scales the precessional frequency by a factor of $\sim m/(l + 1/2)$.

Why the QNM frequency is multiplied by $(l+1/2)$ is a feature that we will explain in greater detail in this paper. Intuitively, this term arises because the in the high-frequency limit, any wavefront

---

[1] By "spherical photon orbits", we mean those orbits that remain on a sphere of constant radius, but do not necessarily close or explore the whole sphere.
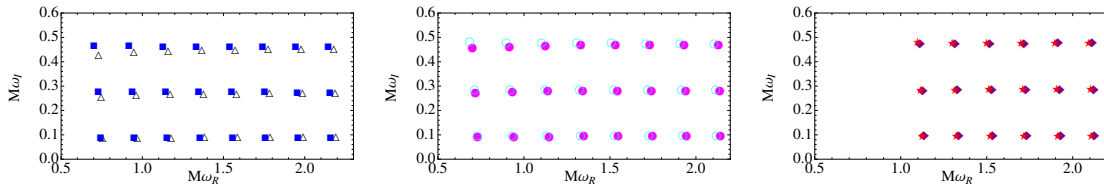
Figure 9.1: Low-overtone QNM spectrum of three Kerr black holes of different spins with approximate degeneracies in their spectra. From left to right, we plot the three lowest-overtone QNM excitations for (i) $a/M = 0.69$ in which $(l, m) = (j, 2)$ are black traignles and $(l', m') = (j + 1, -2)$ are blue squares, where $j = 3, \ldots, 9$; (ii) $a/M = 0.47$ in which $(l, m) = (j, 3)$ are magenta dots and $(l', m') = (j+1, -3)$ are cyan cycles, where $j = 3, \ldots, 9$; (iii) $a/M = 0.35$ in which $(l, m) = (j, 4)$ are red diamonds and $(l', m') = (j + 1, -4)$ are purple stars, where $j = 5, \ldots, 10$. For these spin parameters, the mode with positive values of m and ω_R (a corotating mode) of index l is approximately degenerate with the mode with $m' = -m$, and ω_R (a counterrotating mode) of index $l' = l + 1$.

traveling on null orbits will have an integral number of oscillations in the θ and ϕ directions. For the wave to be periodic and single-valued, there must be m oscillations in the ϕ direction. For the θ direction, it is a Bohr-Sommerfeld quantization condition that requires $l - |m| + 1/2$ oscillations in this direction, which implies that there should be a net spatial frequency of roughly $(l + 1/2)$. This increases the frequency of the radiation seen far from the hole by the same factor.

From this intuitive argument, we expect that the real part of the mode should be

$$\omega_R = L \left(\omega_{\text{orb}} + \frac{m}{L} \omega_{\text{prec}} \right) , \tag{9.3}$$

where we define $L = l + 1/2$. In this paper, we will show that an equation of the form of Eq. (9.3) does, in fact, describe the QNM frequencies of Kerr black holes of arbitrary astrophysical spins (and it recovers the result of Ferrari and Mashhoon for slowly spinning black holes). As we mention in the next part of this section, the exact details of the correspondence between QNMs and photon orbits is richer for rapidly rotating black holes than for slowly rotating or static black holes.

9.1.2 Methods and results of this article

To derive Eq. (9.3) requires that we develop a geometric-optics interpretation of the QNMs of Kerr black holes with arbitrary astrophysical spins. Finding the correspondence requires two steps: first, we need to calculate the approximate frequencies using the WKB method; next, we must articulate a connection between the mathematics of waves propagating in the Kerr spacetime in the geometric-optics approximation and those of the WKB approximation (the first step). Finally, with the geometric-optics description of QNMs, we can make a physical interpretation of the spectrum (for example, the degeneracy or the lack of damping in the extremal limit).

In Sec. 9.2, we describe how we solve the eigenvalue problem that arises from separating the

Teukolsky equation [39] (a linear partial differential equation that describes the evolution of scalar, vector, and gravitational perturbations of Kerr black holes) into two nontrivial linear ordinary differential equations. The two differential equations, the radial and angular Teukolsky equations, share two unknown constants—the frequency, ω, and the angular separation constant, A_{lm}—that are fixed by the boundary conditions that the ordinary differential equations must satisfy (ingoing at the horizon and outgoing at infinity for the radial equation, and well-behaved at the poles for the angular equation). The goal of the WKB method is to compute the frequency and separation constant approximately.

Although there has been work by Kokkotas [40] and Iyer and Seidel [41] using WKB methods to compute QNM frequencies of rotating black holes, their results were limited to slowly rotating black holes, because they performed an expansion of the angular separation constant, A_{lm}, for small, dimensionless spin parameters, a/M, and only applied the WKB method to the radial Teukolsky equation to solve for the frequency. In a different approach, Dolan developed a matched-expansion formalism for Kerr black holes of arbitrary spins that can be applied to compute the frequency of QNMs, but only for modes with $l = |m|$ and $m = 0$ [29].

Therefore, it remains an outstanding problem to compute a WKB approximation to the quasi-normal modes of Kerr black holes of large spins and for any multipolar index m. In Sec. 9.2, we solve the joint eigenvalue problem of the radial and angular Teukolsky equations by applying a change of variables to the angular equation that brings it into the form of a bound-state problem in quantum mechanics. Applying the WKB method to the angular equation, we arrive at a Bohr-Sommerfeld condition that constrains the angular constant in terms of the frequency (and the indices l and m). Simultaneously, we can analyze the radial equation in the WKB approximation, and the two equations together define a system of integral equations, which can be solved for the eigenvalues. When we expand the Bohr-Sommerfeld condition in a Taylor series in terms of the numerically small parameter, $a\omega/l$, the system of integral equations reduces to an algebraic system (which, in turn, leads to a simpler expression for the frequency). The approximate frequency agrees very well with the result that includes all powers of $a\omega/l$, and, in the eikonal limit, it is accurate to order $1/l$ for Kerr black holes of arbitrary spins, for modes with any value of m, and for both the real and the imaginary parts of the frequency.

To interpret the WKB calculation of Sec. 9.2 in the language of propagating waves in the geometric-optics limit within the Kerr spacetime, we analyze waves around a Kerr black hole in Sec. 9.3 using the geometric-optics approximation and the Hamilton-Jacobi formalism. We confirm that the leading-order pieces of the WKB frequencies and angular constants correspond to the conserved quantities of the leading-order, geodesic behavior of the geometric-optics approximation (specifically, the real part of ω, the index m, and the real part of A_{lm} are equivalent to the energy $\mathcal{E}$, the z-component of the specific angular momentum L_z, and Carter's constant $\mathcal{Q}$ plus L_z^2, respec-

tively). The specific geodesics corresponding to a QNM are, in fact, spherical photon orbits. The next-to-leading-order WKB quantities (the imaginary parts of ω and A_{lm}) correspond to dispersive, wavelike corrections to the geodesic motion (they are the Lyapunov exponent and the product of this exponent with the change in Carter's constant with respect to the energy). Table 9.1 in Sec. 9.3 summarizes this geometric-optics correspondence.

In Sec. 9.4, we make several observations about features of the QNM spectrum of Kerr black holes that have simple geometric interpretations. First, we find that for extremal Kerr black holes, a significant fraction of the QNMs have a real frequency proportional to the angular frequency of the horizon and a decay rate that rapidly falls to zero; we explain this in terms of a large number of spherical photon orbits that collect on the horizon for extremal Kerr holes. Second, we expand the WKB expression for the real part of the frequency as in Eq. (9.3), and we interpret these terms as an orbital and a precessional frequency of the corresponding spherical photon orbit. These two frequencies depend on the spin of the black hole and the value of m/L very weakly for slowly-rotating black holes, though quite strongly when the spin of the black hole is nearly extremal. Finally, we use the geometric-optics interpretation given by Eq. (9.3) to explain a degeneracy in the QNM spectrum of Kerr black holes, in the eikonal limit, which also manifests itself, approximately, for small l (see Fig. 9.1). The degeneracy occurs when the orbital and precession frequencies, $\omega_{\rm orb}$ and $\omega_{\rm prec}$ are rationally related (i.e., $\omega_{\rm orb}/\omega_{\rm prec} = p/q$ for integers p and q) for a hole of a specific spin parameter, and when the corresponding spherical photon orbits close. By substituting this result into Eq. (9.3) one can easily see that modes with multipolar indexes l and m become degenerate with those of indexes $l' = l + kq$ and $m' = m - kp$ for any non-negative integer k, in the eikonal limit (note that in Fig. 9.1, we show an approximate degeneracy for $k = 1$ and for three spin parameters, such that $q/p = 1/4$, $1/6$, and $1/8$, respectively.)

9.1.3   Organization of the paper

To conclude this introduction, we briefly summarize the organization of this paper: In Sec. 9.2, we review the Teukolsky equations, and we then describe the WKB formalism that we use to calculate an accurate approximation to the angular eigenvalues $A_{lm} = A_{lm}^R + iA_{lm}^I$ and QNM frequencies $\omega = \omega_R - i\omega_I$, in the eikonal limit $L \gg 1$ and for holes of arbitrary spins. We verify the accuracy of our expressions in Sec. 9.2.4 by comparing the WKB frequencies to exact, numerically calculated frequencies. In Sec. 9.3, we develop a correspondence between the WKB calculation and mathematics of wave propagation within the Kerr spacetime in the geometric-optics limit, using the geometric-optics approximation and the Hamilton-Jacobi formalism. At leading-order, the QNM frequencies and angular eigenvalues correspond to the conserved quantities of motion in the Kerr spacetime for spherical photon orbits; at next-to-leading order in the geometric-optics approximation, we connect the the decaying behavior of the QNMs to dispersive behaviors of the waves. Finally, in Sec. 9.4,

we interpret aspects of the QNM spectrum geometrically, such as the vanishing of the damping rate for many modes of extremal black holes, the decomposition of the frequency into orbital and precessional parts, and the degeneracies in the QNM frequency spectrum. Finally, in Sec. 9.5, we conclude. We use geometrized units in which $G = c = 1$ and the Einstein summation convention throughout this paper.

9.2 WKB approximation for the quasinormal-mode spectrum of Kerr black holes

In this section, we will derive expressions for the frequencies of quasinormal modes of Kerr black holes using the WKB approximation. We will need to compute the real and imaginary parts to an accuracy of $O(1)$ in terms of $l \gg 1$, which implies that we must calculate ω_R to leading and next-to-leading order and ω_I to leading order. Here, we will focus on obtaining an analytic approximation to the frequency spectrum, and we will leave the geometrical interpretation of our results until the next section.

Before specializing our results to the angular and radial Teukolsky equations, we will review a basic result about the WKB expansion that we will use frequently throughout this paper; a more complete discussion of WKB methods can be found in [11]. Given a wave equation for $\psi(x)$

$$\epsilon^2 \frac{d^2\psi}{dx^2} + U(x)\psi = 0 \,, \tag{9.4}$$

we will expand the solution as $\psi = e^{S_0/\epsilon + S_1 + \epsilon S_2 + \cdots}$, where the leading and next-to-leading action variables are given by

$$S_0 = \pm i \int^x \sqrt{U(x)} dx \,, \tag{9.5a}$$

$$S_1 = -\frac{1}{4} \log U(x) \,. \tag{9.5b}$$

The formulas above will be the basis for our analysis of the radial and angular Teukolsky equations in the next sections.

9.2.1 The Teukolsky equations

Teukolsky showed that scalar, vector, and tensor perturbations of the Kerr spacetime all satisfy a single master equation for scalar variables of spin weight s; moreover, the master equation can be solved by separation of variables [39]. We will use u to denote our scalar variable, and we will separate this scalar wave as

$$u(t, r, \theta, \phi) = e^{-i\omega t} e^{im\phi} \mathcal{R}(r) u_\theta(\theta) \,. \tag{9.6}$$

Then, at the relevant order in $l \gg 1$, the angular equation for $u_\theta(\theta)$ can be written as

$$\frac{1}{\sin\theta}\frac{d}{d\theta}\left[\sin\theta\frac{du_\theta}{d\theta}\right] + \left[a^2\omega^2\cos^2\theta - \frac{m^2}{\sin^2\theta} + A_{lm}\right]u_\theta = 0\,,\tag{9.7}$$

where A_{lm} is the angular eigenvalue of this equation. Following the definition in [42], we use the renormalized radial function given by $u_r = \Delta^{s/2}\sqrt{r^2+a^2}\mathcal{R}$. The equation obeyed by the radial function $u_r(r)$ is

$$\frac{d^2u_r}{dr_*^2} + \frac{K^2 - \Delta\lambda_{lm}^0}{(r^2+a^2)^2}u_r = 0\,,\quad \frac{d}{dr_*} \equiv \frac{\Delta}{r^2+a^2}\frac{d}{dr}\tag{9.8a}$$

with

$$K = -\omega(r^2+a^2) + am\,,\tag{9.8b}$$

$$\lambda_{lm}^0 = A_{lm} + a^2\omega^2 - 2am\omega\,,\tag{9.8c}$$

$$\Delta = r^2 - 2Mr + a^2\,.\tag{9.8d}$$

Here we have used the facts that $\omega_R \sim O(l)$, $\omega_I \sim O(1)$, $m \sim O(l)$ to drop terms that are of higher orders in the expansion than those that we treat. Note that the spin s of the perturbation no longer enters into these equations after neglecting the higher-order terms. The only subtlety here is that the s-dependent terms $2ms\cos\theta/\sin^2\theta$ and $s^2\cot^2\theta$ diverge at the poles, $\theta = 0, \pi$. For non-polar modes it will be shown in the following section that the wave function asymptotes to zero near the poles, and therefore these s dependent corrections are not important. For polar modes $m = 0$, the angular wave functions do not vanish at the pole, and so it is not as clear that these terms can be neglected as small. However, numerical evidence presented in Sec. 9.2.4 also shows that neglecting the s dependent terms in the angular Teukolsky equation only contributes a relative error proportional to $1/L^2$.

9.2.2 The angular eigenvalue problem

We will first find an expression for A_{lm} in terms of ω, l, and m, by analyzing the angular equation in the WKB approximation. By defining

$$x = \log\left(\tan\frac{\theta}{2}\right)\tag{9.9}$$

and $dx = d\theta/\sin\theta$, we can write the angular equation as

$$\frac{d^2u_\theta}{dx^2} + V^\theta u_\theta = 0\,,\tag{9.10a}$$

where

$$V^\theta = a^2\omega^2 \cos^2\theta \sin^2\theta - m^2 + A_{lm}\sin^2\theta \,. \tag{9.10b}$$

When written in this form, it is clear that, aside from polar modes where $m = 0$, u_θ must satisfy a boundary condition that it be 0 as $x \to \pm\infty$ (which corresponds to $\theta \to 0, \pi$). In the special case when $m = 0$, u_θ approaches a constant instead. Furthermore, the angular equation is now in a form that is amenable to a WKB analysis (which will be the subject of the next part).

First, however, we outline how we will perform the calculation. Because the frequency $\omega = \omega_R - i\omega_I$ is complex, the angular eigenvalue A_{lm}, a function of ω, must also be complex. We will write

$$A_{lm} = A_{lm}^R + iA_{lm}^I \,, \tag{9.11}$$

to indicate the split between real and imaginary parts. We will treat a real-valued $\omega = \omega_R$ in the first part of this section, and, therefore, a real-valued $A_{lm}^R(\omega_R)$; we shall account for $-i\omega_I$ by including it as an additional perturbation in the next part of this section.

9.2.2.1 Real part of A_{lm} for a real-valued ω

For $\omega_R \in \mathbb{R}$, we will compute the eigenvalues $A_{lm}^R(\omega_R)$, of Eq. (9.10a) for standing-wave solutions that satisfy physical boundary conditions. At the boundary, $\theta = 0, \pi$ (or $x = \mp\infty$) the potential satisfies $V^\theta = -m^2$ independent of the value of A_{lm}^R; this implies that the solutions to Eq. (9.10a) behave like decaying exponential functions at these points (i.e., the wave does not propagate). For there to be a region where the solutions oscillate (i.e., where the wave would propagate), A_{lm} must be sufficiently large to make $V^\theta > 0$ in some region. Depending on the relative amplitudes of A_{lm} and $a^2\omega^2$, V^θ either has one maximum at $\theta = \pi/2$ (when $A_{lm} \geq a^2\omega^2$), or two identical maxima at two locations symmetrically situated around $\theta = \pi/2$ (when $A_{lm} < a^2\omega^2$). It turns out that the region where the maximum of $V^\theta > m^2$ is centered around $\pi/2$; therefore, all solutions fall into the former category rather than the latter.

The length scale over which the function u_θ varies is $1/\sqrt{V^\theta}$, and the WKB approximation is valid only if the potential V^θ does not vary much at this scale. Therefore, to use the WKB approximation, we require that

$$\left| \frac{1}{\sqrt{V^\theta}} \frac{dV^\theta}{d\theta} \right| \ll |V^\theta| \,. \tag{9.12}$$

This condition applies regardless of the sign of V^θ. Empirically, we find this condition to hold for V^θ in Eq. (9.10a), except around points at which $V^\theta = 0$. We will refer to these as *turning points*, and they can be found by solving for the zeros of the potential,

$$a^2\omega_R^2 \cos^2\theta \sin^2\theta - m^2 + A_{lm}^R \sin^2\theta = 0 \,, \tag{9.13}$$

which are given by

$$\sin^2\theta_\pm = \frac{2m^2}{A_{lm} + a^2\omega_{lm}^2 + \sqrt{(A_{lm} + a^2\omega_{lm}^2)^2 + 4m^2}}, \tag{9.14}$$

where we only kept the physical solution and assume $0 < \theta_- < \pi/2$. It is obvious to see that $\theta_+ = \pi - \theta_-$. Using the leading and next-to-leading WKB approximation, we can write the solution to the wave equation in the propagative region, $x_- < x < x_+$, as

$$u_\theta(x) = \frac{a_+ e^{i\int_0^x dx'\sqrt{V^\theta(x')}} + a_- e^{-i\int_0^x dx'\sqrt{V^\theta(x')}}}{[V^\theta(x)]^{1/4}}, \tag{9.15}$$

where $a_\pm$ are constants that must be fixed by the boundary conditions that the solution approach zero at $\theta = 0, \pi$. For $x > x_+$, we find

$$u_\theta(x) = \frac{c_+ e^{-\int_{x_+}^x dx'\sqrt{-V^\theta(x')}}}{[V^\theta(x)]^{1/4}}, \tag{9.16a}$$

and $x < x_-$,

$$u_\theta(x) = \frac{c_- e^{-\int_x^{x_-} dx'\sqrt{-V^\theta(x')}}}{[V^\theta(x)]^{1/4}}, \tag{9.16b}$$

with $c_\pm$ also being constants set by the boundary conditions. Note that outside of the turning points, we have only allowed the solution that decays towards $x \to \pm\infty$.

Around the turning points $x_\pm$, the WKB approximation breaks down, but u_θ can be solved separately by using the fact that $V_\theta(x \sim x_\pm) \propto x - x_\pm$. Solutions obtained in these regions can be matched to Eqs. (9.15)–(9.16b); the matching condition leads to the Bohr-Sommerfeld quantization condition [43]

$$\int_{\theta_-}^{\theta_+} d\theta \sqrt{a^2\omega_R^2 \cos^2\theta - \frac{m^2}{\sin^2\theta} + A_{lm}^R} = (L - |m|)\,\pi\,. \tag{9.17}$$

Here we have defined

$$L \equiv l + \frac{1}{2}, \tag{9.18}$$

which will be used frequently throughout this paper. The limits of the integration are the values of θ where the integrand vanishes [the turning points of Eq. (9.14)].

If we define

$$\mu \equiv \frac{m}{L}, \quad \alpha_R(a,\mu) \equiv \frac{A_{lm}^R}{L^2}, \quad \Omega_R(a,\mu) \equiv \frac{\omega_R}{L}, \tag{9.19}$$

then all three of these quantities are $O(1)$ in our expansion in L. From these definitions, we can re-express the limits of integration as

$$\sin^2\theta_\pm = \frac{2\mu^2}{\alpha + a^2\Omega^2 + \sqrt{(\alpha + a^2\Omega_R^2)^2 + 4\mu^2}}, \tag{9.20}$$

and the integral as

$$\int_{\theta_-}^{\theta_+} d\theta \sqrt{\alpha_R - \frac{\mu^2}{\sin^2\theta} + a^2\Omega^2\cos^2\theta} = (1 - |\mu|)\pi \,. \tag{9.21}$$

For each set of quantities $(\alpha_R, \mu, \Omega_R)$, we can express α_R as an implicit function involving elliptic integrals; however, if we treat $a\Omega_R$ as a small parameter, then the first two terms in the expansion are

$$\alpha_R \approx 1 - \frac{a^2\Omega_R^2}{2}\left(1 - \mu^2\right) \,. \tag{9.22}$$

We derive and discuss this approximation in greater detail in Appendix 9.A. Higher order corrections are on the order of $(a\Omega_R)^4$. For $a = 0$, we note that this is accurate with a relative error of $O(1/L^2)$, because for a Schwarzschild black hole

$$A_{lm}^{\text{Schw}} = l(l + 1) - s(s + 1) \,. \tag{9.23}$$

As we will confirm later in Figs. 9.2 and 9.4, Eq. (9.22) is an excellent approximation even for highly spinning black holes.

To understand intuitively why the approximation works so well, we will focus on corotating modes (i.e., those with positive and large m, or μ near unity), which have the highest frequencies and, therefore, the largest possible values for $a\Omega_R$. For a fixed value of (l, m), ω_R is a monotonically increasing function of a, and

$$\omega_R^{lm}(a) \leq \omega_R^{lm}(a = M) = m\Omega_H^{a=1} = \frac{m}{2M} \,. \tag{9.24}$$

In setting this upper bound, we have used the result that the low-overtone QNM frequencies approach $m\Omega_H$ for $m > 0$ and for extremal black holes (first discussed by Detweiler [44], and discussed further by, e.g. [45, 46]); we have also used Ω_H to denote the horizon frequency of the Kerr black hole,

$$\Omega_H = \frac{a}{2Mr_+} \,, \tag{9.25}$$

and r_+ to indicate the position of the horizon [note that $r_+(a = M) = M$]. Normalizing Eq. (9.24) by L, we find

$$a\Omega_R \leq (\mu/2)(a/M) \leq 1/2 \,. \tag{9.26}$$

Even for the upper bound $a\Omega_R = 1/2$, as can be checked numerically against Eq. (9.21), the relative accuracy of Eq. (9.22) is still better than 0.2%.

9.2.2.2 Complex A_{lm} for a complex ω

To solve for the next-to-leading-order corrections to A_{lm}, we must compute the imaginary part A_{lm}^I. Because $\omega_I \ll \omega_R$, when we allow $\omega = \omega_R - i\omega_I$ to be a complex number in the angular eigenvalue problem (9.7), we can treat the term linear in ω_I as a perturbation to the angular equation. Using the perturbation theory of eigenvalue equations, we find that

$$A_{lm}^I = -2a^2 \omega_R \omega_I \langle \cos^2 \theta \rangle \,, \tag{9.27}$$

where

$$\langle \cos^2 \theta \rangle = \frac{\displaystyle\int \cos^2 \theta |u_\theta|^2 \sin \theta d\theta}{\displaystyle\int |u_\theta|^2 \sin \theta d\theta}$$

$$= \frac{\displaystyle\int_{\theta_-}^{\theta_+} \frac{\cos^2 \theta}{\sqrt{a^2 \omega_R^2 \cos^2 \theta - \frac{m^2}{\sin^2 \theta} + A_{lm}^R}} d\theta}{\displaystyle\int_{\theta_-}^{\theta_+} \frac{1}{\sqrt{a^2 \omega_R^2 \cos^2 \theta - \frac{m^2}{\sin^2 \theta} + A_{lm}^R}} d\theta} \,. \tag{9.28}$$

By taking the derivative of both sides of the Bohr-Sommerfeld condition (9.17) with respect to the variable $z = a\omega_R$ and by treating A_{lm} as a function of z, we can rewrite the above expression as

$$\langle \cos^2 \theta \rangle = -\frac{1}{2z} \frac{\partial A_{lm}^R(z)}{\partial z} \bigg|_{z=a\omega_R} \,. \tag{9.29}$$

Substituting this expectation value into Eq. (9.27), we find

$$A_{lm}^I = a\omega_I \left[\frac{\partial A_{lm}^R(z)}{\partial z} \right]_{z=a\omega_R} \,. \tag{9.30}$$

Equation (9.30) defines a numerical prescription for computing $A_{lm} = A_{lm}^R + iA_{lm}^I$. This approach is quite natural: as ω becomes complex, A_{lm} is the analytic function whose value on the real axis is given by A_{lm}^R. The approximate formula (9.22), therefore, becomes

$$A_{lm} \approx L^2 - \frac{a^2 \omega^2}{2} \left[1 - \frac{m^2}{L^2} \right] \,, \tag{9.31a}$$

or

$$\alpha \approx 1 - \frac{a^2 \Omega^2}{2} \left(1 - \mu^2 \right) \,, \tag{9.31b}$$

for a complex frequency ω, where we have defined Ω to be ω/L.

9.2.3 The radial eigenvalue problem

Now that we have solved for the angular eigenvalues A_{lm} in terms of ω, we turn to the radial Teukolsky equation. From Eq. (10.4a), we see that the radial equation is already in the form

$$\frac{d^2 u_r}{dr_*^2} + V^r u_r = 0, \tag{9.32a}$$

if we define

$$V^r(r, \omega) = \frac{[\omega(r^2 + a^2) - ma]^2 - \Delta \left[A_{lm}(a\omega) + a^2\omega^2 - 2ma\omega\right]}{(r^2 + a^2)^2}. \tag{9.32b}$$

Note here that V^r is an analytic function of ω, and that it is real-valued when ω is real.

In general, the WKB approximant for u_r is given at leading order by

$$u_r = b_+ e^{i \int^{r_*} \sqrt{V^r(r_*')} dr_*'} + b_- e^{-i \int^{r_*} \sqrt{V^r(r_*')} dr_*'}, \tag{9.33}$$

although in order to obtain a mode which is outgoing at $r_* \to +\infty$ (the same as $r \to \infty$) and ingoing at $r_* \to -\infty$ ($r \to r_+$), we must have

$$u_r = b_+ e^{i \int^{r_*} \sqrt{V^r(r_*')} dr_*'}, \tag{9.34a}$$

for the region containing $r \to +\infty$, and

$$u_r = b_- e^{-i \int^{r_*} \sqrt{V^r(r_*')} dr_*'}, \tag{9.34b}$$

for the region containing $r_* \to -\infty$. Intuitively speaking, a solution to Eq. (9.32a) will satisfy the asymptotic behavior above if $V^r \approx 0$ around a point $r = r_0$, and $V_r > 0$ on both sides. Then, the WKB expansion (9.33) is valid in the two regions on both sides of $r = r_0$, and the solution in the vicinity of r_0 must be obtained separately by matching to the WKB approximation. The matching will constrain the frequency, thereby giving a method to determine ω. A detailed calculation of this procedure has been carried out by Iyer and Will [11] to high orders in the WKB approximation; the only difference between our calculation and their result at lower orders comes from the more complex dependence of V^r on ω in our case (particularly because A_{lm} depends on ω in a more involved way).

9.2.3.1 Computing ω_R

From Iyer and Will [11], the conditions at the leading and next-to-leading order that must be solved to find ω_R are

$$V^r(r_0, \omega_R) = \left. \frac{\partial V^r}{\partial r} \right|_{(r_0, \omega_R)} = 0. \tag{9.35}$$

After a short calculation, these conditions can be expressed as

$$\Omega_R = \frac{\mu a}{r_0^2 + a^2} \pm \frac{\sqrt{\Delta(r_0)}}{r_0^2 + a^2} \beta(a\Omega_R), \tag{9.36a}$$

$$0 = \frac{\partial}{\partial r} \left[\frac{\Omega_R(r^2 + a^2) - \mu a}{\sqrt{\Delta(r)}} \right]_{r=r_0}, \tag{9.36b}$$

where we have defined

$$\beta(z) = \sqrt{\alpha(z) + z^2 - 2\mu z} \tag{9.37a}$$

$$\approx \sqrt{1 + \frac{z^2}{2} - 2\mu z + \frac{\mu^2 z^2}{2}}. \tag{9.37b}$$

In deriving Eq. (9.36b), we have used the fact that at $r > r_+$, $(r^2 + a^2)^2/\Delta$ is a monotonically increasing function, and, therefore the extrema of V^r are the same as those of $V^r(r^2 + a^2)^2/\Delta$; we then also used the fact that the quantity within the square brackets in Eq. (9.36b) is always nonzero at points at which $V^r = 0$.

One method of jointly solving Eqs. (9.36a) and (9.36b) would be to use Eq. (9.36b) to express Ω_R in terms of r_0

$$\Omega_R = \frac{(M - r_0)\mu a}{(r_0 - 3M)r_0^2 + (r_0 + M)a^2}, \tag{9.38}$$

and then insert this into Eq. (9.36a) to obtain r_0; finally Ω_R can be obtained by substituting this r_0 back into Eq. (9.38). If we use the approximate formula (9.37b) in this process, the equation for r_0 becomes a sixth-order polynomial in $x = r_0/M$, the roots of which can be found efficiently. For convenience, we write this polynomial here

$$2x^4(x - 3)^2 + 4x^2[(1 - \mu^2)x^2 - 2x - 3(1 - \mu^2)](a/M)^2$$

$$+(1 - \mu^2)[(2 - \mu^2)x^2 + 2(2 + \mu^2)x + (2 - \mu^2)](a/M)^4. \tag{9.39}$$

For each pair $(\mu, a/M)$, there are in general two real roots for x, which correspond to the two possible values of r_0/M (and the two real frequencies with opposite signs).

Note that the procedure above will not work when $m = 0$ [when both the numerator and denominator of Eq. (9.38) vanish]. In this case, we can directly require that

$$(r_p - 3M)r_p^2 + (r_p + M)a^2 = 0. \tag{9.40}$$

The solution, r_p, can be found in closed form [29, 47]. Inserting it into Eq. (9.36a) the result can be
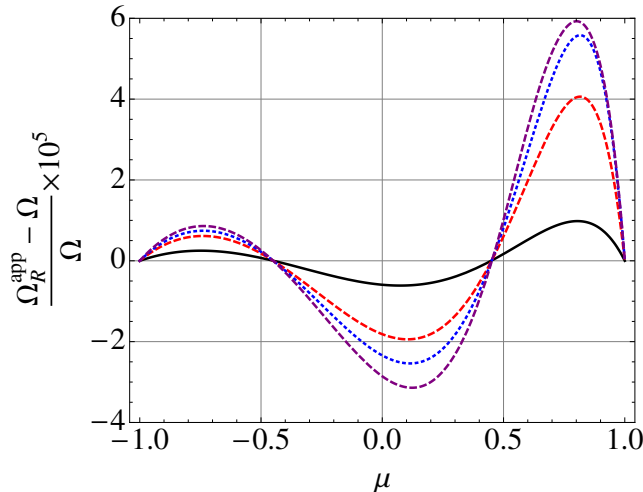
Figure 9.2: Difference in $\Omega_R(a,\mu)$ [Eq. (9.38)] that arises from using the approximate formula for A_{lm} [Eq. (9.31a)] as opposed to the exact formula. Here $a/M = 0.7$, $0.9, 0.95$, and 0.99 correspond to black solid, red dashed, blue dotted, and purple long-dashed curves, respectively. The quantity plotted on the vertical axis has been scaled by 10^5.

expressed in terms of elliptic integrals

$$\Omega_R(a, \mu = 0) = \pm \frac{1}{2} \frac{\pi\sqrt{\Delta(r_p)}}{(r_p^2 + a^2)\text{EllipE}\left[\frac{a^2\Delta(r_p)}{(r_p^2 + a^2)^2}\right]} , \tag{9.41}$$

where EllipE denotes an elliptic integral of the second kind. Here we have used the subscript p for this special case, because this mode will turn out to correspond to polar orbits. Note this formula agrees with the one derived in [29].

We plot in Fig. 9.2 the relative error in Ω_R that comes from using the approximate expression for A_{lm} [Eq. (9.31a)] rather than the exact Bohr-Sommerfeld condition. The error is always less than $\sim 10^{-4}$ (we scale the quantity plotted on the vertical axis by 10^5), and therefore, we will use the approximate expression for A_{lm} for the remaining calculations involving Ω_R throughout this paper. In Fig. 9.3, we plot Ω_R for $a/M = 0$, 0.3, 0.5, 0.9, 0.99, and 1 (the flat curve corresponds to $a/M = 0$, and those with increasing slopes are the increasing values of a/M). While for low values of a/M below ~ 0.5, Ω_R depends roughly linearly upon μ, for higher values of a/M (and for $\mu > 0$), Ω_R grows more rapidly than linearly. For $a/M = 1$, $\Omega_R \to 1/2$ when $\mu \to 1$, as anticipated.
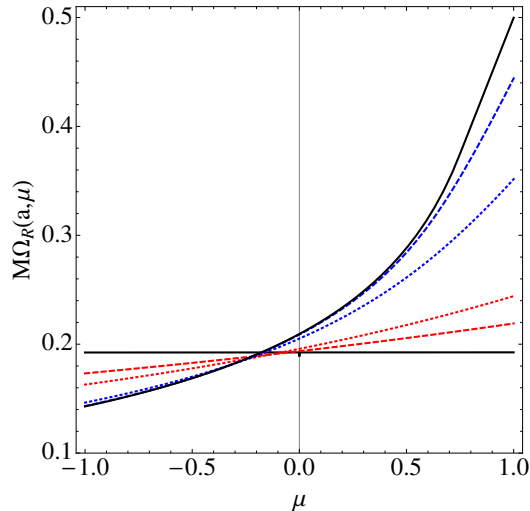
Figure 9.3: Real part of the QNM spectra from the WKB approximation. Black solid curves show Ω for $a/M = 0$ (the flat curve) and $a/M = 1$ (the curve that increases towards 0.5); red (light gray) dashed and dotted curves show $a/M = 0.3$ and 0.5, while blue (dark gray) dotted and dashed curves show $a/M = 0.9$ and 0.99.

9.2.3.2 Computing ω_I

At leading order, the imaginary part ω_I can be calculated using the same procedure set forth by Iyer and Will [11]. They find that

$$
\omega_I = -(n+1/2)\frac{\sqrt{2\left(\frac{d^2V^r}{dr_*^2}\right)_{r_0,\omega_R}}}{\left(\frac{\partial V^r}{\partial\omega}\right)_{r_0,\omega_R}},
$$

$$
= -(n+1/2)\Omega_I(a,\mu). \tag{9.42}
$$

In our calculation, we must also take into account that V^r also depends on ω through the angular eigenvalue's dependence on ω. If we use the approximate formula for α, we obtain a reasonably compact expression for Ω_I:

$$
\Omega_I = \Delta(r_0)\frac{\sqrt{4(6r_0^2\Omega_R^2-1)+2a^2\Omega_R^2(3-\mu^2)}}{2r_0^4\Omega_R - 4aMr_0\mu + a^2r_0\Omega_R[r_0(3-\mu^2)+2M(1+\mu^2)] + a^4\Omega_R(1-\mu^2)}. \tag{9.43}
$$

In Fig. 9.4, we plot the relative error in Ω_I from using the approximate formula for A_{lm} identically to that in Fig. 9.2 (although here we scale the quantity plotted on the vertical axis by 10^4). Because the error is always less than $\sim 10^{-3}$, we will use the approximate expression for A_{lm} for computing Ω_I in the remainder of this paper. In [29], an alternate expression for ω_I (for $m = 0$) was computed by finding an analytic expression for the *Lyapunov exponent* (see Sec. 9.3.3.2, where we discuss the exponent's connection to the QNM's decay rate); this expression gives the same result as (9.43) for

$\mu = 0$ to a high accuracy. In Fig. 9.5, we plot $\Omega_I(a, \mu)$ for several values of a/M (the same as those in Fig. 9.3, though not $a/M = 0.3$). The curve for $a/M = 0$ is flat, and those with larger spins have more rapidly decreasing slopes for increasing values of a/M. It is interesting to note that in the limit $a \to 1$, Ω_I becomes zero for values of μ in a finite interval $0.74 \lesssim \mu \leq 1$ (not only for $\mu = 1$ does Ω_I vanish). We will put forward an explanation for this phenomenon in Sec. 9.4, after we make connections between QNMs and wave propagation in the Kerr spacetime.

The vanishing of the QNM's decay rate for extremal black holes has been discussed by many authors in the past. Detweiler [44] first showed that modes with $l = m$ had vanishing decay. Mashhoon [48] extended the work of Goebel [37] to Kerr-Newman black holes when he calculated the frequency and Lyapunov exponent of equatorial unstable photon orbits. He found that for extremal Kerr-Newman holes (which have $M^2 = a^2 + Q^2$, with Q the charge of the hole) when $a \geq M/2$, the Lyapynov exponent vanished, in analogy with the vanishing decay for $\mu \gtrsim 0.74$ discussed above. For QNMs of a massive scalar field around an extremal Kerr black hole, Hod [49] found that the modes have vanishing damping when the mass of the scalar field is smaller than a critical value. Berti and Kokkotas [50] numerically calculated QNM frequencies for Kerr-Newman black holes using continued fractions, and found good agreement with Mashhoon's result for $l = m = 2$, $s = 2$ modes (i.e., for extremal holes there was zero decay). Cardoso [45] explored Detweiler's calculation of the decay of extremal modes, and could show that some but not all modes with $m \neq l$ and $m > 0$ have vanishing decay rates. Hod also extended Detweiler's calculation to $m \geq 0$ and found that all such modes have zero decay in the extremal Kerr case [46], in contrast to our findings. Hod also computed QNM frequencies and decays for eikonal QNMs in the extremal Kerr limit [51] and found agreement with Mashhoon's result. In the end, the particular value of m at which the QNM mode decay rate for an extremal black hole vanishes is not a settled issue; our results here indicate that for $L \gg 1$, only some subset of the $m > 0$ modes have vanishing decay rates.

9.2.4 Accuracy of the WKB approximation

Because we calculated the leading and next-to-leading orders in the WKB approximation to ω_R, we expect that the relative error for increasing L should scale as $O(1/L^2)$. For the imaginary part, we computed only the leading-order expression, and we would expect that the relative error might scale as $O(1/L)$. In addition, because at this order of approximation we do not account for the spin of the wave, we anticipate that the error for the gravitational modes may be larger than those for scalar modes. In Figs. 9.6–9.9, we confirm most of these expectations, but we find the somewhat unexpected result that the relative error for the imaginary part also scales as $O(1/L^2)$. In fact, this finding is consistent with Eqs. (52) and (53) of [29], where the next order contributions are calculated for the special cases of $m = l$ and $m = -l$, respectively.

In Fig. 9.6, we compare the WKB approximation to ω_R with numerical computations of the
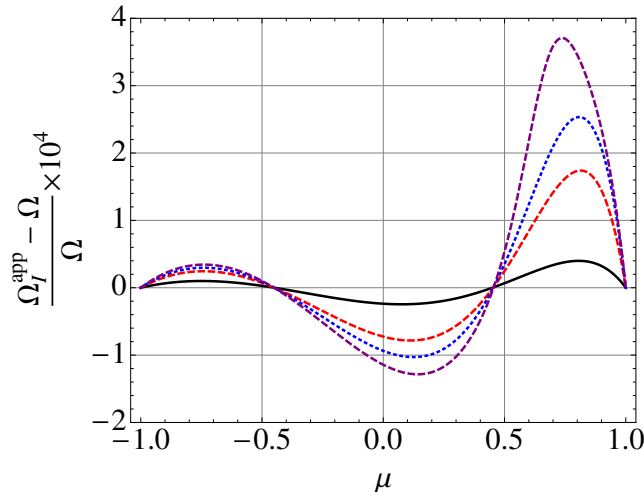
Figure 9.4: Difference in $\Omega_I(a, \mu)$ [Eq. (9.42)] from using the approximate formula for A_{lm} [Eq. (9.31a)] rather than the exact formula. Here $a/M = 0.7$, 0.9, 0.95, and 0.99 correspond to black solid, red dashed, blue dotted, and purple long-dashed curves, respectively. We scale the quantity plotted along the vertical axis by 10^4 in this figure.
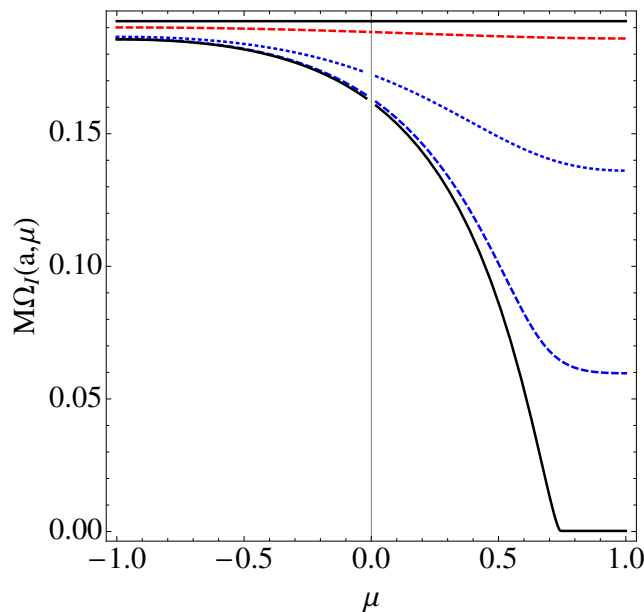

Figure 9.5: Imaginary part of the QNM spectrum computed in the WKB approximation. Black solid curves show Ω_I for $a/M = 0$ (again the flat curve) and $a/M = 1$ the curve that decreases and heads to zero. The red dashed curve shows $a/M = 0.5$, while blue dotted and dashed curves show $a/M = 0.9$ and 0.99, respectively. For $a/M = 1$, modes with $\mu \gtrsim 0.74$ approach zero (modes that do no decay), while others still decay.

$s = 2$, gravitational-wave, quasinormal-mode spectra; specifically, we plot the fractional error against $\mu = m/L$, for $l = 2, 3, \ldots, 14$, and for black holes of spins $a/M = 0.3$, 0.5, 0.9, and 0.95. The relative error clearly converges to $O(L^2)$. Even for $l = 2$, the relative error tends to be $\lesssim 30\%$, and at $l \geq 3$ the relative error stays below $\sim 1.5L^{-2}$ (this means error is $\lesssim 10\%$ for $l = 3$ and higher).
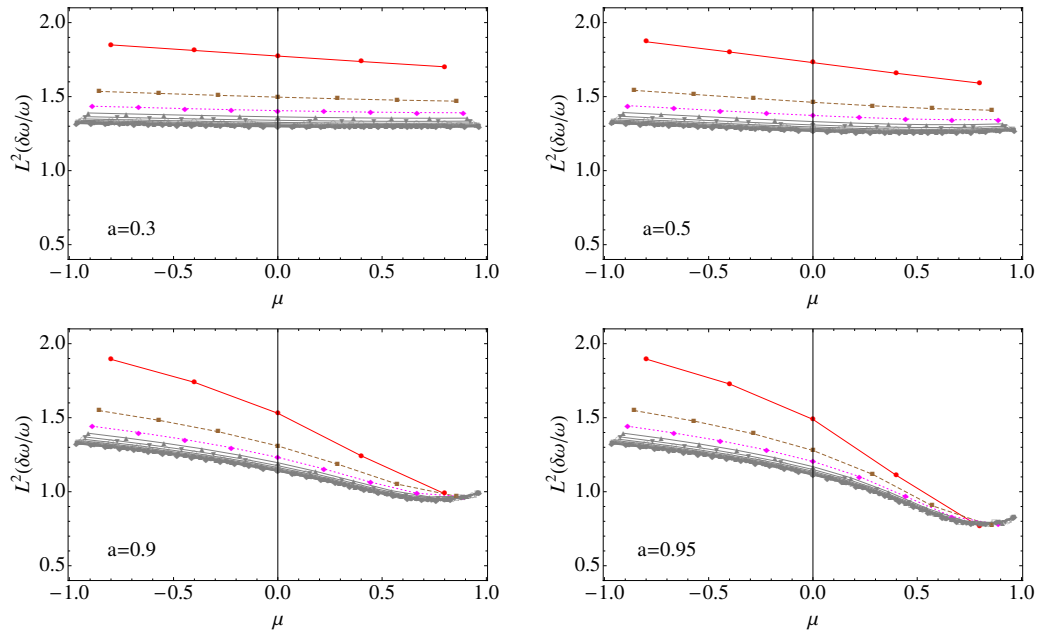
Figure 9.6: Fractional error, $\delta\omega_R/\omega_R$, of the WKB approximation to the $s = 2$, gravitational-wave, quasinormal-mode spectrum, multiplied by L^2. The four panels correspond to four different spins which (going clockwise from the top left) are $a/M = 0.3$, 0.5, 0.95, and 0.9. Errors for $l = 2, 3, 4$ are highlighted as red solid, brown dashed, and pink dotted lines, while the rest ($l = 5, \ldots, 14$) are shown in gray. This shows that the relative error approaches the $O(1/L^2)$ scaling quite quickly.

Figure 9.7: Fractional error, $\delta\omega_R/\omega_R$, of the WKB approximation to the $s = 0$, scalar-wave, quasinormal-mode spectrum, again scaled by L^2. The four panels correspond to the same four spins in Fig. 9.6. The points shown in the four panels are for values of l in the range $l = 2, 3, \ldots, 14$. Because all values of l nearly lie on the same curve, the relative error has converged at an order $O(1/L^2)$ even for very low l. The overall error is also significantly lower than that for the $s = 2$ modes.

Figure 9.8: Fractional error, $\delta\omega_I/\omega_I$, of the WKB approximation to the $s = 2$, gravitational-wave, quasinormal-mode spectrum, also scaled by L^2. The panels and the curves are plotted in the same way as in Fig. 9.6, and the error scales similarly.
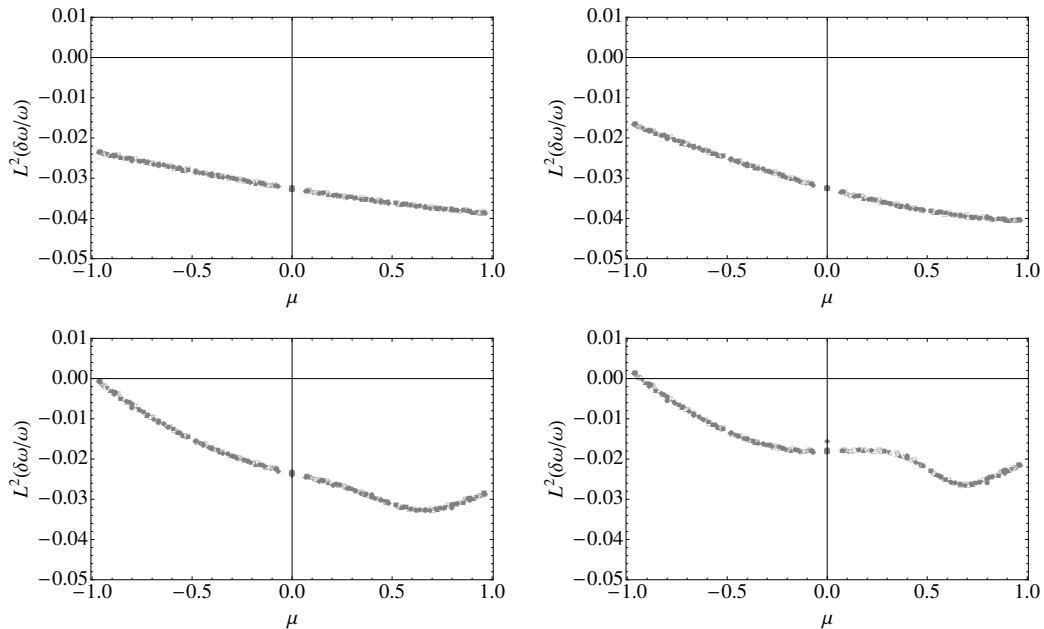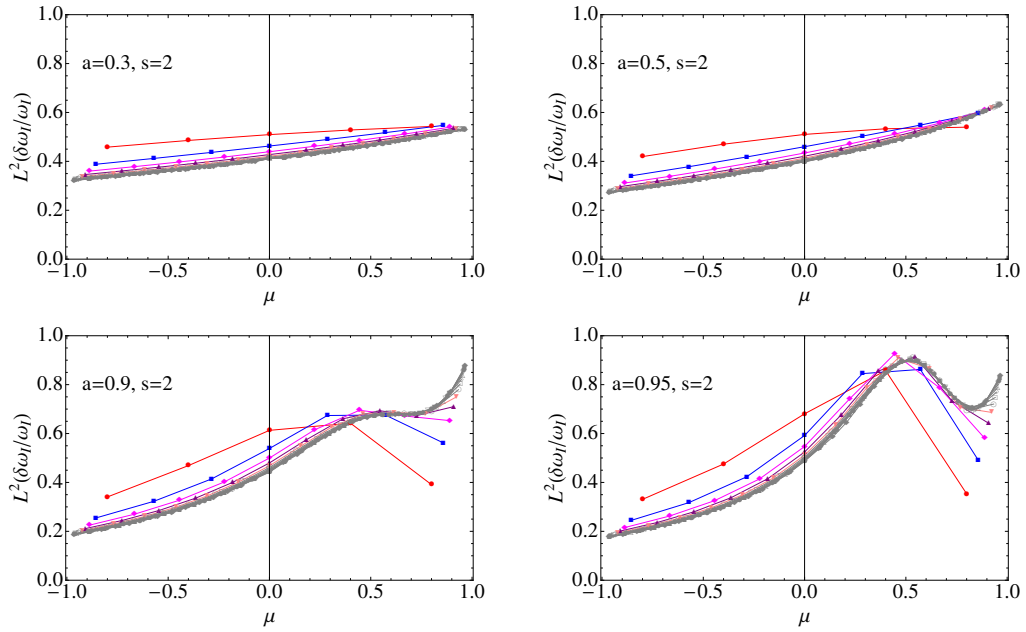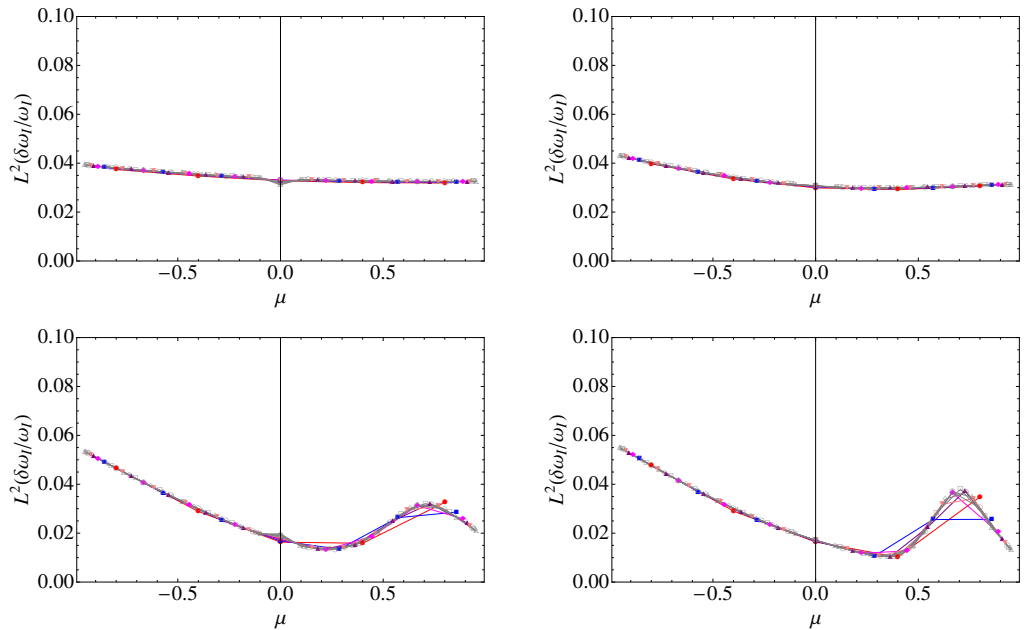

Figure 9.9: Fractional error, $\delta\omega_I/\omega_I$, of the WKB approximation to the $s = 0$, scalar-wave, quasinormal-mode spectrum, again multiplied by L^2. The four panels and the points are shown in the same way as in Fig. 9.7, and there is a similar rapid convergence of the error.

In Fig. 9.7, we compare the WKB spectra with $s = 0$ scalar quasinormal-mode spectra, for the same values of l and the same black-hole spins. We find a much better agreement. For all $l \geq 2$ modes, the relative error stays below $4 \times 10^{-2} L^{-2}$. This suggests that coupling between the spin of the wave (i.e., its tensor polarization) and the background curvature of the Kerr black hole is the main source of error in our WKB approximation.

In Figs. 9.8 and 9.9, we perform the same comparisons as in Figs. 9.6 and 9.7 for the imaginary part of frequency. Surprisingly, we find that for both $s = 0$ and 2, the relative error in ω_I is $O(L^{-2})$. For $s = 0$, the relative error is $\lesssim 6 \times 10^{-2} L^{-2}$, while for $s = 2$, the error is $\lesssim L^{-2}$.

With this comparison, we conclude our direct calculation of the QNM spectrum by WKB techniques. We will discuss additional features of the QNM spectrum in Sec. 9.4, but before doing so, we will develop a geometric interpretation of our WKB results. Doing so will help us to develop more intuition about our WKB expressions.

9.3   Geometric optics in the Kerr spacetime

In this section, we first briefly review the formalism of geometric optics, which describes the propagation of waves with reduced wavelengths λ that are much shorter than the spacetime radius of curvature, R, and the size of the phase front, $\mathcal{L}$. In the geometric-optics approximation, the phase of the waves remains constant along null geodesics (rays), while the amplitude can be expressed in terms of the expansion and contraction of the cross-sectional area of bundles of null rays. We will then specialize the geometric-optics formalism to the Kerr spacetime, and we will write down the most general form of propagating waves in the geometric-optics approximation. Using the Hamilton-Jacobi method, we see that the waves' motion can be related to the null geodesics in the spacetime. By applying boundary conditions to the approximate wave, we obtain expressions for the quasinormal-mode waveforms and their corresponding complex frequency spectra and angular separation constants, in the eikonal limit.

9.3.1   Geometric optics: general theory

Here we briefly review the geometric-optics approximation to scalar-wave propagation (see, e.g., Section 22.5 of Ref. [52] for details). A massless scalar wave u propagating in curved spacetime satisfies the wave equation

$$g^{\mu\nu}\nabla_\mu\nabla_\nu u = 0 \,. \tag{9.44}$$

If we write

$$u = A e^{i\Phi} \,, \tag{9.45}$$

then at leading order in $\lambda/\mathcal{L}$, we have

$$g^{\mu\nu}k_\mu k_\nu = 0\,, \quad k_\mu \equiv \partial_\mu \Phi\,, \tag{9.46}$$

while at next-to-leading order,

$$2k^\mu \partial_\mu \log A + \nabla_\mu k^\mu = 0\,. \tag{9.47}$$

Note that Eq. (9.46) also implies that k^μ is geodesic,

$$k^\mu \nabla_\mu k_\nu = k^\mu \nabla_\mu \nabla_\nu \Phi = k^\mu \nabla_\nu \nabla_\mu \Phi = k^\mu \nabla_\nu k_\mu = 0\,. \tag{9.48}$$

Equations (9.45)–(9.48) encode information about the transport of the amplitude A and phase Φ along a null geodesic (or a *ray*). The phase should be kept constant, because Eq. (9.46) states

$$k^\mu \partial_\mu \Phi = 0\,, \tag{9.49}$$

while the amplitude is transported along the ray in a manner that depends upon the propagation of neighboring rays. Because the 2D area, $\mathcal{A}$, of a small bundle of null rays around the central ray satisfies the equation

$$\nabla_\mu k^\mu = k^\mu \partial_\mu \log \mathcal{A}\,, \tag{9.50}$$

it is possible to show from Eq. (9.47) that

$$k^\mu \partial_\mu \left(\mathcal{A}^{1/2} A\right) = 0\,, \tag{9.51}$$

which implies $A \propto \mathcal{A}^{-1/2}$.

The transport equations (9.49) and (9.51) provide a way to construct a wave solution from a single ray; therefore, any solution to the wave equation (9.44) in a 4D spacetime region can be found from a three-parameter family of null rays (with smoothly varying initial positions and wave vectors) by assigning smoothly varying initial values of (Φ, A) and then transporting these values along the rays. (We use the phrase "smoothly varying" to mean that the values of (Φ, A) must change on the scale of $\mathcal{L} \gg \lambda$.) We note it is often convenient to divide the three-parameter family of initial positions of the null rays into two-parameter families of rays with constant initial values of Φ. The constant-Φ surfaces are the initial phase fronts, which, upon propagation along the rays, become 3D phase fronts of the globally defined wave. The more usual 2D phase fronts, at a given time, are obtained if we take a particular time slicing of the spacetime and find the 2D cross sections of the 3D phase fronts in this slicing.

The above formalism describes wave propagation up to next-to-leading order in $\mathcal{L}/\lambda$, which will

be enough for us to build a geometric correspondence for both the real frequency, the decay rate, and the angular separation constant of QNMs in the Kerr spacetime.

9.3.2 Null geodesics in the Kerr spacetime

Now let us review the description of null geodesics in the Kerr spacetime using the Hamilton-Jacobi formalism. In general, the Hamilton-Jacobi equation states

$$g^{\mu\nu}(\partial_\mu S)(\partial_\nu S) = 0 \,, \tag{9.52}$$

where $S(x^\mu)$ is called the *principal function*. For the Kerr spacetime, the Hamilton-Jacobi equation can be solved via separation of variables (see, e.g., [53]), through which the principal function can be expressed as

$$S(t, \theta, \phi, r) = S_\theta(\theta) + L_z\phi + S_r(r) - \mathcal{E}t \,, \tag{9.53}$$

where $\mathcal{E}$ and L_z are constants that are conserved because of the the timelike and axial Killing vectors of the Kerr spacetime. Physically, $\mathcal{E}$ and L_z represent the energy and z-directed specific angular momentum of the massless scalar particle. The functions $S_r(r)$ and $S_\theta(\theta)$ are given by

$$S_r(r) = \int^r \frac{\sqrt{\mathcal{R}(r')}}{\Delta(r')}dr' , \qquad\qquad S_\theta(\theta) = \int^\theta \sqrt{\Theta(\theta')}d\theta' \,, \tag{9.54a}$$

where $\mathcal{R}(r)$ and $\Theta(\theta)$ are given by

$$\mathcal{R}(r) = [\mathcal{E}(r^2 + a^2) - L_z a]^2 - \Delta[(L_z - a\mathcal{E})^2 + \mathcal{Q}] \,, \tag{9.54b}$$

$$\Theta(\theta) = \mathcal{Q} - \cos^2\theta(L_z^2/\sin^2\theta - a^2\mathcal{E}^2) \,, \tag{9.54c}$$

and $\Delta(r)$ is given in Eq. (10.4b). The constant $\mathcal{Q}$ is the Carter constant of the trajectory, which is a third conserved quantity along geodesics in the Kerr spacetime.

The principal function $S(x^\mu; \mathcal{E}, L_z, \mathcal{Q})$ contains information about all null geodesics; equations of motion for individual null geodesics are given by first choosing a particular set of $(\mathcal{E}, L_z, \mathcal{Q})$, and then imposing

$$\frac{\partial S}{\partial \mathcal{E}} = 0 \,, \ \frac{\partial S}{\partial L_z} = 0 \,, \ \frac{\partial S}{\partial \mathcal{Q}} = 0 \,. \tag{9.55}$$

These conditions lead to a set of first-order differential equations

$$\frac{dt}{d\lambda} = \frac{r^2 + a^2}{\Delta}\left[\mathcal{E}(r^2 + a^2) - L_z a\right] - a(a\mathcal{E}\sin^2\theta - L_z) \,, \tag{9.56a}$$

$$\frac{d\phi}{d\lambda} = -\left(a\mathcal{E} - \frac{L_z}{\sin^2\theta}\right) + \frac{a\left[\mathcal{E}(r^2 + a^2) - L_z a\right]}{\Delta} \,, \tag{9.56b}$$

$$\frac{dr}{d\lambda} = \sqrt{\mathcal{R}}, \qquad \frac{d\theta}{d\lambda} = \sqrt{\Theta}\,, \tag{9.56c}$$

where we have defined

$$\frac{d}{d\lambda} \equiv \Sigma \frac{d}{d\zeta}\,, \quad \Sigma = r^2 + a^2 \cos^2\theta\,, \tag{9.57}$$

and ζ is an affine parameter along the null geodesics.

9.3.3 Correspondence with quasinormal modes

Table 9.1: Geometric-optics correspondence between the parameters of a quasinormal mode, $(\omega, A_{lm}, l, \text{ and } m)$, and the conserved quantities along geodesics, $(\mathcal{E}, L_z, \text{ and } \mathcal{Q})$. To establish a correspondence with the next-to-leading-order, geometric-optics approximation, the geodesic quantities $\mathcal{E}$ and $\mathcal{Q}$ must be complex.

Wave Quantity	Ray Quantity	Interpretation
ω_R	$\mathcal{E}$	Wave frequency is same as energy of null ray (determined by spherical photon orbit).
m	L_z	Azimuthal quantum number $\to z$ angular momentum (quantized to get standing wave in ϕ direction).
A_{lm}^R	$\mathcal{Q} + L_z^2$	Real part of angular eigenvalue $\to$ Carter constant (quantized to get standing wave in θ direction).
ω_I	$\gamma = -\mathcal{E}_I$	Wave decay rate is proportional to Lyapunov exponent of rays neighboring the light sphere.
A_{lm}^I	$\mathcal{Q}_I$	Nonzero because $\omega_I \neq 0$ (see Secs. 9.2.2.2 and 9.3.3.3 for further discussion).

Here we will find connection between the general set of wave solutions in the previous section, and the particular solutions that correspond to a quasinormal modes, in the geometric-optics limit. Specifically, we will look for waves that propagate outwards at infinity and down the horizon. With this correspondence, we will be able to make a geometric interpretation of our WKB results from Sec. 9.2.

9.3.3.1 Leading order: conserved quantities of rays and the real parts of quasinormal-mode parameters

It is straightforward to note that the Hamilton-Jacobi equation (9.52) is identical to the leading-order geometric-optics equations, if we identify the phase, Φ, with the principal function, S. Therefore, at leading order, we can write

$$u = e^{iS} = e^{-i\mathcal{E}t} e^{iL_z\phi} e^{\pm iS_\theta} e^{\pm iS_r}\,, \tag{9.58}$$

where we recall that the amplitude A differs from unity only at next-to-leading order (we will treat it in the following subsections). Here, we have a chosen set of conserved quantities, $(\mathcal{E}, \mathcal{Q}, L_z)$, to

identify the wave we wish to connect with a quasinormal-mode solution. The region in which the wave propagates is identical to the region in which geodesics with these conserved quantities can propagate. In addition, for each point in this region, there is one (and only one) geodesic passing through it; that we have $\pm$ in front of S_θ and S_r means only that either propagation direction could be a solution to the wave equation.

Now we note that u, a scalar wave in the Kerr spacetime, must separate as in Eq. (9.6). By comparing Eq. (9.6) and Eq. (9.58), we can immediately identify that

$$\mathcal{E} = \omega_R \,. \tag{9.59}$$

Because $\mathcal{E}$ is a real quantity (the conserved energy of the null geodesic), we see that at leading order, the wave does not decay. Next, we also observe that in order for u to be consistently defined in the azimuthal direction, L_z (of the null geodesics that S describes) must be an integer. This allows us to make the second identification

$$L_z = m \,. \tag{9.60}$$

Comparing S_θ from Eq. (9.54a) and u_θ from Eqs. (9.15) and (9.10b) (focusing on one direction of θ propagation, and ignoring next-to-leading-order terms), we can also conclude that

$$\mathcal{Q} = A_{lm}^R - m^2 \,. \tag{9.61}$$

At this stage, given any set of $(\mathcal{E}, \mathcal{Q}, L_z)$, we will be able to find a wave solution that exists in the region in which the geodesics travel. Not all such sets of conserved quantities correspond to quasinormal modes, however, because they may not satisfy the correct boundary conditions of QNMs.

We will first explain the conditions on the radial motion of the geodesics that will allow these particular geodesics to correspond to a wave that satisfies outgoing and downgoing conditions at $r_* \to \pm\infty$, respectively. If the radial geodesics satisfy $\mathcal{R} > 0$ everywhere, then there will be traveling waves across the entire r_* axis, which will not satisfy the boundary conditions; if there are two disconnected regions of traveling waves, however, waves will scatter off the potential on each side, and they will also fail to satisfy the boundary conditions. The only way to satisfy the boundary conditions is to have a point r_0 at which $\mathcal{R} = 0$ and $\mathcal{R}' = 0$, in which case there will be a family of geodesics on each side of $r = r_0$ (with each member a *homoclinic orbit* which has $r \to r_0$ on one end) and a *spherical orbit* with constant $r = r_0$. The corresponding wave has zero radial spatial frequency at $r = r_0$, and this frequency increases towards $r < r_0$ and decreases towards $r > r_0$. Noting that

$$\mathcal{R} = V^r \left(r^2 + a^2\right)^2 \,, \tag{9.62}$$

the condition

$$\mathcal{R} = \mathcal{R}' = 0 \tag{9.63}$$

is the same as the condition, Eq. (9.35), which determines ω_R in terms of L and m in the WKB approximation. It is worth mentioning that although the condition of Eq. (9.63) imposed on $(\mathcal{E}, \mathcal{Q}, L_z)$ can be interpreted most easily as the condition for a spherical photon orbit, the wave function for the quasinormal mode we are considering is *not* localized around that orbit. The wave function at leading order, in fact, has a constant magnitude at every location that homoclinic orbits reach (i.e., the entire r axis). We will derive the amplitude corrections in the next section.

The quantization of the frequency ω_R in terms of the multipolar indices l and m arises from the quantization of the motion in the angular directions. For the azimuthal direction, it is easy to see that for the wave function to be single-valued, we need to impose $L_z = m \in \mathbb{Z}$. For the θ direction, we note that

$$\Theta = V^\theta \sin^2 \theta \,, \tag{9.64}$$

and the θ-quantization condition for the wave, Eq. (9.17), is

$$\int_{\theta_-}^{\theta_+} \sqrt{\Theta} \, d\theta = (L - |m|)\pi \,. \tag{9.65}$$

This corresponds to the Bohr-Sommerfeld condition for a particle moving in a potential given by Θ. Consequently, the condition for a standing wave along the θ direction (at leading order) is equivalent to

$$\begin{aligned} \mathcal{Q} &= A_{lm}(\omega_R a) - m^2 \\ &\approx L^2 - m^2 - \frac{a^2 \omega_R^2}{2} \left[1 - \frac{m^2}{L^2} \right] \,. \end{aligned} \tag{9.66}$$

In summary, we connected the QNM's wave function to the Hamilton-Jacobi principal function of homoclinic null geodesics (at leading order). These geodesics have the same energy, Carter constant, and z-component of its angular momentum as a spherical photon orbit; however only spherical orbits with *quantized* Carter constants and z-angular momenta correspond to quasinormal modes. In Table 9.1, we summarize our geometric-optics correspondence; so far we have identified the first three entries on the table. We can find the next two correspondences by investigating next-to-leading-order geometric optics in the next part.
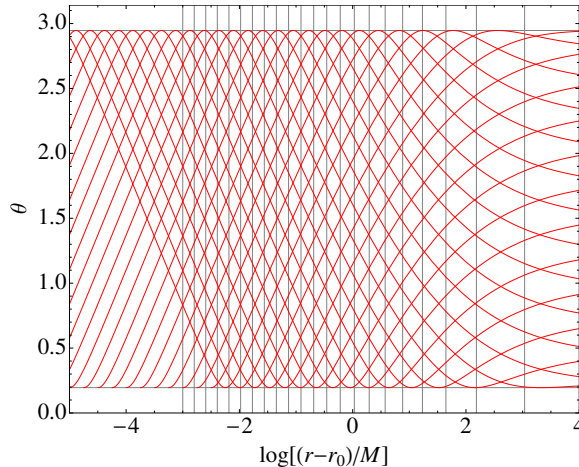
Figure 9.10: Schematic plot of trajectories in the r-θ plane of homoclinic orbits outside of the peak of the potential (specifically for a black hole with spin $a/M = 0.7$ and a photon orbit with radius $r_0/M = 2.584$). The two horizontal grid lines mark the turning points, $\theta = \theta_\pm$; between these turning points, there are two homoclinic orbits passing through every point, while at turning points only one orbit passes through. Vertical grid lines indicate when the value of parameter λ has changed along the orbit by (an arbitrarily chosen value) $\Delta\lambda = 0.046M$. Near the spherical photon orbit, each homoclinic orbit undergoes an infinite number of periodic oscillations in θ while $r - r_0$ is growing exponentially as a function of λ.

9.3.3.2 Next-to-leading order: radial amplitude corrections and the imaginary part of the frequency

We showed in the previous part that the conserved quantities of a spherical photon orbit, $(\mathcal{E}, \mathcal{Q}, L_z)$, correspond simply to the real parts of the quasinormal-mode parameters, (ω_R, A^R_{lm}, m), which are the leading-order quantities of a quasinormal mode. Here, we will show that the behavior of the homoclinic orbits—namely, how the orbits propagate away from the spherical orbit, and how they move between $\theta_\pm$—reveals the spatiotemporal variation of the wave (i.e, the decay rate and the shape of its wave function in space). In Fig. 9.10, we plot the trajectory of a particular series of homoclinic orbits on the r-θ plane, to which we will refer at several points in the discussion below.

With the appropriate values of $(\mathcal{E}, \mathcal{Q}, L_z)$, the function u in Eq. (9.58) solves the wave equation to leading order and satisfies the required boundary conditions. To recover the decaying behavior of quasinormal modes, however, we make corrections to the amplitude of the wave, which appear at next-to-leading order in the geometric-optics approximation. Because of symmetry, there should not be any correction to the amplitude in the ϕ direction, and the correction in the t direction should be a simple decay; therefore, we write

$$u = A\exp(iS) = \underbrace{e^{-\gamma t}A_r(r)A_\theta(\theta)}_{A(t,r,\theta)}\,e^{-i\mathcal{E}t}e^{iL_z\phi}e^{\pm iS_\theta}e^{\pm iS_r}\,. \tag{9.67}$$

This general expression contains four possible directions in which the wave could be propagating:

the $\pm\theta$ direction and the $\pm r$ direction (depending on the signs in front of S_r and S_θ). Because the boundary conditions require that the waves propagate towards $r_* \to +\infty$ for $r > r_0$ and $r_* \to -\infty$ for $r < r_0$, the sign in front of S_r should be positive for $r > r_0$ and negative for $r < r_0$. For θ motion, however, we insist that both directions (signs) be present, because a quasinormal mode is a standing wave in the θ direction. Focusing on $r > r_0$, we write

$$u = e^{-\gamma t} A_r(r) \left[A_\theta^+ e^{iS_\theta} + A_\theta^- e^{-iS_\theta} \right] e^{-i\mathcal{E}t + iL_z\phi + iS_r}$$

$$\equiv u_+ + u_- \,. \tag{9.68}$$

We will next require that both u_+ and u_- satisfy the wave equation to next-to-leading order, separately. By explicitly computing Eq. (9.47) (or $A\sqrt{\mathcal{A}} = \text{const}$) in the Kerr spacetime, we find the amplitude satisfies the relation

$$\Sigma \frac{d\log A}{d\zeta} = -\frac{1}{2} \left[\partial_r(\Delta(r)\partial_r S_r) + \frac{1}{\sin\theta} \partial_\theta(\sin\theta\,\partial_\theta S_\theta) \right] \,. \tag{9.69}$$

Here ζ is an affine parameter along the geodesic specified by $(\mathcal{E}, \mathcal{Q}, \mathcal{L}_z)$. If we use the parameter λ defined by $d/d\lambda = \Sigma d/d\zeta$ then we can separate the left-hand side of the equation as

$$\Sigma \frac{d\log A}{d\zeta} = \frac{d}{d\lambda}\log A_r(r) + \frac{d}{d\lambda}\log A_\theta(\theta) - \gamma\frac{dt}{d\lambda} \,. \tag{9.70}$$

Because the right-hand side of Eq. (9.56a) for $dt/d\lambda$, separates into a piece that depends only upon r and one that depends only upon θ, we will write Eq. (9.56a) schematically as

$$\frac{dt}{d\lambda} = \bar{t} + \tilde{t} \,, \tag{9.71}$$

where $\bar{t}$ is only a function of r and $\tilde{t}$ is only a function of θ. Unlike in Eq. (9.56a), we will require that $\tilde{t}$ average to zero when integrating over λ for half a period of motion in the θ direction (i.e., from θ_- to θ_+). We can ensure this condition is satisfied by subtracting an appropriate constant from $\tilde{t}$ and adding it to $\bar{t}$. Combining Eqs. (9.69)–(9.71) and performing a separation of variables, we obtain

$$\sqrt{\mathcal{R}}\frac{d\log A_r}{dr} - \gamma\bar{t} = -\frac{\mathcal{R}'}{4\sqrt{\mathcal{R}}} \,, \tag{9.72a}$$

$$\sqrt{\Theta}\frac{d\log A_\theta^\pm}{d\theta} \mp \gamma\tilde{t} = -\frac{1}{2\sin\theta}(\sqrt{\Theta}\sin\theta)' \,, \tag{9.72b}$$

where a prime denotes a derivative with respect to r for functions of r only, and a derivative with respect to θ for functions of θ only (whether it is a θ or r derivative should be clear from the context). While it might at first seem possible to add a constant to the definition of $\bar{t}$, and subtract it from $\tilde{t}$

and still have both u_+ and u_- satisfy the next-to-leading order geometric optics, because we have already chosen to have $\tilde{t}$ average to zero,

$$\int_{\theta_-}^{\theta_+} \gamma\tilde{t}\frac{d\theta}{\sqrt{\Theta}} = \int \gamma\tilde{t}d\lambda = 0\,, \tag{9.73}$$

this separation is the only way to guarantee that $|A_\theta^\pm|$ match each other at both ends. We will discuss the angular wave function in greater detail in the next part of this section.

Let us now turn to the radial equation, from which we will be able to compute the decay rate. Close to r_0, we can expand $\mathcal{R}(r)$ to leading order as

$$\mathcal{R}(r) \approx \frac{(r-r_0)^2}{2}\mathcal{R}''(r_0)\,. \tag{9.74}$$

Substituting this result into Eq. (9.72a), we find

$$\frac{d\log A_r}{dr} = \frac{1}{r-r_0}\left[\gamma\bar{t}\sqrt{\frac{2}{\mathcal{R}_0''}} - \frac{1}{2}\right]\,, \tag{9.75}$$

where we used the notation $\mathcal{R}_0'' \equiv \mathcal{R}''(r_0)$. For A_r to be a function that scales as $A_r \sim (r-r_0)^n$ around r_0 for some integer n (namely it scales like a well-behaved function), we need to have

$$\begin{aligned}
\gamma &= \left(n+\frac{1}{2}\right)\frac{\sqrt{\mathcal{R}_0''/2}}{\bar{t}} \\
&= (n+1/2)\lim_{r\to r_0}\frac{1}{r-r_0}\frac{dr/d\lambda}{\langle dt/d\lambda\rangle_\theta}\,. \tag{9.76}
\end{aligned}$$

To arrive at the second line, we used Eq. (9.74), the fact that $dr/d\lambda = \sqrt{\mathcal{R}}$, and that $\bar{t}$ is the part of $dt/d\lambda$ that does not vanish when averaging over one cycle of motion in the θ direction; the limit in the expression comes from the fact that the approximation in Eq. (9.74) becomes more accurate as $r \to r_0$.

The physical interpretation of the rate that multiplies $(n+1/2)$ is somewhat subtle. Because the θ motion is independent from the r motion, a bundle of geodesics at the same r slightly larger than r_0, but at different locations in θ will return to their respective initial values of θ with a slightly increased value of r after one period of motion in the θ direction. The area of this bundle increases in the process, and by Eq. 9.51, the amplitude of the wave must decay; the rate of decay is governed by the quantity that multiplies $(n+1/2)$ in Eq. (9.76).

In addition, as shown in Fig. 9.10, the homoclinic orbits do pass through an infinite number of such oscillations near r_0, because the radial motion is indefinitely slower than the θ motion as r

approaches r_0. It is clear from Fig. 9.10 that

$$\frac{1}{r - r_0}\frac{\Delta r}{\Delta \lambda} = \frac{\Delta \log(r - r_0)}{\Delta \lambda} \tag{9.77}$$

approaches a constant as $r \to r_0$. By multiplying the above equation by the constant value of $(\Delta\lambda)/(\Delta t)$ over one orbit of motion in the θ direction,

$$\frac{1}{r - r_0}\frac{\Delta r}{\Delta t} = \frac{\Delta \log(r - r_0)}{\Delta t} \equiv \gamma_L \tag{9.78}$$

also approaches a constant. This is usually defined as the *Lyapunov exponent* of one-dimensional motion; here, however, we emphasize that it is defined only after averaging over entire cycle of θ motion. By comparing Eq. (9.78) with the second line of Eq. (9.76), and bearing in mind that the Lyapunov exponent is defined after averaging over one period of θ motion, one can write Eq. (9.76) as

$$\gamma = (n + \tfrac{1}{2})\gamma_L \,. \tag{9.79}$$

To put Eq. (9.76) into a form that relates more clearly to Eq. (9.42), we use the conditions on the phase function,

$$\frac{\partial S}{\partial \mathcal{E}} = 0 \,, \quad \frac{\partial S}{\partial \mathcal{Q}} = 0 \,, \tag{9.80}$$

which hold for any point on the trajectory of the particle. We will apply this condition to two points on the particle's trajectory: one at (t, r, θ, ϕ) and the second at $(t + \Delta t, r + \Delta r, \theta, \phi + \Delta\phi)$, where Δt is chosen such that the particle completes a cycle in θ in this time (and it moves to a new location shifted Δr and $\Delta\phi$). Substituting in the explicit expressions for the principal function in Eqs. (9.53) and (9.54a), we find

$$\frac{\partial}{\partial \mathcal{E}}\left[\int_r^{r+\Delta r} \frac{\sqrt{\mathcal{R}(r')}}{\Delta(r')}dr' + \Delta S_\theta\right] = \Delta t \,, \tag{9.81a}$$

$$\frac{\partial}{\partial \mathcal{Q}}\left[\int_r^{r+\Delta r} \frac{\sqrt{\mathcal{R}(r')}}{\Delta(r')}dr' + \Delta S_\theta\right] = 0 \tag{9.81b}$$

where we have defined

$$\Delta S_\theta \equiv 2\int_{\theta_-}^{\theta_+} \sqrt{\Theta(\theta')}d\theta' \equiv \oint \sqrt{\Theta(\theta')}d\theta'. \tag{9.82}$$

Because the change Δr is infinitesimal for r near r_0, the integrand is roughly constant, and the r-dependent part of the integral becomes the product of the integrand with Δr. Then, one can use Eq. (9.74) to write Eqs. (9.81a) and (9.81b) as

$$\frac{1}{\sqrt{2\mathcal{R}_0''\Delta_0}}\frac{\partial \mathcal{R}}{\partial \mathcal{E}}\frac{\Delta r}{r - r_0} + \frac{\partial \Delta S_\theta}{\partial \mathcal{E}} = \Delta t \,, \tag{9.83a}$$

$$\frac{1}{\sqrt{2\mathcal{R}_0''\Delta_0}}\frac{\partial\mathcal{R}}{\partial\mathcal{Q}}\frac{\Delta r}{r-r_0}+\frac{\partial\Delta S_\theta}{\partial\mathcal{Q}}=0\,. \tag{9.83b}$$

Now, we also note that for a given fixed $L_z = m$, the angular Bohr-Sommerfeld condition in Eq. (9.65) makes $\mathcal{Q}$ a function of $\mathcal{E}$ through the condition that $\Delta S_\theta = (L - |m|)\pi$. Because ΔS_θ is a function of $\mathcal{E}$, its total derivative with respect to $\mathcal{E}$ must vanish,

$$\frac{\partial\Delta S_\theta}{\partial\mathcal{E}}+\frac{\partial\Delta S_\theta}{\partial\mathcal{Q}}\left(\frac{d\mathcal{Q}}{d\mathcal{E}}\right)_{\mathrm{BS}}=0\,. \tag{9.84}$$

Therefore, when we multiply Eq. (9.83b) by $(d\mathcal{Q}/d\mathcal{E})_{\mathrm{BS}}$ and add it to Eq. (9.83a), we obtain the condition that

$$\frac{1}{\sqrt{2\mathcal{R}_0''\Delta_0}}\left[\frac{\partial\mathcal{R}}{\partial\mathcal{E}}+\frac{\partial\mathcal{R}}{\partial\mathcal{Q}}\left(\frac{d\mathcal{Q}}{d\mathcal{E}}\right)_{\mathrm{BS}}\right]\frac{\Delta r}{r-r_0}=\Delta t\,. \tag{9.85}$$

Combining this fact with the definition of the Lyapunov exponent in Eq. (9.78) and Eq. (9.79), we find that

$$\gamma=\left(n+\frac{1}{2}\right)\frac{\sqrt{2\mathcal{R}_0''\Delta_0}}{\left[\dfrac{\partial\mathcal{R}}{\partial\mathcal{E}}+\dfrac{\partial\mathcal{R}}{\partial\mathcal{Q}}\left(\dfrac{d\mathcal{Q}}{d\mathcal{E}}\right)_{\mathrm{BS}}\right]_{r_0}}\,, \tag{9.86}$$

where we recall that the quantities should be evaluated at r_0. Equation (9.86) is equivalent to Eq. (9.42). Note, however, that in Eq. (9.86) we explicitly highlight the dependence of $\mathcal{Q}$ on $\mathcal{E}$ through the term $(d\mathcal{Q}/d\mathcal{E})_{\mathrm{BS}}$. There is an analogous term in Eq. (9.42) from the dependence of A_{lm} on ω in the expression for the potential V^r, which we must take into account when computing $\partial V^r/\partial\omega$; however, we did not write it out explicitly in Eq. (9.42).

Summarizing the physical interpretation of the results in this subsection, we note that the Lyapunov exponent γ_L is the rate at which the cross-sectional area of a bundle of homoclinic rays expand, when averaged over one period of motion in the θ direction in the vicinity of r_0. The spatial Killing symmetry along ϕ means the extension of the ray bundle remains the same along that direction. This, therefore, allows us to write

$$\mathcal{A}\sim e^{\gamma_L t}\,. \tag{9.87}$$

Correspondingly, the $A\sqrt{\mathcal{A}}=$ const law requires that

$$A\sim e^{-\gamma_L t/2}\,, \tag{9.88}$$

which agrees with the decay rate of the least-damped QNM. The higher decay rates given by Eq. (9.76) come from an effect related to the intrinsic expansion of the area of a phase front. More specifically, if the amplitude is already nonuniform at points with different $r-r_0$ (but same θ), then shifting the spatial locations of the nonuniform distribution gives the appearance of additional

decay.

9.3.3.3 Next-to-leading order: angular amplitude corrections and the imaginary part of Carter's constant

Having found a relation in Eq. (9.72a) between the imaginary part of the energy, ω_I, and the rate of divergence of rays, we now turn to Eq. (9.72b) to understand the geometric meaning of the complex part of A_{lm}. We recall from Sec. 9.3.3.1 that $\mathcal{Q} = A_{lm}^R - m^2$, at leading order, for a real Carter constant $\mathcal{Q}$. Because A_{lm} becomes complex at next to leading order (and because m remains unchanged), if the correspondence $\mathcal{Q} = A_{lm} - m^2$ holds for a complex A_{lm}, then the Carter constant should also be complex, and its imaginary part should be equivalent to A_{lm}^I. In this part, we argue that this relationship holds.

By integrating Eq. (9.72b), we find that

$$A_\theta^\pm = \sqrt{\frac{1}{\sin\theta\sqrt{\Theta}}}\exp\left[\pm\int_{\theta_-}^\theta \frac{\gamma\tilde{t}}{\sqrt{\Theta}}d\theta'\right]. \tag{9.89}$$

To interpret this equation, we will assume that the orbit is sufficiently close to r_0 that the change in r over the course of a period of motion in θ is negligible. Under this assumption (and with the fact that $d\lambda = d\theta/\sqrt{\Theta}$) we can write the integral in the exponent in Eq. (9.89) as

$$\int_{\theta_-}^\theta \frac{\gamma\tilde{t}}{\sqrt{\Theta}}d\theta'$$
$$=\gamma\left[[t(\theta)-t(\theta_-)]-\left(\frac{\Delta t}{\Delta\lambda}\right)[\lambda(\theta)-\lambda(\theta_-)]\right], \tag{9.90}$$

where $\Delta t/\Delta\lambda$ is the average of $dt/d\lambda$ over a cycle of θ motion. We obtain this expression by using the fact that $dt/d\lambda$ is equivalent to $\tilde{t}$ plus a constant when r (and hence $\bar{t}$) does not change. Because $\tilde{t}$ has zero average (by definition) over a period of θ motion, then when written in the form above, the constant must be $(\Delta t)/(\Delta\lambda)$. We can write this average rate of change in a useful form by noting that, from Eq. (9.56a) and Eqs. (9.54b),

$$\frac{dt}{d\lambda} = \frac{1}{2\Delta}\frac{\partial\mathcal{R}}{\partial\mathcal{E}} + a^2\mathcal{E}\cos^2\theta. \tag{9.91}$$

Averaging this expression over a cycle of θ motion, noting that the first term on the right-hand side is independent of θ, and using Eq. (9.54b) gives

$$\frac{\Delta t}{\Delta\lambda} = \frac{1}{2\Delta}\frac{\partial\mathcal{R}}{\partial\mathcal{E}} + a^2\mathcal{E}\left(\int_{\theta_-}^{\theta^+}\frac{\cos^2\theta}{\sqrt{\Theta}}d\theta\right)\left(\int_{\theta_-}^{\theta^+}\frac{d\theta}{\sqrt{\Theta}}\right)^{-1}$$
$$=\frac{1}{2\Delta}\frac{\partial\mathcal{R}}{\partial\mathcal{E}} + \frac{\partial\Delta S_\theta/\partial\mathcal{E}}{2\partial\Delta S_\theta/\partial\mathcal{Q}}$$

$$= \frac{1}{2\Delta} \frac{\partial \mathcal{R}}{\partial \mathcal{E}} - \frac{1}{2} \left(\frac{d\mathcal{Q}}{d\mathcal{E}} \right)_{\text{BS}} . \tag{9.92}$$

In the last step we have used the Bohr-Sommerfeld condition (9.84). Also according to Eq. (9.56a) and Eq. (9.56c), we can find

$$t(\theta) - t(\theta_-) = \frac{\partial}{\partial \mathcal{E}} \int_{\theta_-}^{\theta} \sqrt{\Theta(\theta')} d\theta'$$
$$+ \frac{1}{2\Delta} \frac{\partial \mathcal{R}}{\partial \mathcal{E}} (\lambda(\theta) - \lambda(\theta_-)) , \tag{9.93a}$$

$$\lambda(\theta) - \lambda(\theta_-) = 2 \frac{\partial}{\partial \mathcal{Q}} \int_{\theta_-}^{\theta} \sqrt{\Theta(\theta')} d\theta' , \tag{9.93b}$$

where to derive these two equations, we can again use the fact that $d\lambda = d\theta/\sqrt{\Theta}$ and also use the definition of Θ; for the first we also make use of Eq. (9.91).

Finally, we insert Eqs. (9.93a), (9.93b), and (9.92) into Eq. (9.90) to find

$$\int_{\theta_-}^{\theta} \frac{\gamma \tilde{t}}{\sqrt{\Theta}} d\theta' = (-i\gamma) \left[\frac{\partial}{\partial \mathcal{E}} + \left(\frac{d\mathcal{Q}}{d\mathcal{E}} \right)_{\text{BS}} \frac{\partial}{\partial \mathcal{Q}} \right] [iS_\theta(\theta)] . \tag{9.94}$$

Substituting Eq. (9.94) into the solution for $A_\theta^\pm$ in Eq. (9.89) gives that

$$A_\theta^\pm = \frac{\exp \left\{ (\pm i\gamma) \left[\frac{\partial}{\partial \mathcal{E}} + \left(\frac{d\mathcal{Q}}{d\mathcal{E}} \right)_{\text{BS}} \frac{\partial}{\partial \mathcal{Q}} \right] [iS_\theta(\theta)] \right\}}{\sqrt{\sin \theta \sqrt{\Theta}}} . \tag{9.95}$$

The phase in this equation, however, is precisely the correction to the leading-order expression for the phase $e^{iS_\theta(\theta)}$ if we allow $\mathcal{E}$ and $\mathcal{Q}$ to be complex, where their imaginary parts are given by

$$\text{Im}\mathcal{E} = -\gamma = -\omega_I , \quad \text{Im}\mathcal{Q} = \left(\frac{d\mathcal{Q}}{d\mathcal{E}} \right)_{\text{BS}} (-\gamma) . \tag{9.96}$$

Through next-to-leading order, therefore, the θ portion of the wave is given by

$$A_\theta^+ e^{iS_\theta(\theta)} + A_\theta^- e^{-iS_\theta(\theta)} = \frac{e^{iS_\theta(\theta)} + e^{-iS_\theta(\theta)}}{\sqrt{\sin \theta \sqrt{\Theta}}} , \tag{9.97}$$

where $\mathcal{E}$ and $\mathcal{Q}$ used in S_θ are complex.

In the geometric-optics approximation, therefore, we have shown that we can account for the amplitude corrections to the wave by allowing the conserved quantities, $\mathcal{E}$ and $\mathcal{Q}$, to be complex [with their imaginary parts given in Eq. (9.96)]. Furthermore, through the geometric-optics correspondence, and the definition of A_{lm}^I in Eq. (9.30) we can confirm that $A_{lm}^I = \mathcal{Q}_I$; therefore, the relationship

$$\mathcal{Q} = A_{lm} - m^2 , \tag{9.98}$$

is true for a complex $\mathcal{Q}$ and A_{lm}.

In closing, we note that at the same θ, the magnitude of the two components of the wave in Eq. (9.95) are not equal. More specifically, the integral involving $\tilde{t}$ makes A^+ have a larger amplitude at $\theta < \pi/2$ and a smaller amplitude at $\theta > \pi/2$; A^- has the opposite profile. Therefore, the net wave function remains symmetric about $\theta = \pi/2$.

9.4 Features of the spectra of Kerr black holes

In this section, we will use the WKB formula and the geometric-optics correspondence in the first two sections of this paper to explain several aspects of the quasinormal-mode spectrum of Kerr black holes. Specifically, we will explain the absence of damping for a significant fraction of modes of extremal Kerr holes. We will also decompose the frequency into orbital and precessional parts and explain a degeneracy in the spectra of Kerr holes in terms of a rational relation of these frequencies when the corresponding photon orbits close.

9.4.1 Spherical photon orbits and extremal Kerr black holes

We will first review the properties of spherical photon orbits. These orbits can be found by setting $\mathcal{R}(r) = \mathcal{R}'(r) = 0$ (see, e.g., [53]), and their conserved quantities are fixed by the radius of the orbit r and the spin of the black hole a to be

$$\mathcal{Q}/\mathcal{E}^2 = -\frac{r^3(r^3 - 6Mr^2 + 9M^2r - 4a^2M)}{a^2(r-M)^2} \quad , \tag{9.99a}$$

$$L_z/\mathcal{E} = -\frac{r^3 - 3Mr^2 + a^2r + a^2M}{a(r-M)} \quad . \tag{9.99b}$$

We will next discuss additional features of these orbits.

For a given spin parameter a, there is a unique spherical photon orbit with parameters $(\mathcal{E}, L_z, \mathcal{Q})$ for any radius between the outermost and innermost photon orbits (the retrograde and prograde equatorial photon orbits). Their radii (which we denote r_1 for prograde and r_2 for retrograde orbits) are given by

$$r_1 = 2M\left[1 + \cos\left(\frac{2}{3}\arccos\left(-\frac{|a|}{M}\right)\right)\right] \quad , \tag{9.100a}$$

$$r_2 = 2M\left[1 + \cos\left(\frac{2}{3}\arccos\left(\frac{|a|}{M}\right)\right)\right] \quad . \tag{9.100b}$$

At each $r_1 \leq r \leq r_2$, the spherical orbit's inclination angle reaches a maximum and minimum of $\theta_\pm$
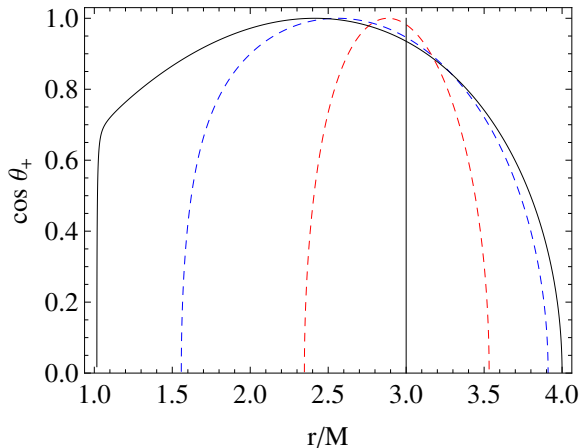
Figure 9.11: The values of r and $\cos\theta_+$ of spherical orbits, for $a/M = 0$ (black, solid vertical line), 0.5 [red (light gray) dashed curve], 0.9 [blue (dark gray) dashed curve] and 0.99999 (black, solid curve). Note that for $a = 0$, all such orbits have $r = 3M$, while for $a = M$, a significant fraction reside at $r = M$.

(at which $\Theta = 0$). These angles are given by

$$
\cos^2\theta_\pm =
$$
$$
\frac{\left[2\sqrt{M\Delta(2r^3 - 3Mr^2 + Ma^2)} - (r^3 - 3M^2r + 2Ma^2)\right]r}{a^2(r-M)^2} , \tag{9.101}
$$

which are equivalent to the turning points of the integral (9.17) (and, therefore, we use the same symbols for these angles).

Using the geometric-optics correspondence between $(\mathcal{E}, L_z, \mathcal{Q})$ and $(\Omega_R, \mu, \alpha_{lm}^R)$, we see that equatorial orbits at r_1 and r_2 correspond to modes with $\mu = -1$ and $+1$, respectively, or modes with $m = \pm l$ and $l \gg 1$ (strictly speaking, though, $\mu = m/(l+1/2)$ never precisely reaches ± 1). We can also relate r_p, the real root of Eq. (9.40), to the polar orbit and modes with $m = 0$. For orbits between the equatorial and polar ones, we can use Eqs. (9.36a) and (9.36b) to obtain a μ between -1 and $+1$. Then, only those modes that can be written as $m/(l+1/2)$ with the allowed integer values of l and m correspond to a QNM (though the photon orbits that correspond to QNMs are a dense subset of all photon orbits).

Note in Fig. 9.11 that for $a \sim M$, a significant fraction of spherical photon orbits of different inclination angles all have nearly the same radius, $r \approx M$. Through the geometric-optics correspondence, a large fraction of modes (a finite range of values of μ) relate to this set of modes with $r \approx M$. In Fig. 9.12, we explicitly show the relation between modes characterized by μ and their corresponding spherical-photon-orbit radii (normalized by the horizon radius) for several values of a/M of slightly less than unity. The radius exhibits an interesting transition between two kinds of behaviors: for $\mu > \mu_* \approx 0.744$, the value of r is very close to M (the horizon radius for an extremal
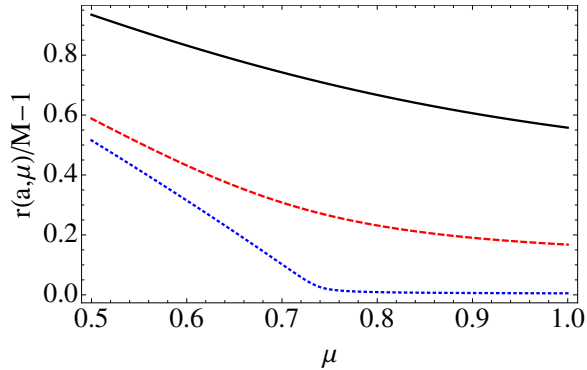
Figure 9.12: Radii of corotating spherical photon orbits as a function of μ, for $a/M = 0.9$ (black solid line), 0.99 (red dashed curve), 0.9999 (blue dotted line). For extremal Kerr black holes, a nonzero fraction of all spherical photon orbits are on the horizon.

Kerr black hole), and for $\mu < \mu_*$ the radii increase linearly. The orbits with $\mu > \mu_*$ have a range of inclination angles. Their $\sin\theta_\pm$ span from 0.731 (at μ_*, the most inclined orbit) to 1 (at $\mu = 1$, the prograde equatorial orbit).

For the extremal black holes, therefore, a nonzero fraction of corotating spherical photon orbits appear to coincide with the horizon in the Boyer-Lindquist coordinate system. Although the proper distance between these orbits will not vanish (see [54]), this does not seem to be a coordinate effect, because there is a definite physical change of the modes for these values of $\mu > \mu_*$. By comparing with Fig. 9.12 with Fig. 9.5, we see that these orbits also have $\Omega_I \approx 0$. A vanishing imaginary part of the frequency corresponds to a vanishing of the radial Lyapunov exponent for this entire nonzero region of spherical photon orbits. This, therefore, would lead to a curious effect for a highly spinning black hole: for perturbations with $\mu \geq \mu_*$, modes do not move away from or into the horizon very quickly. If we were to solve an initial-data problem containing these modes, we would find that they live for a long time. One subtlety here is that QNMs with low damping rates are generally difficult to excite: the black hole excitation factor for a generic Kerr black hole can be proved to be proportional to ω_I (See [30] for Schwarzschild case and [55] for Kerr; see also [56] for Kerr). In the long run the exponential factor $e^{-i\omega_I t}$ over the linear factor ω_I dominates and we would eventually see these long-lived perturbations. Moreover, as these modes are centered around the equatorial plane, we would see these perturbations escaping roughly near the equatorial direction. In fact [56] showed that a long-lived emission in the form of superposed QNMs with zero decay results from the perturbations of an extremal Kerr black hole; their work was for $l = m$ modes only, and together with our eikonal results for generic m can provide a basis for future studies of zero-decay modes.

9.4.2 A mode's orbital and precessional frequencies

In this part, we will define two frequencies associated with individual spherical photon orbits (the orbital and precessional frequencies) and understand their connection to the real part of the QNM frequency. We begin by noting that because spherical photon orbits have only two independent degrees of freedom describing their motion [see, e.g., Eq. (9.99)], the orbit can be characterized by two frequencies. The first is the θ-frequency, Ω_θ, the frequency at which the particle oscillates below and above the equatorial plane. During each θ-cycle, which takes an amount of time given by $T_\theta = 2\pi/\Omega_\theta$, the particle also moves in the azimuthal (or ϕ) direction. If this angle is 2π for a corotating orbit ($m > 0$) or -2π for a counterrotating orbit ($m < 0$), then there is no precession (and these simple, closed orbits have effectively one frequency describing their motion, as the spherical photon orbits of a Schwarzschild black hole do). The difference between the $\Delta\phi$ and $\pm 2\pi$ (its precession-free value) we will denote as the *precession angle*,

$$\Delta\phi_{\mathrm{prec}} \equiv \Delta\phi - 2\pi\,\mathrm{sgn}\,m\,, \tag{9.102}$$

where $\mathrm{sgn}\,m$ is the sign of m. We can also associate the rate of change of ϕ_{prec} with a frequency,

$$\Omega_{\mathrm{prec}} \equiv \Delta\phi_{\mathrm{prec}}/T_\theta = \Delta\phi_{\mathrm{prec}}\Omega_\theta/(2\pi)\,. \tag{9.103}$$

Both T_θ and $\Delta\phi_{\mathrm{prec}}$ can be computed from geodesic motion [see the formulas for Ω_θ and $\Delta\phi_{\mathrm{prec}}$ in Eq. (9.106)].

It is possible to perform a split of the real part of the QNM into two analogous frequencies. To derive this split, start from a single ray, along which the phase of the wave must be constant. Also suppose that the ray originates from θ_- and ends at θ_+ after traveling only one-half of a cycle of motion in the θ direction. During this time, the statement that the phase is unchanged is that

$$0 = -\omega_R T_\theta/2 + (L - |m|)\pi + m\Delta\phi/2\,. \tag{9.104}$$

Using (half of) Eq. (9.102), the real part of the frequency is

$$\omega_R = L\Omega_\theta(m/L) + m\Omega_{\mathrm{prec}}(m/L)\,. \tag{9.105}$$

Note that Ω_θ and Ω_{prec} both depend on m/L.

More explicitly, given the orbital parameters $(\mathcal{E}, \mathcal{Q}, L_z)$, the quantities T_θ and $\Delta\phi$ can be obtained by computing

$$T_\theta = \frac{\partial}{\partial\mathcal{E}}\oint\sqrt{\Theta}d\theta + \frac{1}{2\Delta}\frac{\partial\mathcal{R}}{\partial\mathcal{E}}\oint\frac{d\theta}{\sqrt{\Theta}}\,, \tag{9.106a}$$
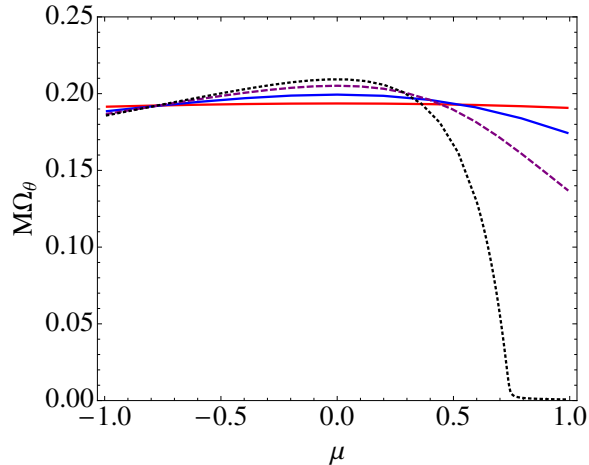
Figure 9.13: Orbital frequency, Ω_θ, plotted against μ, for $a/M = 0.3$ [red (light gray) solid curve], 0.7 [blue (dark gray) solid curve], 0.9 (purple dashed line), and 1 (black dotted line). The orbital frequency vanishes for a significant range of μ for extremal black holes.

$$\Delta\phi = -\frac{1}{L_z}\left[1 - \frac{\partial}{\partial\log\mathcal{E}}\right]\oint\sqrt{\Theta}d\theta + \frac{1}{2\Delta}\frac{\partial\mathcal{R}}{\partial L_z}\oint\frac{d\theta}{\sqrt{\Theta}}, \tag{9.106b}$$

(expressions that hold for any spherical photon orbit—not simply orbits that satisfy the Bohr-Sommerfeld condition) and the two frequencies are given by

$$\Omega_\theta = 2\pi\left(\frac{\partial}{\partial\mathcal{E}}\oint\sqrt{\Theta}d\theta + \frac{1}{2\Delta}\frac{\partial\mathcal{R}}{\partial\mathcal{E}}\oint\frac{d\theta}{\sqrt{\Theta}}\right)^{-1} \tag{9.107a}$$

$$\Omega_{\mathrm{prec}} = \Omega_\theta\frac{\Delta\phi}{2\pi} - (\mathrm{sgn}L_z)\Omega_\theta. \tag{9.107b}$$

These can be expressed in terms of $(\mathcal{E}, \mathcal{Q}, L_z)$ using elliptic integrals (as was done in [47]), but we will not carry this out explicitly.

For very slowly spinning black holes, a short calculation shows that

$$\Omega_\theta \approx \frac{1}{\sqrt{27}M} = \sqrt{\frac{M}{r_0^3}}, \tag{9.108a}$$

$$\Omega_{\mathrm{prec}} \approx \frac{2a}{27M^2} = \frac{2S}{r_0^3}, \tag{9.108b}$$

where r_0 is the circular-photon-orbit radius for a Schwarzschild black hole, $r_0 = 3M$, and $S = aM$. The expression for Ω_θ is the Keplerian frequency of the spherical photon orbit, and $\Omega_{\mathrm{prec}} = 2S/r_0^3$ is the Lense-Thirring precessional frequency. In the slow-rotation limit, therefore, our formula recovers Ferrari and Mashhoon's result Eq. (9.2).

For any value of a, we can normalize Eq. (9.105) by L, and write

$$\Omega_R(a, \mu) = \Omega_\theta(a, \mu) + \mu\Omega_{\mathrm{prec}}(a, \mu). \tag{9.109}$$
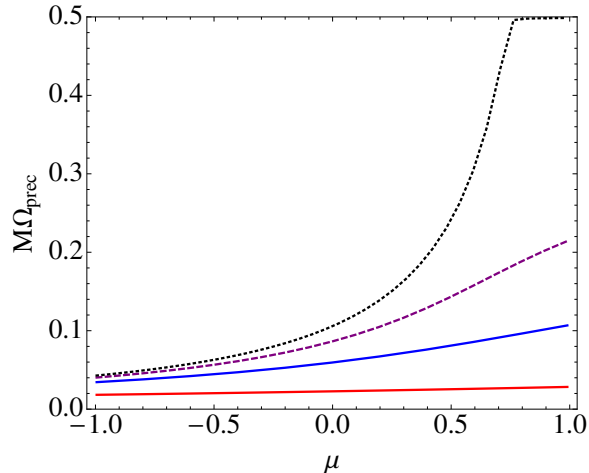
Figure 9.14: Precessional frequency, Ω_ϕ, versus μ plotted identically to those curves in Fig. 9.13 representing the same black-hole spins. The precessional frequency approaches the horizon frequency, Ω_H, for a range of values of μ for extremal black holes.

In Figs. 9.13 and 9.14, we explore the two frequencies in the decomposition of Ω_R by separately plotting Ω_θ and $\Omega_{\rm prec}$, for different values of a.

For small values of a/M, Ω_θ and $\Omega_{\rm prec}$ are consistent with the constant values predicted by Eqs. (9.108a) and (9.108b). For larger values of a/M, Ω_θ does not vary much as a function of μ until $a \sim 0.7M$; for spins greater than this value, it is only for larger values of μ that Ω_θ changes significantly by decreasing from the equivalent values for $a = 0$. Finally, as $a \to M$, Ω_θ vanishes for $\mu \geq \mu_* \approx 0.744$. The precessional frequency, $\Omega_{\rm prec}$, on the other hand, monotonically increases as a function of μ even for small values of a/M; as $a \to M$, $\Omega_{\rm prec}$ grows to Ω_H at $\mu \sim \mu_*$, and stays there for all values of $\mu > \mu_*$. For $a \sim M$ and $\mu > \mu_*$, there is one additional feature worth noting: because $\Omega_\theta \sim 0$ and $\Omega_\phi \sim \Omega_H$, this gives rise to the interpretation of the mode as a ray that sticks on the horizon and corotates with the horizon at its angular frequency of Ω_H; moreover, there seems to be no restoring force along the θ direction.

9.4.3 Degenerate quasinormal modes and closed spherical photon orbits

Finally, in this section, we interpret the degeneracy of QNM frequencies (of which Fig. 9.1 was an example). Recall that in that figure, for $a/M \approx 0.7$, we found pairs of modes such as $(2, 2)$ and $(3, -2)$, $(3, 2)$ and $(4, -2)$, $(4, 2)$ and $(5, -2)$, and so on, all have approximately the same frequency. For another, lower spin $a/M \approx 0.4$, pairs like $(3, 3)$ and $(4, -3)$, $(4, 3)$ and $(5, -3)$, et cetera, have approximately the same frequency.

The approximate degeneracy exists because the ratio between Ω_θ and $\Omega_{\rm prec}$ can be rational, and the photon orbits close. If for a certain mode of a black hole with spin a, with m and L, and for
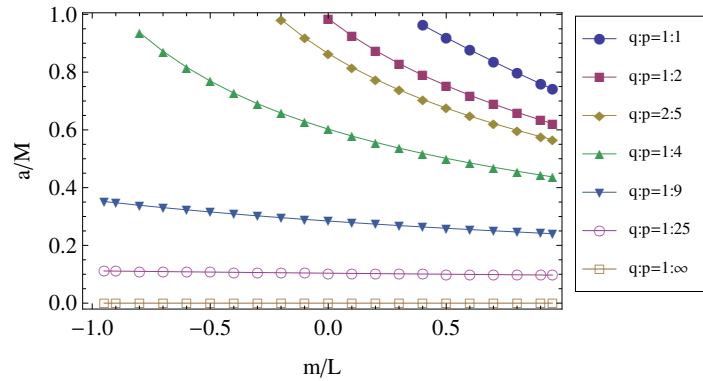
Figure 9.15: A diagram showing the spin parameters, a, and the ratios of the multipolar indexes m/L, at which the orbital and precessional frequencies have a ratio of p/q. Although we only perform our numerical calculations at a discrete set of m/L values (shown by the dots), in the eikonal limit, each set of points for a given ratio of p/q approaches a continuous curve.
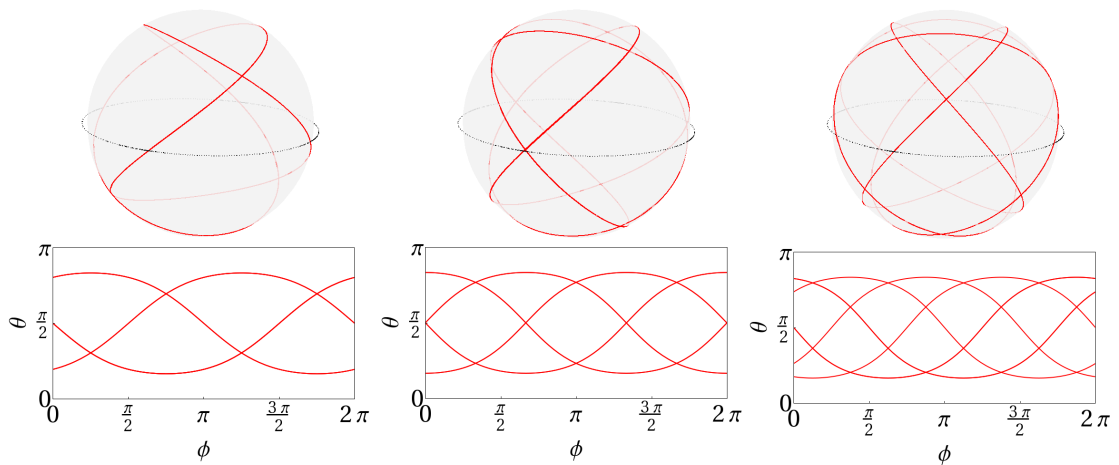

Figure 9.16: For black holes with spins $a/M = 0.768$, 0.612, and 0.502, the spherical photon orbits with $\omega_{\mathrm{orb}} = 2\omega_{\mathrm{prec}}$, on the left, $\omega_{\mathrm{orb}} = 3\omega_{\mathrm{prec}}$ in the center, and $\omega_{\mathrm{orb}} = 4\omega_{\mathrm{prec}}$ on the right, respectively. These orbits correspond to quasinormal modes in the eikonal limit with $m/L = 0.5$. The top figures show the photon orbit, the red, solid curve, on its photon sphere (represented by a transparent sphere). The dashed black line is the equatorial ($\theta = \pi/2$) plane, which was inserted for reference. The bottom figures are the same photon orbits, but plotted in the ϕ-θ plane, instead.

integers p and q,

$$q\Omega_\theta \left(a, \frac{m}{L}\right) = p\Omega_{\text{prec}} \left(a, \frac{m}{L}\right) , \tag{9.110}$$

this means that there exists a closed spherical photon orbit that satisfies the conditions necessary to correspond to a QNM. Equation (9.110) implies that

$$L\Omega_\theta \left(a, \frac{m}{L}\right) + m\Omega_{\text{prec}} \left(a, \frac{m}{L}\right)$$
$$= (L + kq)\Omega_\theta \left(a, \frac{m}{L}\right) + (m - kp)\Omega_{\text{prec}} \left(a, \frac{m}{L}\right) . \tag{9.111}$$

If Ω_θ and Ω_{prec} do not change much from $\mu = m/L$ to $\mu' = (m - kp)/(L + kq)$ (either because spin is small—and therefore Ω_θ and Ω_{prec} depend weakly on μ—or because $L \gg kq$ and $m \gg kp$), then

$$\omega_R^{l,m} \approx \omega_R^{l+kq,m-kp} . \tag{9.112}$$

Because Ω_I depends similarly on μ, under the same conditions,

$$\omega_I^{l,m} \approx \omega_I^{l+kq,m-kp} ; \tag{9.113}$$

therefore, the modes are degenerate. It is also clear from Eq. (9.110) that the degeneracy happens at the same time that the corresponding orbit is closed. The three series mentioned at the beginning of the paper correspond to $p/q = 4$, 6, and 8, respectively (for $k = 1$).

9.4.3.1 Slowly spinning black holes

For $a/M \ll 1$, when Eqs. (9.108a) and (9.108b) apply, the condition for degenerate modes becomes

$$\frac{q\sqrt{27}}{2p} = \frac{a}{M} \ll 1 \tag{9.114}$$

(a statement that holds independent of μ). This implies that orbits of all inclinations close for these spins.

For these specific spins, the QNM spectrum is completely degenerate, by which we mean that all modes have the same decay rate, and all real parts of the frequencies are integer multiples of only one frequency (similar to those of a Schwarzschild black hole). Using this approximate formula to find a for the three instances of degeneracy in Fig. 9.1, we find

$$a_{4/1} \approx 0.65M, \quad a_{6/1} \approx 0.43M, \quad a_{8/1} \approx 0.32M. \tag{9.115}$$

These are not very far away from spins we found empirically.

9.4.3.2 Generic black holes

For a generic spin parameter a, we will explain degeneracies that exist around a mode with $L \gg 1$ and $|m| \gg 1$. If the condition in Eq. (9.110) holds for $p, q \ll \min(L, |m|)$, then there is a range of $|k| \ll \min(L, |m|)/\max(p, q)$ in which there is a degeneracy between all $(L + kq, m - kp)$ and (L, m). These modes must be those close to the mode of indices (L, m), because, strictly speaking, it is only the orbit corresponding to m/L which is precisely closed.

To find this degeneracy, we will search for spin parameters a for which Eq. (9.110) holds for any set of indexes (L, m) and integers (p, q) that satisfy $L, |m| \gg p, q$ (we generally either find one or zero solutions). To visualize this degeneracy, for each pair (p, q), we will mark all possible pairs of $(m/L, a)$ in a 2D plot; the values of the spins are sufficiently dense for each value of m/L that they form a smooth curve when plotted against m/L. Some of these curves are shown in Fig. 9.15. Because for a fixed p/q the degenerate spins for $a/M \lesssim 0.3$ are nearly independent of m/L, Eq. (9.114) should be an accurate prediction for spins less that value. As a concrete illustration of the orbits corresponding to these degenerate modes, we plot closed orbits for $m/L = 0.5$ and for $a/M \approx 0.5$, 0.61, and 0.77 in Fig. 9.16. The values of the spins agree quite well with those predicted in Fig. 9.15.

9.5 Conclusions and discussion

In this paper, we extended the results of several earlier works [9, 29, 40, 41] to compute the quasinormal-mode frequencies and wave functions of a Kerr black hole of arbitrary astrophysical spins, in the eikonal limit ($l \gg 1$). We focused on developing a greater intuitive understanding of their behavior, but, in the process, we calculated expressions for large-l quasinormal-mode frequencies that are reasonably accurate even at low l. Specifically, we applied a WKB analysis to the system of equations defined by the angular and radial Teukolsky equations. Using a Bohr-Sommerfeld condition for the angular equation, we related the angular separation constant to the frequency; when we expanded the constraint to leading order in $a\omega/l$, we found an equally accurate and algebraically simpler relation between the frequency and angular eigenvalue. We then used a well-known WKB analysis on the radial Teukolsky equation to obtain expressions for the QNM frequencies and the angular separation constants. The accuracy of the approximate expressions for the QNM frequency are observed to be of order $O(L^{-2})$ even though we had only expected a $O(L^{-1})$ convergence for the imaginary part.

Next, we reviewed that a massless scalar wave in the leading-order, geometric-optics approximation obeys the Hamilton-Jacobi equations, which are very similar to the Teukolsky equations when $l \gg 1$. By identifying terms in the Hamilton-Jacobi equations and Teukolsky equations, we related the conserved quantities of the Hamilton-Jacobi equations to the eigenvalues of the sepa-

rated Teukolsky equations. Specifically, we confirmed that the energy, angular momentum in the z direction, and Carter constant in the Hamilton-Jacobi equations correspond to the real frequency, the index m, and the angular eigenvalue minus m^2 in the Teukolsky equations, respectively. Furthermore, we found that the conditions that define a quasinormal mode in the WKB approximation are equivalent to the conditions in the geometric-optics approximation that determine a spherical photon orbit that satisfies an identical Bohr-Sommerfeld quantization condition.

By analyzing the next-to-leading-order, geometric-optics approximation, we showed that the corrections to the amplitude of the scalar wave correspond to the imaginary parts of the WKB quantities. Specifically, we saw that the imaginary part of the frequency is equal to a positive half-integer multiplied by the Lyapunov exponent averaged over a period of motion in the θ direction. The imaginary part of the angular eigenvalue is equal to the imaginary part of the Carter constant, which is, in turn, related to an amplitude correction to geometric-optics approximation to the angular function for θ.

We then applied these results to study properties of the QNM spectra of Kerr black holes. We observed that for extremal Kerr black holes a significant fraction of the QNMs have nearly zero imaginary part (vanishing damping) and their corresponding spherical photon orbits are stuck on the horizon (in Boyer-Lindquist coordinates). We plan to study this unusual feature of extremal Kerr black holes in future work. In addition, we showed that for Kerr black holes of any spin, the modes' frequencies (in the eikonal limit) are a linear combination of the orbital and precession frequencies of the corresponding spherical photon orbits. This allows us to study an intriguing feature of the QNM spectrum: namely, when the orbital and precession frequencies are rationally related—i.e, when the spherical photon orbits are closed—then the corresponding quasinormal-mode frequencies are also degenerate.

We hope that the approximate expressions for the quasinormal-mode frequencies in this paper will prove helpful for understanding wave propagation in the Kerr spacetime. This not unreasonable to suppose, because Dolan and Ottewill have shown in [28, 30] that to calculate the Green's function analytically in the Schwarzschild spacetime, one needs to know analytical expressions for the frequency of the quasinormal modes (specifically, this comes from the fact that the frequencies of the quasinormal mode are the poles of the Green's function in the frequency domain). We, therefore, think that our approximate formulas could assist with the calculation of the Green's function in the Kerr spacetime, in future work.

Acknowledgments

spacetime. We would also like to thank the anonymous referee for carefully reviewing our manuscript and offering many helpful suggestions. We base our numerical calculation of the QNM frequencies on the Mathematica notebook provided by Emanuele Berti and Vitor Cardoso [57]. This research is funded by NSF Grants PHY-1068881, PHY-1005655, CAREER Grant PHY-0956189; NASA Grant No.NNX09AF97G; the Sherman Fairchild Foundation, the Brinson Foundation, and the David and Barabara Groce Startup Fund at Caltech.

9.A   The Taylor expanded Bohr-Sommerfeld condition

The Bohr-Sommerfeld constraint (9.17) gives us a way to evaluate A_{lm} in terms of l, m, and ω; the error in this approximation scales as $1/l$. Because it is an integral equation, it is not particularly convenient to solve, and it is beneficial to have an approximate, but algebraic expression for the frequency of a QNM. With the benefit of hindsight, one can confirm through numerical calculations of exact QNM frequencies performed using Leaver's method that the parameter $a\omega/l$ is numerically a small number for all black hole spins. We can then expand the angular separation constant, A_{lm}, in a series in $a\omega/l$ as $A_{lm} = A_{lm}^0 + \delta A_{lm}$, where A_{lm}^0 satisfies the equation

$$\int_{\theta_-^0}^{\theta_+^0} \sqrt{A_{lm}^0 - \frac{m^2}{\sin^2\theta}} = \pi\left(l + \frac{1}{2} - |m|\right) , \tag{9.116}$$

and at leading order, $\theta_+^0, \theta_-^0 = \pm\arcsin[m/(l+1/2)]$. One can easily verify that the solution to this equation is the angular eigenvalue of a Schwarzschild black hole, $A_{lm}^0 = (l+1/2)^2$ (note that we are assuming $l \gg 1$). Now we will compute the lowest-order perturbation in $a\omega/l$, which turns out to be quadratic in this parameter [i.e., $(a\omega/l)^2$] below:

$$\int_{\theta_-^0}^{\theta_+^0} \frac{\delta A_{lm} + a^2\omega^2\cos^2\theta}{\sqrt{(l+1/2)^2 - m^2/\sin^2\theta}}d\theta = 0 . \tag{9.117}$$

The integration limits θ_+, θ_- also can be expanded in a series in $a\omega/l$, and the lowest-order terms of this series are given by θ_+^0, θ_-^0; The perturbation in θ_+, θ_- would result in some quartic corrections in $a\omega/l$ [i.e., $(a\omega/l)^4$] when we evaluate the integrals of Eqs. (9.117) and (9.116), because the integrand is of order $(a\omega/l)^2$ and the width of the correction in θ_+, θ_- are also of order $(a\omega/l)^2$. As a result, we will not need it here. Evaluating the integral in Eq. (9.117) is straightforward, and we find

$$A_{lm} = A_{lm}^0 + \delta A_{lm} = l(l+1) - \frac{a^2\omega^2}{2}\left[1 - \frac{m^2}{l(l+1)}\right] . \tag{9.118}$$

Interestingly, the above expression is consistent with the expansion of A_{lm} for small $a\omega$ given in [58], even in the eikonal limit, where $a\omega$ is large. The reason for this fortuitous agreement is again

that for QNMs of Kerr black holes of any spin, $a\omega/l$ is small, and the expansion only involves even powers of this parameter, $(a\omega/l)^2$. Because the coefficients in the expansion of $a\omega$ scale as $1/l^k$ for even powers of $(a\omega)^k$ and $1/l^{k+1}$ for odd powers of $(a\omega)^k$, in the limit of large l, the two series actually are equivalent in the eikonal limit. In principle, one can also expand and solve Eq. (9.17) to higher orders in the parameter $a\omega/l$ and compare with the expansion in $a\omega$ in [58]; we expect that the two series should agree. This would be useful, because it would effectively let one use the small $a\omega$ expansion in the eikonal limit, where the series would, ostensibly, not be valid.

Bibliography

[1] C. V. Vishveshwara, Nature **227**, 936 (1970).

[2] K. D. Kokkotas and B. Schmidt, Living Rev. Relativity **2**, 2 (1999), http://www.livingreviews.org/lrr-1999-2.

[3] H.-P. Nollert, Classical Quantum Gravity **16**, R159 (1999).

[4] V. Ferrari and L. Gualtieri, Gen. Relativ. Gravit. **40**, 945 (2008).

[5] E. Berti, V. Cardoso, A. O. Starinets, Classical Quantum Gravity **26**, 163001 (2009).

[6] R. A. Konoplya and A. Zhidenko, Rev. Mod. Phys. **83**, 793 (2011).

[7] M. Davis, R. Ruffini, W. H. Press, and R. H. Price, Phys. Rev. Lett. **27**, 1466 (1971).

[8] S. Chandrasekhar and S. Detweiler, Proc. R. Soc. Lond. A **344**, 441 (1975).

[9] V. Ferrari and B. Mashhoon, Phys. Rev. D **30**, 295 (1984).

[10] B. F. Schutz and C. M. Will, Astrophys. J. **291**, L33 (1985).

[11] S. Iyer and C. M. Will, Phys. Rev. D **35**, 3621 (1987).

[12] E. W. Leaver, Proc. R. Soc. Lond. A **402**, 285 (1985).

[13] H.-P. Nollert, Phys. Rev. D **47**, 5253 (1993).

[14] P. P. Fiziev, Classical Quantum Gravity **27**, 135001 (2010).

[15] D. Staicova and P. P. Fiziev, arXiv:1112.0310 (2011).

[16] E. W. Leaver, Phys. Rev. D **34**, 384 (1986).

[17] Y. Sun and R. H. Price, Phys. Rev. D **38**, 1040 (1988).

[18] http://www.ligo.caltech.edu/.

[19] http://www.ego-gw.it/public/virgo/virgo.aspx.

[20] F. Echeverria, Phys. Rev. D **40**, 3194 (1989).

[21] E. E. Flanagan, and S. A. Hughes, Phys. Rev. D **57**, 4566 (1998).

[22] A. Buonanno, G. B. Cook, and F. Pretorius, Phys. Rev. D **75**, 124018 (2007).

[23] E. Berti, V. Cardoso, J. A. Gonzalez, U. Sperhake, M. Hannam, S. Husa, and B. Brügmann, Phys. Rev. D **76**, 064034 (2007).

[24] O. Dreyer, B. Kelly, B. Krishnan, L. S. Finn, D. Garrison, and R. Lopez-Aleman, Classical Quantum Gravity **21**, 787 (2004).

[25] E. Berti, V. Cardoso, and C. M. Will, Phys. Rev. D **73**, 064030 (2006).

[26] A. Zimmerman and Y. Chen, Phys. Rev. D **84**, 084012 (2011).

[27] Y. Mino and J. Brink, Phys. Rev. D **78**, 124015 (2008).

[28] S. R. Dolan and A. C. Ottewill, Classical Quantum Gravity **26**, 225003 (2009).

[29] S. R. Dolan, Phys. Rev. D **82**, 104003 (2010).

[30] S. R. Dolan and A. C. Ottewill, Phys. Rev. D **84**, 104002 (2011).

[31] H. P. Nollert, Phys. Rev. D **47**, 5253 (1993).

[32] N. Andersson, Classical Quantum Gravity **10**, L61 (1993).

[33] L. Motl, Adv. Theor. Math. Phys. **6**, 1135 (2003).

[34] L. Motl and A. Neitzke, Adv. Theor. Math. Phys. **7**, 307 (2003).

[35] T. Padmanabhan, Classical Quantum Gravity **21**, L1 (2004).

[36] V. Cardoso, A. S. Miransa, E. Berti, H. Witek, V. T. Zanchin, Phys. Rev. D **79**, 064016 (2009).

[37] C. J. Goebel, Astrophys. J. **172**, L95 (1972).

[38] C.-M. Claudel, K. S. Virbhadra, and G. F. R. Ellis, J. Math. Phys. **42**, 818 (2001).

[39] S. A. Teukolsky, Phys. Rev. Lett. **29**, 1114 (1972).

[40] K. D. Kokkotas, Classical Quantum Gravity **8**, 2217 (1991).

[41] E. Seidel and S. Iyer, Phys. Rev. D **41**, 374 (1990).

[42] S. A. Teukolsky, Astrophys. J. **185**, 635 (1973).

[43] R. Shankar, *Principals of Quantum Mechanics*, (Plenum Press, New York, 1980).

[44] S. Detweiler, Astrophys. J. **239**, 292 (1980).

[45] V. Cardoso Phys. Rev. D **70**, 127502 (2004).

[46] S. Hod, Phys. Rev. D **78**, 084035 (2008).

[47] E. Teo, Gen. Relativ. and Gravit. **35**, 1909 (2003).

[48] B. Mashhoon, Phys. Rev. D **31**, 290 (1985).

[49] S. Hod, Phys. Rev. D **84**, 044046 (2011).

[50] E. Berti and K. D. Kokkotas, Phys. Rev. D **71**, 124008 (2005).

[51] S. Hod, Phys. Rev. D **80**, 064004 (2009).

[52] C. W. Misner, K. S. Thorne and J. A. Wheeler, *Gravitation*, (W. H. Freeman and Company, New York, 1973).

[53] S. Chandrasekhar, *The Mathematical Theory of Black Holes* (Oxford University Press, Oxford, 1983).

[54] J. M. Bardeen, W. H. Press, and S. A. Teukolsky, Astrophys. J. **178**, 347 (1972).

[55] H. Yang, A. Zimmerman, Z. Y. Zhang and Y. Chen, unpublished.

[56] K. Glampedakis and N. Andersson, Phys. Rev. D **64**, 104021 (2001).

[57] http://www.phy.olemiss.edu/ berti/qnms.html.

[58] E. Berti, V. Cardoso, M. Casals, Phys. Rev. D **73**, 024013 (2006).

Chapter 10

Branching of quasinormal modes for nearly extremal Kerr black holes

We show that a nearly extremal Kerr black hole has two distinct types of quasinormal mode frequencies. One set of frequency modes, the zero-damping modes, approach zero decay in the extremal limit, and exist for all corotating modes ($m \geq 0$). The other set, the damped modes, retain finite decay even for extreme Kerr black holes, and they exist for all counter-rotating modes ($m < 0$) and for a subset of corotating modes. We also show that as the spin approaches its extremal value, when both zero-damping and damped modes are present, the frequency spectrum bifurcates into two distinct branches. We numerically explore the specific case of the fundamental $l = 2$ modes, which have the greatest astrophysical interest, and also discuss the physical reason for the mode branching, in terms of an analogy to the double-well harmonic oscillator of quantum mechanics. Finally, we apply our new analytic expressions to confirm that many superimposed frequency overtones result in a power-law decay for the quasinormal ringing of a nearly extremal Kerr black hole.

10.1 Introduction

Nearly extremal Kerr (NEK) black holes (BHs)—i.e., BHs for which the dimensionless angular momentum $a \approx 1$ in the geometrical units, $G = c = M = 1$, used in this paper—have drawn much attention recently. Besides the mounting evidence for fast-rotating BHs in astronomy [1], NEK
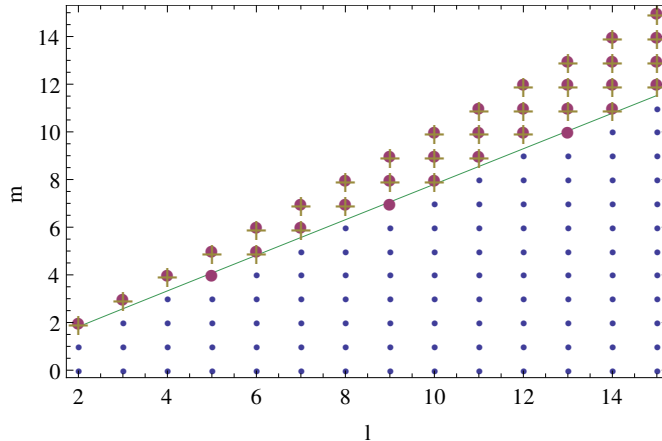
Figure 10.1: (Color online.) Phase diagram for the separation between the single- and double-branch regime for NEK BHs. Large purple dots and gold crosses correspond to (l, m) pairs with only ZDMs for perturbations with spin -2 and 0, respectively. Smaller blue dots correspond to (l, m) pairs with both ZDMs and DMs. The green line is the phase boundary, computed using the eikonal approximation.

BHs have considerable theoretical significance, e.g., in studies of weak cosmic censorship [2] and in calculations of black-hole entropy [3].

For extremal Kerr BHs $(a = 1)$ the near-horizon geometry reduces to $\text{AdS}_2 \times \text{S}^2$ [4]. This observation led to the Kerr/CFT conjecture, which states that extremal Kerr BHs are dual to the chiral limit of a two-dimensional conformal field theory [5]. In the past few years the extremal Kerr spacetime and spacetimes violating the Kerr bound were shown to be unstable [6]. The stability of BHs depends on the sign of the imaginary part of their complex free vibration modes, called quasinormal modes (QNMs) [7]. Therefore the NEK QNM frequencies studied here can shed light on the onset of extremal Kerr instabilities and prove useful in quantum field theory (for example, in the calculation of two-point functions [8]).

Detweiler first used an approximation to the radial Teukolsky equation for NEK BHs (see also [9]) to show that QNMs with angular indices $l = m$ have a long decay time [10]. Using Detweiler's result, Sasaki and Nakamura [11] calculated QNM frequencies analytically and Andersson and Glampedakis proposed long-lived emission from NEK BHs [12]. However, there remains a long-standing controversy in the literature about what set of QNMs decay slowly [13], whether long-lived radiation is possible [14], and whether the imaginary part of the QNM frequencies vanishes as $a \to 1$ (compare [11, 14] with [13]). Despite the importance of this problem, our present understanding of the QNM spectrum of NEK BHs is inconclusive.

In a recent paper [15], some of us used a WKB analysis to relate Kerr QNMs in the eikonal limit to spherical photon orbits around Kerr BHs. We pointed out that a subset of spherical photon orbits of extremal Kerr BHs reside on the horizon and that the corresponding QNMs have zero damping. This happens when the parameter $\mu \equiv m/(l + 1/2) \gtrsim \mu_c \simeq 0.74$. Hod [16] computed μ_c in the

eikonal limit, finding an approximate analytical result in agreement with [15].

In this work, we will show that the NEK geometry has two distinct sets of QNMs: zero-damping modes (ZDMs) and damped modes (DMs). ZDMs are associated with the near-horizon geometry of the BH, and they exist for *all* allowed values of l and $m \geq 0$ (we classify modes using Leaver's conventions [17], but we use units in which the BH has mass $M = 1$). DMs are associated with peaks of the potential barrier; in the eikonal limit, they exist when $\mu \leq 0.74$. This implies that ZDMs and DMs coexist if $0 \leq \mu \leq 0.74$. Figure 10.1 is a "phase diagram" in QNM space, showing the regions where either the ZDMs or both the DMs and the ZDMs exist for scalar and gravitational perturbations with $l \leq 15$. We will discuss this phase diagram further below. When the ZDMs and DMs coexist, and when the BH spin a is small, for each (l, m) there is only a single set of QNMs characterized by the overtone number n (where modes with larger n have stronger damping). For larger a, this set of QNMs appears to break into two branches. The DM branch originates from lower-overtone modes at smaller a, and its modes retain a finite decay rate as $a \to 1$. The ZDM branch originates from higher-overtone modes whose imaginary part becomes smaller than that of DMs as $a \to 1$, thereby forming the second branch. This is similar to the behavior of eigenmodes in quantum mechanics when we parametrically split a single potential well into two potential wells (cf. Fig. 10.2 below, as well as [18] for a somewhat analogous phenomenon in the theory of oscillations of ultracompact stars).

10.2   Matched expansions

For $\epsilon \equiv 1 - a \ll 1$ and $\omega - m/2 \ll 1$, the radial Teukolsky equation can be written in a self-similar form when $(r - 1) \ll 1$ and in an asymptotic form (by setting $a = 1$) when $(r - 1) \gg \sqrt{\epsilon}$ (cf. [9, 10, 19]). The solutions of the Teukolsky equation in these regions (hypergeometric and confluent hypergeometric functions, respectively) can be matched at $\sqrt{\epsilon} \ll (r-1) \ll 1$ to provide the following condition for QNM frequencies:

$$
e^{-\pi\delta - 2i\delta \ln(m) - i\delta \ln(8\epsilon)} \frac{\Gamma^2(2i\delta)\Gamma(1/2 + s - im - i\delta)}{\Gamma^2(-2i\delta)\Gamma(1/2 + s - im + i\delta)}
$$
$$
\times \frac{\Gamma(1/2 - s - im - i\delta)\Gamma[1/2 + i(m - \delta - \sqrt{2}\tilde{\omega})]}{\Gamma(1/2 - s - im + i\delta)\Gamma[1/2 + i(m + \delta - \sqrt{2}\tilde{\omega})]} = 1. \tag{10.1}
$$

Here we denote the eigenvalues of the angular Teukolsky equation by $_sA_{lm}$, and we define $\delta^2 \equiv 7m^2/4 - (s + 1/2)^2 - {}_sA_{lm}$ and $\tilde{\omega} \equiv (\omega - m\Omega_H)/\sqrt{\epsilon}$ [note that $\Omega_H = a/(r_+^2 + a^2)$ is the horizon frequency and $r_+ = 1 + \sqrt{1 - a^2}$ is the horizon radius]. Scalar, electromagnetic, and gravitational perturbations correspond to spin $s = 0, -1, -2$, respectively. If we choose the conventions that $\mathcal{R}e(\delta) \geq 0$ and $\mathcal{I}m(\delta) \geq 0$ when δ^2 is positive and negative, respectively, then the left-hand side of
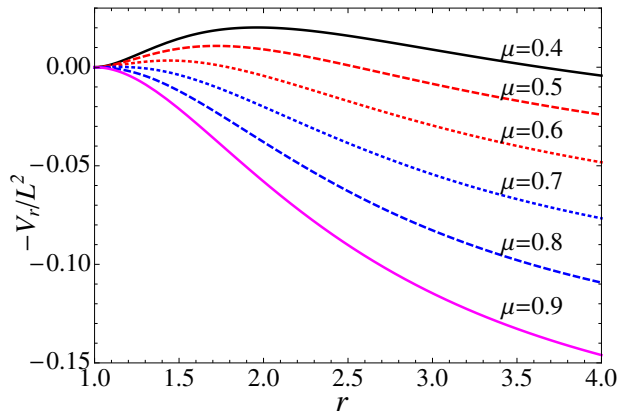
Figure 10.2: (Color online.) Plot of the potential term for $a = 1$, Eq. (10.6), for $\mu = 0.4$, 0.5, 0.6, 0.7, 0.8, and 0.9 (black-solid, red-dashed, red-dotted, blue-dotted, blue-dashed, and magenta-solid curves, respectively). The transition from single-branch to double-branch happens between $\mu = 0.7$ and $\mu = 0.8$.

Eq. (10.1) is usually a very small number, except when it is near the poles of the Γ-functions in the numerator. When $m \geq 0$, we can always find the solution near the poles at negative integers:

$$1/2 + i(m - \delta - \sqrt{2}\tilde{\omega}) \approx -n, \tag{10.2}$$

or

$$\omega \approx \frac{m}{2} - \frac{\delta\sqrt{\epsilon}}{\sqrt{2}} - i\left(n + \frac{1}{2}\right)\frac{\sqrt{\epsilon}}{\sqrt{2}}. \tag{10.3}$$

Note that the overtone index n of these ZDM frequencies need not correspond precisely to the same overtone index of Kerr QNMs at lower spins. This set of solutions was first discovered by Hod [13]. The matched-expansion derivation shows that this set of modes depends on the near-horizon region of the Kerr BH. Equation (10.3) is quite accurate when $|\delta| \gg 1$, but when $|\delta| < 1$ it needs an additional correction [19]. However, the $\sqrt{\epsilon}$ scaling of the decay rate is still correct when $|\delta| < 1$. The solutions to Eq. (10.3) with $m < 0$ are those that arise from the symmetry $\omega_{l,m} = -\omega_{l,-m}^*$; there are no solutions with $m < 0$ and $\mathcal{R}e(\omega) > 0$, when $\omega - m/2$ is not small. Thus, the ZDMs only exist in the *corotating* regime $m \geq 0$.

Another set of solutions of Eq. (10.1) may exist when $\delta^2 < 0$ and $2i\delta \approx -n$, with n a positive integer. A more detailed analysis shows that, in this case, two nearly degenerate hypergeometric functions have comparable contribution to the near-horizon solution [19]. As a result, Eq. (10.1) is no longer valid when $2i\delta \approx -n$. As a consistency check, we looked for solutions with $2i\delta \approx -n$ using Leaver's method and we did not find any.

10.3   WKB analysis

The matched-expansion method assumes that $\omega \approx m/2$, but Eq. (10.1) does not hold for modes which do *not* meet this requirement (i.e., DMs). To compute these modes, we will instead use a WKB analysis in the eikonal limit $l \gg 1$. The radial Teukolsky equation when $l \gg 1$ is [15]

$$\frac{d^2 u_r}{dr_*^2} + V_r u_r = \frac{d^2 u_r}{dr_*^2} + \frac{K^2 - \Delta \lambda_{lm}^0}{(r^2 + a^2)^2} u_r = 0 \,, \tag{10.4a}$$

with

$$K = -\omega(r^2 + a^2) + am, \quad \frac{d}{dr_*} \equiv \frac{\Delta}{r^2 + a^2} \frac{d}{dr},$$

$$\lambda_{lm}^0 = A_{lm} + a^2 \omega^2 - 2am\omega, \quad \Delta = r^2 - 2r + a^2 \,. \tag{10.4b}$$

We define $\omega \equiv \omega_R - i\omega_I$, and we note that the real and imaginary parts scale as $\omega_R \propto l$ and $\omega_I \propto l^0$, while the angular constant scales as $A_{lm} \propto l^2$. We only keep the leading-order terms in the eikonal limit in the following discussion (therefore all s-dependent terms are neglected, and the A_{lm} are real). In Fig. 10.2 and below, we will refer to $-V_r$ as "the potential". According to the WKB analysis and its geometric correspondence in [15], the position of the peak of the potential asymptotes the horizon as $a \to 1$ for some of the corotating modes. For this set of QNMs, one can verify that V_r'' (where primes denote derivatives with respect to r_*) scales as Δ^2; thus, the peak r_0 of the potential becomes broad as r_0 approaches the horizon. It then follows that $\omega_I \propto \sqrt{V_r''}/\partial_\omega V_r \to 0$, and $\omega_R \to m/2$ in order to satisfy $V_r(\omega_R, r_0) = 0$ for these modes. Assuming that $r_0 = 1 + c\sqrt{\epsilon}$ for the nearly extremal modes, where c is some constant, we can apply the eikonal equations in [15] and obtain

$$r_0 \approx 1 + \frac{m\sqrt{2\epsilon}}{\mathcal{F}_0}, \ \omega_R \approx \frac{m}{2} - \frac{\mathcal{F}_0\sqrt{\epsilon}}{\sqrt{2}}, \ \omega_I \approx \left(n + \frac{1}{2}\right)\frac{\sqrt{\epsilon}}{\sqrt{2}} \,, \tag{10.5}$$

with $\mathcal{F}_0 = \sqrt{7m^2/4 - A_{lm}(\omega = m/2)}$. Comparing this result with Eqs. (10.3) and (10.5), we can see the two sets of frequencies are essentially the *same* modes, although obtained in very different ways. Here $\mathcal{F}_0^2$ and δ^2 differ by $1/4$, which is reasonable because in the eikonal limit $\mathcal{F}_0 \propto l$ and $\delta \propto l$ (making $1/4$ a higher-order correction).

To build intuition about $\mathcal{F}_0$ and δ, we look at V_r for extreme Kerr BHs, with ω replaced by $m/2$:

$$V_r = L^2 \frac{(r-1)^2}{(r^2+1)^2} \left[\frac{(r+1)^2}{4}\mu^2 - \alpha(\mu) + \frac{3}{4}\mu^2\right] \,, \tag{10.6}$$

where $L \equiv l + 1/2$ and $\alpha(\mu) \equiv A_{lm}/L^2$. According to the WKB analysis of the radial Teukolsky equation [20], the QNM frequencies are determined by the peak of the potential. As shown in Fig. 10.2, when μ is large the maximum of the potential is at the horizon, $r = 1$, as expected for

ZDMs. As μ decreases and falls below some critical value μ_c, the peak moves outside the horizon, and the horizon becomes a local minimum of the potential. At the peak ω_I is nonzero because $d^2V_r/dr_*^2|_{r_0} \neq 0$, so we have DMs. The criterion for having no peak outside the horizon is

$$\frac{(r+1)^2}{4}\mu^2 - \alpha(\mu) + \frac{3}{4}\mu^2 > 0 \quad \text{for} \quad r = 1, \tag{10.7}$$

i.e., $\mathcal{F}_0^2 > 0$ (or $\delta^2 > 0$). The values at which $\mathcal{F}_0^2$ (or δ^2) vanish lead to the condition for the critical μ_c: $\alpha(\mu_c) = \frac{7}{4}\mu_c^2$. If we use the approximation $\alpha(\mu) \approx 1 - a^2\omega^2(1-\mu^2)/(2L^2)$ [15], this will reproduce Hod's approximate analytical result $\mu_c \approx [(15 - \sqrt{193})/2]^{1/2}$ [16]. We can obtain the exact μ_c (in the eikonal limit) by inserting $\alpha(\mu_c) = \frac{7}{4}\mu_c^2$ into the Bohr-Sommerfeld condition for α derived in [15]:

$$\int_{\theta_-}^{\theta_+} \sqrt{\alpha - \frac{\mu^2}{\sin^2\theta} + \frac{\mu^2}{4}\cos^2\theta} = (1 - |\mu|)\pi, \tag{10.8}$$

where $\theta_+ = \pi - \theta_-$ and $\theta_- = \arcsin(\sqrt{3}-1)$ are the angles at which the integrand vanishes. Therefore we have

$$\mu_c = \frac{1}{1 + \mathcal{I}/\pi}, \quad \mathcal{I} = \int_{\theta_-}^{\theta_+} d\theta \sqrt{\frac{7}{4} - \frac{1}{\sin^2\theta} + \frac{1}{4}\cos^2\theta}, \tag{10.9}$$

which yields the numerical value $\mu_c \simeq 0.74398$. In the eikonal limit, when $\mu > \mu_c$ NEK BHs have only ZDMs ("single-phase regime") ; when $0 \leq \mu \leq \mu_c$, both DMs and ZDMs exist ("double-phase regime").

10.4 Phase boundary

Although there is a clear criterion for determining the boundary between the single-phase regime and the double-phase regime in the eikonal limit (when $\mu < \mu_c$, the peak of the potential no longer resides on the horizon) it is not immediately clear if a similar criterion holds when l is small. For scalar perturbations, however, we can write the radial Teukolsky potential for extreme-Kerr BHs with generic l, m, under the assumption that $\omega = m/2$ (and, therefore, the $_0A_{lm}$ remain real for the ZDMs):

$$V_r = \frac{(r-1)^2}{(r^2+1)^2}\left[\frac{(r+1)^2}{4}m^2 - {_0A_{lm}}\right]$$
$$+ \frac{(r-1)^2}{(r^2+1)^2}\left[\frac{3}{4}m^2 + \frac{(r-1)(2r^2+3r-1)}{(1+r^2)^2}\right]. \tag{10.10}$$

It is not difficult to see that there is still no peak outside the horizon when $\frac{7}{4}m^2 > {_0A_{lm}}$, or $\mathcal{F}_0^2 > 0$. For electromagnetic and gravitational perturbations the potential terms $-V_r$ are complex functions, thereby making the positions of their extrema more difficult to define. Detweiler [21],

however, has shown that the radial function can be transformed so that it satisfies a differential equation with a real potential. Using this potential, the criterion to exclude peaks outside the horizon is [19]:

$$\mathcal{F}_s^2 \equiv \frac{7}{4}m^2 - s(s+1) - {}_sA_{lm}\left(\omega = \frac{m}{2}\right) > 0. \tag{10.11}$$

Note that this expression respects the pairing symmetry ${}_{-s}A_{lm} = {}_sA_{lm} + 2s$, and that for all s, $\mathcal{F}_s^2$ and δ^2 differ from each other only by $1/4$. For $s = 0, -2$ and $2 \leq l \leq 100$, we have searched all QNMs numerically and have not found any mode simultaneously satisfying $\delta^2 < 0$ and $\mathcal{F}_s^2 > 0$; therefore, the sign of δ^2 also determines whether a peak exists outside the horizon. In addition, we have used Leaver's continued-fraction algorithm to determine the phase boundary numerically. As shown in Fig. 10.1, the actual phase boundary matches the criterion predicted by the eikonal limit, $\mu = \mu_c$. In addition, for scalar and gravitational perturbations, we find numerically that modes are in the single-phase regime when $\mathcal{F}_s^2 > 0$ for all $l \leq 15$. This reinforces our physical understanding that DMs are associated with a peak of the potential outside the horizon, while ZDMs are somewhat similar in nature to the s-modes in ultracompact stars [18].

10.5   Bifurcation

10.5.1   Numerical investigation

Schwarzschild and slowly spinning Kerr BHs have a single set of QNMs for each l, m that are characterized by their overtone number n. If the ZDMs originate from modes at higher-n than the DMs when the BH spin is low, then when the spin increases beyond a critical value $a_s = 1 - \epsilon_s$, a single set of QNMs may split into two branches.

We numerically investigate this bifurcation effect by examining the complex QNM frequency plane to search for solutions of Leaver's continued-fraction equations [17, 19]. In Fig. 10.3, we plot the contours of constant value of the logarithm of the continued-fraction expansion, truncating at $N = 800$ terms. The QNM frequencies correspond to the local minima of this sum, where the contours cluster. The shading indicates the value of the fraction, with darker values nearly zero.

When $\mu < \mu_c$, a single set of QNMs splits into two branches for increasing a (see the left-hand panels of Fig. 10.3, where $l = 10$, $m = 7$, as the spin increases from $a = 0.9990$ to $a = 0.9999$ from the upper panel to the lower). The ZDM branch is quite accurately described by Eq. (10.3); the imaginary part of the ZDMs scales like $\sqrt{\epsilon}$, and they move towards the real axis as $\epsilon \to 0$. The DM branch changes relatively little with increasing spin (it is expected that the WKB peak can only support a finite number of modes [19], and there are only 3 DMs in the lower-left panel). In this case, the WKB formulae of [15] are in good agreement with the lowest-overtone DM (marked with a $\times$ in the figure).
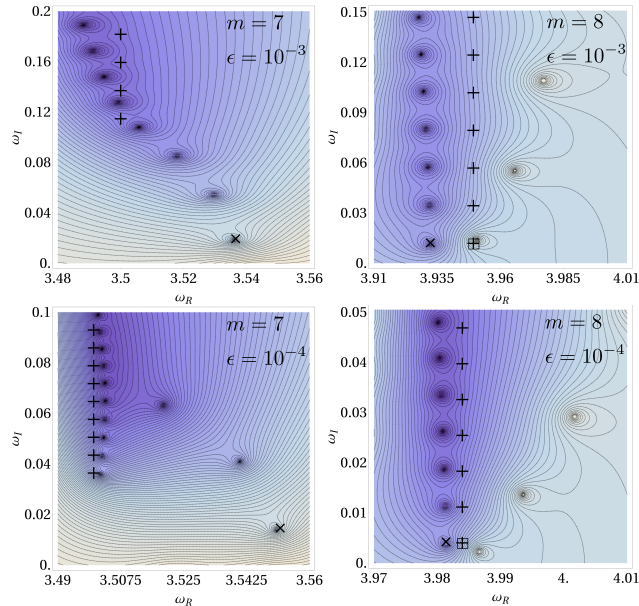
Figure 10.3: (Color online.) QNM frequencies with $l = 10$ for NEK BHs. Contours are constant values of the logarithm of the continued fraction in the complex plane; darker shading indicates values near zero. The + symbols are the ZDM predictions, a × is the lowest-overtone WKB prediction from [15], and the box is centered at the WKB prediction from Eq. (10.5). No branching is observed for modes with $m = 8$. Note that the closed contours with light shading have large values and do not correspond to any QNM. Further discussion of the figure is in the text.

For $\mu > \mu_c$ there is no bifurcation, and the modes are predicted fairly well by Eq. (10.3). We can see this in the right-hand panels of Fig. 10.3, where $l = 10$, $m = 8$ and we again raise the spin from $a = 0.9990$ to $a = 0.9999$. For the $m = 8$ modes, we also mark the leading-order WKB prediction of Eq. (10.5) with a box. For the bifurcation effect, we can define a benchmark $a_c = 1 - \epsilon_c$ as the BH spin at which the imaginary part of the *fundamental* ZDM is equal to that of the *fundamental* DM:

$$\frac{\sqrt{\epsilon_c}}{2\sqrt{2}}(1 + 2|\delta|) = \frac{1}{2}\frac{\sqrt{2V_r''}}{\partial_\omega V_r}\bigg|_{r_0}. \tag{10.12}$$

The right-hand side of Eq. (10.12) can be evaluated using the approximate WKB formula in [15]. Since both sides of Eq. (10.12) depend on ϵ, we solve for ϵ_c iteratively; this converges quickly for a variety of initial spins. By computing ϵ_c for $l \leq 15$ and $0 < m < (l + 1/2)\mu_c$, we find that $L^2\epsilon_c = 10^{-3}(11.6 - 3.12\mu - 18.0\mu^2)$ is a reasonable fitting formula. For the $l = 10$, $m = 7$ case, Eq. (10.12) gives $\epsilon_c \sim 10^{-5}$, which is in agreement with numerical results; for the $l = 2$, $m = 1$ case it gives $\epsilon_c \sim 10^{-3}$.

In Fig. 10.3, however, it is clear that the bifurcation actually starts when the *fundamental* ZDM's imaginary part equals the imaginary part of the *highest-overtone* DM (in Fig. 10.3 it is the third overtone). This happens at a spin $a_s < a_c$. Because we do not have a good estimate of the number

of modes in the DM branch (beyond the fact that it should be proportional to L and a function of μ in the eikonal limit [19]) and because WKB techniques are not accurate for these high-overtone DMs, finding an analytic solution for a_s remains an open problem.

10.5.2   Bound state formulation of the radial Teukolsky equation

The radial Teukolsky equation generally describes a scattering problem, in the WKB approximation. When the boundary condition is specified as describing outgoing waves at infinity and ingoing waves at the horizon, the corresponding eigenmodes are just QNMs. It is often interesting to transform this scattering problem to a bound-state problem, as shown by Mashhoon [25] for slowly rotating BHs in the eikonal approximation. Here we describe a transformation procedure for perturbations of generic Kerr BHs that is similar to Mashoon's for slowly rotating BHs. For generic Kerr BHs, the radial Teukolsky equation is given in Eq. (10.4a) (with general s). The angular eigenvalue can be expressed as a function of $L \equiv l + 1/2$, m, and ω: $A_{lm} = A(L, m, \omega, a)$. After the transformations:

$$r \rightarrow -ir, M \rightarrow -iM, m \rightarrow -im, L \rightarrow -iL,$$

$$a \rightarrow -ia, s \rightarrow s, \omega \rightarrow \Omega, \tag{10.13}$$

the new radial equation becomes

$$\frac{d^2u}{dr_*^2} - \left[\frac{\tilde{K}^2 + 2s(r-M)\tilde{K} - \Delta(4\omega rs + \tilde{\lambda}_{lm}^s)}{(r^2 + a^2)^2} \right] u$$

$$+ \left[G^2 + \frac{dG}{dr_*} \right] u = 0, \tag{10.14}$$

$$\tilde{K} = \Omega(r^2 + a^2) - ma, \tag{10.15}$$

$$\tilde{\lambda}_{lm}^s = -A(-iL, -im, \Omega, -ia) + a^2\Omega^2 - 2ma\Omega. \tag{10.16}$$

Note in the equation above we restored the black hole mass M, because it is also transformed. Because the angular separation constant has the functional form, $A(L, m, \omega, a) = A(L, m/L, a\omega/L)$, then $A(-iL, -im, \Omega, -ia)$ and $\tilde{\lambda}_{lm}^0$ are real if Ω is real. Now Eq. (11.21) describes a bound state problem; when $r_* \rightarrow \pm\infty$, the wavefunction asymptotes to $e^{\Omega r_*}$ or $e^{-(\Omega - ma/(2Mr_+))r_*}$. The eigenvalue $\Omega = \Omega(L, m, n, a)$ should be a real-valued function depending on L, m, and a (n is the overtone number). Knowing the functional form of Ω, we can then apply the inverse transform to obtain ω:

$$\omega = \omega_R - i\omega_I = \Omega(iL, im, n, ia, iM). \tag{10.17}$$

As an example of this idea, we shall take the formula for the QNM frequency in the eikonal limit and study the DMs. In this case, $A(-iL, -im, \Omega, -ia) = -A(L, m, \Omega, a)$ and Eq. (11.21) becomes

$$\frac{d^2u}{dr_*^2} - \left[\frac{\tilde{K}^2 - \Delta(A + a^2\Omega^2 - 2am\Omega)}{(r^2 + a^2)^2} \right] u = \frac{d^2u}{dr_*^2} - V_r u = 0 \qquad (10.18)$$

where we have only kept leading-order terms in L. Because the potential well is very deep as $L \gg 1$, the fundamental mode and the first few overtones should be located near the bottom of the potential well: $V_r(\Omega_0, r_{\text{peak}}) = \partial_r V_r(\Omega_0, r_{\text{peak}}) = 0$. We shall Taylor expand V_r near its extrema:

$$V_r(\Omega_0 + \delta\Omega, r_{*\text{peak}} + \delta r_*) \approx \partial_\Omega V_r \delta\Omega + \frac{1}{2} V_r'' \delta r_*^2 , \qquad (10.19)$$

where primes denote derivatives with respect to r_*. The new equation becomes

$$\frac{d^2u}{dr_*^2} = \left(\partial_\Omega V_r \delta\Omega + \frac{1}{2} V_r'' \delta r_*^2 \right) u . \qquad (10.20)$$

This is now a standard bound-state eigenvalue problem, and the solution is

$$\delta\Omega = \left(n + \frac{1}{2} \right) \frac{\sqrt{2V_r''}}{\partial_\Omega V_r} , \qquad (10.21)$$

or

$$\begin{aligned}
\Omega &= \Omega_0 + \left(n + \frac{1}{2} \right) \frac{\sqrt{2V_r''}}{\partial_\Omega V_r} \\
&= \frac{1}{M} \left[L\omega_0(\mu) + \left(n + \frac{1}{2} \right) \omega_1(\mu) \right] .
\end{aligned} \qquad (10.22)$$

It is then straightforward to obtain

$$\begin{aligned}
\omega &= \Omega(iL, im, n, ia, iM) \\
&= \Omega_0 - i \left(n + \frac{1}{2} \right) \frac{\sqrt{2V_r''}}{\partial_\Omega V_r} ,
\end{aligned} \qquad (10.23)$$

which agrees with the eikonal limit QNM formula in [20].

Besides DMs, the ZDMs can also be examined in the dual bound-state picture. For simplicity, we focus on scalar perturbation $s = 0$ and make the approximation that $A \to -A$. [1] After the transformation in Eq. (10.13), the near-horizon-limit Teukolsky equation becomes:

$$y^2 \frac{d^2u_r}{dy^2} + y \frac{du}{dy} - \left[\tilde{\omega}^2 + \frac{2\sqrt{2}my}{1-y} \left(\tilde{\omega} - \frac{m}{\sqrt{2}} \right) + \frac{2\mathcal{F}_0^2 y}{(1-y)^2} \right] u_r = 0 \qquad (10.24)$$

---

[1] In reality $A \to -A'$, $\mathcal{F}_0^2 \to \mathcal{F}_0^{2\,\prime}$ and $A' \neq A$ for generic s, l, m, and the value of A' can be obtained using the expansion in [28]. Here for illustration purposes we take the approximation $A' = A$.
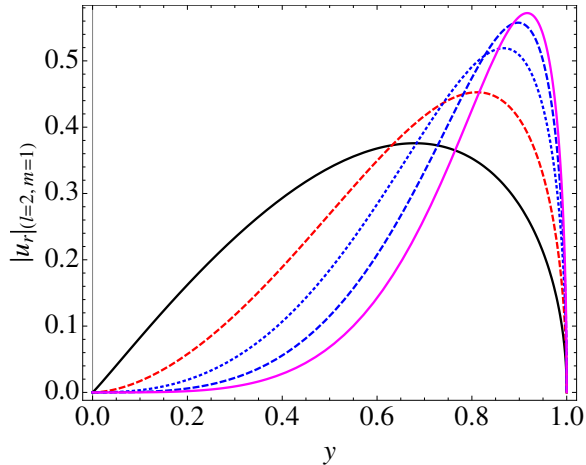
Figure 10.4: $l = 2$, $m = 1$, $s = 0$, ZDM wavefunctions in the bound-state picture. Black solid, red dashed, blue dashed, blue dotted and magenta solid lines correspond to $n = 0, 1, 2, 3, 4$ respectively. The wavefunctions approach 0 when $r \to r_+$ or $\sqrt{\epsilon}r_* \to 0$, and stay negligibly small for $r - 1 \gg \sqrt{\epsilon}$. Therefore the wavefunction is bounded in the near horizon regime, as we expected. In addition, as we increase the overtone n, the wavefunctions monotonically move away from the horizon. This is a general feature for all ZDMs.

The solution can be written as Hypergeometric functions

$$u_r = y^{-p}(1 - y)^{-q}{}_2F_1(\alpha, \beta, \gamma, y), \tag{10.25}$$

but with

$$p = -\tilde{\omega}/\sqrt{2}, \qquad\qquad\qquad q = -1/2 - \delta',$$
$$\alpha = 1/2 + (m + \delta' + \sqrt{2}\bar{\omega}), \qquad\qquad\qquad \beta = 1/2 - m + \delta',$$
$$\gamma = 1 + \sqrt{2}\tilde{\omega}, \tag{10.26}$$

where $y = e^{\sqrt{2\epsilon}r_*}$ and $\delta' = \sqrt{\mathcal{F}_0^2 - 1/2}$. The resonant (bound state) condition is still $\gamma - \beta \approx -n$ or

$$\tilde{\omega} \approx \frac{1}{\sqrt{2}}\left(n + \frac{1}{2} + m - \delta'\right) \tag{10.27}$$

which will transform back to Eq. (10.3) if we apply the inverse transformation of Eq. (10.13). In Fig. (10.4) we plot the wavefunction for the first five overtones of the ZDMs with ($l = 2$, $m = 1$). The wavefunction in the regime $r - 1 \gg \sqrt{\epsilon}$ can be obtained using the matching method as shown in Sec (10.2). It is approximately zero, and is not shown in the plot. One can similarly evaluate the DM wavefunctions in this dual picture, and see their support being close to the WKB peak, which is well separated from these ZDMs as $a \to 1$. Therefore this bound-state transformation serves as a useful technique to study mode bifurcation.

10.6 Late time tails of NEK excitations

It was argued by Glampedakis and Anderson [26] that the perturbation of rapidly rotating black holes decays as $1/t$ at late times. Their argument used the NEK QNM frequency formula which is less accurate. Therefore it would be interesting to reconsider this problem taking advantage of our current understanding of NEK QNM spectrum.

We will consider a generic scalar perturbation of a NEK spacetime at an initial Boyer-Lindquist time slice, and we initially follow the calculation of [26] closely. Suppose we have initial data given in terms of the initial scalar field values $\Phi(t=0, r, \theta, \phi)$ and time derivative $\partial_t \Phi(t=0, r, \theta, \phi)$. This gives a corresponding source function $\mathcal{T}$ which we can separate into angular harmonics, using the spheriodal harmonics,

$$\mathcal{T}_{lm} = \int \sin\theta d\theta d\phi \, \bar{S}_{lm}(\theta) e^{-im\phi} \mathcal{T}(r, \theta, \phi) \,. \tag{10.28}$$

By expanding $\Phi(x)$ in the frequency domain, we can write the scalar field at times $t > r_* + r'_*$ by integrating the source term using the radial Green function $G(r_*, r'_*)$ for the radial function $u(r)$. The result is [26]

$$\Phi(x) = \sum_{l, |m| \leq l} \frac{\Phi_l(t, r, \theta)}{\sqrt{r^2 + a^2}} e^{im\phi} \tag{10.29}$$

$$\Phi_m = \frac{1}{2\pi} \int d\omega dr' e^{-i\omega t} S_{lm}(\omega, \theta) \frac{G(r_*, r'_*) \mathcal{T}_{lm}(\omega, r')}{(r')^2 + a^2} \,. \tag{10.30}$$

Focusing on the QNM contribution to the scalar field, we deform the contour of integration over ω into the lower half plane. Each QNM frequency ω_{lmn} is a simple pole in the lower-half plane, and the contour is converted into a sum over the residues of these poles. For simplicity, we will assume that the source is localized at a large radius and that the observer is also at a large radius. In this case the contour integral resolves as

$$\Phi_m \approx -\frac{i}{2} \int dr' \sum_n \frac{A^{\text{out}}_{lmn}}{\alpha_{lmn}} e^{-i\omega_{lmn}(t - r_* - r'_*)} S_{lm} \frac{\mathcal{T}_{lm}(r')}{i\omega_{lmn}} \tag{10.31}$$

where $\alpha_{lmn} = dA^{\text{in}}/d\omega |_{\omega = \omega_{lmn}}$. The terms A^{out} and A^{in} are the amplitudes for the ingoing and outgoing waves in the "in" wave solution,

$$u^{\text{in}} \sim \begin{cases} e^{-ikr_*}, & r \to r_+ \,, \\ \\ A^{\text{out}} e^{i\omega r_*} + A^{\text{in}} e^{-i\omega r_*}, & r \to +\infty \,, \end{cases} \tag{10.32}$$

For the ZDMs, expressions for A^{in} and A^{out} can be obtained by using the matched-expansion tech-

niques. The important point for the current discussion is that, keeping only the leading order terms in $\epsilon \ll 1$ and $\eta \ll 1$, we can write

$$-\frac{i}{2} \left. \frac{A^{\text{out}}}{\alpha} \right|_{ZDM} \approx C(m,\delta) \frac{e^{i\delta \ln 8\epsilon + in\pi} \sqrt{\epsilon}}{n! \Gamma[-n + 2i\delta]} , \tag{10.33}$$

where the constant $C(m,\delta)$ is only weakly dependent on the overtone number n, through higher order terms in ϵ. Inserting this into Eq. (10.31) allows us to perform the sum over overtones explicitly,

$$\Phi_m \approx C e^{i\delta \ln 8\epsilon} \sqrt{\epsilon} \int dr' \frac{e^{-imT/2 - \sqrt{\epsilon/8}T}}{r'} S_{lm}$$
$$\times \sum_n \frac{e^{-n\sqrt{\epsilon/2}T + in\pi}}{n! \Gamma[-n + 2i\delta]} \frac{2\mathcal{T}_{lm}}{im} \tag{10.34}$$
$$\approx \frac{C e^{i\delta \ln 8\epsilon}}{\Gamma[2i\delta]} \int dr' \frac{\sqrt{\epsilon} \, e^{-imT/2 - \sqrt{\epsilon/8}T}}{1 - e^{-\sqrt{\epsilon/2}T}} \left(1 - e^{\sqrt{\epsilon/2}T} \right)^{2i\delta}$$
$$\times S_{lm} \frac{2\mathcal{T}_{lm}}{im} . \tag{10.35}$$

For early times, $T > 0$ and $T\sqrt{\epsilon/2} \ll 1$, the integrand in Eq. (10.35) reduces to

$$e^{-imT/2} \frac{\sqrt{2}}{T} S_{lm} \frac{2\mathcal{T}_{lm}}{im} \left(\sqrt{\epsilon/2} \, T \right)^{2i\delta} . \tag{10.36}$$

For a fixed r_*, this gives the $\sim 1/t$ dependence of the amplitude of the QNM ringing, provided $\delta^2 > 0$. We see that the power-law decay is only valid for a short period of time, which is $\sim 1/\sqrt{\epsilon}$. At larger times, the decay transitions to an exponential decay, which is quickly dominated by the $n = 0$ overtone decay rate. This explains recent results by Harms et al. [27], whose numerical investigations of perturbed, rapidly rotating Kerr holes shows exponential decay at late times unless $\epsilon \to 0$. In this case, the limit of the integrand gives a decay for the response function equal to $\sqrt{2}/T$. A careful examination of Fig. 17 of [27] show that for large spins at early times, while $T\sqrt{\epsilon/2} < 1$, the asymptotic perturbation decays slower than exponential, and in fact seems to obey a roughly $1/T$ dependence (that figure actually plots the gravitational, $s = -2$ ringdown, but it is clear that the spin dependence enters in only in the coefficient C).

As an example, we take for our initial data $\dot{\Phi}_0 = 0$ and let $\Phi_m(0, r, \theta) = A\delta(r - r_0)S_{22}(\theta)\delta_{m2}$. This simplifies the source term to l

$$\mathcal{T}_{lm} = i\omega_{lmn} A r^2 \delta(r - r_0)\delta_{m2} , \tag{10.37}$$
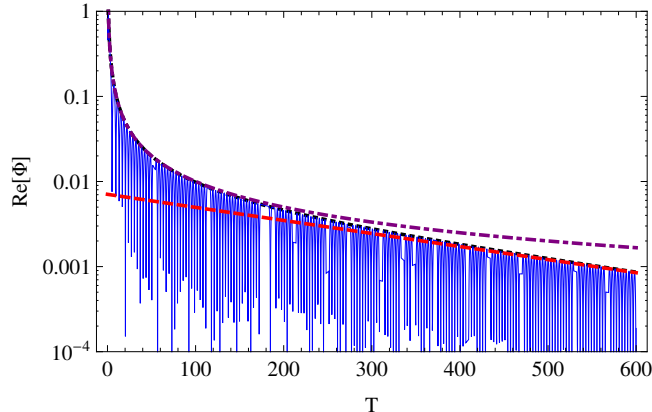
Figure 10.5: The scalar QNM response to an initial perturbation, as described by Eq. (10.35) for a scalar $l = 2$, $m = 2$ perturbation with a radial δ-function distribution. The initial amplitude is normalized to unity. The blue curve plots the logarithm of $\Re[\Phi](T)$, and its envelope is shown by a black dotted line. Also plotted is a curve $1/T$ (purple dot-dashed line) and the decay envelope for the $n = 0$ ZDM (red dashed line).

and the asymptotic scalar field at $r \to \infty$ is then

$$\Phi(x) \approx \frac{Ar_0}{r} S_{22}(\theta) e^{2i\phi} \frac{C' e^{i\delta \ln 8\epsilon}}{(1 - e^{\sqrt{\epsilon/2}\,T})^{2i\delta}} \frac{\sqrt{\epsilon} e^{-iT - \sqrt{\epsilon/8}T}}{1 - e^{-\sqrt{\epsilon/2}T}} \ . \tag{10.38}$$

In Fig. 10.5 we illustrate the time dependence of this QNM ringing by plotting the time dependent amplitude of $\Re[\Phi]$ at some fixed radius and angle, with the amplitude normalized to unity at $T = t - r_* - r_{0*} = 0$, so that at this time the functional behavior limits to $1/T$. Of course, the divergence at $T = 0$ is an artifact of summing the full geometric series from $n = 0$ to $n = \infty$; the ringdown amplitude is in fact finite and proportional to N if the sum is terminated at overtone number N.

We can similarly evaluate DM contribution to Eq. (10.31) according to the WKB QNM frequency formulas [15]. It will be straightforward to see that DM will induce exponential fall off ($\propto e^{-\omega_I t}$), which will be buried under other parts of the tail (ZDM contribution, branch cut contribution and so on).

10.7   Conclusion

We identified two different regimes in the NEK QNM spectrum. In the double-phase regime, we found that the lowest ZDM becomes less damped than the lowest DM at some critical a_c, for which we provided an analytical estimate. For sufficiently large a, Eq. (10.3) is accurate at the least for those ZDMs with smaller decays than the point where the branches bifurcate. We estimate that the number of ZDMs below the bifurcation is $\propto \sqrt{\epsilon_s/\epsilon}$ [19]. In the future, we would like to investigate the behavior of the ZDM branch in the high-overtone limit [22], where these approximations break

down.

Acknowledgement

10.A   Numerical methods

To compute the QNM frequencies more accurately when $a \lesssim 1$, we use a modified version of Leaver's continued-fraction algorithm [17] which we describe below. The most significant difference between Leaver's and our methods arises in the solution to the angular Teukolsky equation. When $s \neq 0$, we use the series expansion of Fackerell and Crossman [23] (see also Appendix B of Fujita and Tagoshi [24]) to express the angular eigenvalue in terms of a continued fraction that depends upon the frequency of the mode. (Fackerell and Crossman expand the angular Teukolsky function in a series of Jacobi polynomials, whereas Leaver finds his solution in terms of powers of $1 + \cos\theta$.) When $s = 0$, we use *Mathematica*'s built-in function for the eigenvalue of the spheroidal harmonic equation to find $_0A_{lm}$. For the radial Teukolsky function, we compute Leaver's expansion, but we specialize his expressions for nearly extremal spins, $a = 1 - \epsilon$. We then compute the continued-fraction solution for the frequency in terms of the angular separation constant. When explicitly find a QNM, we use a nonlinear root-finding algorithm. We can then solve the set of two continued-fraction equations to find the frequency and separation constant of a mode. Because nonlinear root finding often requires an initial condition for the algorithm that is close to the actual solution, we seed the inital conditions at nearly extremal spins using solutions at lower spins.

10.B   Criteria for phase boundaries for electromagnetic and gravitational modes

For electromagnetic and gravitational perturbations, the radial Teukolsky potential is a complex function. To obtain a real potential and a well defined peak, we apply the transformations described

in [21]. Before the transformation, the radial Teukolsky equation is

$$\Delta^{-s} \frac{d}{dr} \left(\Delta^{s+1} \frac{d}{dr} R_s \right) + \frac{K^2 + is\Delta'K - \Delta(2isK' + \lambda_{lm}^s)}{\Delta} R_s$$
$$= 0 , \tag{10.39}$$

where R_s and u are related by $u = \Delta^{s/2}(r^2 + a^2)^{s/2} R_s$. A new field variable X can be defined by

$$X = \Delta^{s/2}(r^2 + a^2)^{1/2} \left[\alpha(r) R_s + \beta(r) \Delta^{s+1} \frac{dR_s}{dr} \right] . \tag{10.40}$$

The functions $\alpha(r)$ and $\beta(r)$ can be chosen such that the master equation satisfied by X has a real valued potential. For electromagnetic perturbations $(s = -1)$ the corresponding transformation is

$$\alpha = \frac{\tilde{a}\Delta + 1}{\kappa^{1/2}[\text{Re}(\tilde{a}\Delta) + 1]^{1/2}} , \quad \beta = \frac{\tilde{b}\Delta}{\kappa^{1/2}[\text{Re}(\tilde{a}\Delta) + 1]^{1/2}} , \tag{10.41}$$

where

$$a = [4K^2 + 2\Delta(iK' - \lambda)]/\Delta^2\kappa, \quad b = -4iK/\Delta\kappa ,$$
$$\kappa = (4\lambda^2 - 16a^2\omega^2 + 16a\omega m)^{\frac{1}{2}} , \tag{10.42}$$

and $\lambda \equiv \lambda_{lm}^s \equiv A_{lm}^s + a^2\omega^2 - 2am\omega$. The potential term is

$$V_r = \frac{-K^2 + \lambda\Delta}{(r^2 + a^2)^2} - \frac{\Delta r(\Delta r + 4Ma^2)}{(r^2 + a^2)^4}$$
$$+ \frac{\Delta[\Delta(10r^2 + 2\nu^2) - (r^2 + \nu^2)(11r^2 - 10rM + \nu^2)]}{(r^2 + a^2)^2[(r^2 + \nu^2)^2 + \eta\Delta]}$$
$$+ \frac{12\Delta r(r^2 + \nu^2)^2[\Delta r - (r^2 + \nu^2)(r - M)]}{(r^2 + a^2)^2[(r^2 + \nu^2)^2 + \eta\Delta]^2}$$
$$- \frac{\Delta(r - M)^2\eta[2(r^2 + \nu^2)^2 - \eta\Delta]}{(r^2 + a^2)^2[(r^2 + \nu^2)^2 + \eta\Delta]^2} , \tag{10.43}$$

where

$$\nu^2 = a^2 - am/\omega, \quad \eta = (\kappa - 2\lambda)/(4\omega^2). \tag{10.44}$$

As with our analysis of scalar modes, we take the limits $a \to 1$ and $\omega \to m/2$ and check whether there is a peak in the potential outside the horizon. After some calculation, we arrive at the condition for the existence of such a peak:

$$_{-1}A_{lm} > \frac{7}{4}m^2 . \tag{10.45}$$

For gravitational perturbations ($s = -2$) the transformation involves the functions

$$\alpha = \frac{2(a_1\Delta^2 i 1 a_2\Delta^2 + |\kappa|)}{|\kappa|(a_1\Delta^2 + |\kappa|)^{\frac{1}{2}}}, \; \beta = \frac{2ib_2\Delta^2}{|\kappa|(a_1\Delta^2 + |\kappa|)^{\frac{1}{2}}}, \tag{10.46}$$

with

$$
\begin{aligned}
a_1 &= \frac{8K^4}{\Delta^4} + \frac{8K^2}{\Delta^3}\left(\frac{M^2 - a^2}{\Delta} - \lambda\right) \\
&\quad + \frac{4\omega K}{\Delta^3}(3r^2 + 2Mr - 5a^2) + \frac{12r^2\omega^2 + \lambda(\lambda + 2)}{\Delta^2}, \\
a_2 &= \frac{-24\omega r K^2}{\Delta^3} - \frac{4\lambda(r - M)K}{\Delta} + 4\omega r\lambda + 12\omega M, \\
b_2 &= -\frac{8K^3}{\Delta^2} - \frac{4K}{\Delta}\left[\frac{2(M^2 - a^2)}{\Delta} - \lambda\right] - \frac{8\omega}{\Delta}(Mr - a^2),
\end{aligned}
\tag{10.47}
$$

and

$$
\begin{aligned}
\kappa &= [\lambda^2(\lambda + 2)^2 + 144a^2\omega^2(m - a\omega)^2 - a^2\omega^2(40\lambda^2 - 48\lambda) \\
&\quad + a\omega m(40\lambda^2 + 48\lambda)]^{\frac{1}{2}} + 12i\omega M,
\end{aligned}
\tag{10.48}
$$

and the new potential term is

$$V_r = \frac{-K^2 + \Delta\lambda}{(r^2 + a^2)^2} + \frac{\Delta(b_2 p'\Delta)'}{(r^2 + a^2)^2 b_2 p} + G^2 + \frac{dG}{dr_*}, \tag{10.49}$$

where $p = (a_1\Delta^2 + |\kappa|)^{-\frac{1}{2}}$. It turns out this potential gives the following criterion for existence of a peak outside the horizon:

$$_{-2}A_{lm} > \frac{7}{4}m^2 - 2. \tag{10.50}$$

There is another transformation listed in [21] which also gives a master equation with real-valued potential. After repeating the calculation above for the alternative transformation, it can be shown that Eq. (10.50) remains valid for the new potential. Combining Eq. (10.45), Eq. (10.50) and the criterion for the scalar modes, the condition for generic spin of the perturbations can be summarized by Eq. (10.11). If there is indeed a peak outside the horizon in the critical-BH-spin limit, it is often helpful to view the radial Teukolsky equation as a bound-state problem, as discussed in Sec. 10.5.2.

For a standard bound state problem in quantum mechanics, no matter how shallow the potential well is, there is always at least one bound state. For generic Kerr BHs (except Schwarzschild BHs), however, the dual bound-state problem has more complicated dependence on the eigenvalue, and it is nontrivial that any shallow potential well can support at least one bound state. In the original scattering problem, this means that even if there is a potential peak outside the horizon, there may not exist a DM associated with it. As the potential well becomes deeper and wider (δ^2 becomes

more and more negative), we know from WKB analysis that DMs must exist for these peaks. Based on our numerical investigations of gravitational QNMs up to $l = 15$ (summarized in Fig. 10.1), the presence of a peak outside the horizon is a necessary and sufficient condition for the existence of DMs.

Bibliography

[1] L. W. Brenneman *et al.*, Astrophys. J. **736**, 103 (2011).

[2] R. Wald, Ann. Phys., **83**, 548, (1974); S. Hod, Phys. Rev. Lett **100** 121101 (2008); T. Jacobson and T. P. Sotiriou, Phys. Rev. Lett **103**, 141101 (2009); E. Barausse, V. Cardoso, and G. Khanna, Phys. Rev. Lett **105**, 261102 (2010); P. Zimmerman, I. Vega, E. Poisson, and R. Haas (2012), arXiv:1211.3889.

[3] A. Strominger and C. Vafa, Phys. Lett. B **379**, 99 (1996).

[4] J. Bardeen and G. T. Horowitz, Phys. Rev. D **60**, 104030 (1999).

[5] M. Guica, T. Hartman, W. Song, and A. Strominger, Phys. Rev. D **80**, 124008 (2009); O. J. C. Dias, H. S. Reall, and J. E. Santos, JHEP **0908**, 101 (2009); I. Bredberg, C. Keeler, V. Lysov, and A. Strominger, Nucl. Phys. Proc. Suppl. **216**, 194 (2011); G. Compere, Living Rev. Rel. **15**, 11 (2012).

[6] G. Dotti, R. J. Gleiser, I. F. Ranea-Sandoval, and H. Vucetich, Class. Quant. Grav. **25**, 245012 (2008); P. Pani, E. Barausse, E. Berti, and V. Cardoso, Phys. Rev. D **82**, 044009 (2010); G. Dotti, R. J. Gleiser, and I. F. Ranea-Sandoval, Class. Quant. Grav. **29**, 095017 (2012); J. Lucietti and H. S. Reall, Phys. Rev. D **86**, 104030 (2012).

[7] E. Berti, V. Cardoso, and A. O. Starinets, Class. Quant. Grav. **26**, 163001 (2009).

[8] I. Bredberg, T. Hartman, W. Song, and A. Strominger, JHEP **1004**, 019 (2010).

[9] S. A. Teukolsky and W. H. Press, Astrophys. J **193**, 443 (1974).

[10] S. Detweiler, Astrophys. J **239**, 292 (1980).

[11] M. Sasaki and T. Nakamura, Gen. Rel. Grav. **22**, 1351 (1990).

[12] N. Andersson and K. Glampedakis, Phys. Rev. Lett. **84**, 4537 (2000).

[13] S. Hod, Phys. Rev. D **78**, 084035 (2008).

[14] V. Cardoso, Phys. Rev. D **70**, 127502 (2004).

[15] H. Yang, D. A. Nichols, F. Zhang, A. Zimmerman, Z. Zhang, and Y. Chen, Phys. Rev. D **86**, 104006 (2012).

[16] S. Hod, Phys. Lett. B **715**, 348 (2012).

[17] E. W. Leaver, Proc. R. Soc. A **402**, 285 (1985); E. W. Leaver, Phys. Rev. D **34**, 384 (1986).

[18] S. Chandrasekhar and V. Ferrari, Proc. Roy. Soc. Lond. A **434**, 449 (1991).

[19] H. Yang, F. Zhang, A. Zimmerman, D. A. Nichols, E. Berti, and Y. Chen, in preparation.

[20] S. Iyer and C. M. Will, Phys. Rev. D **35**, 3621 (1987).

[21] S. Detweiler, Proc. R. Soc. A **352**, 381, (1977).

[22] E. Berti, V. Cardoso, and S. Yoshida, Phys. Rev. D **69**, 124018 (2004); U. Keshet and A. B. Meir (2012), arXiv:1207:2460.

[23] E. D. Fackerell and R. G. Crossman, J. Math. Phys. **18**, 1849 (1977).

[24] R. Fujita and H. Tagoshi, Prog. Theor. Phys. **112**, 415 (2004).

[25] B. Mashhoon, Phys. Rev. D 31 290, (1985).

[26] K. Glampedakis, N. Anderson, Phys. Rev. D 64 104021, (2001).

[27] E. Harms, S. Bernuzzi, B. Brügmann, arXiv:1301.1591 (2013).

[28] E. Berti, V. Cardoso, and M. Casals, Phys. Rev. D **73** 024013 (2006).

Chapter 11

Scalar wave propagation in Kerr spacetime

In this article we try to obtain an analytical understanding of the scalar Green function of the Kerr spacetime. We first apply the spectral representation of the Green function, and obtain an approximate form of the part of Green function due to quasinormal mode contribution. This approximate analytical Green function diverges between points that are connected by null geodesics, and recovers the four-fold singular structure of Green functions that are seen in Schwarzschild [5] and other spacetimes [6]. This Green function also carries signatures of Kerr spacetime such as frame-dragging. We expect this work to benefit the understanding of wave propagation in Kerr spacetime, and perhaps the Kerr self-force problem in the long run.

Based on paper in preparation by H. Yang, A. Zimmerman, F. Zhang, and Y. Chen.

11.1 Introduction

Supermassive Black Holes (SMBHs), sometimes also referred to as Massive Black Holes (MBHs) are the black holes with masses higher than $10^5 \, M_\odot$; they are believed to exist in almost all galaxies. The closest example, Sagittarius A*, is the one at the center of our own galaxy, discovered by radio observations [1]. These stars usually are more than ~ 1000 Schwarzschild radii away from the SMBH, and possible to be driven much closer to the SMBH via the Kozai-mechanism [2] or or due to chaotic 3-body interaction [3]. Once a star moves into orbits close enough to the central SMBH, gravitational wave radiation takes over and the star will eventually merge into the SMBH due to radiation reaction.

One way to compute the effects of radiation reaction for a small object moving in a SMBH background (also referred as extreme mass ratio inspiral or EMRI) was proposed by Mino, Sasaki

and Tanaka [4]. The basic idea is to express the tail part of the metric perturbation as the convolution between Kerr gravitational Green function and the small object's stress energy tensor, and hence obtain the radiation reaction. In this formalism, it is physically clear how the test object sources gravitational perturbation which propagates in the curved spacetime and back-reacts onto its source. However, for realistic EMRI evolutions, it is highly nontrivial to obtain the Green function.

For a Schwarzschild background spacetime, Dolan and Ottewill [5] used a spectral method to relate the scalar Green function to quasinormal modes. By adopting a matched expansion technique, they managed to obtain an approximate analytical form of the Green function. Moreover, they showed the Green's function is singular on the lightcone, and that it has a four-fold singular structure as $\delta(\sigma), 1/\sigma, -\delta(\sigma), -1/\sigma$ (see Sec. V for detailed discussions), where σ is the Synge's world function. This four-fold singular structure matches the earlier expectation by Casals *et al.* [7, 8], which was proved by using the Hadamard ansatz for the Direct part of the Green's function. On the other hand, Zenginoglu and Galley [10] used numerical methods to obtain the time-domain scalar Green function in Schwarzschild background. They also observed the four-fold singular structure as caustic echoes.

In this work, we focus on studying the scalar Green function for a generic Kerr background. We use a spectral representation of the Green function similar to [5], and apply the WKB techniques developed in [12] to compute the quasinormal mode (QNM) contribution to the Green function. We will then show that this Green function is related to spherical photon orbits. In addition, we will compare our analytical Green functions with numerical computations.

This paper is organized as follows. In Sec. 11.2 we discuss the spectral representation of the scalar Green function. In Sec. 11.3 we review the WKB approximation for QNM frequencies and wavefunctions which are useful for later computations. In Sec. 11.4 we explicitly obtain the so-called excitation factors from WKB wave functions. We combine all results in Sec. 11.5, and deduce an approximate formula for the scalar Green function. We then discuss its four-fold singular structure, as well as its relation to trapped photons in spherical orbits. In Sec.V we compare our results with numerical simulations for several configurations. In Sec. 11.6, we summarize our conclusions.

11.2 Spectral decomposition

In this section we review the spectral decomposition of the scalar Green function and discuss its different components. In a generic spacetime, the scalar Green function satisfies the following equation:

$$\Box G_{\rm ret}(x, x') = \frac{1}{\sqrt{-g}} \partial_\mu \left(\sqrt{-g} g^{\mu\nu} \partial_\nu G_{\rm ret} \right) = \delta^{(4)}(x - x') \,. \tag{11.1}$$

We only consider the retarded Green function $G_{\text{ret}}(x, x')$, for which x' lies on or within the future lightcone of x. We shall use the Boyer-Lindquist coordinate, in which the line element is written as:

$$ds^2 = -\left(1 - \frac{2Mr}{\rho^2}\right) dt^2 - \frac{4aMr \sin^2 \theta}{\rho^2} dt d\phi + \frac{\rho^2}{\Delta} dr^2 + \rho^2 d\theta^2 + \sin^2 \theta \left(r^2 + a^2 + \frac{2Ma^2 r \sin^2 \theta}{\rho^2}\right) d\phi^2 .$$

(11.2)

Here $\Delta \equiv r^2 - 2Mr + a^2$ and $\rho^2 = r^2 + a^2 \cos^2 \theta$, M is the mass of the background black hole and a is its spin parameter. The scalar wave equation (11.1) in Kerr spacetime is separable in the frequency domain, and we can write down the following spectral decomposition of the Green function (see Appendix A for detailed derivations):

$$G_{\text{ret}}(x, x') = \frac{1}{2\pi \sqrt{r^2 + a^2} \sqrt{r'^2 + a^2}} \int d\omega e^{-i\omega(t - t')} \sum_m e^{im(\phi - \phi')} \sum_l S_{lm\omega}(\theta) S_{lm\omega}^*(\theta') \tilde{G}_{lm\omega}(r, r') .$$

(11.3)

For $a = 0$, the above expression clearly recovers the Schwarzschild limit in [5]. Here $S_{lm\omega}(\theta)$ is the spheroidal harmonic function; in [12], we obtained its analytical approximation in the case of $l \gg 1$ (we will also review this in Sec. 11.3). The function, $\tilde{G}$ is the radial Green function which satisfies

$$\frac{d^2 \tilde{G}}{dr_*^2} + \left[\frac{K^2 - \Delta \lambda^0}{(r^2 + a^2)^2} - H^2 - \frac{dH}{dr_*}\right] \tilde{G} = -\delta(r_* - r_*') ,$$

(11.4)

where

$$H = r\Delta/(r^2 + a^2)^2, \; K = ma - \omega(r^2 + a^2),$$

(11.5)

$$\frac{dr^*}{dr} = \frac{(r^2 + a^2)}{\Delta}, \; \lambda^0 = A_{lm} + a^2 \omega^2 - 2am ,$$

(11.6)

together with A_{lm} being the eigenvalue of the angular Teukolsky equation (11.20) and in-going (out-going) boundary condition at horizon (spatial infinity).

In order to solve for the Green's function, it is useful to look at the homogeneous solutions of the above equation. The in-going solution u_{in} satisfies Eq. (11.4) but without the source term on the right hand side. Moreover, u_{in} satisfies the in-going boundary condition at the background black hole's horizon

$$u_{\text{in}}(\omega, r) = \begin{cases} e^{-i\bar{\omega} r^*}, & r^* \to -\infty, \\ \\ C_{lm\omega}^- e^{-i\omega r^*} + C_{lm\omega}^+ e^{i\omega r^*}, & r^* \to \infty, \end{cases}$$

(11.7)

where $\bar{\omega} = \omega - ma/(2Mr_+)$ and r_+ is the horizon radius. Similarly, we can define out-going solution

u_{out} which satisfies the out-going boundary condition at spatial infinity:

$$u_{\text{out}}(\omega, r) \equiv \begin{cases} D^-_{lm\omega} e^{-i\bar{\omega}r^*} + D^+_{lm\omega} e^{i\bar{\omega}r^*}, & r^* \to -\infty, \\ \\ e^{i\omega r^*}, & r^* \to \infty. \end{cases} \tag{11.8}$$

The radial Green function can be constructed using the in-going and out-going homogeneous solutions above

$$\tilde{G}_{lm\omega}(r, r') = -\frac{u_{\text{in}}(r_<) u_{\text{out}}(r_>)}{W_{l\omega}}, \tag{11.9}$$

with $r_<$ given by $\min(r, r')$ and $r_>$ given by $\max(r, r')$; the Wronskian W_{lm} is given by

$$W_{l\omega} = u_{\text{in}} \frac{du_{\text{out}}}{dr^*} - u_{\text{out}} \frac{du_{\text{in}}}{dr^*}. \tag{11.10}$$

At some particular complex-valued frequencies ω_{lmn}, the in-going wave solution u_{in} also satisfies out-going boundary condition at infinity: $C^-_{lm\omega} = 0$. Given the boundary condition, apparently this solution must be a multiple of the out-going solution. In other words, u_{in} and u_{out} are degenerate with each other at these frequencies. As a consequence, the outgoing wave solution u_{out} must correspondingly satisfy the ingoing wave condition at the horizon: $D^+_{lm\omega} = 0$. This set of solutions is called the Quasinormal Mode (QNM), and from construction it is easy to see that at these QNM frequencies $D^-_{l\omega_{lmn}} C^+_{l\omega_{lmn}} = 1$ [apply equation (11.7), equation (11.8) and the degeneracy condition]. We can plug Eq. (11.9) back to Eq. (11.3) to perform the integral over frequency ω. Similar to the Schwarzschild case, this integral can be evaluated using the residue theorem and divided into three pieces. The first piece ("direct part") is the integral on the high frequency arc, it is expected to quickly approach zero after the initial pulse [11]. The second piece is the integral on the branch cut on the imaginary frequency axis, it contributes to the power-law decay at later times and is also non-negligible at early times [6]. The final piece comes from residues at poles whose frequencies correspond to those of the QNMs, and it is important only at early and mid times. In this work we shall focus on the QNM contribution to the Green's function and study its early to midtime behavior. It has the following form (with u_{out} replaced by u_{in} for simplicity, as they are degenerate at QNM frequencies):

$$G_{\text{QNM}}(x, x') = \frac{1}{2\pi\sqrt{r^2 + a^2}\sqrt{r'^2 + a^2}} \times$$
$$\left[\text{Re} \sum_m e^{im(\phi - \phi')} \sum_l S_{lm\omega}(\theta) S^*_{lm\omega}(\theta') \sum_n \mathcal{B}_{lmn} \tilde{u}_{\text{in}}(r) \tilde{u}_{\text{in}}(r') e^{-i\omega_{lmn}(t - t' - r^* - r'^*)} \right]. \tag{11.11}$$

As appeared earlier, ω_{lmn} is the quasi-normal mode frequency with spheroidal harmonic index l, m

and overtone number n (except for near extreme Kerr black holes, which may have two branches of QNMs). The coefficient $\mathcal{B}_{lmn}$ is usually referred to as the "black hole excitation number", because it is the multiplication constant characterizing each QNM's contribution to the Green function. It is given by

$$\mathcal{B}_{lmn} \equiv \left[\frac{C^+_{lm\omega}}{2\omega} \left(\frac{\partial C^-_{lm\omega}}{\partial \omega} \right)^{-1} \right]_{\omega=\omega_{lmn}}. \tag{11.12}$$

Apparently, $\mathcal{B}_{lmn}$ depends on the gauge freedom of r_*: if $r_* \to r_* + C$ [see Eq. (11.6)], we have $\mathcal{B}_{lmn} \to \mathcal{B}_{lmn} e^{-2i\omega_{lmn}C}$. In this paper, we will choose

$$r_* = r + \frac{2r_+}{r_+ - r_-} \log\left(\frac{r}{r_+} - 1 \right) - \frac{2r_-}{r_+ - r_-} \log\left(\frac{r}{r_-} - 1 \right), \tag{11.13}$$

where $r_\pm = 1 \pm \sqrt{1 - a^2}$ are the outer- and inner-horizon radii. It is also easy to check that for $a = 0$ the above expression reduces to the commonly used relation: $r_* = r + 2\log(r/2 - 1)$ for Schwarzschild black holes. In Eq. (11.11), we have also used a normalized in-going wave solution $\tilde{u}_{\rm in}(r)$ (see also [5])

$$\tilde{u}_{\rm in}(r) \equiv u_{\rm in}(r) \times \left[C^+_{lm\omega} e^{i\omega_{lmn}r_*} \right]^{-1} \tag{11.14}$$

such that it asymptotically approaches 1 when $r \to +\infty$. In the following sections, we will use WKB analysis and matched expansion techniques to obtain approximate analytical forms of $S_{lm\omega}, \tilde{u}_{\rm in}$ and $\mathcal{B}_{lmn}$. After that we will evaluate the summation in Eq. (11.11) for $G_{\rm QNM}(x, x')$ and discuss its implications.

11.3 QNMs in the eikonal limit

In order to evaluate the summation in Eq. (11.11) to obtain the QNM part of the Green function, we have to insert the frequencies and wavefunctions of all QNMs. While the exact frequencies and wavefunctions can only be obtained numerically, analytical approximations for them are available in the eikonal limit $l \gg 1$. In this section, we will review the WKB analysis on Kerr BH's QNM frequencies and wave functions based on [12]. The same technique will be applied in the next section.

Before we proceed, let us define a set of variables for later convenience: $L \equiv l + 1/2$, $N \equiv n + 1/2$ (where n is the overtone number), $\beta \equiv m/L$. In the eikonal limit, QNM frequencies are given by

$$\omega_{lmn} = \omega_R - i\omega_I = Lf(\beta, a) - iN\lambda(\beta, a) + O(1/L) \tag{11.15}$$

The function dependence of $f(\beta, a)$ and $\lambda(\beta, a)$ can be found in [12] (in which f, λ are referred as Ω_R, Ω_I respectively). In the case of a Schwarzschild background with $a = 0$, $f = \lambda = 1/\sqrt{27}$, they are both constants. In fact, for generic Kerr black holes, the function $f(\beta, a)$ can be determined by

the orbital and precession frequencies of some particular spherical photon orbit (β can be viewed as parameterization of all spherical photon orbits), while $\lambda(\beta, a)$ is given by the Lyapunov exponent of the same orbit. This correspondence gives a geometric meaning to QNMs and interested readers can find more details in [12].

11.3.1   The radial wavefunction

As shown by Teukolsky [9], the angular and radial dependencies can be separated in the frequency domain. QNM wave functions can also be approximated analytically using WKB analysis. The radial wavefunction u_{in} describes a scattering problem

$$\frac{d^2 u_{\text{in}}}{dr_*^2} + Q(\omega, r)u_{\text{in}} = \frac{d^2 u_{\text{in}}}{dr_*^2} + \frac{K^2 - \Delta\lambda^0}{(r^2 + a^2)^2}u_{\text{in}} = 0 \,. \tag{11.16}$$

It is easy to see that $Q(\omega, r)$ is on the order of L^2 and lower order terms of L have been dropped out from the potential (Here ω is a QNM frequency). It is natural to apply a WKB expansion with expansion parameter scaling as $1/L$:

$$u(r) \sim e^{S_0 + S_1 + \cdots}$$

$$S_0 = \pm i \int^{r_*} \sqrt{Q(\omega, r)}dr_*,$$

$$S_1 = -\frac{1}{4}\log[Q(\omega, r)] \,. \tag{11.17}$$

S_0 contributes mostly to the phase and S_1 contributes mostly to the amplitude. Since S_0 scales as L and S_1 scales as $\log L$, the phase varies much faster than the amplitude. In addition, because $\omega = \omega_R - i\omega_I$ is a complex number and $\omega_R \propto L^1$, $\omega_I \propto L^0$ ($\omega_R \gg \omega_I$), $Q(\omega_{lmn}, r)$ is mostly real and S_0 also contains a relatively small real part, which contributes to the amplitude factor. We can single it out by further expanding $Q(\omega_{lmn}, r)$ as $Q(\omega_R, r) - i\omega_I \partial Q/\partial \omega$ and correspondingly S_0 becomes

$$S_0 \approx \pm i \int^{r_*} \sqrt{Q(\omega_R, r)}dr_* \pm \int^{r_*} \frac{1}{2}\frac{\partial_\omega Q|_{\omega_R}\omega_I}{\sqrt{Q(\omega_R, r)}}\,dr_* \,, \tag{11.18}$$

and for obvious reasons we only keep the leading order term for S_1

$$S_1 \approx -\frac{1}{4}\log[Q(\omega_R, r)] \,. \tag{11.19}$$

According to [12] (also see Fig. 11.2), $Q(\omega_R, r)$ is a positive function except at its extrema (also referred as the peak of the potential in [12]), where $r = r_{\text{peak}}$ and $Q(\omega_R, r_{\text{peak}}) = 0$. It is important to notice that this WKB analysis breaks down near the peak of the potential function where $Q(\omega_R, r_{\text{peak}}) \to 0$. This means Eq. (11.17) only works well outside the peak regime, and we

need a separate treatment for the wavefunction in the peak regime to connect to solutions on both sides of the peak. This matched-expansion procedure will be carried out in the next section, where we work out the "black hole excitation factor".

11.3.2 The angular wavefunction

The angular Teukolsky equation has the following form

$$
\frac{d}{\sin\theta d\theta}\left(\sin\theta\frac{du_\theta}{d\theta}\right) + (a^2\omega^2\cos^2\theta - \frac{m^2}{\sin^2\theta} +_s A_{lm})u_\theta
$$
$$
+ \left(-2a\omega s\cos\theta - \frac{2ms\cos\theta}{\sin^2\theta} - s^2\cot^2\theta + s\right)u_\theta = 0\,. \tag{11.20}
$$

where s is the spin index for the perturbation field: $s = 0,\ -1,\ -2$ corresponds to scalar, electromagnetic and gravitational perturbations respectively. All the terms containing s in the potential are sub-leading in L and we shall neglect them from now on. This angular Teukolsky equation can also be written in a form suitable for WKB analysis. Define $x \equiv \log[\tan(\theta/2)]$, the angular Teukolsky equation becomes

$$
\frac{d^2 u_\theta}{dx^2} + V^\theta u_\theta = 0\,, \tag{11.21}
$$

with

$$
V^\theta = a^2\omega^2\cos^2\theta\sin^2\theta - m^2 + A_{lm}\sin^2\theta \equiv \Theta\sin^2\theta\,. \tag{11.22}
$$

It is straightforward to show that this equation describes a bound state problem with V^θ serving as the potential well [12]. For $x \to \pm\infty$ $(\theta \to \pi/0)$, V^θ becomes negative and the wave solution tends to decay to zero: $u_\theta \to e^{-|mx|}$, so the wavefunction is trapped inside the potential well. By applying WKB expansion to the second order it is straightforward to obtain

$$
u_\theta \approx \frac{1}{(\Theta\sin^2\theta)^{1/4}}e^{\pm i\int^\theta\sqrt{\Theta}d\theta}\,. \tag{11.23}
$$

Similar to the radial potential, we can expand Θ as $\Theta_R + i\Theta_I$ and they are separately given by

$$
\Theta_R = a^2\omega_R^2\cos^2\theta - \frac{m^2}{\sin^2\theta} + A_R\,, \tag{11.24}
$$
$$
\Theta_I = A_I - 2a^2\omega_R\omega_I\cos^2\theta\,, \tag{11.25}
$$

where $A_{lm} = A_R + iA_I$. Here $A_R \propto L^2$ and $A_I \propto L$, and hence $\Theta_R \propto L^2$ and $\Theta_I \propto L$. Using the expansion for Θ, we can then separate the phase and amplitude contributions in the wavefunction u_θ, and write as

$$
u_\theta \approx \frac{1}{(\Theta_R\sin^2\theta)^{1/4}}e^{\pm i\int^\theta\sqrt{\Theta_R}d\theta \mp 1/2\int^\theta\Theta_I/\sqrt{\Theta_R}d\theta}\,. \tag{11.26}
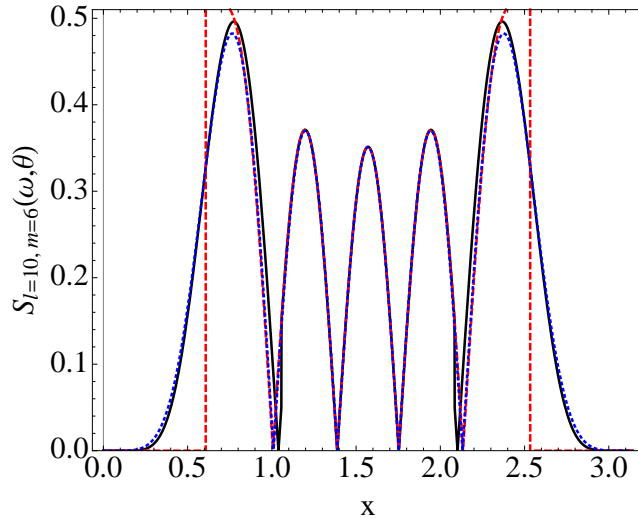$$

Figure 11.1: (Color online.) WKB approximated wavefunction for $l = 10, m = 6$ spherical harmonics. The red dashed line corresponds to the WKB wavefunction described by Eq. (11.27), it blows up at the classical boundary and values outside the boundary are set to zero. The blue dotted line is the exact Y_{lm} function. The solid black line corresponds to the solution we obtained by matching the Airy function near the classical boundary with Eq. (11.27).

We recall that the solutions for Eq. (11.20) are the spin-weighted spheroidal harmonics. After neglecting the spin index s, u_θ should just be the spheroidal harmonic function $S_{lm}(\omega, \theta)$. More precisely speaking, $S_{lm}(\omega, \theta)$ is a linear combination of the above two solutions

$$S_{lm\omega} = \frac{C}{(\Theta_R \sin^2 \theta)^{1/4}} (e^{i \int_{\pi/2}^\theta \sqrt{\Theta_R} d\theta - 1/2 \int_{\pi/2}^\theta \Theta_I / \sqrt{\Theta_R} d\theta} + (-1)^{l+m} e^{-i \int_{\pi/2}^\theta \sqrt{\Theta_R} d\theta + 1/2 \int_{\pi/2}^\theta \Theta_I / \sqrt{\Theta_R} d\theta}),$$
(11.27)

where C is some constant which can be fixed by normalization condition $\int S_{lm\omega} S^*_{lm\omega} d\Omega = 1$, or

$$2\pi C^2 \int \frac{d\theta}{\sqrt{\Theta_R}} (e^{- \int_0^\theta \Theta_I / \sqrt{\Theta_R} d\theta} + e^{\int_0^\theta \Theta_I / \sqrt{\Theta_R} d\theta}) = 1.$$
(11.28)

According to [12], $d\theta/\sqrt{\Theta_R} = d\xi$ where ξ is the "Mino time", and the integral is performed in the "classical regime" where $\Theta_R \geq 0$. In addition, we have

$$\begin{aligned} A_I &= 2a^2 \omega_R \omega_I \langle \cos^2 \theta \rangle \\ &= 2a^2 \omega_R \omega_I \frac{\int d\xi \cos^2 \theta}{\int d\xi} = 2a^2 \omega_R \omega_I \frac{\int d\xi \cos^2 \theta}{\xi_0}. \end{aligned}$$
(11.29)

As a result, Eq. (11.28) can be rewritten in a form that is related to geometric optics and spherical photon orbits

$$2\pi C^2 \int_{\text{one cycle}} d\xi (e^{-2a^2 \omega_R \omega_I \int_0^\xi (\cos^2 \theta - \langle \cos^2 \theta \rangle) d\xi'} + e^{2a^2 \omega_R \omega_I \int_0^\xi (\cos^2 \theta - \langle \cos^2 \theta \rangle) d\xi'}) = 1.$$
(11.30)

Because black hole "rotation" breaks parity symmetry, $S_{lm\omega}$ no longer satisfies the parity relation $S_{lm\omega}(\pi - \theta, \pi + \phi) \neq (-1)^l S_{lm\omega}(\theta, \phi)$ [although for spherical harmonics $Y_{lm}(\pi - \theta, \pi + \phi) = (-1)^l Y_{lm}(\theta, \phi)$ is true].

As WKB approximation breaks down near the classical boundary $\Theta_R(\theta_{\pm}) = 0$, separate treatment has to be taken if we want to extend the wavefunction outside the classical regime. In Fig. 11.1, we compare the wavefunction generated by Eq. (11.27) with exact spherical harmonics (for simplicity, we take $a = 0$). The dashed red line is predicted by Eq. (11.27). It fits the exact spherical harmonic function (blue dotted line) pretty well except near the classical boundary, where the WKB approximation breaks down and the WKB wavefunction blows up. In order to take care of the wavefunction near the classical boundary, we can expand V_θ as $(x - x_{\pm})V' \approx \partial_x V|_{x_{\pm}} (x - x_{\pm})$ and try to solve

$$\frac{d^2 u}{dx^2} + (x - x_{\pm})V'u = 0 \,. \tag{11.31}$$

The solution turns out to be an Airy function,

$$u \sim \text{Airy}[(2L^2\beta^2\sqrt{1 - \beta^2})^{1/3}(x - x_{\pm})] \tag{11.32}$$

which can be matched with Eq. (11.27) in some buffer zone to fix its coefficient. In the end we can just replace Eq. (11.27) with the above wavefunction near the classical boundary and obtain a better estimate. The solid black line in Fig 11.1 is generated using this method, and it fits with Y_{lm} pretty well globally. Since one can show that the boundary treatment only contributes sub-leading WKB terms for Green function, later in the paper we will just use Eq. (11.27) to approximate the angular wavefunction.

11.4   Matched expansions

Given the frequency and wave function of each QNM, the last quantity that needs to be computed is the "black hole excitation factor" $\mathcal{B}_{lmn}$ defined in Eq. (11.12). This quantity determines the weight of each QNM's contribution to the Green function [Cf. Eq. (11.11)]. Because the amplitude of the wave can be expressed as the convolution between the Green function and source, this "black hole excitation factor" also determines the weights of each QNM excitation due to a source distribution.

According to Eq. (11.12), in order to compute $\mathcal{B}_{lmn}$, we have to obtain the frequency dependence of the reflection coefficients of both in-going and out-going wave solutions (i.e. $C^-_{l\omega_{lmn}}$ and $C^+_{l\omega_{lmn}}$). As we recall from WKB analysis on radial Teukolsky equations in Sec. 11.3, the scattering potential term $Q(\omega_R, r)$ is approximately zero near its peak, and that is where all the WKB expansions fail. In fact, the WKB approximation works in two separate regions: one on each side of the scattering potential. In order to relate the boundary conditions at the horizon to those at spatial infinity we
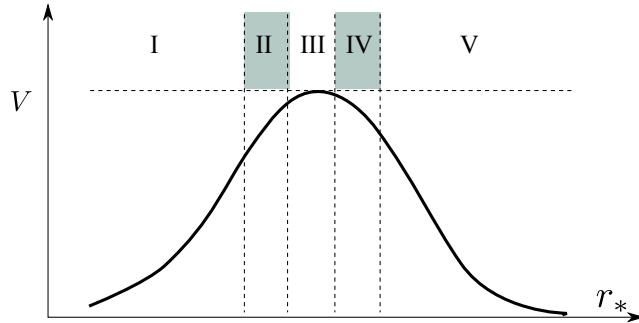
Figure 11.2: (Color online.) Different regimes for the radial wavefunction. WKB analysis are valid in regime I, II, IV and V. The scattering-peak regime is located at II,III and IV. Regime II and IV are the buffer zones to match near-peak and WKB solutions.

have to connect the WKB solutions on both sides of the scattering potential. This can be done by writing down a separate solution near the peak of the potential and then, matching it separately with WKB solutions on both sides and then fixing the reflection coefficients. This matched expansion procedure is also illustrated in Fig 11.2.

11.4.1 Wavefunction near the peak of the scattering potential

We start the matching procedure by solving the radial Teukolsky in the potential-peak regime (regions II, III & IV in Fig. 11.2). Suppose the peak is located at $r = r_p$ or $r_* = r_{*p}$. By definition, we have

$$\frac{\partial Q(\omega_R, r)}{\partial r}\bigg|_{r=r_p} = 0 \,. \tag{11.33}$$

Combing with the fact that the potential term also equals zero at its peak $Q(\omega_R, r_p) = 0$ [12] [1], we can Taylor-expand $Q(\omega, r)$ in the potential-peak regime (assuming $\omega = \omega_R - i\omega_I + \epsilon$) [12],

$$
\begin{aligned}
Q(\omega, r) &= \frac{1}{2} Q_0''(\omega_R, r_p)(r_* - r_{*p})^2 + \frac{\partial Q}{\partial \omega}\bigg|_{\omega_R}(\epsilon - i\omega_I) \\
&= \frac{1}{2} Q_0''(r_* - r_{*p})^2 + (n + \frac{1}{2})\sqrt{2Q_0''}(-i + \frac{\epsilon}{\omega_I}) \\
&\equiv \sqrt{k}z^2 + 2N\sqrt{k}(-i + \frac{\epsilon}{\omega_I}) \,,
\end{aligned}
\tag{11.34}
$$

where $Q_0'' \equiv \partial_{r_*}^2 Q|_{r=r_p}$ is positive near the peak of the potential, and

$$z = (k)^{1/4}(r_* - r_{*p}) = (k)^{1/4}(r - r_p)\frac{r_p^2 + a^2}{\Delta_p}, \; k \equiv \frac{1}{2}Q_0'' \equiv \kappa L^2 \,. \tag{11.35}$$

Since $k \propto L^2$, the rescaled radial position parameter z is proportional to $\sqrt{L}$. Therefore for small

---

[1]Note in the geometric correspondence picture, $Q = Q' = 0$ is the condition for a massless particle to stay on the unstable spherical photon orbit

but finite $r - r_p$, in which case the leading order Taylor expansion is accurate, the corresponding z goes from 0 to infinity as we take the eikonal limit $L \to \infty$. In order to perform the matching, we need to set boundary conditions for the peak-regime. This can be done by taking $z \to \pm\infty$, which is satisfied in region II and IV of Fig. 11.2.

Defining $\psi \equiv u_r$ as the radial wavefunction, with the new set of variables defined above, the radial Teukolsky equation can be re-written in a more compact form

$$\frac{d^2\psi}{dz^2} + \left[z^2 + 2N(-i + \frac{\epsilon}{\omega_I}) \right] \psi = 0 \,. \tag{11.36}$$

The solutions of the above equation can be expressed by parabolic cylinder functions (see the expressions below). The two independent solutions are given by

$$\psi_1 = D_{n+\eta}(z(-1+i)), \ \psi_2 = D_{n+\eta}(z(1-i)) \,, \tag{11.37}$$

where $\eta = i\epsilon/\lambda$ and n is the overtone number. In order to satisfy the ingoing boundary condition at the horizon, we have to pick ψ_1 as the solution (see the following section). In regime II and IV of Fig.2, the asymptotic behavior of ψ_1 is

$$\psi_1 \equiv \begin{cases} 2^{n/2}e^{-in\pi/4}|z|^n e^{iz^2/2} \,, & z \to -\infty \,, \\ \\ 2^{n/2}e^{3in\pi/4}|z|^n e^{iz^2/2} + \eta\Gamma(n+1)(2\pi)^{1/2}e^{-3i\pi(n+1)/4}2^{-(n+1)/2}|z|^{-(n+1)}e^{-iz^2/2} \,, & z \to \infty \,. \end{cases} \tag{11.38}$$

11.4.2 WKB wavefunctions away from the peak of the scattering potential

We must match ψ_1 with the WKB solution away from the peak of the scattering potential. Let us recall the WKB solutions in Eq. (11.17), and single out part of the r dependence for later convenience:

$$u_\pm = \frac{1}{(Q(\omega_R, r))^{1/4}} |r_* - r_{*p}|^{\pm(n+1/2)} e^{\bar{S}_0} \,, \tag{11.39}$$

where $\bar{S}_0$ is given by

$$\bar{S}_0 = \begin{cases} \pm i \int_{r_{*p}}^{r_*} \sqrt{Q(\omega_R, r)} dr_* \pm \int_{r_{*p}}^{r_*} \left[\frac{1}{2} \frac{\frac{\partial Q}{\partial \omega}|_{\omega_R} \omega_I}{\sqrt{Q(\omega_R, r)}} - \frac{n+1/2}{|r_* - r_{*p}|} \right] dr_* \,, & z > 0 \,, \\ \\ \pm i \int_{r_p}^{r_{*p}} \sqrt{Q(\omega_R, r)} dr_* \pm \int_{r_p}^{r_{*p}} \left[\frac{1}{2} \frac{\frac{\partial Q}{\partial \omega}|_{\omega_R} \omega_I}{\sqrt{Q(\omega_R, r)}} - \frac{n+1/2}{|r_* - r_{*p}|} \right] dr_* \,, & z < 0 \,. \end{cases} \tag{11.40}$$

The $r \to r_p$ limit of this solution should match with the $z \to \pm\infty$ limit of ψ_1. As discussed in Sec. 11.3, the first integral in the above expression for $\bar{S}_0$ corresponds to the phase and the second integral contributes to the amplitude. With the $(r_* - r_{*p})^{\pm(n+1/2)}$ being singled out, the amplitude factor in $\bar{S}_0$ asymptotes zero in the $r \to r_p$ limit. Taking the limit that $r \to r_p$ but keeping $|z| \to \infty$, [2], i.e, in the buffer zone II and IV, the WKB solution in Eq. (11.39) can be greatly simplified using the rescaled radial position z:

$$u_{\pm} = k^{-1/4} \left(\frac{|z|}{k^{1/4}} \right)^{-1/2 \pm (n+1/2)} e^{\pm i z^2 / 2} \,. \tag{11.41}$$

It is worth pointing out that u_+ is the "out-going" solution when $r > r_p$ and the "in-going" solution when $r < r_p$ (and vice versa for u_-). This is because $\sqrt{Q(\omega_R, r)} \approx k^{1/4} z$ for $z > 0$ and $-k^{1/4} z$ for $z < 0$. With this property, we will show that for QNMs u_+ will be the only surviving solution.

For generic frequencies, in order to compute the "black hole excitation factor", we also have to know the asymptotic behavior of $u_{\pm}$ in the limit $r_* \to \pm\infty$. For later convenience we will define the following phase factor:

$$-\omega_R r_{*p} + \int_{r_{*p}}^{\infty} (\sqrt{Q(\omega_R, r)} - \omega_R) dr_* \equiv L\alpha_1(\beta, a) \,,$$

$$\bar{\omega}_R r_{*p} + \int_{-\infty}^{r_{*p}} (\sqrt{Q(\omega_R, r)} - \bar{\omega}_R) dr_* \equiv L\alpha_2(\beta, a) \,. \tag{11.42}$$

Here $\bar{\omega}_R \equiv \omega_R - ma/(2Mr_+)$ is the radial frequency for QNMs approaching the horizon. The phases α_1 and α_2 are both finite numbers, which have the physical meaning of the accumulated phase errors at the position of the peak, if we were to extrapolate the $|r_*| \to \infty$ wavefunctions to the near zone. Similarly, we can define the accumulated amplitude factor as follows:

$$\int_{r_{*p}}^{r_1} \left[\frac{1}{2} \frac{\frac{\partial Q}{\partial \omega}|_{\omega_R} \omega_I}{\sqrt{Q(\omega_R, r)}} - \frac{N}{r_* - r_{*p}} \right] dr_* + N \log(r_1 - r_{*p}) - \omega_I r_1 + \int_{r_1}^{\infty} \left[\frac{1}{2} \frac{\frac{\partial Q}{\partial \omega}|_{\omega_R} \omega_I}{\sqrt{Q(\omega_R, r)}} - \omega_I \right] dr_*$$

$$\equiv N\gamma_1(\beta, a) \,,$$

$$\int_{r_2}^{r_{*p}} \left[\frac{1}{2} \frac{\frac{\partial Q}{\partial \omega}|_{\omega_R} \omega_I}{\sqrt{Q(\omega_R, r)}} - \frac{N}{r_{*p} - r_*} \right] dr_* + N \log(r_{*p} - r_2) + \omega_I r_2 + \int_{-\infty}^{r_2} \left[\frac{1}{2} \frac{\frac{\partial Q}{\partial \omega}|_{\omega_R} \omega_I}{\sqrt{Q(\omega_R, r)}} - \omega_I \right] dr_*$$

$$\equiv N\gamma_2(\beta, a) \,, \tag{11.43}$$

where r_1, r_2 are two constants satisfying $r_1 > r_{*p}$ and $r_2 < r_{*p}$. By taking the derivative of the above expressions with respect to r_1, r_2, it is straightforward to show that γ_1 and γ_2 are independent of the choices of r_1, r_2. We introduce extra terms $N/(r_* - r_{*p})$ and ω_I into the integrands to make

---

[2]For example, this can be achieved by requiring $r_* - r_{*p} \propto L^{-1/4}$. In the $L \to \infty$ limit, obviously we have $r \to r_p$ and $|z| \to \infty$.
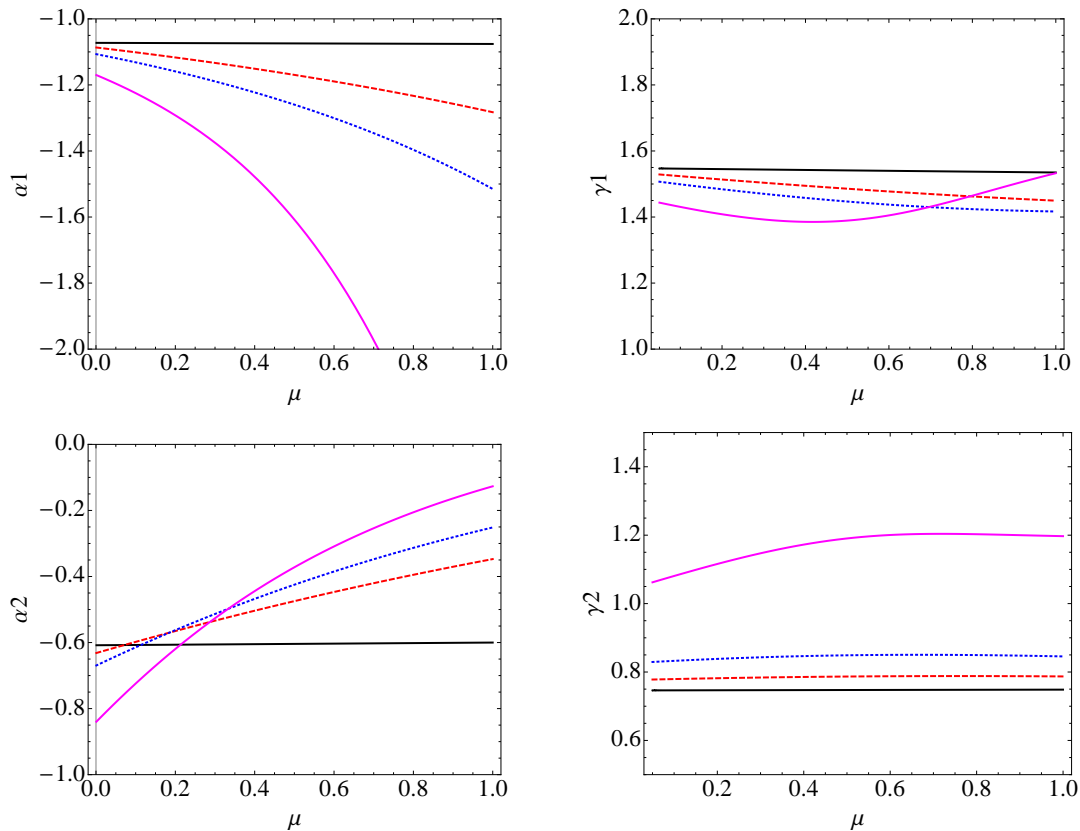
Figure 11.3: (Color online.) Amplitude and phase factors for different a and μ. Black solid lines correspond to $a = 0$, they are flat because of the spherical symmetry. Red dashed lines correspond to $a = 0.4$. Blue dotted lines correspond to $a = 0.6$. Magenta solid lines are for $a = 0.9$.

sure the integrals are well defined in the $r \to r_p$ or $|r_*| \to \infty$ limit.

We explore the dependence of $\alpha_1, \alpha_2, \gamma_1, \gamma_2$ on a and β in Fig. 11.3. For Schwarzschild black holes with $a = 0$, the corresponding $\gamma_1, \gamma_2, \alpha_1, \alpha_2$ are all constants, because Schwarzschild QNMs do not depend on β or azimuthal quantum number m. As a increases towards 1, all these phase and amplitude factors quickly gain their dependence on β.

11.4.3 Matching solutions

The next step is to match the interior and exterior solutions in the buffer zone II and IV. The solution ψ_1 of the scattering-peak regime can be written as

$$\psi_1 \equiv \begin{cases} C_{\text{in}} u_+ & z \to -\infty \,, \\ \\ B_{\text{in}} u_- + B_{\text{out}} u_+ \,, & z \to \infty \,, \end{cases} \tag{11.44}$$

by comparing it with Eq. (11.41), we can read off the coefficients C_{in}, B_{in}, B_{out},

$$C_{\text{in}} = k^{(n+1)/4} 2^{n/2} e^{-in\pi/4}, \ B_{\text{out}} = C_{\text{in}}(-1)^n \,, \tag{11.45}$$

$$B_{\text{in}} = \eta \Gamma(n+1)(2\pi)^{1/2} e^{-3i\pi(n+1)/4} 2^{-(n+1)/2} k^{-n/4} \,. \tag{11.46}$$

For QNMs η and ϵ are both zero. According to Eq. (11.45), B_{in} is zero and u_+ is the only surviving solution, as we expected. Now we can write down the asymptotic behavior of u_+ near horizon or spatial infinity:

$$u^+ = \begin{cases} (\bar{\omega}_R)^{-1/2} e^{-i\bar{\omega}_{lmn} r_* + iL\alpha_2 + N\gamma_2}, & r_* \to -\infty \,, \\ \\ (\omega_R)^{-1/2} e^{i\omega_{lmn} r_* + iL\alpha_1 + N\gamma_1}, & r_* \to +\infty \,, \end{cases} \tag{11.47}$$

and similarly for u^- in the case of $r_* \to +\infty$ (u^- in the $r_* \to -\infty$ limit turns out to be not useful in our case);

$$u^- = (\omega_R)^{-1/2} e^{-i\omega_{lmn} r_* - iL\alpha_1 - N\gamma_1}, \ r_* \to +\infty \,. \tag{11.48}$$

By comparing Eq. (11.47) and Eq. (11.48) with Eq. (11.7), Eq. (11.44) and Eq. (11.45), we can show that

$$C_{lm\omega}^+ = \sqrt{\frac{\bar{\omega}_R}{\omega_R}} \frac{B_{\text{out}}}{C_{\text{in}}} e^{iL(\alpha_1 - \alpha_2) + N(\gamma_1 - \gamma_2)}$$

$$C_{lm\omega}^- = \sqrt{\frac{\bar{\omega}_R}{\omega_R}} \frac{B_{\text{in}}}{C_{\text{in}}} e^{iL(-\alpha_1 - \alpha_2) + N(-\gamma_1 - \gamma_2)} \,. \tag{11.49}$$

Therefore the back hole excitation factor is just given by

$$\begin{aligned} \mathcal{B}_{lmn} &= \left[\frac{C_{lm\omega}^+}{2\omega} \left(\frac{\partial C_{lm\omega}^-}{\partial \omega} \right)^{-1} \right]_{\omega = \omega_{lmn}} \\ &= e^{2iL\alpha_1 + 2N\gamma_1} \frac{\lambda}{2\omega_{lmn}} 2^n k^{n/2} \sqrt{\frac{i\sqrt{k}}{\pi}} \frac{(-i)^n}{n!} \\ &\approx e^{2iL\alpha_1 + 2N\gamma_1} \frac{\lambda\sqrt{L}}{2\omega_R} \sqrt{\frac{i\sqrt{\kappa}}{\pi}} \frac{(-i2\sqrt{\kappa}L)^n}{n!} \\ &\equiv \frac{B}{\sqrt{L}} e^{2iL\alpha_1} \frac{(-i\xi L)^n}{n!} \end{aligned} \tag{11.50}$$

with the constants B, ξ given by (note $\omega_R = Lf(\beta, a)$),

$$B = \frac{e^{\gamma_1}\Omega_I}{2\Omega_R} \sqrt{\frac{i\sqrt{\kappa}}{\pi}}, \ \xi = 2\sqrt{\kappa} e^{2\gamma_1} \,. \tag{11.51}$$

As we neglected the sub-leading terms in L, the error of the expression for $\mathcal{B}_{lmn}$ scales as $L^{n-3/2}$

(relative error $1/L$). For $a = 0$, it is straightforward to check that $\mathcal{B}_{lmn}$ recovers the Schwarzschild "black hole excitation factor" derived in [5]. For generic Kerr black holes, we can check our WKB "black hole excitation factor" against the numerical value obtained using Leaver's methods [13], and the agreement is decent, even for a close to 1.

11.5   The Green fucntion

In this section, we will combine all previous results on QNM frequencies, wave functions and the "black hole excitation factor" to obtain an approximate Green function in the analytical form.

11.5.1   Summation over of all QNM contributions and the singular structure

Now we are ready to evaluate the summation in Eq. (11.11) to obtain the Green function in the eikonal limit. The spheroidal harmonic function $S_{lm\omega}(\theta)$ in the eikonal is discussed in Sec. 11.3 and the normalized "in-going" radial function $\tilde{u}_{\mathrm{in}}(r)$ can be expressed by (for now we are only interested in the case r, r' both outside potential barrier)

$$\tilde{u}_{\mathrm{in}}(r) = U(r)[\rho(r)]^n e^{-iL\tilde{\alpha}_1(r)}, \tag{11.52}$$

with $U(r), \rho(r)$ and $\tilde{\alpha}_1(r)$ given by

$$\tilde{\alpha}_1(r) \equiv \frac{1}{L} \int_{r_*}^{\infty} (\sqrt{Q(\omega_R, r)} - \omega_R) dr_* \tag{11.53}$$

$$\log(\rho(r)) \equiv -\int_{r_*}^{\infty} \lambda(\beta, a) \left[\frac{1}{2} \frac{\frac{\partial Q}{\partial \omega}|_{\omega_R}}{\sqrt{Q(\omega_R, r)}} - 1 \right] dr_* \tag{11.54}$$

$$U(r) \equiv \omega_R^{1/2} \sqrt{\frac{\rho(r)}{\sqrt{Q(\omega_R, r)}}}. \tag{11.55}$$

Note that $\rho(r) \propto (r_* - r_{*p})$ and $Q(\omega_R, r) \propto k(r_* - r_{p*})^2$ when $r \to r_p$, so $U(r)$ converges to a constant when $r \to r_p$. Equation (11.11) contains the summation over n, m, l. We can first evaluate the summation over overtone in Eq. (11.11)

$$\sum_n \mathcal{B}_{lmn} e^{\pm \int_0^\theta \Theta_I / \sqrt{\Theta_R} d\theta} \tilde{u}_{\mathrm{in}}(r) \tilde{u}_{\mathrm{in}}(r') e^{-N(t-t'-r_*-r'_*)}$$

$$= \frac{B}{\sqrt{L}} e^{iL(2\alpha_1 - \tilde{\alpha}_1(r) - \tilde{\alpha}(r'))} e^{\lambda/2T} e^{\pm \Upsilon(\theta,\theta')/2} U(r) U(r')$$

$$\times \sum_n \frac{(-i\kappa\gamma_1 \rho(r)\rho(r')L)^n e^{-n\lambda(\beta,a)T} e^{\pm n\Upsilon(\theta,\theta')} + O(L^{n-1})}{n!}$$

$$\approx \frac{B}{\sqrt{L}} e^{iL\left[\bar{\alpha}_1(r)+\bar{\alpha}_1(r')-\kappa\gamma_1\rho(r)\rho(r')e^{-\lambda(\beta,a)T\pm\Upsilon(\theta,\theta')}\right]} e^{\lambda/2T} U(r)U(r') e^{\pm\Upsilon(\theta,\theta')/2} \tag{11.56}$$

with $T = t - t' - r_* - r_{*'}$ and

$$\Upsilon(\theta,\theta') = \int_{\pi/2}^{\theta} \frac{2a^2\omega_R\lambda(\beta,a)(\langle\cos^2\theta\rangle - \cos^2\theta)}{\sqrt{\Theta_R}} + \int_{\pi/2}^{\theta'} \frac{2a^2\omega_R\lambda(\beta,a)(\langle\cos^2\theta\rangle - \cos^2\theta)}{\sqrt{\Theta_R}}$$

$$\bar{\alpha}_1(r) \equiv \frac{1}{L}\int_{r_{*p}}^{r_*} (\sqrt{Q(\omega_R,r)} - \omega_R)dr_* . \tag{11.57}$$

After dealing with the summation over overtone n, we compute the summation over m next. Now the relevant terms are

$$\sum_m e^{-i\omega_R T + im(\phi-\phi')} e^{\pm i\int_{\theta'}^{\theta}\sqrt{\Theta_R}d\tilde{\theta}} e^{iL(\bar{\alpha}_1(r)+\bar{\alpha}_1(r')-\kappa\gamma_1\rho(r)\rho(r')e^{-\lambda(\beta,a)T\pm\Upsilon(\theta,\theta')})}$$

$$\times \frac{B}{\sqrt{L}} e^{\lambda/2T} U(r)U(r') e^{\pm\Upsilon(\theta,\theta')/2} \frac{C^2}{(\Theta_R(\theta)\sin^2\theta)^{1/4}(\Theta_R(\theta')\sin^2\theta')^{1/4}} . \tag{11.58}$$

All the terms in the first line are rapidly changing in phase, because the exponential indices are all $\propto O(L)$. The functions in the second line also depend on m but they are slowly changing in amplitude. In addition, we recall that $\beta = m/L$ and we will apply the approximation that $\sum_m \to L\int d\beta$, as $L \gg 1$. As a result, we can apply the method of steepest descent to evaluate the summation, which basically says in the eikonal limit

$$\int d\beta e^{iLg(\beta)} \approx \sqrt{\frac{2\pi}{iLg''(\beta_0)}} e^{iLg(\beta_0)} , \tag{11.59}$$

with β_0 being the extrema point of $g(\beta)$: $g'(\beta)|_{\beta_0} = 0$. In fact, one can view the above integral as a simplified version of path integral, and in the classical limit $L \gg 1$, we only pick the paths near the classical trajectory $g'(\beta) = 0$, where $g(\beta)$ here is explicitly given by

$$Lg_\pm(\beta) = -\omega_R T + m(\phi-\phi') \pm \int_{\theta'}^{\theta}\sqrt{\Theta_R}d\theta + L[\bar{\alpha}_1(r) + \bar{\alpha}_1(r') - \kappa\gamma_1\rho(r)\rho(r')e^{-\lambda(\beta,a)T\pm\Upsilon(\theta,\theta')}] . \tag{11.60}$$

As argued in [5], the Schwarzschild Green function becomes singular when all terms in the summation over l are resonant in phase. This can be translated into $g(\beta_0) = 2\pi j$ where j is an integer. On the other hand, the Green function should be singular along the null geodesic [6]. This observation gives a consistent check of our method, by examining whether $g(\beta_0) = 2\pi j$ gives a null geodesic connecting points (r,θ,ϕ) and (r',θ',ϕ'). It may be helpful to first look at some special cases:

1. Suppose $r = r' = r_p(\beta_0)$, and we have $\bar{\alpha}_1(r) = \bar{\alpha}_1(r') = \rho(r) = \rho(r') = 0$. Consequently $Lg(\beta) = -\omega_R T + S_\phi \pm S_\theta$, and the requirement that $g'(\beta)|_{\beta_0} = 0$ basically means that the stationary-

phase trajectory is the Kerr spherical photon geodesic.

2. For $a = 0$, i.e., Schwarzschild spacetime, Eq. (11.60) agrees with the one derived by Dolan et al. [5]. It is actually easy to see this point: when $a = 0$, only $m(\phi - \phi') \pm \int_{\theta'}^{\theta} \sqrt{\Theta_R} d\theta = S_\phi \pm S_\theta$ in Eq. (11.60) depends on m and its extrema are just $\pm L\gamma$, where γ is the angle between (θ, ϕ) and (θ', ϕ') on the photon sphere and it satisfies $\cos\gamma = \cos\theta \cos\theta' + \sin\theta \sin\theta' \cos(\phi - \phi')$. So $g(\beta_0) = 2\pi j$ (j is an integer) reduces to Eq. (41) in [5], hence the results are consistent with each other.

3. For arbitrary r, r', we believe the optimal trajectory is a null geodesic connecting points (r, θ, ϕ) and (r', θ', ϕ'). But since we made an approximation when computing the black hole excitation number $\mathcal{B}_{lmn}$, Eq. (11.60) is only an approximate formula for the total phase factor and the best way to demonstrate this point maybe through numerical investigation. Dolan *et al.* [5] encountered the same problem for Schwarzschild Green's function. They found that $g(\beta_0) = 2\pi j$ in Schwarzschild gives a slightly different prediction to the geodesic requirement but nevertheless the error is very small. In principle we can do the same thing here and demonstrate $g(\beta_0) = 2\pi j$ is also a good approximation for a geodesic in Kerr. This part of the numerical verification will be left to future work.

11.5.2   The Green function

In order to compute the Green function (not only its singular structure), we still need to evaluate the summation in L. We will apply the trick in [5, 7] by converting the summation over L to an integral. The QNM Green's function under eikonal approximation is just

$$
\begin{aligned}
G_{\text{eik}} &= \text{Re} \sum_l i^{1/2} (\chi_+(l, x, x') e^{i\pi/4} e^{iLg_+(\beta_0)} + \chi_-(l, x, x') e^{-i\pi/4} e^{iLg_-(\beta_0)}) \\
&= \sum_{k=-\infty}^{k=+\infty} (-1)^s \text{Re} \int_0^\infty d\nu e^{2\pi i k \nu} (\chi_+ i e^{i\nu g_+(\beta_0)} + \chi_- e^{i\nu g_-(\beta_0)})
\end{aligned}
\tag{11.61}
$$

with $\chi_\pm(l, x, x')$ given by

$$
\begin{aligned}
\chi_\pm(l, x, x') = &\frac{L}{2\pi\sqrt{r^2 + a^2}\sqrt{r'^2 + a^2}} \sqrt{\frac{2\pi}{Lg''(\beta_0)}} \\
&\times \left\{ \frac{|B|}{\sqrt{L}} e^{\lambda/2T} U(r) U(r') e^{\pm \Upsilon(\theta, \theta')/2} \frac{C^2}{(\Theta_R(\theta) \sin^2\theta \Theta_R(\theta') \sin^2\theta')^{1/4}} \right\}_{\beta = \beta_0(x, x')}.
\end{aligned}
\tag{11.62}
$$

Since $C \propto L^{1/2}$ and $\Theta_R \propto L^2$, $\chi(l, x, x')$ is independent of l and we can move it out of the

integral in Eq. (11.61)

$$G_{\text{eik}} = \text{Re} \sum_{k=0}^{s=\infty} I_k \tag{11.63}$$

where

$$I_{s'} = \begin{cases} \int_0^\infty d\nu (-1)^{k/2} \left(\chi_- e^{ik\pi\nu} e^{i\nu g_-(\beta_0)} + i\chi_+ e^{-ik\pi\nu} e^{i\nu g_+(\beta_0)} \right), & k \quad \text{even}, \\[3mm] \int_0^\infty d\nu (-1)^{(k+1)/2} \left(\chi_+ i e^{i(k+1)\pi\nu} e^{i\nu g_+(\beta_0)} + \chi_- e^{-i(k+1)\pi\nu} e^{i\nu g_-(\beta_0)} \right), & k \quad \text{odd}. \end{cases} \tag{11.64}$$

The integral can be evaluated using the identity

$$\int_0^\infty d\nu e^{i\nu(q+i\epsilon^+)} = \frac{i}{q} + \pi\delta(q), \tag{11.65}$$

where ϵ^+ is a positive infinitesimal running constant and the Green function is singular when the phase factor q becomes zero. Here we are only interested in the case that $T > 0$ (required for the QNM sum to converge) and the singular time T increases with increasing m. Therefore we drop the latter terms in Eq. (11.64) and it becomes

$$\text{Re} \, I_k = \begin{cases} (-1)^{k/2} \chi_- \pi\delta[\pi k + g_-(\beta_0)], & k \quad \text{even}, \\[3mm] \frac{-i\chi_+ (-1)^{(k+1)/2}}{\pi(k+1) + g_+(\beta_0)}, & k \quad \text{odd}, \end{cases} \tag{11.66}$$

which recovers the four-fold singular structure similar to the Schwarzschild background case [5] and other spacetimes [6]. In addition, it confirms our earlier argument that the Green function becomes singular when $g(\beta_0) = 2\pi j$, where j is an integer.

11.6   Conclusion and future work

In this chapter, we applied a WKB method and obtained an approximate expression for the QNM part of Kerr spacetime's scalar Green function, which arises due waves scattering off the strong-field-region of the Kerr black hole. An immediate next step of this work would be to compare our analytical formula with numerical Green functions [14]. Besides the application in EMRI modeling, we also think this Green function could be useful for electromagnetic (EM) observation from stars near SMBHs. More specifically, if the star moves in the strong-gravity regime of the SMBH, it is natural to expect a series of pulses to arrive at the earth at different times, as the EM signal can orbit around the black hole a few times before propagating towards the earth. The time interval

between these pulses can be obtained by examining the singular structure of the Green function, or equivalently by solving the geodesics in Kerr spacetime. More importantly, the shapes of these sequential pulses depend strongly on the non-singular part of the Green function. As a result, given the signal from a series of pulses, one can try to decode the information about the orbit of the star as well as the spin of the central SMBH. In the future, we plan to explore the application of the Kerr Green function in this direction.

Acknowledgments

Bibliography

[1] D. C. Backer and R. A. Sramek, Astrophys. J. **524** 805, (1999).

[2] P. B. Polnarev, A. G. Polnarev and P. Saha, Mon. Not. R. Astron. Soc., **358**, 1361, (2005).

[3] X. Chen, P. Madau, A. Sesana and F. K. Liu, Astrophys. J. **697** L149, (2009).

[4] Y. Mino, M. Sasaki and T. Tanaka, Phys. Rev. D. **56** 3457, (1997).

[5] S. Dolan, A. Ottewill, Phys. Rev. D. **84**, 104002, 2011.

[6] M. Casals, B. C. Nolan, arXiv:1204.0407.

[7] M. Casals, S. R. Dolan, A. C. Ottewill and B. Wardell, Phys. Rev. D. **79**, 124043, (2009).

[8] M. Casals, S. R. Dolan, A. C. Ottewill and B. Wardell, Phys. Rev. D. **79**, 124044, (2009).

[9] S. A. Teukolsky, Phys. Rev. Lett. **29**, 1114, (1972); Astrophys. J. **185**, 635, (1973).

[10] A. Zenginoglu, C. R. Galley, Phys. Rev. D. **86** 064030, (2012).

[11] E. W. Leaver, Proc. R. Soc. A **402**, 285, (1985).

[12] H. Yang, D. Nichols, F. Zhang, A. Zimmerman, Y. Chen, Phys. Rev. D. **86**, 104006, (2012).

[13] E. Berti and V. Cardoso, Phys. Rev. D. **74**, 104020, (2006).

[14] A. Zenginouglu, private communication.